International Journal of Photoenergy

Solar Energy and PV Systems

Guest Editors: Ismail H. Altas and Adel M. Sharaf

Solar Energy and PV Systems

International Journal of Photoenergy

Solar Energy and PV Systems

Guest Editors: Ismail H. Altas and Adel M. Sharaf

Editorial Board

M. S. A. Abdel-Mottaleb, Egypt
Xavier Allonas, France
Nicolas Alonso-Vante, France
Wayne A. Anderson, USA
Yanhui Ao, China
Raja S. Ashraf, UK
V. Augugliaro, Italy
Detlef W. Bahnemann, Germany
I. R. Bellobono, Italy
Raghu N. Bhattacharya, USA
Pramod H. Borse, India
Alessio Bosio, Italy
Stephan Buecheler, Switzerland
Gion Calzaferri, Switzerland
C. Chen, China
Sung Oh Cho, Republic of Korea
V. Cimrová, Czech Republic
Juan M. Coronado, Spain
Ying Dai, China
D. D. Dionysiou, USA
Pingwu Du, China
M. M. El-Nahass, Egypt
Polycarpos Falaras, Greece
Chris Ferekides, USA
Paolo Fornasiero, Italy
Hermenegildo García, Spain
Germà Garcia-Belmonte, Spain
E. I. Garcia-Lopez, Italy
Beverley Glass, Australia
M. A. Gondal, Saudi Arabia
Jr-Hau He, Taiwan
Shinya Higashimoto, Japan
Cheuk-Lam Ho, Hong Kong
Wing-Kei Ho, Hong Kong
Fuqiang Huang, China
Adel A. Ismail, Egypt
Chun-Sheng Jiang, USA
Misook Kang, Republic of Korea
Shahed Khan, USA
Sun-Jae Kim, Republic of Korea
Jong Hak Kim, Republic of Korea
Sungjee Kim, Republic of Korea
Cooper H. Langford, Canada
Tae-Woo Lee, Republic of Korea
Lecheng Lei, China
Xinjun Li, China
Zhaosheng Li, China
Yuexiang Li, China
Stefan Lis, Poland
Vittorio Loddo, Italy
Gongxuan Lu, China
Dongge Ma, China
N. M. Mahmoodi, Iran
Nai Ki Mak, Hong Kong
Rajaram S. Mane, India
D. Mantzavinos, Greece
Ugo Mazzucato, Italy
Sheng Meng, China
Jacek Miller, Poland
Claudio Minero, Italy
Antoni Morawski, Poland
Franca Morazzoni, Italy
F. Morlet-Savary, France
M. Muneer, India
Kun Na, Republic of Korea
Ebinazar B. Namdas, Australia
Maria Neves, Portugal
Tebello Nyokong, South Africa
Kei Ohkubo, Japan
Haridas Pal, India
Leonidas Palilis, Greece
Leonardo Palmisano, Italy
Ravindra K. Pandey, USA
H. Park, Republic of Korea
Pierre Pichat, France
Gianluca Li Puma, UK
Tijana Rajh, USA
Peter Robertson, UK
Avigdor Scherz, Israel
Elena Selli, Italy
Ganesh D. Sharma, India
Jinn Kong Sheu, Taiwan
Panagiotis Smirniotis, USA
Zofia Stasicka, Poland
Elias Stathatos, Greece
J. Subbiah, Australia
M. Swaminathan, India
Kazuhiro Takanabe, Saudi Arabia
Mohamad-Ali Tehfe, Canada
K. R. Justin Thomas, India
Yang Tian, China
Nikolai V. Tkachenko, Finland
Ahmad Umar, Saudi Arabia
Thomas Unold, Germany
Veronica Vaida, USA
Roel van De Krol, Germany
Mark van Der Auweraer, Belgium
Rienk Van Grondelle, The Netherlands
Wilfried Van Sark, The Netherlands
Sheng Wang, China
Xuxu Wang, China
Mingkui Wang, China
Ezequiel Wolcan, Argentina
Man Shing Wong, Hong Kong
David Worrall, UK
Jeffrey C. S. Wu, Taiwan
Yanfa Yan, USA
Jiannian Yao, China
Minjoong Yoon, Republic of Korea
Jiangbo Yu, USA
Hongtao Yu, USA
Ying Yu, China
Klaas Zachariasse, Germany
Juan Antonio Zapien, Hong Kong
Tianyou Zhai, China
Lizhi Zhang, China
Guijiang Zhou, China
Yong Zhou, China
Rui Zhu, China

Contents

Hindawi Publishing Corporation
International Journal of Photoenergy
Volume 2014, Article ID 408285, 2 pages
http://dx.doi.org/10.1155/2014/408285

Editorial

Solar Energy and PV Systems

Ismail H. Altas[1] and Adel M. Sharaf[2]

[1] *Karadeniz Technical University, 61080 Trabzon, Turkey*
[2] *Sharaf Energy Systems Inc., Fredericton, NB, Canada E3C 2P2*

Correspondence should be addressed to Ismail H. Altas; ihaltas@altas.org

Received 20 November 2014; Accepted 20 November 2014; Published 22 December 2014

The utilization of solar photovoltaic (PV) systems has gained a tremendous momentum due to decreasing costs of PV arrays and interface systems by as much as 50% during the last five years. The advancements on electric utility grid interface systems and utilization of PV arrays in standalone local power generation and smart buildings with storage battery and back-up hybrid systems are increasing the PV system utilization as the emerging form of renewable/alternative energy source. In many countries, the government has instituted special incentives and tax credits as well as feed-in tariff and energy purchase back legislation programs in order to promote and encourage manufacturers and consumers and boost new investments in solar PV energy use in different sectors.

As the solar PV systems emerge as viable and economic source of green energy with increasing installation sites every year, attempts are made to find economic and technological solutions to the problems arising from various aspects of the PV utilization schemes. The state of the art research is continuing in all areas from material sciences to manufacturing and interfacing in order to ensure efficient utilization and commercial viability in terms of cost, security, and durability of PV and hybrid PV-wind-storage systems. Specific areas focus on PV array topologies, dynamic sun tracking, maximum power point control, storage devices, and efficient decoupled interface with smart grid and smart building to ensure dynamic matching of energy to load requirements with minimal impact on the host utility grid. Besides, energy management studies in smart grids and distributed generation have become other additional areas of demand side management and energy efficient hybrid utility-renewable energy.

We invited investigators to contribute original research articles as well as review articles that will stimulate the continuing efforts and promote new research directions to address the undergoing challenges and technological requirements in PV systems utilization in order to ensure commercial viability and improve usability, security, reliability, and integration of sustainability of converting sun power to electricity.

Hybrid PV-wind-fuel cell-microgas turbines with storage Li-ion batteries and super capacitors are promising to modify the way smart grid manages efficient electrical energy and ensure demand-side management and peak shifting as well as shaving of peak demand during summer months due to massive air-conditioning loads.

The inherent problems of PV interfacing include the effects of solar insulation and temperature changes affecting the PV array power/energy as well as interface power quality and required dc-ac isolation and grid supply security and reliability.

The effects of mismatching conditions and partial shading/clouding problems require novel control and power tracking algorithms, new architecture using multi converters, and sitting/location dynamic exchanges of PV arrays using series-parallel (SP) topologies.

The special edition is a collection of accepted papers focused on photovoltaic systems emerging technology and current applications including interfacing, energy efficient utilization, emerging technologies, fabrication, and new control strategies for maximum power point tracking under contingencies, mismatching, and cloudy/partial shading conditions with PV farm/park utilization and field studies. Technologies using solar energy in heating and cooling systems, advancements in manufacturing processes, developments in power electronic devices for utility interfacing issues, shading effects, maximum power point tracking algorithms, and efficient energy management for higher efficiency in PV systems are some other topics presented in this special issue.

Ismail H. Altas
Adel M. Sharaf

Hindawi Publishing Corporation
International Journal of Photoenergy
Volume 2014, Article ID 626251, 10 pages
http://dx.doi.org/10.1155/2014/626251

Research Article

Performance Analysis of Hybrid PV/Diesel Energy System in Western Region of Saudi Arabia

Makbul A. M. Ramli,[1] Ayong Hiendro,[2] and H. R. E. H. Bouchekara[3]

[1] Department of Electrical and Computer Engineering, King Abdulaziz University, Jeddah 21589, Saudi Arabia
[2] Department of Electrical Engineering, Universitas Tanjungpura, Pontianak 78124, Indonesia
[3] Constantine Electrical Engineering Laboratory (LEC), Department of Electrical Engineering, University of Constantine 1, 25000 Constantine, Algeria

Correspondence should be addressed to Makbul A. M. Ramli; makbul.anwari@gmail.com

Received 29 October 2013; Accepted 24 March 2014; Published 13 May 2014

Academic Editor: Adel M. Sharaf

The potential implementation of hybrid photovoltaic (PV)/diesel energy system in western region of Saudi Arabia is analyzed in this paper. The solar radiation intensity considered in this study is in the range of 4.15–7.17 kWh/m^2/day. The HOMER software is used to perform the technical and economical analysis of the system. Three different system configurations, namely, stand-alone diesel system, and hybrid PV/diesel system with and without battery storage element, will be evaluated and discussed. The analysis will be addressed to the impact of PV penetration and battery storage on energy production, cost of energy, number of operational hours of diesel generators, fuel savings, and reduction of carbon emission for the given configurations. The simulation results indicate that the energy cost of the hybrid PV/diesel/battery system with 15% PV penetration, battery storage of 186.96 MWh, and energy demand of 32,962 MWh/day is $0.117/kWh.

1. Introduction

The Kingdom of Saudi Arabia is blessed with abundant energy resources. It has the world's largest oil reserves and the world's fourth largest proven gas reserves. In addition, the Kingdom also has abundant wind and solar renewable energy resources. However, in this country, the use of its renewable energy resources to generate electricity is negligibly small and almost all its electricity is produced from the combustion of fossil fuels [1]. During the last two decades, electrical energy consumption in Saudi Arabia increased significantly due to rapid economic development and the absence of energy conservation measures. It is expected that peak loads will reach 60 GW in 2023 which causes total investment may exceed $90 billion. Therefore, there is an urgent need to develop energy conservation policies for sustainable development [2].

Remarkable efforts to diversify energy sources and to intensify the deployment of renewable energy options have been increasing around the world. In recent years, a set of renewable energy scenarios for Saudi Arabia has been proposed to examine the prospects of renewable sources from the perspective of major oil producers. The drive towards renewable energy in Saudi Arabia should not be regarded as being a luxury but rather a must, as a sign of good governance, concern for the environment, and prudence in oil-production policy [3, 4].

The first priority in intensifying renewable energy deployment in the 21st century is the combined effects of the depletion of fossil fuels and the awareness of environmental degradation [5]. Therefore, policy makers and researchers are paying more attention to research in this field. For instance, Alnatheer has conducted researches on environmental impacts of electric energy system expansion in Saudi Arabia. It has been concluded that the use of renewable energy and energy efficiency resources gives significant environmental benefits [6, 7]. Apart from local conservation efforts, the country has an option to reduce domestic diesel consumption and increase its oil exports. By reducing domestic diesel consumption, subsidies can be used to promote the use of renewable energy. This, in turn, contributes to reducing air pollution and greenhouse gas emissions [3, 8].

As one of renewable energy sources, solar energy is a site-dependent, inexhaustible, benign (does not produce emissions that contribute to the greenhouse effect), and potential source of renewable energy that is being developed by a number of countries with high solar radiation as an effort to reduce their dependence on fossil-based nonrenewable fuels [9]. Saudi Arabia, located in the heart of one of the world's most productive solar regions, receives the most potent kind of sunlight [10]. With the average annual solar radiation of 2200 kWh/m^2 in the Arabian Peninsula, applications of solar energy have been growing since 1960 [9, 10]. Now and in the future, exploitation of this important energy resource becomes more imperative for Saudi Arabia [11].

Makkah is the most populous province of Saudi Arabia. It is located in western region of Saudi Arabia and has annual solar radiation of 247.5 W/m^2. There are many factors affecting the electricity demand in this area, such as weather changes, social life activities (work, school, and prayer times), and special events (Ramadan and Hajj) [12]. With the high electricity demand during both day- and nighttime, replacing diesel generators with PV/battery system is not a wise solution. Therefore, very large sizes of PV and battery are needed to meet the electricity demand; otherwise, electricity shortages will occur.

Many researchers have reported that hybrid PV/diesel/battery system is more economically viable than stand-alone diesel system [13–16]. It is not happening in Makkah at the present time. Operation cost for the stand-alone diesel generators is relatively cheap in Makkah because of the low diesel fuel price. However, diesel generators are not environmentally friendly. Although hybrid PV/diesel/battery system is more expensive than the stand-alone diesel, the hybrid system gives other various advantages, such as improved reliability and reduced pollution and emission.

In this paper, a hybrid PV/diesel system is designed to reach its optimum performance to meet load demand in Makkah. Diesel generators are used as a backup for the hybrid system. Minimum sizes of the hybrid system components required to achieve zero unmet electric loads are determined using hybrid optimization model for electric renewable (HOMER) software [17].

2. Solar Irradiance Data

Saudi Arabia is one of the driest and hottest countries in the world. The global solar irradiation in Saudi Arabia is shown in Figure 1. Either the clearness index or the solar irradiation data can be used to represent the solar resource. Based on data from NASA surface meteorology and solar energy (http://eosweb.larc.nasa.gov), the solar irradiation in Makkah (21°26′ North, 39°49′ East) is between 4.15 kWh/m^2/day and 7.17 kWh/m^2/day. The scaled annual average of the solar radiation is estimated to be 5.94 kWh/m^2/day. Figure 2 shows the solar irradiation data; on the right axis is the clearness index of the solar irradiation. It is clearly shown that solar irradiance is high (above the average) in March–September with a peak in June, while solar irradiance is low in January, February, October, November, and December as shown in Figure 3.

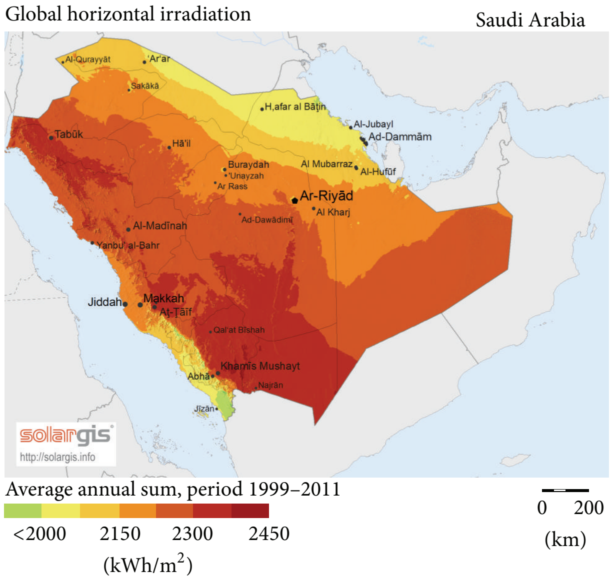

Figure 1: Solar irradiation map in Saudi Arabia.

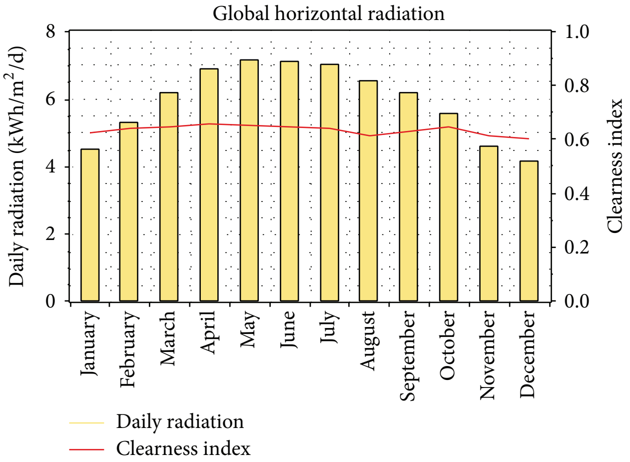

Figure 2: Solar irradiation data.

3. Design and System Specifications

3.1. Primary Load. The load demand in Makkah varies monthly. Three different reasons for increases in the load demand in Makkah are due to (1) special occasions (Eid al-Fitr, National Day), (2) religious occasions (Hajj, Ramadan, and Umra), and (3) climate conditions. The maximum peak load occurs in the summer season. Sometimes there is an overlapping between the summer season and the Hajj or Ramadan month resulting in a much higher load demand for that period.

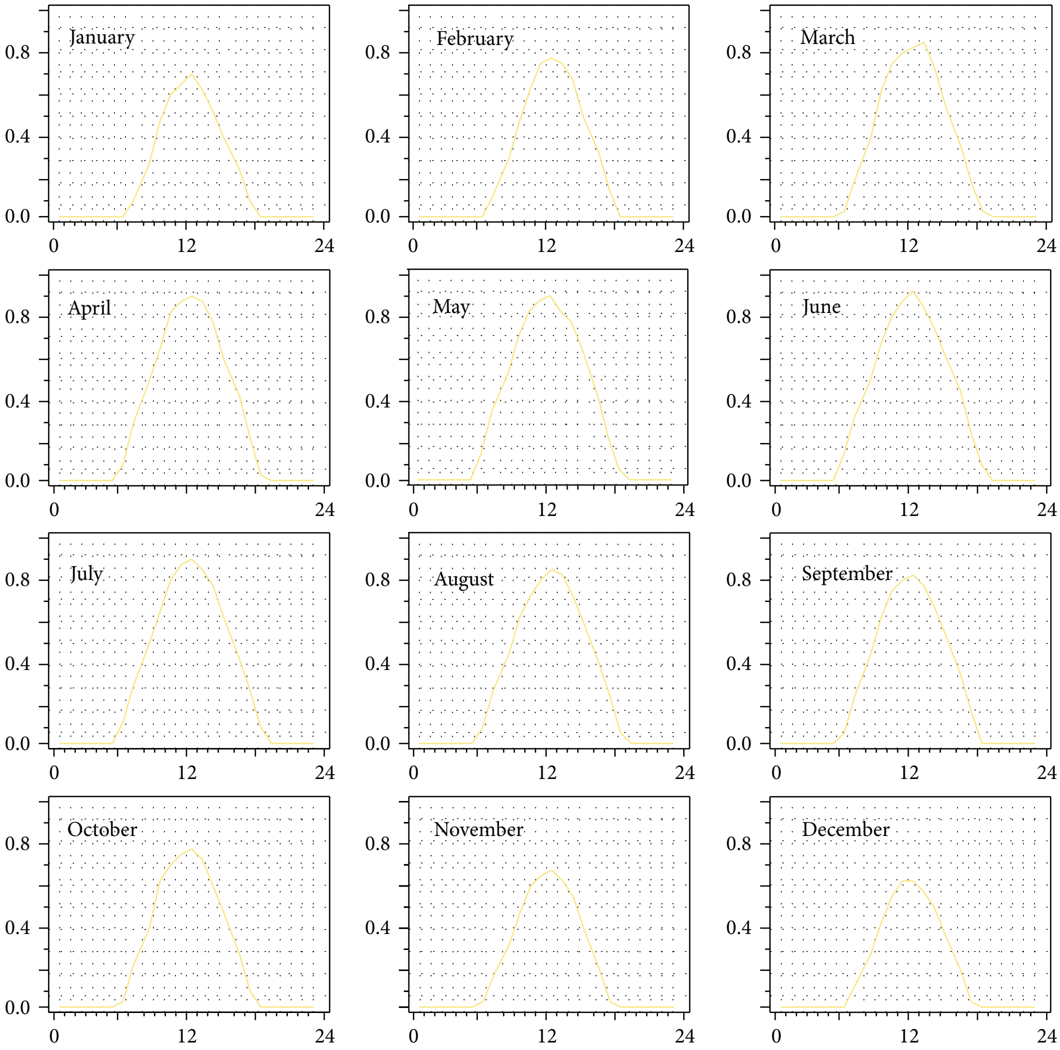

Figure 3: Monthly solar irradiation data.

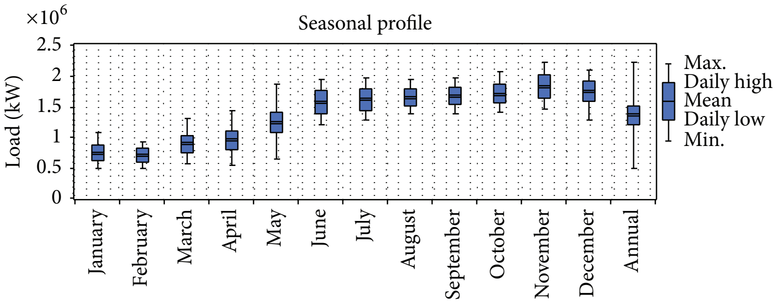

Figure 4: Monthly load profile of Makkah.

Load profile of Makkah is presented in Figure 4. From the load profile, it is shown that peak load in Makkah is 2,213 MW with energy consumption of 32,962 MWh/day. The peak load is about 0.023% or 2 hours during the year.

3.2. Design Specification. In this design, the hybrid PV/diesel/battery system consists of four main system components: (1) PV modules, (2) storage batteries, (3) diesel generators, and (4) inverters. The configuration of the hybrid PV/diesel/battery system is shown in Figure 5.

3.2.1. Diesel Generator (DG). A diesel generator (DG) is characterized by its fuel consumption and efficiency. The fuel characteristic describes the amount of fuel the generator

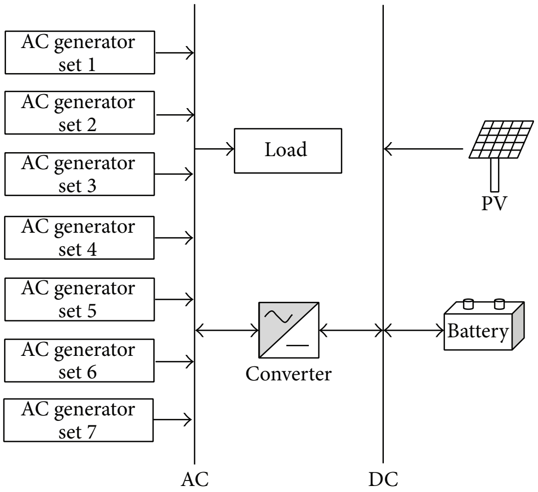

Figure 5: Configuration of hybrid PV/diesel/battery system.

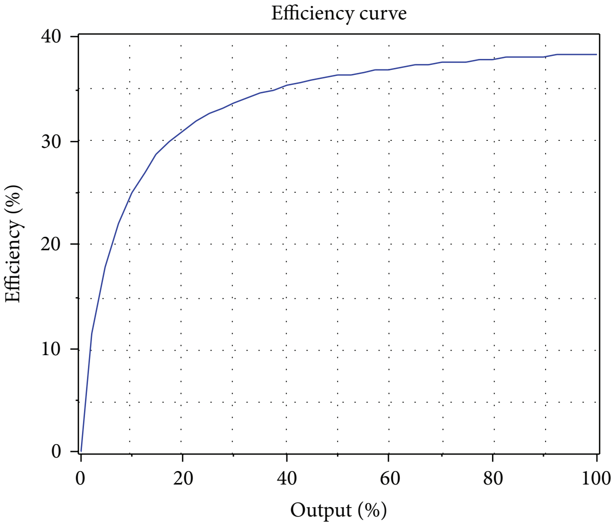

Figure 6: Efficiency curve.

Table 1: Generator groups.

Group	Number of units	Total capacity (MW)
Generator 1	4	320
Generator 2	4	320
Generator 3	4	320
Generator 4	4	320
Generator 5	4	320
Generator 6	4	320
Generator 7	2	160

consumes to produce electricity. The efficiency curve defines electrical energy coming out divided by the chemical energy of fuel going in.

In this design, the DGs have the fuel intercept coefficient of 0.01609 L/kWh and the fuel slope of 0.2486 L/kWh. The efficiency curve of the DGs is shown in Figure 6. The DGs are used as a backup during peak demand periods which cannot be fulfilled by PV and battery. The DGs also support the battery at nighttime when the PV has stopped producing electricity. In order to cover the peak load of 2,213 MW, 80 MW/unit DG is used in the simulation. There are 26 DGs employed in this design to meet the load demand. They are distributed into 7 groups of generators as illustrated in Figure 5. Table 1 presents amount of DGs in each group. The DG cost and technical data are provided in Table 2.

Table 2: DG data.

DG	
Size	80 MW
Lifetime	15000 hr
Min. load ratio	40%
Capital cost	$400/kW
Replacement cost	$350/kW
Operating and maintenance cost	$0.05/hr

Table 3: PV data.

PV system	
Size	1.1–2.2 GW
Lifetime	20 yr
Derating factor	90%
Capital cost	$2500/kW
Replacement cost	$2000/kW
Operating and maintenance cost	$3/yr

3.2.2. Photovoltaic (PV). Solar energy is used as the base-load power source. PV array size is dependent on the load profile, solar radiation, and renewable fraction. The renewable fraction is the fraction of the energy delivered to the load that originated from renewable power sources, and in this case the renewable fraction is related to the PV production.

With the peak load of 2.2 GW, the initial PV size of 2.2 GW is fair enough for the PV/diesel/battery hybrid system. The PV size can be either increased or decreased, according to the amounts of unmet electric load and renewable fraction set in the design. This PV size will be used to cater for the variety of load demand in a year. PV array will only generate electricity at daytime, from 6 a.m. to 6 p.m. The excess generated power will be used to charge the battery. The PV cost and technical data are provided in Table 3.

3.2.3. Inverter. The PV arrays produce direct current (DC) at a voltage that depends on the design and the solar radiation. The DC power then runs to an inverter, which converts it into standard AC voltage. The inverter size is rated based on the selected PV size, in order to maximize the quantity of energy which is harvested from the PV arrays. For 2.2 GW rated output PV, the inverter is rated at 2.2 GW to fully supply the power from the PV. However, it is frequently sized below the PV rated output because the PV does not always produce its full rated power. Smaller size inverter will minimize inverter

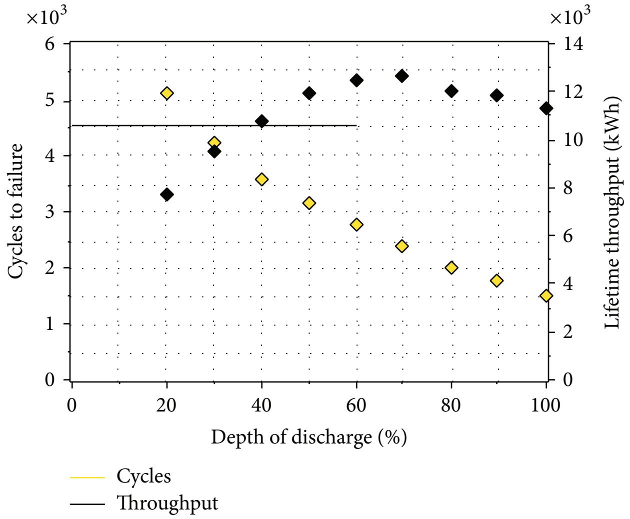

Figure 7: Lifetime curve.

Table 4: Inverter data.

Inverter	
Size	<2.2 GW
Lifetime	10 yr
Efficiency	90%
Capital cost	\$400/kW
Replacement cost	\$375/kW
Operating and maintenance cost	\$20/yr

Table 5: Battery data.

Battery	
Type	Surrette 4KS25P
Lifetime	12 yr
Batteries per string	12
Nominal voltage	4 V (48 V)
Nominal capacity	1900 Ah
Nominal energy capacity of each battery	7.60 kWh
Capital cost	\$1200/quantity
Replacement cost	\$1200/quantity
Operating and maintenance cost	\$60/yr

cost but does not reduce the system performance. A brief summary on the data for inverter is provided in Table 4.

3.2.4. Battery. Battery is used as a storage device which has two operation modes: charging and discharging. Excess electricity from PV or other sources can be stored in the battery. The purpose of the battery is to alleviate the mismatch between the load demand and electricity generation.

State of charge (SOC) indicates the level of battery charge. When the battery is fully charged, the SOC level is 100%. Battery has its specific minimum SOC allowed to operate, and it is usually recommended by the battery manufacturers.

The battery chosen is Surrette 4KS25P. It is a 4-volt deep cycle battery rated at 1,900 Ah at 100 hour rate. The battery's safe operating SOC is between 40% and 100%. Lifetime of the battery is 12 years for operating within the safe region. It will shorten the battery's lifetime if operated below the SOC of 40% or over DOD of 60% as shown in Figure 7. The battery lifetime throughput is 10,569 kWh when operated with minimum SOC of 40% or maximum DOD of 60%. The data for battery is provided in Table 5.

4. Cost of Carbon Emissions

Carbon emissions cause economic costs of damage and resulting climate change. The cost of carbon emissions is calculated by multiplying tons of CO_2 emitted for each type of plant system by an assumed cost per ton for carbon emission. The cost per ton for carbon emissions is not set in Saudi Arabia since there is currently no CO_2 market mechanism. However, emission penalties can be added to analyze the total annual cost of the power system on the assumption that the penalties are \$50/t for CO_2, \$900/t for SO_2, \$2600/t for NO_x, and \$2800/t for PM [18, 19].

5. Simulation Results and Discussions

Performance of the stand-alone diesel system, hybrid PV/diesel system without battery, and hybrid PV/diesel system with battery is discussed in this section. Simulations for various configurations are performed by considering the total battery storage sizes of 186.96 MWh for 5 min/autonomy (equivalent to 5 min of average load), while the hourly average load is 1,373.434 MWh/hr.

5.1. Stand-Alone Diesel System. From the simulation results, it can be found that stand-alone diesel system without renewable penetration gives total net present cost (NPC) of \$17,335,490,560 and CO_2 emission of 8,460,421,632 kg/yr. This system offers 0% for both the unmet load and excess electricity. This is according to the diesel price of \$0.067/L. The cost of energy (COE) for this stand-alone diesel system is \$0.102/kWh.

Monthly average electric production and cash flow summary are shown in Figures 8 and 9, respectively.

5.2. Hybrid PV/Diesel System without Battery. To determine the feasibility of hybrid PV/diesel installation, four configuration options will be analyzed:

(1) option 1: PV (1.1 GW) with DGs;
(2) option 2: PV (2.2 GW) with DGs;
(3) option 3: PV (3.3 GW) with DGs;
(4) option 4: PV (4.4 GW) with DGs.

5.2.1. Option 1: PV (1.1 GW) with DGs. From the simulation results, it can be noticed that this system gives total NPC of \$20,139,882,496 and CO_2 emission of 7,198,296,576 kg/yr. The COE for this system is \$0.119/kWh with PV penetration of 15%.

Monthly average electric production and cash flow summary are illustrated in Figures 10 and 11, respectively.

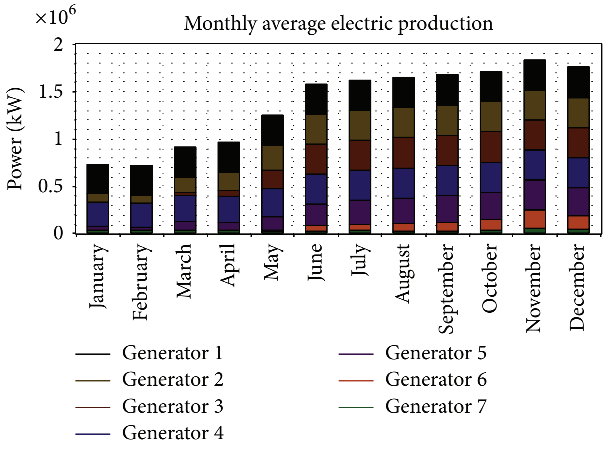

FIGURE 8: DGs monthly average electric production.

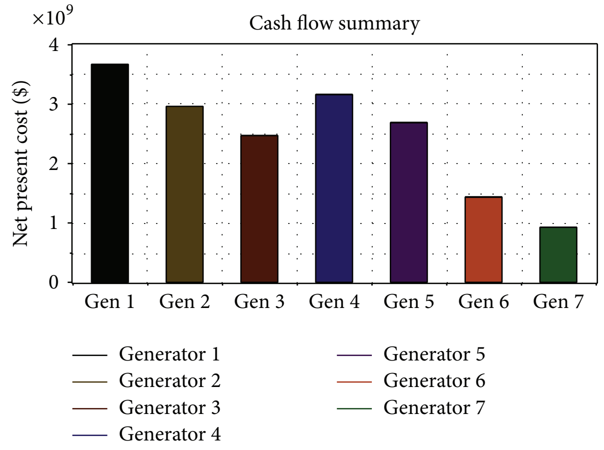

FIGURE 9: DGs cash flow summary.

5.2.2. Option 2: PV (2.2 GW) with DGs. From the simulation results, it can found that this system gives total NPC of \$20,995,399,680 and CO_2 emission of 6,276,211,200 kg/yr. The COE for this system is \$0.124/kWh with PV penetration of 26%.

Monthly average electric production and cash flow summary are shown in Figures 12 and 13, respectively.

5.2.3. Option 3: PV (3.3 GW) with DGs. From the simulation results, it can be seen that this system gives total NPC of \$22,260,590,592 and CO_2 emission of 5,742,476,288 kg/yr. The COE for this system is \$0.131/kWh with PV penetration of 32%.

Monthly average electric production and cash flow summary are illustrated in Figures 14 and 15, respectively.

5.2.4. Option 4: PV (4.4 GW) with DGs. From the simulation results, it can be noticed that this system gives total NPC of \$23,976,376,320 and CO_2 emission of 5,408,787,456 kg/yr. The COE for this system is \$0.141/kWh with PV penetration of 36%.

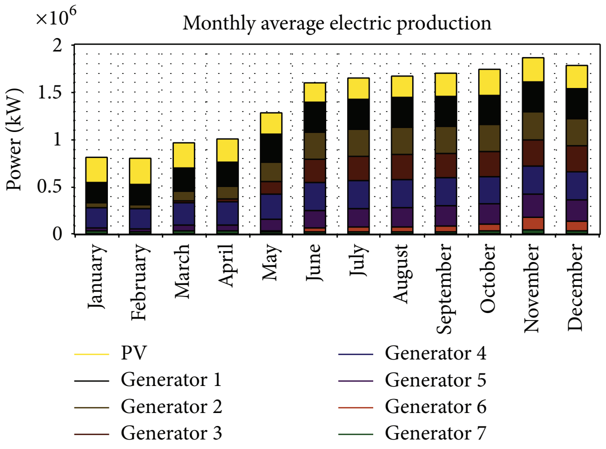

FIGURE 10: Monthly average electric production.

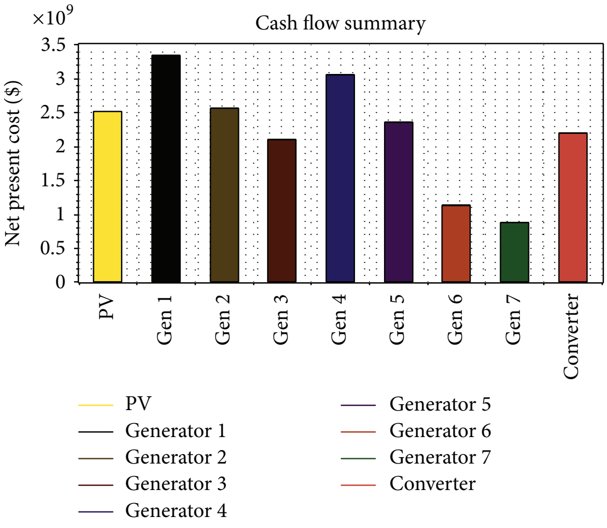

FIGURE 11: Cash flow summary.

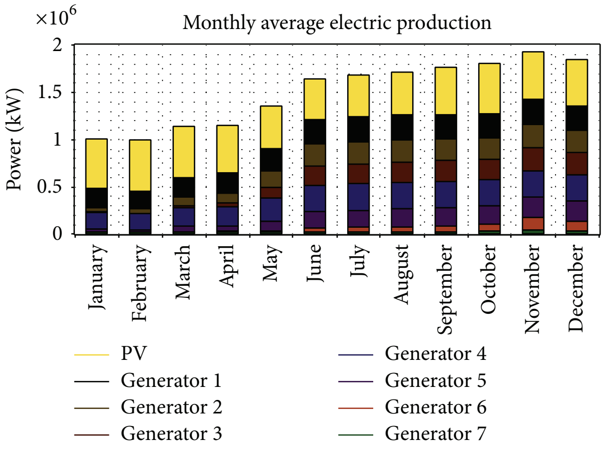

FIGURE 12: Monthly average electric production.

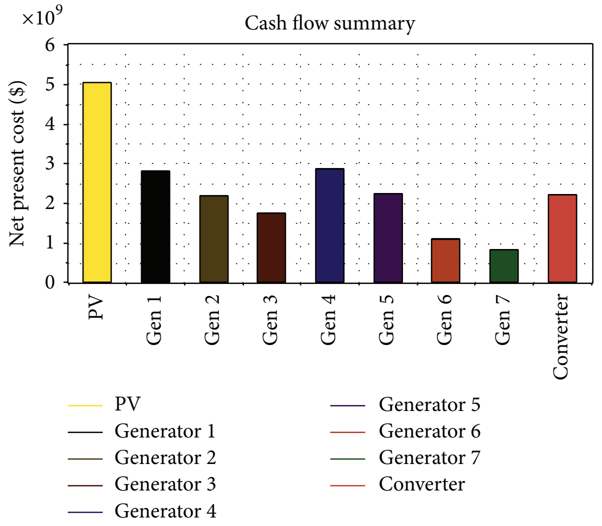

Figure 13: Cash flow summary.

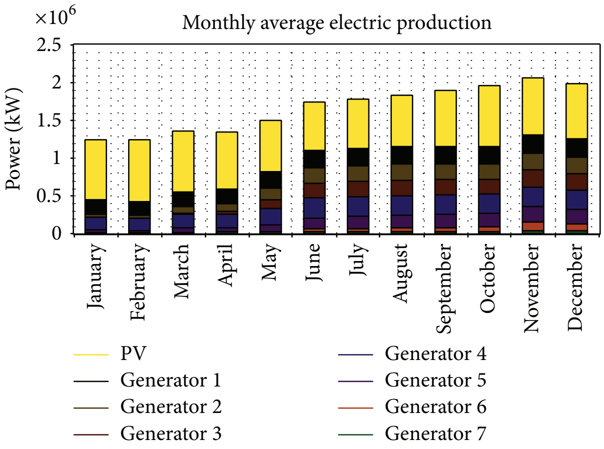

Figure 14: Monthly average electric production.

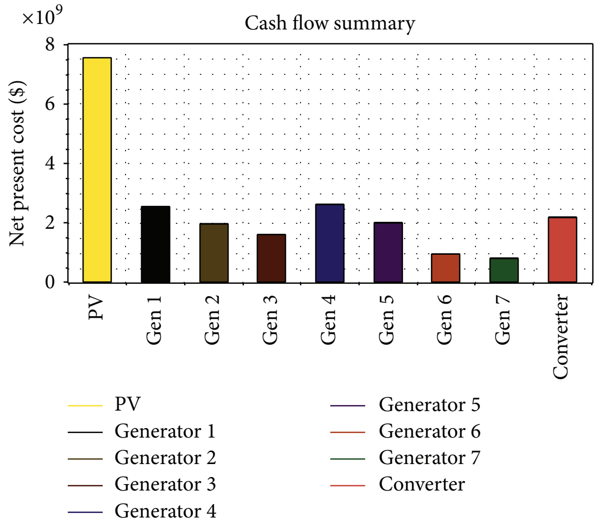

Figure 15: Cash flow summary.

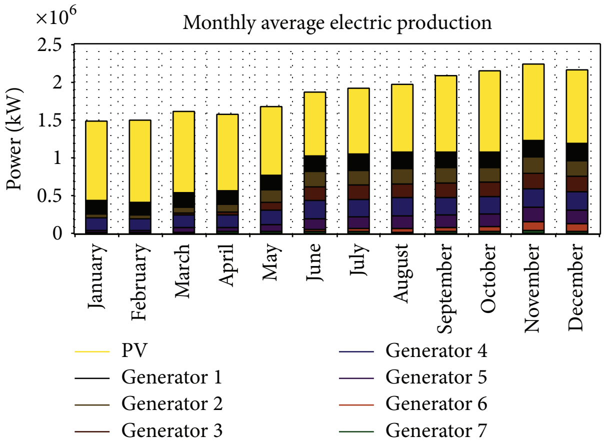

Figure 16: Monthly average electric production.

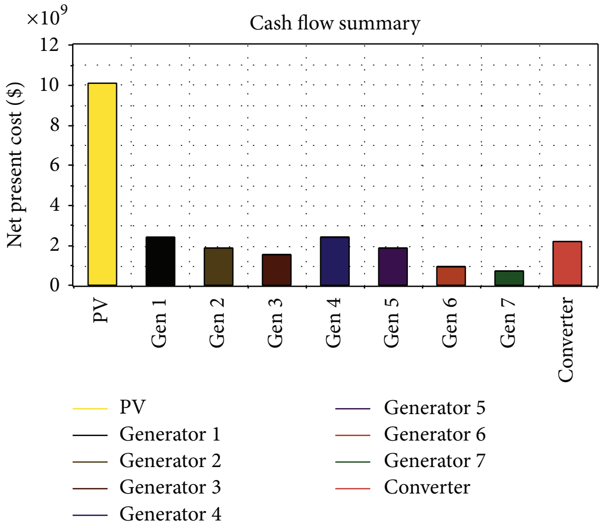

Figure 17: Cash flow summary.

Monthly average electric production and cash flow summary are shown in Figures 16 and 17, respectively.

From the simulation results, it can be found that option 1 is the cheapest and the minimum system requirement to meet all demands. All of them offer the unmet load of 0% as summarized in Table 6.

High PV penetration might result in difficulties in control while maintaining stable voltage and frequency. The level of renewable energy penetration in real application is generally in the range of 11–25%. The utilization of the bigger PV array size will result in a higher value of the total NPC as well as the COE. On the other hand, reducing the PV size will result in higher dependence of DGs and give more CO_2 emission. Therefore, the use of PV array size between 1.1 and 2.2 GW is justified.

5.3. Hybrid PV/Diesel System with Battery. From the simulation results, it can be seen that this system gives total NPC of $19,849,900,032 and CO_2 emission of 7,176,592,896 kg/yr.

Table 6: Hybrid PV/diesel system without battery performance.

Config.	Unmet load (%)	Excess elect. (%)	NPC ($)	COE ($/kWh)	PV penet.n (%)	CO_2 emissions (kg/yr)
Option 1	0%	0.94	20,139,882,496	0.119	15	7,198,296,576
Option 2	0%	6.09	20,995,399,680	0.124	26	6,276,211,200
Option 3	0%	14.60	22,260,590,592	0.131	32	5,742,476,288
Option 4	0%	23.20	23,976,376,320	0.141	36	5,408,787,456

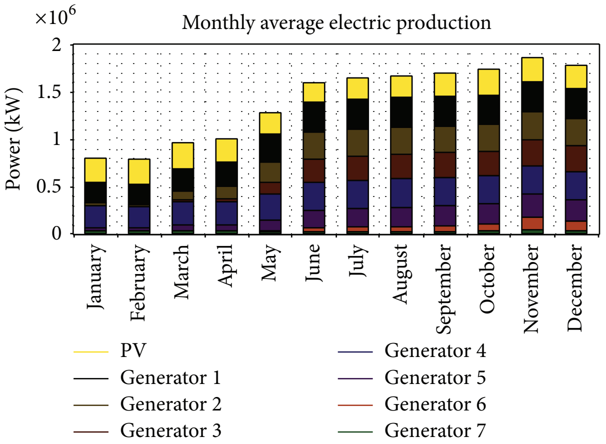

Figure 18: Monthly average electric production.

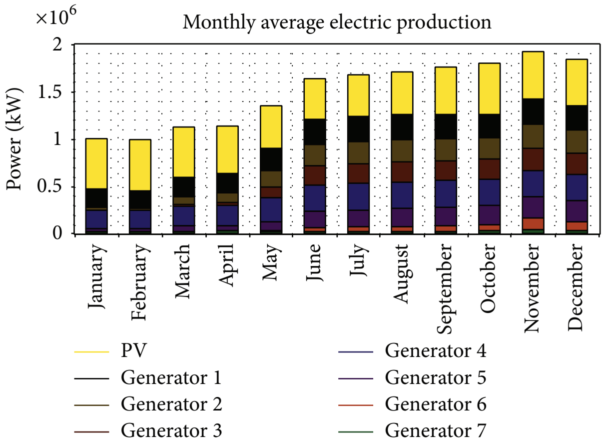

Figure 20: Monthly average electric production.

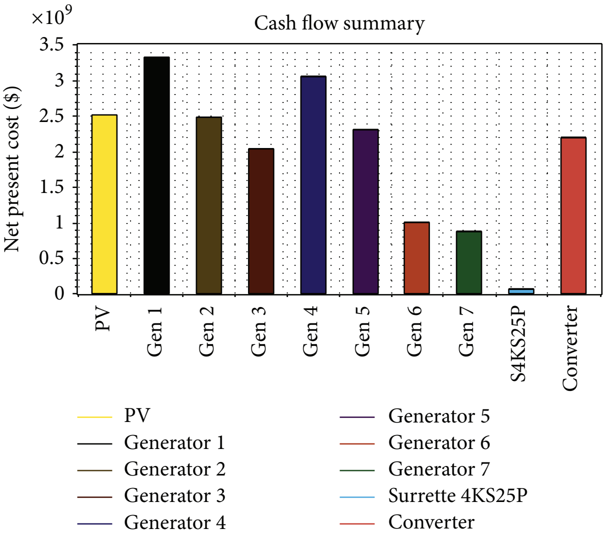

Figure 19: Cash flow summary.

The COE for this system is \$0.117/kWh with PV penetration of 15%.

From the previous results, it is shown that PV array size between 1.1 and 2.2 GW offers satisfying options. To determine the feasibility of hybrid PV/diesel with battery installation, two options of configurations are considered:

(1) option 1: PV (1.1 GW) with battery and DGs;

(2) option 2: PV (2.2 GW) with battery and DGs.

5.3.1. Option 1: PV (1.1 GW) with Battery and DGs. Monthly average electric production and cash flow summary are illustrated in Figures 18 and 19, respectively.

5.3.2. Option 2: PV (2.2 GW) with Battery and DGs. From the simulation results, it can be found that this system gives total NPC of \$20,690,055,168 and CO_2 emission of 6,247,786,496 kg/yr. The COE for this system is \$0.122/kWh with the PV penetration of 26%.

Monthly average electric production and cash flow summary are shown in Figures 20 and 21, respectively.

The summaries of hybrid PV/diesel system with battery are presented in Table 7.

5.4. Comparing Designs. The hybrid PV/diesel system using PV array size of 1.1 GW gives 15% renewable penetration. This penetration value makes sense for real-world application. Further, the utilization of PV array size more than 1.1 GW is out of consideration, since it would result in higher values of the total NPC as well as the COE. In addition, higher contribution of renewable energy penetration might give problems related to system instability.

The summaries of the stand-alone diesel system, hybrid PV/diesel system without battery, and hybrid PV/diesel system with battery are presented in Table 8. By using the proposed hybrid PV/diesel system without battery, the total NPC is \$20,139,882,496. This system is the most expensive system configuration as can be seen in Table 8. One of the main reasons is that the power generated by PV is not being fully utilized. If there are no storage devices, the excess solar electricity

Table 7: Performance of hybrid PV/diesel system with battery.

Config.	Unmet load (%)	Excess elect. (%)	NPC ($)	COE ($/kWh)	PV penet.n (%)	CO_2 emissions (kg/yr)
Option 1	0%	0.84	19,849,900,032	0.117	15	7,176,592,896
Option 2	0%	5.93	20,690,055,168	0.122	26	6,247,786,496

Table 8: Stand-alone diesel and hybrid PV/diesel with and without battery.

Config.	Unmet load (%)	Excess elect. (%)	NPC ($)	COE ($/kWh)	PV penet.n (%)	CO_2 emissions (kg/yr)
Diesel	0%	0.00	17,335,490,560	0.102	0	8,460,421,632
PV/diesel	0%	0.94	20,139,882,496	0.119	15	7,198,296,576
PV/diesel/battery	0%	0.84	19,849,900,032	0.117	15	7,176,592,896

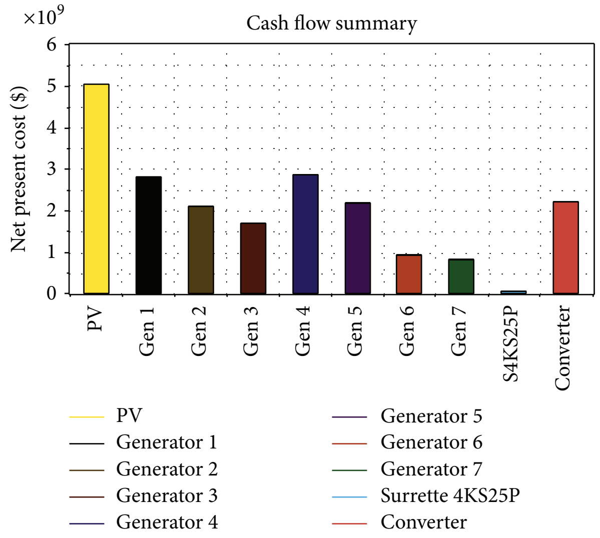

Figure 21: Cash flow summary.

cannot be stored and is considered as losses. When the PV cannot meet the load demand, the DGs will be then operated to cope for the demand. The yearly load has to be provided by DGs if the PV/diesel system does not use battery storages [20].

Although storage devices are typically very expensive, they are very important to ensure that the excess electricity produced from PV can be stored for later use. It would greatly optimize the system and, as a result, the PV/diesel system with battery is less expensive than the PV/diesel system without battery.

The COE of hybrid PV/diesel/battery system (15% PV penetration) with 5-minute battery autonomy is \$0.117/kWh (diesel fuel price of \$0.067/L). This value is lower than the COE of hybrid PV/diesel system under similar condition which is \$0.119/kWh. As reported in some pieces of literature, the COE of PV/diesel system in some countries is in the range of \$0.22–0.96/kWh [14, 21–27]. The COE varies depending on diesel fuel prices, PV penetrations, and interest rates.

The present cost of electricity production by diesel power plant in Makkah is about \$0.10/kWh. This cost of electricity production matches the simulation result for the stand-alone diesel as shown in Table 8. The average electricity price for residence in Makkah is about \$0.0133–0.0693/kWh (1 \$ = 3.75 SAR). Residential buildings consume most of electricity in Saudi Arabia and estimated 45–47% of the total electrical energy generated in the country [20, 28]. The difference between cost and price is paid from the government resources which subsidize fuel and electricity prices.

As shown in Table 8, the stand-alone diesel system is cheaper than the hybrid PV/diesel system either with or without battery for application in Makkah. It is because of the cheap subsidized diesel fuel price in Makkah.

By renewable energy penetration of 15% (as in hybrid PV/diesel with battery), the use of diesel fuel can be reduced from 3,212,823,296 L/yr to 2,725,292,544 L/yr. In this case, the country can save 487,530,752 L of diesel fuel per year. From environmental viewpoint, the use of hybrid PV/diesel system will significantly reduce CO_2 emission from 8,460,421,632 kg/yr to 7,176,592,896 kg/yr.

6. Conclusion

The HOMER software has simulated three different system configurations, namely, stand-alone diesel system, hybrid PV/diesel system, and hybrid PV/diesel/battery system, for two options of PV array size, that is, 1.1 GW and 2.2 GW. The hybrid PV/diesel system using PV array size of 1.1 GW gives 15% renewable penetration. This penetration value makes sense for the real-world application. From the simulation, it has been clearly demonstrated that the stand-alone diesel system has the lowest COE but the highest CO_2 gas emission. The use of hybrid PV/diesel system will significantly reduce CO_2 gas emission from environmental point of view. On the other hand, the configuration of hybrid PV/diesel system without battery is the most expensive system. One of the main reasons is that the power generated by PV is not being fully utilized. Since the storage devices are very important to ensure that the excess electricity produced by PV array can be stored for later use, it would greatly optimize the system. As a conclusion, the PV/diesel system with battery is more economical than the PV/diesel system without battery.

Conflict of Interests

The authors declare that there is no conflict of interests regarding the publication of this paper.

Acknowledgment

This paper was funded by the Deanship of Scientific Research (DSR), King Abdulaziz University, Jeddah. Therefore, the authors acknowledge, with thanks, the DSR financial support.

References

[1] Y. Alyousef and P. Stevens, "The cost of domestic energy prices to Saudi Arabia," *Energy Policy*, vol. 39, no. 11, pp. 6900–6905, 2011.

[2] S. A. Al-Ajlan, A. M. Al-Ibrahim, M. Abdulkhaleq, and F. Alghamdi, "Developing sustainable energy policies for electrical energy conservation in Saudi Arabia," *Energy Policy*, vol. 34, no. 13, pp. 1556–1565, 2006.

[3] Y. Al-Saleh, "Renewable energy scenarios for major oil-producing nations: the case of Saudi Arabia," *Futures*, vol. 41, no. 9, pp. 650–662, 2009.

[4] H. A. Saleh, "Renewable energy research, development and applications in Saudi Arabia," in *World Renewable Energy Congress VI*, A. A. M. Sayigh, Ed., chapter 345, pp. 1665–1668, Pergamon, Oxford, UK, 2000.

[5] H. H. Chen, H.-Y. Kang, and A. H. I. Lee, "Strategic selection of suitable projects for hybrid solar-wind power generation systems," *Renewable and Sustainable Energy Reviews*, vol. 14, no. 1, pp. 413–421, 2010.

[6] O. Alnatheer, "The potential contribution of renewable energy to electricity supply in Saudi Arabia," *Energy Policy*, vol. 33, no. 18, pp. 2298–2312, 2005.

[7] O. Alnatheer, "Environmental benefits of energy efficiency and renewable energy in Saudi Arabia's electric sector," *Energy Policy*, vol. 34, no. 1, pp. 2–10, 2006.

[8] S. M. Rahman and A. N. Khondaker, "Mitigation measures to reduce greenhouse gas emissions and enhance carbon capture and storage in Saudi Arabia," *Renewable and Sustainable Energy Reviews*, vol. 16, no. 5, pp. 2446–2460, 2012.

[9] S. M. Shaahid and I. El-Amin, "Techno-economic evaluation of off-grid hybrid photovoltaic-diesel-battery power systems for rural electrification in Saudi Arabia-A way forward for sustainable development," *Renewable and Sustainable Energy Reviews*, vol. 13, no. 3, pp. 625–633, 2009.

[10] J. Dargin, "Saudi Arabia, UAE promote energy from sun and wind," *Oil & Gas Journal*, vol. 107, no. 12, pp. 18–22, 2009.

[11] S. H. Alawaji, "Evaluation of solar energy research and its applications in Saudi Arabia—20 years of experience," *Renewable & sustainable energy reviews*, vol. 5, no. 1, pp. 59–77, 2001.

[12] A. J. Al-Shareef and M. F. Abbod, "The application of committee machine model in power load forecasting for the western region of Saudi Arabia," *Engineering Sciences Journal*, vol. 22, no. 1, pp. 19–38, 2011.

[13] S. M. Shaahid and M. A. Elhadidy, "Economic analysis of hybrid photovoltaic-diesel-battery power systems for residential loads in hot regions-A step to clean future," *Renewable and Sustainable Energy Reviews*, vol. 12, no. 2, pp. 488–503, 2008.

[14] E. S. Hrayshat, "Techno-economic analysis of autonomous hybrid photovoltaic-diesel-battery system," *Energy for Sustainable Development*, vol. 13, no. 3, pp. 143–150, 2009.

[15] D. P. Papadopoulos and E. Z. Maltas, "Design, operation and economic analysis of autonomous hybrid PV-diesel power systems including battery storage," *Journal of Electrical Engineering*, vol. 61, no. 1, pp. 3–10, 2010.

[16] J. Dekker, M. Nthontho, S. Chowdhury, and S. P. Chowdhury, "Economic analysis of PV/diesel hybrid power systems in different climatic zones of South Africa," *International Journal of Electrical Power & Energy Systems*, vol. 40, no. 1, pp. 104–112, 2012.

[17] HOMER Energy, http://www.homerenergy.com/.

[18] N. Kulichenko and E. Ereira, *Carbon Capture and Storage in Developing Countries: A Perspective on Barriers to Deployment*, World Bank, Washington, DC, USA, 2012.

[19] J. Bergerson and L. Lave, "The long-term life cycle private and external costs of high coal usage in the US," *Energy Policy*, vol. 35, no. 12, pp. 6225–6234, 2007.

[20] S. M. Shaahid and M. A. Elhadidy, "Opportunities for utilization of stand-alone hybrid (photovoltaic + diesel + battery) power systems in hot climates," *Renewable Energy*, vol. 28, no. 11, pp. 1741–1753, 2003.

[21] S. Rehman and L. M. Al-Hadhrami, "Study of a solar PV-diesel-battery hybrid power system for a remotely located population near Rafha, Saudi Arabia," *Energy*, vol. 35, no. 12, pp. 4986–4995, 2010.

[22] K. Karakoulidis, K. Mavridis, D. V. Bandekas, P. Adoniadis, C. Potolias, and N. Vordos, "Techno-economic analysis of a stand-alone hybrid photovoltaic-diesel-battery-fuel cell power system," *Renewable Energy*, vol. 36, no. 8, pp. 2238–2244, 2011.

[23] G. Rohani and M. Nour, "Techno-economical analysis of stand-alone hybrid renewable power system for Ras Musherib in United Arab Emirates," *Energy*, vol. 64, pp. 828–841, 2014.

[24] K. Y. Lau, M. F. M. Yousof, S. N. M. Arshad, M. Anwari, and A. H. M. Yatim, "Performance analysis of hybrid photovoltaic/diesel energy system under Malaysian conditions," *Energy*, vol. 35, no. 8, pp. 3245–3255, 2010.

[25] M. S. Ismail, M. Moghavvemi, and T. M. I. Mahlia, "Techno-economic analysis of an optimized photovoltaic and diesel generator hybrid power system for remote houses in a tropical climate," *Energy Conversion and Management*, vol. 69, pp. 163–173, 2013.

[26] M. S. Adaramola, S. S. Paul, and O. M. Oyewola, "Assessment of decentralized hybrid PV solar-diesel power system for applications in Northern part of Nigeria," *Energy for Sustainable Development*, vol. 19, pp. 72–82, 2014.

[27] N. E. Mbaka, N. J. Mucho, and K. Godpromesse, "Economic evaluation of small-scale photovoltaic hybrid systems for minigrid applications in far north Cameroon," *Renewable Energy*, vol. 35, no. 10, pp. 2391–2398, 2010.

[28] S. M. Shaahid and M. A. Elhadidy, "Prospects of autonomous/stand-alone hybrid (photo-voltaic + diesel + battery) power systems in commercial applications in hot regions," *Renewable Energy*, vol. 29, no. 2, pp. 165–177, 2004.

Hindawi Publishing Corporation
International Journal of Photoenergy
Volume 2014, Article ID 637468, 16 pages
http://dx.doi.org/10.1155/2014/637468

Research Article

New Multiphase Hybrid Boost Converter with Wide Conversion Ratio for PV System

Ioana-Monica Pop-Calimanu[1] **and Folker Renken**[2]

[1] *Applied Electronics Department, "Politehnica" University of Timisoara, 300223 Timisoara, Romania*
[2] *Power Electronics/Department of Engineering, "Jade University," University of Applied Sciences, 26389 Wilhelmshaven, Germany*

Correspondence should be addressed to Ioana-Monica Pop-Calimanu; ioanamonica.pop@gmail.com

Received 1 December 2013; Accepted 2 March 2014; Published 30 April 2014

Academic Editor: Ismail H. Altas

A new multiphase hybrid boost converter, with wide conversion ratio as a solution for photovoltaic energy system, is presented in this paper. To ensure that all the phases of the converter operate at the same switching frequency we use interleaving topology. The proposed converter can be used as an interface between the PV system and the DC load/inverter. This multiphase converter has the advantage of reduced value and physical size of the input and output capacitor as well as the effort for the inductors. To validate the operation of the converter we provide the analyses and the simulation results of the converter.

1. Introduction

Photovoltaic (PV) energy has attracted interest as an energy source capable of solving the problems of the energy crisis. Solar PV energy is becoming an increasingly important part of the renewable energy resources. It is considered one of the most promising energy resources due to its infinite power delivered directly for free, and many other advantages. These include reliability, availability, zero pollution or destruction of the land, reasonable installation and production cost, long life-span, and the capability of supporting microgrid systems and connecting to electrical grids [1–5]. One of the challenges in the case of grid connection applications or high voltage DC applications requirements is the low voltage of the PV module. For this reason, many PV modules should be either connected in series to meet these application requirements, or to use a step-up DC/DC converter. This type of converter is widely used in PV systems. Theoretically, a traditional step-up converter can achieve a high step-up voltage gain with an extremely high duty ratio near to 100% [6]. The step-up voltage gain in practice is limited due to the effect of power switches, rectifier diodes, the equivalent series resistance of inductors and capacitors, and the saturation effects of the inductors and capacitors [7]. Due to the fact that these traditional converters are not able to operate efficient with a high duty ratio near to 100%, scientific literature presents many topologies [8–11] that provide a high step-up voltage gain without an extremely high duty ratio. A very good review of nonisolated high step-up DC/DC converters used in renewable energy applications is presented in [12, 13], where the advantages and disadvantages of these converters and the major challenges are summarized. In [14] the architecture of a high step-up converter, which contains seven parts including a PV module input circuit, a primary-side circuit, a secondary-side circuit, a passive regenerative snubber circuit, a filter circuit, a DC output circuit, and a feedback control mechanism, is presented. The authors from [14], for raising the voltage gain, are using a coupled inductor with a low-voltage rated switch. In [15] three types of step-up converters with high-efficiency by using PV system with reduced diode stresses sharing are proposed. Through the employ of coupled inductor and switched capacitor, the

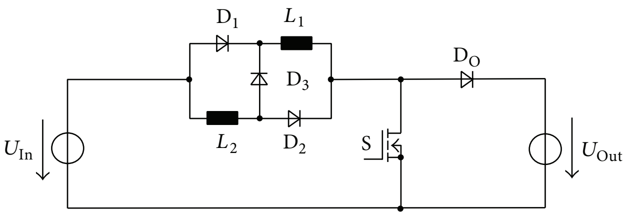

FIGURE 1: Single-phase hybrid boost DC/DC converter.

proposed converters attain high step-up conversion ratio without operating at extreme duty ratio. Very often in the literature is presented high step-up DC/DC converter that utilizes at least one coupled inductor. One of these structures is presented in [16] where the operating principle and steady state analyses are discussed in detail, and a prototype of the circuit is implemented. Another configuration of step-up converter with coupled inductor is presented in [17]. This converter achieves a high step-up voltage conversion ratio, without extreme duty ratios and the numerous turn's ratios of a coupled inductor. The leakage inductor energy of the coupled inductor is efficiently recycled to the load. Other high step-up DC/DC converters with coupled inductor are presented in [18–21].

In this paper is presented and analysed the structures of the step-up hybrid boost converter [7, 22], or as named in some papers switched inductor boost type.

One of the main disadvantages of this circuit is that the effort for the input and output capacitor, in the case of a single-phase DC/DC converter is very high. This is the same with the effort of the inductors. Based on the structure of the hybrid boost converter built in multiphase design, we present a method for reducing this disadvantage through a new multiphase hybrid boost converter.

2. Single-Phase Hybrid Boost Converter

Figure 1 shows the step-up hybrid boost converter which was introduced in [22]. The hybrid boost DC/DC converter consists of a classical boost converter in which is inserted an L-switching structure. The L-switching structure consists of two inductors and three diodes. We can simply say that the input inductor from a classical boost converter was replaced by the two inductors in the new hybrid converter. This type of converter provides high gain and high efficiency and is used for many applications such as solar cell energy conversion systems [7], fuel cell energy conversion systems, battery backup systems for uninterruptible power supplies, and high intensity discharge lamp ballast for automobile head lamps [23].

The gain of the hybrid boost converter is higher than the traditional boost converter by a factor of $(d + 1)$. Figure 2 shows a comparison between the gain of the hybrid boost converter and the traditional boost converter.

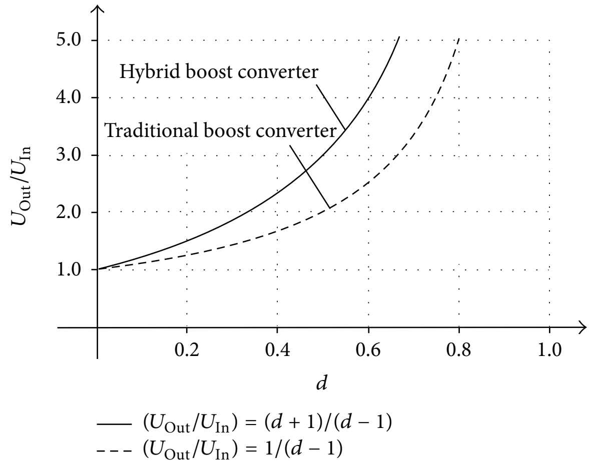

FIGURE 2: Conversion ratio of a hybrid boost and traditional boost DC/DC converter.

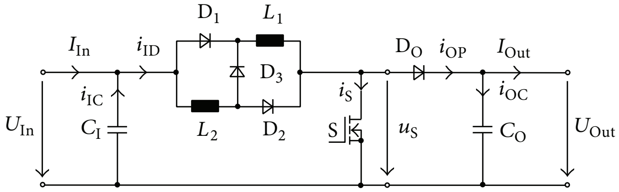

FIGURE 3: Single-phase hybrid boost DC/DC converter.

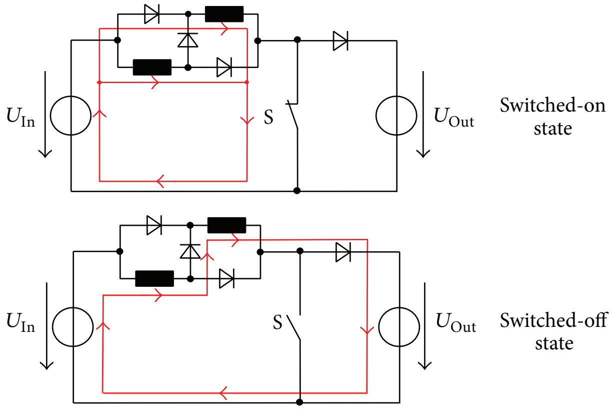

FIGURE 4: Current flow in switched-on and switched-off state of the hybrid boost DC/DC converter.

To ensure a better understanding, this section continues by presenting and discussing the power part of the hybrid converter, which is presented in Figure 3.

The power part consists of an input network with two inductors and three diodes, a step-up circuit with the power switch S and diode D_O, as well as a DC-link capacitor at the input and output side of the converter. Based only on the circuit structure, we can observe that the energy can be transferred only in one direction from input to output.

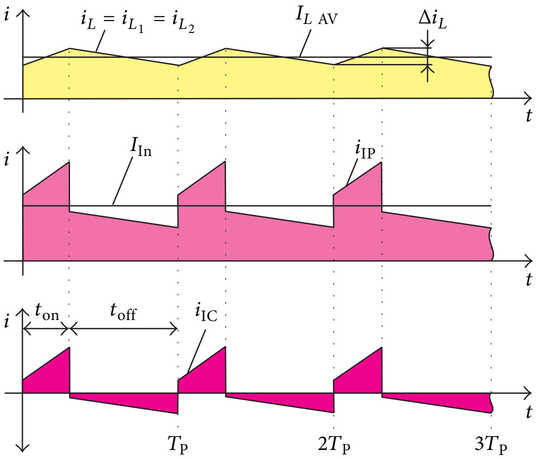

FIGURE 5: Current waveforms at the input of a single-phase hybrid boost DC/DC converter ($d = 0.3$).

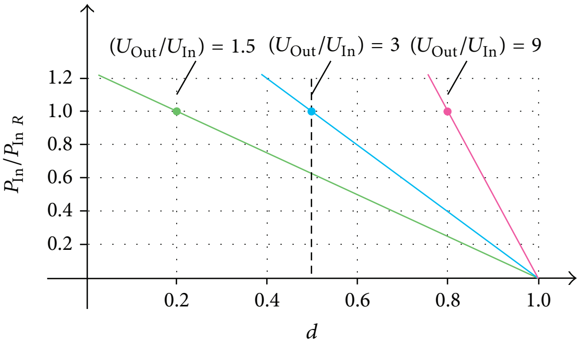

FIGURE 6: Maximum power transfer in case of fixed output voltage.

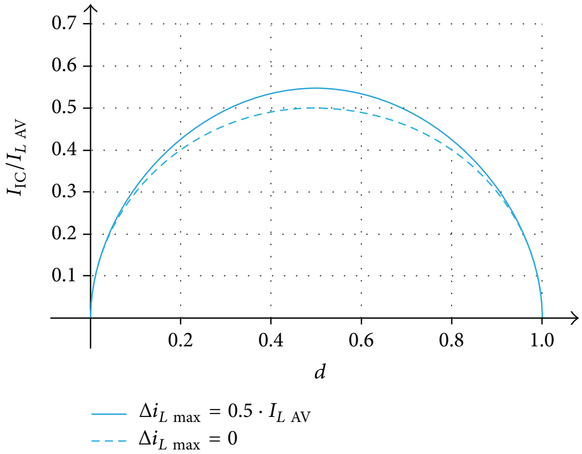

FIGURE 7: RMS current in the input capacitors of a single-phase hybrid boost DC/DC converter.

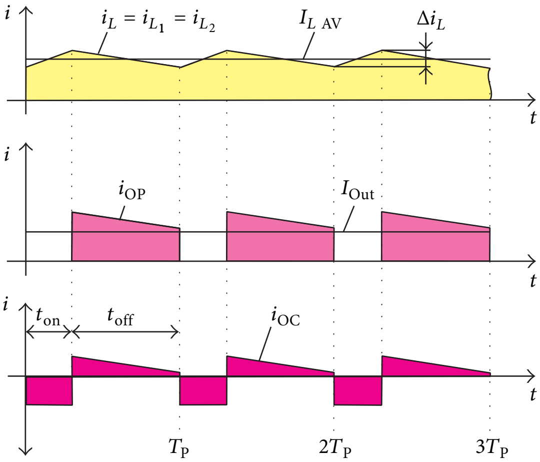

FIGURE 8: Current waveforms at the output of a single-phase hybrid boost DC/DC converter ($d = 0.3$).

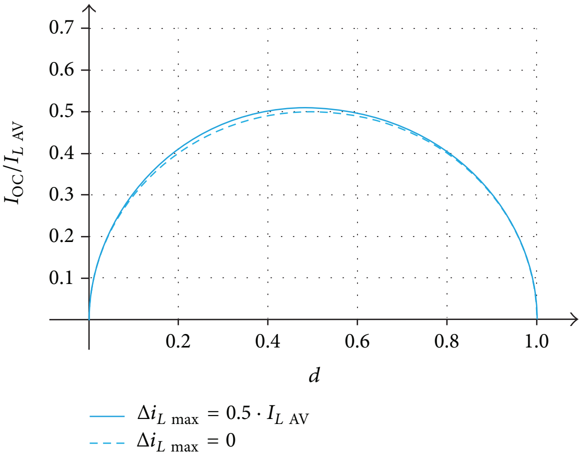

FIGURE 9: RMS current in the output capacitors of a single-phase hybrid boost DC/DC converter.

For operation of the converter we use a pulse control method. Figure 4 shows the current flow in the circuit in the switched-on and the switched-off state.

In the switched-on state the inductors are connected in parallel and the current of both inductors flows in the input phase and in the switch element. For this reason during the switched-on state the current in the output phase i_{OP} is zero (Figure 8). In the switched-off state the inductance current flows in series through the inductors and the output diode. In this moment the inductors are connected in series, while the input phase current i_{IP} and output phase current i_{OP} are the same as the inductor current. The expectation being that only the average value of the input phase current would flow in the converter input current, I_{In}, while the AC-current component would flow in to the capacitor C_I and the average value of the output phase current would flow in the converter output I_Out.

For calculations, we assumed that all elements of the converter would work without losses, the voltage and currents at the input and output were ideally DC-values, and the converter would be controlled with pulse width modulation [24]. With these requirements in the converter switching states, the voltage at the inductors can be determined by applying the voltage-second balance on the inductor as follows:

$$\begin{aligned} t_\mathrm{on}&: \quad u_L = U_\mathrm{In}, \\ t_\mathrm{off}&: \quad u_L = -\frac{U_\mathrm{Out} - U_\mathrm{In}}{2}, \end{aligned} \tag{1}$$

where u_L is the inductor voltage, U_In is the input voltage, and U_Out is the output voltage.

As we can see from the above formulas, the voltage at the inductors is positive in the switched-on state and negative in the switched-off state. In circuit operation the positive and negative voltage-time-area at the inductors must always be the same. With this condition the conversion ratio of the hybrid boost DC/DC converter can be calculated. Consider

$$U_\mathrm{Out} = \frac{1+d}{1-d} \cdot U_\mathrm{In} \quad \text{with } d = \frac{t_\mathrm{on}}{T_\mathrm{P}},\ 1-d = \frac{t_\mathrm{off}}{T_\mathrm{P}}. \tag{2}$$

2.1. DC/DC Converter Input Circuit. In Figure 5 the current waveforms at the input of the hybrid boost converter is presented. The first waveform shows the currents in both inductors, and we can see that they are the same. The inductor current rises in switched-on state and fall in switched-off state, so that a triangular shape current is generated. The middle waveform presents the input phase current i_IP, and the lower waveform presents the input capacitor current i_IC.

The average current $I_{L\,\mathrm{AV}}$ depends on the duty cycle d. Consider

$$I_{L\,\mathrm{AV}} = \frac{I_\mathrm{In}}{1+d}. \tag{3}$$

In order to calculate the required inductance and capacitance in the circuit we needed to fix conditions for the circuit operation. We first needed to know the rated output voltage, as well as the minimal input voltage at rated power which should be transferred. With these conditions the conversion ratio of the circuit for rated input power $P_{\mathrm{In}\,R}$ transfer is fixed.

In this operation point the DC-input current and the average current $I_{L\,\mathrm{AV}}$ in the inductors can be calculated. It is assumed that this average current $I_{L\,\mathrm{AV}}$ is the maximum DC-value in the inductances. Figure 6 shows the possible power transfer dependent on the duty cycle for three different converter designs. The inductivity must be calculated for the maximum inductor voltage-time-area within the pulse periods and the maximum acceptable current variation during this time. In the switched-on state t_on, the input voltage U_In is connected at the inductors. The voltage U_In is described in formula (5) as a function of the output voltage and the duty cycle. Consider

$$L_1 = L_2 = \frac{U_\mathrm{In} \cdot t_\mathrm{on}}{\Delta i_L}, \tag{4}$$

$$L_1 = L_2 = \frac{U_\mathrm{Out} \cdot T_\mathrm{P}}{\Delta i_L} \cdot \frac{d \cdot (1-d)}{1+d}. \tag{5}$$

Considering the full duty cycle range, the voltage-time-area within the pulse periods reaches its maximum for a duty cycle of approximately 41%. For this duty cycle in general the converter inductance is specified. The maximum acceptable current variation $\Delta i_{L\,\max}$ is chosen normally between 10% and 30% of the rated average inductance current $I_{L\,\mathrm{AV}\,R}$. These inductances can be realized as individual or mutual coupled inductances.

$$\begin{gathered} L_1 = L_2 = \frac{U_\mathrm{Out} \cdot T_\mathrm{P}}{\Delta i_{L\,\max}} \cdot \left(3 - 2 \cdot \sqrt{2}\right) \\ \text{with } \Delta i_{L\,\max} = (0.1\text{–}0.3) \cdot I_{L\,\mathrm{AV}\,R}. \end{gathered} \tag{6}$$

We continue with the calculation of the capacity of the input side. We begin with the worst case scenario which could happen when the converter input current is an ideally average value and the overall AC-current of the input phase flows in the capacitor (see Figure 4). This AC-current in the capacitor produces an AC-voltage at the input that is overlaid with the DC-input voltage. For this reason the maximum acceptable voltage variation at the capacitor must be chosen during the capacity dimension. Consider

$$\begin{aligned} C_\mathrm{I} &= \frac{i_\mathrm{C} \cdot t_\mathrm{on}}{\Delta u_\mathrm{C}}, \\ C_\mathrm{I} &= \frac{I_{L\,\mathrm{AV}} \cdot T_\mathrm{P}}{\Delta u_{\mathrm{In}\,\max}} \cdot d \cdot (1-d). \end{aligned} \tag{7}$$

The current-time-area depends on the duty cycle having its maximum at 50% and at the rated inductance current $I_{L\,\mathrm{AV}}$. In practice, the acceptable static voltage variation at the converter input is chosen smaller than 1% of the rated input voltage $U_{\mathrm{In}\,R}$.

$$C_\mathrm{I} = \frac{I_{L\,\mathrm{AV}\,R} \cdot T_\mathrm{P}}{4 \cdot \Delta u_{\mathrm{In}\,\max}} \quad \text{with } \Delta u_{\mathrm{In}\,\max} \le 0.01 \cdot U_{\mathrm{In}\,R}. \tag{8}$$

In the input of the DC/DC converters, electrolytic capacitors are often used [25]. The main design criteria for these capacitors are the RMS current loads. The RMS current in the input capacitor is calculated as a function of the duty cycle for an average inductance current $I_{L\,\mathrm{AV}}$ and a maximum current variation $\Delta i_{L\max}$. Consider

$$\begin{aligned} I_\mathrm{IC} &= I_{L\,\mathrm{AV}} \\ &\quad \cdot \sqrt{d \cdot (1-d) + \left(\frac{\Delta i_{L\max}}{I_{L\,\mathrm{AV}}}\right)^2 \cdot \frac{d^2 \cdot (1-d)^2 \cdot (1 + 3 \cdot d)}{12 \cdot (1+d)^2 \cdot \left(3 - 2 \cdot \sqrt{2}\right)}}. \end{aligned} \tag{9}$$

The result can be split into two. One is dependent on the average current $I_{L\,\mathrm{AV}}$ and the other is dependent on the triangle current variation in the inductances. In Figure 7, the current in the RMS capacitor is shown. The maximum value of the capacitor current is higher than the half average inductance current $I_{L\,\mathrm{AV}}$. The current variation has, however, only a small influence on the total RMS current in the capacitor.

2.2. DC/DC Converter Output Circuit. Figure 8 shows the current and voltage waveforms at the output of the hybrid boost DC/DC converter.

The first waveform in Figure 8 shows the current in both inductors. The middle waveform presents the output phase current i_{OP}. The lower waveform shows the AC-current in the output capacitor. This current can be calculated by subtraction of output phase current i_{OP} and output current I_{Out}.

We continue with the calculation for the capacity of the output side. We begin with the worst case scenario which would happen when the converter output current is an ideally average value and the overall AC component of the output phase current flows in the capacitor (see Figure 8). This AC-current in the capacitor produces an AC-voltage at the output that is overlaid with the DC-output voltage. For this reason the maximum acceptable voltage variation at the capacitor must be chosen during the capacity dimension. The current-time-area in the capacitor within the pulse periods can be described as a function of the output current and the duty cycle. Consider

$$C_{\mathrm{O}} = \frac{I_{\mathrm{Out}} \cdot T_{\mathrm{P}}}{\Delta u_{\mathrm{Out\,max}}} \cdot d,$$
$$C_{\mathrm{O}} = \frac{I_{L\,\mathrm{AV}} \cdot T_{\mathrm{P}}}{\Delta u_{\mathrm{Out\,max}}} \cdot d \cdot (1-d)\,. \tag{10}$$

The current-time-area depends on the duty cycle with its maximum at 50% and at rated inductance current $I_{L\,\mathrm{AV}}$. In practice, the acceptable static voltage variation is chosen smaller than 1% of the nominal output voltage U_{Out}. Consider

$$C_{\mathrm{O}} = \frac{I_{L\,\mathrm{AV}\,R} \cdot T_{\mathrm{P}}}{4 \cdot \Delta u_{\mathrm{Out\,max}}} \quad \text{with } \Delta u_{\mathrm{Out\,max}} \le 0.01 \cdot U_{\mathrm{Out}\,R}. \tag{11}$$

Also on the output side of the hybrid boost converters, electrolytic capacitors are often used. For design of the capacitors, the RMS current in the output must be calculated. In the next formula the RMS current is determined as a function of the duty cycle for an average inductance current $I_{L\,\mathrm{AV}}$ and a maximum inductance current variation $\Delta i_{L\,\max}$. Consider

$$I_{\mathrm{OC}} = I_{L\,\mathrm{AV}} \cdot \sqrt{d \cdot (1-d) + \left(\frac{\Delta i_{L\max}}{I_{L\,\mathrm{AV}}}\right)^2 \cdot \frac{d^2 \cdot (1-d)^3}{12 \cdot (1+d)^2 \cdot \left(3 - 2 \cdot \sqrt{2}\right)}}. \tag{12}$$

The result can also be split into two: one is dependent on the average inductor current $I_{L\,\mathrm{AV}}$, and the other is dependent on the triangle current variation in the inductances. In Figure 9, the current in the RMS capacitor is shown. The maximum value is more than the half average inductance current $I_{L\,\mathrm{AV}}$. The current variation also has only a small influence on the total RMS current in the capacitor.

The effort for the input and output capacitor in the case of a single-phase DC/DC converter is very high. In the next section a method for reducing the capacitor currents is presented. With this method, the effort for the inductors can also be reduced.

3. Multiphase DC/DC Converter

Several solutions and their control were presented in the literature for interconnection of the converters [26–32]. Multiphase configuration is one of them [33–35]. Although the physical connection of the multiphase looks exactly the same like parallel connection, the main difference between them is the method of how they time/control their main switches. The parallel configuration is operated by having the switching signals for main switches coincide with each other (e.g., when switch from first power converter turns on, so does the switch from the second power converter and vice versa). The main advantage of parallel configuration is that the control circuit must only provide a single switching signal.

In multiphase converter each switch operates at a different time with a phase shift between the switch gate drivers [36] but with common frequency. The result of the phase delay allows multiphase configurations to exhibit higher overall efficiency due to ripple cancelation, smaller output filter requirements, and smaller output voltage ripple [37–40]. The output voltage ripple is reduced because the output frequency is increased by the number of phase times of the individual switch frequency. Higher output frequency makes the output ripple easier to filter which allows smaller components and further increase in efficiency [36]. In [41] is presented another two-phase boost converter topology, which due to the fact that the multiphase configuration, at the output the circuit, will have just a single capacitor and the output voltage will have ripple component twice the operating switching frequency of each individual boost converter. The frequency multiplication effect also occurs at the input side of the converter and will reduce the input filters and will improve the quality of the input current [41].

The hybrid boost DC/DC converter presented in this paper can also be built in multiphase design. Therefore the different phases are connected at a common input and output capacitor. The total current is subdivided in the different phases. By interleaving switching topology the AC-currents in the input C_{I} and output capacitor C_{O} can be reduced clearly. In addition the frequency of the capacitor currents is increased. With suitable circuit design the effort of the inductances can be decreased. Figure 10 shows a DC/DC converter in two-phase design.

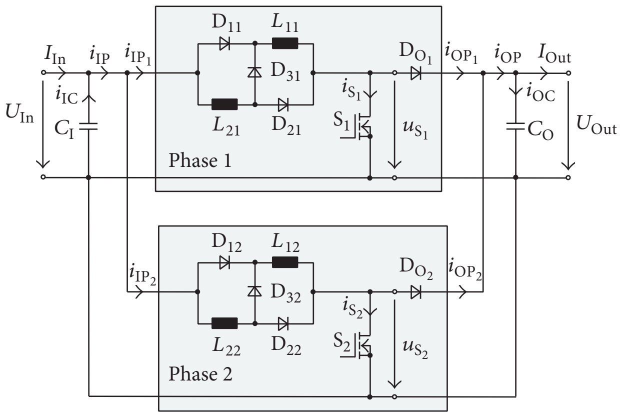

FIGURE 10: Two-phase hybrid boost DC/DC converter.

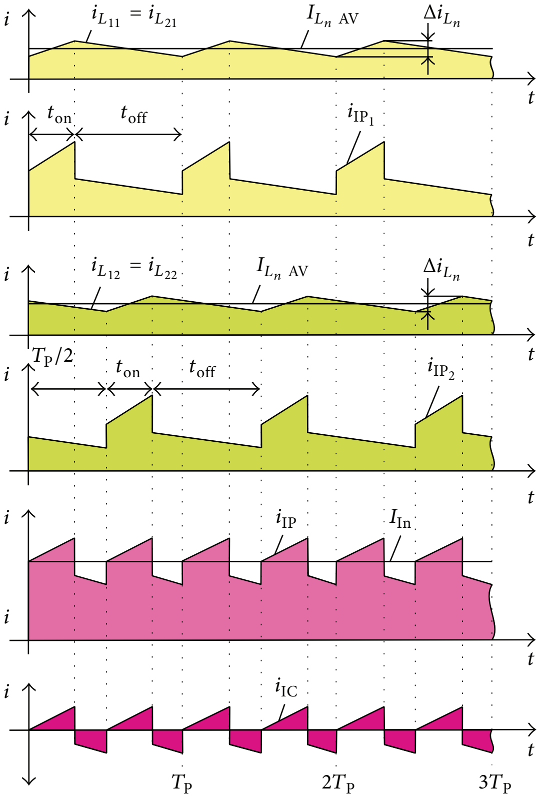

FIGURE 11: Current waveforms at the input of a two-phase hybrid boost DC/DC converter ($n = 2$, $d = 0.3$).

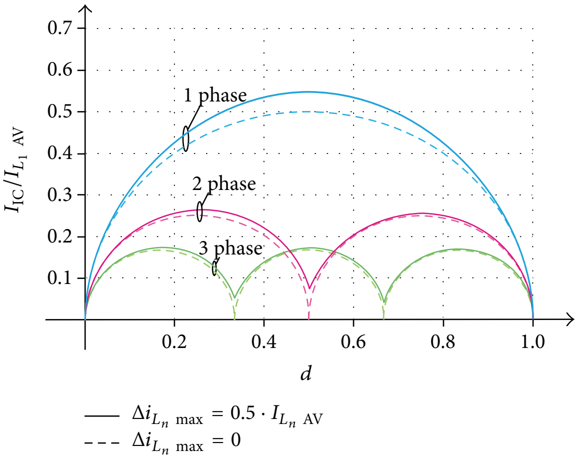

FIGURE 12: RMS current in the input capacitors of a one-, two-, and three-phase hybrid boost DC/DC converter.

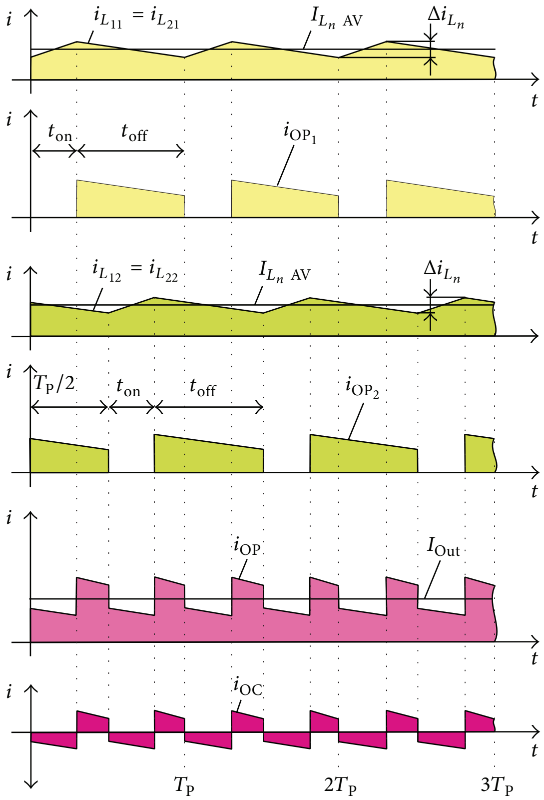

FIGURE 13: Current waveforms at the output of the two-phase hybrid boost DC/DC converter ($n = 2$, $d = 0.3$).

3.1. DC/DC Converter Input Circuit. In Figure 11 the current waveforms at the input of a two-phase hybrid boost converter are shown. First, the currents in both inductances and the input current of phase one are shown. Represented underneath in green are the same currents of phase two. The triangle shaped inductance currents of the two phases are shifted with about a half pulse period. At switched-on time the input current of each phase is twice as small as the inductance current from a single-phase converter. But in this circuit the overall input phase current I_{IP} consists of the sum of all the input phase currents. The overall input phase current I_{IP}, with the DC-component I_{In} is shown in Figure 11. Also for this circuit it is assumed that only the DC-current is flowing in the circuit input. With these conditions, for multiphase converters, the function between the input current I_{In} and the average inductance current of the individual phases $I_{L_n\,\mathrm{AV}}$ can be calculated. Consider

$$I_{L_n\,\mathrm{AV}} = \frac{I_{\mathrm{In}}}{n \cdot (1 + d)}. \tag{13}$$

The total AC-component of the overall input phase current I_{IP} flows in the input capacitor (Figure 11). This current is clearly smaller in comparison to a single-phase hybrid boost converter. In addition, the frequency of the capacitor current is doubled. For these reasons the filter effort is reduced.

We continue with the calculation of the inductances and capacitors of a multiphase hybrid boost converter. The same technical conditions for a single-phase converter are applied and the calculation of inductances for an n-phase design can be accomplished in the same way as for single-phase circuits. Taking into account the input current which is subdivided into the different phases, the maximum current variation in the inductances must be based on the maximum DC-current at rated power in the individual phases. For design, the maximum current variation is selected between 10% and 30% of the phase DC-current in the inductances at rated power. Consider

$$\begin{gathered} L_{1n} = L_{2n} = \frac{U_{\mathrm{Out}} \cdot T_{\mathrm{P}}}{\Delta i_{L_n\,\max}} \cdot \left(3 - 2 \cdot \sqrt{2}\right) \\ \text{with } \Delta i_{L_n\,\max} = (0.1\text{–}0.3) \cdot I_{L_n\,\mathrm{AV}\,R}. \end{gathered} \tag{14}$$

The amplitude of the triangle current variation in the inductors is dependent on the duty cycle of the converter. Because the duty cycle in all phases has the same value, the current variations in all inductors are equivalent. Consider

$$\Delta i_{L_n} = \frac{(d) \cdot (1 - d)}{(1 + d) \cdot \left(3 - 2 \cdot \sqrt{2}\right)} \cdot \Delta i_{L_n\,\max}. \tag{15}$$

The necessary input capacity of the multiphase hybrid boost converter will now be calculated. Compared to a single-phase design, the capacitor current is reduced and the current frequency is increased by the number of phases. As a consequence the current in the capacitor has a voltage variation at the input. For the capacitor design, the permissible static voltage variation in general is selected smaller than 1% of the rated input voltage. Consider

$$C_{\mathrm{I}} = \frac{T_{\mathrm{P}} \cdot I_{L_n\,\mathrm{AV}}}{4 \cdot n \cdot \Delta u_{\mathrm{In}\,\max}} \quad \text{with } \Delta u_{\mathrm{In}\,\max} \le 0.01 \cdot u_{\mathrm{In}\,R}. \tag{16}$$

In these DC/DC converters, electrolytic capacitors are used often. A main design criterion of these capacitors is the RMS current load. For this reason, for multiphase DC/DC converters the RMS current in the input capacitor C_{I} will be calculated. Therefore the switching processes in the phases are assumed as ideal. Moreover, it is accepted that the current in the input is an ideal DC-current. The worst case scenario will happen when the capacitor is loaded with the total AC-current component.

The input capacitor current for two-phase converters is represented in Figure 12. In the case of closer inspection the capacitor current can be split into two different components: a rectangle part and a triangle part. The RMS current of these two components has been calculated. The RMS result of the rectangle portion for multiphase converters is shown in the formula below:

$$I_{\mathrm{IC\,\Pi}} = \left| \begin{array}{ll} \sqrt{I_{L_n\,\mathrm{AV}}^2 \cdot n^2 \cdot \left(d - \dfrac{0}{n}\right) \cdot \left(\dfrac{1}{n} - d\right)} & \text{if } \dfrac{0}{n} \le d \le \dfrac{1}{n} \\ \sqrt{I_{L_n\,\mathrm{AV}}^2 \cdot n^2 \cdot \left(d - \dfrac{1}{n}\right) \cdot \left(\dfrac{2}{n} - d\right)} & \text{if } \dfrac{1}{n} \le d \le \dfrac{2}{n} \\ \sqrt{I_{L_n\,\mathrm{AV}}^2 \cdot n^2 \cdot \left(d - \dfrac{2}{n}\right) \cdot \left(\dfrac{3}{n} - d\right)} & \text{if } \dfrac{2}{n} \le d \le \dfrac{3}{n} \\ \vdots & \vdots \\ \sqrt{I_{L_n\,\mathrm{AV}}^2 \cdot n^2 \cdot \left(d - \dfrac{n-1}{n}\right) \cdot \left(\dfrac{n}{n} - d\right)} & \text{if } \dfrac{n-1}{n} \le d \le \dfrac{n}{n}. \end{array} \right. \tag{17}$$

In this formula it is necessary to consider that the average inductance current $I_{L_n\,\mathrm{AV}}$ becomes smaller with an increasing number of phases. For example, the average inductance current $I_{L_n\,\mathrm{AV}}$ in a two-phase converter is only half as big as in a single-phase converter. With this fact in mind the rectangle component of the input capacitor current can clearly be reduced with a multiphase design.

In addition, the RMS current of the triangle has been calculated. The next formula shows the RMS results for a multiphase circuit design. Consider

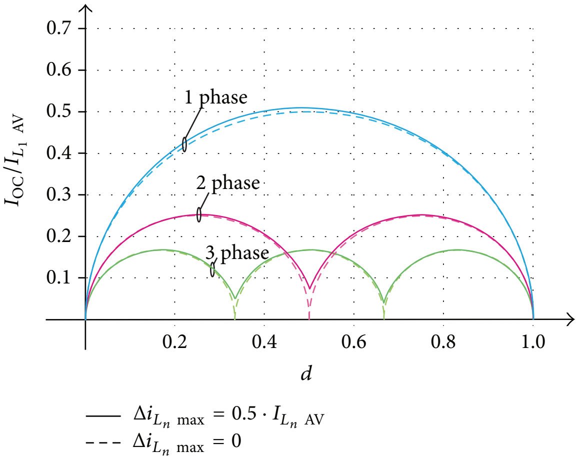

FIGURE 14: RMS current in the output capacitors of a one-, two-, and three-phase hybrid boost DC/DC converter.

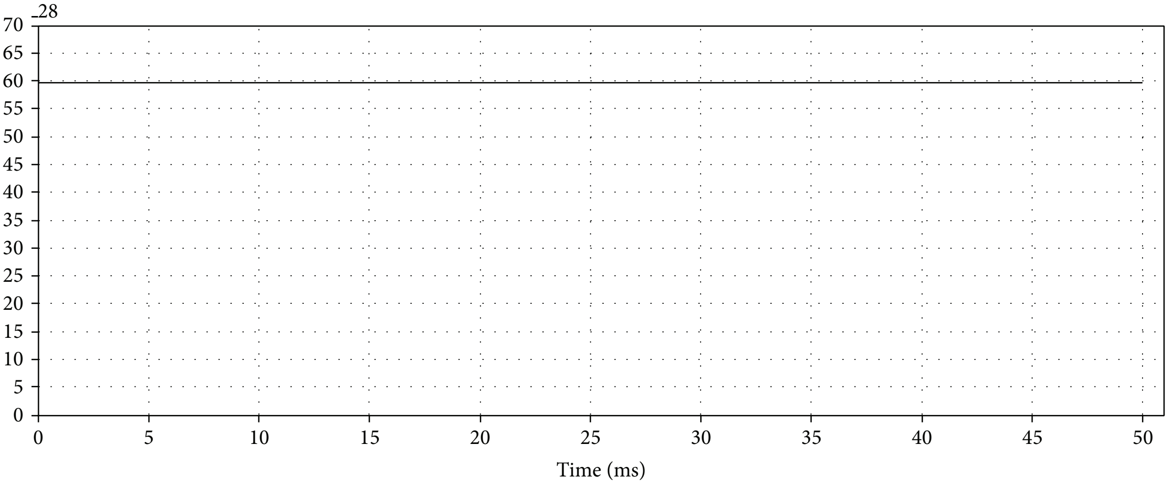

y	MinX	MaxX	MinY	MaxY	Mean	RMS	Peak-peak	Abs mean	RMS ac	Integral	Ripple	Ripple fac. . .	Harmonic. . .	Form fact. . .
	0	50 m	0	60	60	60	60	60	84.853 m	3	1	1	1.414 m	1

FIGURE 15: Input voltage.

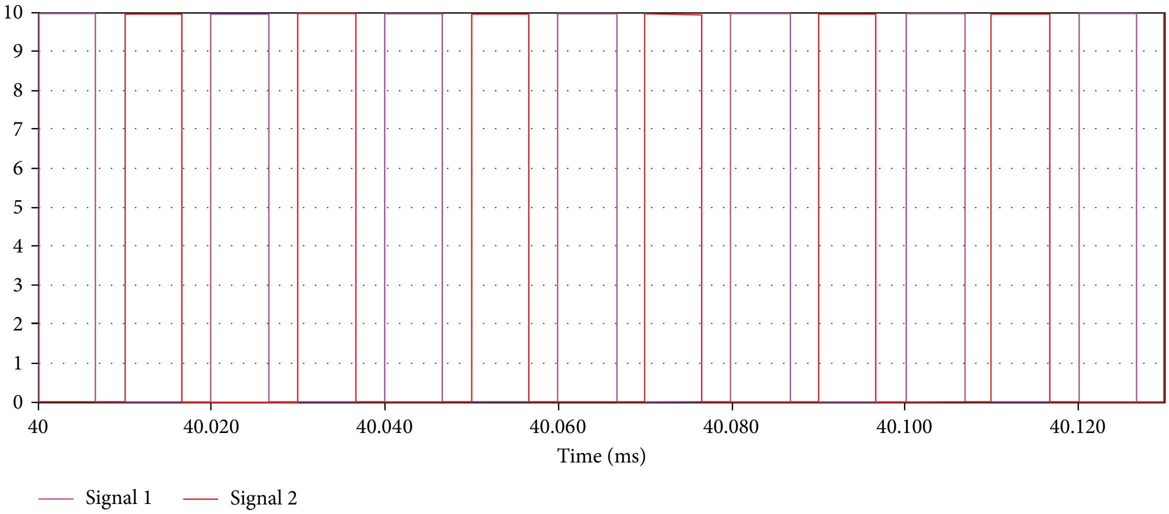

t	y	MinX	MaxX	MinY	MaxY	Mean	RMS	Peak-peak	Abs mean	RMS ac	Integral	Ripple	Ripple fac. . .	Harmonic. . .	Form fact. . .
40.007 m	10	0	50 m	0	10	3.320	5.762	10	3.320	4.709	165.982 m	1.736	3.012	817.335 m	1.736
40.007 m	0	0	50 m	0	10	3.320	5.762	10	3.320	4.709	165.980 m	1.736	3.012	817.335 m	1.736

FIGURE 16: PWM pulse applied to switch one (pink signal), respective switch two (red signal).

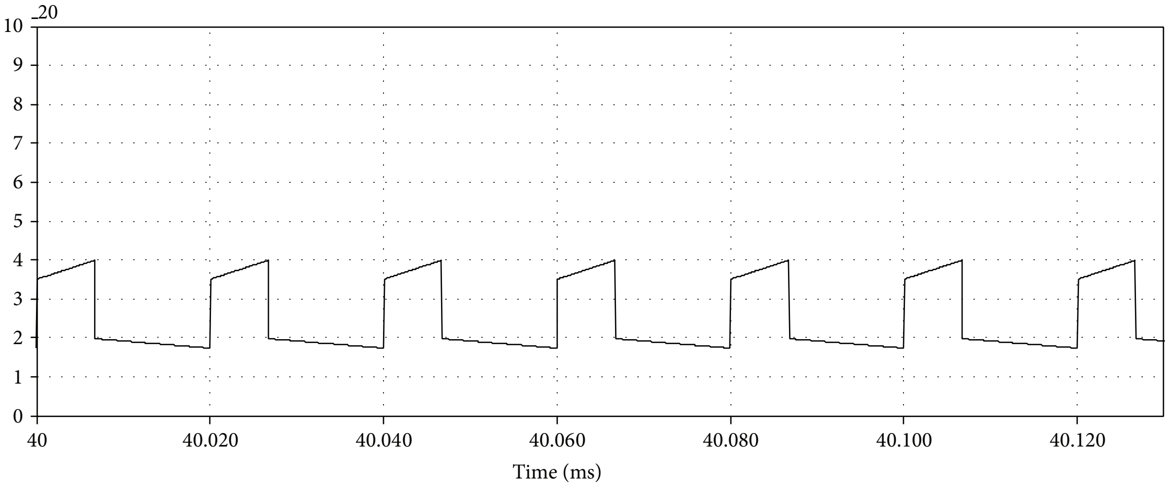

y	MinX	MaxX	MinY	MaxY	Mean	RMS	Peak-peak	Abs mean	RMS ac	Integral	Ripple	Ripple fac...	Harmonic...	Form fact...
	0	50 m	0	6.973	2.494	2.653	6.973	2.494	904.460 m	124.694 m	1.064	2.796	340.942 m	1.064

FIGURE 17: Input current of phase one, i_{IP_1}.

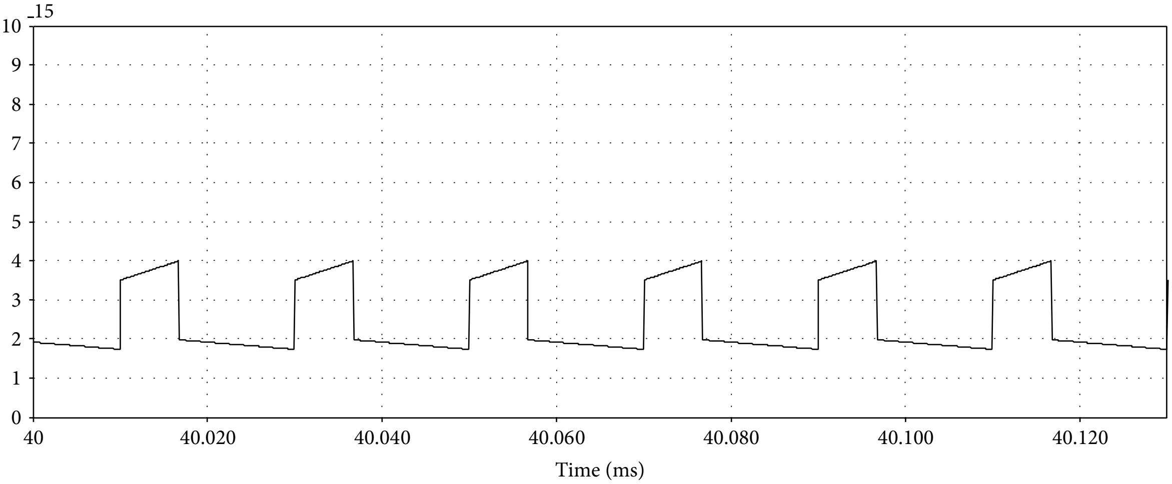

y	MinX	MaxX	MinY	MaxY	Mean	RMS	Peak-peak	Abs mean	RMS ac	Integral	Ripple	Ripple fac...	Harmonic...	Form fact...
0	0	50 m	0	6.992	2.496	2.655	6.992	2.496	905.309 m	124.809 m	1.064	2.801	340.948 m	1.064

FIGURE 18: Input current of phase two, i_{IP_2}.

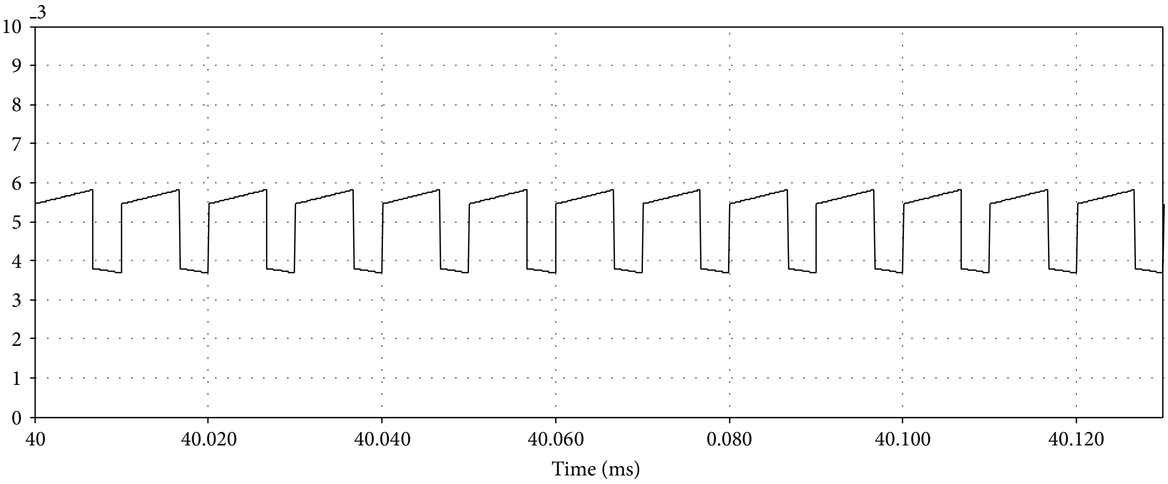

y	MinX	MaxX	MinY	MaxY	Mean	RMS	Peak-peak	Abs mean	RMS ac	Integral	Ripple	Ripple fac...	Harmonic...	Form fact...
	0	50 m	0	10.296	4.990	5.080	10.296	4.990	949.092 m	249.503 m	1.018	2.063	186.847 m	1.018

FIGURE 19: Overall input phase current, i_{IP}.

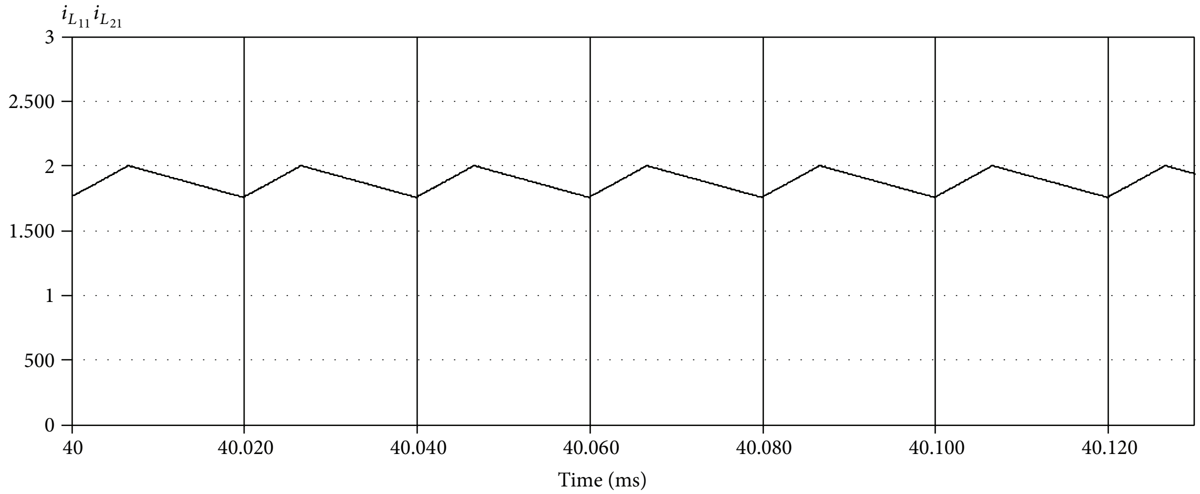

Trace	t	y	Min$X$	Max$X$	Min$Y$	Max$Y$	Mean	RMS	Peak-peak	Abs mean	RMS ac	Integral	Ripple	Ripple fac...	Harmonic...	Form fact...
(1) $i_{L_{11}}$	0	0	0	50 m	0	3.487	1.871	1.875	3.487	1.871	135.711 m	93.529 m	1.003	1.864	72.360 m	1.003
(2) $i_{L_{21}}$	0	0	0	50 m	0	3.487	1.871	1.875	3.487	1.871	135.711 m	93.529 m	1.003	1.864	72.360 m	1.003

FIGURE 20: Current through inductors L_{11} and L_{21}, $i_{L_{11}}$, $i_{L_{21}}$.

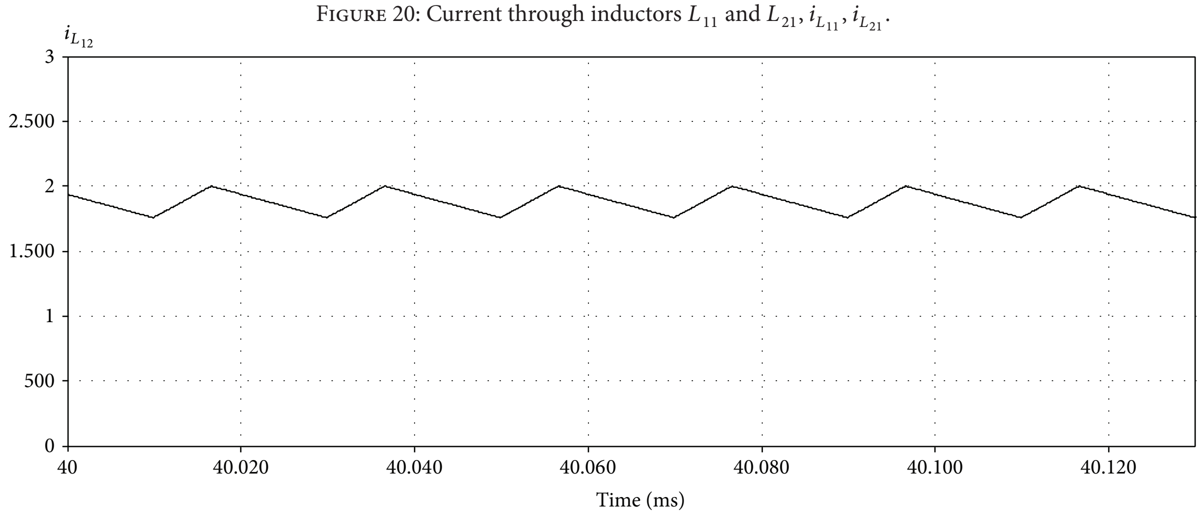

t	y	Min$X$	Max$X$	Min$Y$	Max$Y$	Mean	RMS	Peak-peak	Abs mean	RMS ac	Integral	Ripple	Ripple fac...	Harmonic...	Form fact...
40.024 m	1.879	0	50 m	0	3.496	1.872	1.877	3.496	1.872	135.792 m	93.608 m	1.003	1.867	72.343 m	1.003

FIGURE 21: Current through inductor L_{12}, $i_{L_{12}}$.

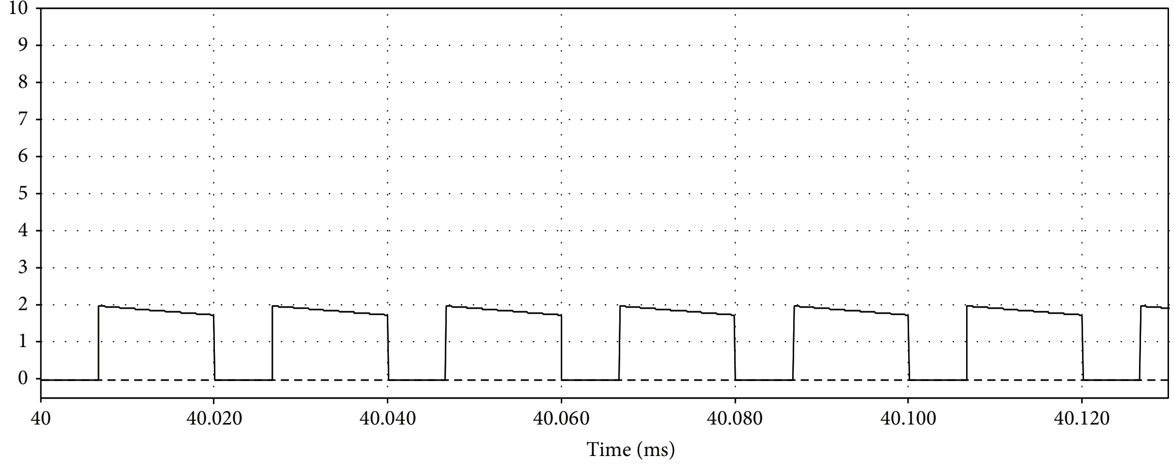

y	Min$X$	Max$X$	Min$Y$	Max$Y$	Mean	RMS	Peak-peak	Abs mean	RMS ac	Integral	Ripple	Ripple fac...	Harmonic...	Form fact...
0	0	50 m	−157.172 μ	5.081	1.251	1.535	5.081	1.251	890.262 m	62.531 m	1.227	4.063	579.928 m	1.227

FIGURE 22: Output current of phase one, i_{OP_1}.

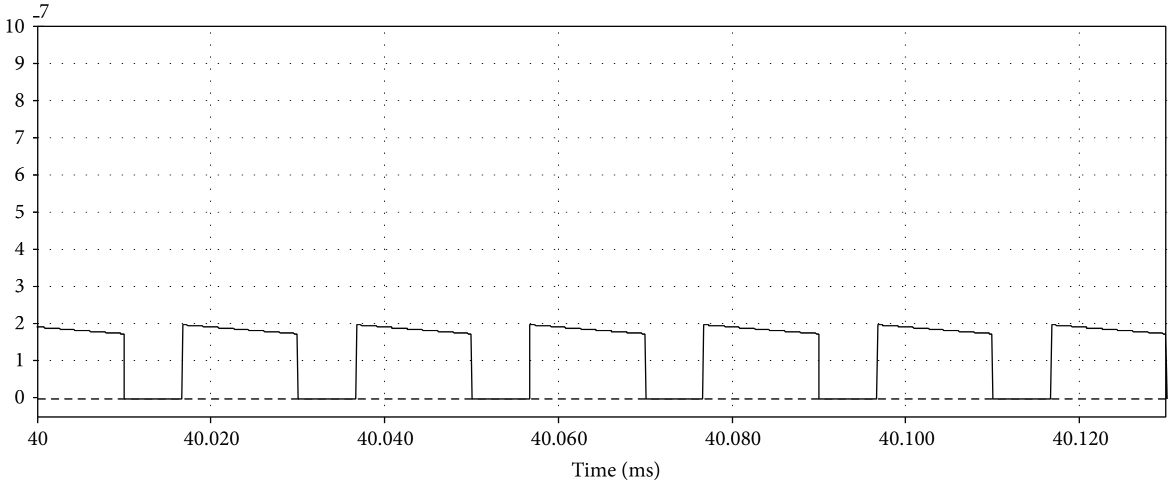

y	Min$X$	Max$X$	Min$Y$	Max$Y$	Mean	RMS	Peak-peak	Abs mean	RMS ac	Integral	Ripple	Ripple fac...	Harmonic...	Form fact...
1.828	0	50 m	−157.115 μ	4.851	1.252	1.537	4.851	1.252	891.238 m	62.581 m	1.228	3.876	580.038 m	1.228

FIGURE 23: Output current of phase two, i_{OP_2}.

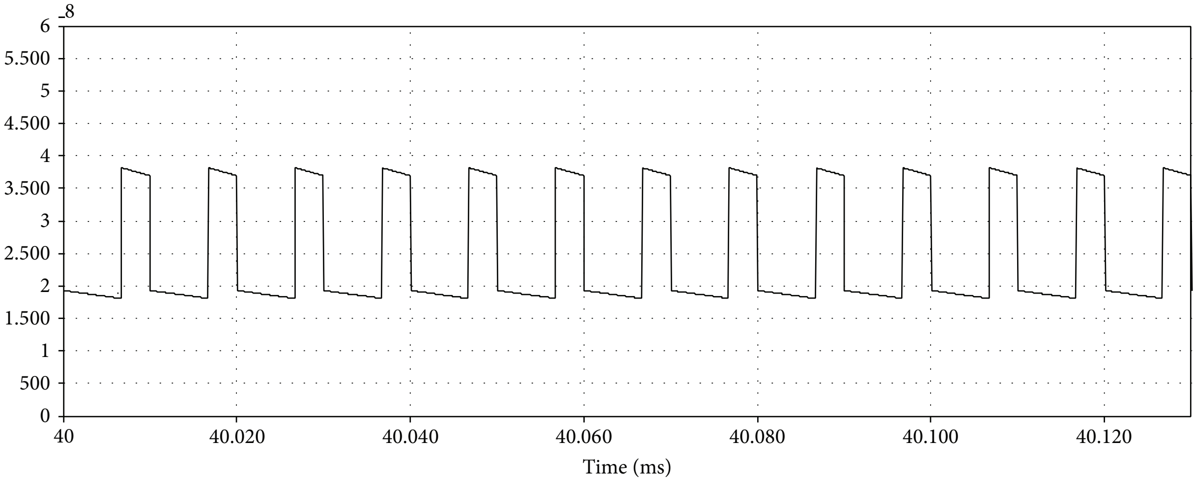

t	y	Min$X$	Max$X$	Min$Y$	Max$Y$	Mean	RMS	Peak-peak	Abs mean	RMS ac	Integral	Ripple	Ripple fac...	Harmonic...	Form fact...
40.007 m	1.828	0	50 m	0	9.931	2.502	2.661	9.931	2.502	905.742 m	125.112 m	1.063	3.969	340.360 m	1.063

FIGURE 24: Overall output phase current, i_{OP}.

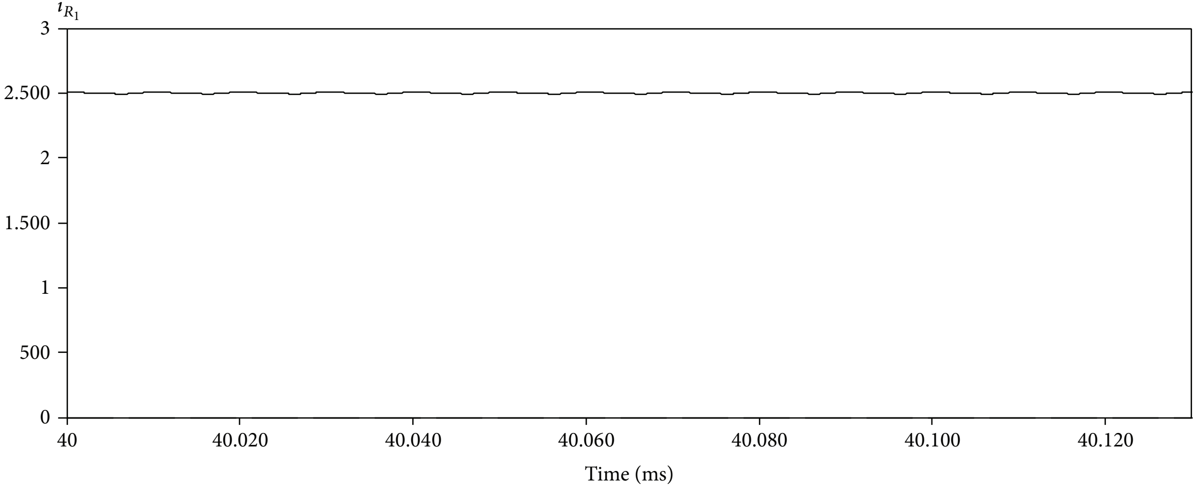

t	y	Min$X$	Max$X$	Min$Y$	Max$Y$	Mean	RMS	Peak-peak	Abs mean	RMS ac	Integral	Ripple	Ripple fac...	Harmonic...	Form fact...
40.007 m	2.501	0	50 m	0	3.275	2.490	2.492	3.275	2.490	112.534 m	124.483 m	1	1.315	45.154 m	1

FIGURE 25: Output current, I_{Out}.

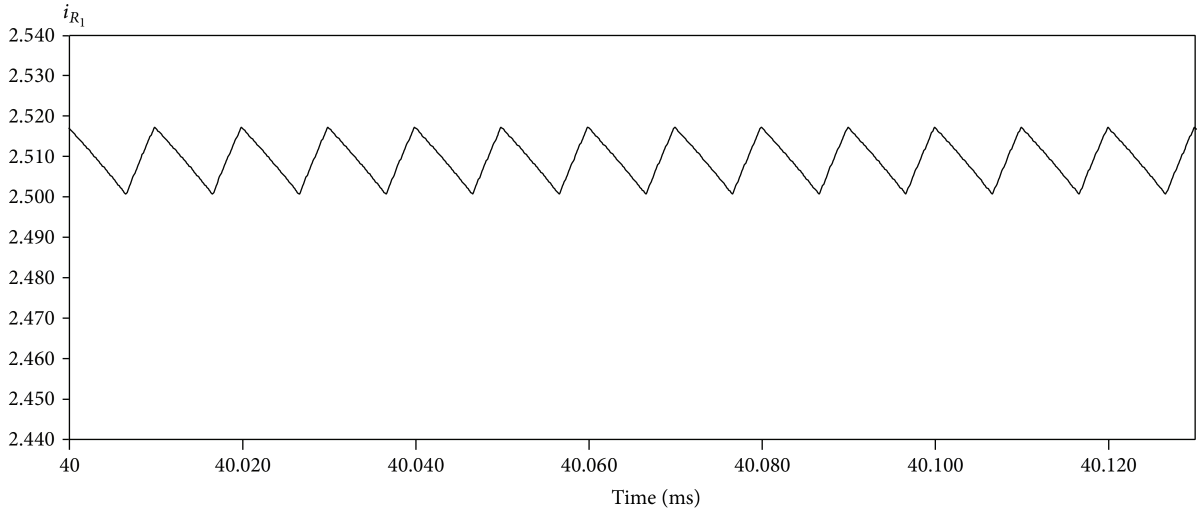

t	y	Min$X$	Max$X$	Min$Y$	Max$Y$	Mean	RMS	Peak-peak	Abs mean	RMS ac	Integral	Ripple	Ripple fac. . .	Harmonic. . .	Form fact. . .
40.007 m	2.501	0	50 m	0	3.275	2.490	2.492	3.275	2.490	112.534 m	124.483 m	1	1.315	45.154 m	1

Figure 26: Zoom on output current.

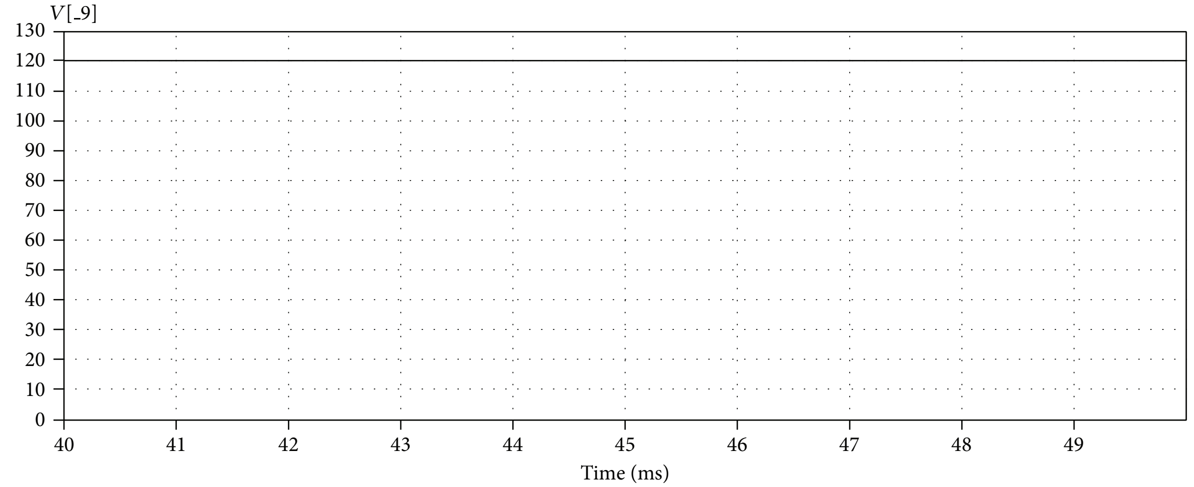

t	y	Min$X$	Max$X$	Min$Y$	Max$Y$	Mean	RMS	Peak-peak	Abs mean	RMS ac	Integral	Ripple	Ripple fac. . .	Harmonic. . .	Form fact. . .
40.007 m	120.029	0	50 m	0	157.198	119.504	119.626	157.198	119.504	5.402	5.975	1	1.315	45.154 m	1

Figure 27: Output voltage, V_{Out}.

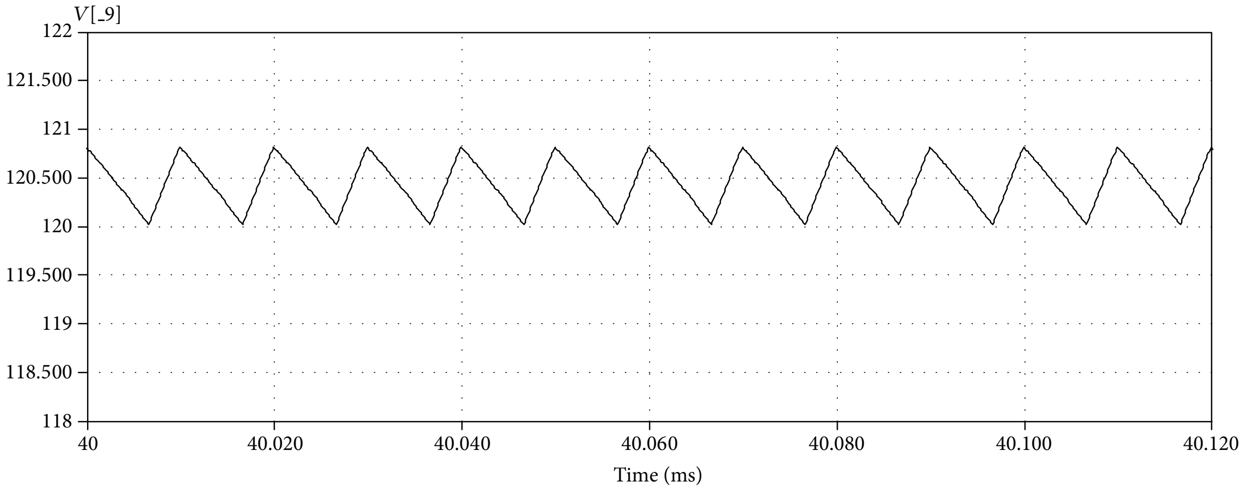

t	y	Min$X$	Max$X$	Min$Y$	Max$Y$	Mean	RMS	Peak-peak	Abs mean	RMS ac	Integral	Ripple	Ripple fac. . .	Harmonic. . .	Form fact. . .
40.007 m	120.029	0	50 m	0	157.198	119.504	119.626	157.198	119.504	5.402	5.975	1	1.315	45.154 m	1

Figure 28: Zoom on output voltage, V_{Out}.

$$I_{\mathrm{IC}\,\Delta} = \begin{cases} \sqrt{\Delta i^2_{L_n\,\max} \cdot \dfrac{n\cdot\left[[2-(n+1)\cdot d]^2\cdot(d-0/n)^3+[0-(n+0)\cdot d]^2\cdot(1/n-d)^3\right]}{12\cdot\left(3-2\cdot\sqrt{2}\right)^2\cdot(1+d)^2}} & \text{if } \dfrac{0}{n}\le d\le\dfrac{1}{n} \\ \sqrt{\Delta i^2_{L_n\,\max} \cdot \dfrac{n\cdot\left[[4-(n+2)\cdot d]^2\cdot(d-1/n)^3+[2-(n+1)\cdot d]^2\cdot(2/n-d)^3\right]}{12\cdot\left(3-2\cdot\sqrt{2}\right)^2\cdot(1+d)^2}} & \text{if } \dfrac{1}{n}\le d\le\dfrac{2}{n} \\ \sqrt{\Delta i^2_{L_n\,\max} \cdot \dfrac{n\cdot\left[[6-(n+3)\cdot d]^2\cdot(d-2/n)^3+[4-(n+2)\cdot d]^2\cdot(3/n-d)^3\right]}{12\cdot\left(3-2\cdot\sqrt{2}\right)^2\cdot(1+d)^2}} & \text{if } \dfrac{2}{n}\le d\le\dfrac{3}{n} \\ \vdots & \vdots \\ \sqrt{\Delta i^2_{L_n\,\max} \cdot \dfrac{n\cdot\left[[2\cdot n-(n+n)\cdot d]^2\cdot(d-(n-1)/n)^3+[(2\cdot n-2)-(n+n-1)\cdot d]^2\cdot(n/n-d)^3\right]}{12\cdot\left(3-2\cdot\sqrt{2}\right)^2\cdot(1+d)^2}} & \text{if } \dfrac{n-1}{n}\le d\le\dfrac{n}{n}. \end{cases} \tag{18}$$

The current variation $\Delta i_{L_n\,\max}$ in this formula is selected in relation to the rated average inductance current $I_{L_n\,\mathrm{AV}}$ during the circuit dimension. This will mean that with the same circuit dimension and increasing number of phases, the current variation is reduced.

The geometrical addition of rectangle and triangle RMS components results in the total capacitor current for an n-phase hybrid boost DC/DC converter. Consider

$$I_{\mathrm{IC}} = \sqrt{I^2_{\mathrm{IC}\,\Pi} + I^2_{\mathrm{IC}\,\Delta}}. \tag{19}$$

Figure 12 shows the RMS current in the input capacitors of multiphase DC/DC converters. The current load of the capacitor decreases with the increasing number of phases. The influence of the rectangle RMS component is clearly dominant (dotted lines, $i_{L_n\,\max} = 0$). The maximum capacitor current component produced from the rectangle portion is smaller by a factor of $1/n$ for n-phase converters. The triangle capacitor current is not dependent on the converter power and has, for all loads, the same value. In case of rated power the additional load from the triangle current in the capacitors is small.

3.2. DC/DC Converter Output Circuit. Figure 13 shows the current waveforms at the output of a two-phase hybrid boost DC/DC converter. First, the currents in both inductors and the output current of phase 1 are represented. In the middle the current of phase 2 is shown. The triangle inductance current of the two phases is shifted within about a half pulse period of each other. At switched-off times, the inductors are connected in series and the current flows to the output phase, just as in a single-phase converter. However, in this circuit, the overall output phase current I_{OP} consists of the sum of all the output phase currents. The overall output phase current I_{OP} with the DC-component I_{Out} is shown Figure 13. It is assumed that only the DC-current is flowing in the circuit output; the total AC-component of the overall output phase current I_{OP} flows in the output capacitor. In comparison to a single-phase hybrid boost converter this current is clearly smaller. In addition, the frequency of the capacitor current has been doubled.

The necessary output capacity of the multiphase hybrid boost converter will next be calculated. Compared to a single-phase design, the output capacitor current is reduced and the current frequency is increased by the number of phases. As a consequence the current in the capacitor has a voltage variation at the output. For the capacitor design the permissible static voltage variation in general is selected at less than 1% of the rated output voltage. Consider

$$C_{\mathrm{O}} = \frac{T_{\mathrm{P}}\cdot I_{L_n\,\mathrm{AV}}}{4\cdot n\cdot\Delta u_{\mathrm{Out\,max}}} \quad \text{with } \Delta u_{\mathrm{Out\,max}} \le 0.01\cdot u_{\mathrm{Out}\,R}. \tag{20}$$

The RMS current in the output capacitor C_{O} will next be calculated for multiphase hybrid boost DC/DC converters. The output capacitor current for a two-phase converter is represented in Figure 13. Like the input capacitor, the output capacitor current can also be split into a rectangle and a triangle component. The RMS current of the rectangle portion for multiphase converters is shown in the formula below:

$$I_{\mathrm{OC}\,\Pi} = \begin{cases} \sqrt{I^2_{L_n\,\mathrm{AV}}\cdot n^2\cdot\left(d-\dfrac{0}{n}\right)\cdot\left(\dfrac{1}{n}-d\right)} & \text{if } \dfrac{0}{n}\le d\le\dfrac{1}{n} \\ \sqrt{I^2_{L_n\,\mathrm{AV}}\cdot n^2\cdot\left(d-\dfrac{1}{n}\right)\cdot\left(\dfrac{2}{n}-d\right)} & \text{if } \dfrac{1}{n}\le d\le\dfrac{2}{n} \\ \sqrt{I^2_{L_n\,\mathrm{AV}}\cdot n^2\cdot\left(d-\dfrac{2}{n}\right)\cdot\left(\dfrac{3}{n}-d\right)} & \text{if } \dfrac{2}{n}\le d\le\dfrac{3}{n} \\ \vdots & \vdots \\ \sqrt{I^2_{L_n\,\mathrm{AV}}\cdot n^2\cdot\left(d-\dfrac{n-1}{n}\right)\cdot\left(\dfrac{n}{n}-d\right)} & \text{if } \dfrac{n-1}{n}\le d\le\dfrac{n}{n} \end{cases} \tag{21}$$

The output capacitor RMS current, that is, produced by the rectangle component is exactly the same as that in the input capacitor. It is necessary to also consider that the average inductance current $I_{L_n\,\mathrm{AV}}$ becomes smaller with the increasing number of phases. The next formula shows the output capacitor RMS component produced by the triangle part of multiphase converters. Consider

$$I_{\mathrm{OC}\,\Delta}=\begin{cases}\sqrt{\Delta i^2_{L_n\,\max}\cdot\dfrac{n\cdot d^2\cdot\left[(n-1)^2\cdot(d-0/n)^3+(n-0)^2\cdot(1/n-d)^3\right]}{12\cdot\left(3-2\cdot\sqrt{2}\right)^2\cdot(1+d)^2}} & \text{if } \dfrac{0}{n}\le d\le\dfrac{1}{n}\\ \sqrt{\Delta i^2_{L_n\,\max}\cdot\dfrac{n\cdot d^2\cdot\left[(n-2)^2\cdot(d-1/n)^3+(n-1)^2\cdot(2/n-d)^3\right]}{12\cdot\left(3-2\cdot\sqrt{2}\right)^2\cdot(1+d)^2}} & \text{if } \dfrac{1}{n}\le d\le\dfrac{2}{n}\\ \sqrt{\Delta i^2_{L_n\,\max}\cdot\dfrac{n\cdot d^2\cdot\left[(n-3)^2\cdot(d-2/n)^3+(n-2)^2\cdot(3/n-d)^3\right]}{12\cdot\left(3-2\cdot\sqrt{2}\right)^2\cdot(1+d)^2}} & \text{if } \dfrac{2}{n}\le d\le\dfrac{3}{n}\\ \vdots & \vdots\\ \sqrt{\Delta i^2_{L_n\,\max}\cdot\dfrac{n\cdot d^2\cdot\left[(n-n)^2\cdot(d-(n-1)\,/n)^3+[n-(n-1)]^2\cdot(n/n-d)^3\right]}{12\cdot\left(3-2\cdot\sqrt{2}\right)^2\cdot(1+d)^2}} & \text{if } \dfrac{n-1}{n}\le d\le\dfrac{n}{n}.\end{cases}\tag{22}$$

The geometrical addition of rectangle and triangle RMS components results in the total capacitor current for n-phase converters. Consider

$$I_{\mathrm{OC}}=\sqrt{I^2_{\mathrm{OC}\,\Pi}+I^2_{\mathrm{OC}\,\Delta}}.\tag{23}$$

In Figure 14 the RMS current in the output capacitors of multiphase DC/DC converters is shown. The current load of the capacitor decreases with the increasing number of phases. If neglecting the current variation ($\Delta i_{L_n\,\max}=0$, dotted lines), the maximum current in the output capacitor C_{O} is smaller for n-phase converters by a factor of $1/n$ compared to a single-phase design. The load in the output capacitors produced by the triangle current is fixed by the inductance converter design. This capacitor current is not dependent on the converted power. If the converter is operated with rated output power, this current has only a small influence on the overall capacitor current. In the figure, the output capacitor current is represented with a current variation of $\Delta i_{L_n\,\mathrm{N}\max}=0.5I_{L_n\,\mathrm{AV}}$. The influence of the triangle current at the output capacitors is smaller than at the input side of the converter.

The calculations indicate that the triangle current load in the input and output capacitor for multiphase converters is clearly reduced. Putting this knowledge into practice, the triangle current in the inductances can be selected more largely [42, 43]. The dynamics of the hybrid boost DC/DC converter can be improved and beyond that the inductance and capacitor effort of the circuit can be reduced substantially.

Besides the calculated current in the capacitors also is flowing harmonics current produced by switching processes of the phases [44]. This current has been examined in [45–47] for different converters. In consequence, these results can also be used for a hybrid boost converter. The additional current can contribute substantially to the output capacitors, heating up the capacitors during the small load of the converter. However, with higher power the calculated capacitor current dominates. A statement for all semiconductor types cannot be made. Beyond that, this additional current is dependent on the pulse frequency of the converter.

3.3. Simulation of the Two-Phase Hybrid Boost DC/DC Converter.

We made this simulation of the two-phase hybrid boost DC/DC converter in CASPOC simulation program with a power source, not with a PV module. The following parameters are used for simulation: $P_{\mathrm{In}}=300$ W, $U_{\mathrm{In}}=60$ V, $I_{\mathrm{In}}=5$ A, $L_{11}=L_{21}=L_{12}=L_{22}=823.55\,\mu$H, $C_{\mathrm{I}}=15.625\,\mu$F, $C_{\mathrm{O}}=5.208\,\mu$F, and $f_s=50$ kHz.

In previous Figures 15, 16, 17, 18, 19, 20, 21, 22, 23, 24, 25, 26, 27, and 28 are presented the results of simulation. Figure 16 presents the PWM pulses applied to switch 1, corresponding to first phase of the converter, respective the PWM pulses applied to switch 2, corresponding to the second phase of the converter. Figure 17 show the input current of phase 1, Figure 18 show the input current of phase 2, and the overall input phase current which consists of the sum of all the input phase currents, in our case phase one and phase two it is presented in Figure 19. It is obvious from Figure 20 that the currents of phase one through inductors L_{11} and L_{21} ($i_{L_{11}}$, $i_{L_{21}}$) are equal. The currents of phase two through inductors L_{12} and L_{22} ($i_{L_{12}}$, $i_{L_{22}}$) are equal, but here is represented just one of them in Figure 21. Output current of phase 1, respective 2, and the overall output phase current which consists of the sum of all the output phase currents, in our case phase one and phase two, are presented in Figures 22, 23, and 24. In the last figures are presented the output current and voltage, and the ripple of them.

4. Conclusion

Beginning from a step-up hybrid boost converter which was introduced in [22], after analyses this circuit and seeing if it is suitable for a PV system, we realize that one of the main disadvantages of this circuit is that the effort for the input and output capacitor, in the case of a single-phase DC/DC converter, is very high. This is the same with the effort of the inductors. A method for reducing this disadvantage was based on the same structure of the hybrid boost converter but built in a multiphase design. To ensure that all the phases of the converter operate at the same switching frequency and with phase-shift between them, we used interleaving switching strategy. After we analyze this new multiphase hybrid boost converter, made the theoretical calculation, and sketch the waveform, our presumption became true. The effort of the inductors, of the input and output capacitor, is decreased and at the same time their size is reduced. The frequency of the capacitor currents is increased with the number of phase. To validate and confirm our theoretical calculation, we simulate this circuit in CASPOC [48] simulation program.

Therefore, how it is obvious from theoretical calculation and waveforms associated to it, compared with the simulation waveforms, we can see a very good accordance. Based on this, next step will be to put this circuit into practice.

Conflict of Interests

The authors declare that there is no conflict of interests regarding the publication of this paper.

Acknowledgments

This work was partially supported by the strategic Grant POSDRU 107/1.5/S/77265, inside POSDRU Romania 2007–2013 cofinanced by the European Social Fund—Investing in People.

References

[1] A. Campoccia, L. Dusonchet, E. Telaretti, and G. Zizzo, "Comparative analysis of different supporting measures for the production of electrical energy by solar PV and Wind systems: four representative European cases," *Solar Energy*, vol. 83, no. 3, pp. 287–297, 2009.

[2] T. Andrejašič, M. Jankovec, and M. Topič, "Comparison of direct maximum power point tracking algorithms using en 50530 dynamic test procedure," *IET Renewable Power Generation*, vol. 5, no. 4, pp. 281–286, 2011.

[3] S. S. W. Walker, N. K. Sooriyaarachchi, N. D. B. Liyanage, P. A. G. S. Abeynayake, and S. G. Abeyratne, "Comparative analysis of speed of convergence of MPPT techniques," in *Proceedings of the 2011 6th International Conference on Industrial and Information Systems (ICIIS '11)*, pp. 522–526, Kandy, Sri Lanka, August 2011.

[4] M. Liserre, T. Sauter, and J. Y. Hung, "Future energy systems: integrating renewable energy sources into the smart power grid through industrial electronics," *IEEE Industrial Electronics Magazine*, vol. 4, no. 1, pp. 18–37, 2010.

[5] J. M. Carrasco, L. G. Franquelo, J. T. Bialasiewicz et al., "Power-electronic systems for the grid integration of renewable energy sources: a survey," *IEEE Transactions on Industrial Electronics*, vol. 53, no. 4, pp. 1002–1016, 2006.

[6] A. Das, V. K. Rajput, A. Chakraborty, M. Dhar, S. Ray, and R. Dutta, "A new transformerless DC-DC converter with high voltage gain," in *Proceedings of the 2010 International Conference on Industrial Electronics, Control and Robotics (IECR '10)*, pp. 91–94, December 2010.

[7] O. Abdel-Rahim, M. Orabi, E. Abdelkarim, M. Ahmed, and M. Z. Youssef, "Switched inductor boost converter for PV applications," in *Proceedings of the 27th Annual IEEE Applied Power Electronics Conference and Exposition (APEC '12)*, pp. 2100–2106, February 2012.

[8] R. J. Wai, C. Y. Lin, R. Y. Duan, and Y. R. Chang, "High-efficiency dc-dc converter with high voltage gain and reduced switch stress," *IEEE Transactions on Industrial Electronics*, vol. 54, no. 1, pp. 354–364, 2007.

[9] B. R. Lin and F. Y. Hsieh, "Soft-switching zeta-flyback converter with a buck-boost type of active clamp," *IEEE Transactions on Industrial Electronics*, vol. 54, no. 5, pp. 2813–2822, 2007.

[10] K. C. Tseng and T. J. Liang, "Novel high-efficiency step-up converter," *IEE Proceedings: Electric Power Applications*, vol. 151, no. 2, pp. 182–190, 2004.

[11] T. F. Wu, Y. S. Lai, J. C. Hung, and Y. M. Chen, "Boost converter with coupled inductors and buck-boost type of active clamp," *IEEE Transactions on Industrial Electronics*, vol. 55, no. 1, pp. 154–162, 2008.

[12] W. Li, X. Lv, Y. Deng, J. Liu, and X. He, "A review of non-isolated high step-up DC/DC converters in renewable energy applications," in *Proceedings of the 24th Annual IEEE Applied Power Electronics Conference and Exposition (APEC '09)*, pp. 364–369, IEEE, February 2009.

[13] A. Tomaszuk and A. Krupa, "High efficiency high step-up DC/DC converters—a review," *Bulletin of the Polish Academy of Sciences: Technical Sciences*, vol. 59, no. 4, pp. 475–483, 2011.

[14] R. J. Wai, W. H. Wang, and C. Y. Lin, "High-performance stand-alone photovoltaic generation system," *IEEE Transactions on Industrial Electronics*, vol. 55, no. 1, pp. 240–250, 2008.

[15] V. M. E. Thirumurugan and S. B. E. Sugumar, "High-efficiency step-up converter by using PV system with reduced diode stresses sharing," *International Journal of Engineering and Advanced Technology*, vol. 4, no. 2, pp. 319–324, 2014.

[16] Y. P. Hsieh, J. F. Chen, T. J. Liang, and L. S. Yang, "Novel high step-up dc-dc converter for distributed generation system," *IEEE Transactions on Industrial Electronics*, vol. 60, no. 4, pp. 1473–1482, 2013.

[17] S. M. Chen, T. J. Liang, L. S. Yang, and J. F. Chen, "A safety enhanced, high step-up DC-DC converter for AC photovoltaic module application," *IEEE Transactions on Power Electronics*, vol. 27, no. 4, pp. 1809–1817, 2012.

[18] S. Y. Tseng and H. Y. Wang, "A photovoltaic power system using a high step-up converter for DC load applications," *Energies*, vol. 6, no. 2, pp. 1068–1100, 2013.

[19] S. M. Chen, T. J. Liang, L. S. Yang, and J. F. Chen, "A cascaded high step-up DC-DC converter with single switch for microsource applications," *IEEE Transactions on Power Electronics*, vol. 26, no. 4, pp. 1146–1153, 2011.

[20] Y. P. Hsieh, J. F. Chen, T. J. Liang, and L. S. Yang, "A novel high step-up DC-DC converter for a microgrid system," *IEEE Transactions on Power Electronics*, vol. 26, no. 4, pp. 1127–1136, 2011.

[21] K. Varuna and S. Kumar, "Modeling & simulation of grid connected photovoltaic system using high step up DC/DC converter," *International Journal of Latest Advances in Electronic and Electric Engineering*, vol. 2, no. 2, pp. 153–158, 2013.

[22] B. Axelrod, Y. Berkovich, and A. Ioinovici, “Switched-capacitor/switched-inductor structures for getting transformerless hybrid DC-DC PWM converters,” *IEEE Transactions on Circuits and Systems I: Regular Papers*, vol. 55, no. 2, pp. 687–696, 2008.

[23] L. Huber and M. M. Jovanovic, “Design approach for server power supplies for networking applications,” in *Proceedings of the 15th Annual IEEE Applied Power Electronics Conference and Exposition (APEC ’00)*, pp. 1163–1169, February 2000.

[24] F. Renken and V. Karrer, “DC/DC converters for automotive board-net structures,” in *Proceedings of the International Power Electronics and Motion Control Conference (EPE-PEMC ’04)*, Riga, Latvia, September 2004.

[25] F. Renken, “High temperature electronics for future hybrid drive systems,” in *Proceedings of the 13th European Conference on Power Electronics and Applications (EPE ’09)*, pp. 1–7, Barcelona, Spain, September 2009.

[26] L. Huber and M. M. Jovanovic, “Design approach for server power supplies for networking applications,” in *Proceedings of the 15th Annual IEEE Applied Power Electronics Conference and Exposition (APEC ’00)*, pp. 1163–1169, New Orleans, La, USA, February 2000.

[27] K. P. Yalamanchili, M. Ferdowsi, and K. Corzine, “New double input DC-DC converters for automotive applications,” in *Proceedings of the 2006 IEEE Vehicle Power and Propulsion Conference (VPPC ’06)*, Windsor, UK, September 2006.

[28] M. Gavriş, O. Cornea, and N. Muntean, “Multiple input DC-DC topologies in renewable energy systems—a general review,” in *Proceedings of the 3rd IEEE International Symposium on Exploitation of Renewable Energy Sources (EXPRES ’11)*, pp. 123–128, Subotica, Serbia, March 2011.

[29] M. J. V. Vázquez, J. M. A. Márquez, and F. S. Manzano, “A methodology for optimizing stand-alone PV-system size using parallel-connected DC/DC converters,” *IEEE Transactions on Industrial Electronics*, vol. 55, no. 7, pp. 2664–2673, 2008.

[30] T. Hosi, “Control circuit for parallel operation of self-commutating inverters,” Japanese Patent S56-13101, 1975.

[31] R. Gules, J. D. P. Pacheco, H. L. Hey, and J. Imhoff, “A maximum power point tracking system with parallel connection for PV stand-alone applications,” *IEEE Transactions on Industrial Electronics*, vol. 55, no. 7, pp. 2674–2683, 2008.

[32] S. V. G. Oliveira and I. Barbi, “A three-phase step-up DC-DC converter with a three-phase high frequency transformer,” in *Proceedings of the IEEE International Symposium on Industrial Electronics 2005 (ISIE ’05)*, vol. 2, pp. 571–576, June 2005.

[33] P. Thounthong and B. Davat, “Study of a multiphase interleaved step-up converter for fuel cell high power applications,” *Energy Conversion and Management*, vol. 51, no. 4, pp. 826–832, 2010.

[34] G. Y. Choe, J. S. Kim, H. S. Kang, and B. K. Lee, “An optimal design methodology of an interleaved boost converter for fuel cell applications,” *Journal of Electrical Engineering and Technology*, vol. 5, no. 2, pp. 319–328, 2010.

[35] H. B. Shin, J. G. Park, S. K. Chung, H. W. Lee, and T. A. Lipo, “Generalised steady-state analysis of multiphase interleaved boost converter with coupled inductors,” *IEE Proceedings: Electric Power Applications*, vol. 152, no. 3, pp. 584–594, 2005.

[36] T. Soepraptob, S. Sidopeksoc, and M. Taufik, “A Comparison of multiple boost configurations for small renewable energy battery storage systems,” in *Proceedings of the International Conference on Sustainable Energy Engineering and Application*, pp. 93–96, Yogyakarta, Indonesia, 2012.

[37] W. Xiao, B. Zhang, and D. Qiu, “Analysis and design of an automatic-current-sharing control based on average-current mode for parallel boost converters,” in *Proceedings of the CES/IEEE 5th International Power Electronics and Motion Control Conference (IPEMC ’06)*, pp. 1293–1297, August 2006.

[38] T. Taufik, R. Prasetyo, D. Dolan, and D. Garinto, “A new multiphase multi-interleaving buck converter with bypass LC,” in *Proceedings of the 36th Annual Conference of the IEEE Industrial Electronics Society (IECON ’10)*, pp. 291–295, Phoenix, Ariz, USA, November 2010.

[39] Z. Lukí, S. M. Ahsanuzzaman, A. Prodí, and Z. Zhao, “Self-tuning sensorless digital current-mode controller with accurate current sharing for multi-phase DC-DC converters,” in *Proceedings of the 24th Annual IEEE Applied Power Electronics Conference and Exposition (APEC ’09)*, pp. 264–268, Washington, DC, USA, February 2009.

[40] P. L. Wong, P. Xu, B. Yang, and F. C. Lee, “Performance improvements of interleaving VRMs with coupling inductors,” *IEEE Transactions on Power Electronics*, vol. 16, no. 4, pp. 499–507, 2001.

[41] T. Taufik, T. Gunawan, D. Dolan, and M. Anwari, “Design and analysis of two-phase boost DC-DC converter,” in *World Academy of Science, Engineering and Technology*, pp. 912–916, 2010.

[42] F. Renken, V. Karrer, and P. Skotzek P, “The starter generator—systems, functions and components,” in *Proceedings of the 30th FISITA World Automotive Congress*, Barcelona, Spain, May 2004.

[43] V. Karrer and F. Renken, “Power electronics for the integrated starter generator,” in *Proceedings of the Optimization of the Power Train in Vehicles by Using the Integrated Starter Generator (ISG ’02)*, pp. 222–247, Haus der Technik e. V., Munich, Germany, 2002.

[44] F. Renken, “Analytic calculation of the DC-link capacitor current for pulsed single-phase H-bridge inverters,” *European Power Electronics and Drives Journal*, vol. 13, no. 4, pp. 13–19, 2003.

[45] F. Renken, “Analytic calculation of the DC-link capacitor current for pulsed single-phase H-bridge inverters,” *European Power Electronics and Drives Journal*, vol. 13, no. 4, pp. 13–19, 2003.

[46] F. Renken, “Analyses of the DC-link current in discontinuous modulated three-phase inverters,” in *Proceedings of the 12th International Power Electronics and Motion Control Conference (EPE-PEMC ’06)*, Portorož, Slovenia, August-September 2006.

[47] F. Renken, “DC-link current in pulsed H-bridge inverters,” in *Proceedings of the International Exhibition & Conference for Power Electronics, Intelligent Motion and Power Quality (PCIM ’09)*, Nürnberg, Germany, May 2009.

[48] “CASPOC Simulation program,” http://www.caspoc.com/.

Hindawi Publishing Corporation
International Journal of Photoenergy
Volume 2014, Article ID 437641, 9 pages
http://dx.doi.org/10.1155/2014/437641

Research Article

Reconfigurable Charge Pump Circuit with Variable Pumping Frequency Scheme for Harvesting Solar Energy under Various Sunlight Intensities

Jeong Heon Kim, Sang Don Byeon, Hyun-Sun Mo, and Kyeong-Sik Min

School of Electrical Engineering, Kookmin University, Seoul 136-702, Republic of Korea

Correspondence should be addressed to Kyeong-Sik Min; mks@kookmin.ac.kr

Received 13 November 2013; Revised 1 March 2014; Accepted 1 March 2014; Published 15 April 2014

Academic Editor: Ismail H. Altas

We propose variable pumping frequency (VPF) scheme which is merged with the previous reconfigurable charge pump (RCP) circuit that can change its architecture according to a given sunlight condition. Here, merging the VPF scheme with the architecture reconfiguration can improve percentage output currents better by 21.4% and 22.4% than RCP circuit with the fixed pumping frequencies of 7 MHz and 15 MHz, respectively. Comparing the VPF scheme with real maximum power points (MPP), the VPF can deliver 91.9% of the maximum amount of output current to the load on average. In terms of the power and area overheads, the VPF scheme proposed in this paper consumes the power by 0.4% of the total power consumption and occupies the layout area by 1.61% of the total layout area.

1. Introduction

Solar energy is one of the most popular energy sources that can be harvested from environment because of its ubiquitous availability and high power density, and that DC voltage and current can be directly obtained from sunlight [1–3]. Due to these advantages that are mentioned just earlier, harvesting solar energy becomes more popular and useful in various applications such as wireless sensor networks (WSN) [4, 5]. Among various solar energy harvesting systems, in this paper, we consider a simple capacitor-based charge pump circuit for harvesting a small amount of solar energy [6, 7]. The charge pump circuit with small-scale energy harvesting can be implemented with low cost and simple architecture; thus, it can be suitable to tiny low-power and low-cost systems such as WSN systems.

One problem in developing solar energy harvesting systems is that sunlight is not static but changes dynamically. As a result of this dynamic variation of sunlight, an amount of solar energy that can be converted to electrical voltage and current by energy harvesting systems can be changed. When sunlight is very strong, the amount of solar energy that can be converted to electrical voltage and current is large. On the contrary, for weak sunlight, the amount of solar energy is small; thereby, the converted amounts of voltage and current become small, too. Figure 1(a) shows the current-voltage relationship of solar cell for various sunlight conditions. For the sunlight intensity as strong as 38 mA, maximum power point (MPP) that means a bias point that can deliver maximum amount of current-voltage product of solar cell is given at V_{SC} = 2.97 V and I_{SC} = 32.7 mA. Here V_{SC} and I_{SC} are the solar cell's voltage and current, respectively. If the sunlight intensity becomes as small as 2 mA in weak sunlight condition, the MPP moves to V_{SC} = 1.81 V and I_{SC} = 1.61 mA, as shown in Figure 1(a). Figure 1(b) shows the relationship of solar cell's voltage and power, where the solar cell's power is calculated with the product of V_{SC} and I_{SC}. One more thing to note here is that the sunlight intensity should be expressed by lumen or candela unit. In this paper, however, we expressed the sunlight intensity by amount of solar cell's photocurrent, because the solar cell's photocurrent is directly depending on the sunlight intensity [8]. Instead of using lumen or candela, the solar cell's photocurrent

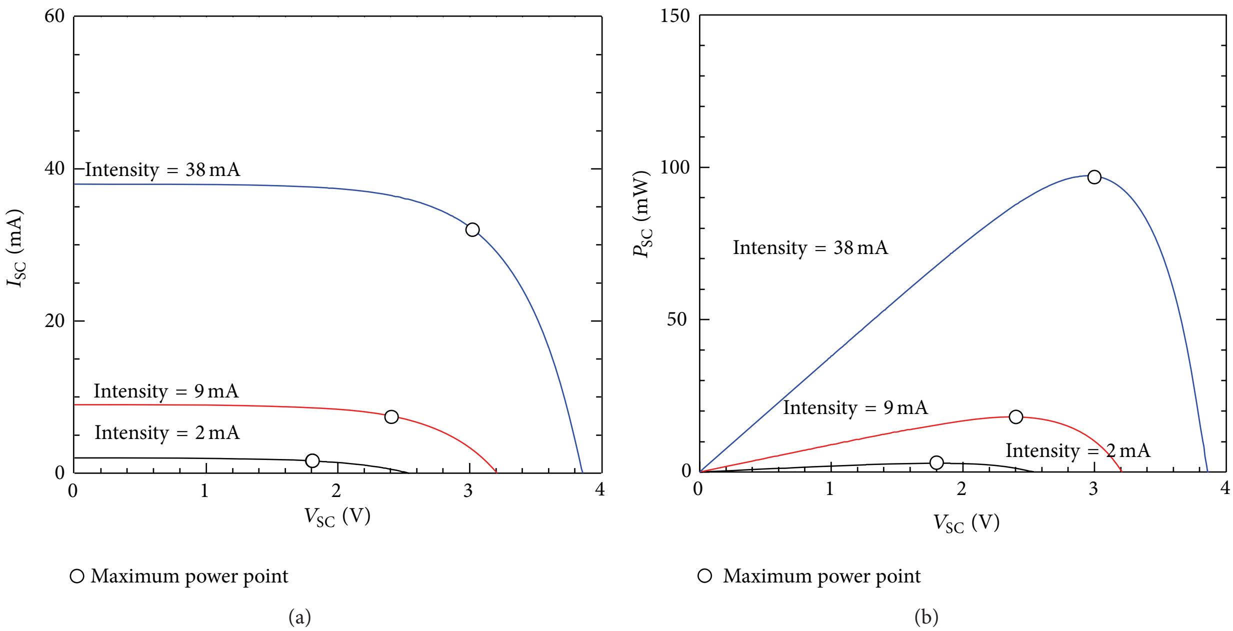

FIGURE 1: (a) Relationship of solar cell's current (I_{SC}) and voltage (V_{SC}) according to sunlight intensity variation. (b) Relationship of solar cell's power (P_{SC}) and voltage (V_{SC}) according to sunlight intensity variation.

for representing sunlight intensity can make us easier in understanding the energy harvesting system.

Lee et al. proposed a reconfigurable charge pump (RCP) circuit that can adjust the architecture among the serial, the parallel-serial, and the parallel modes according to sunlight variation to deliver the largest amount of power to the output at a given sunlight condition [9]. The conceptual diagrams of operation of RCP circuit are shown in Figures 2(a), 2(b), and 2(c), where weak, moderate, and strong sunlight conditions are illustrated, respectively. In Figure 1(a), we can know that V_{SC} and I_{SC} in weak sunlight are smaller than moderate and strong sunlight conditions. In Figure 2(a) V_{SC} in weak sunlight is as low as 1.81 V which is about 71.3% of the open-circuit voltage (V_{OC}) in Figure 1(a). On the contrary, the output voltage, V_{BAT}, should be the same with the charging voltage of lithium ion batteries, that is, as high as 4.2 V. Thus the number of stages of charge pump's architecture should be large enough to generate 4.2 V from 1.81 V.

One more thing to consider here is that an amount of pumping current should be small in weak sunlight because the solar cell can deliver only small amounts of V_{SC} and I_{SC} to the load. Here we can think that the serial architecture of charge pump in Figure 2(a) is more suitable than the parallel-serial and parallel architectures that are shown in Figures 2(b) and 2(c), respectively. In the serial architecture, 4 unit pumps (UPs) are connected in series, as shown in Figure 2(a).

In Figure 2(b), we assume that sunlight intensity is moderate, where V_{SC} becomes 2.40 V, that is, higher than $V_{SC} = 1.81$ V in weak sunlight. For the amount of I_{SC}, I_{SC} in moderate sunlight is larger than weak sunlight, as shown in Figure 1(a). Owing to these higher V_{SC} and larger I_{SC} in the moderate sunlight condition than the weak condition, we can consider the parallel-serial architecture more suitable than the serial in Figure 2(a) in delivering larger output current to the load. In the parallel-serial architecture, two UPs are in parallel and two parallel-connected pumps are in series, as shown in Figure 2(b). Figure 2(c) shows the parallel architecture that has four UPs in parallel. This parallel architecture can be thought to be suitable to deliver the largest amount of output current to the load than the serial and parallel-serial architectures in Figures 2(a) and 2(b), respectively.

As explained just earlier, RCP circuit can maximize the amount of output current, by choosing the most suitable architecture among the serial, parallel-serial, and parallel architectures at a given sunlight condition [9]. However, performance of RCP circuit can be improved more by adding variable pumping frequency (VPF) scheme to the reconfigurable architecture. By merging the VPF scheme with the reconfigurable architecture, the charge pump which is proposed in this paper can track MPPs better than charge pumps only with the reconfigurable architecture.

2. Variable Pumping Frequency Scheme with Reconfigurable Charge Pump's Architecture

Figures 3(a), 3(b), and 3(c) show the amounts of output current of RCP circuit for weak, moderate, and strong sunlight, respectively, with varying the pumping frequency. In Figure 3(a) with weak sunlight intensity from 1.5 mA to 2.5 mA, the pumping frequency is varied from 1 MHz to 30 MHz to find the best pumping frequency at which the charge pump can deliver the largest amount of output current [10]. From Figure 3(a), it is indicated that the MPP is found around $f_{PUMP} = 2.5$ MHz for the sunlight intensity as low as 1.5 mA. If the sunlight intensity becomes 2 mA, the best

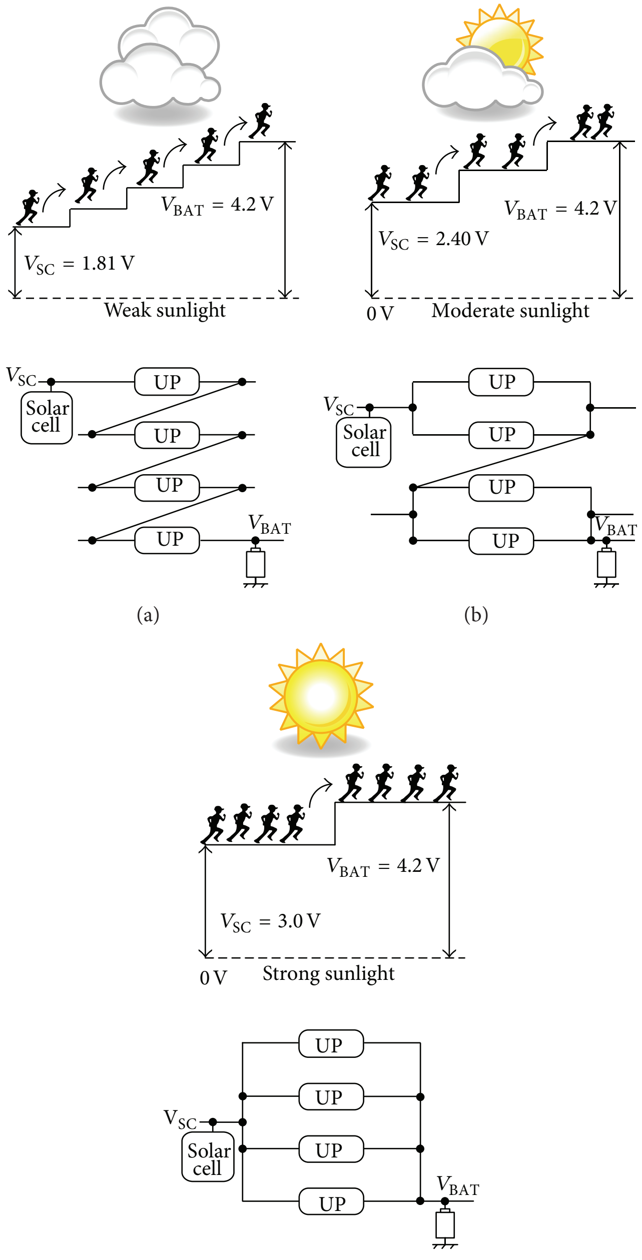

Figure 2: (a) Conceptual diagram of operation of RCP circuit and the serial architecture in weak sunlight condition, (b) conceptual diagram of operation of RCP circuit and the parallel-serial architecture in moderate sunlight condition, and (c) conceptual diagram of operation of RCP circuit and the parallel architecture in strong sunlight condition.

pumping frequency of delivering the maximum power to the load moves to around 2.75 MHz. For the light intensity as much as 2.5 mA in Figure 3(a), the charge pump can be the best in harvesting solar energy around $f_{PUMP} = 3$ MHz. Here we can know that pumping frequency for MPP becomes higher with increasing the sunlight intensity.

Similarly, with moderate sunlight, we varied the pumping frequency to find the MPPs, where the largest amount of power can be harvested from environmental solar energy. For the moderate sunlight intensities of 3 mA, 9 mA, and 15 mA, respectively, in Figure 3(b), the pumping frequencies of MPPs are found at 3 MHz, 7 MHz, and 9 MHz, respectively. Figure 3(c) shows the amounts of output current with strong sunlight intensities such as 18 mA, 38 mA, and 58 mA. The circuit simulation indicates that the pumping frequencies of 9 MHz, 15 MHz, and 23 MHz can deliver the maximum amounts of output current to the load for the sunlight intensities of 18 mA, 38 mA, and 58 mA, respectively.

From Figures 3(a), 3(b), and 3(c), we can know that the VPF scheme that is merged with the reconfigurable

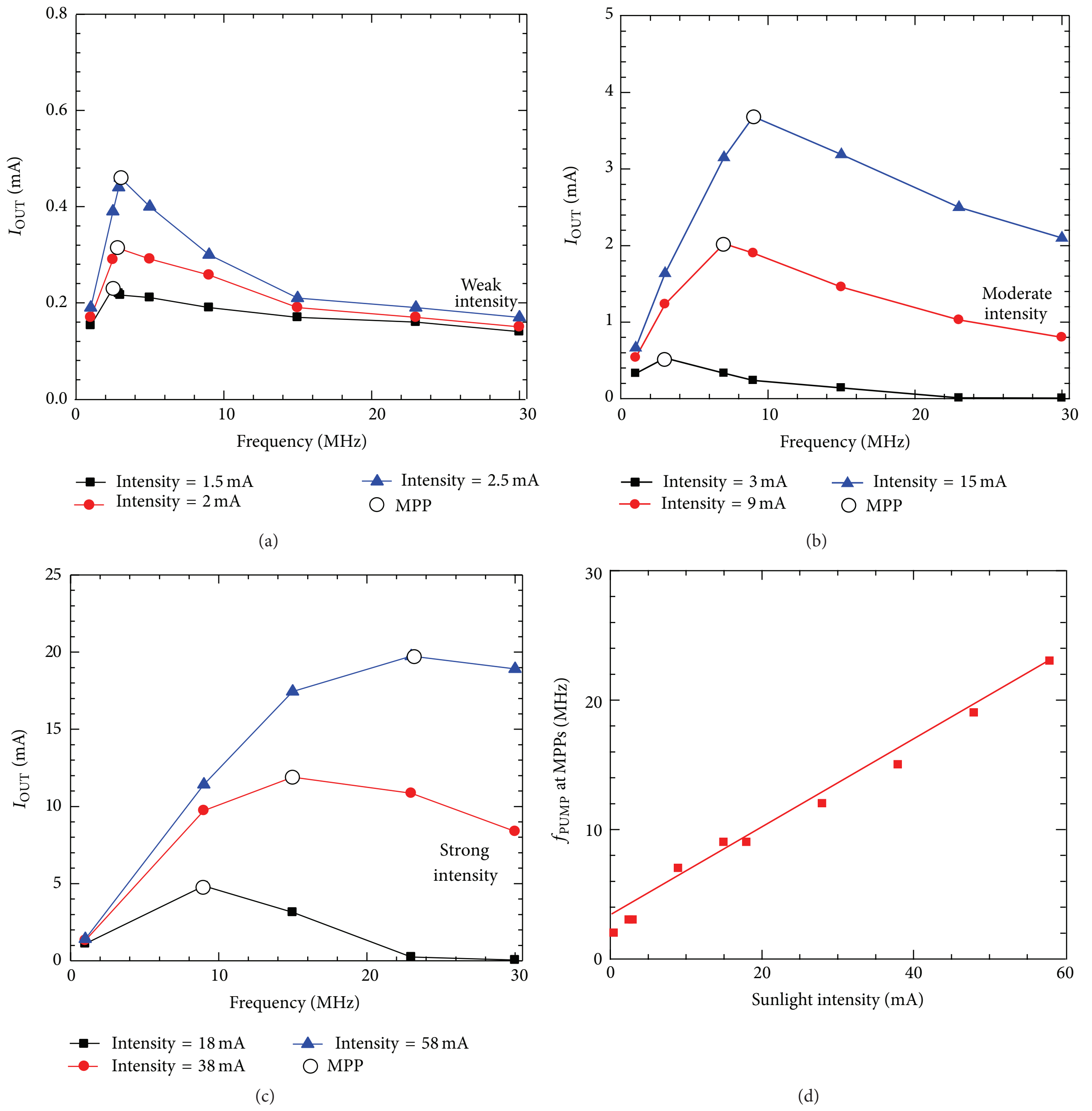

FIGURE 3: (a) Output current of RCP circuit in weak sunlight intensities with varying pumping frequency. (b) Output current in moderate sunlight with varying pumping frequency. (c) Output current in strong sunlight with varying pumping frequency. (d) The pumping frequencies at MPPs with varying sunlight intensity from 1.5 mA to 58 mA.

architecture can harvest more power from environment than the charge pump circuit with only the fixed pumping frequency. Figure 3(d) shows the pumping frequencies at MPPs with varying sunlight intensity from 1.5 mA to 58 mA that includes weak, moderate, and strong sunlight intensities. From Figure 3(d), it is indicated that the pumping frequency as low as 2.5 MHz for the sunlight intensity = 1.5 mA can harvest the largest amount of power from solar energy. If the sunlight intensity becomes 28 mA, the frequency at MPP is increased to 12 MHz. For the largest sunlight intensity as large as 58 mA, the best frequency for delivering the maximum amount of output current can be found around 23 MHz.

Figure 4 compares output currents of RCP circuit with the fixed pumping frequencies of f_{PUMP} = 7 MHz and f_{PUMP} = 15 MHz and the found MPPs that are shown in Figures 3(a), 3(b), and 3(c). Here the fixed pumping frequency of f_{PUMP} = 7 MHz is decided by the MPP of moderate sunlight intensity as low as 9 mA. If we fix pumping frequency of RCP circuit by 7 MHz, the amounts of output current at f_{PUMP} = 7 MHz are very similar with the maximum output currents in moderate

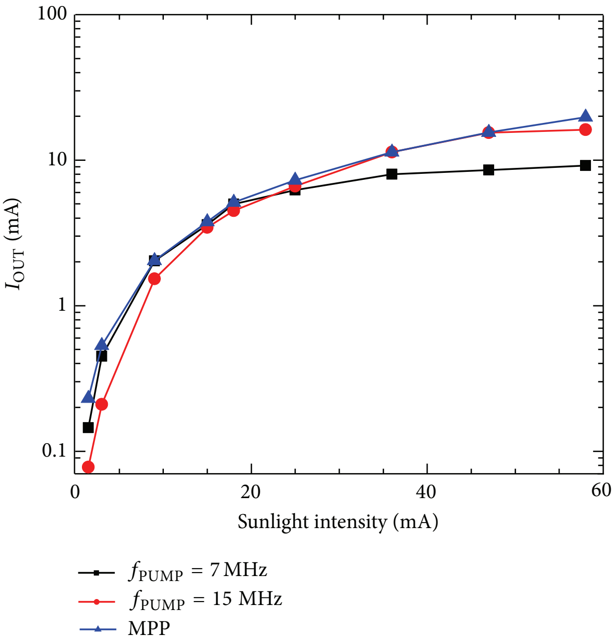

Figure 4: Comparison of output currents of RCP circuit with the fixed pumping frequencies (f_{PUMP} = 7 MHz and f_{PUMP} = 15 MHz) and MPPs that are shown in Figures 3(a), 3(b), and 3(c).

sunlight intensities from 2.5 mA to 15.5 mA. On the contrary, if the intensity is increased stronger than 15.5 mA, the output current of RCP circuit with f_{PUMP} = 7 MHz begins to deliver much smaller output current than MPPs. For the fixed pumping frequency of 15 MHz, the amounts of output current with f_{PUMP} = 15 MHz are very comparable to the MPPs in strong sunlight intensities from 15.5 mA to 58 mA. However, for lighter intensities, the fixed pumping frequency of 15 MHz cannot give the output current as much as MPPs.

From Figure 4, we can know that no fixed frequency can have the amounts of output current that are similar with the MPPs in the entire range of sunlight intensity. Thus, we need to propose the VPF scheme that can be added to the previous RCP circuit, where the pumping frequency can be changed according to a given sunlight condition to deliver the largest amount of output current to the load at this given intensity.

To give more analytical explanation on relationship of MPP and f_{PUMP}, we can start from the following equation of the input current of RCP circuit, I_{IN} [10]:

$$I_{IN} = \frac{1}{\eta} I_{OUT} + \alpha_1 f_{PUMP}. \tag{1}$$

Here, η is the ideal current efficiency of RCP circuit and α_1 is the proportional coefficient between the charge pump's input current and the pumping frequency that accounts for switching loss and reverse current of RCP circuit that depend on the pumping frequency [10]. In this paper, we can think that the solar cell delivers the input current to RCP circuit with the additional control circuit which is needed to adjust the architecture and pumping frequency according to a sunlight variation. The solar cell's current can be expressed with [10]

$$I_{SC} = I_{IN} + I_{DC} + \alpha_2 f_{PUMP}. \tag{2}$$

Here I_{DC} means the static current which is consumed in RCP circuit and the controller circuit. α_2 means the switching loss in the additional control circuit. By combining (1) and (2), we can calculate I_{OUT} with

$$I_{OUT} = \eta \left(I_{SC} - I_{DC} - (\alpha_1 + \alpha_2) f_{PUMP} \right). \tag{3}$$

As we increase f_{PUMP}, I_{SC} becomes larger; thus, we can have more I_{OUT} at the load. However, once I_{SC} starts to saturate, I_{OUT} should be lowered because of $-(\alpha_1 + \alpha_2) f_{PUMP}$ in spite of increasing f_{PUMP}. Thus, we can have an optimum pumping frequency for a given sunlight condition, at which the charge pump circuit can deliver the largest amount of output current to the load.

From (3), we can extract three parameters of η, I_{DC}, and $\alpha_1 + \alpha_2$ using the least-square fitting method [11]. For the strong sunlight condition with the parallel architecture, the extracted values of η, I_{DC}, and $\alpha_1 + \alpha_2$ are 0.607, 3.89 μA, and 0.744 mA/Hz, respectively.

If we know the value of η, we can rewrite (3) as follows:

$$\eta I_{SC} - I_{OUT} = \eta \left(\alpha_1 + \alpha_2 \right) f_{PUMP} + \eta I_{DC}. \tag{4}$$

Equation (4) is shown in Figure 5, where the symbols represent the simulated values of $\eta I_{SC} - I_{OUT}$ and the line is calculated with $\eta(\alpha_1 + \alpha_2) f_{PUMP} + \eta I_{DC}$ using the values of η, I_{DC}, and $\alpha_1 + \alpha_2$ that are stated just earlier, as we increase the pumping frequency from 1 MHz to 30 MHz. From Figure 5, we can see that the simulated values of $\eta I_{SC} - I_{OUT}$ are in good agreement with the calculated values of $\eta(\alpha_1 + \alpha_2) f_{PUMP} + \eta I_{DC}$. The good agreement between the simulation and the model in (4) indicates that (3) can describe the charge pump's output current well.

3. New Reconfigurable Charge Pump Circuit Merged with Variable Pumping Frequency Scheme

In this session, a new RCP circuit is proposed, where the reconfigurable architecture is merged with the VPF scheme, as shown in Figure 6(a). Here the solar cell is connected to the voltage divider with the division ratio as much as 0.5. Thus we can have a voltage as high as $0.5 \cdot V_{SC}$ using the divider. By applying the sampling frequency, f_{SAMPLE} which is much slower than f_{PUMP} for the open-circuit condition, the divided voltage, $0.5 \cdot V_{OC}$ can be sampled by the sample and hold circuit (S&H). In this paper, f_{SAMPLE} used in the simulation is as slow as 1 KHz [9]. Comparing f_{SAMPLE} with f_{PUMP}, f_{SAMPLE} is ~1000x slower than f_{PUMP}; thus, the timing overhead due to the sampling of the open-circuit voltage can be ignored. Here it should be noted that $0.5 \cdot V_{OC}$ is half the sampled solar cell's voltage with the open-circuit condition. The S&H's output, $0.5 \cdot V_{OC}$, goes into the architecture reconfiguration block (ARB), where the charge pump's architecture can be

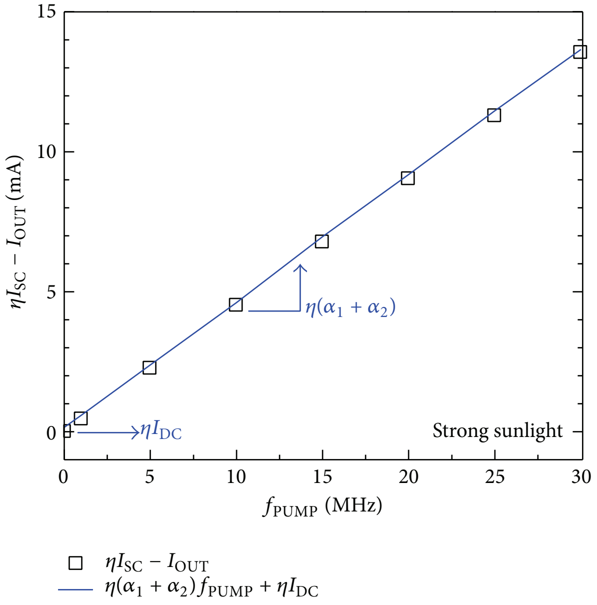

FIGURE 5: $\eta I_{SC} - I_{OUT}$ versus $\eta(\alpha_1 + \alpha_2) f_{PUMP} + \eta I_{DC}$ with increasing f_{PUMP}. The good agreement between $\eta I_{SC} - I_{OUT}$ and $\eta(\alpha_1 + \alpha_2) f_{PUMP} + \eta I_{DC}$ indicates that (3) can describe the charge pump's output current driven by the solar cell well.

reconfigured by controlling the reconfiguration switches [9]. As well explained in [9], three modes of RCP circuit are available in Figure 6(a). They are the serial, parallel-serial, and parallel architecture, respectively. The sampled $0.5 \cdot V_{OC}$ is compared with the predetermined reference voltages such as V_{REF_PM} and V_{REF_SM}; thereby, the charge pump architecture can be reconfigured. C1 and C2 are the comparators for the architecture reconfiguration. If $0.5 \cdot V_{OC} < V_{REF\_SM}$, the architecture is changed to the serial mode [9]. If $0.5 \cdot V_{OC}$ is between V_{REF_SM} and V_{REF_PM}, the circuit is reconfigured by the parallel-serial mode. When $0.5 \cdot V_{OC}$ is larger than V_{REF_PM}, the mode is fixed by the parallel architecture.

The $0.5 \cdot V_{OC}$, that is, a signal before the S&H circuit in Figure 6(a) goes into the variable frequency block (VFB), where the solar cell's voltage, V_{SC} is compared with $0.5 \cdot k \cdot V_{OC} - \Delta$ and $0.5 \cdot k \cdot V_{OC} + \Delta$ to decide the optimum pumping frequency, at which the maximum solar power can be harvested from environment. Here k is a fractional constant of V_{OC} and the value used in this simulation is 0.8. It is well known that the solar cell can deliver the maximum power to the load, when V_{SC} is close to a fractional open-circuit voltage, $k \cdot V_{OC}$, even though k can be different for various kinds of solar cells [12]. If the optimum pumping frequency is found, the voltage-controlled oscillator (VCO) applies the obtained f_{PUMP} of MPP to RCP circuit. The schematic of UP circuit is shown in the inset of Figure 6(a), where M_1 and M_3 are the precharging NMOSFETs and M_2 and M_4 are the transferring PMOSFETs. The width and length of M_1 and M_3 are 120 μm and 0.35 μm, respectively. The width and length of M_2 and M_4 are 240 μm and 0.35 μm, respectively. The pumping capacitors are CAP_1 and CAP_2 in Figure 6(a). The capacitance used in the simulation is 50 pF. CLKB and CLK are the two-phase clocking signals that enter CAP_1 and CAP_2, respectively. Figure 6(b) shows the detailed schematic of VFB with VCO circuit. For VCO circuit, the general scheme which is based on simple ring oscillator is used in this paper [13].

Figure 6(c) shows the voltage and current waveforms in Figure 6(a). If $0.5 \cdot V_{SC}$ is between $0.5 \cdot k \cdot V_{OC} - \Delta$ and $0.5 \cdot k \cdot V_{OC} + \Delta$, the charge pump (CP) in VFB keeps its output voltage, V_C, which controls the VCO. If V_C is not changed, the VCO's output frequency, f_{PUMP}, is not changed, too. Now let us explain the closed-loop operation of VPF scheme in Figure 6(a) more in detail, as shown in Figure 6(c). First, we can assume that $0.5 \cdot V_{SC}$ is larger than $0.5 \cdot k \cdot V_{OC} + \Delta$. At this time, the two comparators of C_3 and C_4 can give UP signal to CP and VCO in Figure 6(a) to increase the pumping frequency higher. As the pumping frequency becomes higher, $0.5 \cdot V_{SC}$ becomes lower. If $0.5 \cdot V_{SC}$ is between $0.5 \cdot k \cdot V_{OC} - \Delta$ and $0.5 \cdot k \cdot V_{OC} + \Delta$, the two comparators of C_3 and C_4 give STOP signal to CP and VCO; thereby, the pumping frequency is stabilized. If $0.5 \cdot V_{SC}$ is lower than $0.5 \cdot k \cdot V_{OC} - \Delta$, the comparators C_3 and C_4 generate DOWN signal to CP and VCO; thus, the pumping frequency becomes lower and $0.5 \cdot V_{SC}$ can be raised little by little until $0.5 \cdot V_{SC}$ is between $0.5 \cdot k \cdot V_{OC} - \Delta$ and $0.5 \cdot k \cdot V_{OC} + \Delta$.

4. Simulation Results and Layout

The proposed circuit is verified by SPECTRE circuit simulation which is provided by Cadence Inc. The SPECTRE simulation model was obtained from Magna 0.35 μm CMOS process technology. Figure 7(a) compares the percentage amounts of output current among 3 schemes of the reconfigurable charge pump circuit, with respect to MPPs. Here "$f_{PUMP} = 7$ MHz" in Figure 7(a) means that the output current of RCP circuit is obtained when the pumping frequency is fixed at 7 MHz. For "$f_{PUMP} = 7$ MHz", even though the sunlight condition is changed, the pumping frequency is fixed at 7 MHz for all the sunlight conditions. In Figure 7(a), the fixed pumping frequency as low as 7 MHz is decided by the fact that the charge pump circuit can deliver the maximum output current at $f_{PUMP} = 7$ MHz for the moderate sunlight condition of the intensity = 9 mA, as shown in Figure 3(b). In Figure 7(a), $f_{PUMP} = 15$ MHz is the output current of RCP circuit when the pumping frequency of Figure 6(a) is fixed at 15 MHz. Similarly, with "$f_{PUMP} = 7$ MHz", the fixed pumping frequency as high as 15 MHz is decided because the charge pump can have the largest output current for the strong sunlight condition of intensity = 38 mA, as shown in Figure 3(c). In Figure 7(a), "VPF" means that the pumping frequency of the reconfigurable charge pump can be variable according to the sunlight conditions. Here the pumping frequency is decided to meet the condition where the solar cell's voltage, $0.5 V_{SC}$, should be between $0.5 \cdot k \cdot V_{OC} - \Delta$ and $0.5 \cdot k \cdot V_{OC} + \Delta$. This variable frequency for each sunlight condition can be tracked by the circuit shown in Figures 6(a) and 6(b). In Figure 7(a), "MPP" means the amounts of output current of RCP circuit at the maximum power points for various sunlight conditions. The maximum amounts of I_{OUT}

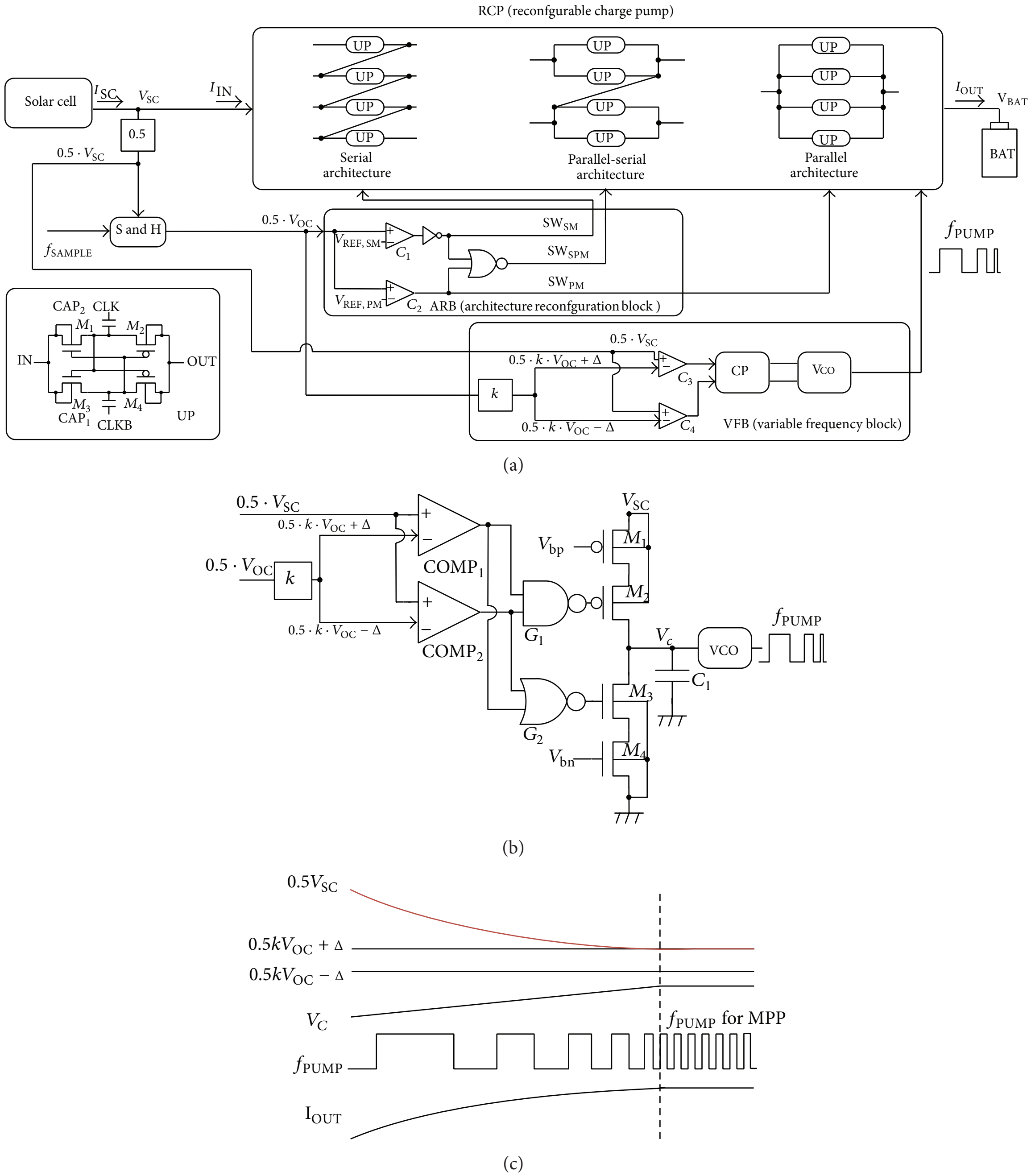

Figure 6: (a) Block diagram of the new RCP circuit that is proposed in this paper. (b) Circuit schematic of the VFB. (c) Voltage and current waveforms of the VFB.

for various sunlight conditions are obtained by the circuit simulation of the charge pump with varying the pumping frequency from 1 MHz to 30 MHz.

From Figure 7(a), "$f_{PUMP} = 7$ MHz" shows 99.6% of the maximum output current, at the moderate sunlight condition. However, "$f_{PUMP} = 7$ MHz" shows only 63.1% and 48.9% at the weak and strong sunlight conditions, respectively. This fact tells us that f_{PUMP} as low as 7 MHz can deliver the largest amount of I_{OUT} in only moderate sunlight intensity compared to weak and strong sunlight intensities. If sunlight intensity becomes different from the moderate condition, percentage of I_{OUT} with respect to the MPP becomes much smaller. "$f_{PUMP} = 15$ MHz" can deliver 99.9% of the maximum output current in strong sunlight. In spite of this large output current in strong intensity, RCP circuit at the fixed pumping frequency of 15 MHz can generate as low as 33.8% and 74.7% of the maximum I_{OUT}, in the weak and moderate sunlight condition, respectively. Unlike the cases of the fixed pumping frequencies of f_{PUMP} = 7 MHz and 15 MHz, the VPF scheme which is proposed in

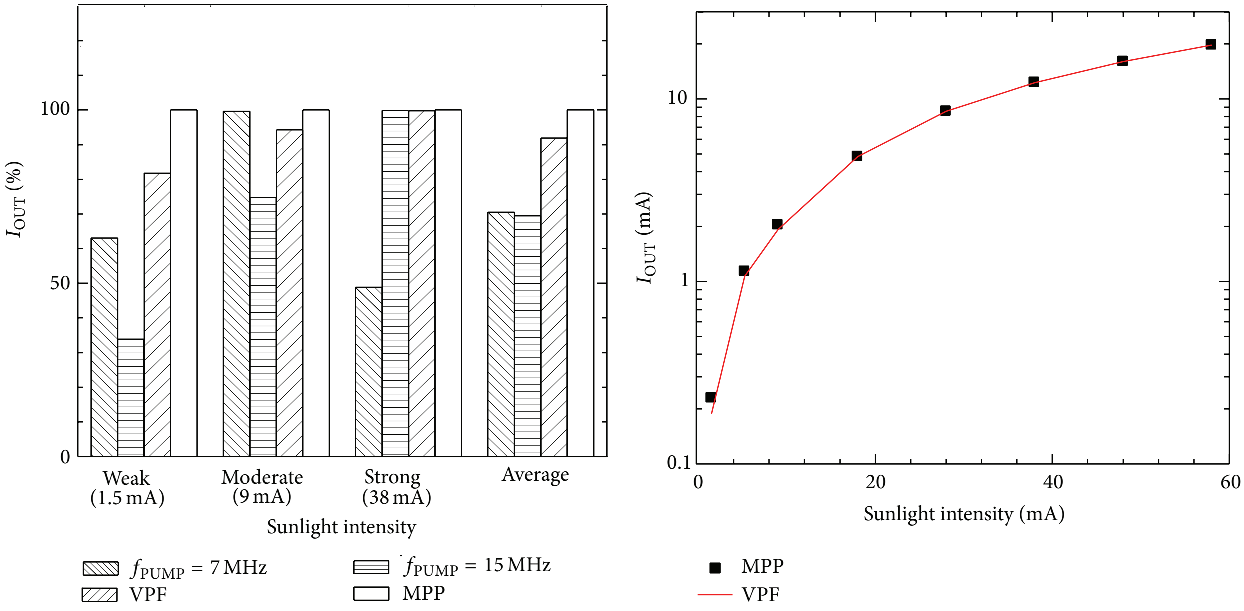

(a)

(b)

Figure 7: (a) The percentage I_{OUT} for various sunlight conditions with the fixed pumping frequencies of 7 MHz and 15 MHz and the VPF scheme. Here MPP means the simulated maximum output currents. (b) The output current comparison between the proposed VPF scheme and the simulated maximum output currents (MPP).

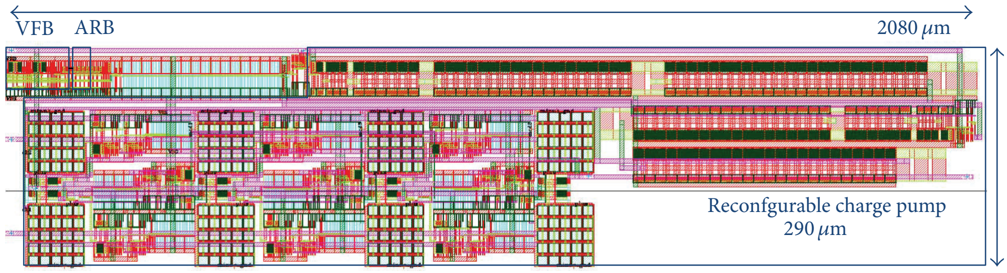

Figure 8: Layout of RCP circuit with the added VPF scheme.

this paper shows 91.9% of the maximum amounts of current for all the sunlight conditions from weak to strong intensity, on average. The large amounts of output current in the VPF scheme can be delivered to the load in a wide range of sunlight intensity from weak to strong. Figure 7(b) compares the VPF scheme with respect to MPPs from the sunlight intensity from 1.5 mA to 58 mA. For the entire range of sunlight intensity, the VPF scheme shows that amounts of the output current are similar with MPPs that are obtained from Figures 3(a), 3(b), and 3(c).

Figure 8 shows the layout of the proposed RCP circuit with VPF scheme. The VPF scheme which is added in this paper occupies an area as small as 1.61% of the total layout area. The power overhead which is caused by the added VPF scheme is estimated only as small as 0.4% of the total power consumption, for the sunlight condition as strong as 38 mA. If the sunlight conditions become as weak as 9 mA, the power overhead is increased to 1.7%. This is due to the fact that the solar cell's current becomes smaller with decreasing the sunlight intensity, while the amount of power consumption of the VPF scheme is changed very little. Thus the percentage power overhead becomes worse with decreasing sunlight intensity.

5. Conclusion

In this paper, the VPF scheme was proposed to be merged with the previous RCP circuit that can change its architecture according to a given sunlight condition. Merging the VPF scheme with the architecture reconfiguration can improve the percentage I_{OUT} better by 21.4% and 22.4% than the fixed pumping frequencies of 7 MHz and 15 MHz, respectively. Comparing the VPF scheme with the available maximum output currents, the VPF can deliver 91.9% of the maximum I_{OUT} to the load on average. In terms of the power and area overheads, the VPF scheme proposed in this paper consumes the power by 0.4% of the total power consumption and occupies the layout area by 1.61% of the total layout area.

Conflict of Interests

The authors declare that there is no conflict of interests regarding the publication of this paper.

Acknowledgments

The work was financially supported by NRF-2011-220-D00089, NRF-2011-0030228, NRF-2013K1A3A1A25038533, NRF-2013R1A1A2A10064812, and BK Plus with the Educational Research Team for Creative Engineers on Material-Device-Circuit Co-Design (Grant no. 22A20130000042), funded by the National Research Foundation of Korea (NRF) and the Industrial Strategic Technology Development Program funded by the Ministry of Trade, Industry and Energy (MOTIE, Korea) (10039239). The CAD tools were supported by IC Design Education Center (IDEC), Daejeon, Korea.

References

[1] J. Kim, J. Kim, and C. Kim, “A regulated charge pump with a low-power integrated optimum power point tracking algorithm for indoor solar energy harvesting,” *IEEE Transactions on Circuits and Systems II: Express Briefs*, vol. 58, no. 12, pp. 802–806, 2011.

[2] C. Lu, S. P. Park, V. Raghunathan, and K. Roy, “Low-overhead maximum power point tracking for micro-scale solar energy harvesting systems,” in *Proceedings of the 25th International Conference on VLSI Design (VLSID ’12)*, pp. 215–220, January 2012.

[3] J. Schmid, T. Gaedeke, T. Scheibe, and W. Stork, “Improving energy efficiency for small-scale solar energy harvesting,” in *Proceedings of the European Conference on Smart Objects, Systems and Technologies*, pp. 1–9, June 2012.

[4] C. Alippi and C. Galperti, “An adaptive system for opimal solar energy harvesting in wireless sensor network nodes,” *IEEE Transactions on Circuits and Systems I: Regular Papers*, vol. 55, no. 6, pp. 1742–1750, 2008.

[5] S. Bader and B. Oelmann, “Short-term energy storage for wireless sensor networks using solar energy harvesting,” in *Proceedings of the IEEE International Conference on Networking, Sensing and Control*, pp. 71–76, April 2013.

[6] P. Favrat, P. Deval, and M. J. Declercq, “A high-efficiency CMOS voltage doubler,” *IEEE Journal of Solid-State Circuits*, vol. 33, no. 3, pp. 410–416, 1998.

[7] F. Pen and T. Samaddar, *Charge Pump Circuit Design*, McGraw-Hill, New York, NY, USA, 2006.

[8] J. Nelson, *The Physics of Solar Cells*, Imperial College Press, London, UK, 2003.

[9] E. S. Lee, J. M. Choi, Y. S. Kim et al., “Sunlight-variation-adaptive charge pump circuit with self-reconfiguration for small-scale solar energy harvesting,” *IEICE Electronics Express*, vol. 9, no. 17, pp. 1423–1433, 2012.

[10] H. Shao, C.-Y. Tsui, and W.-H. Ki, “An inductor-less micro solar power management system design for energy harvesting applications,” in *Proceedings of the IEEE International Symposium on Circuits and Systems (ISCAS ’07)*, pp. 1353–1356, May 2007.

[11] T. Kariya and H. Kurata, *Generalized Least Squares*, John Wiley & Sons, New York, NY, USA, 2004.

[12] J. Ahmad, “A fractional open circuit voltage based maximum power point tracker for photovoltaic arrays,” in *Proceedings of the 2nd International Conference on Software Technology and Engineering (ICSTE ’10)*, pp. 247–250, October 2010.

[13] P. E. Allen and D. R. Holberg, *CMOS Analog Circuit Design*, Oxford University, Oxford, UK, 2002.

Hindawi Publishing Corporation
International Journal of Photoenergy
Volume 2014, Article ID 819637, 6 pages
http://dx.doi.org/10.1155/2014/819637

Research Article

Optimization of p-GaN/InGaN/n-GaN Double Heterojunction p-i-n Solar Cell for High Efficiency: Simulation Approach

Aniruddha Singh Kushwaha,[1,2,3] Pramila Mahala,[4] and Chenna Dhanavantri[2,3]

[1] *Indian Institute of Technology, Bombay (IIT-B) Powai, Maharashtra 400076, India*
[2] *Academy of Scientific and Innovative Research, New Delhi 110001, India*
[3] *Council of Scientific and Industrial Research-Central Electronics Engineering Research Institute (CSIR-CEERI) Pilani, Rajasthan 333031, India*
[4] *School of Solar Energy, Pandit Deendayal Petroleum University (PDPU), Gandhinagar, Gujarat 382007, India*

Correspondence should be addressed to Pramila Mahala; pramila.mahala98@gmail.com

Received 29 May 2013; Accepted 13 March 2014; Published 10 April 2014

Academic Editor: Adel M. Sharaf

We have conducted numerical simulation of p-GaN/$In_{0.12}Ga_{0.88}N$/n-GaN, p-i-n double heterojunction solar cell. The doping density, individual layer thickness, and contact pattern of the device are investigated under solar irradiance of AM1.5 for optimized performance of solar cell. The optimized solar cell characteristic parameters for cell area of $1 \times 1\,mm^2$ are open circuit voltage of 2.26 V, short circuit current density of $3.31\,mA/cm^2$, fill factor of 84.6%, and efficiency of 6.43% with interdigitated grid pattern.

1. Introduction

The direct and tunable band gap of InGaN semiconductor offers a unique opportunity to develop high efficiency solar cell. The direct band gap of the InGaN semiconductor can vary from 0.7 to 3.4 eV [1], which covers a broad solar spectrum from near-infrared to near-ultraviolet wavelength region. InGaN alloys show the unique properties such as tunable band gap, high carrier mobility, and high radiation resistance which offers a great advantage in design and fabrication of high efficiency devices for photovoltaic applications [2–4]. High absorption coefficient of InGaN alloys also makes it suitable to use in solar cells [5–7]. Earlier theoretical calculations have shown that it is possible to achieve efficiency up to 50% with InGaN alloys [8]. In spite of high efficiency prediction, fabricated solar cells could not demonstrate high efficiency [9–13]. The epitaxial growth of InGaN layers faces many issues such as lack of defect-free substrate, indium segregation at higher composition, and large lattice mismatch between InN and GaN which leads to phase separation [14]. In addition, there are significant polarization charges at the InGaN/GaN interface which alter the electric field in InGaN layer [15]. As a consequence the fabricated InGaN solar cell shows very low conversion efficiency compared to theoretical calculation.

In this paper, a simulation work is carried out to optimize p-GaN/InGaN/n-GaN/sapphire device structure of solar cells with 12% indium composition under AM1.5 illumination. Simulation is carried out by optimizing doping concentration and thickness of p-GaN, InGaN, and n-GaN layer, respectively, by changing only one material parameter at a time and keeping other parameters constant. Simulation verifies that device efficiency is strongly dependent on the intrinsic-layer (InGaN) thickness, as most of the spectrum is absorbed in this layer. We simulate p-GaN/InGaN/n-GaN/Sapphire solar cell to investigate the effect of incorporating grid contact pattern on the device characteristic parameter. It is observed that optimization of grid contact spacing helps greatly in device efficiency enhancement.

TCAD SILVACO, Version: ATLAS 5.16.3.R, is used for simulation. The simulator works on mathematical models which consist of fundamental equations such as Poisson's equation, continuity equation, and transport equations. In our simulation, we have used the models such as AUGER for

Table 1: Material parameter used in simulation.

Parameter	GaN	$In_{0.12}Ga_{0.88}N$	InN
Band gap E_g (ev) [10]	3.42	2.93	0.7
Lattice constant (A$^\circ$) [11]	3.18	3.23	3.6
Minority carrier life time (ns) [21]	1	1	1
Spontaneous polarization (sheet charge per cm^2) [22]	$-2.12e13$	$-2.18e13$	$-2.63e13$
Piezoelectric polarization (sheet charge per cm^2) [22]	0	$-8.87e12$	$9.98e13$
Auger coefficient n-type [11]	$1e-34$	$1e-34$	$1e-34$
Auger coefficient p-type [11]	$1e-34$	$1e-34$	$1e-34$

Auger recombination, SRH for Shockley Read Hall recombination, OPTR for optical recombination, KP model for effective masses, and band edge energies for drift diffusion simulation. Mathematical models are used in simulation which consists of fundamental equations such as Poisson's equation, continuity equation, and transport equations. Newton's method is used as the solution method in simulation. All the above models are used from standard TCAD library.

This paper is organized as follows: in Section 2 material parameters are described which are used in simulation models. Section 3 discusses simulation and results. Finally, conclusion is presented in Section 4.

2. Material Parameters

The absorption coefficient $\alpha(E)$ of $In_xGa_{1-x}N$ semiconductor as a function of energy [16], energy band gap and electron affinity as a function of band gap energy, $E_g(x)$ [17, 18], and electron and hole mobility as a function of doping [19] can be expressed as

$$\begin{gathered}\alpha\left[E(\lambda)\right]=\alpha_0\sqrt{\frac{E(\lambda)-E_g(x)}{E_g(x)}},\\ E_g(x)=0.7x+3.4(1-x)-1.43x(1-x)\ \text{eV},\\ \chi=4.1+0.7\times\left(3.4-E_g(x)\right),\\ \mu_i(N)=\mu_{\min,i}+\frac{\mu_{\max,i}-\mu_{\min,i}}{1+\left(N/N_{g,i}\right)^{\gamma_i}},\end{gathered}\tag{1}$$

where $E(\lambda)$ is the energy of photon corresponding to respective wavelength and $E_g(x)$ is the band gap of $In_xGa_{1-x}N$ semiconductor. It is assumed that α_0 for $In_xGa_{1-x}N$ is the same as that of GaN, i denotes electrons (e) or holes (h), N is doping concentration, and $\mu_{\min}$, $\mu_{\max}$, γ, and N_g are the parameter given for a specific semiconductor [19]. The material parameters for InGaN such as absorption coefficient, lattice constant, and polarization charges are derived and extracted by interpolation of known material parameters of InN and GaN. Some of important material parameters used during simulation are listed in Table 1.

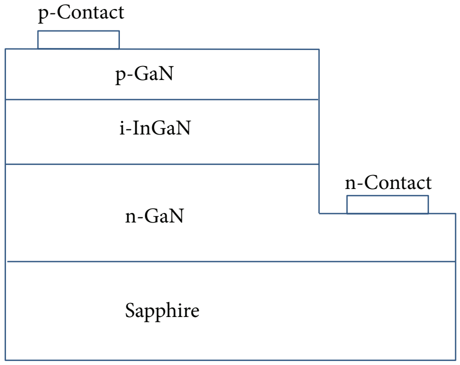

Figure 1: p-i-n InGaN/GaN double heterojunction solar cell structure.

3. Simulation Results and Discussion

3.1. Optimization of p-i-n Structure. The schematic diagram of InGaN/GaN p-i-n solar cell is shown in Figure 1. The p-GaN layer thickness is varied from 70 to 120 nm. The InGaN and n-GaN layer thicknesses 100 nm and 1.5 μm and their doping densities 1×10^{16} cm^{-3} and 6×10^{18} cm^{-3}, respectively, are kept constant while optimizing p-GaN layer thickness and doping density.

The effect of p-GaN layer thickness and doping concentration on solar cells characteristic parameters such as short circuit current density, open circuit voltage, fill factor, and efficiency is shown in Figure 2. The short circuit current density, J_{sc}, increases with p-GaN layer thickness. As the thickness of p-GaN layer increases more photon absorption occurs in the p-region, resulting in more electron and hole carrier generation that contributes to enhancement of current density. On the contrary, thicker p-GaN layer increases surface recombination rate after a certain thickness; current density starts decreasing. The open circuit voltage, V_{oc}, and fill factor, FF, do not show significant change with respect to p-GaN layer thickness as these parameters largely depend on the bulk property of semiconductor rather than surface property.

The effect of doping density is analyzed by simulating the structure for different doping concentrations of 1×10^{16} cm^{-3}, 1×10^{17} cm^{-3}, and 1×10^{18} cm^{-3}, respectively. The simulation result shows that the short circuit current density is higher for doping concentration of 1×10^{16} cm^{-3}. However,

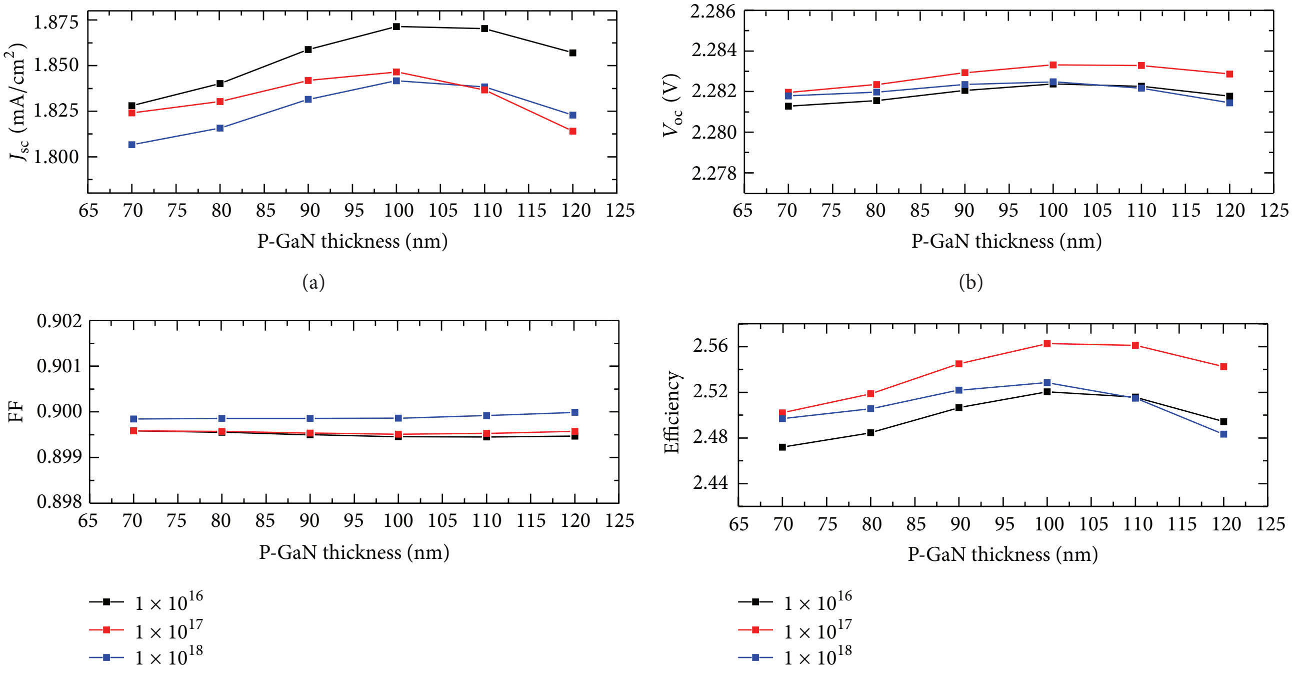

(a)

(b)

(c)

(d)

FIGURE 2: Effect of p-GaN layer thickness and doping concentrations on GaN/InGaN solar cell characteristic parameters: (a) short circuit current density, (b) open circuit voltage, (c) fill factor, and (d) efficiency.

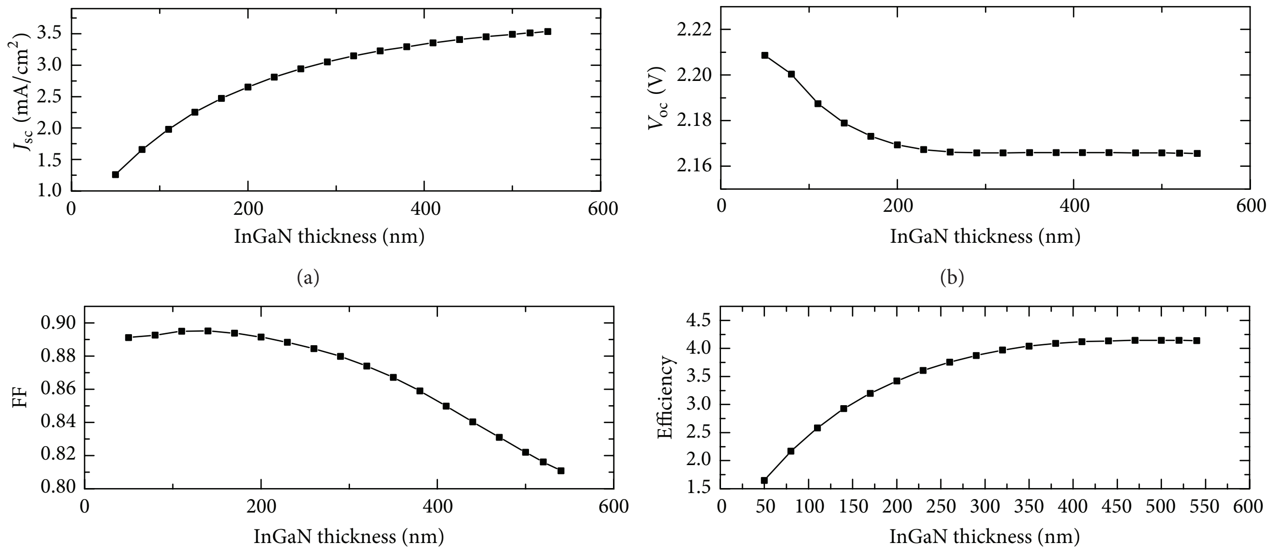

(a)

(b)

(c)

(d)

FIGURE 3: Effect of InGaN layer thickness on characteristic parameters of solar cells. (a) Short circuit current density. (b) Open circuit voltage. (c) Fill factor. (d) Efficiency.

it is found that V_{oc} is higher for doping concentration of 1×10^{17} cm^{-3}. The combined effect of J_{sc} and V_{oc} determines the efficiency curve which follows curve pattern of J_{sc} and shows higher efficiency for the doping concentration of 1×10^{17} cm^{-3}, where V_{oc} is high.

The effect of intrinsic InGaN layer thickness on solar cell characteristic parameters of p-GaN/InGaN/n-GaN p-i-n solar cell is shown in Figure 3. The InGaN layer thickness is varied from 50 to 550 nm. The p-GaN and n-GaN layer thicknesses 100 nm and 1.5 μm and their doping densities 5

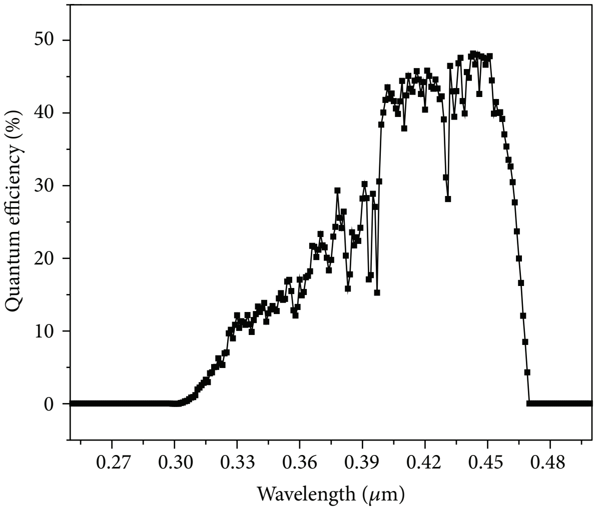

Figure 4: Quantum efficiency of optimized p-i-n GaN/InGaN double heterojunction solar cell.

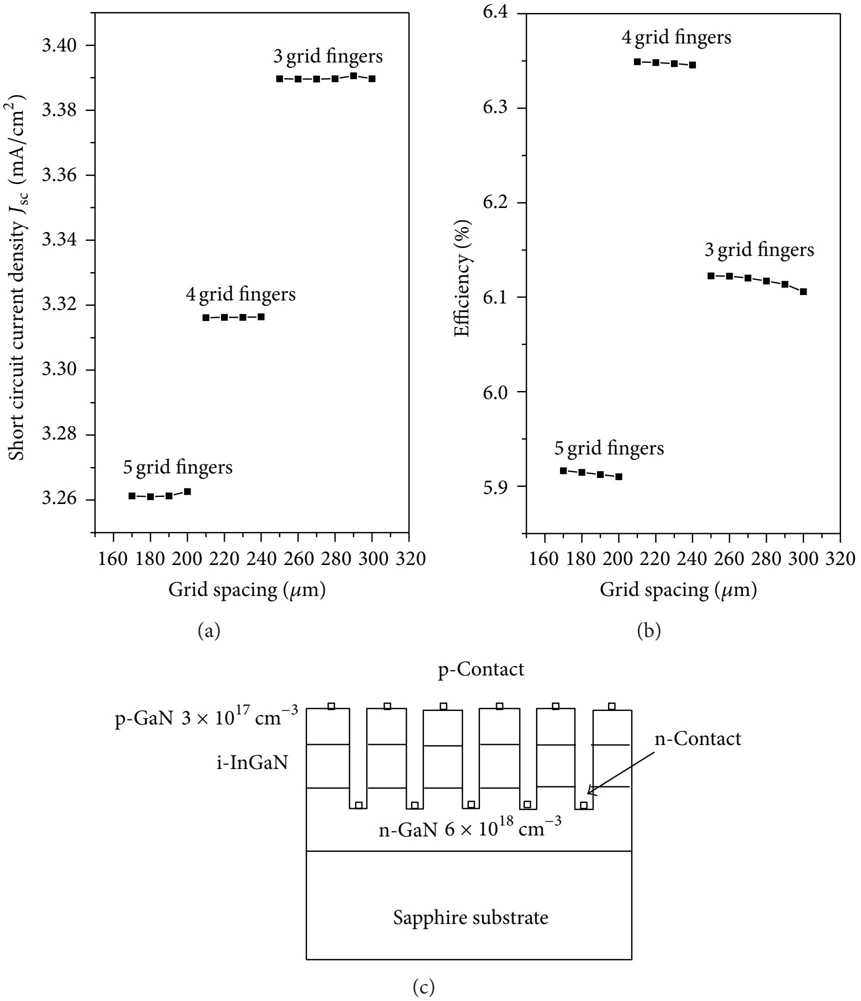

Figure 5: Effect of (a) short circuit current density, (b) efficiency on grid spacing for different number of grids, and (c) p-i-n InGaN/GaN double heterojunction solar cell with grid type contact.

Table 2: Characteristic parameters of simulated InGaN p-i-n solar cell.

Contact type	Effective device area (mm^2)	Grid spacing (μm)	Indium (%)	J_{sc} (mA/cm^2)	V_{oc} (V)	FF (%)	η (%)
Square pad	0.96	—	12	5.64	2.27	82	4.16
Grid pattern							
5 grid fingers	0.90	180	12	3.26	2.17	83.6	5.92
4 grid fingers	0.92	210	12	3.31	2.26	84.6	6.34
3 grid fingers	0.94	260	12	3.39	2.17	83.2	6.12

$\times 10^{17}$ cm^{-3} and 6×10^{18} cm^{-3}, respectively, are kept constant while optimizing InGaN layer thickness.

It is found that J_{sc} increases with InGaN layer thickness since photons get longer path for absorption and also unabsorbed lower energy photons from p-GaN layer get absorbed in this region. Photon absorption is also supported by higher absorption coefficient of InGaN material [20]. On the other hand, the open circuit voltage is found to be decreased and remain nearly constant after layer thickness of 250 nm. Higher thickness generates more carriers and recombination results in decreased open circuit voltage.

The fill factor also starts decreasing with respect to increased InGaN layer thickness. The series resistance increases with increasing InGaN layer thickness. The efficiency curve resembles that of current density which represents the combined effect of all parameters S_C, V_{ic}, and FF. After the p-GaN and InGaN-layers, the n-GaN layer thickness and doping density concentration are optimized. The n-GaN thickness is varied from 0.4 to 2.4 μm. The p-GaN and InGaN layers thicknesses are 100 nm and 450 nm and doping densities 5×10^{17} cm^{-3} and 1×10^{16} cm^{-3}, respectively, are kept constant while optimizing n-GaN layer thickness and doping density. The n-GaN layer thickness and doping density do not play an important role with respect to solar cell parameters. It may be because most of the available photons are already absorbed in the p-GaN and InGaN layer, and very few carriers are generated in n-GaN layer.

The final p-i-n structure consists of n-type GaN layer, 1.5 μm thickness and doping density of 6×10^{18} cm^{-3}, unintentionally doped InGaN layer, 450 nm thickness and doping density of 1×10^{16} cm^{-3} with 12 percent indium composition, and top p-type GaN layer, 100 nm thickness, with acceptor density of 5×10^{17} cm^{-3}. The quantum efficiency of optimized structure is calculated and shown in Figure 4 and the maximum quantum efficiency is found to be in the wavelength range of 0.4 nm to 0.45 nm wavelength, which corresponds to GaN/InGaN material band gap region.

3.2. Effect of using Interdigitated Grid Pattern. We simulated the p-i-n structure with interdigitated grid pattern, in order to further enhance the efficiency by use of grid type contact which helps in increasing the carrier collection. Simulation results of incorporating grid patterns on × and efficiency with different numbers of grid fingers such as 3, 4, and 5 and different grid spacing from 175 to 375 μm are shown in Figure 5. The size of the cell considered here is 1 × 1 mm^2. The number of grids will be reduced with increasing finger-to-finger grid spacing. The short circuit current density decreases with increasing grid numbers due to decrease in effective area available for photon absorption. However there is an enhancement in efficiency due to more carrier collection. The characteristic parameters for different contact patterns along with square pad are compared in Table 2.

4. Conclusion

The optimization of p-GaN/InGaN/n-GaN double heterojunction p-i-n solar cell with square contact and grid pattern is studied. The photovoltaic parameter of solar cell strongly depends on p-GaN and InGaN layers thickness and doping density. Photovoltaic parameters, such as V_{oc}: 2.27 V, J_{sc}: 5.64 mA/cm^2, FF: 82%, and η: 4.16, are obtained for square contact type under 1 sun AM1.5 illumination with optimized p-GaN (100 nm, 5e17 am-3) and InGaN (In = 0.12, 450 nm) layers and high quantum efficiency of ~50% is also achieved in wavelength range of 0.4 nm to 0.45 nm which corresponds to In$_{0.12}$Ga$_{0.88}$N absorption region. In addition to optimizing structure, use of grid contact pattern with finger spacing of 210 nm improves conversion efficiency to 6.34.

Conflict of Interests

The authors declare that there is no conflict of interests regarding the publication of this paper.

Acknowledgments

The authors gratefully acknowledge the Director of CSIR-CEERI, Pilani, for his encouragement in this work. They also thank all ODG members for their help and cooperation.

References

[1] J. Wu, W. Walukiewicz, K. M. Yu et al., "Small band gap bowing in In$_{1-x}$Ga$_x$N alloys," *Applied Physics Letters*, vol. 80, no. 25, pp. 4741–4743, 2002.

[2] X. M. Cai, S. W. Zeng, and B. P. Zhang, "Fabrication and characterization of InGaN p-i-n homojunction solar cell," *Applied Physics Letters*, vol. 95, Article ID 173504, 2009.

[3] Y. Nanishi, Y. Saito, and T. Yamaguchi, "RF-molecular beam epitaxy growth and properties of InN and related alloys," *Journal of Applied Physics*, vol. 42, part 1, pp. 2549–2559, 2003.

[4] X. Zheng, R. H. Horng, D. S. Wuu et al., "High-quality InGaN/GaN heterojunctions and their photovoltaic effects," *Applied Physics Letters*, vol. 93, Article ID 261108, 2008.

[5] C. J. Neufeld, N. G. Toledo, S. C. Cruz et al., "High quantum efficiency InGaN/GaN solar cells with 2.95 eV band gap," *Applied Physics Letters*, vol. 93, Article ID 143502, 2008.

[6] R. Singh, D. Doppalapudi, T. D. Moustakas, and L. T. Romano, "Phase separation in InGaN thick films and formation of InGaN/GaN double heterostructures in the entire alloy composition," *Applied Physics Letters*, vol. 70, no. 9, pp. 1089–1091, 1997.

[7] J. F. Muth, J. H. Lee, I. K. Shmagin et al., "Absorption coefficient, energy gap, exciton binding energy, and recombination lifetime of GaN obtained from transmission measurements," *Applied Physics Letters*, vol. 71, no. 18, pp. 2572–2574, 1997.

[8] A. De Vos, *Endoreversible Thermodynamics of Solar Energy Conversion*, Oxford University Press, Oxford, UK, 1992.

[9] X. Zhang, X. L. Wang, H. L. Xiao et al., "Simulation of $In_{0.65}Ga_{0.35}$ N single-junction solar cell," *Journal of Physics D: Applied Physics*, vol. 40, no. 23, p. 7335, 2007.

[10] H. Hamzaoui, A. S. Bouazzi, and B. Rezig, "Theoretical possibilities of $In_xGa_{1-x}N$ tandem PV structures," *Solar Energy Materials and Solar Cells*, vol. 87, no. 1–4, pp. 595–603, 2005.

[11] Md. R. Islam, A. N. M. E. Kabir, and A. G. Bhuiyan, "Projected Performance of $In_xGa_{1-x}N$-based multi-junction solar cells," *Istanbul University-Journal of Electrical and Electronics Engineering*, vol. 6, no. 2, pp. 251–255, 2006.

[12] L. Hsu and W. Walukiewicz, "Modeling of InGaN/Si tandem solar cells," *Journal of Applied Physics*, vol. 104, Article ID 024507, 2008.

[13] B. W. Liou, "$In_xGa_{1-x}N$-GaN-based solar cells with a multiple-quantum-well structure on SiCN–Si(111) substrates," *IEEE Photonics Technology Letters*, vol. 22, no. 4, 2010.

[14] Y.-S. Lin, K.-J. Ma, C. Hsu et al., "Dependence of composition fluctuation on indium content in InGaN/GaN multiple quantum wells," *Applied Physics Letters*, vol. 77, no. 19, pp. 2988–2990, 2000.

[15] J. Wierer, A. Fischer, and D. Koleske, "The impact of piezoelectric polarization and nonradiative recombination on the performance of (0001) face GaN/InGaN photovoltaic devices," *Applied Physics Letters*, vol. 96, Article ID 051107, 2010.

[16] J. Hubin and A. V. Shah, "Effect of the recombination function on the collection in a p-i-n solar cell," *Philosophical Magazine B*, vol. 72, no. 6, pp. 589–599, 1995.

[17] M. E. Levinshtein, S. L. Rumyantsev, and M. S. Shur, *Properties of Advanced Semiconductor Materials*, Wiley, Chichester, UK, 2001.

[18] N. Li, *Simulation and analysis of GaN-based photoelectronics devices [Ph.D. dissertation]*, Institute of Semiconductors, Chinese Academy of Sciences, Beijing, China, 2005, (Chinese).

[19] T. T. Mnatsakanov, M. E. Levinshtein, L. I. Pomortseva, S. N. Yurkov, G. S. Simin, and M. A. Khan, "Carrier mobility model for GaN," *Solid-State Electronics*, vol. 47, no. 1, pp. 111–115, 2003.

[20] K. Kumakura, T. Makimoto, N. Kobayashi, T. Hashizume, T. Fukui, and H. Hasegawa, "Minority carrier diffusion length in GaN: dislocation density and doping concentration dependence," *Applied Physics Letters*, vol. 86, Article ID 052105, 2005.

[21] G. F. Brown, J. W. Ager III, W. Walukiewicz, and J. Wu, "Finite element simulations of compositionally graded InGaN solar cells," *Solar Energy Materials and Solar Cells*, vol. 94, no. 3, pp. 478–483, 2010.

[22] ATLAS User's Manual: Device Simulation Software, 06/11/08 Ed., Silvaco Data Systems, Inc., Santa Clara, Calif, USA, 2008.

Hindawi Publishing Corporation
International Journal of Photoenergy
Volume 2014, Article ID 392394, 14 pages
http://dx.doi.org/10.1155/2014/392394

Research Article

Buck-Boost/Forward Hybrid Converter for PV Energy Conversion Applications

Sheng-Yu Tseng, Chien-Chih Chen, and Hung-Yuan Wang

Department of Electrical Engineering, Chang-Gung University, 259 Wen-Hwa 1st Road, Tao-Yuan 333, Taiwan

Correspondence should be addressed to Sheng-Yu Tseng; sytseng@mail.cgu.edu.tw

Received 16 August 2013; Revised 28 February 2014; Accepted 28 February 2014; Published 7 April 2014

Academic Editor: Ismail H. Altas

This paper presents a charger and LED lighting (discharger) hybrid system with a PV array as its power source for electronic sign indicator applications. The charger adopts buck-boost converter which is operated in constant current mode to charge lead-acid battery and with the perturb and observe method to extract maximum power of PV arrays. Their control algorithms are implemented by microcontroller. Moreover, forward converter with active clamp circuit is operated in voltage regulation condition to drive LED for electronic sign applications. To simplify the circuit structure of the proposed hybrid converter, switches of two converters are integrated with the switch integration technique. With this approach, the proposed hybrid converter has several merits, which are less component counts, lighter weight, smaller size, and higher conversion efficiency. Finally, a prototype of LED driving system under output voltage of 10 V and output power of 20 W has been implemented to verify its feasibility. It is suitable for the electronic sign indicator applications.

1. Introduction

In recent years, light emitting diodes (LEDs) are becoming more prevalent in a wide application. Due to material advances over the past few decades, efficiencies of LEDs have increased many times [1], and their applications have rapidly grown for automotive taillights, LCD back lights, traffic signals, and electronic signs [2, 3]. Moreover, serious greenhouse effect and environmental pollution caused by overusing fossil fuels have disturbed the balance of global climate. In order to reduce emission of exhausted gases, zero-emission renewable energy sources have been rapidly developed. One of these sources is photovoltaic (PV) arrays, which is clean and quiet and an efficient method for generating electricity. As mentioned above, this paper proposes an LED driving system, which adopts the PV arrays for electronic sign applications.

In electronic sign applications using PV arrays, the power system will inevitably need batteries for storing energy during the day and for releasing energy to LED lighting during the night. Therefore, it needs a charger and discharger (LED driving circuit), as shown in Figure 1. Since the proposed power system belongs to the low power level applications, buck, boost, buck-boost, flyback, or forward converter is more applied to the proposed one [4–12]. In these circuit structures, according to the relationships among PV output voltage V_{PV}, battery voltage V_B, and output voltage V_{O}, the proposed hybrid converter can choose functions, which are of step-up and -down simultaneously as the charger or discharger for a wider application. Due to the previously described reasons, the charger of the proposed one adopts buck-boost converter and the discharger uses forward converter. Moreover, since forward converter exits two problems, which are the energies trapped in leakage inductor and magnetizing inductor of transformer T_f, it needs a snubber or circuit to recover these energies. Therefore, forward converter can use an active clamp circuit to solve these problems. In order to simplify the proposed hybrid converter and increase its conversion efficiency, a bidirectional buck-boost converter and active clamp forward converter are used, as shown in Figure 2. Since charger and discharger (LED driving circuit) of the proposed hybrid converter are operated in complement and they use switch S_1 to control their operational states, inductor L_1 of buck-boost converter and magnetizing inductor L_m of transformer T_f can be merged. Therefore, switches of the bidirectional buck-boost converter and active clamp forward

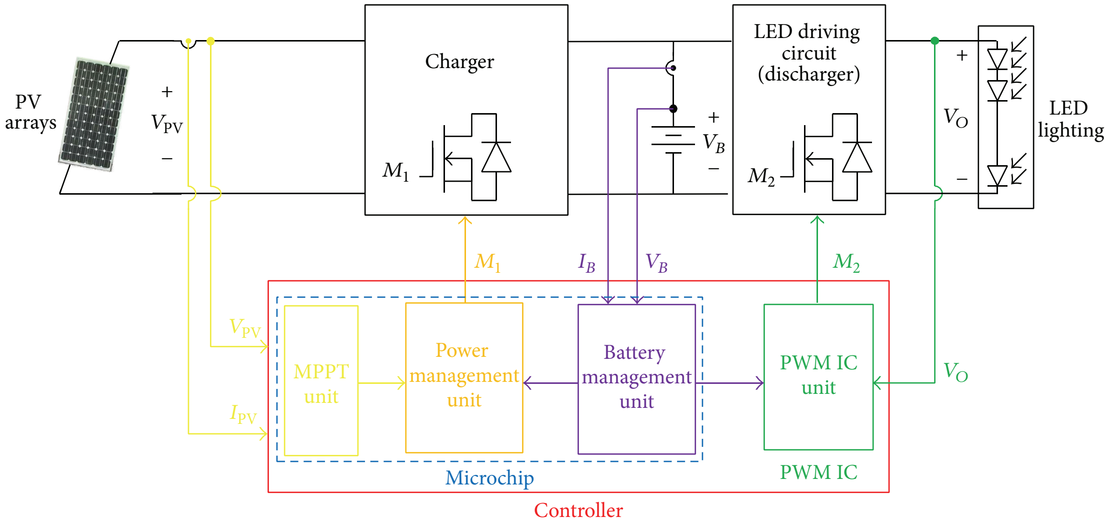

FIGURE 1: Block diagram of the proposed hybrid converter for electronic sign applications.

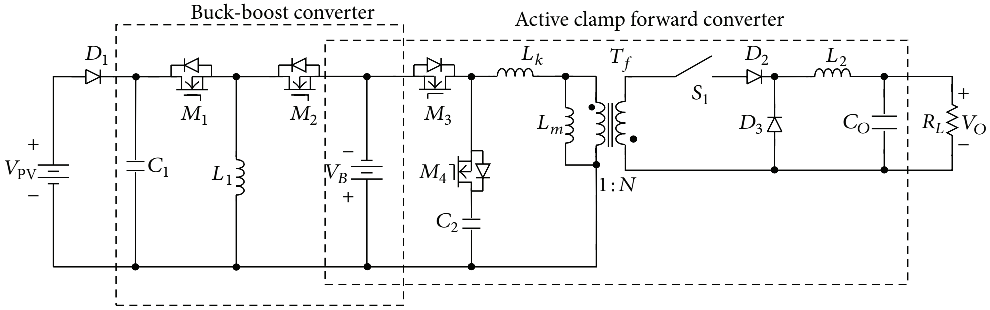

FIGURE 2: Schematic diagram of the hybrid converter for electronic sign applications.

converter are integrated with synchronous switch technique [13] to reduce their component counts, as shown in Figure 3. With this circuit structure, the proposed one can yield higher efficiency, reduce weight, size, and volume and increase the discharging time of battery under the same storing energy, significantly.

The proposed hybrid converter using PV arrays supplies power to LED lighting for electronic sign applications. The proposed one includes charger and discharger. Since the proposed one uses PV arrays as its power source, it must be operated at the maximum power point (MPP) of PV arrays to extract its maximum power. Many maximum power point tracking (MPPT) methods of PV arrays have been proposed [14–21]. They are, respectively, power matching [14, 15], curve-fitting [16, 17], perturb-and-observe [18, 19], and incremental conductance [20, 21] methods. Since power matching method requires a specific insolation condition or load, it will limit its applications. MPPT using curve-fitting technique needs prior establishment characteristic curve of PV arrays. It cannot predict the characteristics including other factors, such as aging, temperature, and a possible breakdown of individual cell. The incremental conductance technique requires an accurate mathematical operation. Its controller is more complex and higher cost. Due to a simpler control and lower cost of perturb and observe method, the proposed hybrid converter adopts the perturb and observe method to implement MPPT.

For electronic sign applications using LED, the power system needs battery to store energy during day and to discharge energy for driving LED during night. In order to generate better performances of battery charging, many battery charging methods have been proposed. They are constant trickle current (CTC), constant current (CC), and CC and constant-voltage (CC-CV) hybrid charge methods [22]. Among these methods, the CTC charging method needs a larger charging time. Battery charging using CC-CV method requires to sense battery current and voltage, resulting in a more complex operation and higher cost. Due to a simpler controller of battery charger using CC charging method, it is adopted in the proposed hybrid converter. According to description above, the proposed hybrid converter uses the perturb and observe method to track MPP of PV arrays and

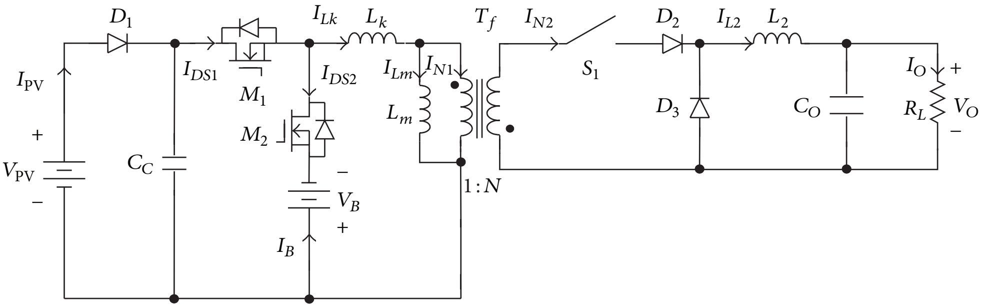

FIGURE 3: Schematic diagram of the proposed hybrid converter for electronic sign applications.

adopts the CC charging method to simplify battery charging. All overall power system can achieve battery charging and LED driving.

2. Circuit Structure Derivation of the Proposed Hybrid Converter

The hybrid converter consists of a bidirectional buck-boost and active clamp forward converter, as shown in Figure 2. Due to complementary operation between two converters, two switch pairs of (M_1, M_4) and (M_2, M_3) can be operated in synchronous. It will do not affect the operation of the proposed original converter. Since switch pairs of (M_2, M_3) has a common node, they meet the requirements of switch integration technique [11]. According to principle of switch integration technique, switches M_2 and M_3 can be merged, as shown in Figure 4(a). Since charger and LED driving circuit (discharger) are operated in complementary, switch M_2 and M_3 are also regarded as an independent operation. Therefore, voltages across switches M_2 and M_3 are the same value in each operation state. Diode D_{F231} and D_{F232} can be removed, while diode D_{B231} and D_{B232} can be shorted, as shown in Figure 4(b). In Figure 4(b), since $L_K \ll L_m$, L_K can be neglected. The inductor L_1 and magnetizing L_m are connected in parallel. Although features of inductors L_1 and L_m are different, their design rules are to avoid them to operate in saturation condition. Therefore, they can be merged as inductor L_{1m}, as shown in Figure 4(c).

From Figure 4(c), it can be seen that switch M_1 and M_4 have a common node. They can use switch integration technique to combine them, as shown in Figure 4(d). Since voltages across M_1 and M_4 are the same values, diodes D_{B141} and D_{B142} are shorted and diodes D_{F141} and D_{F142} can be removed, as shown in Figure 4(e). From Figure 4(e), it can be found that capacitors C_1 and C_2 are connected in parallel. They can be integrated as capacitor C_C, as illustrated in Figure 4(f). To simplify symbols of components illustrated in Figure 4(f), component symbols will be renamed, as shown in Figure 3. Note that switch S_1 can be operated by manual or automatic method to control the operational states of the proposed hybrid converter.

Buck-boost and forward converters are combined to form the proposed hybrid converter. Since operation of buck-boost converter is the same as the conventional buck-boot converter, its operational principle is described in [8]. It will not be described in this paper. The forward converter with the active clamp circuit recovers the energies stored in magnetizing and leakage inductors of transformer T_f and achieves zero-voltage switch (ZVS) at turn-on transition for switches M_1 and M_2. It operational mode can be divided into 9 modes and their Key waveforms are illustrated in Figure 5, since their operational modes are similar to those modes of the conventional converter illustrated in [23]. It is also not described in this paper.

3. Design of the Proposed Hybrid Converter

The proposed hybrid converter consists of buck-boost converter and active clamp forward converter. Since switches and inductors in two converters are integrated with the synchronous switch technique, design of the proposed one must satisfy requirements of each converter. Since design of the active clamp forward converter is illustrated in [23], buck-boost converter is only analyzed briefly in the following.

3.1. Buck-Boost Converter. Since buck-boost converter is regarded as the battery charger under constant current charging. Its design consideration is to avoid a completely saturation of inductor. Therefore, duty ratio D_{11} and inductor L_m are analyzed in the following.

3.1.1. Duty Ratio D_{11}. Within charging mode, since battery voltage V_B is regarded as a constant voltage during a switching cycle of the proposed hybrid converter, maximum duty ratio $D_{11(\max)}$ of the proposed one can be determined by volt-second balance of inductor L_m. Its relationship is expressed as

$$V_{PV(\min)} D_{11(\max)} T_s + \left(-V_{B(\max)}\right)\left(1 - D_{11(\max)}\right) T_s = 0, \tag{1}$$

where $V_{PV(\min)}$ is the minimum output voltage of PV arrays, $V_{B(\max)}$ is the maximum voltage across battery, and T_s represents the period of the proposed hybrid converter. From (1), it can be found that $D_{11(\max)}$ can be illustrated by

$$D_{11(\max)} = \frac{V_{B(\max)}}{V_{PV(\min)} + V_{B(\max)}}. \tag{2}$$

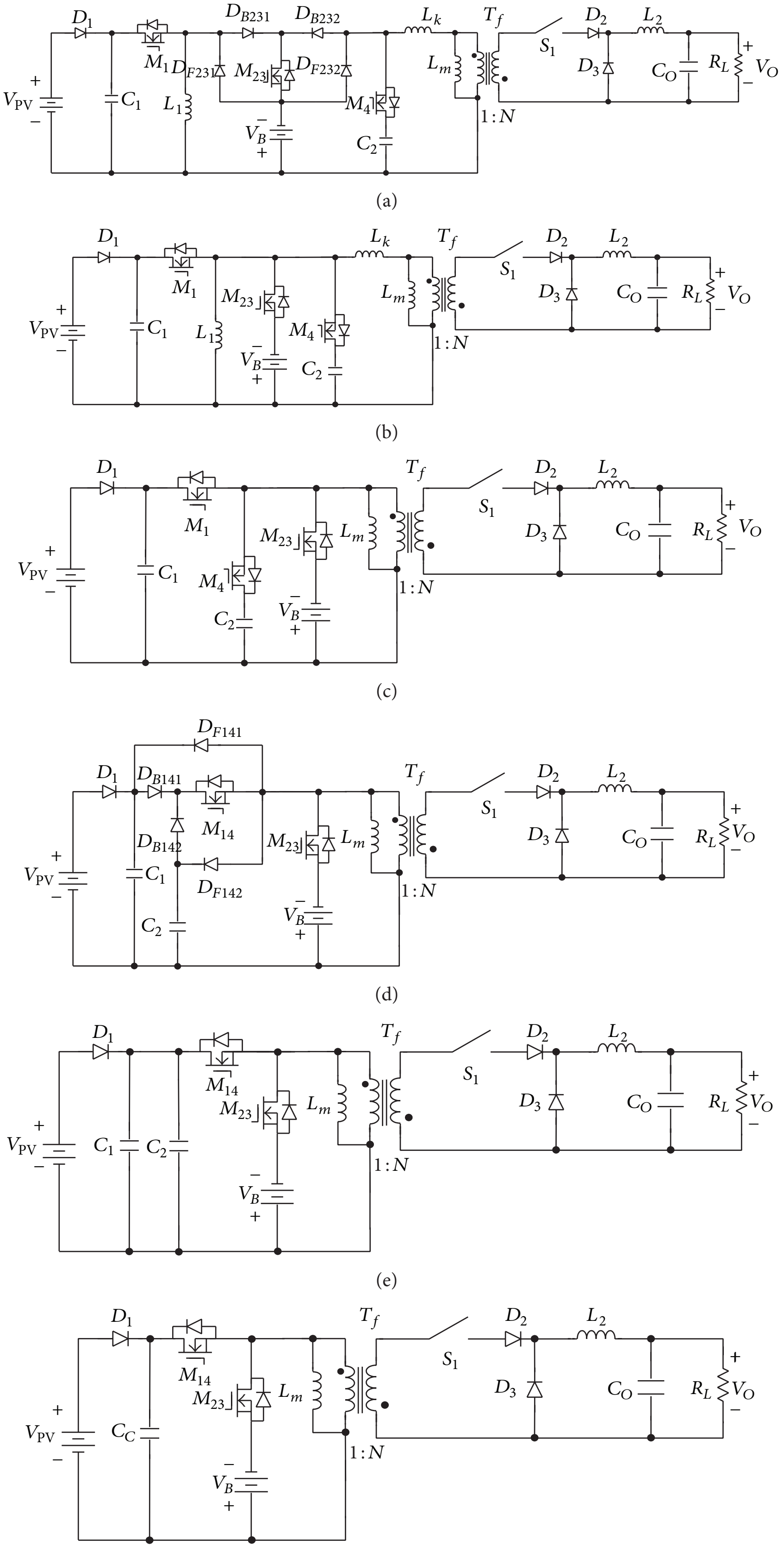

(a)

(b)

(c)

(d)

(e)

(f)

Figure 4: Derivation of the proposed hybrid converter for battery charger.

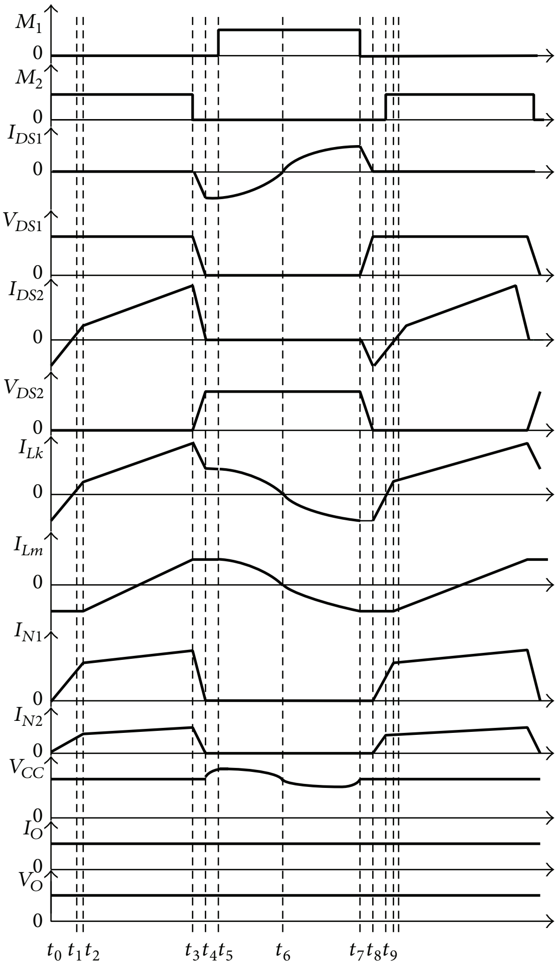

Figure 5: Key waveforms of forward converter with active clamp circuit over one switching cycle.

Moreover, transfer ratio $M_{11(\max)}$ can be also determined as follows:

$$M_{11(\max)} = \frac{D_{11(\max)}}{1 - D_{11(\max)}}. \tag{3}$$

When type of battery is chosen, its maximum charging current $I_{B(\max)}$ is also determined. The charging current I_B can be changed from its maximum charging current $I_{B(\max)}$ to 0 by variation duty ratio D_{11} of switch M_1.

3.1.2. Inductor L_m. Since the proposed hybrid converter is operated in CCM to obtain the maximum charging current $I_{B(\max)}$, its conceptual waveforms of inductor current I_{Lm} and charging current I_B are illustrated in Figure 6. If the proposed one is operated in the boundary of discontinuous conduction mode (DCM) and CCM, the charging current I_B is expressed by

$$I_{B(\mathrm{av})} = \frac{(1 - D_{11})^2 V_B T_s}{2L_{mB}}, \tag{4}$$

where L_{mB} is the inductance L_m at the boundary condition. According to (4), variation of duty ratio D_{11} can obtain a different charging current I_B. In general, the maximum charge current $I_{B(\mathrm{av})\max}$ occurs at the maximum battery voltage $V_{B(\max)}$ and the maximum output voltage $V_{\mathrm{PV}(\max)}$ of PV arrays. Therefore, the boundary inductor L_{mB} can be determined by

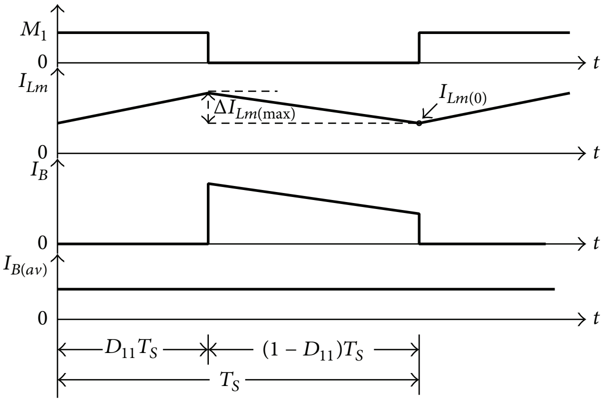

Figure 6: Conceptual waveforms of inductor current I_{Lm} and charging current I_B in buck-boost converter.

$$I_{B(\mathrm{av})\max} = \frac{(1 - D_{11B})^2 V_{B(\max)} T_s}{2L_{mB}}, \tag{5}$$

where D_{11B} is duty ratio of switch M_1 under $V_{B(\max)}$ and $V_{\mathrm{PV}(\max)}$. From (5), it can be found that the maximum boundary inductor $L_{mB(\max)}$ can be expressed as

$$L_{mB(\max)} = \frac{(1 - D_{11B})^2 V_{B(\max)} T_s}{I_{B(\mathrm{av})\max}}. \tag{6}$$

Since the proposed hybrid converter is operated in CCM, inductor L_m must be greater than $L_{mB(\max)}$. Therefore, when $V_{\mathrm{PV}(\max)}$, $V_{B(\max)}$, $I_{B(\mathrm{av})\max}$, and T_s are specified, the minimum inductance $L_{m(\min)}$ ($=L_{mB(\max)}$) can be determined.

In order to avoid the core of transformer T_f operated in saturation state, the working flux density $B_{\max}$ must be less than the saturation flux density B_{sat} of core. Since $B_{\max}$ is proportional to the maximum inductor current $I_{Lm(\mathrm{peak})}$, $I_{Lm(\mathrm{peak})}$ must be first determined. In Figure 6, $I_{Lm(\mathrm{peak})}$ can be expressed as

$$I_{Lm(\mathrm{peak})} = I_{Lm(0)} + \Delta I_{Lm(\max)}, \tag{7}$$

where $I_{Lm(0)}$ is the initial value of inductor current I_{Lm} operated in CCM and $\Delta I_{Lm(\max)}$ represents its maximum variation value. In general, its maximum value $\Delta I_{Lm(\max)}$ can be determined by

$$\Delta I_{Lm(\max)} = \frac{V_{\mathrm{PV}(\max)} D_{11R} T_s}{L_m}, \tag{8}$$

where D_{11R} represents the duty ratio of switch M_1 under $V_{\mathrm{PV(max)}}$ and $V_{B(\mathrm{max})}$. Furthermore, the maximum charging current $I_{B(\mathrm{av})\max}$ can be expressed as

$$\begin{aligned} I_{B(\mathrm{av})\max} &= \frac{(1-D_{11R})}{2}\left(I_{Lm(\mathrm{peak})}+I_{Lm(0)}\right) \\ &= \frac{(1-D_{11R})}{2}\left(2I_{Lm(0)}+\frac{V_{\mathrm{PV(max)}}D_{11R}T_s}{L_m}\right). \end{aligned} \quad (9)$$

From (9), the initial value $I_{Lm(0)}$ can be determined as follows:

$$I_{Lm(0)} = \frac{I_{B(\mathrm{av})\max}}{1-D_{11R}} - \frac{V_{\mathrm{PV(max)}}D_{11R}T_s}{2L_m}. \quad (10)$$

From (7), (8), and (10), $I_{Lm(\mathrm{peak})}$ can be denoted as

$$I_{Lm(\mathrm{peak})} = \frac{I_{B(\mathrm{av})\max}}{1-D_{11R}} + \frac{V_{\mathrm{PV(max)}}D_{11R}T_s}{2L_m}. \quad (11)$$

According to datasheet of core which is supplied by core manufacturer, the number of turns N_1 on the primary side of transformer T_f can be obtained by

$$N_1 = \sqrt{\frac{L_m}{A_L}}, \quad (12)$$

where A_L represents nH per turns^2. That is, $L_m = N_1^2 A_L$. By applying Faraday's law, $B_{\max}$ can be determined as

$$B_{\max} = \frac{L_m I_{Lm(\mathrm{peak})} \times 10^4}{N_1 A_c}, \quad (13)$$

where A_c is the effective cross-section area of the transformer core. In order to avoid saturation condition of core, $B_{\max}$ must be less than saturation flux density B_{sat} of core.

4. Configuration of the Proposed PV Hybrid Converter

Since the proposed PV power system includes charger and discharger and adopts PV arrays as its power source, its circuit structure and control algorithm are described in the following.

4.1. Circuit Structure of the Proposed PV Power System. The proposed PV power system consists of battery charger, LED driving circuit (discharger), and controller, as shown in Figure 1. The battery charger and LED driving circuit using buck-boost and active clamp forward hybrid converter are shown in Figure 3. In addition, controller adopts microchip and PWM IC for managing battery charging and LED driving circuit. The microchip is divided into 3 units (MPPT, power management, and battery management units) to implement MPPT of PV arrays and battery charging. The PWM IC is used to regulate output voltage of LED driving circuit. In the microchip of the controller, the MPPT unit senses PV voltage V_{PV} and current I_{PV} to achieve MPPT, which adopts perturb and observe method. The battery management unit acquires battery voltage V_B and current I_B for implementing CC charging of battery. Since the proposed hybrid converter is required to match MPPT of PV arrays and CC charging mode, the power management unit can manage the power flow between PV arrays and battery, depending on the relationship of the generated power of PV arrays and the required power of battery charging. All of protections are implemented by microchip. The protections include overcurrent and overvoltage protections of the proposed hybrid converter and undercharge and overcharge of battery. Therefore, the proposed one can achieve the optimal utility rate of PV arrays and a better performance of battery charging.

Table 1: Parameter definitions of control signals shown in Figure 4.

Symbol	Definition
V_{PV}	Output voltage of PV arrays
I_{PV}	Output current of PV arrays
P_P	Maximum power of PV arrays
P_B	Charging power of battery ($P_B = V_B I_B$)
$P_{B(\mathrm{max})}$	Maximum charging power of battery ($P_{B(\mathrm{max})} = V_B I_{B(\mathrm{max})}$)
I_B	Charging current of battery
V_B	Battery voltage
V_O	Output voltage of forward converter
I_O	Output current of forward converter
$V_{B(\mathrm{max})}$	Maximum voltage of battery
$V_{B(\mathrm{min})}$	Minimum voltage of battery
$V_{O(\mathrm{max})}$	Maximum output voltage of forward converter
$I_{O(\mathrm{max})}$	Maximum output current of forward converter
$I_{B(\mathrm{max})}$	Maximum current of battery
V_{ref}	Reference voltage for obtaining the desired output voltage V_O
I_C	Current command for obtaining the desired charging current I_B
S_M	Control signal of operational mode (S_M = 0, battery charging; S_M = 1, LED driving)
S_n	Insolation level judgment (S_n = 1, low insolation level; S_n = 0, high insolation level)
V_f	Feedback signal of PWM IC
V_e	Error value
G_1, G_2	pwM signals
M_1, M_2	Gate signals of switches M_1 and M_2

4.2. Control Algorithm of the Proposed Hybrid Converter. In Figure 1, the controller of the proposed hybrid converter includes microchip and PWM IC to achieve battery charging and LED driving. In order to implement battery charging and LED driving, block diagram of the hybrid converter is shown in Figure 7. In Figure 7, control signals are defined in Table 1.

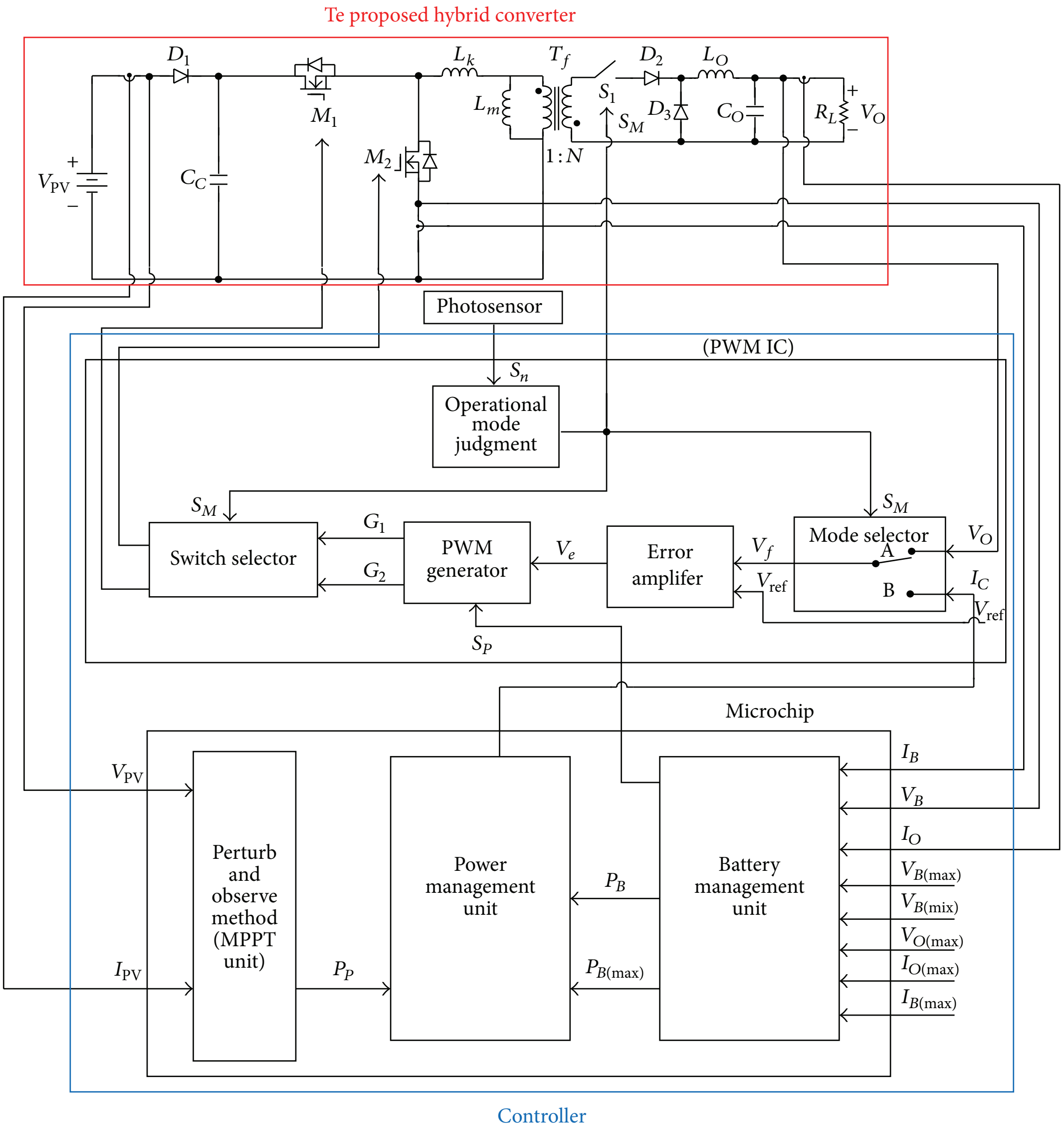

FIGURE 7: Block diagram of the proposed hybrid converter.

In the following, control algorithms for battery charging and LED driving are briefly described.

4.2.1. Battery Charging. Since the proposed hybrid converter supplies power to load from PV arrays, the proposed one must perform MPPT for PV arrays and battery charging for battery. The MPPT control method and battery charging method are described as follows.

MPPT Algorithm. Since solar cell has a lower output voltage and current, a number of solar cells are connected in series and parallel to form PV arrays for attaining the desired PV voltage and current. Their output characteristic variations depend on ambient temperature and insolation of sun. Figure 8 illustrates *P-V* curve of PV arrays at different insolation of sun, from which it can be seen that each insolation level has a maximum power P_{max} where $P_{max\,1}$ is the most insolation of sun, while $P_{max\,3}$ is the one at the least insolation. Three maximum power point $P_{max\,1} \sim P_{max\,3}$ can be connect by a straight line. The operational area is divided into two areas: A area and B area. When operational point of PV arrays locates in A area, output current I_{PV} of PV arrays is decreased to make the operational point close to its maximum power point (MPP). If operational point is set in B area, current I_{PV} will be increased to operate PV arrays at its MPP.

The proposed power system adopts perturb and observe method to implement MPPT. Its flowchart is shown in Figure 9. In Figure 9, V_n and P_p separately represent their old voltage and power, and P_n $(=V_nI_n)$ is its new power. According to flowchart procedures of MPPT using perturb and observe method, first step is to read new voltage V_n and current I_n of PV arrays and then to calculate new PV power P_n. Next step is to judge relationship of P_n and P_p. Since the relationship of P_n and P_p has three different relationships, they are separately

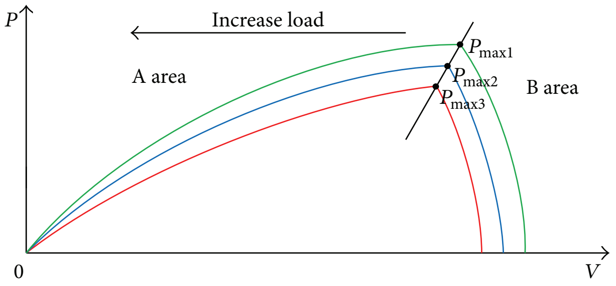

Figure 8: Plot of P-V curve for PV arrays at different isolation of sun.

$P_n > P_p$, $P_n = P_p$, and $P_n < P_p$. Each relationship can be corresponded to the different relationship of V_n and V_p. Therefore, when the relationship of P_n and P_p is decided, next step is to find the relationship of V_n and V_p. According to the relationship of P-V curve of PV arrays, when the relationships of P_n and P_p and V_n an V_p are decided, working point of PV arrays can be specified. When working point of PV arrays locates in A area, power system connected in PV arrays to supply load power must decrease output power to close the distance between working point and MPP of PV arrays. On the other hand, when working point sets in B area, power system must increase output power to make working point to approach MPP of PV arrays. Finally, V_p is replaced by V_n and P_p is also substituted by P_n. The procedure of flowchart returns first step to judge next working point of PV arrays. Moreover, when $P_n = P_P$ and $V_n = V_P$, working point of PV arrays set in the MPP of PV arrays. The maximum power P_P of PV arrays is transferred to power management unit for regulating power of battery charging.

Battery Charging Method. The proposed hybrid converter uses CC charging method to charge battery. According to battery specifications, charging voltage and current are limited for extending its life cycle. Therefore, the power limitation curve for battery charger will be limited. Figure 10 depicts conceptual waveforms of charging current, voltage, and power for battery charger with CC charging method. The battery charging time is from T_0 to T_c. When $t = T_0$, the proposed power system begins to charge battery and battery voltage V_B is at the minimum value $V_{B(\min)}$. When $t = T_c$, battery is charged to its maximum voltage $V_{B(\max)}$. According to limitation of the maximum battery charging current $I_{B(\max)}$, power limitation curve of battery charging can be determined from T_0 to T_c. The charging power of battery follows the power limitation curve for extending its life cycle.

Since power limitation curve of battery has upper and lower values, they are, respectively, $P_{B(\min)}$ $(=V_{B(\min)}I_{B(\max)})$ and $P_{B(\max)}$ $(=V_{B(\max)}I_{B(\max)})$. According to relationship among $P_{\mathrm{PV}(\max)}$, $P_{B(\min)}$, and $P_{B(\max)}$, they can be divided into three operational states: $P_{\mathrm{PV}(\max)} < P_{B(\min)}$, $P_{B(\min)} \leq P_{\mathrm{PV}(\max)} < P_{B(\max)}$, and $P_{\mathrm{PV}(\max)} > P_{B(\max)}$, as shown in Figure 11. When $P_{\mathrm{PV}(\max)} < P_{B(\min)}$, power curve of battery charging follows $P_{\mathrm{PV}(\max)}$. When $P_{B(\min)} \leq P_{\mathrm{PV}(\max)} < P_{B(\max)}$, power limitation curve and $P_{\mathrm{PV}(\max)}$ intersects at A point where its intersecting time is T_A. Power curve tracks power limitation curve before $t = t_A$, while it traces $P_{\mathrm{PV}(\max)}$ after $t = t_A$, as shown in Figure 11(b). If operational state of $P_{\mathrm{PV}(\max)} > P_{B(\max)}$, power curve is regulated by power limitation curve, as shown in Figure 11(c). As mentioned above, battery charging can be operated in a better charging mode.

In order to implement a better battery charging, power management and battery management units are adopted and they are implemented by microchip. In the following, power management and battery management are briefly described.

(1) Power Management. In Figure 7, the controller includes microchip and PWM IC. When the microchip is used to execute power management, its control procedures are depicted in Figure 12. First step is to set $S_P = 0$ and then is to read control signals. The control signals include $V_{O(\max)}$, $V_{B(\max)}$, $V_{B(\min)}$, V_B, I_B, $I_{B(\max)}$, I_O, $I_{O(\max)}$, V_{ref}, and P_P. When control signals are obtained by microchip, next step is to calculate $P_{B(\max)}$ $(=V_B I_{B(\max)})$ and P_B $(=V_B I_B)$. Since P_P, which is attained by MPPT control method, is the maximum output power of PV arrays, when $P_P \geq P_{B(\max)}$ is confirmed, P_{set} is set to equal $P_{B(\max)}$. If $P_P \geq P_{B(\max)}$ is denied, $P_{\mathrm{set}} = P_P$. The P_P is the power command of battery charging. Therefore, power error value ΔP can be determined. It is equal to $(P_{\mathrm{set}} - P_B)$. When ΔP is determined, current command I_C can be obtained. It is equal to $(\Delta P/V_B)$. The current command I_C is sent to PWM IC to determine gate signals G_1 and G_2. Next step is to judge next current command.

(2) Battery Management. In Figure 12, the right hand side of flowchart shows procedures of battery management. When the microchip reads control signals, the procedure of battery management is to judge overcurrent condition. When $I_O \geq I_{O(\max)}$ is confirmed, overcurrent condition of the proposed hybrid converter occurred. When overcurrent condition occurred, signal S_P is set to 1. The S_P is sent to PWM IC to shutdown PWM generator and the proposed hybrid converter is also shutdown. Next step is to judge next current command. Moreover, when $V_O \geq V_{O(\max)}$ (overcharge condition), $V_B \leq V_{B(\min)}$ (undercharge condition) and $V_B \geq V_{B(\max)}$ (overcharge condition), the control procedure enters to set $S_P = 1$ and to shutdown the proposed hybrid converter. According to previously describing procedures, battery can be properly controlled to complete a better charging condition.

(3) PWM IC. In the battery charging mode, PWM IC is used to control charging current with CC method. First, photosensor is used to detect insolation level of sun. When insolation is a high level, $S_n = 0$. If insolation is a low level, $S_n = 1$. The signal S_n is sent to operational mode judgment to obtain mode control signal S_M. When $S_M = 0$, the hybrid converter enters battery charging mode. That is, the insolation of sun is at a high level and $S_n = 0$. If $S_M = 1$, the one is in LED driving mode. The signal $S_n = 1$ and insolation is at a low level. The mode control signal S_M is sent to mode selector, switch selector, and switch S_1. When mode selector

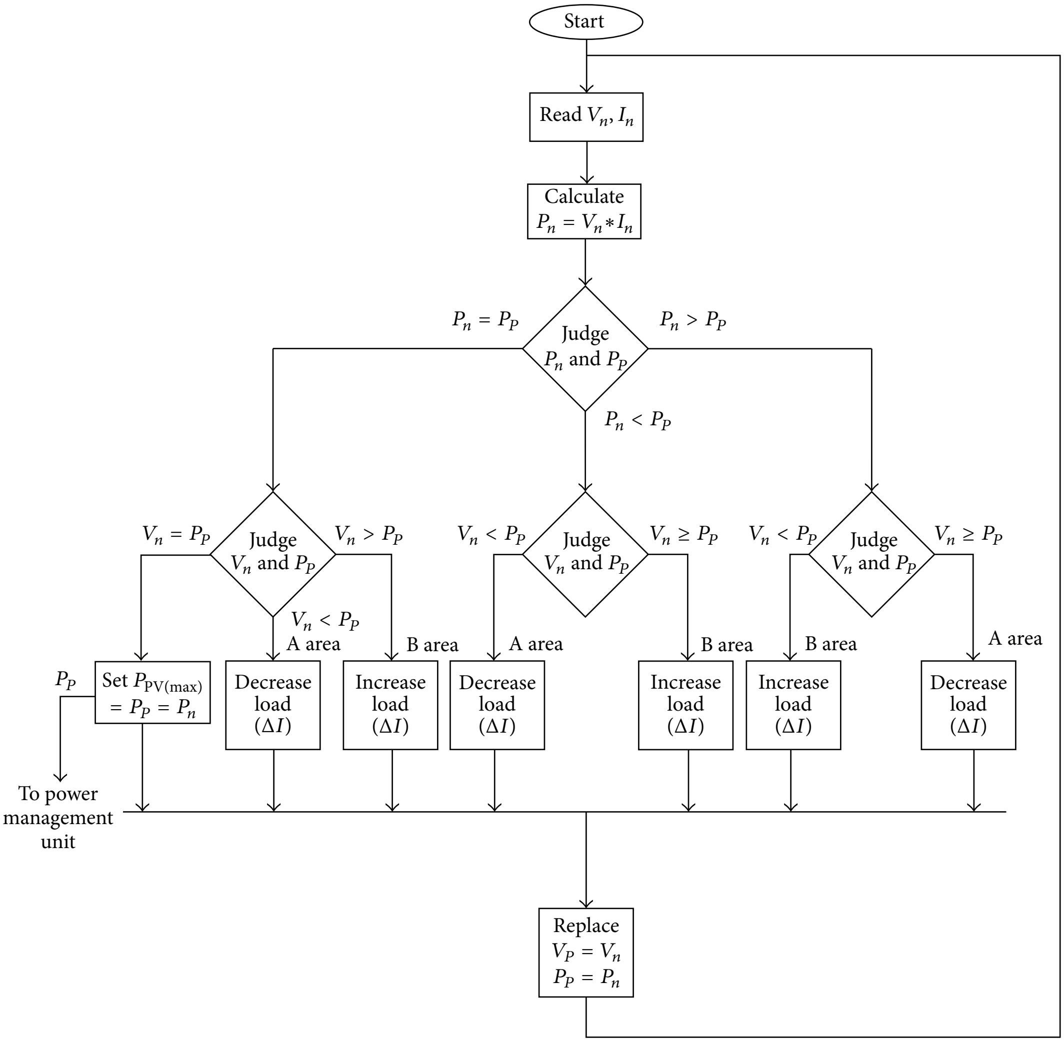

FIGURE 9: Flowchart of MPPT using perturb and observe method for PV arrays system.

receives $S_M = 0$, the feedback signal V_f is set to equal IC. The feedback signal V_f and reference single V_{ref} are sent to error amplifier to obtain error value V_e. When error value V_e is attained, PWM generator can depend on V_e to determine duty ratios of PWM signals G_1 and G_2. When G_1 and G_2 are specified and $S_M = 0$, switch selector can set that $M_1 = G_1$ and $M_2 = G_2$ to control the charging current I_B of battery. As mentioned above, the proposed hybrid converter can use microchip and PWM IC to achieve battery charging.

4.2.2. LED Driving. The LED driving mode is regarded as battery discharging mode. When operational mode enters LED driving mode, $S_M = 1$. The mode selector can be operated to set $V_f = V_O$. The V_f and V_{ref} are sent to error amplifier to attain V_e. The V_e is through PWM generator to generate signals G_1 and G_2. Since $S_M = 1$, switch selector is controlled by S_M to set $M_1 = G_2$ and $M_2 = G_1$. Therefore, the proposed hybrid converter can depend on duty ratios of gate signals M_1 and M_2 to supply power to LED until battery voltage V_B is equal to or less than $V_{B(\min)}$. When $V_B \leq V_{B(\min)}$, the proposed hybrid converter is shutdown.

5. Experimental Results

In order to verify the circuit analysis and component design of the proposed power system, a prototype, which is composed of a charger and LED driving circuit (discharger), with the following specifications was implemented.

5.1. Buck-Boost Converter (Charger)

(i) Input voltage V_{PV} : DC 17 V~21 V (PV arrays)
(ii) Switching frequency f_{s1} : 250 KHz
(iii) Output voltage V_B : DC 5~7 V (lead-acid battery: 6 V/2.3 Ah)
(iv) Maximum output current $I_{B(\max)}$: 2.3 A.

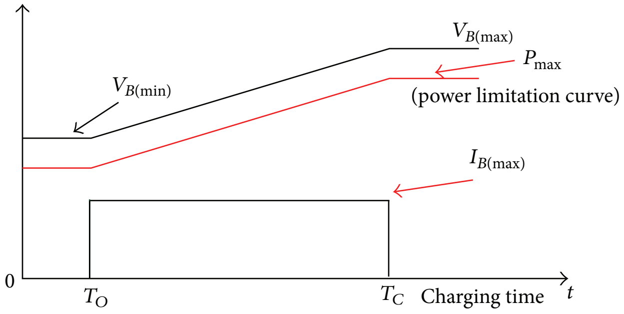

FIGURE 10: Conceptual waveforms of charging current, voltage, and power for battery charger with CC charging method.

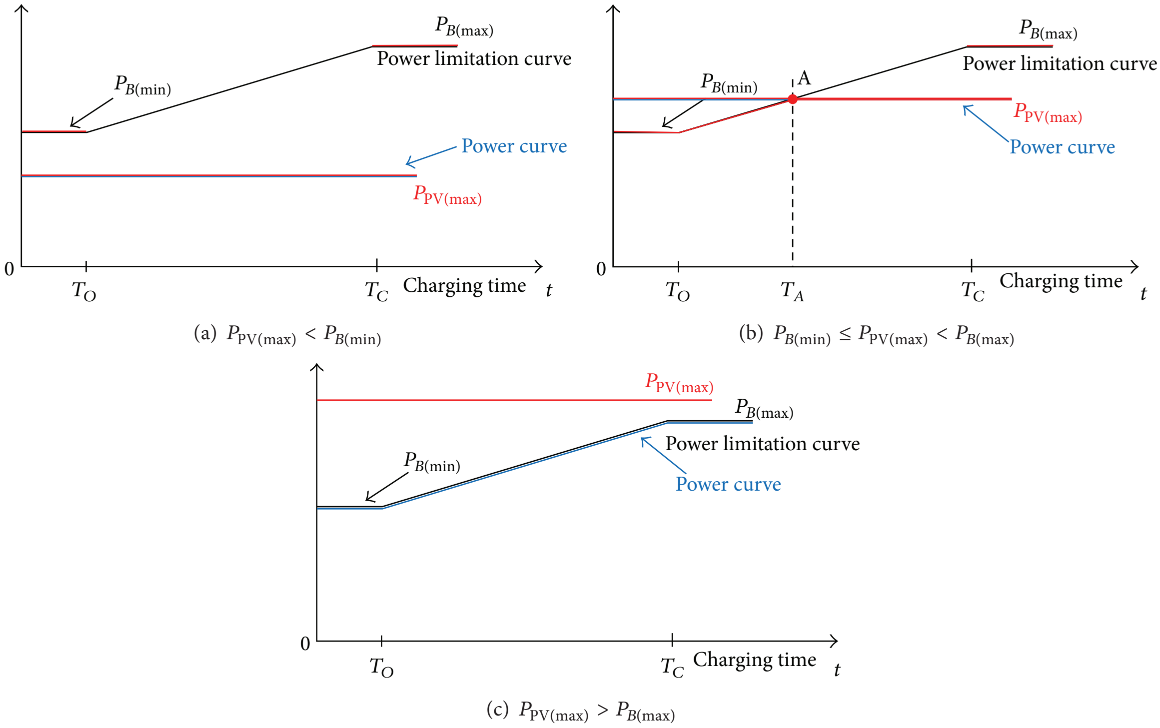

(a) $P_{PV(\max)} < P_{B(\min)}$

(b) $P_{B(\min)} \leq P_{PV(\max)} < P_{B(\max)}$

(c) $P_{PV(\max)} > P_{B(\max)}$

FIGURE 11: Conceptual waveforms of maximum output power of PV arrays and power limitation and power curves of battery from T_O to T_C: (a) $P_{PV(\max)} < P_{B(\min)}$, (b) $P_{B(\min)} \leq P_{PV(\max)} < P_{B(\max)}$, and (c) $P_{PV(\max)} > P_{B(\max)}$.

5.2. Active Clamp Forward Converter (LED Driving Circuit)

(i) Input voltage V_B : DC 5 V~7 V

(ii) Switching frequency f_{s2} : 250 KHz

(iii) Output voltage V_O : DC 10 V

(iv) Maximum output current $I_{O(\max)}$: 2 A.

According to previously specifications and design of the hybrid converter, inductors L_2 and L_m and capacitor C_C can be determined. In (17) illustrated in [23], since inductor L_m must be greater than 7.09 uH under $V_O = 10$ V, $V_B = 7$ V, and $V_{PV} = 17$ V, L_2 is chosen by 40 uH. According to (6) and (22) illustrated in [23], the magnetizing inductor L_m must be greater than 6.8 uH under $N = 5$, $V_B = 7$ V, and $L_2 = 40$ uH. Therefore, magnetizing inductor L_m is determined by 40 uH, while its leakage inductor L_K is obtained by 0.2 uH. Moreover, capacitor C_C can be attained by (29) illustrated in [23]. Its capacitance C_C is 0.22 nF under $N = 5$ and $V_B = 7$ V. Therefore, C_C is chosen by 0.24 uF. The components of power stage in the proposed hybrid converter was determined as follows:

(i) switches M_1, M_2: PSMN005-75B,

(ii) diodes D_1, D_2: UF601,

(iii) transformer T_f: EE-25 core,

(iv) inductor L_2: EE-22 core,

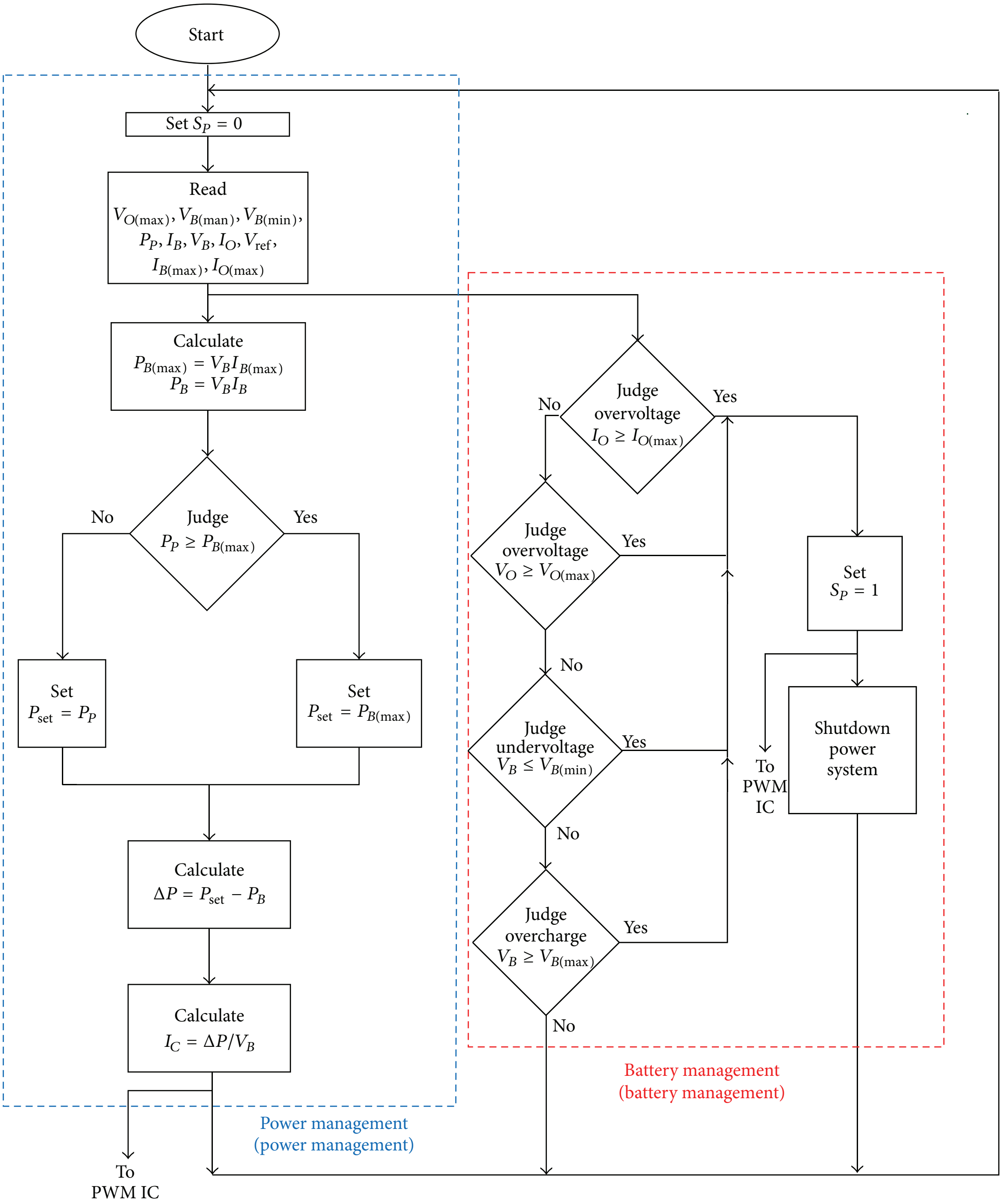

FIGURE 12: Flowchart of power and battery managements of the proposed hybrid converter.

(v) capacitor C_O: 47 μF/25 V, and

(vi) switch S_1: IRFP540.

Since the charging current I_B of battery can be varied by duty ratio of switch M_1 in buck-boost converter, its value is proportional to duty ratio D_{11}. Figures 13(a) and 13(b), respectively, depict the measured voltage V_{DS} waveform of switch M_1 and current I_B waveform under duty ratio of 0.31 and 0.35, illustrating that the charging current I_B can be increased by duty ratios increase. Measured waveforms of PV arrays current I_{PV} and voltage V_{PV} using the perturb and observe method are illustrated in Figure 14. Figure 14(a) illustrates the MPP of PV arrays at 10 W, while Figure 14(b) depicts that at 20 W. Figure 15 shows the measured battery voltage V_B and current I_B under MPP of PV arrays at 10 W, from which it can be found that the maximum charging

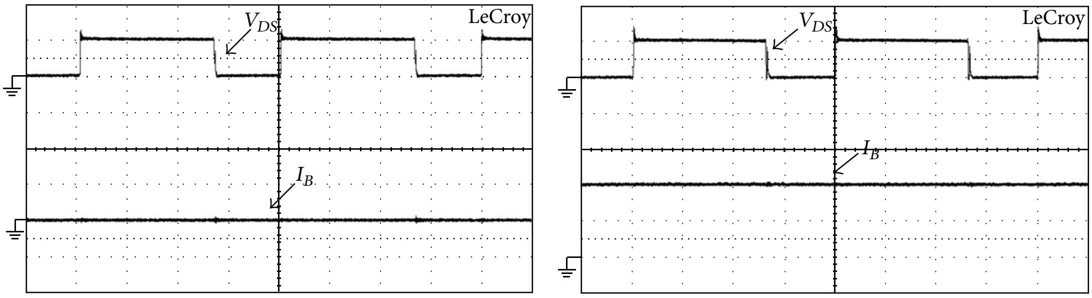

(V_{DS}: 25 V/div, I_{DS}: 500 mA/div, 1 μs/div) (V_{DS}: 25 V/div, I_{DS}: 500 mA/div, 1 μs/div)

(a) (b)

FIGURE 13: Measured voltage V_{DS} waveform of switch M_1 and the charged current I_B waveform operated in duty ratio of (a) 0.31 and (b) 0.35 for working in the charging state.

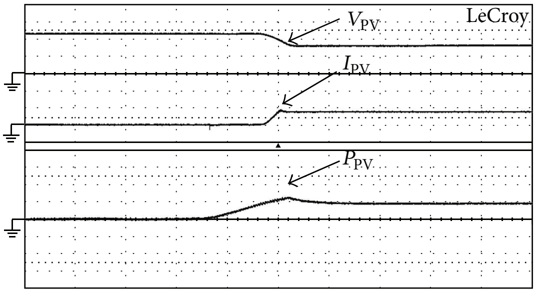

(V_{PV}: 20 V/div, I_{PV}: 2 A/div, P_{PV}: 50 W/div, time: 100 ms/div)

(a)

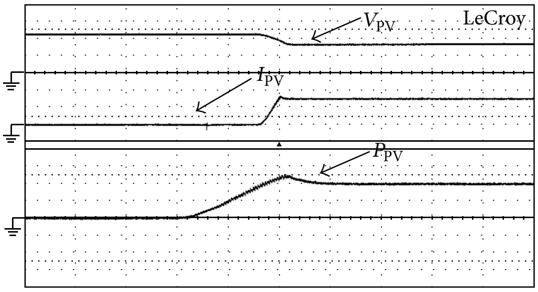

(V_{PV}: 20 V/div, I_{PV}: 2 A/div, P_{PV}: 50 W/div, time: 100 ms/div)

(b)

FIGURE 14: Measured voltage V_{PV}, current I_{PV}, and power P_{PV} waveforms of PV arrays using the perturb and observe method to track MPPT of arrays (a) under $P_{PV(max)} = 10$ W and (b) under $P_{PV(max)} = 20$ W.

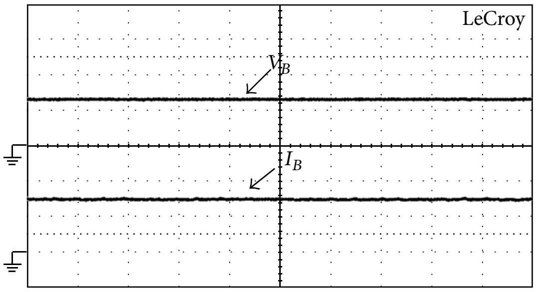

(V_B: 5 V/div, I_B: 1 A/div, time: 10 ms/div)

FIGURE 15: Measured battery voltage V_B and current I_B waveforms under $P_{PV(max)} = 10$ W.

current I_B is limited at 1.5 A under battery voltage V_B of 6.5 V due to control of power management.

When the proposed hybrid converter is operated in the discharging state (LED driving state), active clamp forward is in working. Measured voltage V_{DS} and current I_{DS} waveforms of switched M_1 and M_2 are, respectively, illustrated in Figures 16 and 17. Figures 16(a) and 16(b) show those waveforms under 20% of full load, while Figures 17(a) and 17(b) depict those waveforms under full load. From Figures 16 and 17, it can be seen that switches M_1 and M_2 are operated with ZVS at turn-on transition. Comparison of conversion efficiency between forward converter with hard-switching circuit and with the proposed active clamp circuit from light load to heavy load is depicted in Figure 18, from which it can be found that the efficiency of the proposed converter is higher than that of hard-switching one. Its maximum efficiency is 90% under 80% of full load and its efficiency is 83% under full load. Figure 19 illustrates step-load change between 20% of full load and full load, illustrating that the voltage regulation V_O has been limited within ±2%. From experimental results, it can be found that the proposed hybrid converter is suitable for electronic sign applications.

6. Conclusion

In this paper, the buck-boost converter combined with active clamp forward converter to form the proposed hybrid converter is used to implement battery charger and driving LED. Circuit derivation of the hybrid converter with switch integration technique is presented in this paper to reduce component counts. Operational principle, steady-state analysis, and design of the proposed hybrid converter have been described in detail. From efficiency comparison between forward converter with hard-switching circuit and with the proposed active clamp circuit, the proposed active clamp converter can yield higher efficiency. An experimental

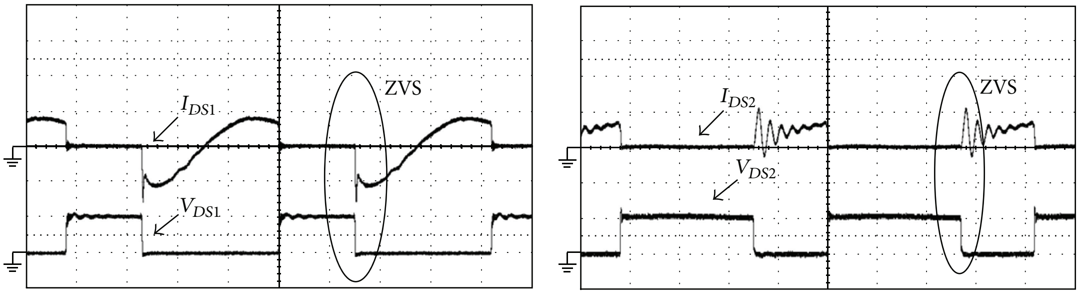

(V_{DS1}: 10 V/div, I_{DS1}: 4 A/div, 1 μs/div)

(a)

(V_{DS2}: 10 V/div, I_{DS2}: 4 A/div, 1 μs/div)

(b)

FIGURE 16: Measured voltage V_{DS} and current I_{DS} waveforms of (a) switch M_1 and (b) switch M_2 for working under 20% of full load.

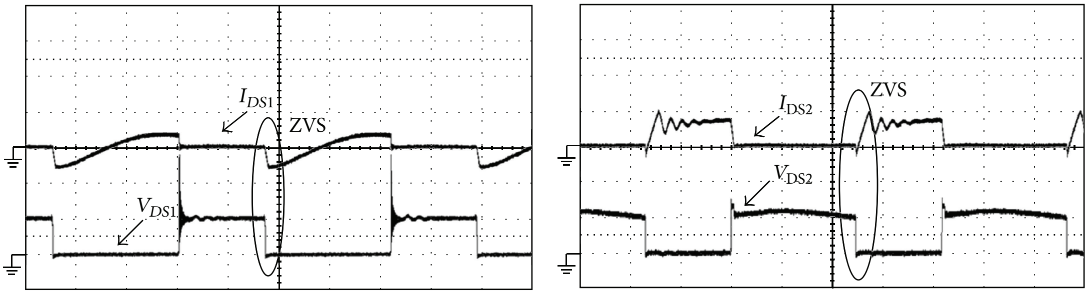

(V_{DS1}: 10 V/div, I_{DS2}: 15 A/div, 1 μs/div)

(a)

(V_{DS2}: 10 V/div, I_{DS2}: 15 A/div, 1 μs/div)

(b)

FIGURE 17: Measured voltage V_{DS} and current I_{DS} waveforms of (a) switch M_1 and (b) switch M_2 for working under full load.

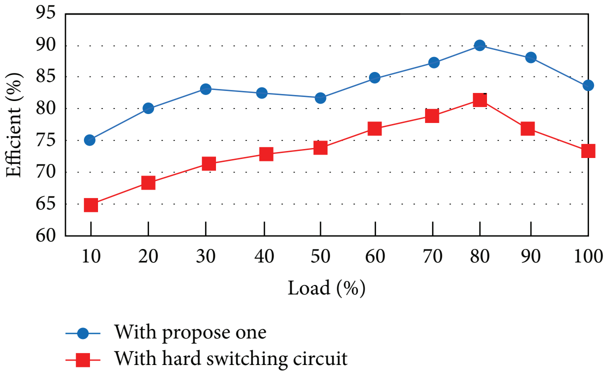

FIGURE 18: Comparison conversion efficiency between the conventional hard-switching forward converter and the proposed one from light load to heavy load for working in the discharging state.

prototype for a battery charger for lead-acid battery of 6 V/2.3 Ah and discharger for LED driving under 10 V/2 A has been built and evaluated, achieving the maximum efficiency of 90% under 80% of full load and verifying the feasibility of the proposed hybrid converter. Moreover, constant current charging method, MPPT with perturb and observe method, and power management have been implemented by microchip and PWM IC.

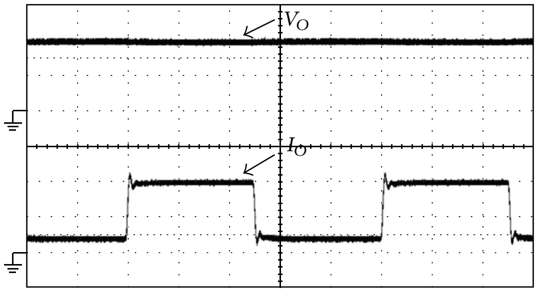

(V_O : 5 V/div, I_O : 1 A/div, 500 μs/div)

FIGURE 19: Output voltage V_O and output current I_O under step-load charges between 30% and 100% of full load of the proposed forward converter operated in the discharging state.

Conflict of Interests

The authors declare that there is no conflict of interests regarding the publication of this paper.

References

[1] Y. Jiang, A. W. Leung, J. Xiang, and C. Xu, "LED light-activated hypocrellin B induces mitochondrial damage of ovarian cancer cells," *International Journal of Photoenergy*, vol. 2012, Article ID 186752, 5 pages, 2012.

[2] C.-H. Liu, C.-Y. Hsieh, Y.-C. Hsieh, T.-J. Tai, and K.-H. Chen, "SAR-controlled adaptive off-time technique without sensing resistor for achieving high efficiency and accuracy LED lighting system," *IEEE Transactions on Circuits and Systems I*, vol. 57, no. 6, pp. 1384–1394, 2010.

[3] C. C. Chen, C.-Y. Wu, and T.-F. Wu, "LED back-light driving system for LCD panels," in *Proceedings of The Applied Power Electronics Conference and Exposition*, pp. 19–23, 2006.

[4] S.-Y. Tseng and C.-T. Tsai, "Photovoltaic power system with an interleaving boost converter for battery charger applications," *International Journal of Photoenergy*, vol. 2012, Article ID 936843, 15 pages, 2012.

[5] J.-H. Park and B.-H. Cho, "Nonisolation soft-switching buck converter with tapped-inductor for wide-input extreme step-down applications," *IEEE Transactions on Circuits and Systems I*, vol. 54, no. 8, pp. 1809–1818, 2007.

[6] K. Mehran, D. Giaouris, and B. Zahawi, "Stability analysis and control of nonlinear phenomena in boost converters using model-based Takagi-Sugeno fuzzy approach," *IEEE Transactions on Circuits and Systems I*, vol. 57, no. 1, pp. 200–212, 2010.

[7] B. Bryant and M. K. Kazimierczuk, "Open-loop power-stage transfer functions relevant to current-mode control of boost PWM converter operating in CCM," *IEEE Transactions on Circuits and Systems I*, vol. 52, no. 10, pp. 2158–2164, 2005.

[8] M. R. Yazdani, H. Farzanehfard, and J. Faiz, "EMI analysis and evaluation of an improved ZCT flyback converter," *IEEE Transactions on Power Electronics*, vol. 26, no. 8, pp. 2326–2334, 2011.

[9] K. I. Hwu and T. J. Peng, "A novel buck-boost converter combining KY and buck converters," *IEEE Transactions on Power Electronics*, vol. 27, no. 5, pp. 2236–2241, 2012.

[10] F. Xie, R. Yang, and B. Zhang, "Bifurcation and border collision analysis of voltage-mode-controlled flyback converter based on total ampere-turns," *IEEE Transactions on Circuits and Systems I*, vol. 58, no. 9, pp. 2269–2280, 2011.

[11] B.-R. Lin and H.-Y. Shih, "Implementation of a parallel zero-voltage switching forward converter with less power switches," *IET Power Electronics*, vol. 4, no. 2, pp. 248–256, 2011.

[12] D. Wang, X. He, and J. Shi, "Design and analysis of an interleaved flybackforward boost converter with the current autobalance characteristic," *IEEE Transactions on Power Electronics*, vol. 25, no. 2, pp. 489–498, 2010.

[13] T.-F. Wu and T.-H. Yu, "Unified approach to developing single-stage power converters," *IEEE Transactions on Aerospace and Electronic Systems*, vol. 34, no. 1, pp. 211–223, 1998.

[14] K. I. Hwu, W. C. Tu, and C. R. Wang, "Photovoltaic energy conversion system constructed by high step-up converter with hybrid maximum power point tracking," *International Journal of Photoenergy*, vol. 2013, Article ID 275210,, 9 pages, 2013.

[15] A. Braunstein and Z. Zinger, "On the dynamic optimal coupling of a solar cell array to a load and storage batteries," *IEEE transactions on Power Apparatus and Systems*, vol. 100, no. 3, pp. 1183–1188, 1981.

[16] A. S. Weddell, G. V. Merrett, and M. A.-H. Bashir, "Photovoltaic sample-and-hold circuit enabling MPPT indoors for low-power systems," *IEEE Transaction on Circuits and Systems*, vol. 59, no. 6, pp. 1196–1204, 2012.

[17] S. M. M. Wolf and J. H. R. Enslin, "Economical, PV maximum power point tracking regulator with simplistic controller," in *Proceedings of the EEE 24th Annual Power Electronics Specialist Conference*, pp. 581–587, June 1993.

[18] C.-L. Shen and S.-H. Yang, "Multi-input converter with MPPT feature for wind-PV power generation system," *International Journal of Photoenergy*, vol. 2013, Article ID 129254, 13 pages, 2013.

[19] R. Leyva, C. Olalla, H. Zazo et al., "MPPT based on sinusoidal extremum-seeking control in PV generation," *International Journal of Photoenergy*, vol. 2012, Article ID 672765, 7 pages, 2012.

[20] N. Onat, "Recent developments in maximum power point tracking technologies for photovoltaic systems," *International Journal of Photoenergy*, vol. 2010, Article ID 245316, 11 pages, 2010.

[21] K. H. Hussein, I. Muta, T. Hoshino, and M. Osakada, "Maximum photovoltaic power tracking: an algorithm for rapidly changing atmospheric conditions," *IEE Proceedings: Generation, Transmission and Distribution*, vol. 142, no. 1, pp. 59–64, 1995.

[22] S. R. Rajwade, K. Auluck, J. B. Phelps, K. G. Lyon, J. T. Shaw, and E. C. Kan, "A ferroelectric and charge hybrid nonvolatile memory—Part II: experimental validation and analysis," *IEEE Transactions on Electron Devices*, vol. 59, no. 2, pp. 450–458, 2012.

[23] S. Y. Tseng, H. Y. Wang, and C. C. Chen, "PV power system using hybrid converter for LED indictor applications," *Energy Conversion and Management*, vol. 75, pp. 761–772, 2013.

Hindawi Publishing Corporation
International Journal of Photoenergy
Volume 2014, Article ID 209028, 10 pages
http://dx.doi.org/10.1155/2014/209028

Research Article

A Novel Parabolic Trough Concentrating Solar Heating for Cut Tobacco Drying System

Jiang Tao Liu, Ming Li, Qiong Fen Yu, and De Li Ling

Solar Energy Research Institute, Yunnan Normal University, Kunming 650092, China

Correspondence should be addressed to Ming Li; lmllldy@126.com

Received 31 October 2013; Accepted 4 February 2014; Published 26 March 2014

Academic Editor: Adel M. Sharaf

A novel parabolic trough concentrating solar heating for cut tobacco drying system was established. The opening width effect of V type metal cavity absorber was investigated. A cut tobacco drying mathematical model calculated by fourth-order Runge-Kutta numerical solution method was used to simulate the cut tobacco drying process. And finally the orthogonal test method was used to optimize the parameters of cut tobacco drying process. The result shows that the heating rate, acquisition factor, and collector system efficiency increase with increasing the opening width of the absorber. The simulation results are in good agreement with experimental data for cut tobacco drying process. The relative errors between simulated and experimental values are less than 8%, indicating that this mathematical model is accurate for the cut tobacco airflow drying process. The optimum preparation conditions are an inlet airflow velocity of 15 m/s, an initial cut tobacco moisture content of 26%, and an inlet airflow temperature of 200°C. The thermal efficiency of the dryer and the final cut tobacco moisture content are 66.32% and 14.15%, respectively. The result shows that this parabolic trough concentrating solar heating will be one of the heat recourse candidates for cut tobacco drying system.

1. Introduction

Solar energy currently represents the most abundant inexhaustible, nonpolluting, and free energy resources that could have a positive meaning in alleviating the global energy shortage and environmental pollution. There are abundant solar energy resources and good economic tobacco industry in Yunnan Province, located in the southwest of China. However, drying cut tobacco of the production process in cigarette factory needs a large amount of heat energy (150°C~300°C). If abundant solar energy resources are used for drying cut tobacco of the production process in cigarette factory, we can not only save a large amount of fossil energy but also widen the field of utilization of solar energy. In this paper, solar energy drying cut tobacco process will be investigated.

However, the solar energy is intermittent in nature and that received on earth is of small flux density due to atmospheric scattering and abortion, making it necessary to use large surfaces to collect solar energy for drying cut tobacco process utilization. The major technologies used for solar energy conversion to heat are thermal processes comprising of solar collectors. There are two basic types of solar collectors, the flat-plate and the concentrating solar collectors. The flat-plate collector has advantage of absorbing both beam and diffused radiation and, therefore, still functions when beam radiation is cut off by the cloud. The area absorbing solar radiation is the same as the area intercepting solar radiation. However, flat-plate collectors are designed for applications requiring energy delivered at temperatures quite lower than 100°C, indicating that they are not suitable for drying cut tobacco process. The concentrating collector utilizes optical systems like reflectors, refractors, and so forth to increase the intensity of solar radiation incidents on energy-absorbing surfaces. It has the main advantage of generating high temperatures and may be used for drying cut tobacco process.

Parabolic trough solar collector (PTC) is one type of the intermediate/high concentrating collectors, being widely used in the field of electricity generation, air-conditioning, heating, desalination, and so on. Conventional receiver used in PTC is the vacuum tube. Because of different expanding coefficients between the metallic tube and the glass tube, the cost of vacuum tube receiver is relatively high, and its useful life is short. Therefore, many researches focus on investigation of cavity absorbers. Boyd et al. [1] firstly developed a receiver that consists of an annular cylindrical tube with an aperture parallel to the axis of the cylinder. The aperture is illuminated by means of a focusing concentrator, such as a lens, and the radiation energy is scattered inside the cavity, absorbed by the walls and transmitted, as heat, to the working fluid flowing axially inside the annulus. To reduce radiative losses the tube is surrounded by a layer of a thermal insulator. Principal advantages of this design lie in exclusive use of commonly available materials and current fabrication technology. In order to minimize the heat loss, this annular cylindrical tube was improved by Barra and Franceschi [2]. Eight small cylindrical tubes were scattered inside the big cylindrical tube and used for fluid transferring. Qiaoli et al. [3] proposed the scheme of tightly connecting cluster and the inner wall of pipe. Moreover, Zhang et al. [4] established a series of absorbers with triangular, circular, hemispherical and square, and simulated the optical performance and thermal property using the software programs TracePro and Fluent. The results showed that the triangular cavity absorber structure owned the best optical performance and thermal property, which could gain collecting efficiency above 40%, under the condition of collecting temperature 150°C. Based on these above studies, a novel cavity absorber was investigated by this paper. PTC system with V type metal cavity absorber similar to triangle structure would be used for drying cut tobacco process and the thermal loss is constrained by the cavity radiation. In order to lower the absorber cost, aluminum alloy was selected as the material of absorber.

Because of the coupling effect among the heat transfer, mass transfer, and energy, air drying process became complex. In order to analyze air drying cut tobacco process, simulation model was discussed. Fukuchi et al. [5] regarded the cut tobacco as equal volume sphere and simulated the motion characteristics, indicating the simulation results agreed well with the experimental results. The model equivalent sphere was established to simulate drying process of superheated steam by Pakowski et al. [6]. The result showed the moisture content of shredded tobacco simulated and the outlet temperature simulated agreed well with the experimental values. Based on these simulation results, simulation model of air drying cut tobacco process was studied and the process parameters of process of drying cut tobacco were optimized in this research.

In this paper, parabolic trough concentrating system with V type metal cavity absorber was used for providing heat for cut tobacco drying system. In order to reduce the incident light energy loss and prevent cavity absorber from deformation, the width of V type metal cavity absorber was calculated, ensuring that stable heat energy provided by the PTC system is enough for cut tobacco drying process. Moreover, a mathematical model of cut tobacco drying process was calculated by using fourth-order Runge-Kutta numerical solution method and the accuracy of the model compared with the experimental results was analyzed.

Table 1: Main parameters of cut tobacco drying system.

Parabolic trough concentrator mirror	
Reflectivity	0.9
Opening width	3.2 m
Lighting area	30 m^2
Length	10 m
Metallic V cavity absorber	
Opening width	4 cm, 7 cm
Internal surface coating	Aluminum anodic oxide film
Absorptivity	0.85~0.9
Emissivity	0.1~0.2
Variable diameter drying pipe	
Part 1	Height: 1.2 m, diameter: 200 mm
Part 2	Height: 2 m, diameter: 300 mm
Total height	3.25 m

2. Materials and Methods

2.1. Materials. Before solar energy drying process, the cut tobacco samples were pretreated by humidifier and equilibrated water content for 24 h in conditions of temperature 20±2°C and relative humidity 60±2%. Moisture content of cut tobacco samples was determined by YC/T31-1996 standard test methods [7].

2.2. Experimental Equipment

2.2.1. Parabolic Trough Concentrating Solar Heating for Cut Tobacco Drying System. Diagram of parabolic trough concentrating solar heating for cut tobacco drying system was shown in Figure 1(a). The main parameters of the design are given in Table 1. The parabolic trough concentrating solar heating for cut tobacco drying process was illustrated as follows. Firstly, when sunlight arrived at the parabolic trough concentrator mirror, the solar tracker was adjusted to make the metal V cavity body coincide with focal length of the PTC. Because of photothermal conversion, heat transfer oil was used to exchange heat with the cavity body and then heated to the predetermined temperature. Secondly, the circulating fan was opened and the hot air exchanged with heat transfer oil was transferred into the drying pipe. When temperature of the hot air reached target temperature in the drying pipe, cut tobacco pretreated was put into the drying pipe for drying process. Thirdly, when finishing the drying process, product of cut tobacco dried was followed with airflow into the whirlwind separator and separated from the airflow. Fourthly, part of airflow was recycled into next drying process and the left airflow was supplied by the valve S2. The electric heater was used to keep the output temperature of heat conduction oil stable when solar irradiance changed.

2.2.2. Test Schematic of Energy Flux Density Distribution. In order to analyze the effect of cavity opening width on energy flux density distribution, the test schematic was shown in Figure 2. As shown in Figure 2, the width and the focal length of parabolic trough concentrator mirror were 3.2 m

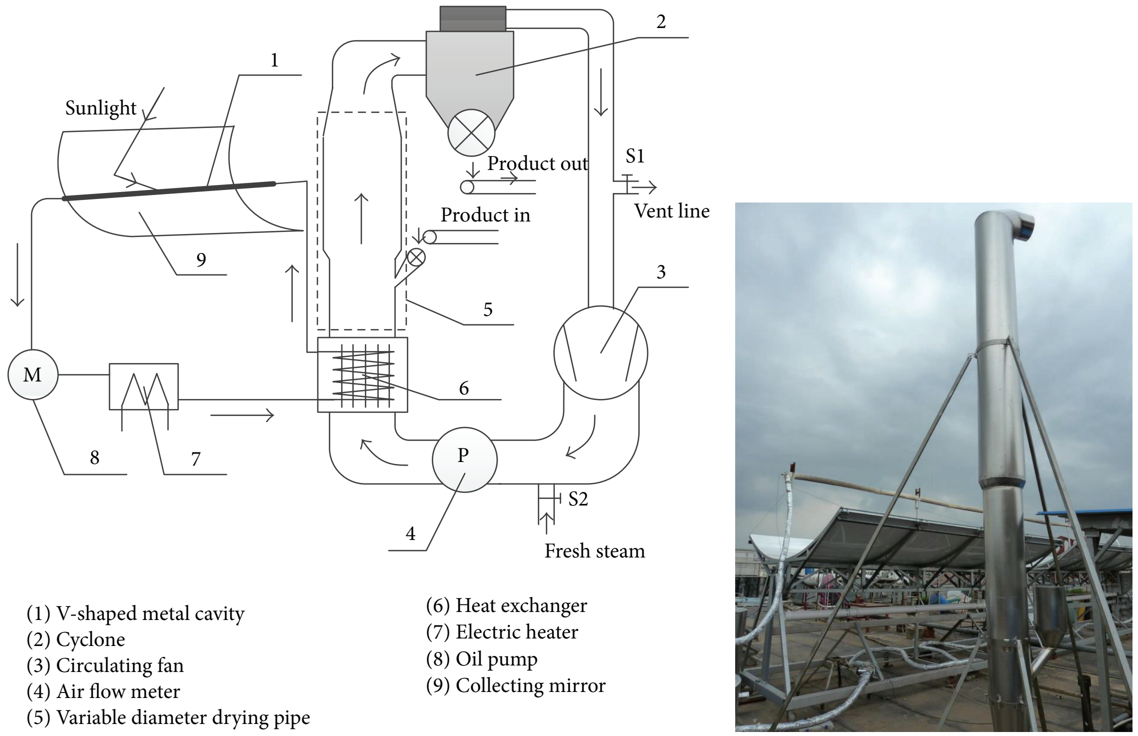

(a) Diagram of parabolic trough concentrating solar heating for cut tobacco drying system

(b) Photograph of parabolic trough concentrating solar heating for cut tobacco drying system

Figure 1: Parabolic trough concentrating solar heating for cut tobacco drying system.

and 117 cm, respectively. There were a width of 10 cm Lambert target, neutral density attenuator (ND-filter), CCD industrial cameras, computers and solar tracking control system, and other parts. Test method was detailed by our previous work [8].

3. Cut Tobacco Drying Mathematical Model

3.1. Assumption. In this work, a relatively simple one-dimensional model [9, 10] was adopted assuming no radial or axial dispersion of flow. The shape of cut tobacco particles was considered as equal volume sphere and had a uniform size. Diameter and density variations of cut tobacco particles were ignored in the drying process. The wall of drying pipe has good insulation and there was no heat exchange with the atmospheric environment.

3.2. Mathematical Model of the Drying Process. The momentum equation of cut tobacco particle was as follows:

$$\frac{dv_p}{dz} = \frac{3}{4}\xi\frac{\rho_g\left(v_g - v_p\right)^2}{v_p d_p \rho_p} - \left(1 - \frac{\rho_g}{\rho_p}\right)\frac{g}{v_p} - \frac{0.1}{D}. \quad (1)$$

The relationship between ξ and Re in (1) was shown in Table 2 [11].

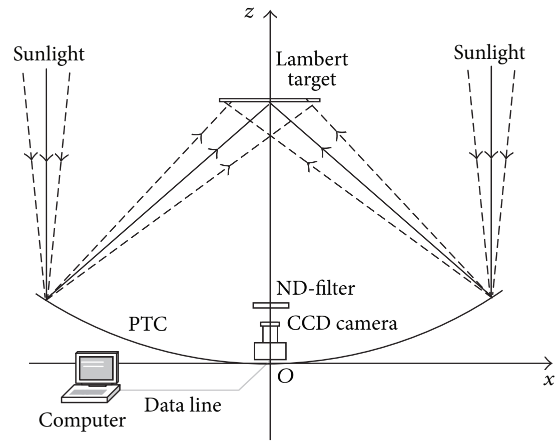

Figure 2: The measurement schematic of focal line energy flux density distribution.

The movement equation of air stream was as follows:

$$\frac{dv_g}{dz} = -\frac{dP}{\rho_g v_g dz} - \frac{g}{v_g} - \frac{3N\xi\left(v_g - v_p\right)^2}{4v_g d_p} - \frac{\lambda v_g}{2D}. \quad (2)$$

The parameter N of (2) was the number of particles per unit volume in the drying pipe and identified according to the experimental conditions.

Table 2: The relationship between ξ and Re.

Parameter	Numerical value		
Re	0-1	1–500	500–15000
ξ	24/Re	$24/\mathrm{Re}^{0.5}$	0.44

The differential equations of cut tobacco particles and airflow humidity distribution were as follows:

$$G_p dX + G_g dY = 0 \tag{3}$$

$$G_P dX + W_d dA = 0. \tag{4}$$

The equation of dry mass transfer rate was as follows:

$$W_d = K_y \left(Y_{\mathrm{eq}} - Y\right). \tag{5}$$

The differential equation of cut tobacco particles humidity was as follows:

$$\frac{dX}{dz} = -\frac{6K_y \left(Y_{\mathrm{eq}} - Y\right)(1 + X)}{\rho_p d_p v_p}. \tag{6}$$

The mass transfer coefficient K_y, the Schmidt number Sc, and the Prandtl number Pr in (6) were associated and calculated according to the correlation proposed by literature [12]:

$$\frac{h}{K_y} = C_g (1 + Y) \left(\frac{\mathrm{Sc}}{\mathrm{Pr}}\right)^{0.56}$$
$$\mathrm{Pr} = \frac{\left(C_g v_g \rho_g\right)}{\lambda_g}, \tag{7}$$
$$\mathrm{Sc} = \frac{v_g}{D_{va}}.$$

Combining (3) and (6), the differential equation of airflow and humidity could be obtained as

$$\frac{dY}{dz} = -\frac{6G_p K_y \left(Y_{\mathrm{eq}} - Y\right)(1 + X)}{G_g \rho_p d_p v_p}. \tag{8}$$

The heat balance equation of cut tobacco particles was

$$\frac{dt_p}{dz} = -\frac{C_w t_p}{C_s + C_w X} \frac{dX}{dz} + \frac{6(1 + X)\left[h\left(t_g - t_p\right) - K_y \left(Y_{\mathrm{eq}} - Y\right)\left(r_0 + C_w t_p\right)\right]}{\rho_p v_p d_p \left(C_s + C_w X\right)}. \tag{9}$$

The convective heat transfer coefficient h between the air stream and cut tobacco particles in (9) was associated with Russell number Nu and also calculated by literature [12].

The equation of gas heat balance was as follows:

$$\frac{dt_g}{dz} = -\frac{r_0}{C_g} \frac{dY}{dz} - \frac{6G_p (1 + X)\left[h\left(t_g - t_p\right) - K_y \left(Y_{\mathrm{eq}} - Y\right)\left(r_0 + C_w t_p\right)\right]}{G_g v_p d_p C_g}. \tag{10}$$

The differential equation of pipe diameter was as follows:

$$\frac{dD}{dz} = 2 \cot \theta. \tag{11}$$

There, θ was the expansion angle of the adjustable pipe.

According to the equations from (1) to (2) and (6) to (11), the tapered tubular air drying cut tobacco mathematical model was formed. Then this mathematical model was calculated using fourth-order Runge-Kutta method and Matlab software program.

4. Results and Discussion

4.1. The heating Experiments of Parabolic Trough Concentrating System. Experiments were studied to analyze the effect of cavity opening width on collector temperatures as shown in Figure 3.

As can be seen from Figure 3, when the solar irradiation intensity is low, the cavity with opening width of 7 cm has faster heating rate because the cavity with opening width of 4 cm has relatively larger heat loss. When the run time increases to about 1 month, the cavity opening width of 4 cm has larger deformation. As for the cavity with opening width of 7 cm, it was almost not deformed except in enclosure seams of insulated enclosure. These changes before and after heating about the cavity shape are shown in Figure 4.

In order to analyze the effect of cavity opening width on energy flux density distribution, the test results were shown in Figure 5. During test process, the direct solar radiation during measurement was 568 W/m^2. As can be seen from Figure 5, the 95% of energy is concentrated in the focal line of concentration at the 0–7.5 cm. When the cavity absorber with opening width of 4 cm is used, there is part of the energy outside the cavity focused on the insulation enclosure. This may be because the insulation housing material and the absorber material were different. The cavity absorber with opening width of 4 cm has severe deformation when it is stressed. The cavity absorber with opening width of 7 cm can absorb most of the energy. The insulation enclosure absorbs less energy and only causes deformation of shell commissure.

When the impact of tracking accuracy is ignored, the optical efficiency of this collector system is equal to the product of mirror reflectivity, acquisition factor, and the cavity absorptivity. The acquisition factors of the cavity absorber with the opening width of 4 cm and 7 cm are

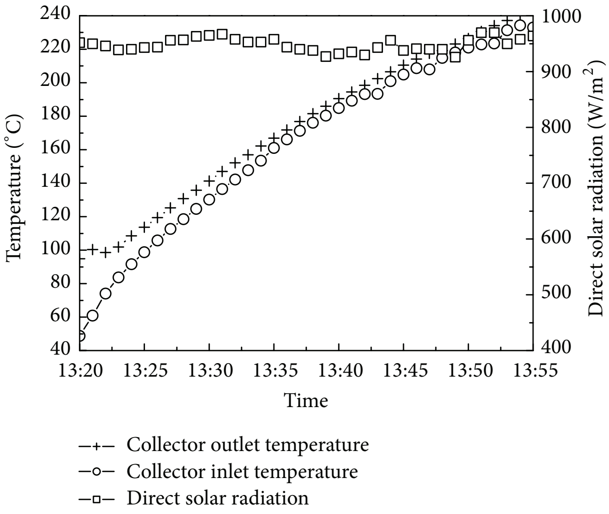

(a) 7 cm

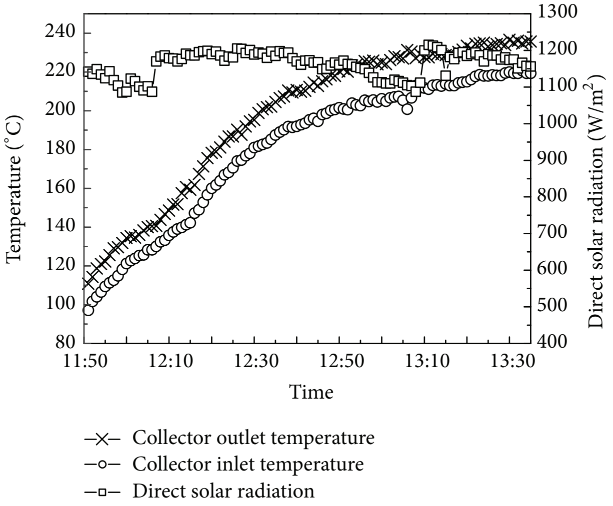

(b) 4 cm

Figure 3: Effect of cavity opening width on collector temperature (experimental conditions: mass of heat conduction oil = 42.65 kg and flow rate = 0.15 kg/s).

0.81 and 0.96, respectively. The collector system efficiency is calculated using the following formula:

$$\eta_{\text{sys}} = \frac{mC_{\text{oil}}\left(t_{\text{out}} - t_{\text{in}}\right)}{A_a H_b}. \tag{12}$$

When the heat conduction oil temperature is 230°C, the collector system efficiency of the cavity absorber with the opening width of 4 cm and 7 cm is 10.9% and 25.2%, respectively. The result shows that the heating rate, acquisition factor, and collector system efficiency increase with increasing the opening width of the absorber and can also prevent the cavity from deformation. It naturally follows that stability of heat conduction oil output temperature can be improved.

(a) 4 cm

(b) 7 cm

Figure 4: The changes about the cavity shape before and after heating.

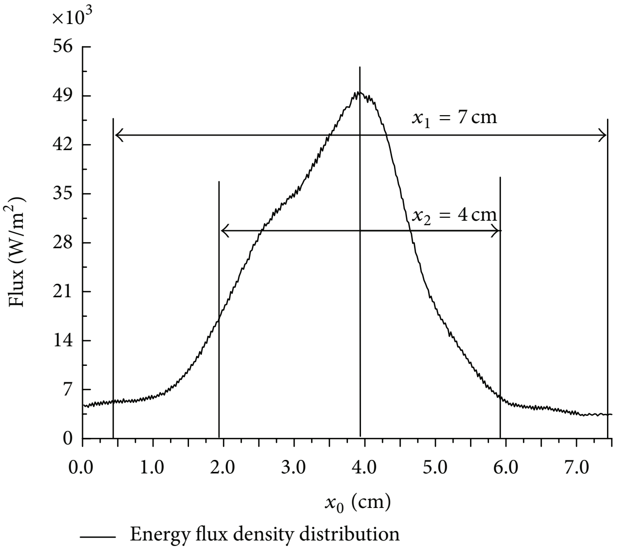

Figure 5: The test results of focal line energy flux density distribution.

4.2. Design and Construction of the Variable Diameter Drying Pipe

4.2.1. Approximation of Variable Diameter Drying Pipe. This paper uses the Fedorov method on the drying tube diameter and height of approximate calculation.

The number K_i is calculated by the following equation:

$$K_i = d_p \times \sqrt[3]{\frac{4g\left(\rho_p - \rho_g\right)}{3\mu_g^2 \rho_g}}. \tag{13}$$

Through the Figure 6 found the relationship between Re_p and K_i and through the Figure 7 found the relationship between Re_p and Nu, the heat transfer coefficient of K between air and material particles is as follows:

$$K = \frac{\text{Nu} \cdot \lambda_g}{d_p}. \tag{14}$$

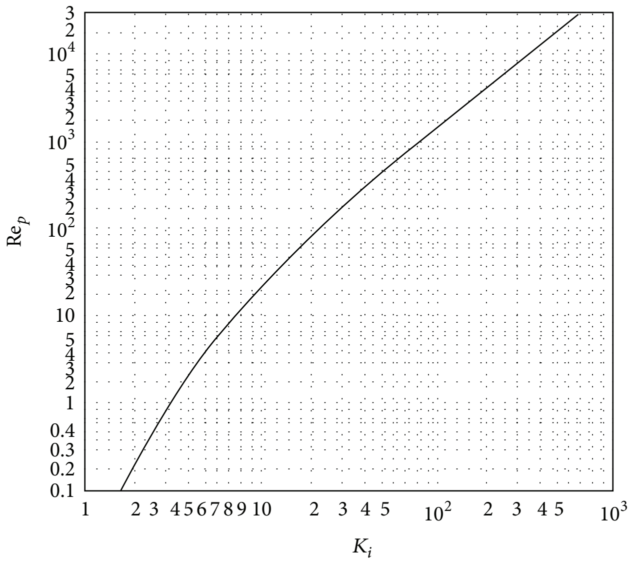

FIGURE 6: The relationship between Re_p and K_i.

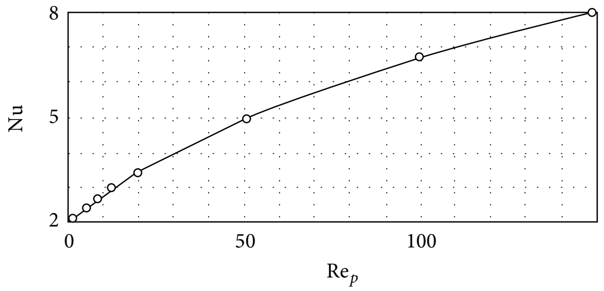

FIGURE 7: The relationship between Re_p and Nu.

Suspension velocity of particles is as follows:

$$v_a = \frac{\mathrm{Re}_p \mu_g}{d_p}. \tag{15}$$

The total surface area of the particle is as follows:

$$A_s = \frac{6G_p}{d_p \rho_p}. \tag{16}$$

The mean temperature difference between the material and the air is

$$\Delta t = \frac{t_1 + t_2}{2} - t_s. \tag{17}$$

The time of the drying process is

$$\tau = \frac{Q}{K A_s \Delta t}. \tag{18}$$

The length z of the drying pipe is as follows:

$$z = \left(v_g - v_a\right)\tau. \tag{19}$$

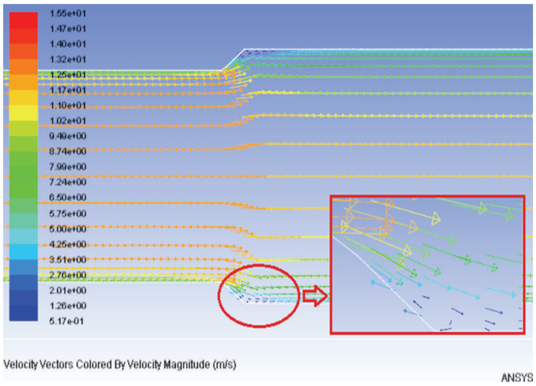

(a) $\theta = 50^\circ$

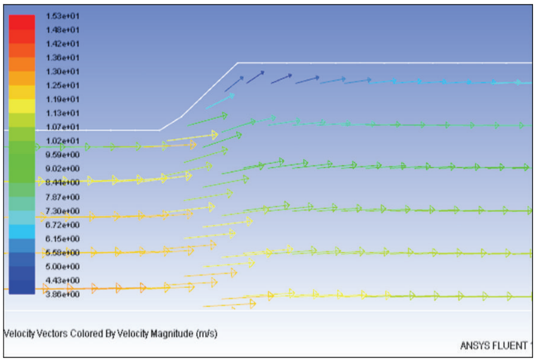

(b) $\theta = 52^\circ$

FIGURE 8: The velocity of flow field in variable diameter drying pipe.

The diameter D of the drying pipe is

$$D = \sqrt{\frac{4G_g \rho_s}{3600 \pi v_g}}. \tag{20}$$

The design parameters are substituted into the above formula of cut tobacco drying. The parameters are shown in Table 3.

4.2.2. The Simulation Speed Flow of Variable Diameter Drying Pipe. Reducing type dry pipe consists of two different diameters of straight pipe and an expansion pipe connection. In the actual environment, the improper value of θ will lead to sediment in the drying pipe on drying process. According to the actual model using ANSYS Fluent for the fluid flow model the sediment will make the flow channel blockage and have a great influence on the drying effect even an accident.

Figure 8 shows the entrance of hot air temperature is 200°C, velocity of 15 m/s; the variable angle θ is 50° and 52°, respectively. We get the velocity of flow field in variable diameter drying pipe through ANSYS Fluent.

Figure 8 shows that, when the θ is 50°, there is reflux area in variable diameter of variable diameter drying pipe. The reflux area will make sediment in the drying pipe on drying process. When the θ is 52°, there is no reflux area in variable diameter drying pipe. In practical design, the height and heat loss of variable diameter drying pipe are considered;

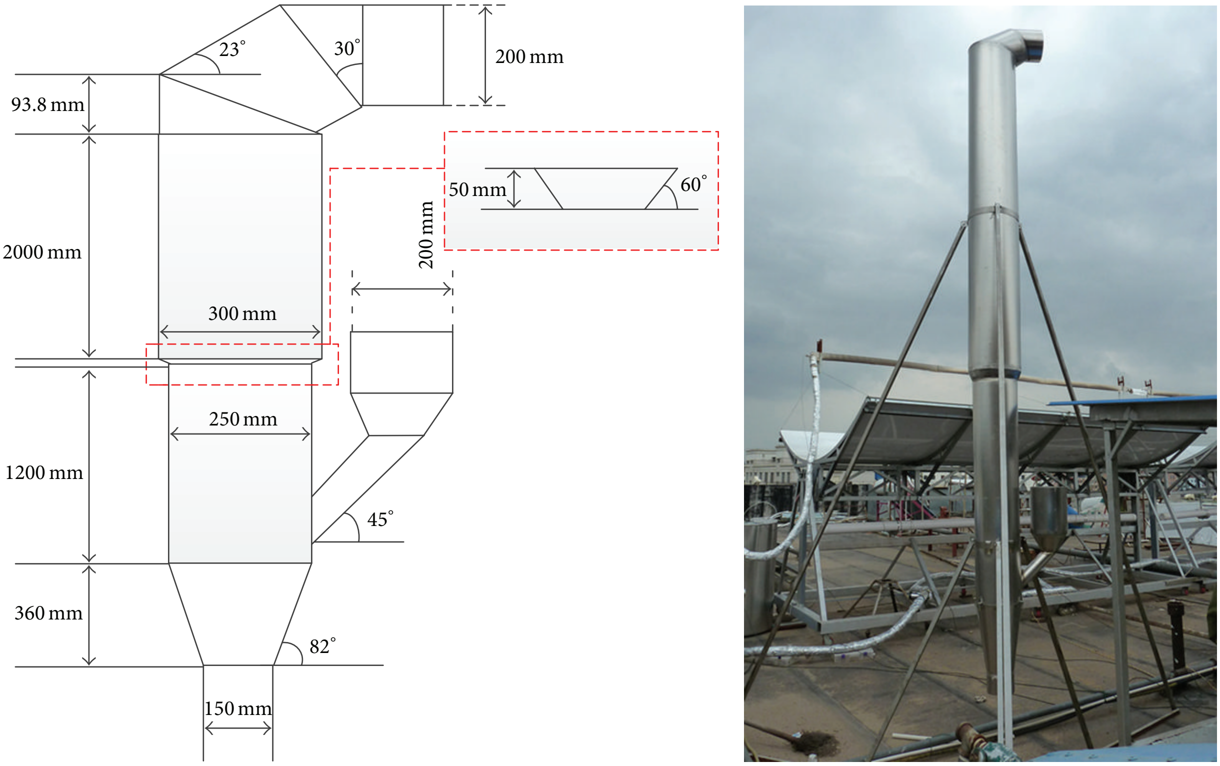

(a) The parameters of the drying pipe

(b) The photo of variable diameter drying pipe

FIGURE 9: The diagram of variable diameter drying pipe.

TABLE 3: The design parameters of cut tobacco drying.

Parameters	Density (kg/m^3)	Specific heat (kJ/kg·°C)	Initial velocity (m/s)	Initial moisture content (kg/kg)	Initial temperature (°C)	The water content after drying (kg/kg)	Diameter (m)
Cut tobacco	800	1.467	0	0.25	20	0.115~0.14	1.2×10^{-3}
Air	0.75	1.025	15	0.025	190	—	—

the variable angle θ of 60° can well meet the requirements of cut tobacco drying process.

4.2.3. Production of the Variable Diameter Drying Pipe. According to the above calculation and analysis, the variable diameter drying pipe is designed and is made of stainless steel 304 with the thickness of 2 mm. It is fixed through the bracket to ensure the drying tube vertically. The parameters of the drying pipe and the photo are shown in Figure 9.

4.3. Cut Tobacco Drying Process

4.3.1. Simulation of Cut Tobacco Drying Process. The distribution simulation of airflow and cut tobacco parameters is shown in Table 4. The velocities shown in Figure 10 vary with the height of drying process. In the accelerating section (range from 0 m to 1.2 m), the airflow velocity decreases slightly and that of cut tobacco increases quickly with increasing the height of drying pipe. In the transition section (from 1.2 m to 1.25 m), the airflow velocity decreases sharply and that of cut tobacco increases slowly with increasing the height of drying pipe. But in the constant section (from 1.25 m to 3.25 m), the velocities of the airflow and the cut tobacco decrease gradually with the height increasing.

As shown in Figure 10(b), the temperature of air flow decreases with the increases of drying pipe height. The temperature of cut tobacco increases rapidly in the accelerating section and then increases slowly with the increases of drying pipe height. This is the cut tobacco is put into the drying pipe and separated quickly by high-speed airflow. Then the contact area between the airflow and the cut tobacco is increased, indicating that both heat and mass transfer rates are improved. In the accelerating section, because the relative speed of cut tobacco particles is large, both heat transfer areas for gas phase together with solid phase and the volumetric heat transfer coefficient are improved. It naturally follows that cut tobacco temperature increases rapidly in the accelerating section. But in the constant section, the relative speed of airflow and cut tobacco particles basically keeps unchanged, so the speed of cut tobacco particles no longer increases and the time of cut tobacco in drying pipe is prolonged.

Table 4: Parameters of cut tobacco drying (cut tobacco).

Intensity/kg·m^{-3}	Specific heat/J·(kg·°C)$^{-1}$	Initial moisture content/%	Diameter/m	Solids-gas ratio	Airflow temperature/°C	Airflow speed/ms^{-1}	Initial temperature /°C
255	1467	25.05	1.2×10^{-3}	0.1	200	15	20

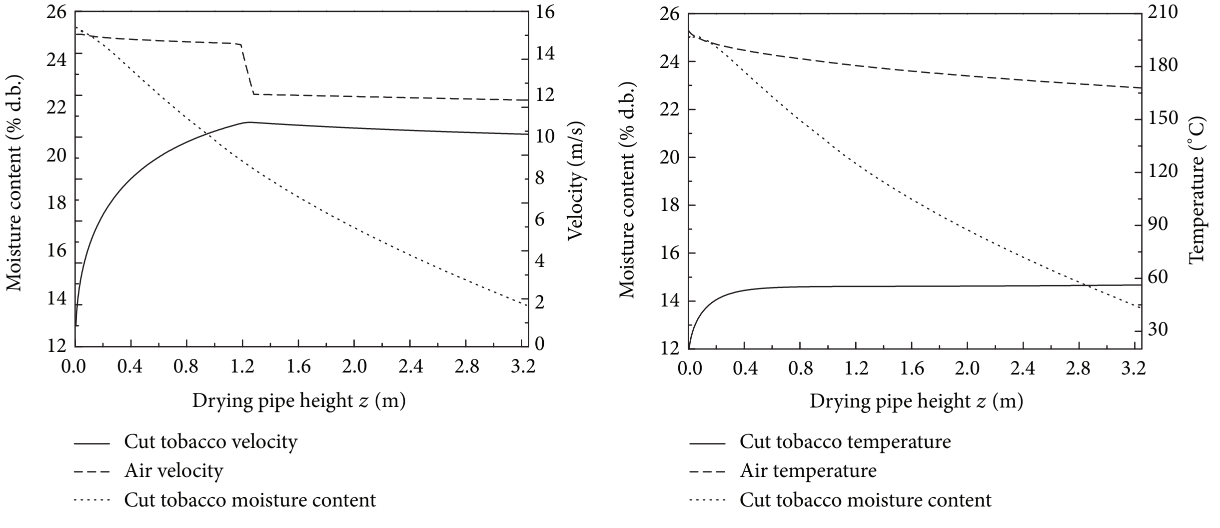

(a)

(b)

Figure 10: Distribution simulation of airflow and cut tobacco parameters (simulation experimental conditions: inlet air temperature = 200°C, flow rate = 15 m/s, and initial moisture content of cut tobacco = 25%).

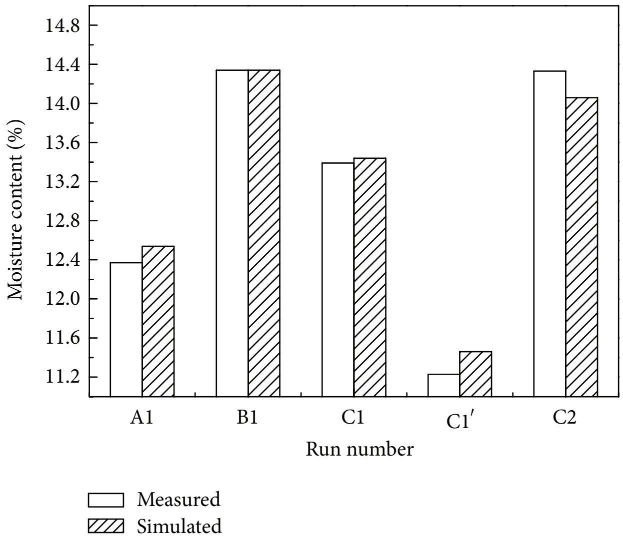

Figure 11: Final cut tobacco moisture contents of simulation and experiment results.

4.3.2. Validation of Mathematical Model. The mathematical model of the cut tobacco particles drying process was calculated using fourth-order Runge-Kutta numerical solution method. Experimental conditions [12] and the results of both simulation and experiment are shown in Table 5 and Figures 11, 12, and 13, respectively.

Figures 11, 12, and 13 show the final cut tobacco moisture contents, temperatures, and the final airflow temperatures along with the simulation results for the same. It can be seen from it that the simulation results are in good agreement with experimental data for cut tobacco drying process. The relative errors between simulated and experimental values are less than 8%, indicating that this mathematical model is accurate for the cut tobacco airflow drying process.

4.4. Optimization Parameters of Cut Tobacco Drying Process. The effects of initial cut tobacco moisture content, inlet airflow velocity, and temperature on cut tobacco drying process are studied by the orthogonal experiment in three factors and three levels. Criteria for determining the optimum parameter conditions are the final cut tobacco moisture content and thermal efficiency of the dryer. The optimization results are shown in Table 6.

According to the orthogonal test result, it can be seen that the thermal efficiency increases with increasing the airflow temperature and the inlet cut tobacco moisture content but decreases with the decrease of airflow velocity. The result shows the optimum preparation conditions are an inlet airflow velocity of 15 m/s, an initial cut tobacco moisture content of 26%, and an inlet airflow temperature of 200°C. The thermal efficiency of the dryer and the final cut tobacco moisture content are 66.32% and 14.15%, respectively. The

TABLE 5: Summaries of experimental conditions.

Run number	t_{gin}	v_{gin}	v_{gout}	t_{pout}	X_{in}	X_{out}
A1	199.5	15	163.4	53.2	24.03	12.37
B1	199.8	15	156.9	58.7	26.02	14.15
C1	200.4	15	157.7	59.3	25.05	13.39
C1′	200.4	20	152.6	61.2	25.05	11.23
C2	190.3	15	148.5	52.8	25.05	14.33

TABLE 6: Result of orthogonal experiment.

Run number	v_{gin} (m/s)	X_{in} (%)	t_{gin} (°C)	η (%)
1	15	24	180	62.46
2	15	25	190	63.54
3	15	26	200	66.32
4	18	24	190	59.46
5	18	25	200	61.34
6	18	26	180	60.64
7	20	24	200	54.56
8	20	25	180	52.35
9	20	26	190	57.49
K1	64.107	58.827	58.483	—
K2	60.480	59.077	60.163	—
K3	54.800	61.483	60.740	—
Range	9.307	2.656	2.257	—

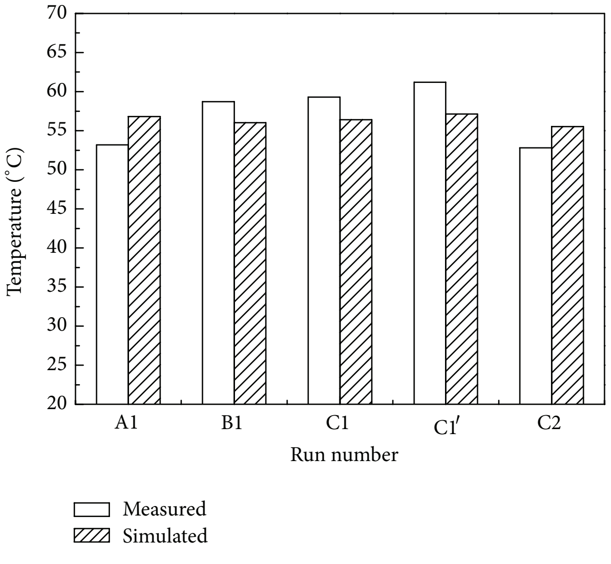

FIGURE 12: Final cut tobacco temperatures of simulation and experiment results.

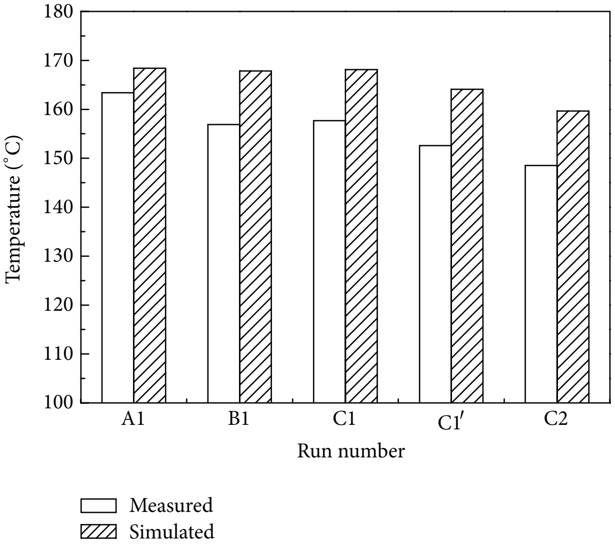

FIGURE 13: Final airflow temperatures of simulation and experiment results.

final cut tobacco moisture content meets the requirements of cut tobacco drying process. The result shows that this parabolic trough concentrating solar heating will be a potential heat recourse for cut tobacco drying system.

5. Conclusion

A novel parabolic trough concentrating solar heating for cut tobacco drying system was established. The result shows that the heating rate, acquisition factor, and collector system efficiency increase with increasing the opening width of the absorber and can also prevent the cavity from deformation. The simulation results using the cut tobacco drying mathematical model were in good agreement with experimental data for cut tobacco drying process. The optimum preparation conditions were an inlet airflow velocity of 15 m/s, an initial cut tobacco moisture content of 26%, and an inlet airflow temperature of 200°C. The thermal efficiency of the dryer and the final cut tobacco moisture content were 66.32% and 14.15%, respectively. The result showed that this parabolic trough concentrating solar heating would be one of the heat recourse candidates for cut tobacco drying system.

Nomenclature

A: Drying pipe cross-sectional area, m^2
C_s: Specific heat capacity of dry material, kJ/(kg·°C)
C_w: Specific heat capacity of water, kJ/(kg·°C)
C_g: Specific heat capacity of moist air, kJ/(kg·°C)
C_{oil}: Specific heat capacity of heat transfer oil, kJ/(kg·°C)
D: Drying pipe diameter, m
d_p: Particle size, m
G_g: Oven dry air flow, kg/s
G_p: Oven dry particle size flow, kg/s
h: Convective heat transfer coefficients, W/(m^2 · °C)
K_y: Mass transfer coefficient, kg/(m^2·s)
N: The number of particles per unit volume, 1/m^3
Nu: Nusselt number
P_{sat}: Saturated vapor pressure, Pa
Pr: Prandtl number
r_0: 0°C latent heat of vaporization of water, kJ/(kg·°C)
Re: Reynolds number
t_g: Air temperature, °C
t_p: Particle temperature, °C
v_g: Steam velocity, m/s
v_p: Particle velocity, m/s
W_d: Mass transfer rate, W/(m^2 · °C·s)
X: The moisture content of the material, % d.b.
Y: Absolute humidity of air, % d.b.
Y_{eq}: Moisture content of air saturation
z: Drying pipe length, m.

Greek

ξ: Drag coefficient
λ_g: Thermal conductivity of air, J/(m·°C ·s)
ρ_p: Wet density of the material, kg/m^3
ρ_g: Wet density of the air, kg/m^3
ρ_s: Oven dry density of the material, kg/m^3
θ: Variable diameter angle
η_{sys}: Collector system efficiency
η: Drying pipe thermal efficiency.

Subscript

In: inlet
Out: outlet.

Conflict of Interests

The authors declare that there is no conflict of interests regarding the publication of this paper.

Acknowledgments

The present study was supported by the National Natural Science Foundation, China (Grant no. U1137605), and the Applied Basic Research Programs of Science and Technology Department Foundation of Yunnan Province, China (Grant no. 2011DFA60460).

References

[1] D. A. Boyd, R. Gajewski, and R. Swift, "A cylindrical blackbody solar energy receiver," *Solar Energy*, vol. 18, no. 5, pp. 395–401, 1976.

[2] O. A. Barra and L. Franceschi, "The parabolic trough plants using black body receivers: experimental and theoretical analyses," *Solar Energy*, vol. 28, no. 2, pp. 163–171, 1982.

[3] C. Qiaoli, G. Xinshi, C. Shuxin et al., "Numerical analysis of thermal characteristics of solar cavity receiver with absorber of a bundle of pipes," *Acta Energiae Solaris Sinica*, vol. 16, no. 1, pp. 21–28, 1995.

[4] L. Zhang, H. Zhai, Y. Dai, and R.-Z. Wang, "Thermal analysis of cavity receiver for solar energy heat collector," *Journal of Engineering Thermophysics*, vol. 29, no. 9, pp. 1453–1457, 2008.

[5] J. Fukuchi, Y. Ohtaka, and C. Hanaoka, "A numerical fluid simulation for a pneumatics conveying dryer of cut tobacco," in *Proceedings of the CORESTA Congress*, pp. 201–212, Lisbon, Portugal, 2000.

[6] Z. Pakowski, A. Druzdzel, and J. Drwiega, "Validation of a model of an expanding superheated steam flash dryer for cut tobacco based on processing data," *Drying Technology*, vol. 22, no. 1-2, pp. 45–57, 2004.

[7] L. Huimin and M. Ming, *YC/T31-1996 Tobacco and Tobacco Products—Preparation of Test Specimens and Determination of Moisture Content—Oven Method*, China Standard Press, Beijing, China, 1996.

[8] X. Chengmu, L. Ming, J. Xu et al., "Frequency statistics analysis for energy-flux-density distribution on focal plane of parabolic trough solar concentrators," *Acta Optica Sinica*, vol. 33, no. 4, Article ID 040800, pp. 1–7, 2013.

[9] R. Legros, C. A. Millington, and R. Clift, "Drying of tobacco particles in a mobilized bed," *Drying Technology*, vol. 12, no. 3, pp. 517–543, 1994.

[10] R. Blasco, R. Vega, and P. I. Alvarez, "Pneumatic drying with superheated steam: bi-dimensional model for high solid concentration," *Drying Technology*, vol. 19, no. 8, pp. 2047–2061, 2001.

[11] P. Yongkang and W. Zhong, *Modern Drying Technology*, Chemical Industry Press, Beijing, China, 1998.

[12] W. E. Ranz and W. R. Marshall, "Evaporation from drops, part I," *Chemical Engineering Progress*, vol. 48, no. 3, pp. 141–146, 1952.

Hindawi Publishing Corporation
International Journal of Photoenergy
Volume 2014, Article ID 946360, 10 pages
http://dx.doi.org/10.1155/2014/946360

Research Article

Very Fast and Accurate Procedure for the Characterization of Photovoltaic Panels from Datasheet Information

Antonino Laudani,[1] Francesco Riganti Fulginei,[1] Alessandro Salvini,[1]
Gabriele Maria Lozito,[1] and Salvatore Coco[2]

[1] *Department of Engineering, Università di Roma Tre, Via Vito Volterra 62, 00146 Roma, Italy*
[2] *DIEEI, Università di Catania, Viale A. Doria 6, 95125 Catania, Italy*

Correspondence should be addressed to Francesco Riganti Fulginei; riganti@uniroma3.it

Received 1 November 2013; Accepted 12 February 2014; Published 24 March 2014

Academic Editor: Ismail H. Altas

In recent years several numerical methods have been proposed to identify the five-parameter model of photovoltaic panels from manufacturer datasheets also by introducing simplification or approximation techniques. In this paper we present a fast and accurate procedure for obtaining the parameters of the five-parameter model by starting from its reduced form. The procedure allows characterizing, in few seconds, thousands of photovoltaic panels present on the standard databases. It introduces and takes advantage of further important mathematical considerations without any model simplifications or data approximations. In particular the five parameters are divided in two groups, independent and dependent parameters, in order to reduce the dimensions of the search space. The partitioning of the parameters provides a strong advantage in terms of convergence, computational costs, and execution time of the present approach. Validations on thousands of photovoltaic panels are presented that show how it is possible to make easy and efficient the extraction process of the five parameters, without taking care of choosing a specific solver algorithm but simply by using any deterministic optimization/minimization technique.

1. Introduction

The one-diode model for the photovoltaic (PV) panel characterization has been widely used within both specific software toolboxes for the estimation and the prediction of the electrical power produced by PV plants [1–4] and algorithms for the Maximum Power Point Tracking [5–7] or irradiance measurements [8, 9]. Indeed, it guarantees a good tradeoff between accuracy and complexity for its setup [10, 11]. On the other hand, the extraction of the five-parameter model at standard reference conditions (SRC) (i.e., an inverse problem) has been widely faced in the literature. Although two approaches are generally the most adopted (the one that uses the datasheet information and the other one that exploits the experimental data on I-V curves), the use of only data provided by manufacturer on datasheet appears more interesting because it does not require a specific experimental study on PV module. Nevertheless, the approaches proposed the in literature differ between them and often it is difficult to understand what is the best one to be used. Indeed, on one hand several works proposed different equations/approaches for the extraction of the five parameters; on the other hand, almost any kinds of optimization techniques have been presented to solve the inverse problem of the extraction of the five parameters. This is essentially due to the nature of the involved equations which are transcendental and hard to manage. Just to give some references within the wide literature regarding this issue, hereafter some of the more recent works are briefly reported. Regarding the techniques for finding the inverse problem solutions, in [12] an improved differential evolution algorithm is presented for the extraction of five parameters from both synthetic data and experimental IV data, in [13] penalty differential evolution is used in a similar way, in [14, 15] pattern search and Bacterial Foraging Algorithm are used, respectively, and so on (see the reference within these works for further journal articles). Regarding the alternative analytical approaches, in [16] an explicit I-V model of a solar cell which uses Padé

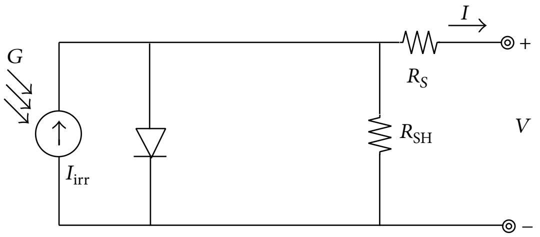

Figure 1: One-diode equivalent model for a PV module.

approximation is presented, that is, the exponential function is approximated by means of a rational function; in [17] the Taylor series is instead used; in [18–20] the I-V relations are more explicitly written by means of the W Lambert function [21], and then the extraction of the five parameters is performed by numerical techniques. Although the aim of these works is to effectively solve the problem, they suffer from unsuitable mathematical approximations (which lead to errors in the results) or complicated implementations and high computational costs. As a consequence these approaches are not so easy to be applied.

In this paper we present a fast and accurate procedure for obtaining the parameters of the five-parameter model by starting from its reduced form [22] which allows the identification of thousands of PV panels available on the standard databases (such as Californian Energy Commission database [23]). Indeed, by using suitable initial guesses it is possible to fully characterize thousands of PV panel in few seconds without any model simplifications or data approximations, simply by introducing further important mathematical considerations about the five-parameter model. The paper is structured as follows: in Section 2 the traditional one-diode model and the problem related to its characterization are presented; in Section 3 the reduced form of the five-parameter model is described; the validation results obtained on thousands of PV panels are shown in Section 4; finally, Section 5 is for the conclusions.

2. The One-Diode Model and Its Reduced Form

The equivalent circuit of the one-diode model is shown in Figure 1. The relation between current I and voltage V for a PV array/panel of arbitrary dimension (N_P parallel connected strings of N_S series-connected PV cells) at the equivalent port is [10]

$$I = N_P I_{irr} - N_P I_0 \left[e^{q(V+I(N_S/N_P)R_S)/N_S nkT} - 1 \right] - \frac{V + I(N_S/N_P)R_S}{(N_S/N_P)R_{SH}}, \tag{1}$$

where I_{irr} is the irradiance current (photocurrent), I_0 is the cell reverse saturation current (diode saturation current), q is the electron charge ($q = 1.602 \times 10^{-19}$ C), n is the cell ideality factor, k is the Boltzmann constant ($k = 1.3806503 \times 10^{-23}$ J/K), T is the cell temperature, and R_S and R_{SH} represent the cell series and shunt resistance, respectively. In (1), the governing variables n, R_S, I_{irr}, I_0, and R_{SH} can be assumed as dependent or not on the irradiance (G) and the temperature (T) but in any case they are in function of certain reference (ref) parameters at SRC ($G_{ref} = 1000\,\text{W/m}^2$, $T_{ref} = 25^\circ\text{C}$) (hereafter we present and utilize the relations proposed by De Soto et al. in [11]; other slightly different relations are presented in several works, such as [24, 25], but their use does not affect the effectiveness and validity of the presented procedure):

$$n = n_{ref}, \tag{2}$$

$$R_S = R_{S,ref}, \tag{3}$$

$$I_{irr} = \frac{G}{G_{ref}} \left[I_{irr,ref} + \alpha_T \left(T - T_{ref} \right) \right], \tag{4}$$

$$I_0 = I_{0,ref} \left[\frac{T}{T_{ref}} \right]^3 e^{[E_{g,ref}/kT_{ref} - E_g/kT]}, \tag{5}$$

$$R_{SH} = \frac{G}{G_{ref}} R_{SH,ref}. \tag{6}$$

In (5) $E_g = 1.17 - 4.73 \times 10^{-4} \times (T^2/(T + 636))$ is the bandgap energy for silicon in eV. Thus, there are five unknown parameters at SRC, n_{ref}, $R_{S,ref}$, $I_{irr,ref}$, $I_{0,ref}$, and $R_{SH,ref}$ to be found within (2)–(6). Then, by starting from their values and by using the above relations, it is possible to write the I-V curves for every temperature and irradiance values. In order to determine these five unknowns we need five independent equations based on datasheet information. Usually the PV panel manufacturers provide several information on datasheet at standard reference conditions (SRC), that is, for the irradiance G_{ref} and the temperature T_{ref}: the values of the short-circuit current ($I_{SC,ref}$) and the open-circuit voltage ($V_{OC,ref}$), the current and voltage values at the maximum power point ($I_{mp,ref}$ and $V_{mp,ref}$). In addition, the datasheets report the temperature coefficients (or percentage) of both the short-circuit current (α_T or $\alpha_T^{\%}$) and the open-circuit voltage (β_T or $\beta_T^{\%}$). On the basis of the three characteristic points, open-circuit, short-circuit, and maximum power points at SRC, it is possible to write the first four equations of the five-parameter model [10, 11, 15, 22, 26]: indeed the first equation arises by writing (1) for the open-circuit (OC) condition; the second equation arises by using (1) for the short-circuit (SC) condition; the third equation arises by exploiting the current and voltage values at the maximum power point (MPP) condition. The fourth equation is written by imposing the slope of the P-V curve (power versus voltage) over the MPP equal to zero, $d(V \cdot I)/dV = 0$, that can be also expressed in terms of $I_{mp,ref}/V_{mp,ref}$ ratio. The last fifth equation used to complete the five-parameter model is written by exploiting the temperature dependence of (1) at the open-circuit condition and irradiance $G = G_{ref}$ by using the previously stated temperature coefficients (α_T and β_T) [10–12]. Before showing the five equations, it is useful to briefly recall the constants specified in (7) adopted in order to simplify the writing of the mathematical expressions. Furthermore, the temperature-dependent factor

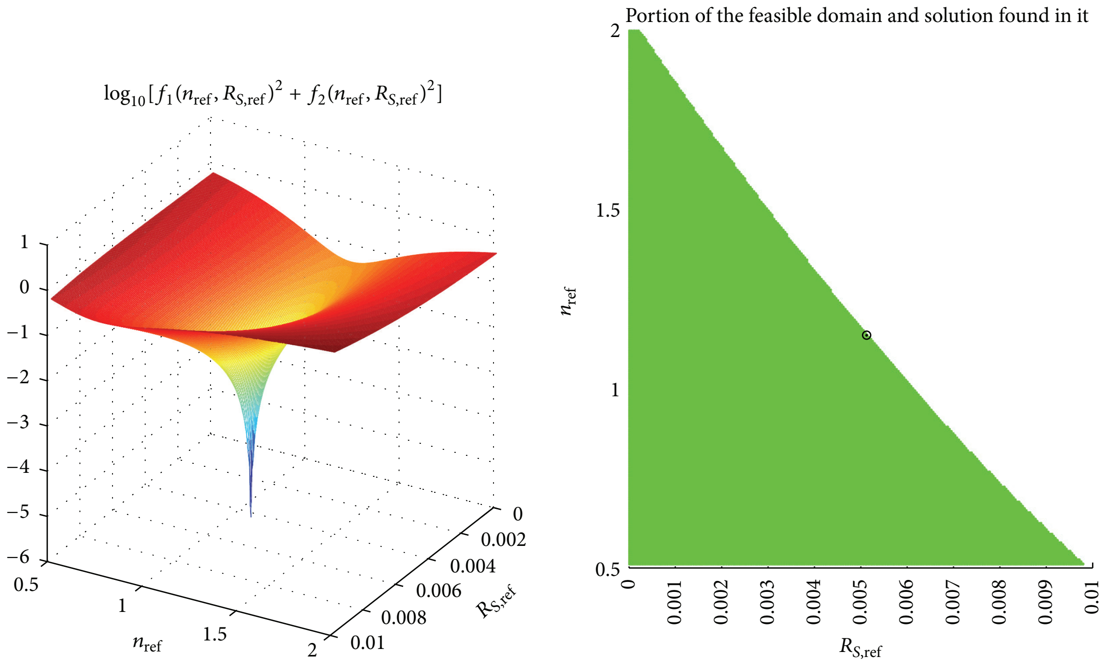

(a)

(b)

Figure 2: Graph of the functional (25) and the feasible domain for the BP 3 235 T PV panel (multi-Si technology). A unique physical solution exists.

$K_T = [T/T_{\text{ref}}]^3 e^{[E_{g,\text{ref}}/kT_{\text{ref}} - E_g/kT]}$ is used in (5) and the shunt conductance $G_{\text{SH,ref}} = R_{\text{SH,ref}}^{-1}$ is adopted as unknown in (6) instead of $R_{\text{SH,ref}}$:

$$C_1 = \frac{kT_{\text{ref}}}{q}; \qquad C_2 = \frac{V_{\text{OC,ref}}}{N_S C_1}; \qquad C_3 = \frac{V_{\text{mp,ref}}}{N_S C_1}; \qquad C_4 = \frac{I_{\text{mp,ref}}}{N_P C_1}; \qquad C_5 = \frac{I_{\text{SC,ref}}}{N_P C_1}. \tag{7}$$

Thus, the five equations are the following:

$$0 = I_{\text{irr,ref}} - I_{0,\text{ref}}\left(e^{C_2/n_{\text{ref}}} - 1\right) - G_{\text{SH,ref}} C_1 C_2, \tag{8}$$

$$C_1 C_5 = I_{\text{irr,ref}} - I_{0,\text{ref}}\left(e^{C_5 R_{S,\text{ref}}/n_{\text{ref}}} - 1\right) - C_1 C_5 G_{\text{SH,ref}} R_{S,\text{ref}}, \tag{9}$$

$$C_1 C_4 = I_{\text{irr,ref}} - I_{0,\text{ref}}\left(e^{(C_3 + C_4 R_{S,\text{ref}})/n_{\text{ref}}} - 1\right) - G_{\text{SH,ref}} C_1 \left(C_3 + C_4 R_{S,\text{ref}}\right), \tag{10}$$

$$\frac{C_4}{C_3} = \frac{\left(I_{0,\text{ref}}/n_{\text{ref}} C_1\right) e^{(C_3 + C_4 R_{S,\text{ref}})/n_{ref}} + G_{\text{SH,ref}}}{1 + \left(I_{0,\text{ref}} R_{S,\text{ref}}/n_{\text{ref}} C_1\right) e^{(C_3 + C_4 R_{S,\text{ref}})/n_{\text{ref}}} + G_{\text{SH,ref}} R_{S,\text{ref}}}, \tag{11}$$

$$\begin{aligned} 0 = {} & I_{\text{irr,ref}} + \alpha_T \left(T - T_{\text{ref}}\right) \\ & - I_{0,\text{ref}} K_T \left(e^{q(N_S C_1 C_2 + \beta_T (T - T_{\text{ref}}))/N_S n_{\text{ref}} kT} - 1\right) \\ & - G_{\text{SH,ref}} \frac{N_S C_1 C_2 + \beta_T \left(T - T_{\text{ref}}\right)}{N_S}. \end{aligned} \tag{12}$$

In (12), a value of $T = T_{\text{ref}} \pm 10$ K is used, even if variations of temperature ΔT belonging to the range $[-10, +10]$ with respect to T_{ref} return very similar solutions [10, 11].

The five-parameter model is thus defined by a system of five equations, (8)–(12), with the five unknowns (parameters), n_{ref}, $R_{S,\text{ref}}$, $I_{\text{irr,ref}}$, $I_{0,\text{ref}}$, and $G_{\text{SH,ref}}$. Due to the presence of transcendental equations this problem is not so simple to manage and it can be only solved by means of numerical methods. Since it is practically an inverse problem, many minimization algorithms can be used and almost any kinds of computing techniques have been tested in the literature: for example, in [27] the comparison between several techniques to extract the five parameters is presented and compared by using the criteria of applicability, convergence, stability, calculation speed, and error on various types of *IV* data. In addition, due to its nonlinear nature, the system returns solutions that are very sensitive to the choice of the initial guesses [22, 26, 27]. As the following section shows, this problem can be easily overwhelmed by using a reduced form of the model employing only a set of two equations in two unknowns. For the reader's convenience, the list of the technical parameters used in this work is reported at the end of the paper.

3. Reduction to a Two-Parameter Model

In [22] it has been proven that the five-parameter model can be reduced to a two-parameter model improving the efficiency of the algorithm finding the solution. By using this reduced form of the system instead of the original one, it is also possible to demonstrate: (i) the uniqueness of

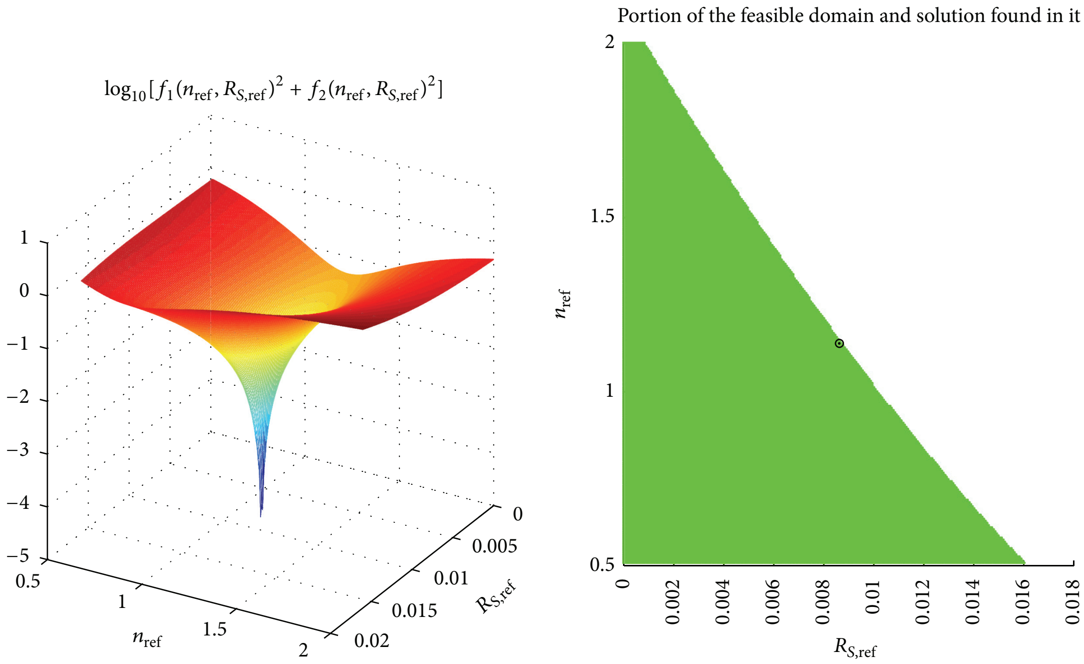

(a)

(b)

Figure 3: Graph of the functional (25) and feasible domain for the Sharp NT175 panel (mono-Si technology). A unique physical solution exists.

the solution for the problem; (ii) the existence of a unique solution without physical meaning for some PV panels; (iii) the matter of the optimal choice of the initial guesses that make easy and effective the solution of the inverse problem. As first thing, let us show the way to reduce the five-parameter model to a two-parameter model. This is obtained by simple algebraic manipulations of three of the five equations (8)–(11). Indeed from the first equation (8) it is possible to obtain $I_{irr,ref}$ as a function of n_{ref}, $R_{S,ref}$ and $R_{SH,ref}$ as follows:

$$I_{irr,ref} = I_0\left(e^{C_2/n_{ref}} - 1\right) + G_{SH,ref}C_1C_2. \qquad (13)$$

By substituting (13) in (10), it is possible to write

$$\begin{aligned} C_1C_4 &= I_{0,ref}\left(e^{C_2/n_{ref}} - 1\right) - I_{0,ref}\left(e^{(C_3+C_4R_{S,ref})/n_{ref}} - 1\right) \\ &\quad - G_{SH,ref}C_1\left(C_3 - C_2 + C_4R_{S,ref}\right) \end{aligned} \qquad (14)$$

that can be written also as

$$I_{0,ref} = \frac{C_1C_4 + G_{SH,ref}C_1\left(C_3 - C_2 + C_4R_{S,ref}\right)}{\left(e^{C_2/n_{ref}} - e^{(C_3+C_4R_{S,ref})/n_{ref}}\right)}. \qquad (15)$$

On the other hand, from (11) we can also obtain $I_{0,ref}$

$$I_{0,ref} = \frac{C_3G_{SH,ref} - C_4 - C_4G_{SH,ref}R_{S,ref}}{e^{(C_3+C_4R_{S,ref})/n_{ref}}\left(\left(C_4R_{S,ref} - C_3\right)/n_{ref}C_1\right)}. \qquad (16)$$

Furthermore, by posing the expression (15) equal to the (16), we can write

$$\begin{aligned} &\frac{C_1C_4 + G_{SH,ref}C_1\left(C_3 - C_2 + C_4R_{S,ref}\right)}{\left(e^{C_2/n_{ref}} - e^{(C_3+C_4R_{S,ref})/n_{ref}}\right)} \\ &\quad = \frac{C_3G_{SH,ref} - C_4 - C_4G_{SH,ref}R_{S,ref}}{e^{(C_3+C_4R_{S,ref})/n_{ref}}\left(\left(C_4R_{S,ref} - C_3\right)/n_{ref}C_1\right)} \end{aligned} \qquad (17)$$

from which it is possible to obtain $G_{SH,ref}$ as a function of n_{ref} and $R_{S,ref}$,

$$\begin{aligned} G_{SH,ref} &= \frac{C_4}{C_4R_{S,ref} - C_3} \\ &\quad \cdot \frac{\left(1 + \left(C_3 - C_4R_{S,ref}\right)/n_{ref}\right)e^{(C_3+C_4R_{S,ref}-C_2)/n_{ref}} - 1}{1 + \left(\left(C_4R_{S,ref} + C_3 - C_2\right)/n_{ref} - 1\right)e^{(C_3+C_4R_{S,ref}-C_2)/n_{ref}}}. \end{aligned} \qquad (18)$$

Now, substituting (18) in (15) or (16) also allows expressing $I_{0,ref}$ as a function of n_{ref} and $R_{S,ref}$,

$$\begin{aligned} I_{0,ref} &= \frac{C_1C_4}{C_3 - C_4R_{S,ref}} \\ &\quad \cdot \frac{\left(2C_3 - C_2\right)}{e^{C_2/n_{ref}} + \left(\left(C_4R_{S,ref} + C_3 - C_2\right)/n_{ref} - 1\right)e^{(C_3+C_4R_{S,ref})/n_{ref}}}. \end{aligned} \qquad (19)$$

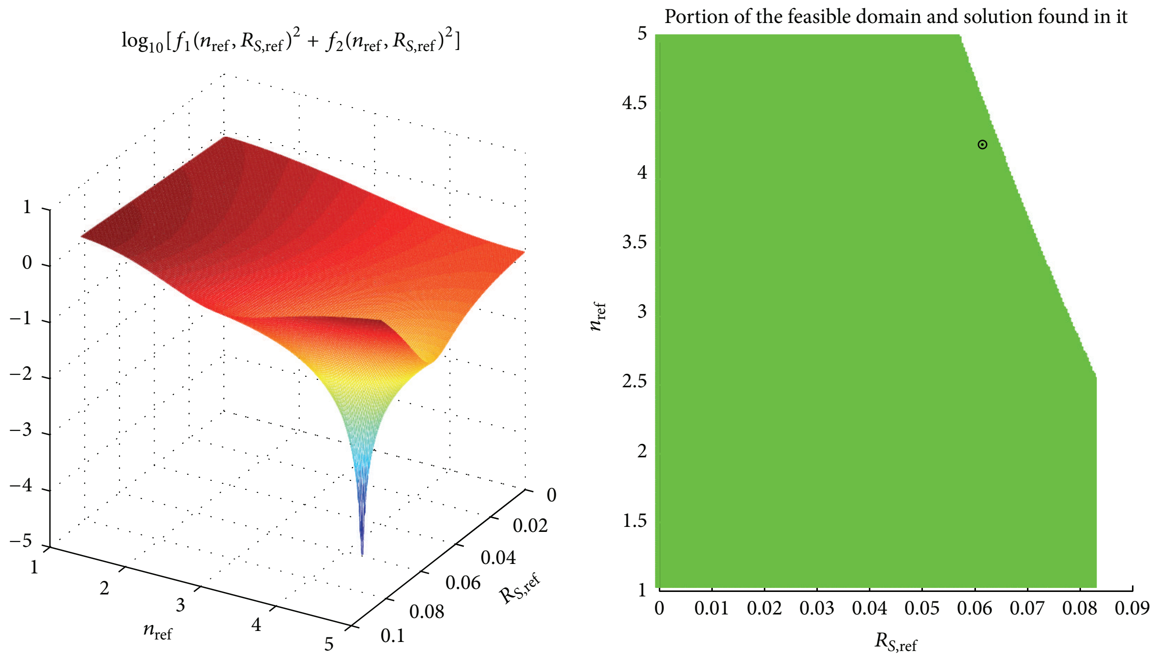

(a) (b)

FIGURE 4: Graph of the functional (25) and feasible domain for the PV panel Xunlight XR12–88 panel (thin film technology). A unique physical solution exists.

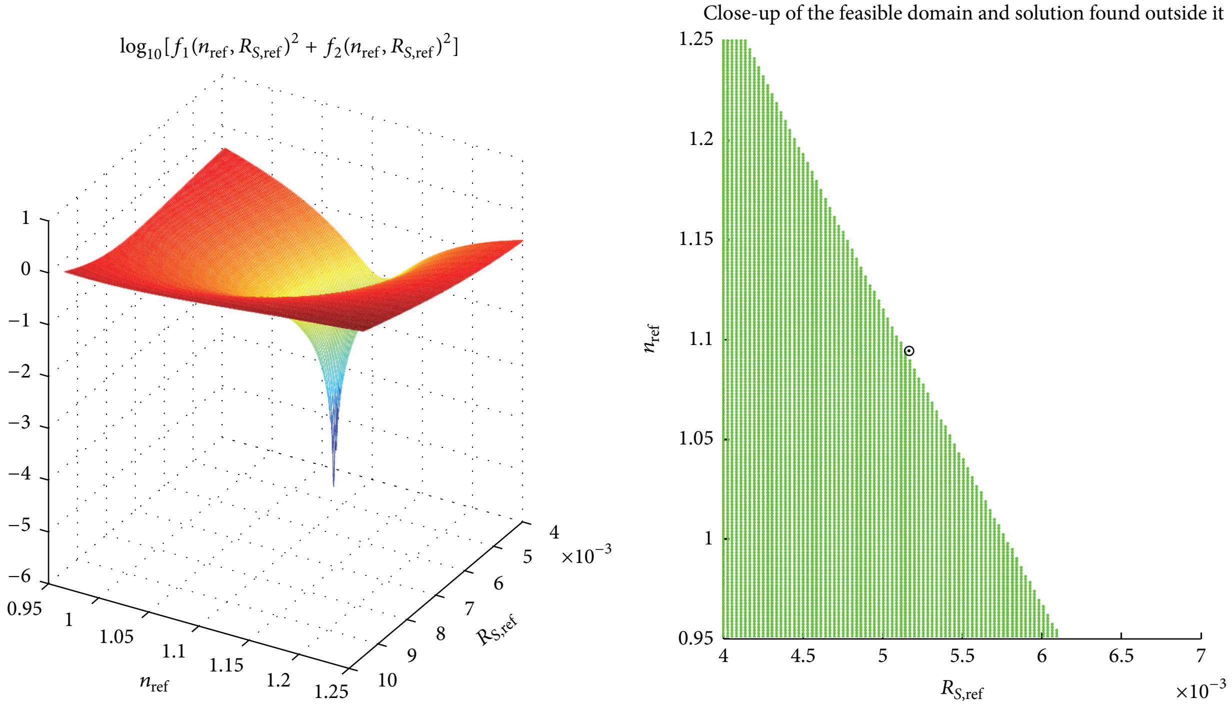

(a) (b)

FIGURE 5: Graph of the functional (25) and feasible domain for the PV panel BP Q 230 panel (multi-Si technology). A unique unphysical solution exists (it lies outside the feasible domain); that is, this panel cannot be modelled by using the five-parameter model.

Finally, (19) and (18) are utilized together with (13) so that $I_{\mathrm{irr,ref}}$ can be written as a function of n_{ref} and $R_{S,\mathrm{ref}}$,

$$I_{\mathrm{irr,ref}} = \frac{C_1 C_4 C_2}{\left(C_3 - C_4 R_{S,\mathrm{ref}}\right)} + \frac{\left(C_1\ C_4\ \left(2C_3 - C_2\right)\right) / \left(C_3 - C_4\ R_{S,\mathrm{ref}}\right) \left(e^{C_2/n_{\mathrm{ref}}} - 1 - \left(C_2/n_{\mathrm{ref}}\right) e^{\left(C_3 + C_4 R_{S,\mathrm{ref}}\right)/n_{\mathrm{ref}}}\right)}{e^{C_2/n_{\mathrm{ref}}} + \left(\left(C_4 R_{S,\mathrm{ref}} + C_3 - C_2/n_{\mathrm{ref}}\right) - 1\right) e^{\left(C_3 + C_4 R_{S,\mathrm{ref}}\right)/n_{\mathrm{ref}}}}. \tag{20}$$

In (18), (19), and (20) we have written $G_{\mathrm{SH,ref}}$, $I_{0,\mathrm{ref}}$, and $I_{\mathrm{irr,ref}}$ as functions of n_{ref} and $R_{S,\mathrm{ref}}$, respectively. This means that now there are only two independent unknowns, called n_{ref} and $R_{S,\mathrm{ref}}$, to be found by using the two equations coming out from the other two conditions not yet utilized in the previous steps. They are (9) and (12) obtained from the evaluation of (1) at short-circuit ($V = 0$, $I = I_{\mathrm{SC,ref}}$) condition and for $\beta_T \approx (V_{\mathrm{OC}} - V_{\mathrm{OC,ref}})/(T - T_{\mathrm{ref}})$ condition, respectively. Thus, the reduced form of the original five-equation system is the following:

$$\begin{aligned}
&\frac{C_3\left(2C_4 - C_5\right)}{C_3 - R_{S,\mathrm{ref}} C_4} + \frac{C_4\left(C_2 - 2C_3\right)}{C_3 - R_{S,\mathrm{ref}} C_4} e^{\left(\left(C_5 R_{S,\mathrm{ref}} - C_2\right)/n_{\mathrm{ref}}\right)} \\
&\quad + \left[\frac{C_5 C_3 - C_4 C_2}{C_3 - R_{S,\mathrm{ref}} C_4} - \frac{C_2 C_4 + C_5 C_3 - C_5 C_2}{n_{\mathrm{ref}}}\right] \\
&\quad \times e^{\left(\left(C_3 + R_{S,\mathrm{ref}} C_4 - C_2\right)/n_{\mathrm{ref}}\right)} = 0, \\
&\left[\alpha_T\left(T - T_{\mathrm{ref}}\right) - \frac{\beta_T\left(T - T_{\mathrm{ref}}\right) C_4}{N_S\left(C_3 - R_{S,\mathrm{ref}} C_4\right)} + \frac{C_1 C_4\left(2C_3 - C_2\right)}{\left(C_3 - R_{S,\mathrm{ref}} C_4\right)}\right] \\
&\quad + \left[\alpha_T\left(T - T_{\mathrm{ref}}\right)\left(\frac{C_3 + R_{S,\mathrm{ref}} C_4 - C_2}{n_{\mathrm{ref}}} - 1\right)\right] \\
&\quad \times e^{\left(\left(C_3 + R_{S,\mathrm{ref}} C_4 - C_2\right)/n_{\mathrm{ref}}\right)} \\
&\quad + \left[\frac{C_4 \beta_T\left(T - T_{\mathrm{ref}}\right)}{N_S} \frac{\left(n_{\mathrm{ref}} - R_{S,\mathrm{ref}} C_4 + C_3\right)}{n_{\mathrm{ref}}\left(C_3 - R_{S,\mathrm{ref}} C_4\right)}\right] \\
&\quad \times e^{\left(\left(C_3 + R_{S,\mathrm{ref}} C_4 - C_2\right)/n_{\mathrm{ref}}\right)} \\
&\quad + \frac{C_1 C_4 K_T\left(C_2 - 2C_3\right)}{\left(C_3 - R_{S,\mathrm{ref}} C_4\right)} \\
&\quad \times e^{\left(q\beta_T\left(T - T_{\mathrm{ref}}\right)/N_S k T n_{\mathrm{ref}} + \left(C_2/n_{\mathrm{ref}}\right)\left(T_{\mathrm{ref}}/T - 1\right)\right)} \\
&\quad + \frac{C_1 C_4\left(K_T - 1\right)\left(2C_3 - C_2\right)}{\left(C_3 - R_{S,\mathrm{ref}} C_4\right)} e^{\left(-C_2/n_{\mathrm{ref}}\right)} = 0.
\end{aligned} \tag{21}$$

3.1. Solution of the Reduced form of the Five-Parameter Model. Although the two equations (21) of the reduced form of the five-parameter model are transcendental equations, they are quite affordable that simple and fast numerical methods can be utilized to find the solutions instead of more complex and expensive algorithms in terms of computational costs [28–31]. On the other hand, the effectiveness of the reduced form with respect to the original system based on five equations is evident since it returns the same unique solution also by using different numerical methods. Moreover, (18)–(21) allows making several important considerations about the solutions of the five-parameter model.

(i) Since the values of $I_{\mathrm{irr,ref}}$, $I_{0,\mathrm{ref}}$, and $R_{\mathrm{SH,ref}}$ must be positive in order to obtain a physical meaning for these three parameters, it is possible to find the conditions for the range of the independent unknowns n_{ref} and $R_{S,\mathrm{ref}}$ from (18), (19), and (20). In particular, the maximum admissible value for $R_{S,\mathrm{ref}}$ is a function of n_{ref}, according to the following relations [22]:

$$\begin{gathered}
R_{S,\mathrm{ref}} \neq \frac{\left(C_2 - C_3\right)}{C_4}, \\
0 < R_{S,\mathrm{ref}} < R_{S,\mathrm{ref}}^{\max}\left(n_{\mathrm{ref}}\right)
\end{gathered} \tag{22}$$

with $R_{S,\mathrm{ref}}^{\max}$ as a function of n_{ref}

$$R_{S,\mathrm{ref}}^{\max}\left(n_{\mathrm{ref}}\right) = \frac{n_{\mathrm{ref}}}{C_4}\left[1 + W_{-1}\left(-e^{\left(C_2 - n_{\mathrm{ref}} - 2C_3\right)/n_{\mathrm{ref}}}\right)\right] + \frac{C_3}{C_4} \tag{23}$$

whereas the Lambert W function [8] in (23) has been used: this special mathematical function allows obtaining a closed form representation for the I-V curves and it is often successfully used for the analysis of PV modules [14, 15].

(ii) Thus it is possible to individuate the feasible domain for the two remaining independent unknowns by assuming

$$0.5 \leqslant n_{\mathrm{ref}} \leqslant 2.5. \tag{24}$$

(iii) It is also possible to graph the 2D functional used for solving the system (21):

$$F\left(n_{\mathrm{ref}}, R_{S,\mathrm{ref}}\right) = f_1\left(n_{\mathrm{ref}}, R_{S,\mathrm{ref}}\right)^2 + f_2\left(n_{\mathrm{ref}}, R_{S,\mathrm{ref}}\right)^2, \tag{25}$$

where $f_1(n_{\mathrm{ref}}, R_{S,\mathrm{ref}}) = 0$ and $f_2(n_{\mathrm{ref}}, R_{S,\mathrm{ref}}) = 0$ represent the first and the second equation of the system (21), respectively. The graph of the functional $F(n_{\mathrm{ref}}, R_{S,\mathrm{ref}})$ is smooth and free from local minima (some examples are shown in the next section). The presence of only one minimum (i.e., one global minimum) makes the problem of finding the solution of the system (21) a convex problem allowing the use of simple initial guesses without choosing specific optimization algorithms. Indeed, as also discussed in [26] where an empirical approach is adopted,

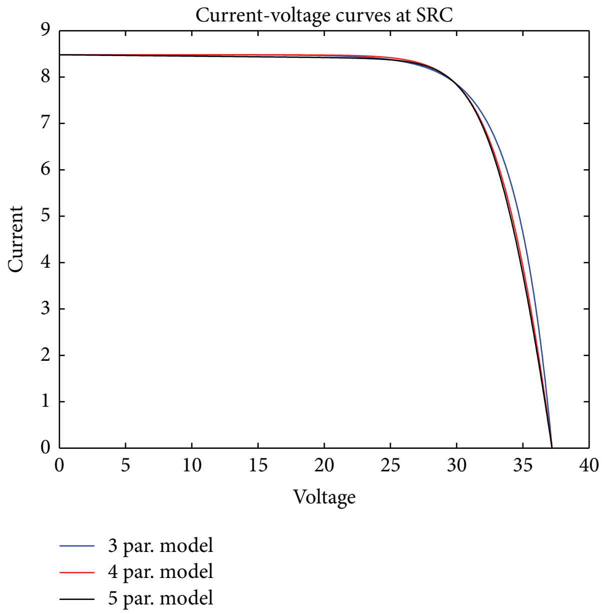

Figure 6: Current-Voltage curves at SRC of BP 3 235T, traced by using 3/4/5 parameter models.

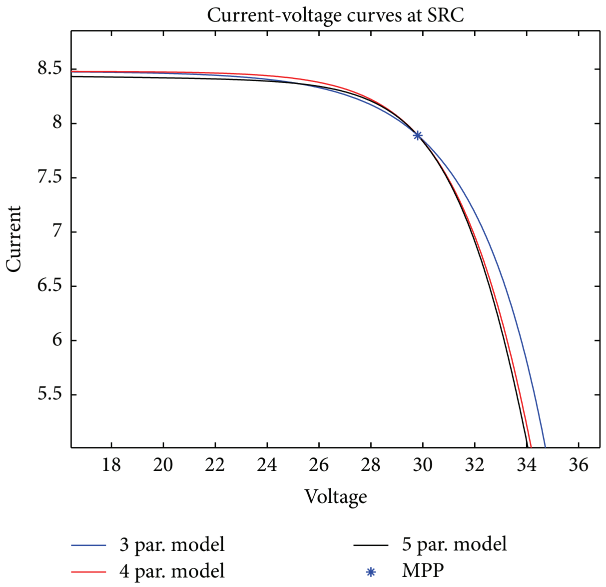

Figure 7: Close-up around maximum power point of Current-Voltage curves at SRC of BP 3 235T, traced by using 3/4/5 parameter models.

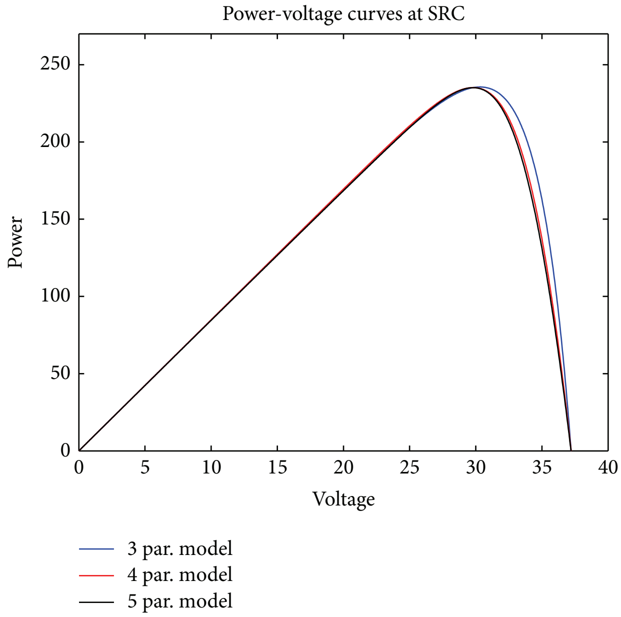

Figure 8: Power-Voltage curves at SRC of BP 3 235T, traced by using 3/4/5 parameter models.

the choice of the initial guesses is one of the more critical aspects regarding the identification of the five-parameter model [22].

(iv) As a consequence, it is also possible to state that the system (21), that is, the reduced form of the original five-equation system, has a unique solution that corresponds to the one with physical meaning.

(v) By observing the graph of the functional $F(n_{\text{ref}}, R_{\text{S,ref}})$ it is also possible to verify that some PV panels have the minimum (i.e., the solution of the problem) lying outside the feasible domain. This means that the solution still exists but it is not physical (i.e., at least one among the five parameters is negative).

3.2. Some Examples and Graphs. In order to prove the above considerations, in Figures 2, 3, 4, and 5 the results of four different panel modules are shown: a mono-Si PV panel (Sharp NT-175UC1), a multi-Si PV panel (BP 3235 T), a thin film PV panel (Xunlight XR12–88), and another multi-Si PV panel (BP Q Series 230 W). Each figure shows the graph of the functional $F(n_{\text{ref}}, R_{\text{S,ref}})$ together with its feasible domain (i.e., the set of points of the two independent parameters n_{ref} and $R_{\text{S,ref}}$ for which the dependent parameters $I_{0,\text{ref}}$, $I_{\text{irr,ref}}$ and $G_{\text{SH,ref}}$, have physical meaning) and the solution (minimum of the functional) of the reduced system (21). Figures 2–5 clearly prove the uniqueness of the solutions of the four panels. Furthermore, the quasi-monotonic behaviours of the functionals allow for an easy search of the solution (convex optimization). The initial guesses chosen for the search procedure of the solutions were the following:

$$R_{\text{S}}^{\text{guess}} = 0.9 \cdot R_{\text{S,ref}}^{\max}\left(n^{\text{guess}}\right) \qquad (26)$$

with $n^{\text{guess}} = 1.0$ for multi-Si and mono-Si PV panels and $n^{\text{guess}} = 2.0$ for thin film PV panels. It can be noted by observing Figure 5 that the PV panel BP Q Series 230 W does not provide for physical solutions of the five parameters model (i.e., the solution exists but it lies outside the feasible domain and then at least one among the dependent parameters is lower than zero). It is worth noting that all the PV panels of BP Q series cannot be modelled by using the five-parameter model. The issue about the existence or not of the solution

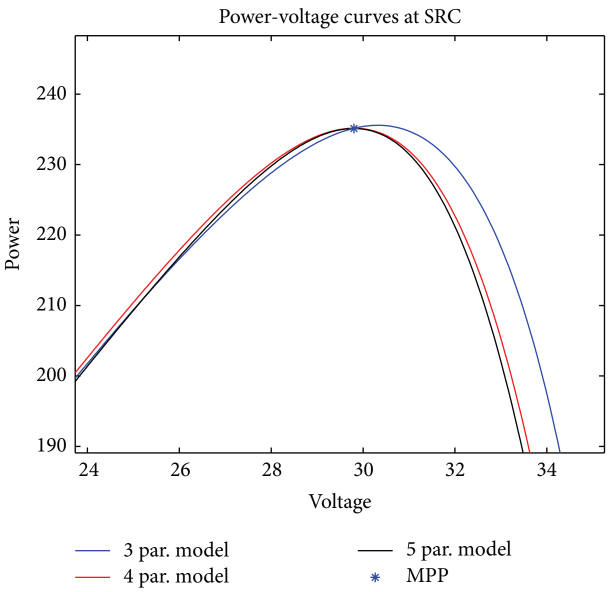

Figure 9: Close-up around maximum power point of Power-Voltage curves at SRC of BP 3 235T, traced by using 3/4/5 parameter models.

is really complex and nothing can be said a priori by simply observing the datasheets of the PV panels.

4. Tests on California Energy Commission Database

In order to prove the effectiveness of the proposed procedure, aimed at the identification of the five-parameter model simply by starting from PV datasheets, in this section a statistical validation is presented. In particular, the tests have involved around 11000 PV panels belonging to the California Energy Commission (CEC) database [23] (updated monthly). Table 1 shows the number of tested PV panels (# PV panels) from CEC database grouped by type of technology. With the aim to demonstrate both the robustness and the fastness of the proposed approach, several initial guesses have been chosen and three different numerical algorithms/functions have been used in Matlab: *fsolve* (suitable for systems with nonlinear equations), *fminsearch* (generic unconstrained minimization function), and *lsqnonlin* (function aimed to solve least squares problems). The simulations showed very accurate results (i.e., with functional values less than $1E-20$) which are independent of the adopted algorithm and the unique solutions have been found at first launch for almost all panels. The execution time for the extraction of the five parameters of all the 11764 PV shown in Table 1 performed on an Intel i5 core 2.5 GHz based notebook with 4 GB of RAM was around 90 seconds for the most efficient algorithm (fsolve with trust-region-dogleg) and 400 seconds for the slowest algorithm (fsolve with trust-region-reflective). This means that, also for the worst cases, the herein proposed extraction procedure of the five parameters spent less than 30 msec for each panel.

Table 1: Number of tested PV panels from CEC database grouped by type of technology.

Technology	# PV panels
Mono-Si	4801
Multi-Si	6435
Amorphous and thin films	253
Other (CIS, CIGS, CdTe, etc.)	275
Total	11764

Table 2: Results obtained with Matlab *fsolve* for $R_S^{\text{guess}} = 0.5R_{S,\text{ref}}^{\max}(n^{\text{guess}})$.

Algorithm	Trust-region-dogleg	Trust-region-reflective	Levenberg-marquardt
Mean # steps	15.56	17.55	17.52
Std # steps	9.48	5.91	9.89
Mean # FEs	41.16	55.65	80.84
Std # FEs	26.38	17.85	34.57

Table 3: Results obtained with Matlab *fsolve* for $R_S^{\text{guess}} = 0.9R_{S,\text{ref}}^{\max}(n^{\text{guess}})$.

Algorithm	Trust-region-dogleg	Trust-region-reflective	Levenberg-marquardt
Mean # steps	6.28	11.83	7.18
Std # steps	2.28	4.35	2.42
Mean # FEs	20.57	32.45	42.60
Std # FEs	4.69	13.09	9.23

Table 4: Results obtained with different Matlab functions with $R_S^{\text{guess}} = 0.9R_{S,\text{ref}}^{\max}(n^{\text{guess}})$.

Matlab function	fminsearch	lsqnonlin	lsqnonlin
Algorithm	Nelder-Mead simplex method	Trust-region-reflective	Levenberg-marquardt
Mean # steps	127.2	9.80	7.14
Std # steps	20.09	3.74	1.69
Mean # FEs	254.8	32.35	44.70
Std # FEs	19.95	11.28	7.24

The comparisons of the performance achievable by using various algorithms and initial guesses are reported in Tables 2, 3, and 4: in particular the results are expressed in terms of average number (mean # steps) and standard deviation (std # steps) of iterations steps, average number (mean # FEs) and standard deviation (std # FEs) of function evaluations (FEs) (in Table 2 the initial guesses are the ones proposed in [22]).

It is worth noting that the proposed initial guess (26) allows obtaining effective results also by using one of the most generic solvers for minimization problems, *fminsearch*, which employs the Nelder-Mead simplex method discussed in Lagarias et al. [32]. By using instead more effective Matlab functions (such as *fsolve* or *lsqnonlin*) and algorithms (such as *Levenberg-Marquardt* [33] or *trust-region-dogleg* [34] algorithms) the number of iterations and FEs becomes extremely low (around 7 for the average number of iterations and 45 for the one of FEs). Consequently the computational costs of the proposed procedure is quite negligible, as the various soft computing based approaches, like the ones in [12–15], typically require thousands of FEs. In addition, it is worth noting that the obtained results have physical meaning for more than 97% of the total number of panels (11488 on 11764 PV panels). The unphysical solutions could be due to the impossibility of identifying the five-parameter model as was for the previous case of BP Q series PV panels. Nevertheless, since we do not have any information about how the datasheets are loaded into the CEC database, we assumed they were correct and no check was made about the exactness of data. Thus, some unphysical solutions could be also due to this last matter and caused by the presence of some errors within the CEC database. Finally, with the aim to show the importance of adopting an accurate 5-parameter model rather than approximated ones (such as for example the 3-parameter and 4-parameter models [35]) the *I*-*V* and *P*-*V* curves at SRC for BP 3 235T module have been considered as last test. The 3-parameter and 4-parameter models seem to be very similar to the 5-parameter one. Nevertheless, with the aim to simplify the characterization problem, $R_{S,\mathrm{ref}} = 0$ and $R_{\mathrm{SH,ref}} = \inf$ conditions are used for the 3-parameter model and $R_{\mathrm{SH,ref}} = \inf$ condition is used for the 4-parameter model. The *I*-*V* and *P*-*V* curves for the three models are shown in Figures 6 and 8, whereas the close-up around the maximum power point (MPP) is shown in Figures 7 and 9. It is evident, by observing the *P*-*V* curves, that (1) the 5-parameter and 4-parameter models are both accurate in the evaluation of MPP, whereas the 3-parameter model is not; (2) the 4-parameter model overestimates the power around the MPP, causing possible errors in the prediction of electric power produced by a PV plant.

5. Conclusions

In this paper a fast and accurate procedure has been presented for the characterization of thousands of photovoltaic modules in few seconds, by starting from the manufacturer datasheets. The proposed procedure utilizes the five-parameter model and takes advantage from its reduced form [22] in order to decrease the dimensions of the search space. Indeed, the reduced system provides a strong advantage in terms of convergence, computational costs, and execution time of the present approach (less than 30 msec for each panel was spent on a simple Intel i5 core 2.5 GHz based notebook). In particular, it allows (1) choosing suitable initial guesses within a well-defined feasible domain; (2) using very simple and standard numerical algorithms for finding parameters; (3) proving the existence, or not, of the unique physical solution of the five-parameter model for each PV panel; (4) proving the existence of only unphysical solutions for the cases in which the five-parameter model cannot be identified. The results of the tests performed on around 11.000 photovoltaic modules belonging to the CEC database demonstrated both the fastness and the effectiveness of the proposed method.

Technical Parameters

q:	1.602×10^{-19} (C)
k:	$1.3806503 \times 10^{-23}$ (J/K)
E_g:	Bandgap energy
G:	Irradiance
T:	Cell temperature
I_0:	Reverse saturation current
I_{irr}:	Photocurrent
n:	Ideality factor
R_S:	Series resistance
R_{SH}:	Shunt resistance
N_s:	Number of series modules/cells
N_p:	Number of parallel connected strings
T_{ref}:	25°C at SRC
G_{ref}:	1000 W/m^2 at SRC
n_{ref}:	Ideality factor at SRC
$R_{S,\mathrm{ref}}$:	Series resistance at SRC
$I_{\mathrm{irr,ref}}$:	Photocurrent at SRC
$I_{0,\mathrm{ref}}$:	Reverse saturation current at SRC
$G_{\mathrm{SH,ref}} = R_{SH,\mathrm{ref}}^{-1}$:	Shunt resistance at SRC
V_{OC}:	Open circuit voltage
I_{SC}:	Short circuit current
V_{mp}:	Maximum power voltage
I_{mp}:	Maximum power current
$V_{\mathrm{OC,ref}}$:	Open circuit voltage at SRC
$I_{\mathrm{SC,ref}}$:	Short circuit current at SRC
$V_{\mathrm{mp,ref}}$:	Maximum power voltage at SRC
$I_{\mathrm{mp,ref}}$:	Maximum power current at SRC
α_T:	Temperature coeff. for I_{SC}
$\alpha_T^{\%}$:	Percentage temperature coeff. for I_{SC}
β_T:	Temperature coeff. for V_{OC}
$\beta_T^{\%}$:	Percentage temperature coeff. for V_{OC}
C_1:	kT_{ref}/q
C_2:	$V_{\mathrm{OC,ref}}/N_S C_1$
C_3:	$V_{\mathrm{mp,ref}}/N_S C_1$
C_4:	$I_{\mathrm{mp,ref}}/N_P C_1$
C_5:	$I_{\mathrm{SC,ref}}/N_P C_1$.

Conflict of Interests

The authors declare that there is no conflict of interests regarding the publication of this paper.

References

[1] A. D. Rajapakse and D. Muthumuni, "Simulation tools for photovoltaic system grid integration studies," in *Proceedings of the IEEE Electrical Power and Energy Conferenc (EPEC '09)*, pp. 1–5, October 2009.

[2] D. Menicucci and J. Fernandez, *User's Manual for PVFORM, SAND85-0376: A Photovoltaic System Simulation Program For Stand-Alone and Grid-Interactive Applications*, Sandia National Laboratories, Albuquerque, NM, USA, 1988.

[3] "PVWATTS," 2011, http://www.nrel.gov/rredc/pvwatts/.

[4] N. J. Blair, A. P. Dobos, and P. Gilman, “Comparison of photovoltaic models in the system advisor model,” in *Proceedings of the Solar*, Baltimore, Md, USA, April 2013.

[5] J. Ma, K. Man, T. Ting, N. Zhang, S. U. Guan, and P. W. Wong, “Dem: direct estimation method for photovoltaic maximum power point tracking,” *Procedia Computer Science*, vol. 17, pp. 537–544, 2013, 1st International Conference on Information Technology and Quantitative Management.

[6] I. T. Papaioannou and A. Purvins, “Mathematical and graphical approach for maximum power point modelling,” *Applied Energy*, vol. 91, no. 1, pp. 59–66, 2012.

[7] M. Carrasco, F. Mancilla-David, F. R. Fulginei, A. Laudani, and A. Salvini, “A neural networks-based maximum power point tracker with improved dynamics for variable dc-link grid-connected photovoltaic power plants,” *International Journal of Applied Electromagnetics and Mechanics*, vol. 43, no. 1, pp. 127–135, 2013.

[8] B. Schulz, T. Glotzbach, C. Vodermayer, G. Wotruba, M. Mayer, and S. Grünsteidl, “Evaluation of calibrated solar cells and pyranometers regarding the effective irradiance detected by pv modules,” in *Proceedings of the 25th European Photovoltaic Solar Energy Conference and Exhibition/5th World Conference on Photovoltaic Energy Conversion*, pp. 4797–4800, October 2012.

[9] F. Mancilla-David, F. Riganti-Fulginei, A. Laudani, and A. Salvini, “A neural network-based low-cost solar irradiance sensor,” *IEEE Transactions on Instrumentation and Measurement*, vol. 63, no. 3, pp. 583–591, 2014.

[10] H. Tian, F. Mancilla-David, K. Ellis, E. Muljadi, and P. Jenkins, “A cell-to-module-to-array detailed model for photovoltaic panels,” *Solar Energy*, vol. 86, no. 9, pp. 2695–2706, 2012.

[11] W. de Soto, S. A. Klein, and W. A. Beckman, “Improvement and validation of a model for photovoltaic array performance,” *Solar Energy*, vol. 80, no. 1, pp. 78–88, 2006.

[12] L. L. Jiang, D. L. Maskell, and J. C. Patra, “Parameter estimation of solar cells and modules using an improved adaptive differential evolution algorithm,” *Applied Energy*, vol. 112, pp. 185–193, 2013.

[13] K. Ishaque, Z. Salam, S. Mekhilef, and A. Shamsudin, “Parameter extraction of solar photovoltaic modules using penalty-based differential evolution,” *Applied Energy*, vol. 99, pp. 297–308, 2012.

[14] M. F. AlHajri, K. M. El-Naggar, M. R. AlRashidi, and A. K. Al-Othman, “Optimal extraction of solar cell parameters using pattern search,” *Renewable Energy*, vol. 44, pp. 238–245, 2012.

[15] N. Rajasekar, N. K. Kumar, and R. Venugopalan, “Bacterial foraging algorithm based solar {PV} parameter estimation,” *Solar Energy*, vol. 97, pp. 255–265, 2013.

[16] S. Xian Lun, C. Jiao Du, G. Hong Yang et al., “An explicit approximate iv characteristic model of a solar cell based on pad approximants,” *Solar Energy*, vol. 92, pp. 147–159, 2013.

[17] S. Xian Lun, C. Jiao Du, T. Ting Guo, S. Wang, J. Shu Sang, and J. Pei Li, “A new explicit iv model of a solar cell based on taylors series expansion,” *Solar Energy*, vol. 94, pp. 221–232, 2013.

[18] A. Jain and A. Kapoor, “Exact analytical solutions of the parameters of real solar cells using Lambert W-function,” *Solar Energy Materials and Solar Cells*, vol. 81, no. 2, pp. 269–277, 2004.

[19] A. Jain and A. Kapoor, “A new method to determine the diode ideality factor of real solar cell using Lambert W-function,” *Solar Energy Materials and Solar Cells*, vol. 85, no. 3, pp. 391–396, 2005.

[20] Y. Chen, X. Wang, D. Li, R. Hong, and H. Shen, “Parameters extraction from commercial solar cells I-V characteristics and shunt analysis,” *Applied Energy*, vol. 88, no. 6, pp. 2239–2244, 2011.

[21] R. M. Corless, G. H. Gonnet, D. E. G. Hare, D. J. Jeffrey, and D. E. Knuth, “On the Lambert W function,” *Advances in Computational Mathematics*, vol. 5, no. 4, pp. 329–359, 1996.

[22] A. Laudani, F. Mancilla-David, F. Riganti-Fulginei, and A. Salvini, “Reduced-form of the photovoltaic five-parameter model for efficient computation of parameters,” *Solar Energy*, vol. 97, pp. 122–127, 2013.

[23] California Energy Commission, “CECPV calculator version 4.0,” 2013, http://www.gosolarcalifornia.org/tools/nshpcalculator/index.php.

[24] V. lo Brano, A. Orioli, G. Ciulla, and A. di Gangi, “An improved five-parameter model for photovoltaic modules,” *Solar Energy Materials and Solar Cells*, vol. 94, no. 8, pp. 1358–1370, 2010.

[25] A. Mermoud and T. Lejeune, “Performance assessment of a simulation model for PV modules of any available technology,” in *Proceedings of the 25th European PV Solar Energy Conference*, pp. 4786–4791, 2010.

[26] A. P. Dobos, “An improved coefficient calculator for the california energy commission 6 parameter photovoltaic module model,” *Journal of Solar Energy Engineering, Transactions of the ASME*, vol. 134, no. 2, Article ID 021011, pp. 1–6, 2012.

[27] Y. Li, W. Huang, H. Huang et al., “Evaluation of methods to extract parameters from currentvoltage characteristics of solar cells,” *Solar Energy*, vol. 90, pp. 51–57, 2013.

[28] J. Fourie, R. Green, and Z. W. Geem, “Generalised adaptive harmony search: a comparative analysis of modern harmony search,” *Journal of Applied Mathematics*, vol. 2013, Article ID 380985, 13 pages, 2013.

[29] A. Laudani, F. Riganti-Fulginei, and A. Salvini, “Closed forms for the fully-connected continuous flock-of-starlings optimization algorithm,” in *Proceedings of the 15th International Conference on Computer Modeling and Simulation (UKSim ’13)*, April 2013.

[30] A. Laudani, F. Riganti-Fulginei, A. Salvini, M. Schmid, and S. Conforto, “CFSO^3: a new supervised swarm-based optimization algorithm,” *Mathematical Problems in Engineering*, vol. 2013, Article ID 560614, 13 pages, 2013.

[31] F. R. Fulginei, A. Salvini, and G. Pulcini, “Metric-topological-evolutionary optimization,” *Inverse Problems in Science and Engineering*, vol. 20, no. 1, pp. 41–58, 2012.

[32] J. C. Lagarias, J. A. Reeds, M. H. Wright, and P. E. Wright, “Convergence properties of the Nelder-Mead simplex method in low dimensions,” *SIAM Journal on Optimization*, vol. 9, no. 1, pp. 112–147, 1998.

[33] J. J. Moré, “The levenberg-marquardt algorithm: implementation and theory,” in *Numerical Analysis*, pp. 105–116, Springer, New York, NY, USA, 1978.

[34] T. F. Coleman and Y. Li, “An interior trust region approach for nonlinear minimization subject to bounds,” *SIAM Journal on Optimization*, vol. 6, no. 2, pp. 418–445, 1996.

[35] A. Luque and S. Hegedus, *Handbook of Photovoltaic Science and Engineering*, John Wiley & Sons, New York, NY, USA, 2011.

Hindawi Publishing Corporation
International Journal of Photoenergy
Volume 2014, Article ID 346704, 9 pages
http://dx.doi.org/10.1155/2014/346704

Research Article

An Improved Mathematical Model for Computing Power Output of Solar Photovoltaic Modules

Abdul Qayoom Jakhrani,[1] Saleem Raza Samo,[1] Shakeel Ahmed Kamboh,[2] Jane Labadin,[3] and Andrew Ragai Henry Rigit[4]

[1] *Energy and Environment Engineering Department, Quaid-e-Awam University of Engineering, Science and Technology (QUEST), Nawabshah, Sindh 67480, Pakistan*
[2] *Department of Mathematics and Computational Science, Faculty of Computer Science and Information Technology, Universiti Malaysia Sarawak, Kota Samarahan, 94300 Sarawak, Malaysia*
[3] *Faculty of Computer Science and Information Technology, Universiti Malaysia Sarawak, Kota Samarahan, 94300 Sarawak, Malaysia*
[4] *Faculty of Engineering, Universiti Malaysia Sarawak, Kota Samarahan, 94300 Sarawak, Malaysia*

Correspondence should be addressed to Abdul Qayoom Jakhrani; aqunimas@hotmail.com

Received 31 May 2013; Revised 26 December 2013; Accepted 9 January 2014; Published 17 March 2014

Academic Editor: Ismail H. Altas

It is difficult to determine the input parameters values for equivalent circuit models of photovoltaic modules through analytical methods. Thus, the previous researchers preferred to use numerical methods. Since, the numerical methods are time consuming and need long term time series data which is not available in most developing countries, an improved mathematical model was formulated by combination of analytical and numerical methods to overcome the limitations of existing methods. The values of required model input parameters were computed analytically. The expression for output current of photovoltaic module was determined explicitly by Lambert W function and voltage was determined numerically by Newton-Raphson method. Moreover, the algebraic equations were derived for the shape factor which involves the ideality factor and the series resistance of a single diode photovoltaic module power output model. The formulated model results were validated with rated power output of a photovoltaic module provided by manufacturers using local meteorological data, which gave ±2% error. It was found that the proposed model is more practical in terms of precise estimations of photovoltaic module power output for any required location and number of variables used.

1. Introduction

The photovoltaic (PV) modules are generally rated under standard test conditions (STC) with the solar radiation of $1000\,\mathrm{W/m^2}$, cell temperature of $25^\circ\mathrm{C}$, and solar spectrum of 1.5 by the manufacturers. The parameters required for the input of the PV modules are relying on the meteorological conditions of the area. The climatic conditions are unpredictable due to the random nature of their occurrence. These uncertainties lead to either over- or underestimation of energy yield from PV modules. An overestimation up to 40% was reported as compared to the rated power output of PV modules [1, 2]. The growing demand of photovoltaics technologies led to research in the various aspects of its components from cell technology to the modeling, size optimization, and system performance [3–5]. Modeling of PV modules is one of the major components responsible for proper functioning of PV systems. Modeling provides the ways to understand the current, voltage, and power relationships of PV modules [6–8]. However, the estimation of models is affected by various intrinsic and extrinsic factors, which ultimately influence the behavior of current and voltage. Therefore, perfect modeling is essential to estimate the performance of PV modules in different environmental conditions. Hernanz et al. [9] compared the performance of solar cells with different models and pointed out that the manufacturers did not provide the values of the resistance in series and parallel of the manufactured cell. Andrews et al. [10] proposed an improved methodology for fine resolution modeling of PV systems using module short circuit current

(I_{sc}) at 5 min time scales. Their work was a modified version of the Sandia array performance model by incorporating new factors for the calculation of short circuit current (I_{sc}) to justify errors (including instrumentation alignment and spectral and module power tolerance errors). Chakrasali et al. [11] investigated the performance of Norton's circuit model of solar PV module with the existing models using Matlab and reported that it is a well-suited way to predict the behavior of PV modules operated for longer periods of time. Chouder et al. [12] modeled a PV module by a single diode lumped circuit and evaluated its main parameters by considering the power conversion efficiency. Chouder et al. [13] presented a detailed characterization of the performance and dynamic behavior of PV systems by using the LabVIEW platform. The Lambert W function was applied for the solution of equations by Jain and Kapoor [14], Jain et al. [15], Ortiz-Conde et al. [16], and others [17–19]. Picault et al. [17] presented a novel method to forecast existing PV array production in diverse environmental conditions and concluded that Lambert W function facilitates a direct relationship between current and voltage of modules as it significantly reduces calculation time. Chen et al. [18] proposed an optimized method based on polynomial curve fitting and Lambert W function for extraction of parameters from the current-voltage (*I-V*) characteristics of commercial silicon solar cells. The Lambert W function was used for translation of transcendental equation into explicit analytical solution. Fathabadi [19] presented a novel method for characterization of silicon solar cells, modules, and plastic solar cells. Artificial neural network together with Lambert W function was employed for determination of *I-V* and *P-V* curves of silicon and plastic solar cells and modules [20].

Moreover, Krismadinata et al. [21] used a single diode electrical equivalent circuit model for determination of PV cell characteristics and found that output of PV modules were strongly affected by the intensity of solar irradiation and ambient temperature. Lu et al. [22] investigated various PV module layouts using full size as well as halved solar cells. The performance of module layouts was investigated by partially shading the PV cells using a solar cell equivalent circuit model with SPICE software. They found that the series-parallel hybrid connection of cells within a module has a significant improvement on the power output of the PV module under partial shading conditions. Mellit et al. [23] employed a methodology for estimation power profile of a 50 Wp Si-polycrystalline PV module by developing two artificial neural networks (ANNs) for cloudy and sunny days and found that the ANN-models performed better than the existing models and also did not need more parameters unlike implicit models. Singh [24] reviewed various models of PV cells and concluded that the accuracy of models can be improved by including series and shunt resistance into the model. In addition, the author also discovered that the estimation of models can further be improved by either introducing two parallel diodes with independent set saturation current or considering the diode quality factor as a variable parameter instead of fixed value like 1 or 2. Thevenard and Pelland [25] reported that the uncertainties of model predictions can be reduced by increasing the reliability and spatial coverage of solar radiation estimates, appropriate familiarity of losses due to dirt, soiling, and snow, and development of better tools for PV system modeling. Tian et al. [26] presented a modified *I-V* relationship for the single diode model. The alteration in the model was made in the parallel and series connections of an array. The derivation of the adapted *I-V* relationship was begun with a single solar cell and extended up to a PV module and finally an array. The modified correlation was investigated with a five-parameter model based on the data provided by the manufacturers. The performance of the model was examined with a wide range of irradiation levels and cell temperatures for prediction of *I-V* and *P-V* curves, maximum power point values, short circuit current, and open circuit voltage. Vincenzo and Infield [27] developed a detailed PV array model to deal explicitly with nonuniform irradiance and other nonuniformities across the array and it was validated against data from an outdoor test system. However, the authors reduced the complexity of the simulations by assuming that the cell temperatures are homogeneous for each module. Yordanov et al. [28] presented a new algorithm for determination of the series resistance of crystalline-Si PV modules from individual illuminated *I-V* curves. The ideality factor and the reverse saturation current were extracted in the typical way. They found that the ideality factor at open circuit is increased by about 5%. It was established from the review that Lambert W function is a simple technique to give the analytical explicit solution of solar photovoltaic module characteristics as compared to the other methods. However, some problems still exist for the derivation of the required model equations.

Equivalent electrical circuit model is one of the key models under study since the last few decades. It is configured with either single or double diode for investigation of current-voltage relationships. The single diode models usually have five, four, or three unknown parameters with only one exponential term. The five unknown parameters of a single diode model are light-generated current (I_L), diode reverse saturation current (I_o), series resistance (R_s), shunt resistance (R_{sh}), and diode ideality factor (A) [29, 30]. The four-parameter model infers the shunt resistance as infinite and it is ignored [31]. The three-parameter model assumes that the series resistance is zero and shunt resistance is infinite and, thus, both of these parameters are ignored, whereas, the double diode models have six unknown parameters with two exponential terms [32, 33].

In fact, both single and double diode models require the knowledge of all unknown parameters, which is usually not provided by manufacturers. Nevertheless, the current-voltage equation is a transcendental expression. It has no explicit analytical solution. It is also time consuming to discover its exact analytical solution due to the limitation of available data for the extraction of required parameters [34–36]. For that reason, the researchers gradually focused on searching out the approximate methods for the calculation of unknown parameters. The analytical methods give exact solutions by means of algebraic equations. However, due to implicit nature and nonlinearity of PV cell or module characteristics, it is hard to find out the analytical solution of all unknown parameters. Analytical methods have also some limitations and could not give exact solutions when the functions are not given. Thus, numerical methods such as Newton-Raphson method or Levenberg-Marquardt algorithm were preferred. It is because of the fact that numerical methods give approximate solution of the nonlinear problems without searching for exact solutions. However, numerical methods are time consuming and need long term time series data which is not available in developing countries.

It was revealed from the review that a wide variety of models exist for estimation of power output of PV modules. However, these were either complicated or gave approximate solutions. To overcome the limitations of both numerical and analytical methods an improved mathematical model using combination of numerical and analytical methods is presented. It makes the model simple as well as comprehensive to provide acceptable estimations for PV module power outputs. The values of required unknown parameters of *I-V* curve, namely, light-generated current, diode reverse saturation current, shape parameter, and the series resistance, are computed analytically. The expression for output current of PV module is determined explicitly by Lambert W function and voltage output is computed numerically by Newton-Raphson method.

2. Formulated Model for Computing Power Output of PV Modules

The power produced by a PV module depends on intrinsic electrical characteristics (current and voltage) and extrinsic atmospheric conditions. The researchers generally incorporate the most important electrical characteristics and influential meteorological parameters in the models for the sake of simplicity. It is almost unfeasible to obtain a model that accounts each parameter which influences the performance of PV modules. The models generally include those parameters, which are commonly provided by manufacturers, such as the electrical properties of modules at standard rating conditions [37]. The standard equivalent electrical circuit model of PV cell denoted by a single diode is expressed as [38]

$$I = I_L - I_D - I_{\text{sh}}, \tag{1}$$

where I_L is light-generated current, I_D is diode current, and I_{sh} is shunt current. The diode current (I_D) is expressed by the Shockley equation as [39, 40]:

$$I_D = I_o\left[e^{\xi(V+IR_s)} - 1\right]. \tag{2}$$

The shunt current (I_{sh}) is defined by Petreus et al. [41] as

$$I_{\text{sh}} = \frac{V + IR_s}{R_{\text{sh}}}. \tag{3}$$

Therefore, the final structure of five-parameter one diode electrical equivalent circuit model is graphically shown in Figure 1. It is also algebraically expressed as [40, 42–44]

$$I = I_L - I_o\left[e^{\xi(V+IR_s)} - 1\right] - \frac{V + IR_s}{R_{\text{sh}}}, \tag{4}$$

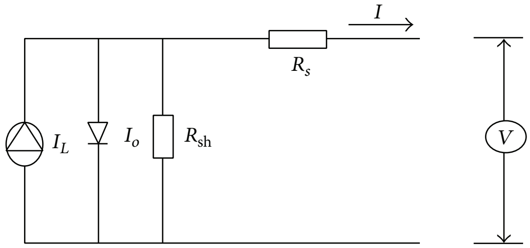

Figure 1: Equivalent electrical circuit model of a PV module.

where I_o is the reverse saturation current and ξ is a term incorporated for the simplicity of (4), which is expressed as

$$\xi = \frac{q}{\lambda k T_c}, \tag{5}$$

where q is electronic charge, k is Boltzmann's constant, T_c is the cell temperature, and λ is the shape factor, which is given as

$$\lambda = A \times N_{\text{CS}}, \tag{6}$$

where A is the ideality factor and N_{CS} is the number of series cells in a module. The ideality factor (A) does not depend on the temperature as per definition of shape factor (λ) from semiconductor theory [45]. The five unknown parameters, namely, I_L, I_o, R_s, R_{sh}, and A, can only be found through complicated numerical methods from a nonlinear solar cell equation. It requires a close approximation of initial parameter values to attain convergence. Otherwise, the result may deviate from the real values [32, 43]. It is impractical to find a method, which can properly extract all required parameters to date [40, 46]. Thus, for simplicity, the shunt resistance (R_{sh}) is assumed to be infinity. Hence, the last term in (4) is ignored [47]. Therefore, the simplified form of four-parameter single diode equivalent circuit model, which is used for this study, is defined as [48]

$$I = I_L - I_o\left[e^{\xi(V+IR_s)} - 1\right]. \tag{7}$$

From (7), a continuous relationship of current as function of voltage for a given solar irradiance, cell temperature, and other cell parameters can be obtained.

2.1. Determination of Unknown Parameters of Formulated Model. The expressions for unknown parameters such as light-generated current (I_L) and reverse saturation current (I_o) were adopted from previous available models. The expressions for the shape factor (λ) which involve the ideality factor (A) and the series resistance (R_s) were algebraically derived from existing equations. The PV module used for this study was NT-175 (E1) manufactured by Sharp Energy Solution Europe, a division of Sharp Electronics (Europe) GmbH, Sonninstraße 3, 20097, Hamburg, Germany.

2.1.1. Light-Generated Current (I_L). Light-generated current (I_L) is a function of solar radiation and module temperature, if the series resistance (R_s) and the shape factor (λ) are taken as constants. For any operating condition, I_L is related to the light-generated current measured at some reference conditions as [14, 29]

$$I_L = \left(\frac{S_T}{S_{T,r}}\right)\left[I_{L,r} + \mu_{I_{\mathrm{sc}}}\left(T_c - T_{c,r}\right)\right], \tag{8}$$

where S_T and $S_{T,r}$ are the absorbed solar radiation and T_c and $T_{c,r}$ are the cell temperatures at outdoor conditions and reference conditions, respectively. $I_{L,r}$ is light-generated current at reference conditions and $\mu_{I_{\mathrm{sc}}}$ is coefficient of temperature at short circuit current. The cell temperature (T_c) can be computed from the ambient temperature and other data tested at nominal operating cell temperature (NOCT) conditions, provided by the manufacturers.

2.1.2. Reverse Saturation Current (I_o). The reverse saturation current (I_o) is a function of temperature only [49]. It is given as

$$I_o = DT_c^3 e^{\xi\varepsilon_g/A}. \tag{9}$$

The reverse saturation current (I_o) is a diminutive number, but its value increases by a factor of two with a temperature increase of 10°C [50]. It is actually computed by taking the ratio of (9) at two different temperatures, thereby, eliminating the diode diffusion factor (D). It is related to the temperature only. Thus, it is estimated at some reference conditions as the same technique used for the determination of light current [49]. Consider

$$I_o = \left(\frac{T_c}{T_{c,r}}\right)^3 e^{\xi\lambda\varepsilon_g(T_{c,r}-T_c)/A}. \tag{10}$$

2.1.3. Shape Factor (λ). Mostly, manufacturers provide information of *I-V* characteristic curve at three different points using reference conditions, at open circuit voltage (V_{oc}), at short circuit current (I_{sc}), and at optimum power point for both current and voltage. The correlation for the given points are $I = 0$ and $V = V_{\mathrm{oc}}$ at open circuit conditions, $I = I_{\mathrm{sc}}$ and $V = 0$ at short circuit conditions, and $I = I_{\mathrm{mp}}$ and $V = V_{\mathrm{mp}}$ at maximum power point [48]. By substituting these expressions in (7), it yields

$$I_{\mathrm{sc},r} = I_{L,r} - I_{o,r}\left[e^{(\xi_r I_{\mathrm{sc},r} R_s)} - 1\right], \tag{11}$$

where

$$\xi_r = \frac{q}{\lambda k T_{c,r}}, \tag{12}$$

$$I_{L,r} - I_{o,r}\left[e^{(\xi_r V_{\mathrm{oc},r})} - 1\right] = 0, \tag{13}$$

$$I_{\mathrm{mp},r} = I_{L,r} - I_{o,r}\left[e^{\xi_r(V_{\mathrm{mp},r} + I_{\mathrm{mp},r}R_s)} - 1\right]. \tag{14}$$

The reverse saturation current (I_o) is a very small quantity on the order of 10^{-5} to 10^{-6} A [47]. It lessens the influence of the exponential term in (11). Hence, it is assumed to be equivalent to I_{sc} [32]. One more generalization can be made regarding the first term in (13) and (14), which could be ignored. Regardless of the system size, the exponential term is much greater than the first term. Thus, the equations become

$$I_{L,r} \cong I_{\mathrm{sc},r}, \tag{15}$$

$$I_{\mathrm{sc},r} - I_{o,r}\left[e^{(\xi_r I_{\mathrm{sc},r} R_s)}\right] \cong 0, \tag{16}$$

$$I_{\mathrm{mp},r} \cong I_{L,r} - I_{o,r}\left[e^{\xi_r(V_{\mathrm{mp},r} + I_{\mathrm{mp},r}R_s)}\right]. \tag{17}$$

Solving (16) for reverse saturation current at reference conditions, ($I_{o,r}$) is obtained as

$$I_{o,r} = I_{\mathrm{sc},r}\left[e^{-(\xi_r V_{\mathrm{oc},r})}\right]. \tag{18}$$

By substituting the value of reverse saturation current at reference conditions ($I_{o,r}$) from (18) into (17), it yields

$$I_{\mathrm{mp},r} \cong I_{\mathrm{sc},r} - I_{\mathrm{sc},r}\left[e^{\xi_r(V_{\mathrm{mp},r} - V_{\mathrm{oc},r} + I_{\mathrm{mp},r}R_s)}\right]. \tag{19}$$

The Equation (17) can also be solved for ξ_r, which is given as

$$\xi_r = \frac{\ln\left(1 - I_{\mathrm{mp},r}/I_{\mathrm{sc},r}\right)}{V_{\mathrm{mp},r} - V_{\mathrm{oc},r} + I_{\mathrm{mp},r}R_s}. \tag{20}$$

Finally, the value of the shape factor (λ) can be obtained by comparing (12) and (20) as

$$\lambda = \frac{q\left(V_{\mathrm{mp},r} - V_{\mathrm{oc},r} + I_{\mathrm{mp},r}R_s\right)}{kT_{c,r}\ln\left(1 - I_{\mathrm{mp},r}/I_{\mathrm{sc},r}\right)}. \tag{21}$$

2.1.4. Series Resistance (R_s). The series resistance (R_s) is an essential parameter when the module is not operating near the reference conditions. This characterizes the internal losses due to current flow inside the each cell and in linkages between cells. It alters the shape of *I-V* curve near optimum power point and open circuit voltage; however, its effect is small [29, 36]. *I-V* curve without considering R_s would be somewhat dissimilar than the curves outlined including its value. On the basis of annual simulation, the predicted power output from PV systems will be 5% to 8% lower when correct series resistance is not used [32, 51]. It can be determined as

$$\left.\frac{dV}{dI}\right|_{V_{\mathrm{oc},r}} - R_s = 0. \tag{22}$$

To obtain differential coefficient for (22), first the current (I) can be extracted explicitly as a function of voltage (V) by using Lambert W function from (7) and is expressed as

$$I = \left(I_L + I_o\right) - \frac{W\left(\xi R_s e^{\xi(V + I_L R_s + I_o R_s)}\right)}{\xi R_s}. \tag{23}$$

By differentiating (23) with respect to V and taking its reciprocal at $V = V_{\mathrm{oc},r}$ and $I_L = I_{L,r}$ and substituting into (22), it gives

$$\frac{W\left(\xi R_s I_o e^{\xi(V_{\mathrm{oc},r} + I_{L,r}R_s + I_o R_s)}\right)}{\left[1 + W\left(\xi R_s I_o e^{\xi(V_{\mathrm{oc},r} + I_{L,r}R_s + I_o R_s)}\right)\right] R_s} - R_s = 0. \tag{24}$$

A number of simplifications have been made in order to solve (24) analytically for R_s. For example, I_o is usually taken in the order of 10^{-5} to 10^{-6} [47]. Its value for this study was taken as the order of 10^{-6}. Similarly, the values of $I_{L,r}$ and $V_{\mathrm{oc},r}$ were taken from the manufacturers data. The expression for R_s is obtained based on the above simplifications and by putting the value of ξ in (24) as

$$R_s = 1.8\,\mathrm{Re}\left(\frac{T_c W\left(-1.5\times 10^7 e^{0.022(47+(1.7\times 10^5/T_c))}\right)}{T_c W\left(-1.5\times 10^7 e^{0.022(47+(1.7\times 10^5/T_c))}\right)+4400}\right), \quad (25)$$

where Re represents the real part, because the negative expression inside the Lambert W function results in a complex number. However, in practical problems only real values are to be considered.

2.2. Determination of Optimum Power Output Parameters of Proposed Model. The optimum power output parameters of model were determined by deriving the equations for current (I) and voltage (V) by putting the values of unknown parameters, namely, I_L, I_o, R_s, and λ, in the respective equations. The power (P) is the product of current (I) and voltage (V) [48]; therefore, it can be expressed as

$$P = IV. \quad (26)$$

By substituting I from (23) into (26), the value of P is computed as [52]

$$P = \left\{\left(I_L + I_o\right) - \frac{W\left[\xi R_s e^{\xi(V+I_L R_s+I_o R_s)}\right]}{\xi R_s}\right\} V. \quad (27)$$

Mathematically, the optimum power occurs at the point $V_{\max}$ of P-V curve, where the slope of tangent line is equal to zero as follows:

$$\left.\frac{dP}{dV}\right|_{V_{\max}} = 0. \quad (28)$$

By differentiating (27) with respect to voltage (V) and taking the R.H.S equal to zero,

$$\frac{W\left[\xi R_s I_o e^{\xi(V+I_L R_s+I_o R_s)}\right] V}{\left\{1 + W\left[\xi R_s I_o e^{\xi(V+I_L R_s+I_o R_s)}\right]\right\} R_s} + \frac{1}{\xi R_s} \times \left\{W\left[\xi R_s I_o e^{\xi(V+I_L R_s+I_o R_s)}\right] - \xi R_s\left(I_L + I_o\right)\right\} = 0. \quad (29)$$

Newton-Raphson method is applied to (29) in order to find the critical value of V for $V_{\max}$. The value of $V_{\max}$ is substituted into (27) in order to solve the maximum power ($P_{\max}$). Consider

$$P_{\max} = \left\{\left(I_L + I_o\right) - \frac{W\left[\xi R_s e^{\xi(V_{\max}+I_L R_s+I_o R_s)}\right]}{\xi R_s}\right\} V_{\max}. \quad (30)$$

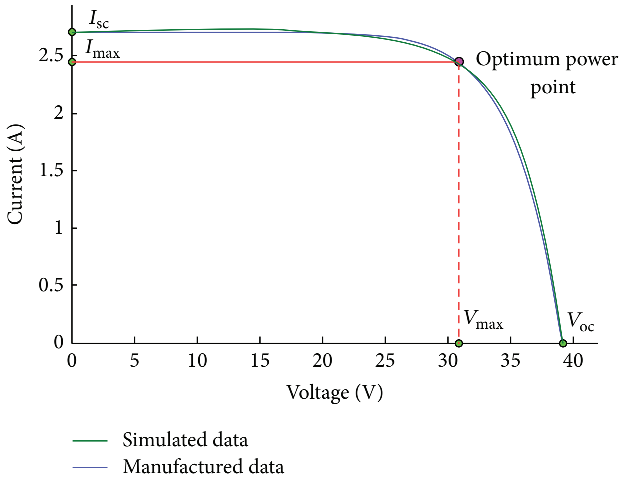

FIGURE 2: Typical *I-V* characteristic curve of a PV module.

Consequently, the desired maximum current ($I_{\max}$) can be obtained from (30) by dividing the maximum power ($P_{\max}$) with maximum voltage ($V_{\max}$). Consider

$$I_{\max} = \frac{P_{\max}}{V_{\max}}. \quad (31)$$

3. Simulation of *I-V* and *P-V* Characteristic Curves of a Selected PV Module

The familiarity of current and voltage relationship of photovoltaic modules under real operating conditions is essential for the determination of their power output. Normally, the cells are mounted in modules, and multiple modules are used in arrays to get desired power output. Individual modules may have cells connected in series and parallel combinations to obtain the required current and voltage. Similarly, the array of modules may be arranged in series and parallel connections. When the cells or modules are connected in series, the voltage is additive, and when they are attached in parallel, the currents are additive [52–56]. The power output of PV modules could be predicted from the behavior of current-voltage, *I-V*, and power-voltage, *P-V*, characteristic curves. The current-voltage and power-voltage characteristic curves are graphically shown in Figures 2 to 9.

The current-voltage, *I-V*, characteristic of a typical PV module is shown in Figure 2. When the output voltage $V = 0$, the current is the short circuit current (I_{sc}) and when the current $I = 0$, the output voltage is the open circuit voltage (V_{oc}). Mostly the current decreases slowly at a certain point and then decreases rapidly to the open circuit conditions. The power as a function of voltage is given in Figure 3. The maximum power that can be obtained corresponds to the rectangle of maximum area under *I-V* curve. At the optimum power point the power is P_{mp}, the current is I_{mp}, and the voltage is V_{mp}. Ideally, the cells would always operate at the optimum power point that matches the *I-V* characteristic of the load. Hence, the load matching is essential for extracting the maximum power from the solar photovoltaic modules.

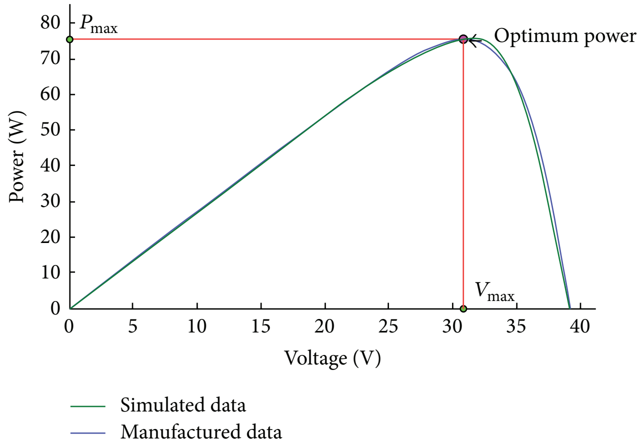

FIGURE 3: Typical *P-V* characteristic curve of a PV module.

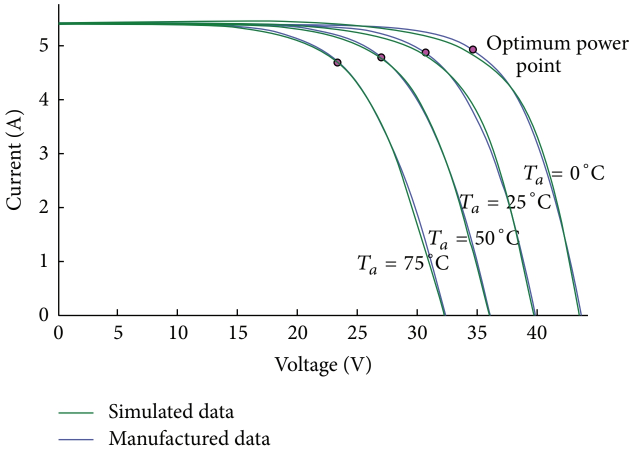

FIGURE 5: *I-V* characteristic curves at various temperatures.

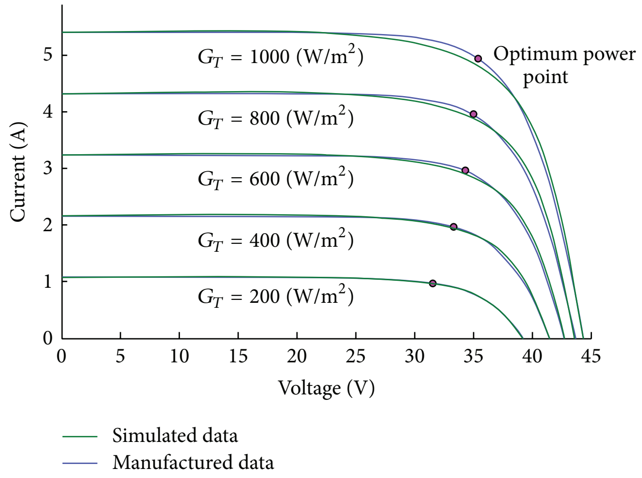

FIGURE 4: *I-V* characteristic curves at various solar radiation levels.

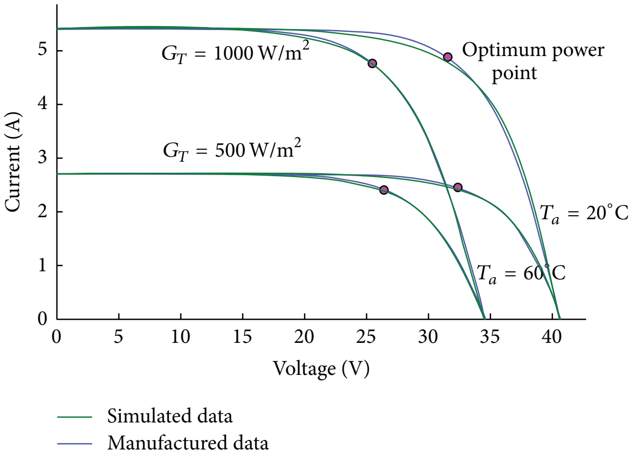

FIGURE 6: *I-V* characteristic curves for various set of solar radiation and temperature.

Therefore, the maximum power point tractors are preferred to optimize the output power from solar PV systems.

I-V characteristic curves at various solar irradiation levels and temperatures are shown in Figures 4 and 5, respectively. The locus of maximum power point is indicated on the curves. The short circuit current increases in proportion to the solar radiation while the open circuit voltage increases logarithmically with solar radiation. As long as the curved portion of the *I-V* characteristic does not intersect, the short circuit current is nearly proportional to the incident solar radiation. If the incident solar radiation is assumed to be a fixed spectral distribution, the short circuit current can be used as a measure of incident solar radiation. *I-V* characteristics curves for the combination of irradiance and temperatures are illustrated in Figure 6. It was observed that the temperature linearly decreases the output voltage as compared to current. Consequently, the decrease of voltage lowers the power output of PV module at constant solar irradiation level. However, the effect of temperature is small on short circuit current but increases with the increase of incident solar radiation.

The *P-V* characteristics curves for various solar irradiation levels at constant temperature of 25°C and at several temperatures with constant solar irradiance of 1000 W/m^2 is illustrated in Figures 7 and 8, respectively. Increasing temperature leads to decreasing the open circuit voltage and slightly increasing the short circuit current. Operating of cell temperature at that region of the curve leads to a significant power reduction at high temperatures. The *P-V* characteristics curves for the combination of irradiance and temperatures are shown in Figure 9.

The power output of photovoltaic module by formulated model gave a ±2% error when compared with the rated power of PV module provided by manufacturers on average basis. However, at higher solar radiation and temperature values, the model simulated results were somehow deviated from the rated power of PV module. Since, the shunt resistance (R_{sh}) was assumed to be infinity in the proposed model. It was found from the analysis that the increase of temperature and decrease of incident solar radiation levels lead to lower power output and vice versa. The power output from PV modules

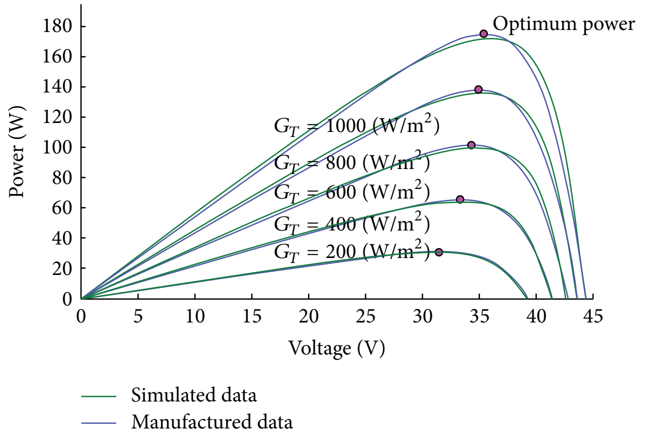

FIGURE 7: *P-V* characteristic curve at constant temperature of 25°C.

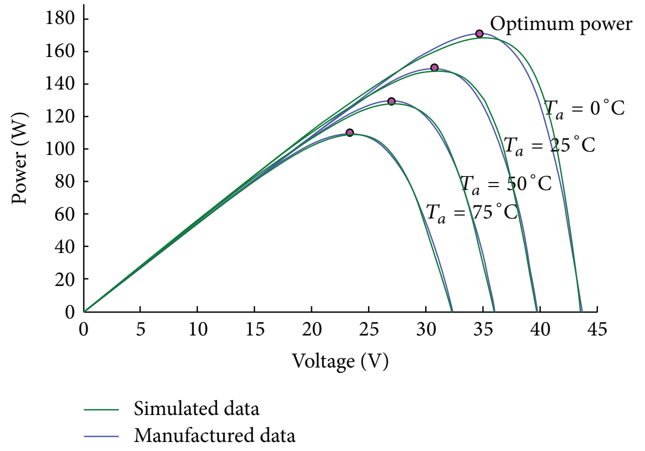

FIGURE 8: *P-V* characteristic curve at constant solar radiation of 1000 W/m^2.

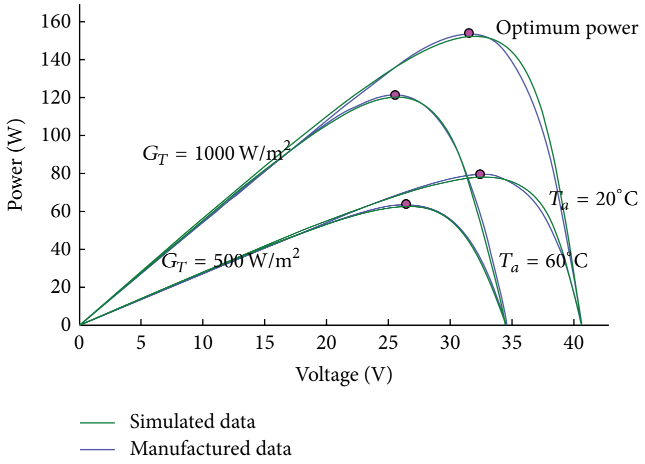

FIGURE 9: *P-V* characteristic curve at various set of solar radiation and temperature.

approaches zero, if the amount of solar radiation tends to decrease and the temperature goes up.

4. Conclusions

The proposed mathematical model is formulated by integration of both analytical and numerical methods. The required parameters of current-voltage (*I-V*) curve such as the light-generated current, diode reverse saturation current, shape parameter, and the series resistance are computed analytically. The expression for output current from PV module is determined explicitly by Lambert W function and voltage output is computed numerically by Newton-Raphson method. The main contribution of this study is algebraic derivation of equations for the shape factor (λ) which involve the ideality factor (A) and the series resistance (R_s) of single diode model of PV module power output. These equations will help to find out the predicted power output of PV modules in precise and convenient manner.

The current-voltage (*I-V*) and the power-voltage (*P-V*) characteristic curves obtained from the proposed model were matching with the curves drawn from the PV module at standard test conditions. The variation of incident solar radiation and temperature were found to be the main cause of modifications in the amount of PV module power output. A linear relationship between the power output of PV module and the amount of incident solar radiation were observed if other factors were kept constant.

The estimated results of the proposed model are validated by PV module rated power output provided by manufacturer, which gave a ±2% error. The model is found to be more practical in terms of the number of variables used and predicted satisfactory performance of PV modules.

Nomenclature

S_T: absorbed solar radiation, W/m^2
k: Boltzmann's constant, 1.381×10^{-23} J/K
T_c: Cell temperature at actual conditions, K
I: Current output of cell, A
I_D: Diode current or dark current, A
D: Diode diffusion factor, -
I_o: Diode reverse saturation current, A
A: Ideality factor, 1 for ideal diodes and between 1 and 2 for real diodes
W: Lambert W function, -
I_L: Light-generated current, A
ε_g: Material band gap energy, eV, 1.12 eV for silicon and 1.35 eV for gallium arsenide
I_{mp}: Maximum current of PV module, A
P_{mp}: Maximum power of PV module, W
V_{mp}: Maximum voltage of PV module, V
N_{cs}: Number of cells in series, -
V_{oc}: Open circuit voltage of PV module, V
ξ: Parameter, $q/kT_c\lambda$
R_s: Series resistance, Ω
λ: Shape factor of *I-V* curve, -

I_{sc}: Short circuit current of PV module, A
R_{sh}: Shunt resistance, Ω
$\mu_{I_{sc}}$: Temperature coefficient of short circuit current, -
$\mu_{V_{oc}}$: Temperature coefficient of voltage, V/K
V: Voltage output of cell, V
G_T: Solar radiation, W/m^2
q: Electron charge, 1.602×10^{-19}C
T_a: Ambient temperature, °C.

The Subscript

r: In any notation the corresponding value of parameter at reference conditions.

Conflict of Interests

The authors declare that there is no conflict of interests regarding the publication of this paper.

References

[1] W. Durisch, D. Tille, A. Wörz, and W. Plapp, "Characterisation of photovoltaic generators," *Applied Energy*, vol. 65, no. 1–4, pp. 273–284, 2000.

[2] A. Q. Jakhrani, A. K. Othman, A. R. H. Rigit, S. R. Samo, and S. R. Kamboh, "A novel analytical model for optimal sizing of standalone photovoltaic systems," *Energy*, vol. 46, no. 1, pp. 675–682, 2012.

[3] A. N. Celik, "A simplified model based on clearness index for estimating yearly performance of hybrid pv energy systems," *Progress in Photovoltaics: Research and Applications*, vol. 10, no. 8, pp. 545–554, 2002.

[4] A. H. Fanney and B. P. Dougherty, "Building integrated photovoltaic test facility," *Journal of Solar Energy Engineering*, vol. 123, no. 3, pp. 194–199, 2001.

[5] M. A. Green, "Short communication: price/efficiency correlations for 2004 photovoltaic modules," *Progress in Photovoltaics: Research and Applications*, vol. 13, pp. 85–87, 2005.

[6] A. Q. Jakhrani, A. K. Othman, A. R. H. Rigit, and S. R. Samo, "Model for estimation of global solar radiation in Sarawak, Malaysia," *World Applied Sciences Journal*, vol. 14, pp. 83–90, 2011.

[7] A. Q. Jakhrani, A. K. Othman, A. R. H. Rigit, and S. R. Samo, "Assessment of solar and wind energy resources at five typical locations in Sarawak," *Journal of Energy & Environment*, vol. 3, pp. 8–13, 2012.

[8] R. Ramaprabha and B. L. Mathur, "Development of an improved model of SPV cell for partially shaded solar photovoltaic arrays," *European Journal of Scientific Research*, vol. 47, no. 1, pp. 122–134, 2010.

[9] J. A. R. Hernanz, J. J. C. ampayo Martin, I. Z. Belver, J. L. Lesaka, E. Z. Guerrero, and E. P. Perez, "Modelling of photovoltaic module," in *Proceedings of the International Conference on Renewable Energies and Power Quality (ICREPQ '10)*, Granada, Spain, March 2010.

[10] R. B. Andrews, A. Pollard, and J. M. Pearce, "Improved parametric empirical determination of module short circuit current for modelling and optimization of solar photovoltaic systems," *Solar Energy*, vol. 86, pp. 2240–2254, 2012.

[11] R. L. Chakrasali, V. R. Sheelavant, and H. N. Nagaraja, "Network approach to modeling and simulation of solar photovoltaic cell," *Renewable and Sustainable Energy Reviews*, vol. 21, pp. 84–88, 2013.

[12] A. Chouder, S. Silvestre, N. Sadaoui, and L. Rahmani, "Modeling and simulation of a grid connected PV system based on the evaluation of main PV module parameters," *Simulation Modelling Practice and Theory*, vol. 20, no. 1, pp. 46–58, 2012.

[13] A. Chouder, S. Silvestre, B. Taghezouit, and E. Karatepe, "Monitoring, modeling and simulation of PV systems using LabVIEW," *Solar Energy*, vol. 91, pp. 337–349, 2013.

[14] A. Jain and A. Kapoor, "A new approach to study organic solar cell using Lambert W-function," *Solar Energy Materials and Solar Cells*, vol. 86, no. 2, pp. 197–205, 2005.

[15] A. Jain, S. Sharma, and A. Kapoor, "Solar cell array parameters using Lambert W-function," *Solar Energy Materials and Solar Cells*, vol. 90, no. 1, pp. 25–31, 2006.

[16] A. Ortiz-Conde, F. J. García Sánchez, and J. Muci, "New method to extract the model parameters of solar cells from the explicit analytic solutions of their illuminated I-V characteristics," *Solar Energy Materials and Solar Cells*, vol. 90, no. 3, pp. 352–361, 2006.

[17] D. Picault, B. Raison, S. Bacha, J. de la Casa, and J. Aguilera, "Forecasting photovoltaic array power production subject to mismatch losses," *Solar Energy*, vol. 84, no. 7, pp. 1301–1309, 2010.

[18] Y. Chen, X. Wang, D. Li, R. Hong, and H. Shen, "Parameters extraction from commercial solar cells I-V characteristics and shunt analysis," *Applied Energy*, vol. 88, no. 6, pp. 2239–2244, 2011.

[19] H. Fathabadi, "Novel neural-analytical method for determining silicon/plastic solar cells and modules characteristics," *Energy Conversion and Management*, vol. 76, pp. 253–259, 2013.

[20] Y. Chen, X. Wang, D. Li, R. Hong, and H. Shen, "Parameters extraction from commercial solar cells I-V characteristics and shunt analysis," *Applied Energy*, vol. 88, no. 6, pp. 2239–2244, 2011.

[21] Krismadinata, N. A. Rahim, H. W. Ping, and J. Selvaraj, "Photovoltaic module modeling using simulink/matlab," *Procedia Environmental Sciences*, vol. 17, pp. 537–546, 2013.

[22] F. Lu, S. Guo, T. M. Walsh, and A. G. Aberle, "Improved PV module performance under partial shading conditions," *Energy Procedia*, vol. 33, pp. 248–255, 2013.

[23] A. Mellit, S. Sağlam, and S. A. Kalogirou, "Artificial neural network-based model for estimating the produced power of a photovoltaic module," *Renewable Energy*, vol. 60, pp. 71–78, 2013.

[24] G. K. Singh, "Solar power generation by PV, (photovoltaic) technology: a review," *Energy*, vol. 3, pp. 1–13, 2013.

[25] D. Thevenard and S. Pelland, "Estimating the uncertainty in long-term photovoltaic yield predictions," *Solar Energy*, vol. 91, pp. 432–445, 2013.

[26] H. Tian, F. Mancilla-David, K. Ellis, E. Muljadi, and P. Jenkins, "A cell-to-module-to-array detailed model for photovoltaic panels," *Solar Energy*, vol. 86, pp. 2695–2706, 2012.

[27] M. C. D. Vincenzo and D. Infield, "Detailed PV array model for non-uniform irradiance and its validation against experimental data," *Solar Energy*, vol. 97, pp. 314–331, 2013.

[28] G. H. Yordanov, O.-M. Midtgård, and T. O. Saetre, "Series resistance determination and further characterization of c-Si PV modules," *Renewable Energy*, vol. 46, pp. 72–80, 2012.

[29] W. De Soto, S. A. Klein, and W. A. Beckman, "Improvement and validation of a model for photovoltaic array performance," *Solar Energy*, vol. 80, no. 1, pp. 78–88, 2006.

[30] E. Karatepe, M. Boztepe, and M. Colak, "Neural network based solar cell model," *Energy Conversion and Management*, vol. 47, no. 9-10, pp. 1159–1178, 2006.

[31] Y.-C. Kuo, T.-J. Liang, and J.-F. Chen, "Novel maximum-power-point-tracking controller for photovoltaic energy conversion system," *IEEE Transactions on Industrial Electronics*, vol. 48, no. 3, pp. 594–601, 2001.

[32] R. Chenni, M. Makhlouf, T. Kerbache, and A. Bouzid, "A detailed modeling method for photovoltaic cells," *Energy*, vol. 32, no. 9, pp. 1724–1730, 2007.

[33] A. Wagner, *Peak-Power and Internal Series Resistance Measurement under Natural Ambient Conditions*, EuroSun, Copenhagen, Denmark, 2000.

[34] M. Chegaar, G. Azzouzi, and P. Mialhe, "Simple parameter extraction method for illuminated solar cells," *Solid-State Electronics*, vol. 50, no. 7-8, pp. 1234–1237, 2006.

[35] K. Bouzidi, M. Chegaar, and A. Bouhemadou, "Solar cells parameters evaluation considering the series and shunt resistance," *Solar Energy Materials and Solar Cells*, vol. 91, no. 18, pp. 1647–1651, 2007.

[36] J. C. Ranuárez, A. Ortiz-Conde, and F. J. García Sánchez, "A new method to extract diode parameters under the presence of parasitic series and shunt resistance," *Microelectronics Reliability*, vol. 40, no. 2, pp. 355–358, 2000.

[37] M. A. De Blas, J. L. Torres, E. Prieto, and A. García, "Selecting a suitable model for characterizing photovoltaic devices," *Renewable Energy*, vol. 25, no. 3, pp. 371–380, 2002.

[38] D. Petreus, C. Frcas, and I. Ciocan, "Modelling and simulation of photovoltaic cells," *Acta Technica Napocensis: Electronica-Telecomunicatii*, vol. 49, pp. 42–47, 2008.

[39] V. D. Dio, D. La Cascia, R. Miceli, and C. Rando, "A mathematical model to determine the electrical energy production in photovoltaic fields under mismatch effect," in *Proceedings of the International Conference on Clean Electrical Power (ICCEP '09)*, pp. 46–51, Capri, Italy, June 2009.

[40] W. Kim and W. Choi, "A novel parameter extraction method for the one-diode solar cell model," *Solar Energy*, vol. 84, no. 6, pp. 1008–1019, 2010.

[41] D. Petreus, I. Ciocan, and C. Farcas, *An Improvement on Empirical Modelling of Photovoltaic Cells*, ISSE, Madrid, Spain, 2008.

[42] M. S. Benghanem and N. A. Saleh, "Modeling of photovoltaic module and experimental determination of serial resistance," *Journal of Taibah University for Science*, vol. 1, pp. 94–105, 2009.

[43] A. N. Celik, "Effect of different load profiles on the loss-of-load probability of stand-alone photovoltaic systems," *Renewable Energy*, vol. 32, no. 12, pp. 2096–2115, 2007.

[44] Q. Kou, S. A. Klein, and W. A. Beckman, "A method for estimating the long-term performance of direct-coupled PV pumping systems," *Solar Energy*, vol. 64, no. 1–3, pp. 33–40, 1998.

[45] J. A. Duffie and W. A. Beckman, *Solar Engineering of Thermal Processes*, John Wiley & Sons, 3rd edition, 2006.

[46] A. H. Fanney, B. P. Dougherty, and M. W. Davis, "Evaluating building integrated photovoltaic performance models," in *Proceedings of the 29th IEEE Photovoltaic Specialists Conference (PVSC '02)*, New Orleans, La, USA, May 2002.

[47] R. L. Boylestad, L. Nashelsky, and L. Li, *Electronic Devices and Circuit Theory*, Prentice-Hall, 10th edition, 2009.

[48] E. Saloux, A. Teyssedou, and M. Sorin, "Explicit model of photovoltaic panels to determine voltages and currents at the maximum power point," *Solar Energy*, vol. 85, no. 5, pp. 713–722, 2011.

[49] J. Crispim, M. Carreira, and C. Rui, "Validation of photovoltaic electrical models against manufacturers data and experimental results," in *Proceedings of the International Conference on Power Engineering, Energy and Electrical Drives (POWERENG '07)*, pp. 556–561, Setubal, Portugal, April 2007.

[50] F. M. González-Longatt, *Model of Photovoltaic Module in Matlab*, II CIBELEC, Puerto La Cruz, Venezuela, 2006.

[51] D. Sera and R. Teodorescu, "Robust series resistance estimation for diagnostics of photovoltaic modules," in *Proceedings of the 35th Annual Conference of the IEEE Industrial Electronics Society (IECON '09)*, pp. 800–805, Porto, Portugal, November 2009.

[52] A. Q. Jakhrani, A. K. Othman, A. R. H. Rigit, R. Baini, S. R. Samo, and L. P. Ling, "Investigation of solar photovoltaic module power output by various models," *NED University Journal of Research*, pp. 25–34, 2012.

[53] A. Q. Jakhrani, A. K. Othman, A. R. H. Rigit, and S. R. Samo, "Comparison of solar photovoltaic module temperature models," *World Applied Sciences Journal*, vol. 14, pp. 1–8, 2011.

[54] A. Q. Jakhrani, A. K. Othman, A. R. H. Rigit, and S. R. Samo, "Determination and comparison of different photovoltaic module temperature models for Kuching, Sarawak," in *Proceedings of the IEEE 1st Conference on Clean Energy and Technology (CET '11)*, pp. 231–236, Kuala Lumpur, Malaysia, June 2011.

[55] A. Q. Jakhrani, S. R. Samo, A. R. H. Rigit, and S. A. Kamboh, "Selection of models for calculation of incident solar radiation on tilted surfaces," *World Applied Sciences Journal*, vol. 22, no. 9, pp. 1334–1341, 2013.

[56] A. Q. Jakhrani, A. K. Othman, A. R. H. Rigit, S. R. Samo, and S. A. Kamboh, "Sensitivity analysis of a standalone photovoltaic system model parameters," *Journal of Applied Sciences*, vol. 13, no. 2, pp. 220–231, 2013.

Hindawi Publishing Corporation
International Journal of Photoenergy
Volume 2014, Article ID 895271, 17 pages
http://dx.doi.org/10.1155/2014/895271

Research Article

A Virtual PV Systems Lab for Engineering Undergraduate Curriculum

Emre Ozkop and Ismail H. Altas

Department of Electrical and Electronics Engineering, Karadeniz Technical University, 61080 Trabzon, Turkey

Correspondence should be addressed to Emre Ozkop; emreozkop@hotmail.com

Received 28 October 2013; Accepted 4 February 2014; Published 13 March 2014

Academic Editor: Adel M. Sharaf

Design and utilization of a Virtual Photovoltaic Systems Laboratory for undergraduate curriculum are introduced in this paper. The laboratory introduced in this study is developed to teach students the basics and design steps of photovoltaic solar energy systems in a virtual environment before entering the field. The users of the proposed virtual lab will be able to determine the sizing by selecting related parameters of the photovoltaic system to meet DC and AC loading conditions. Besides, the user will be able to analyze the effect of changing solar irradiation and temperature levels on the operating characteristics of the photovoltaic systems. Common DC bus concept and AC loading conditions are also included in the system by utilizing a permanent magnet DC motor and an RLC load as DC and AC loading examples, respectively. The proposed Virtual Photovoltaic Systems Laboratory is developed in Matlab/Simulink GUI environment. The proposed virtual lab has been used in Power Systems Lab in the Department of Electrical and Electronics Engineering at Karadeniz Technical University as a part of undergraduate curriculum. A survey on the students who took the lab has been carried out and responses are included in this paper.

1. Introduction

As the utilization of photovoltaic (PV) solar energy systems gain importance day by day, training seminar sessions, short courses, and certificate programs are offered by companies in order to close the gap of the experienced professionals in designing and utilizing the PV systems. As a part of encouraging the use of renewable energy sources, government in many countries recommend schools and universities to include the renewable energy sources such as solar and wind in their curriculum. Modeling, analyzing, and designing of PV solar energy systems are taught in a course called Design of Low Voltage Power Systems and a set of PV experiments are included in Power Systems Lab in the Department of Electrical and Electronics Engineering at Karadeniz Technical University, Turkey. In order to teach the modeling and characteristic behaviors of the PV arrays, a virtual PV Systems Lab is developed and offered to be used by the students as a part of undergraduate curriculum.

The changes and developments such as globalization, economic crisis, and technological innovations involve reconsidering education system curriculum [1]. In conventional education system, courses have been based on the principal of printed word and blackboard [2]. Studying mainly mathematics and basic concepts to understand the dynamic system responses causes students to be less interested in essential subject. If the students are provided with various ways to reach learning sources of information, which is one of the flexible education aims, classical education based on textbooks and chalkboards becomes time consuming and insufficient in completion realize the dynamic system responses, nowadays [3, 4].

While students attain theoretical knowledge in the classroom, practical knowledge and experiences are given in laboratories [2]. Laboratory is an integral part of undergraduate studies particularly in engineering education [1]. Laboratory works give students the ability to design and conduct experiments, analyze and interpret data, design a system and component, and develop social and team work skills and also increase learning efficiency in engineering education [2, 5, 6]. There are many studies to improve engineering students' skills [7].

Even though students get theoretical background very well in detail in classroom, and they are provided lab manuals to study and become familiar with the experiments they are going to do in laboratory, they always face difficulties in practice when it comes to setting up and performing the actual experimental tests. It has been always a task to have the students gain the ability to turn the theoretical knowledge into practical reality. In particular, the engineering students should be able to combine the theory with the practice. Course laboratories in schools and universities are the first and important places for the students to put their knowledge into practice. However, every student does not have the chance to use the labs for practicing before the lab hour for the course starts. Every student does not have the income to establish his/her own high cost test laboratory for checking the experiment designed to be performed.

Experimental setup has a high cost and also lacks doing experiments again and again in nonlinear range [8, 9]. There are generally limited laboratory equipments, space, time period, and danger for laboratory experiments such that it is not possible for the students to do an experiment alone in laboratory. Besides, the increasing number of the students every year becomes a heavy burden to departments with laboratories [1, 5]. Consequently, either the number of experiment groups or the number of students in the experiment groups must be increased. In any case more teaching assistants and lab equipments are required to deliver the experiments efficiently. Otherwise, the students will not be able to learn and interpret effectively in the experiments [1, 9–11]. If the required conditions for a high quality or a normal laboratory are not provided, then the practical experiment part of the education will be insufficient resulting in inexperienced graduates deprived of scientific knowledge and abilities [3]. Insufficient laboratory conditions and experiments decrease the education quality and result in the presence of incompetent graduates with less ability [1]. Therefore, new alternatives are always the challenge to keep the laboratory experiments and the practical abilities of the graduates high. That is where the virtual laboratories become important. Virtual laboratories are software based simulators of the actual systems and require only the computers to be performed.

Since computer prices decrease and it is possible to find easily variable versatile software programs, computer-aided education has become a part of both classroom and laboratory experiments [12]. With new technological innovations, computers have been benefited as auxiliary equipments and teaching tools in many universities [13]. The uses of computers make a positive impact in lectures and laboratory work and also contribute economically towards mitigating the education cost [1]. A lack of concentration lessons and students' performances are positively affected with computer applications as compared to hands-on labs alone [1]. Computer based virtual lab software has been used as a part of education tools to develop the students' comprehension in both theoretical and experimental topics [14]. When the comparison is made between the hands-on experiments and the virtual learning experiments, it is obvious that the virtual one provides a flexible, time invariant and location free learning environment, to perform many different and less costly experiments. Moreover, each student can realize more complex and extensive experiments alone so that self-learning potential of the students is brought to forward [14]. The virtual laboratory enables easy interaction for students and has flexible parameter variations for ongoing experiments and gives prominent understanding into experimental dynamics [6]. Virtual learning environments give students opportunity to establish a connection from theoretical concepts to practical applications [14]. The virtual learning environments corroborate students to design experiments based on the concept they are studying and also provide immediate graphical feedback. It is obvious that the virtual learning has a comprehensive and interactive environment [1]. Nowadays, many universities and institutions have applied virtual laboratories. A virtual laboratory can be utilized by the means of combining both physical experiments and numerical simulations [14].

Commercially available software packages have been progressively used for educational purposes as the high performance and cost efficient computers developed [15, 16]. There are many different software packages developed using independent language platforms. These virtual labs are usually developed for certain purposes and are not expandable for more detailed experiments. On the other hand, there are some software platforms that are suitable for developing virtual laboratories. MATLAB is one of these software platforms used by a great number of universities throughout the world and it might be the better choice since engineering students are generally acquainted with MATLAB [2, 12, 16–19]. The user can design, develop, expand, simulate, analyze, and visualize data with MATLAB and its toolbox Simulink software [16, 20].

Graphical user interface (GUI) ability of Matlab/Simulink software environment is used to develop the Virtual PV Systems lab introduced in this paper. Mathematical model of the PV cell and PV array given in [21] is modified and used in this study. The Virtual PV Systems lab provides the measurement and analysis of PV arrays *I-V* and *P-V* characteristics at constant and variable solar irradiation and temperature levels. The user is able to modify the number of panels in series and in parallel so that a desired array combination can be designed to match the load requirements. The virtual lab also includes a power electronics converter to give the opportunity of controlling the output voltage of the PV arrays. A permanent magnet DC motor is also used as a load to analyze the operational characteristics of the PV system under variable load. The proposed virtual lab has been used in Power Systems laboratory in the Department of Electrical and Electronics Engineering at Karadeniz technical University, Turkey, and the responses from the students are evaluated.

2. System Architecture

The Virtual PV Systems Lab (VPVSL) is intended to be used as an auxiliary supporting virtual environment for the actual PV System lab. The idea behind the combination of the virtual and actual labs is based on student outcome requirements described by ABET as A-K engineering education criteria's

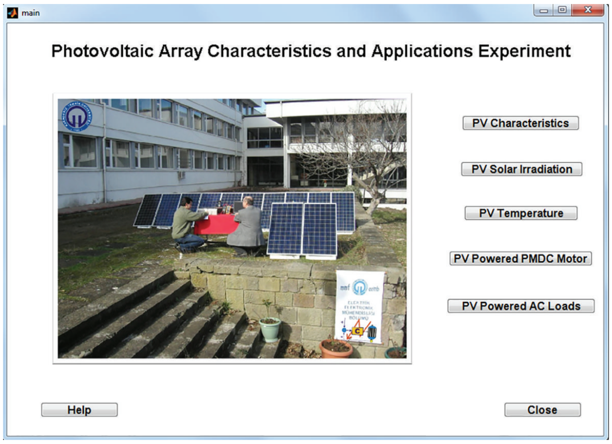

Figure 1: The main menu of VPVSL.

[22]. Two of the A-K criteria's highlight the importance of the "ability to design and conduct experiments as well as to analyze and interpret data" and "ability to design a system, component, or process to meet desired needs within realistic constraints..." [22]. In order to have the students gain the ability of designing and conducting experiments on PV systems, proposed VPVSL is developed.

The lab is conducted in the following order.

(i) Define the size and operational specifications of the system.
(ii) Determine the values of required parameters and enter them into the VPVSL software using the user data interfacing windows shown in Figures 1, 2, 3, 4, 5, and 6.
(iii) Select the configuration (DC or AC load) type to be used.
(iv) Obtain *I-V* and *P-V* characteristics of the PV array for various solar irradiation and temperature levels and analyze them.
(v) Obtain the optimum operating power points for various operating conditions.
(vi) Run the VPVSL, record the results, and analyze them.

Students write their lab reports based upon the data they obtained from the VPVSL and keep them to compare with those obtained using actual PV system lab. The use of the VPVSL before the actual lab is that students get to know the PV system and its operational characteristics so that they become familiar with the designing steps and characteristics. Therefore, they have no difficulties when performing the real time PV system experiments as well as designing real time PV system applications. The VPVSL software is developed using Matlab/Simulink GUI environment. Figure 1 shows the first user interfacing screen, which is also called the main window. This window includes the following five modules, which are explained in the next sections:

1. PV characteristics,
2. PV solar irradiation,
3. PV temperature,
4. PV powered PMDC motor,
5. PV powered AC loads.

2.1. Module 1: PV Array Characteristics. This module uses the PV cell model described by

$$V_C = \frac{AkT_C}{e} \ln\left(\frac{I_{\text{ph}} + I_0 - I_C}{I_0}\right) - R_S I_C, \tag{1}$$

where A is curve fitting constant used in solar cell *I-V* characteristics, e is electron charge, k is Boltzmann constant, I_C is the cell output current, I_{ph} is photocurrent, I_0 is the reverse saturation current of diode, R_S is series resistance of cell, T_C is reference cell operating temperature, and V_C is the cell output voltage. The cell parameters values used in this study are given in the Appendix. All these cell parameters and modelling details are given in [21]. The module runs the characteristic equation in the back and offers the user to enter the simulation parameters that are needed to obtain the PV array current-voltage and power-voltage characteristics under certain solar irradiance and ambient temperature. The user interface window of Module 1 is shown in Figure 2. Number of cells in series (N_S) in a branch and number of parallel connected series branches (N_P) are the main inputs for sizing the PV array to get the required power. Solar irradiation and ambient temperature are the other two inputs in order to obtain the PV array characteristics for these light and temperature levels.

Students are able to resize the PV array to meet the load requirements and obtain the *I-V* and *P-V* characteristics. After entering the panel configuration and external condition, the module returns the characteristics along with the maximum power point operating quantities. This module teaches the student how the resizing affect the power output of a PV array under constant solar irradiation and ambient temperature.

2.2. Module 2: Solar Irradiation Effects on PV Array Characteristics. This module shows how the changes in solar irradiation affect the output current and voltage and the power of a PV array. The inclusion of the effects of the changes in solar irradiation level in PV array modeling is described by the following equations, which are discussed in [23, 24]:

$$C_{TV} = 1 + \beta_T (T_a - T_x), \tag{2}$$

$$C_{TI} = 1 + \frac{\gamma_T}{S_C} (T_x - T_a), \tag{3}$$

$$C_{SV} = 1 + \beta_T \alpha_S (S_x - S_C) = 1 + \beta_S (S_x - S_C), \tag{4}$$

$$C_{SI} = 1 + \frac{1}{S_C} (S_x - S_C) = 1 + \gamma_S (S_x - S_C), \tag{5}$$

$$\Delta T_C = \alpha_S (S_x - S_C), \tag{6}$$

$$V_{CX} = C_{TV} C_{SV} V_C, \tag{7}$$

$$I_{\text{ph}x} = C_{TI} C_{SI} I_{\text{ph}}, \tag{8}$$

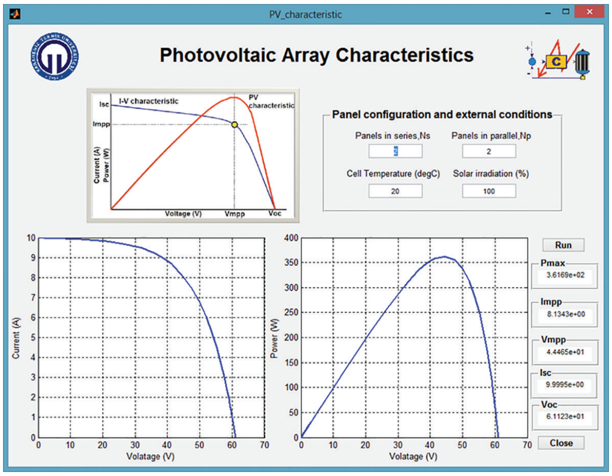
PV_characteristic

Photovoltaic Array Characteristics

Panel configuration and external conditions

Panels in series,Ns: 2

Panels in parallel,Np: 2

Cell Temperature (degC): 20

Solar irradiation (%): 100

Pmax: 3.6169e+02

Impp: 8.1343e+00

Vmpp: 4.4465e+01

Isc: 9.9995e+00

Voc: 6.1123e+01

FIGURE 2: The photovoltaic array characteristics interface.

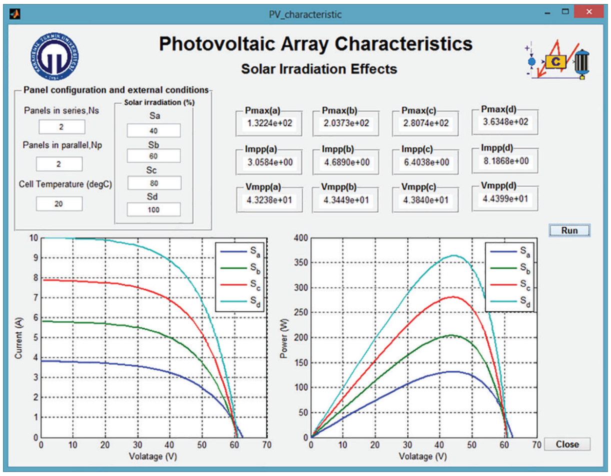
PV_characteristic

Photovoltaic Array Characteristics

Solar Irradiation Effects

Panel configuration and external conditions

Panels in series,Ns: 2

Panels in parallel,Np: 2

Cell Temperature (degC): 20

Solar irradiation (%)

Sa: 40

Sb: 60

Sc: 80

Sd: 100

Pmax(a)	Pmax(b)	Pmax(c)	Pmax(d)
1.3224e+02	2.0373e+02	2.8074e+02	3.6348e+02

Impp(a)	Impp(b)	Impp(c)	Impp(d)
3.0584e+00	4.6890e+00	6.4038e+00	8.1868e+00

Vmpp(a)	Vmpp(b)	Vmpp(c)	Vmpp(d)
4.3238e+01	4.3449e+01	4.3840e+01	4.4399e+01

FIGURE 3: The photovoltaic array solar irradiation interface.

where T_a is the reference ambient temperature, S_C is the reference solar irradiation, and T_x and S_x are the current values of the ambient temperature and solar irradiation, respectively. β_T and γ_T are constants representing the effect of temperature on PV cell voltage and current, respectively. The constant α_S represents the slope of the change in the cell operating temperature due to a change in the solar irradiation. Constants β_S and γ_S represent effect of the solar irradiation on cell voltage and photocurrent, respectively. Equations (2) and (3) yield the temperature gain parameters C_{TI} and C_{TV} for current and voltage, respectively, while (4) and (5) give the solar irradiation gain parameters C_{SI} and C_{SV} for current and voltage. These gain parameters are used in (7) and (8) in order to update the values of PV cell voltage and current to the new cell voltage and new photocurrent under new cell temperature T_x and solar irradiation S_x. Temperature constants (β_T and γ_T) and solar irradiation constants (α_S, β_S, and γ_S) are obtained experimentally for the PV cell type used in both simulation and test studies. Since the PV cell types and the properties are assumed to be the same in a PV panel, these constants may also be obtained by running the similar tests with the PV panels used. After recording the reference values at known temperature and solar irradiation levels, the same quantities are measured at another known temperature and solar irradiation level and the differences are compared. The same test may be repeated for a few times at different temperature and solar irradiation levels for better correlation. Then (2) to (8) are used backwards to obtain the constant parameters used in these formulas. After this process, the obtained constant can only be used for the models of the PV cells that are used in the testing.

As shown in Figure 3, panel configuration and cell temperature are given as the constant inputs besides the four different solar irradiation values. After running the module, the students get four different normalized *I-V* and *P-V* curves, one for each solar irradiation. The module also returns the maximum power point operating power, voltage, and current values $P_{\max}$, I_{mpp}, and V_{mpp} for all four solar irradiation levels. It is clear that this module gives a good understanding and interfacing to the student to analyze the effects of variable solar irradiation levels on PV array characteristics.

2.3. Module 3: Temperature Effects on PV Array Characteristics.

This module uses the same equation set (2) to (8) given in previous section about Module 2. The students are able to configure the array and analyze the effects of variable temperature on PV array characteristics while the solar irradiation is kept constant. Figure 4 shows the user interface screen for Module 3. After running the module, the students get four different normalized *I-V* and *P-V* curves, one for each temperature level. The module also returns the maximum power point operating power, voltage, and current values $P_{\max}$, I_{mpp}, and V_{mpp} for all four temperature levels. It is clear that this module gives a good understanding and interfacing to the students to analyze the effects of variable temperature on PV array characteristics.

2.4. Module 4: PMDC Motor Load Fed from PV Array.

Once the students learn and understand the PV array characteristics under different environmental conditions, they can continue the simulation based experiments by starting to feed the loads. The first load in VPVSL is a permanent magnet DC (PMDC) motor. This scheme includes a PV array with the required voltage and power configuration, a filter circuit to eliminate the discontinuities in current, a PID controlled DC/DC chopper, a PID controller, and a PMDC motor. Figure 5 shows the user interfacing windows and the connection diagram of the PV powered PMDC motor scheme. The user interface scheme has PV array data, motor data, and PID controller data as three input areas and four graphic windows as the output areas. Time response of the PMDC motor speed, PMDC motor voltage, and PV array *I-V* and *P-V* characteristics under loading conditions are plotted in the output section. Since a maximum power point tracker (MPPT) is not added to the scheme, the operating power may not be at its maximum value and may be changed as the reference voltage is changed by the user. An MPPT may be

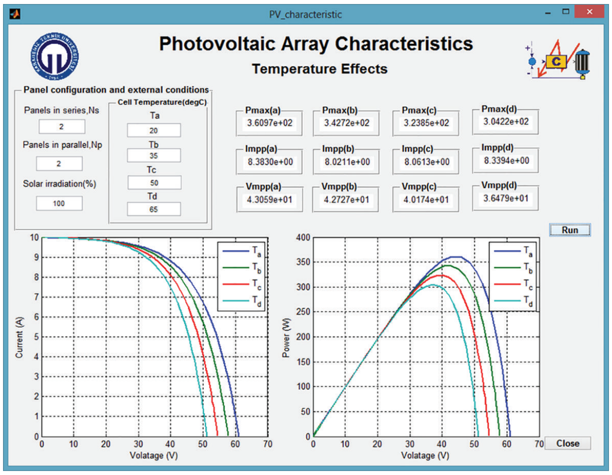

PV_characteristic

Photovoltaic Array Characteristics

Temperature Effects

Panel configuration and external conditions

Panels in series,Ns: 2

Panels in parallel,Np: 2

Solar irradiation(%): 100

Cell Temperature(degC)

Ta: 20

Tb: 35

Tc: 50

Td: 65

Pmax(a)	Pmax(b)	Pmax(c)	Pmax(d)
3.6097e+02	3.4272e+02	3.2385e+02	3.0422e+02
Impp(a)	**Impp(b)**	**Impp(c)**	**Impp(d)**
8.3830e+00	8.0211e+00	8.0613e+00	8.3394e+00
Vmpp(a)	**Vmpp(b)**	**Vmpp(c)**	**Vmpp(d)**
4.3059e+01	4.2727e+01	4.0174e+01	3.6479e+01

Figure 4: The photovoltaic array temperature interface.

considered to be added to the scheme for a more complete simulation model.

This module gives the students an opportunity of understanding DC load operation and control. A PID controller is employed to operate the PMDC motor at a constant voltage while the temperature and solar irradiation levels of the PV array change. The module can be simulated without and with the controller to see the effects of the changes in sunlight level. In order to have a constant motor speed, the voltage to the motor must be kept constant. Therefore, the constant speed means constant DC voltage, which may be assumed as a DC bus used to collect the DC power from different sources in distributed generation networks. Therefore, this module also teaches the common DC bus concept with the control in practice.

2.5. Module 5: AC Loads Fed from PV Array. The DC chopper in previous module is replaced by a three-phase inverter in order to obtain a three-phase AC voltage with nominal voltage and constant frequency. As shown in user interface screen of Module 5 in Figure 6, this module includes six input areas, which are used for panel configuration, RLC AC load, filter parameters, RL DC load, controller parameters, and a three-phase isolation transformer.

There are six output plots in the user window. The students are able to plot and observe the voltage at the output terminals of the inverter, the voltage of the PV array under load, *I-V* characteristics of the array under loading, the AC voltage at load terminals, PV array current under load, and *P-V* characteristics of the panel under loading conditions. A DC load is connected before the inverter in order to initiate the operation of the PV array.

3. Simulation Results

This section gives the results from the virtual experiments done to test the proposed VPVSL. Five modules described above are tested in given order. First the PV array characteristics, then the effects of the solar irradiation, the effects of temperature, DC load operation, and finally the AC load operation are tested.

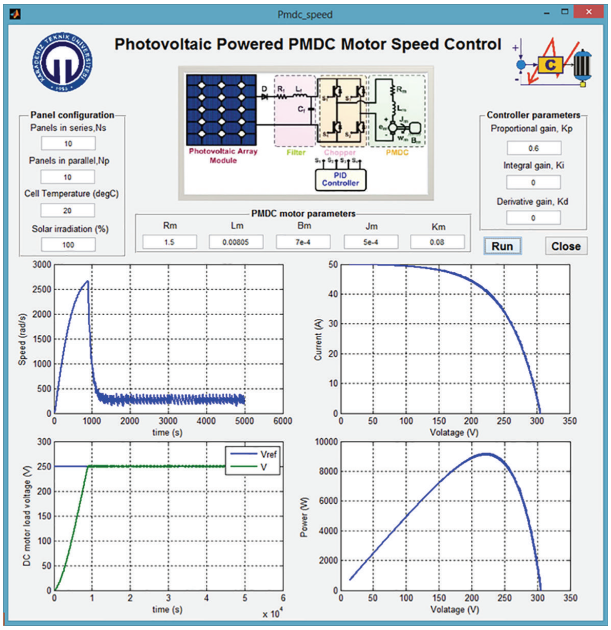

Pmdc_speed

Photovoltaic Powered PMDC Motor Speed Control

Panel configuration

Panels in series,Ns: 10

Panels in parallel,Np: 10

Cell Temperature (degC): 20

Solar irradiation (%): 100

PMDC motor parameters

Rm	Lm	Bm	Jm	Km
1.5	0.00805	7e-4	5e-4	0.08

Controller parameters

Proportional gain, Kp: 0.6

Integral gain, Ki: 0

Derivative gain, Kd: 0

Figure 5: The PV powered PMDC motor interface.

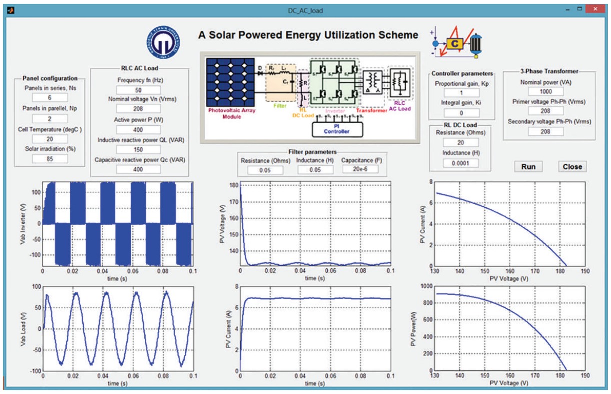

DC_AC_load

A Solar Powered Energy Utilization Scheme

Panel configuration

Panels in series, Ns: 6

Panels in parellel, Np: 2

Cell Temperature (degC): 20

Solar irradiation (%): 85

RLC AC Load

Frequency fn (Hz): 50

Nominal voltage Vn (Vrms): 208

Active power P (W): 400

Inductive reactive power QL (VAR): 150

Capacitive reactive power Qc (VAR): 400

Filter parameters

Resistance (Ohms)	Inductance (H)	Capacitance (F)
0.05	0.05	20e-6

Controller parameters

Proportional gain, Kp: 1

Integral gain, Ki: 0

RL DC Load

Resistance (Ohms): 20

Inductance (H): 0.0001

3-Phase Transformer

Nominal power (VA): 1000

Primer voltage Ph-Ph (Vrms): 208

Secondary voltage Ph-Ph (Vrms): 208

Figure 6: The PV powered AC loads interface.

3.1. PV Array Characteristics. The GUI screen given in Figure 2 for Module 1 is used to perform the tests for PV array characteristics. The system is simulated for eight different PV array configurations under reference temperature and solar irradiation levels, which are 20°C and 100 mW/cm^2. The array configurations and corresponding maximum power point operating values are given in Table 1 for a sample case study. These sets of experiments give the students an insight look at the design of PV systems in terms of sizing.

Results from the sample case study are depicted in Figure 7. The size of the PV array is changed by different combinations of series and parallel connected PV panels, and the resultant operating parameters are recorded from each case. The sizing effect on open circuit voltage (V_{oc}), short circuit current (I_{sc}), maximum power (P_{max}), maximum power point current (I_{mpp}), and maximum power point

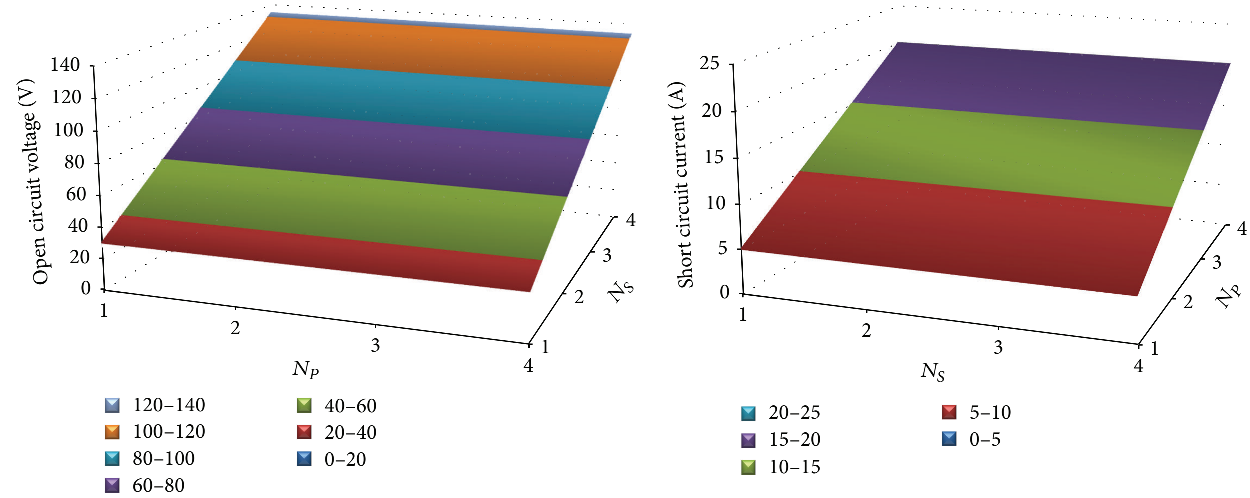

(a) Open circuit voltage surface

(b) Short circuit current surface

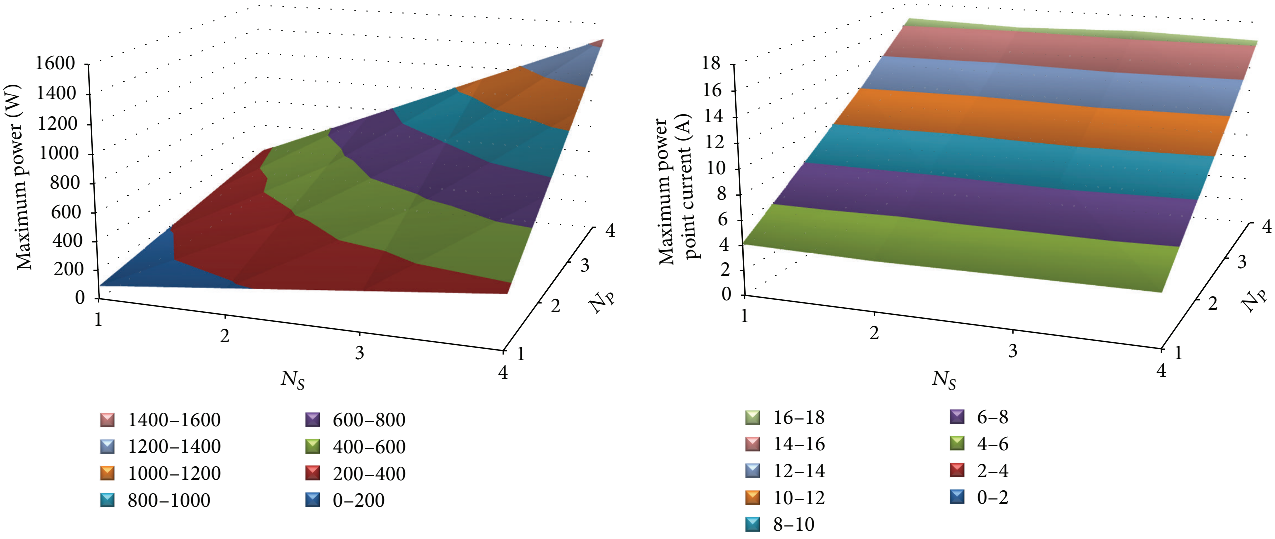

(c) Maximum power surface

(d) Maximum power point current surface

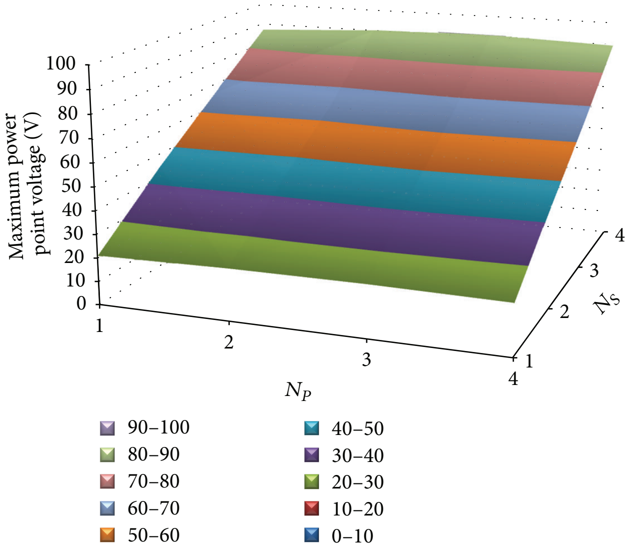

(e) Maximum power point voltage surface

Figure 7: The sizing effects on the array characteristics at reference temperature and solar irradiation levels. (a) Open circuit voltage surface, (b) short circuit current surface, (c) maximum power surface, (d) maximum power point current surface, and (e) maximum power point voltage surface.

Table 1: The PV array characteristics experiment parameters and outputs.

Case	I	II	III	IV	V	VI	VII	VIII
N_S	1,000	2,000	3,000	4,000	1,000	1,000	1,000	2,000
N_P	1,000	1,000	1,000	1,000	2,000	3,000	4,000	2,000
P_{max} (W)	90,147	180,90	271,38	361,00	180,80	271,52	362,48	361,69
I_{mpp} (A)	4,210	4,043	4,121	4,186	8,077	12,037	16,533	8,134
V_{mpp} (V)	21,416	44,741	65,803	86,234	22,384	22,558	21,925	44,465
I_{sc} (A)	4,998	5,000	5,000	5,000	9,996	14,992	19,985	9,999
V_{oc} (V)	30,561	61,123	91,664	122,25	30,561	30,561	30,561	61,123
Case	IX	X	XI	XII	XIII	XIV	XV	XVI
N_S	2,000	2,000	3,000	3,000	3,000	4,000	4,000	4,000
N_P	3,000	4,000	2,000	3,000	4,000	2,000	3,000	4,000
P_{max} (W)	542,05	723,39	541,61	813,81	1085,50	723,72	1085,1	1446,7
I_{mpp} (A)	11,914	16,262	8,364	12,233	16,550	8,118	12,042	16,332
V_{mpp} (V)	45,496	44,483	64,751	66,524	65,592	89,146	90,109	88,582
I_{sc} (A)	14,998	19,998	10,002	15,002	20,001	10,001	15,001	20,003
V_{oc} (V)	61,123	61,123	91,684	91,684	91,684	122,25	122,25	122,25

Table 2: Maximum power point surface, P_{max} (W), at a fixed configuration.

$N_s = 2$		T_x			
$N_p = 2$		−20	0	20	40
	80	316	298	280	261
	100	410	386	362	337
	120	512	481	451	418
S_x	140	618	581	543	505
	160	733	688	642	595
	180	850	797	745	691
	200	977	915	853	790

voltage (V_{mpp}) are shown in Figure 7 by surface plots where solar irradiation and temperature levels are kept constant. The surfaces in Figure 7 are called *the Design Surfaces* and used as the base load power matching in design process. These design surfaces can be extended to include the effects of the changes in solar irradiation and temperature levels. Therefore these surfaces can be converted into *dynamic design surfaces* so that both the maximum power operating point values can be tracked when the environmental conditions are changed and the configuration switching for load power matching can be done.

3.2. Solar Irradiation and Temperature Effects. Simulation results of Modules 2 and 3 of VPVSL are discussed in this section. The students get the *I-V* and *P-V* curves of the PV array at different solar irradiation and temperature levels for a fixed configuration by keeping N_S and N_P unchanged. For the sample case study, the array configuration is set to $N_S = 2$ and $N_P = 2$.

First, operating temperature is assumed to be constant in Module 2 and only the solar irradiation is changed. Therefore, tests from Module 2 give the characteristics for changing sunlight levels at constant temperature as given in Figure 8. Solar irradiation is assumed to be constant in Module 3 and only the temperature is changed to see the effects of temperature on the PV array characteristics. The results from Module 3 are given in Figure 9.

Both Module 2 and Module 3 show that the generated power from the PV array changes when temperature and solar irradiation levels change. Therefore the recordings from these two modules can be combined to yield the maximum power generated by the PV array at different pairs of solar irradiation and temperature as given in Table 2.

A similar table can also be obtained easily for maximum power point current and voltages. However, for the sake of using optimum number of pages, these tables are not given here. The plots of the maximum power points, maximum power point operating currents, and maximum power point operating voltages are given in Figure 10 instead.

The results from Module 2 and Module 3 are evaluated together in order to see the solar irradiation and temperature effects at the same time. The combination of the results from these two modules enables the user to obtain maximum power points, maximum power point operating currents, and maximum power point operating voltages at different solar irradiation and temperature levels. Three-dimensional surface plots of these maximum power point quantities are shown in Figure 10. Actually these surfaces are used as *dynamic design surfaces* as expressed before. These surfaces are called *the dynamic design surfaces* because the maximum power operating points move on these surfaces when the solar irradiation and temperature levels change as unpredictable and uncontrolled input variables. The users of the VPVSL or the students can use these surfaces as design surfaces within an interval of solar irradiation and temperature universes. The array configuration is used to expand the power output range while the maximum power point surfaces are used to track and operate the PV array at its maximum power output [25].

Table 3: The PV powered PMDC motor GUI interface parameters.

PV Array and PID controller			PMDC Motor		
Number of solar cells connected in series	N_s	10	Resistance	R_m	1.5 Ohm
Number of solar cells connected in parallel	N_p	10	Inductance	L_m	0.00805 H
Ambient temperature	T	20°C	Back emf constant	K_m	0.08 V·s/rad
Ambient solar irradiation (%)	S	100%	Viscous friction constant	B_m	7×10^{-4} Nms/rad
Proportional constant	K_p	0.6	Rotor moment of inertia constant	J_m	5×10^{-4} kg·m^2
Integral constant	K_i	0	Actual rated speed	w_n	1265 rad/s
Derivative constant	K_d	0	Voltage source	V_m	300 V

Table 4: The PV powered AC load experiment parameters.

PV array			AC load		
Number of solar cells connected in series	N_s	8	Frequency	f_n	60 Hz
Number of solar cells connected in parallel	N_p	1	Nominal phase-phase voltage	V_n	208 V
Ambient temperature	T	16°C	Active power	P	500 W
Ambient solar irradiation (%)	S	103%	Inductive reactive power	Q_L	200 VAR
			Capacitive reactive power	Q_C	500 VAR
Controller			DC Load		
Proportional constant	K_p	1	Resistance	R	40 Ohm
Integral constant	K_i	0	Inductance	L	0.0002 H
Filter			Three-phase transformer		
Resistance	R_f	0.05 Ohm	Nominal power	S	1000 VA
Inductance	L_f	0.05 H	Primary winding phase-phase voltage (rms)	V_1	208 V
Capacitance	C_f	20×10^{-6} F	Secondary winding phase-phase voltage (rms)	V_2	208 V

3.3. PV Array with a PMDC Motor Load. The VPVSL is tested under two loading conditions. First, a PMDC motor load is fed from the PV system. A PMDC motor is selected as the DC load in order to give an example of stand-alone DC load feeding. A controlled DC-DC chopper is used to control the voltage to DC loads. DC chopper is controlled for two different purposes, which are constant DC voltage operation and constant motor speed operation. The first one is to obtain a constant DC voltage at the output terminals of the DC-DC chopper in order to have a common DC bus. This operating condition gives the student the importance of common DC bus in distributed generation systems. The second purpose of controlling DC-DC chopper is for testing the system control to meet the load operating conditions. The motor is operated at a constant speed without considering a constant DC voltage. The purpose here is to operate the motor at constant speed whatever the voltage from PV array to DC-DC chopper is. Therefore the second operating case shows the user how to eliminate the effects of the changes in solar irradiation and temperature levels on the load performance while the first case shows how the same effects are eliminated for the common DC bus voltage.

The GUI screen shown in Figure 5 is used with the sample case parameters given in Table 3. The connection diagram, in Figure 5, includes a reverse current blocking diode (D), a current smoothing input filter (R_f and L_f), and a storage capacitor (C_f) to overcome voltage discontinuities. A PID controlled type-D DC-DC chopper is used to adjust the voltage at load terminals.

The PID controller used in VPVSL generates the control signal, which is sent to a pulse width modulator (PWM) to generate the required switching pulses. For the two-quadrant DC-DC chopper, four pulses are generated.

The system outputs, which are observed, are shown in Figures 11, 12, 13, 14, 15, and 16. Figure 11 shows the controlled output voltage of DC-DC chopper. This voltage is kept constant considering that it is a voltage of common DC bus, which acts as a station to connect different power generating units together in a distributed power system. The speed variation of the PMDC motor load is given in Figure 12. For this operating case, the DC chopper is controlled to keep the speed constant. *I-V* and *P-V* characteristics of the PV system during the constant DC bus voltage operating condition are shown in Figures 13 and 14, respectively. Since there is no MPP tracking controller in the system, the operating point on *I-V* and *P-V* curves swings along the characteristics until it settles down at operating values that match the load side values. The operating voltage and power values can be seen clearly in Figures 15 and 16, in which the time responses of the PV array voltage and power are shown.

3.4. The PV Powered AC Load. The second loading condition of the VPVSL is a three-phase AC load. The connection diagram given in Figure 6 is used for the AC load operation. The connection scheme includes reverse current blocking diode (D) and input filter (R_f, L_f, and C_f) for input current smoothing and input voltage continuity, a DC *R-L* load for the system initiation, a PI controlled three-phase inverter, an

Table 5: Assessment data student evaluations (Section-A).

(1) When I compare this experiment with other experiments belonging to this laboratory, this experiment is				
Very easy (1)	Easy (2)	Reasonable (3)	Difficult (4)	Very difficult (5)
(2) When I compare this experiment with other experiments belonging to this laboratory, workload of this experiment is				
Too much (1)	Much (2)	Reasonable (3)	Few (4)	Too few (5)
(3) Experiment realization speed is				
Very fast (1)	Fast (2)	Reasonable (3)	Slow (4)	Very slow (5)
(4) This experiment is completely				
Very good (1)	Good (2)	Reasonable (3)	Inadequate (4)	Highly inadequate (5)
(5) This experiment instructor is completely				
Very good (1)	Good (2)	Reasonable (3)	Inadequate (4)	Highly inadequate (5)

Table 6: Assessment data student evaluations using a Likert-scale (Section-B).

6	I understood the main idea
7	Experiment coordination was very poor
8	The experiment was attractive
9	Experiment sheet (laboratory handout) was well arranged
10	I learned something that I will remember future
11	Experiment sheet helped me to comprehend orders effectively
12	Using Matlab/Simulink GUI environment was good
13	Using Matlab/Simulink GUI environment helped me to interpret the experiment results
14	Using the model development of the system for Matlab/Simulink GUI environment enhanced my knowledge and skills
15	I find the model development of the system for Matlab/Simulink GUI environment useful for learning related issue in corresponding course
16	Using the model development of the system for Matlab/Simulink GUI environment make me be more interested in this subject
17	Experiment goal was clear and understandable
18	I was able to fully use the model development of the system for Matlab/Simulink GUI environment by following the instructions provided?
19	It was difficult to gather from this experiment?
20	Instructor showed effective control and guidance during the experiment
21	How experiment will be done was explicitly explained in experiment sheet
22	It was easy to attend the order since experiment sheet was well organized
23	I will need more information to prepared experiment report

Note: strongly agree: 1; agree: 2; neither agree or disagree: 3; disagree: 4; strongly disagree: 5.

isolation transformer for filtering and isolation purposes, and a three-phase AC RLC load. The input parameters used in Figure 6 for the sample study case are given in Table 4.

As mentioned earlier, the students or the users are able to plot and observe the voltage at the output terminals of the inverter, the voltage of the PV array under load, *I-V* characteristics of the array under loading, the AC voltage at load terminals, PV array current under load and *P-V* characteristics of the panel under loading conditions. The controller gains (K_P, K_I) can be adjusted to provide the AC load demands (required voltage and frequency with minimum disturbances). PV array characteristics can also be observed from this operating process. The virtual experiment outputs are shown in Figures 17, 18, 19, 21, and 22. Figures 17 and 18 show the time variations of the PV array voltage and current, respectively. These two figures show the steady-state operating voltage and current of the array. The array voltage given in Figure 17 is the DC voltage converted to three-phase AC voltage by the inverter.

The output voltage of the inverter is given in Figure 19. Since the voltage at the output terminals of the inverter is not pure AC, an isolation transformer is used as a filtering device to minimize the voltage harmonics so that the AC voltage waveform shown in Figure 20 is obtained with less harmonics.

I-V and *P-V* characteristics of the PV array are shown in Figures 21 and 22. After the initial swinging of the operating point on the curves, it settles down to steady-state operating values as depicted in Figures 17 and 18. The operating points of the PV array on *I-V* and *P-V* characteristics in Figures 21 and 22 are marked using the information from Figures 17 and 18.

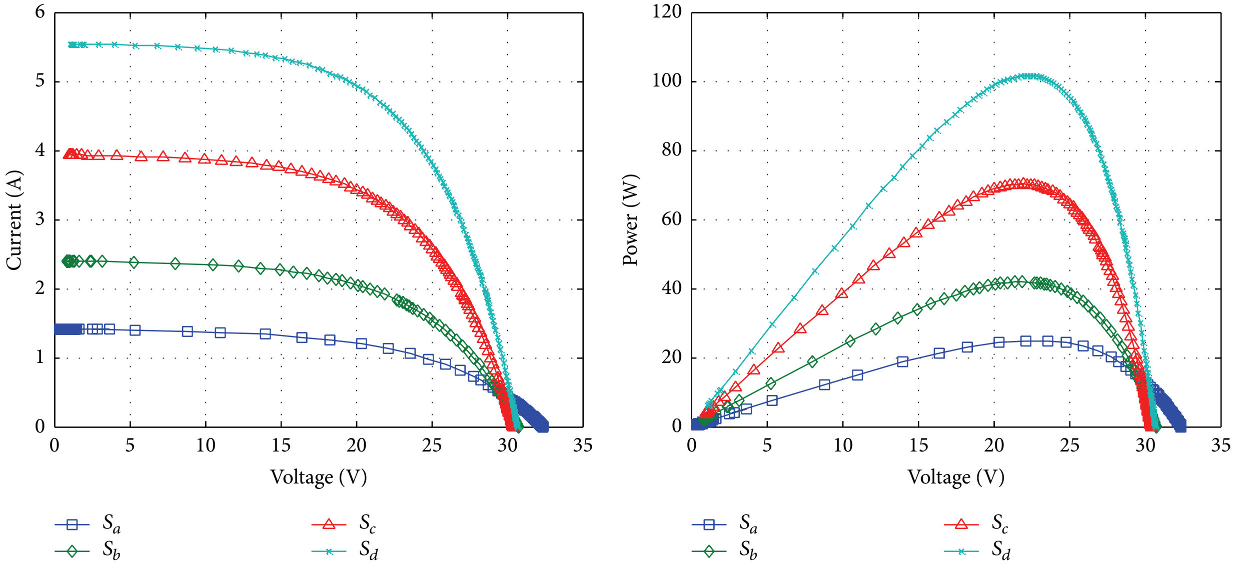

(a) *I-V* characteristics (b) *P-V* characteristics

Figure 8: The effect of solar irradiation on *I-V* and *P-V* characteristics of the PV array.

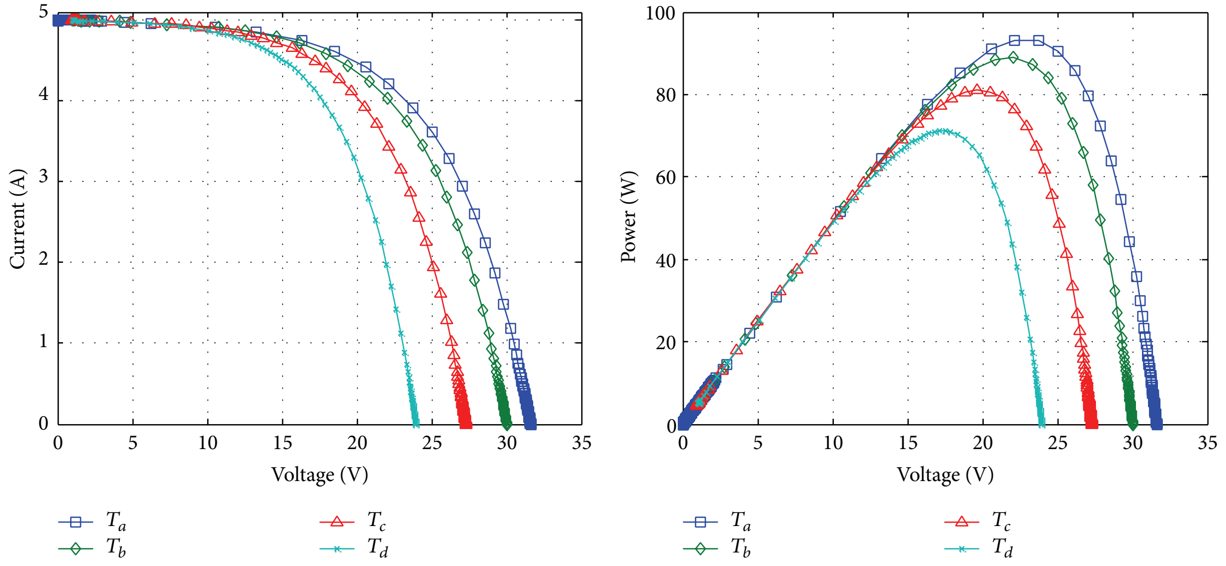

(a) *I-V* characteristics (b) *P-V* characteristics

Figure 9: The effect of temperature on *I-V* and *P-V* characteristics of the PV array.

4. Student Assessment and Evaluation

The effectiveness of learning based on the GUI environment is determined by experiment report and questionnaire. The experiment report is based on the GUI interface explained thoroughly in the experiment sheet (laboratory handout). A questionnaire is an important source to observe the students' reactions. Individual students share their perceptions of the experiment. Thus, the students were asked to fill in a questionnaire about the experiment, characteristics of the environment, and opinion about instructor during experiment. The students can specify the pros and cons of the environment and experiment. The questionnaire consisted of thirty-three questions, as shown in Tables 5, 6, and 7. The questionnaire consists of three sections (Section-A, Section-B, and Section-C). We used Likert scales most commonly applied rating scales in spite of some limitations [26]. General opinion about experiment and instructor are roughly researched in Section-A. The students' observations and comments about effectiveness of the experiment and instructor are deeply taken on in Section-B and Section-C, respectively.

The students gave a grade between 5 (strongly disagree) and 1 (strongly agree) based on Likert Scale. The students' observations and comments given in Tables 5–7 are evaluated

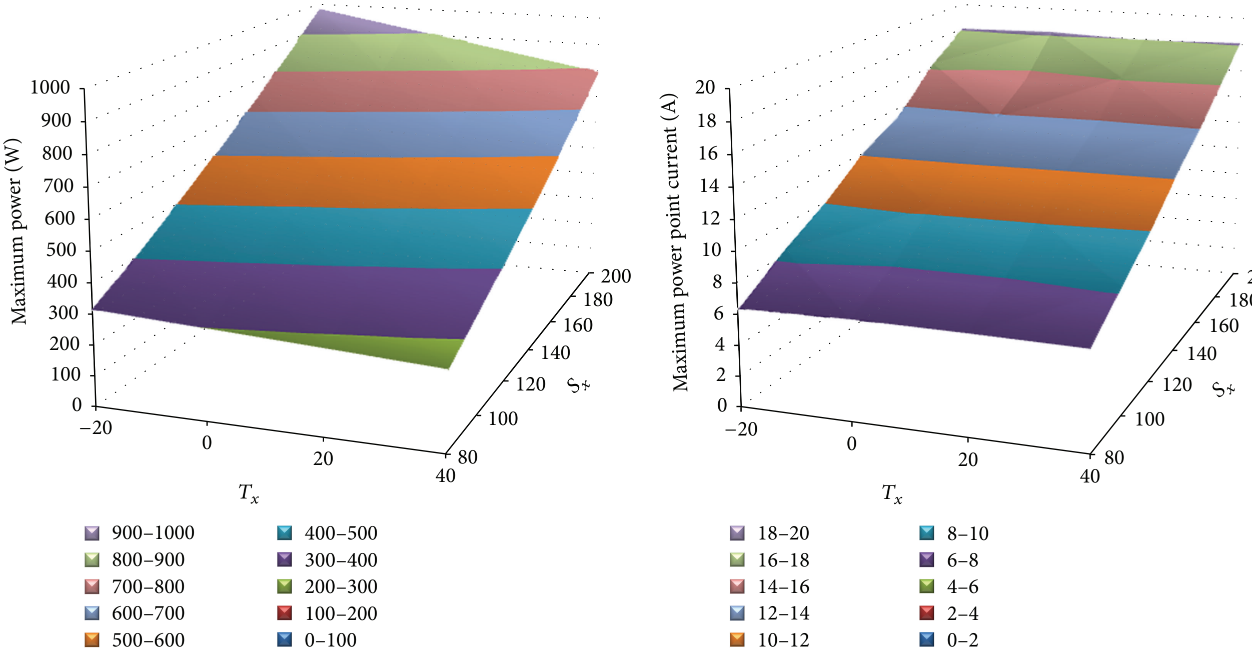

(a) Maximum power point surface

(b) Maximum power point operating current surface

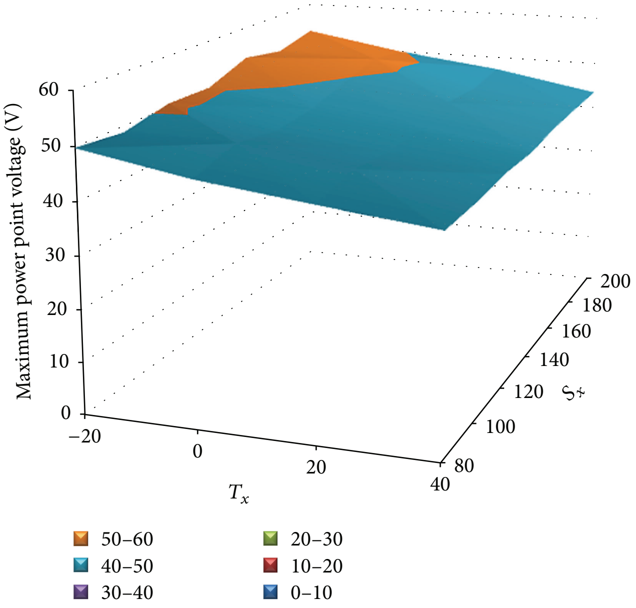

(c) Maximum power point operating voltage surface

Figure 10: Maximum power point surfaces under variable solar irradiation and temperature levels with fixed sizing. (a) Maximum power point surface, (b) maximum power point operating current surface and, (c) maximum power point operating voltage surface.

and their success based on their laboratory reports, due a week after the completion of the laboratory, is described in percentages for each group shown in Figure 23. The reports were marked according to experiment sheet (hand-out) explained above. The global result gotten from the questionnaire (average scores of each question) is shown in Figures 24, 25, and 26 and Table 8.

5. Conclusion

Design and utilization of a Virtual Photovoltaic Systems Laboratory for engineering undergraduate curriculum are introduced in this paper. The Virtual Photovoltaic System Laboratory described in this study is developed to teach students the basics and design steps of photovoltaic solar

Table 7: Assessment data student evaluations using a Likert-scale (Section-C).

24	Instructor was powerful communicator
25	Instructor was eager to teach
26	Instructor performance interacted with me
27	Instructor explanation was explicit and fluent
28	Instructor explanation complicated taking notes
29	Instructor enabled me to concentrate more
30	Instructor behavior was friendly and pleasant
31	Instructor was well prepared
32	Instructor was self-confident
33	I do not ask for instructor help for other things

Note: strongly agree: 1; agree: 2; neither agree nor disagree: 3; disagree: 4; strongly disagree: 5.

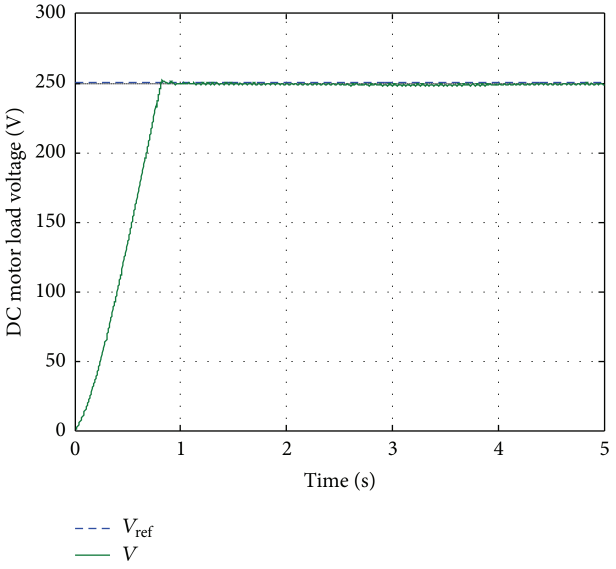

Figure 11: DC motor load voltage waveform.

energy systems in a virtual environment before entering the field. Proposed VPVSL offers five modules to the users. The first module can be used to analyze the *I-V* and *P-V* characteristics of PV systems based on sizing, solar irradiation, and temperature conditions. Module 1 provides a GUI window to the user to change solar irradiation level, temperature and the sizing parameters so that both design and the effects of the changing environmental conditions are set and analyzed. Module 2 can be used to analyze the effect of solar irradiation level under constant temperature and fixed sizing conditions. The effects of the changes in temperature can be analyzed using Module 3 under constant solar irradiation and fixed sizing conditions. The proposed system is tested under two loading conditions. Module 4 provides the testing GUI window for a PMDC motor load. A PID controller is included in this module along with a DC-DC chopper in order to have a constant DC voltage to be treated as a common DC bus, at which a PMDC motor is connected. Module 5 is used to test the VPVSL for AC loading. A three-phase inverter and

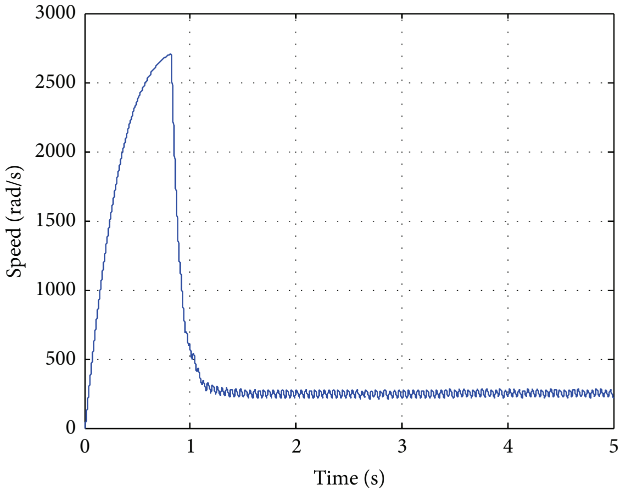

Figure 12: Speed-time waveform.

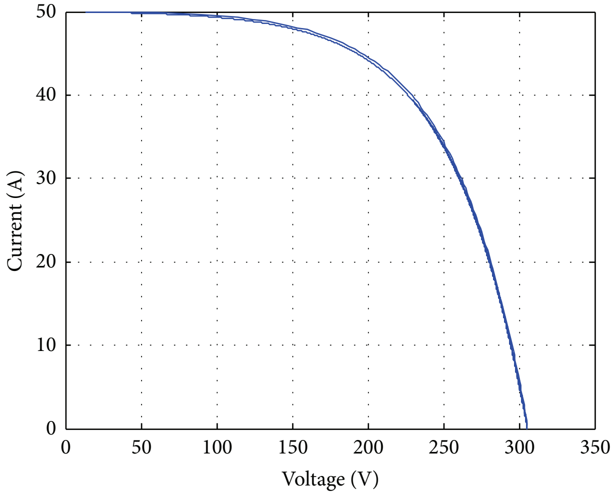

Figure 13: PV current-voltage waveform.

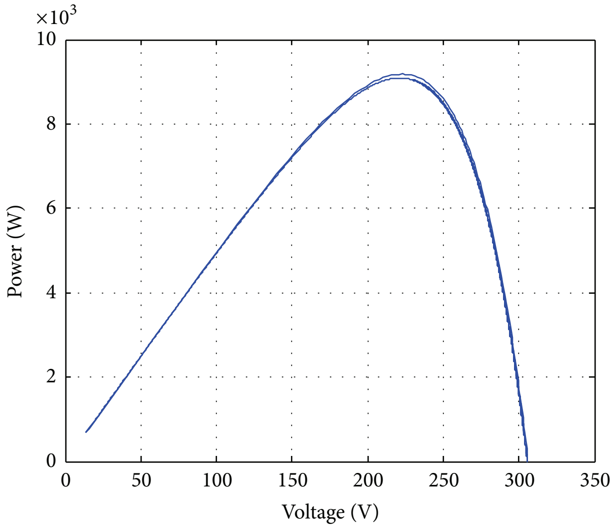

Figure 14: PV power-voltage waveform.

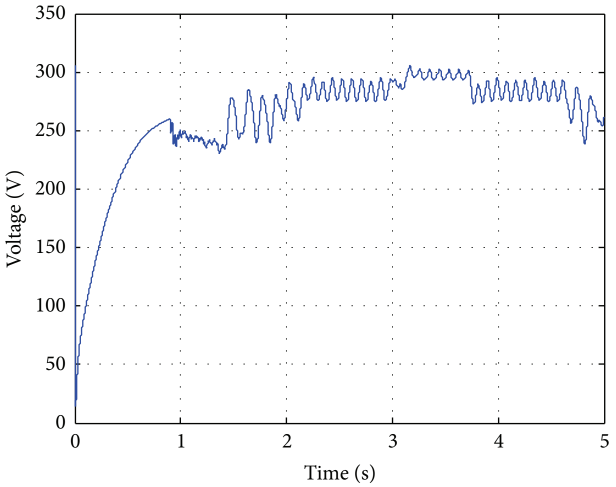

Figure 15: Variation of PV array voltage in time domain.

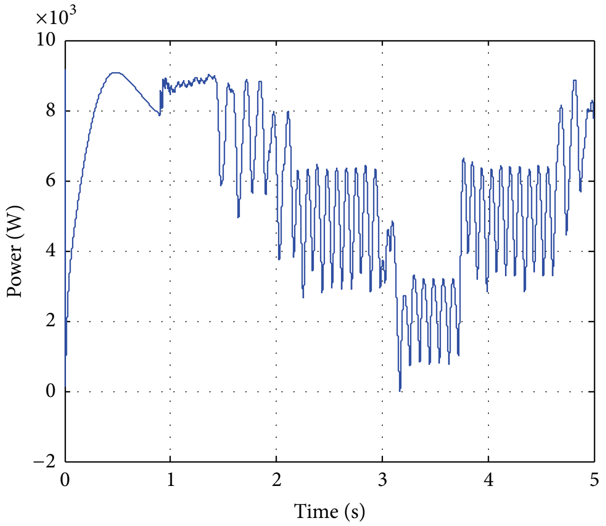

Figure 16: Variation of PV array power in time domain.

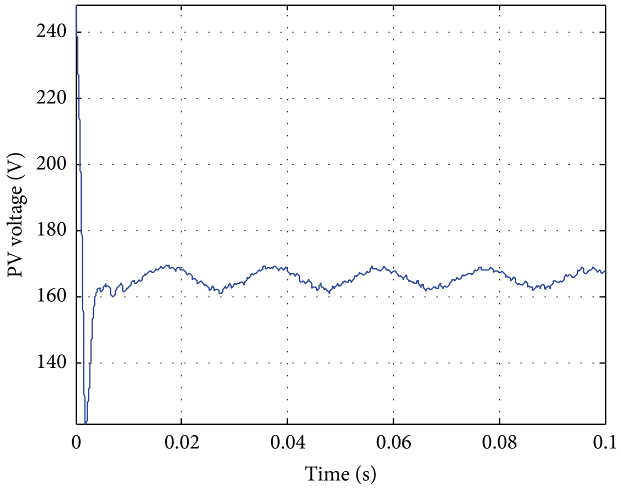

Figure 17: Load PV voltage waveform.

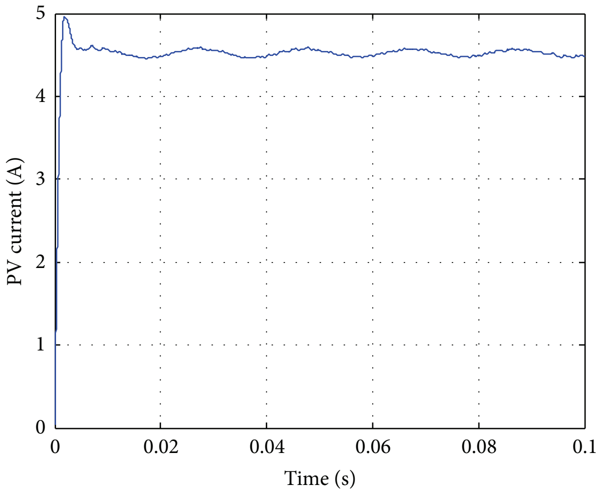

Figure 18: PV current waveform.

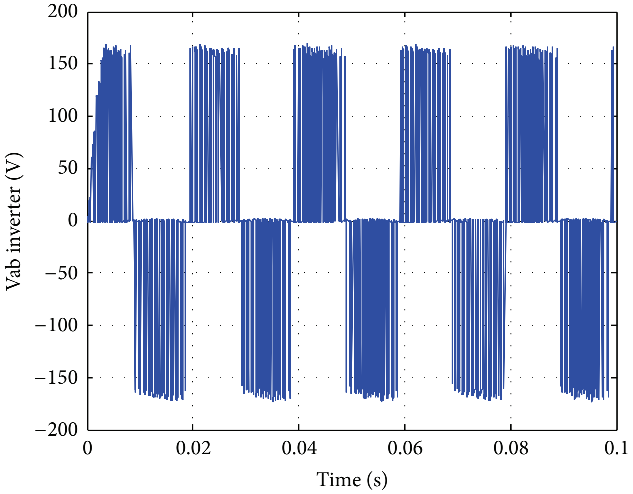

Figure 19: Inverter voltage waveform.

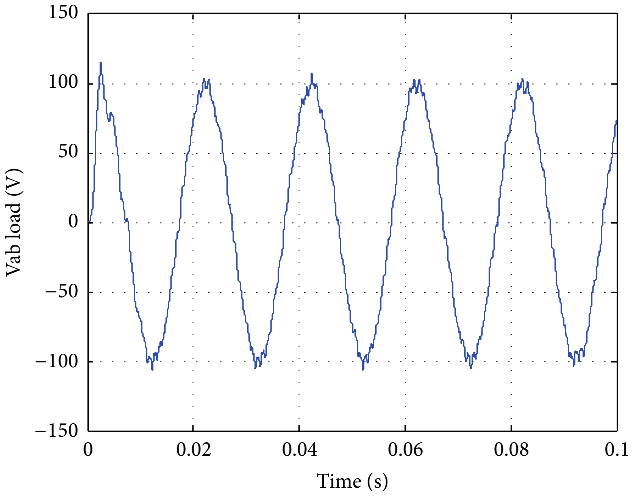

Figure 20: AC load voltage waveform.

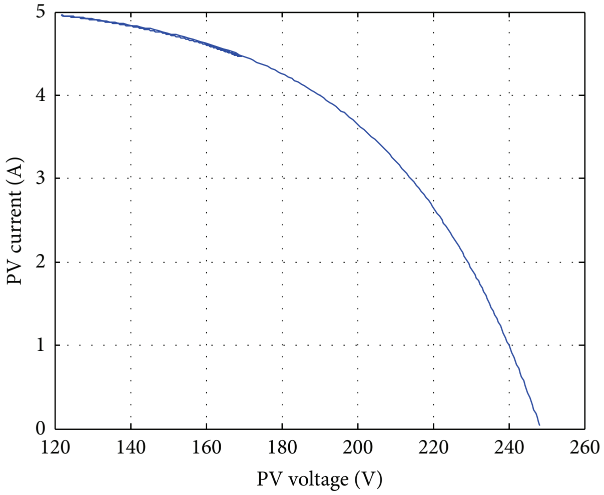

Figure 21: PV current-voltage waveform.

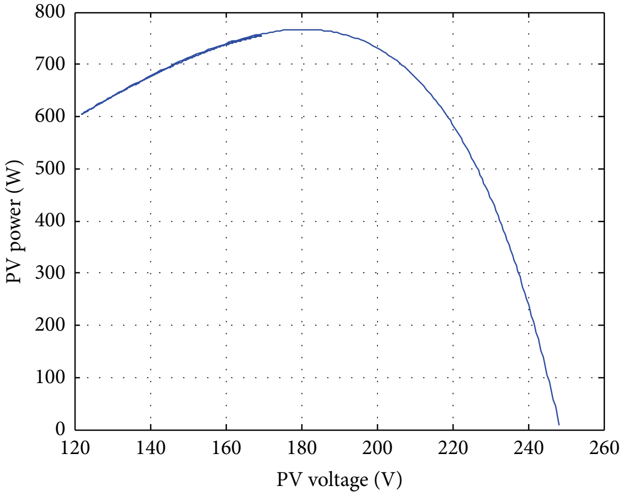

Figure 22: PV power-voltage waveform.

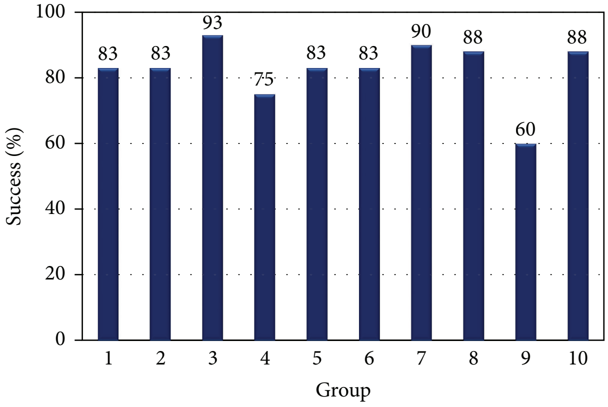

Figure 23: The group success in experiment in percentages.

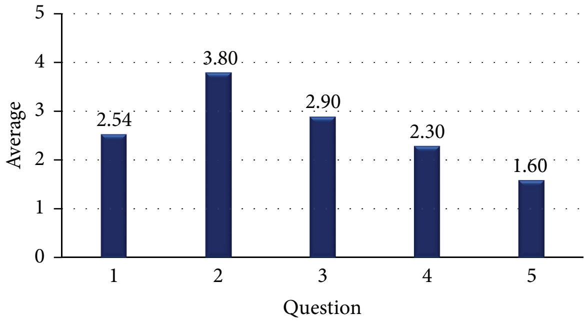

Figure 24: Summary of responses to student opinion survey (Section-A).

Table 8: Student evaluation results.

Question	SD (%)	D (%)	N (%)	A (%)	SA (%)
6	2	2	6	46	44
7	28	34	22	12	4
8	2	4	18	44	32
9	0	10	14	33	43
10	0	6	4	56	34
11	0	6	24	38	32
12	2	4	6	32	56
13	0	6	28	38	28
14	0	12	28	32	28
15	2	12	32	36	18
16	0	8	24	34	34
17	2	2	12	32	52
18	8	12	14	40	26
19	12	42	16	20	10
20	0	6	8	34	52
21	2	8	6	37	47
22	2	4	10	40	44
23	4	28	26	22	20
24	0	0	2	37	60
25	2	0	12	30	56
26	2	0	14	42	42
27	0	0	6	28	66
28	32	38	22	2	6
29	0	6	16	42	36
30	2	0	0	18	80
31	0	0	6	28	66
32	2	0	4	20	74
33	78	16	2	2	2

SD: strongly disagree, D: disagree, N: neutral, A: agree, SA: strongly agree.

a three-phase transformer are included in this module to supply power to an RLC load.

Virtual test results for sample cases are obtained and discussed in the paper. It has been shown that the proposed VPVSL can be used in designing and analyzing purposes. The students can analyze and understand the operational characteristics of the PV systems as well as being able to step in to the design stage of the PV systems. The proposed VPVSL

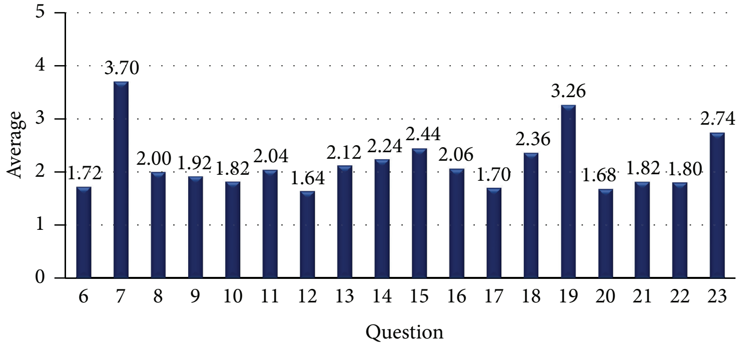

Figure 25: Summary of responses to student opinion survey (Section-B).

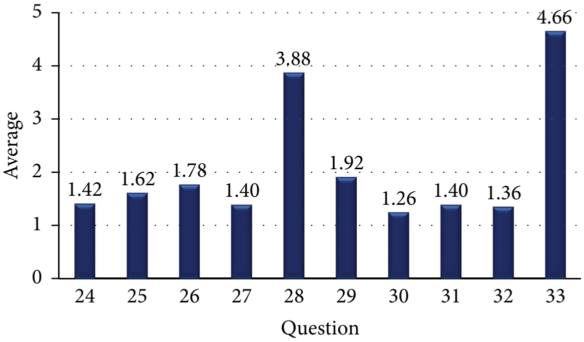

Figure 26: Summary of responses to student opinion survey (Section-C).

has been used in Power Systems Lab in the Department of Electrical and Electronics Engineering at Karadeniz Technical University as a part of undergraduate curriculum. A survey on the students who took the lab has been carried out and responses are included in this paper. The survey indicates that the students get benefit of using the lab. They found it usable, easy, and understandable.

A maximum power point tracker, a battery charging unit, and power conditioning filter circuit options can be added to this study to expand the scope of the virtual lab. A wind energy conversion module, a fuel cell module, and a small hydro module can also be added to this system to develop a general virtual renewable energy laboratory. Besides, the proposed VPVSL can be expanded to handle real time experiments remotely. However, if the VPVSL is combined with a real time measurement and experimental system, some additional components and software will be needed. In order to perform the real time experiments remotely, a communication link and a device on/off switching control software are required. In this case, the connection and data transferring speed will be important as well as the bandwidth of the communication channels to handle the density of coinciding user demands. Due to large size and additional research in a different area such as communication and networking, the idea of establishing a remote VPVSL is left for the future work and is not studied in this paper.

Appendix

The Photovoltaic Cell Parameters

$$T_C\,(^\circ\mathrm{C}) = 20$$
$$S_C\,(\%) = 100$$
$$\beta_T = 0.004$$
$$\gamma_T = 0.06$$
$$T_a\,(^\circ\mathrm{C}) = 20$$
$$\alpha_S = 0.2$$
$$A = 62$$
$$k\,(\mathrm{JK}^{-1}) = 1.3806488 \times 10^{-23}$$
$$e\,(\mathrm{coulombs}) = 1.603 \times 10^{-19}$$
$$I_0\,(\mathrm{A}) = 0.01$$
$$R_S\,(\Omega) = 0.02.$$

Nomenclature

PV:	Photovoltaic
GUI:	Graphical user interface
VPVSL:	Virtual photovoltaic systems lab
PMDC:	Permanent magnet DC
MPPT:	Maximum power point tracker
V_C:	Solar cell output voltage
A:	Curve fitting constant used in solar cell *I-V* characteristics
k:	Boltzmann constant
T_C:	Reference solar cell operating temperature
e:	Electron charge
I_{ph}:	Solar cell photocurrent
I_0:	Diode reverse saturation current
I_C:	Solar cell output current
R_S:	Series resistance of solar cell equivalent circuit
N_S:	Number of cells in series
N_P:	Number of cells in parallel
C_{TV}:	Temperature dependent scaling factor of solar cell voltage
β_T:	Temperature constant affecting solar cell voltage

T_a: Reference ambient temperature
T_x: Current values of ambient temperature
C_{TI}: Temperature dependent scaling factor of solar cell current
γ_T: Temperature constant affecting solar cell current
S_C: Reference solar irradiation
α_S: Solar irradiation constant
S_x: Current values of solar irradiation
S_C: Reference solar irradiation
β_S: Effect of the solar irradiation on cell voltage
C_{SV}: Solar irradiation dependent scaling factor of solar cell voltage
C_{SI}: Solar irradiation dependent scaling factor of solar cell current
γ_S: Effect of the solar irradiation on photocurrent
ΔT_C: Temperature change due to changing solar irradiation level
V_{CX}: Solar cell operating voltage
$I_{\mathrm{ph}\,x}$: Solar cell operating photocurrent
$P_{\max}$: Maximum power photovoltaic array
I_{mpp}: Maximum power point current photovoltaic array
V_{mpp}: Maximum power point voltage photovoltaic array
I_{sc}: Short circuit current photovoltaic array
V_{oc}: Open circuit voltage photovoltaic array.

Conflict of Interests

The authors declare that there is no conflict of interests regarding the publication of this paper.

References

[1] M. Hashemipour, H. F. Manesh, and M. Bal, "A modular virtual reality system for engineering laboratory education," *Computer Applications in Engineering Education*, vol. 19, no. 2, pp. 305–314, 2011.

[2] B. Balamuralithara and P. C. Woods, "Virtual laboratories in engineering education: the simulation lab and remote lab," *Computer Applications in Engineering Education*, vol. 17, no. 1, pp. 108–118, 2009.

[3] J. A. Kypuros and T. J. Connolly, "Student-configurable, web-accessible virtual systems for system dynamics and controls courses," *Computer Applications in Engineering Education*, vol. 16, no. 2, pp. 92–104, 2008.

[4] R. Dormido, H. Vargas, N. Duro et al., "Development of a web-based control laboratory for automation technicians: the three-tank system," *IEEE Transactions on Education*, vol. 51, no. 1, pp. 35–44, 2008.

[5] E. Tanyildizi and A. Orhan, "A virtual electric machine laboratory for effect of saturation of the asynchronous machine application," *Computer Applications in Engineering Education*, vol. 17, no. 4, pp. 422–428, 2009.

[6] E. Lindsay and M. Good, "The impact of audiovisual feedback on the learning outcomes of a remote and virtual laboratory class," *IEEE Transactions on Education*, vol. 52, no. 4, pp. 491–502, 2009.

[7] H. Rehman, R. A. Said, and Y. Al-Assaf, "An integrated approach for strategic development of engineering curricula: focus on students' design skills," *IEEE Transactions on Education*, vol. 52, no. 4, pp. 470–481, 2009.

[8] G. C. Goodwin, A. M. Medioli, W. Sher, L. B. Vlacic, and J. S. Welsh, "Emulation-based virtual laboratories: a low-cost alternative to physical experiments in control engineering education," *IEEE Transactions on Education*, vol. 54, no. 1, pp. 48–55, 2011.

[9] S. Azaklar and H. Korkmaz, "A remotely accessible and configurable electronics laboratory implementation by using LabVIEW," *Computer Applications in Engineering Education*, vol. 18, no. 4, pp. 709–720, 2010.

[10] C. Elmas and Y. Sönmez, "An educational tool for power electronics circuits," *Computer Applications in Engineering Education*, vol. 18, no. 1, pp. 157–165, 2010.

[11] A. See and A. J. Leong, "An advanced-automated system for equipotential field lines mapping utilizing motion control," *Computer Applications in Engineering Education*, vol. 19, no. 1, pp. 171–182, 2011.

[12] H. Y. Yamin, I. A. Altawil, A. F. Al-Ajlouni, and A. S. Al-Fahoum, "A new developed educational approach to improve conventional teaching methodology of the power electronics laboratory," *Computer Applications in Engineering Education*, vol. 19, no. 1, pp. 193–200, 2011.

[13] A. F. Al-Ajlouni, H. Y. Yamin, and B. Harb, "Effect of instructional software on achievement of undergraduate students in Digital Signal Processing," *Computer Applications in Engineering Education*, vol. 18, no. 4, pp. 703–708, 2010.

[14] E. S. Aziz, S. K. Esche, and C. Chassapis, "Content-rich interactive online laboratory systems," *Computer Applications in Engineering Education*, vol. 17, no. 1, pp. 61–79, 2009.

[15] T. Yigit and C. Elmas, "An educational tool for controlling of SRM," *Computer Applications in Engineering Education*, vol. 16, no. 4, pp. 268–279, 2008.

[16] J. R. R. Ruiz, A. G. Espinosa, and J. A. Ortega, "Validation of the parametric model of a DC contactor using Matlab-Simulink," *Computer Applications in Engineering Education*, vol. 19, no. 2, pp. 337–346, 2011.

[17] J. A. Calvo, M. J. Boada, V. Díaz, and E. Olmeda, "SIMPERF: SIMULINK based educational software for vehicle's performance estimation," *Computer Applications in Engineering Education*, vol. 17, no. 2, pp. 139–147, 2009.

[18] I. Colak, S. Demirbas, S. Sagiroglu, and E. Irmak, "A novel web-based laboratory for DC motor experiments," *Computer Applications in Engineering Education*, vol. 19, no. 1, pp. 125–135, 2011.

[19] J. R. R. Ruiz, A. G. Espinosa, and X. A. Morera, "Electric field effects of bundle and stranded conductors in overhead power lines," *Computer Applications in Engineering Education*, vol. 19, no. 1, pp. 107–114, 2011.

[20] E. Aziz, "Teaching and learning enhancement in undergraduate machine dynamics," *Computer Applications in Engineering Education*, vol. 19, no. 2, pp. 244–255, 2011.

[21] I. H. Altas and A. M. Sharaf, "A photovoltaic array simulation model for matlab-simulink GUI environment," in *Proceedings of the International Conference on Clean Electrical Power (ICCEP '07)*, pp. 341–345, Capri, Italy, May 2007.

[22] Criteria for Accrediting Engineering Programs: Effective for Reviews during the 2012–2013 Accreditation Cycle, ABET Engineering Accreditation Commission, 2011.

[23] M. Buresch, *Photovoltaic Energy Systems Design and Installation*, McGraw-Hill, New York, NY, USA, 1983.

[24] I. H. Altas and A. M. Sharaf, "A fuzzy logic power tracking controller for a photovoltaic energy conversion scheme," *Electric Power Systems Research*, vol. 25, no. 3, pp. 227–238, 1992.

[25] I. H. Altas and A. M. Sharaf, "A novel on-line MPP search algorithm for PV arrays," *IEEE Transactions on Energy Conversion*, vol. 11, no. 4, pp. 748–754, 1996.

[26] D. R. Hodge and D. F. Gillespie, "Phrase completion scales: a better measurement approach than Likert scales?" *Journal of Social Service Research*, vol. 33, no. 4, pp. 1–12, 2007.

Hindawi Publishing Corporation
International Journal of Photoenergy
Volume 2014, Article ID 502628, 6 pages
http://dx.doi.org/10.1155/2014/502628

Research Article

Effect of Ambient Temperature on Performance of Grid-Connected Inverter Installed in Thailand

Kamonpan Chumpolrat, Vichit Sangsuwan, Nuttakarn Udomdachanut, Songkiate Kittisontirak, Sasiwimon Songtrai, Perawut Chinnavornrungsee, Amornrat Limmanee, Jaran Sritharathikhun, and Kobsak Sripapha

National Electronics and Computer Technology Center, 112 Thailand Science Park, Phahonyotin Road, Klong 1, Klong Luang, Pathumthani 12120, Thailand

Correspondence should be addressed to Kamonpan Chumpolrat; kamonpan.chumpolrat@nectec.or.th

Received 28 October 2013; Revised 7 January 2014; Accepted 4 February 2014; Published 6 March 2014

Academic Editor: Adel M. Sharaf

The effects of temperature on performance of a grid-connected inverter, and also on a photovoltaic (PV) system installed in Thailand have been investigated. It was found that the maximum efficiency of the inverter showed 2.5% drop when ambient temperature was above 37°C. The inverter performed efficiently in November and December, the months of high irradiance, and monthly average ambient temperature of lower than 35°C, allowing relatively high system performance ratio in this period. Our results show that high temperature provides negative impacts not only on the PV modules, but also on the performance of the inverter. Thus, the effect of temperature on the inverter efficiency should be taken into account when predicting energy yield or analyzing losses of the PV systems—especially in high temperature regions.

1. Introduction

Thailand receives an annual average solar irradiation of 18.2 MJ/m^2—day, which is relatively high compared to other tropical and mid-latitude counties [1]. Owing to abundant solar energy and government support scheme for megawatts solar farms, Thailand is expected to be an emerging photovoltaic (PV) market of Southeast Asia. Nonetheless, severe climatic conditions of tropical countries—high temperature and high humidity—have negative impacts on performance and reliability of PV systems. Since high temperature causes a reduction in output power of PV modules, the temperature effects are one of main concerns when forecasting energy production or analyzing losses of the PV systems. There are, thus, many reports regarding the effects of temperature on the performance of various types of PV modules operating in tropical countries including Thailand [2–5]. Besides the performance of the PV modules, inverter efficiency is also a critical factor which greatly influences the system performance; therefore, its actual behavior needs to be evaluated. Furthermore, temperature-dependent performance of inverter is also worth investigating because the efficiency of electronic devices including inverter also depends on the operating temperature [6–9]. Since the temperature-dependent behavior of the inverter for PV systems has not yet been reported, in this study we have investigated performance of a high-efficient grid-connected inverter installed in Thailand, in particular with respect to the temperature effect. The findings of our work are expected to be useful information for energy yield prediction and loss analysis of the PV systems, especially in high temperature regions.

2. System Installation and Monitoring

The 2.24 kWp grid-connected PV system has been installed at National Science and Technology Development Agency (NSTDA), Pathumthani province, Thailand—latitude 14° 4′ 46″ N, longitude 100° 36′ 4″ E—in March 2010, supplying electricity for load of the office building. This PV system consists of tandem amorphous silicon (a-Si:H/a-Si:H) prototype modules manufactured by NSTDA. The characteristics of the PV modules, inverter, and the PV system in this study are described in Table 1. The PV modules have been installed in an open rack at a tilt of 14° facing

Table 1: PV module and system characteristics.

Item	Details	
Module	Type	Thin film a-Si
	Peak power output	40 W
	Peak power voltage	47.5 V
	Peak power current	0.84 A
	Temperature coefficient for power	−0.20%/°C
	Area	1.2 m × 0.65 m (0.78 m^2)
Inverter	Type	Single-phase string, transformer based, grid-connected
	Nominal output power	5 kW
	Maximum efficiency	96%
System	Number of modules	56 (8 modules/string, 7 strings)
	Nominal power output	2.24 kW
	Peak power voltage	380 V
	Peak power current	5.89 A

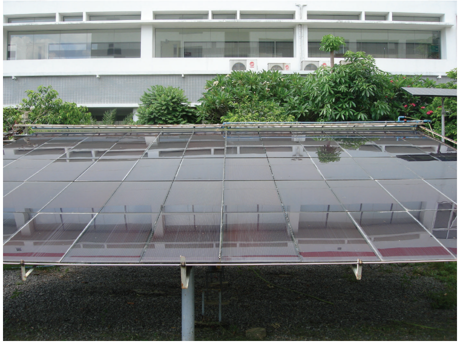

Figure 1: PV test site at NSTDA, Thailand.

South, as shown in Figure 1. An automated measuring system was constructed to collect data of the system, that is, system output, module temperature (T_m), ambient temperature (T_a), and in-plane solar irradiance, at 1 min interval. The collected data from 5 AM to 7 PM during the period of 7 months (from October 2010 to April 2011) was used for the system performance analysis in this study.

3. Results and Discussion

The DC output power as a function of the solar intensity and a variation of the module temperature are shown in Figure 2. It can be seen that the module temperature was about 30°C under the irradiance of lower than 250 W/m^2 and then gradually increased with increasing irradiance, rising to 60°C at the irradiance of 800–1000 W/m^2. It should be noted that in this test site the average module temperature ranged from 42°C to 47°C, rarely being 25°C or lower during the operating hours. Figure 3 indicates a linear relationship between the DC output from the PV modules (inverter input power) and the AC output from the inverter. The inverter started to produce the AC output at the DC output power of about 58 W, suggesting energy consumption of 58 W at its operating mode.

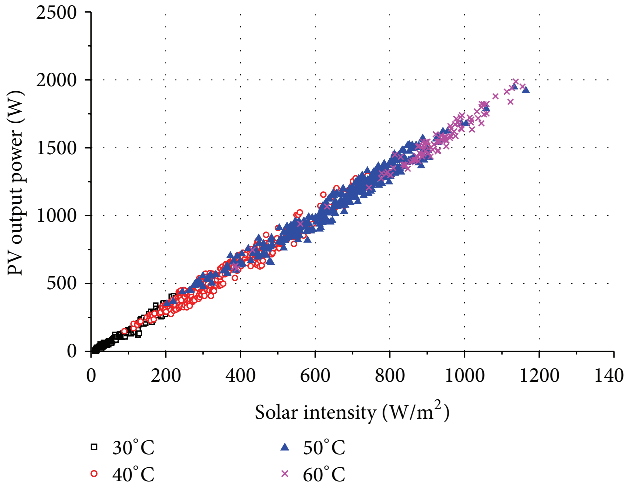

Figure 2: Relation of solar irradiance to PV output power and variation in module temperature.

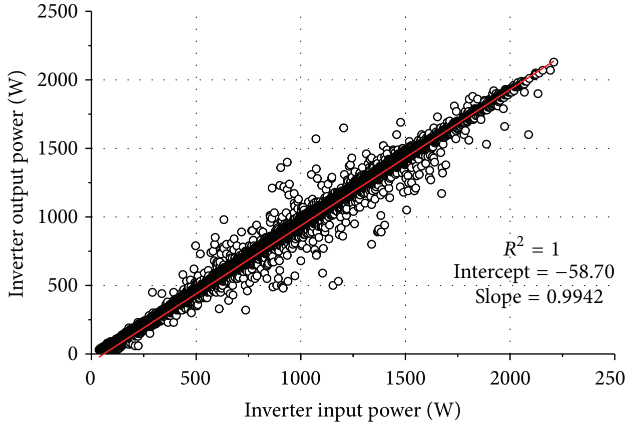

Figure 3: Relation between input and output power of inverter.

Interestingly, it was found that the actual maximum efficiency of the inverter strongly depended on the ambient temperature. As shown in Figure 4, the inverter efficiency

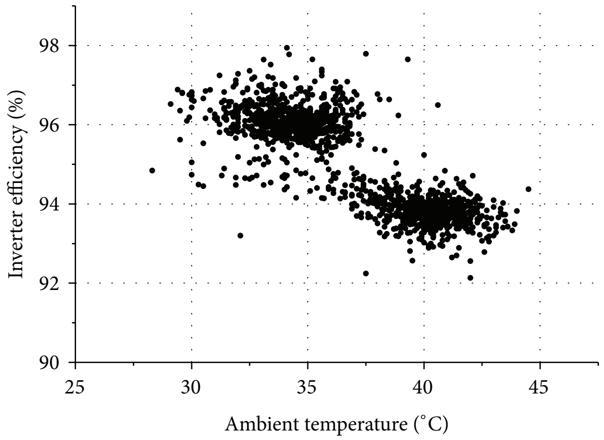

FIGURE 4: Relation between inverter efficiency and ambient temperature.

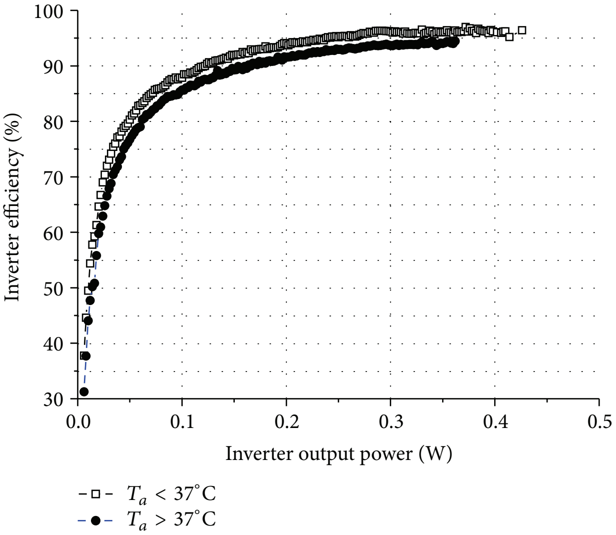

FIGURE 5: Average inverter efficiency of two different operating conditions: $T_a < 37^\circ$C and $T_a > 37^\circ$C.

(η_{ivt}) reaches its maximum value of 96–96.5% when the ambient temperature is below 37°C and shows 2.5% drop when the temperature increases above 37°C—under the same solar irradiance of 1000–1100 W/m^2. An obvious difference in the inverter efficiency of two different operating conditions, of which 37°C is set as a borderline, is displayed in Figure 5. In both cases the inverter efficiency similarly tended to remain constant when the AC output power exceeded 1500 W or 27% of the inverter's rated capacity; however, the difference in the inverter efficiency of these two different temperatures was obvious.

It is well known that the characteristics of the inverter are dependent on the temperature of the electronic circuit—temperature inside the inverter case. Although we did not collect continuous data of the temperature inside the inverter, we occasionally checked it and found its relation to the ambient temperature. The inverter temperature is always higher than the ambient temperature. During the day time, a temperature difference of about 10–14°C is found when the ambient temperature rises higher than 32°C. This implies that the ambient temperature of 37°C corresponds to the inverter temperature of about 47–51°C. The grid-connected inverter in this study is a single-phase string inverter with transformer. It contains 3 major parts; Maximum Power Point (MPP) tracking, bridge, and transformer. Among these three parts, bridge is the part that is the most sensitive to the operating temperature because it contains switching devices. The temperature effects possibly can be mitigated by optimizing inverter topology and its internal design. A separation of different types of components into different temperature zones within the inverter's overall enclosure is concerned to be an effective way. This approach is generally utilized in low frequency transformer-based inverter design [10]. Since transformer causes heating and also induces power loss, development of a transformerless inverter is likely to be preferable in respect to the temperature effect. Additionally, an efficient cooling system is essential to maintain performance and extend lifetime of the inverter.

The experimental results have revealed the temperature-dependent behavior of the inverter and moreover clearly pointed out negative impact of high temperature on the inverter performance [7]. In high temperature regions, the operating temperature of the inverter, thus, is a critical factor, which should be concerned when analyzing the losses in the PV systems.

Normalized frequency distributions of four different inverter operating conditions are shown in Table 2. Here, the input power of 27% of the inverter's rated capacity and the ambient temperature of 37°C are used as borderline conditions. It can be seen that the conditions whose $T_a > 37^\circ$C (numbers 2 and 4) occupied 33% of the total frequency distribution, indicating relatively high possibility of undesirable operating conditions for the inverter. Furthermore, the ideal condition, normalized input power >27% and $T_a < 37^\circ$C, occupied only 11%. In this test site the normalized frequency distribution of the low input conditions (numbers 3 and 4) was found to be as high as 80%. This was because the installed PV module capacity was 2.24 kWp, only 45% of the inverter's rated capacity.

The monthly cumulative solar irradiance—which is here denoted by solar energy received (E_r)—and the monthly average ambient temperature are shown in Figure 6. The average ambient temperature from October 2010 to December 2010 was found to be lower than 35°C, while from January 2011 to April 2011 the temperature increased above 35°C. In this test site the E_r ranged from 5 to 6.5 MWh, especially being high in January. The monthly average inverter efficiency, performance ratio (PR) of the PV modules, and PR of the PV system are indicated in Figure 7. It is obvious that the inverter efficiency was strongly affected by the ambient temperature, that is, high efficiency during low-temperature period and less efficient performance during high-temperature months. The high average inverter efficiency was observed in November and December, when the average ambient temperature was lower than 35°C and their monthly cumulative irradiance was relatively high. Since the inverter efficiency is directly proportional to the

Table 2: Normalized frequency distributions of four different inverter's operating conditions.

Number	Inverter's operating conditions		Normalized frequency (%)
	Normalized input power (%)	T_a (°C)	
1	>27	<37	11
2	>27	>37	9
3	<27	<37	56
4	<27	>37	24

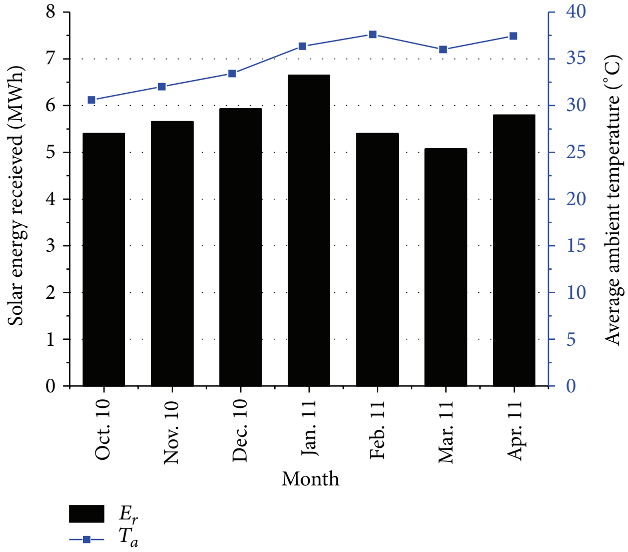

Figure 6: Trends of monthly solar energy received (E_r) and average ambient temperature (T_a).

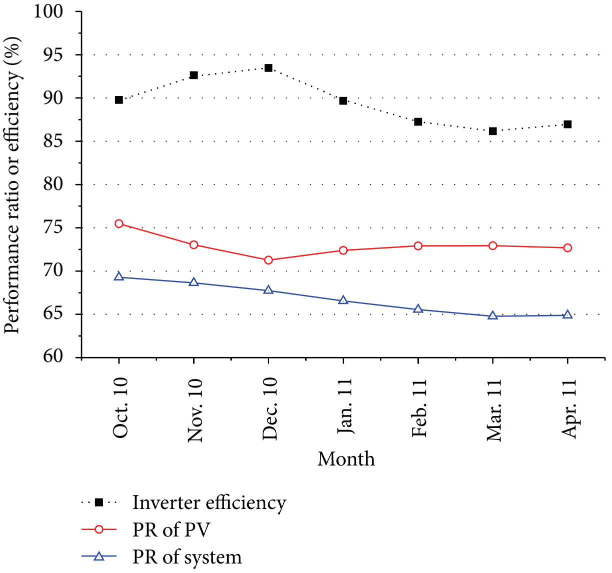

Figure 7: Trends of monthly inverter efficiency, PR of PV modules, and PR of PV system.

solar intensity, higher efficiency should be observed in the month of higher irradiance; however, in January, the month of the highest monthly cumulative irradiance, the inverter efficiency was found to be relatively low. This was perhaps due to high temperature in January, demonstrating the temperature effects on the inverter performance. Although the highest inverter efficiency was obtained in December, the PR of the thin film a-Si:H modules significantly dropped, which was likely to be caused by the red-shift spectrum distribution during this period [11–14]. The PR of the PV modules tended to recover in January; however, it was still low due to high temperature during January 2011–April 2011, which eventually resulted in the low system PR. According to the results, the PR of the PV system depended on both PV module and inverter performance, both of which were strongly influenced by the operating temperature.

The output energy of the PV system can be expressed by the following equation, which is the modified equation of a method previously used for field-test analysis of PV system output [15]:

$$P_{\text{out}} = K_T \cdot K_{\text{ivt}} \cdot K_e \cdot P_{\text{in}} \cdot \eta_s, \tag{1}$$

where P_{out} is AC output energy, P_{in} is in-plane irradiance, and η_s is conversion efficiency of the PV modules under the standard testing conditions (STC)—irradiance of 1000 W/m^2, module temperature of 25°C, and air mass 1.5 global spectrum. K_T denotes a correction coefficient for module temperature, which can be given by

$$K_T = 1 + \alpha \cdot (T_m - 25), \tag{2}$$

where α is a temperature coefficient for power of the PV module, which is −0.20%/°C in this case. K_{ivt} is a correction coefficient for inverter performance. Here, the K_{ivt} is expressed by the following equation:

$$K_{\text{ivt}} = \eta^{\circ}_{\text{ivt}} \cdot \alpha_{\text{ivt}} = \eta^{*}_{\text{ivt}}, \tag{3}$$

where $\eta^{\circ}_{\text{ivt}}$ is the nominal maximum efficiency of the inverter, α_{ivt} is a correction factor for inverter efficiency, and η^{*}_{ivt} is the actual efficiency of the inverter. It is well known that the inverter efficiency depends mainly on the input DC power, which corresponds directly to the solar irradiance, thus the variation of the inverter efficiency can be presented in terms of the solar irradiance. However, the inverter efficiency under high-irradiance condition—irradiance >500 W/m^2—tended to be saturated and remained constant; the correction factor for the inverter performance is, therefore, presented as the approximate equation (3). A correction coefficient for factors except module temperature and inverter performance, which includes effects of shading, reflection, soiling, and

Table 3: The monthly basis of irradiance, average ambient temperature, average module temperature, and correction coefficients.

Month	Irradiance (MWh)	Ambient temp. (°C)	Irradiance weighted module temp. (°C)	K_T	K_{ivt}	K_e
Oct. 10	5.398	30.6	47.5	0.955	0.898	0.807
Nov. 10	5.654	32.0	49.8	0.950	0.926	0.778
Dec. 10	5.926	33.4	49.7	0.951	0.935	0.761
Jan. 11	6.648	36.3	49.6	0.951	0.897	0.779
Feb. 11	5.398	37.6	49.2	0.952	0.873	0.788
Mar. 11	5.071	36.0	46.5	0.957	0.862	0.784
Apr. 11	5.795	37.4	49.2	0.952	0.870	0.783

degradation, is denoted by K_e. The P_{in}, P_{out}, T_m, and η^*_{ivt} were obtained from the field-test data, while the η_s and η°_{ivt} were known values; therefore, the K_T, K_{ivt}, and K_e can be derived to evaluate the effects of module temperature, inverter efficiency, and other factors on the PV system performance.

We have derived the correction coefficients, K_T, K_{ivt}, and K_e and summarized in Table 3. These correction coefficients, whose value must be >0 and <1 can be used as primary indicators of energy loss; thus, we can simply compare the losses due to module temperature, inverter, and other factors. It can be seen that the K_T did not show obvious variation, while the K_{ivt} tended to depend on the monthly average ambient temperature. During high-temperature period, the K_{ivt} was found to be small, suggesting a large amount of energy loss of the inverter. Interestingly, the K_e in December was obviously smaller than that of the other months. This was perhaps due to increased spectrum mismatch loss during that period which resulted in the PR drop of the thin film a-Si:H modules.

The efficiency of the inverter, needless to say, certainly influences the total performance of the PV systems. The temperature effects on the inverter is thus a meaningful finding, and the quantitative analysis of this kind of loss is useful for forecasting energy yield of the PV systems—especially in high temperature regions. Although, at present we have evaluated and analyzed the results of only one high-efficient inverter, it is certain that high operating temperature has negative effects on all inverters. However, the amount of loss perhaps depends on inverter's type and manufacture, which is worth investigating further.

4. Conclusion

High temperature has negative impacts also on the performance of the inverter, not only on the PV modules. According to our experimental results, the ambient temperature of higher than 37°C caused 2.5% drop in the inverter's maximum efficiency. During high-temperature period, when the monthly average ambient temperature was >35°C, the PR of the PV system was found to be low, which was likely to be due to a large amount of loss arising from high operating temperature. Consequently, in high temperature regions like Thailand the effect of temperature on the inverter performance cannot be neglected, and it must be taken into account in the energy yield prediction or the loss analysis of the PV systems.

Conflict of Interests

The authors declare that there is no conflict of interests regarding the publication of this paper.

References

[1] S. Janjai, *Solar Radiation Maps from Satellite Data for Thailand*, Department of Alternative Energy Development and Efficiency, Ministry of Energy, Bangkok, Thailand, 2010.

[2] W. Suponthana, N. Ketjoya, W. Rakwichian, and P. Inthanon, "Performance evaluation AC solar home systems in Thailand: system using multi crystalline silicon PV module versus system using thin film amorphous silicon PV module," *International Journal of Renewable Energy*, vol. 2, no. 2, pp. 35–52, 2007.

[3] K. Phaobkaew, N. Ketjoy, W. Rakwichian, and S. Yammen, "Performance of a-Si, p-Si, and HIT PV technological comparison under tropical wet climate condition," *International Journal of Renewable Energy*, vol. 2, no. 2, pp. 23–34, 2007.

[4] A. Sasitharanuwat, W. Rakwichian, N. Ketjoy, and S. Yammen, "Performance evaluation of a 10 kWp PV power system prototype for isolated building in Thailand," *Renewable Energy*, vol. 32, no. 8, pp. 1288–1300, 2007.

[5] P. Kamkird, N. Ketjoy, W. Rakwichian, and S. Sukchai, "Investigation on temperature coefficients of three types photovoltaic module technologies under Thailand operating condition," *Procedia Engineering*, vol. 32, pp. 376–383, 2012.

[6] D. Wolpert and P. Ampadu, *Managing Temperature Effects in Nanoscale Adaptive Systems*, Springer, New York, NY, USA, 2012.

[7] S. Islam, A. Woyte, R. Belmans, P. J. M. Heskes, and P. M. Rooij, "Investigating performance, reliability and safety parameters of photovoltaic module inverter: test results and compliances with the standards," *Renewable Energy*, vol. 31, no. 8, pp. 1157–1181, 2006.

[8] B. Burger and R. Rüther, "Inverter sizing of grid-connected photovoltaic systems in the light of local solar resource distribution characteristics and temperature," *Solar Energy*, vol. 80, no. 1, pp. 32–45, 2006.

[9] M. Eltawil and Z. Zhao, "Grid-connected photovoltaic power systems: technical and potential problems—a review," *Renewable and Sustainable Energy Reviews*, vol. 14, no. 1, pp. 112–129, 2010.

[10] J. Worden and M. Martinson, “How inverters work: what goes on inside the magic box,” *Solarpro*, no. 2.3, pp. 68–85, 2009.

[11] Y. Nakada, H. Takahashi, K. Ichida, T. Minemoto, and H. Takakura, “Influence of clearness index and air mass on sunlight and outdoor performance of photovoltaic modules,” *Current Applied Physics*, vol. 10, no. 2, supplement, pp. S261–S264, 2010.

[12] T. Minemoto, S. Nagae, and H. Takakura, “Impact of spectral irradiance distribution and temperature on the outdoor performance of amorphous Si photovoltaic modules,” *Solar Energy Materials and Solar Cells*, vol. 91, no. 10, pp. 919–923, 2007.

[13] A. Limmanee and K. Chumpolrat, “Changes in spectral irradiance and their effects on PV module performance,” in *Proceeding of the 6th Conference on Energy Network of Thailand (ENETT ’10)*, 2010.

[14] R. Rüther, G. Kleiss, and K. Reiche, “Spectral effects on amorphous silicon solar module fill factors,” *Solar Energy Materials and Solar Cells*, vol. 71, no. 3, pp. 375–385, 2002.

[15] K. Nishioka, T. Hatayama, Y. Uraoka, T. Fuyuki, R. Hagihara, and M. Watanabe, “Field-test analysis of PV system output characteristics focusing on module temperature,” *Solar Energy Materials and Solar Cells*, vol. 75, no. 3-4, pp. 665–671, 2003.

Hindawi Publishing Corporation
International Journal of Photoenergy
Volume 2014, Article ID 385720, 12 pages
http://dx.doi.org/10.1155/2014/385720

Research Article

Grid Connected Solar PV System with SEPIC Converter Compared with Parallel Boost Converter Based MPPT

T. Ajith Bosco Raj,[1] R. Ramesh,[1] J. R. Maglin,[1] M. Vaigundamoorthi,[1] I. William Christopher,[1] C. Gopinath,[1] and C. Yaashuwanth[2]

[1] *Department of Electrical and Electronics Engineering, Anna University, Chennai 600 025, India*
[2] *Department of Computer Science Engineering, SRM University, Tamil Nadu 603 203, India*

Correspondence should be addressed to T. Ajith Bosco Raj; ajithboscoraj@gmail.com and R. Ramesh; rramesh@annauniv.edu

Received 22 August 2013; Revised 13 January 2014; Accepted 14 January 2014; Published 3 March 2014

Academic Editor: Ismail H. Altas

The main objective of this work is to study the behaviour of the solar PV systems and model the efficient Grid-connected solar power system. The DC-DC MPPT circuit using chaotic pulse width modulation has been designed to track maximum power from solar PV module. The conversion efficiency of the proposed MPPT system is increased when CPWM is used as a control scheme. This paper also proposes a simplified multilevel (seven level) inverter for a grid-connected photovoltaic system. The primary goal of these systems is to increase the energy injected to the grid by keeping track of the maximum power point of the panel, by reducing the switching frequency, and by providing high reliability. The maximum power has been tracked experimentally. It is compared with parallel boost converter. Also this model is based on mathematical equations and is described through an equivalent circuit including a PV source with MPPT, a diode, a series resistor, a shunt resistor, and dual boost converter with active snubber circuit. This model can extract PV power and boost by using dual boost converter with active snubber. By using this method the overall system efficiency is improved thereby reducing the switching losses and cost.

1. Introduction

Because of constantly growing energy demand, grid-connected photovoltaic (PV) systems are becoming more and more popular, and many countries have permitted, encouraged, and even funded distributed-power-generation systems. Currently, solar panels are not very efficient with only about 12–20% efficiency in their ability to convert sunlight to electrical power. The efficiency can drop further due to other factors such as solar panel temperature and load conditions. In order to maximize the power derived from the solar panel, it is important to operate the panel at its optimal power point. To achieve this, a maximum power point tracker will be designed and implemented.

The MATLAB/PSPICE model of the PV module is developed [1–4] to study the effect of temperature and insolation on the performance of the PV module. The power electronics interface, connected between a solar panel and a load or battery bus, is a pulse width modulated (PWM) DC-DC converter or their derived circuits used to extract maximum power from solar PV panel. *I-V* characteristic curve of photovoltaic generators based on various DC-DC converters [5–8] was proposed and concluded that SEPIC converter is the best alternative to track maximum power from PV panel. The various types of nonisolated DC-DC converters for the photo voltaic system is reviewed [9].

The maximum power tracking for PV panel using DC-DC converter is developed [10] without using microcontroller. This approach ensures maximum power transfer under all atmospheric conditions. The analogue chaotic PWM is used to reduce the EMI in boost converter. The conversion efficiency is increased when CPWM is used as a control technique [11–13]. To increase conversion efficiency, an active clamp circuit is introduced into the proposed one to provide soft switching features to reduce switching losses. Moreover, switches in the converter and active clamp circuit are integrated with a synchronous switching technique to reduce circuit complexity and component counts, resulting in a lower cost and smaller volume [14].

Multilevel inverter consists of an array of power semiconductor switches, capacitor voltage sources, and clamping diodes. The multilevel inverter produces the stepped voltage waveforms with less distortion, less switching frequency, higher efficiency, lower voltage devices, and better electromagnetic compatibility [15]. The commutation (process of turn off) of the switches permits the addition of the capacitor voltages, which reach high voltages at the output [16].

A modular grid-connected PV generation system presents an actual behavioural model of a grid tied PV system suitable for system level investigations. Simplified means for modelling the PV array and investigating a gradient based MPPT into a very simple averaged model of the power converter was developed, and the model has been experimentally vetted [17, 18]. A single-phase grid-connected inverter which is usually used for residential or low-power applications of power ranges that are less than 10 kW [15]. Types of single-phase grid-connected inverters have been investigated [19]. A common topology of this inverter is full-bridge three-level. The three-level inverter can satisfy specifications through its very high switching, but it could also unfortunately increase switching losses, acoustic noise, and level of interference to other equipment. Improving its output waveform reduces its harmonic content and, hence, also the size of the filter used and the level of electromagnetic interference (EMI) generated by the inverter's switching operation [20].

MATLAB-based modelling and simulation scheme which is suitable for studying the *I*-*V* and *P*-*V* characteristics of a PV array under a nonuniform insolation due to partial shading [21] was proposed. The mathematical model of solar PV module is useful for the computer simulation. The power electronics interface, connected between a solar panel and a load or battery bus, is a pulse width modulated (PWM) DC-DC converter or their derived circuits used to extract maximum power from solar PV panel [22]. The main drawback of PV systems is that the output voltage of PV panels is highly dependent on solar irradiance and ambient temperature. Therefore PV panels outputs cannot connect directly to the load. To improve this, a DC-DC boost converter is required to interface between PV panels and loads [23]. The boost converter is fixing the output voltage of the PV system. Converter receives the variable input voltage which is the output of PV panels and gives up constant output voltage across its output capacitors where the loads can be connected. In general, a DC-DC boost converter operates at a certain duty cycle. In this case, the output voltage depends on that duty cycle. If the input voltage is changed while the duty cycle is kept constant, the output voltage will vary. Duty cycle is varied by using a pulse width modulation (PWM) technique [24].

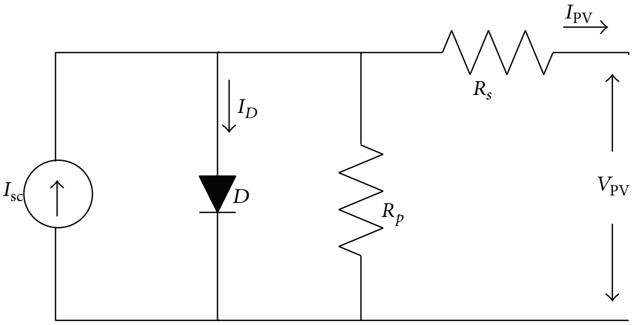

Figure 1: Equivalent circuit of solar PV module.

Silicon carbide (SiC) represents an advance in silicon technology because it allows a larger energy gap. SiC is classified as a wide-band-gap (WBG) material, and it is the mainstream material for power semiconductors [25, 26]. Among the different types of power semiconductors, the power diode was the best device to adopt SiC technology. The main advantage of SiC is high-breakdown voltage and reverse-recovery current is small [27–29]. As a result, higher efficiency and higher power density can be brought to power electronic systems in different applications [30, 31]. In this research, a new active snubber circuit is proposed to contrive a new family of PWM converters. This proposed circuit provides perfectly ZVT turn on and ZCT turn off together for the main switch of a converter by using only one quasiresonant circuit without an important increase in the cost and complexity of the converter. This paper proposes to implement Chaotic PWM as a control method to improve the steady state performance of the DC-DC SEPIC converter based MPPT system for solar PV module. The nominal duty cycle of the main switch of DC-DC SEPIC converter is adjusted so that the solar panel output impedance is equal to the input resistance of the DC-DC converter which results in better spectral performance in the tracked voltages when compared to conventional PWM control. The conversion efficiency of the proposed MPPT system is increased when CPWM is used; this will be compared with parallel boost converter. Multilevel inverters are promising as they have nearly sinusoidal output-voltage waveforms, output current with better harmonic profile, less stressing of electronic components owing to decreased voltages, switching losses that are lower than those of conventional two-level inverters, a smaller filter size, and lower EMI, all of which make them cheaper, lighter, and more compact [29].

2. MATLAB Model of L1235-37W Solar PV Module

The output characteristics of the solar PV module depend on the irradiance and the operating temperature of the cell. The equivalent circuit of PV module is shown in Figure 1.

From Figure 1, the current and voltage equation is given by

$$\begin{gathered} I_{\text{sc}} = I_D + I_{\text{PV}} + \left(\frac{V_D}{R_p}\right), \\ V_{\text{PV}} = V_D - \left(I_{\text{PV}} * R_s\right), \end{gathered} \tag{1}$$

where diode current is $I_D = I_o + (e^{(V_D/V_T)} - 1)$.

Based on the electrical equation (1) and the solar PV module are modelled in MATLAB as shown in Figure 2, which is used to enhance the understanding and predict the V-I characteristics and to analyze the effect of temperature and irradiation variation. If irradiance increases, the fluctuation of the open-circuit voltage is very small. But the short circuit

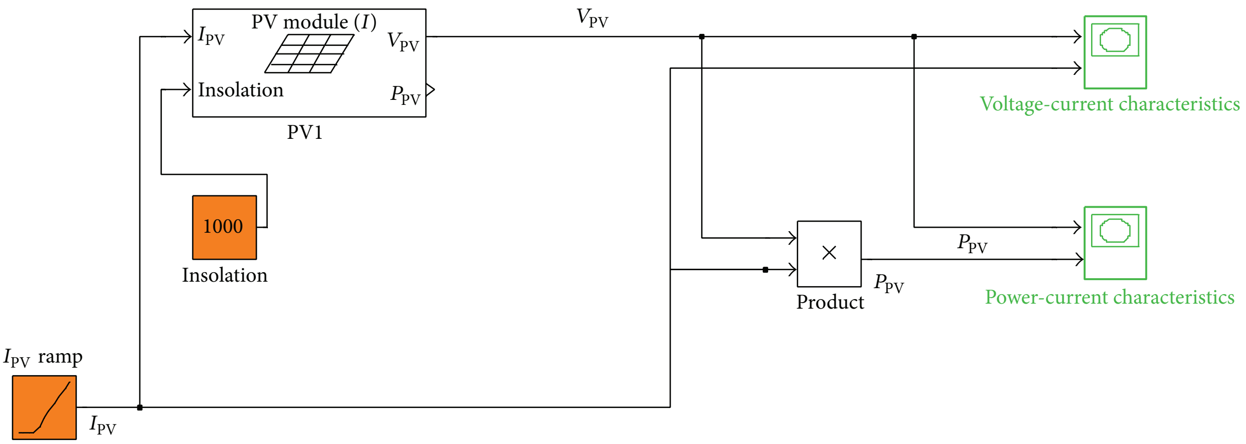

Figure 2: MATLAB model for PV module.

Figure 3: L1235-37W solar module under test.

current has sharp fluctuations with respect to irradiance. However, for a rising operating temperature, the open-circuit voltage is decreased in a nonlinear fashion [4].

The V-I characteristics are validated experimentally in the L1235-37Wp solar module as shown in Figure 3. The technical specifications of L1235-37Wp solar module under test are given in Table 1. Figure 4 shows the V-I characteristics of L1235-37Wp which is based on the experimental results under irradiation $(G) = 1000\ \mathrm{W/m^2}$ and temperature = 25°C.

2.1. Space Modelling of SEPIC Converter Input at MPP. The relation between input and output currents and voltage are given by

$$\frac{V_{\mathrm{OUT}}}{V_{\mathrm{IN}}} = \frac{D}{(1-D)}, \qquad \frac{I_{\mathrm{IN}}}{I_{\mathrm{OUT}}} = \frac{D}{(1-D)}. \tag{2}$$

The duty cycle of the SEPIC converter under continuous conduction mode is given by

$$D = \frac{V_{\mathrm{OUT}} + V_D}{V_{\mathrm{IN}} + V_{\mathrm{OUT}} + V_D}. \tag{3}$$

Table 1: Specifications of L1235-37W solar PV panel.

Short circuit current (I_{sc})	2.5 A
Voltage at MPP (V_m)	16.4
Current at MPP (I_m)	2.25
Open circuit voltage (V_{oc})	21 V
Length	645 mm
Width	530 mm
Depth	34 mm
Weight	4 kg
Maximum power ($P_{\max}$)	37 W

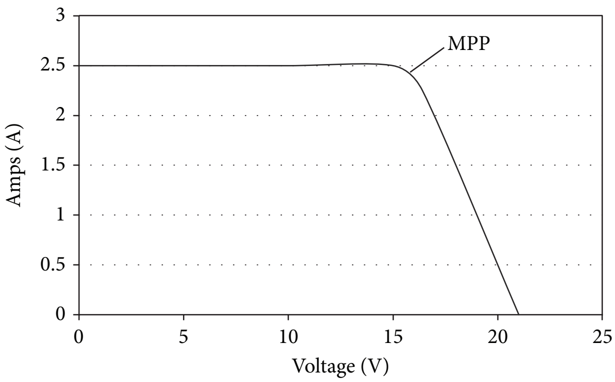

Figure 4: V-I characteristics of L 1235-37W solar panel.

V_D is the forward voltage drop across the diode (D). The maximum duty cycle is

$$D_{\max} = \frac{V_{\mathrm{OUT}} + V_D}{V_{\mathrm{IN(MIN)}} + V_{\mathrm{OUT}} + V_D}. \tag{4}$$

The value of the inductor is selected based on the below equations

$$L_1 = L_2 = L = \frac{V_{\mathrm{IN(MIN)}} * D_{\max}}{\Delta I_L * f_S}. \tag{5}$$

ΔI_L is the peak-to-peak ripple current at the minimum input voltage and f_S is the switching frequency. The value of C_1 depends on RMS current, which is given by

$$I_{C_1(\text{RMS})} = I_{\text{OUT}} * \sqrt{\frac{V_{\text{OUT}} + V_D}{V_{\text{IN(MIN)}}}}. \tag{6}$$

The voltage rating of capacitor C_1 must be greater than the input voltage. The ripple voltage on C_1 is given by

$$\Delta V_{C_1} = \frac{I_{(\text{OUT})} * D_{\max}}{C_1 * f_S}. \tag{7}$$

The parameters governing the selection of the MOSFET are the minimum threshold voltage $V_{\text{th(min)}}$, the on-resistance $R_{\text{DS(ON)}}$, gate-drain charge Q_{GD}, and the maximum drain to source voltage $V_{\text{DS(max)}}$. The peak switch voltage is equal to $V_{\text{IN}} + V_{\text{OUT}}$. The peak switch current is given by

$$I_{Q_1(\text{Peak})} = I_{L_1(\text{PEAK})} + I_{L_2(\text{PEAK})}. \tag{8}$$

The RMS current is given by

$$I_{Q_1(\text{RMS})} = I_{\text{OUT}} \sqrt{\left(V_{\text{OUT}} + V_{\text{IN(MIN)}}\right) * \frac{V_{\text{OUT}}}{V_{\text{IN(MIN)}^2}}}. \tag{9}$$

The total power dissipation for MOSFETs includes conduction loss (as shown in the first term of the above equation) and switching loss (as shown in the second term). I_G is the gate drive current. The $R_{\text{DS(ON)}}$ value should be selected at maximum operating junction temperature and is typically given in the MOSFET datasheet

$$\begin{aligned} P_{\text{switch}} = {} & \left(I_{Q_1(\text{RMS})} * R_{\text{DS(ON)}} * D_{\text{MAX}}\right) \\ & + \left(V_{\text{IN(MIN)}} + V_{\text{OUT}}\right) * I_{Q_1(\text{Peak})} * \frac{\left(Q_{\text{GD}} * f_S\right)}{I_G}. \end{aligned} \tag{10}$$

The output diode must be selected to handle the peak current and the reverse voltage. In a SEPIC converter, the diode peak current is the same as the switch peak current $I_{Q_1(\text{Peak})}$. The minimum peak reverse voltage the diode must withstand is

$$V_{\text{RD}} = V_{\text{IN(MAX)}} + V_{\text{OUT(MAX)}}. \tag{11}$$

2.2. Dynamic Input Characteristics of a SEPIC Converter at MPP. The input voltage and the equivalent input resistance of the converter are V_S and R_i, respectively. As the input power ρ_i to the converter is equal to the output power ρ_o of the solar PV module

$$\rho_i = \rho_o = \frac{V_S^2}{R_i}. \tag{12}$$

The rate of change ρ_i with respect to V_S and R_i can be shown below

$$\partial \rho_i = \frac{2V_S}{R_i}\partial V_S - \frac{V_S^2}{R_i^2}\partial R_i. \tag{13}$$

At the MPP, the rate of change of ρ_i equals zero and $R_i = r_g$

$$\partial \rho_i = 0, \quad \text{hence } \frac{\partial V_S}{\partial R_i} = \frac{V_S}{2R_i}. \tag{14}$$

The equation gives the required dynamic resistance characteristics of the tracker at MPP.

2.3. Generation of Chaotic PWM. In order to improve the steady state performance of solar powered system, direct control Chaotic Pulse width modulated (CPWM) SEPIC converter is proposed to track maximum power from solar PV module. Therefore, in order to get chaotic frequency f_Δ or chaotic amplitude A_Δ, chaos-based PWM (CPWM) is analyzed to generate chaotic PWM. The MATLAB simulation is carried out as shown in Figure 5. The analogue chaotic PWM has its advantages over the digital in its low costs and easy-to-design, making it suitable for high-frequency operation and situations when design flexibility, high converter conversion efficiency, and low cost. In order to generate chaotic pulse width modulation, Chua's diode is used to trigger the main switch of SEPIC converter and to be used for reducing spectral peaks in tracked converter voltage.

The CPWM adopts sawtooth to modulate, but its carrier period T'_Δ changes according to

$$T'_\Delta = \frac{X_i}{\text{Mean}(x)} * T_\Delta, \tag{15}$$

where T_Δ is invariant period, X_i, $i = 1, 2, \ldots N$, a chaotic sequence, $x = (x_1, x_2 \ldots x_N)$, and Mean$(x)$ average of the sequence defined as

$$\text{Mean}(x) = \text{Lim} \sum_{i=1}^{N} \left|X_i\right| \frac{1}{N}; \quad N \longrightarrow \infty. \tag{16}$$

Similarly the CPWM also adopts sawtooth to modulate, but its carrier amplitude A'_Δ changes according to

$$A'_\Delta = \left\{1 + K\frac{X_i}{\text{Mean}(x)}\right\} A_\Delta, \tag{17}$$

where A_Δ is the invariant amplitude, X_i, $i = 1, 2, \ldots N$, a chaotic sequence, $x = (x_1, x_2 \ldots x_N)$ and Mean(x), average of the sequence, and K is the modulation factor of the amplitude which can be set required in practice. The value of K is selected as low so that the ripple in the output voltage of the SEPIC converter is low. Also the ripple in the output voltage controlled by chaotic PWM is low. The analog chaotic carrier is generated based on the circuit; the resistances $(R_{d1} \cdots R_{d6})$ are used to realise linear resistor called Chua diode. The parameters for Chua's diode are designed and chosen as $R_{d1} = 2.4\,\text{k}\Omega$, $R_{d2} = 3.3\,\text{k}\Omega$, $R_{d3} = R_{d4} = 220\,\Omega$, and $R_{d5} = R_{d6} = 20\,\text{k}\Omega$. The other parameters of Chua's oscillator used in the experiment are $L_1 = 2.2\,\text{mH}$, $C_1 = 4.7\,\text{nF}$, $C_2 = 500\,\text{pF}$, and $R = 1.75\,\text{K}\Omega$.

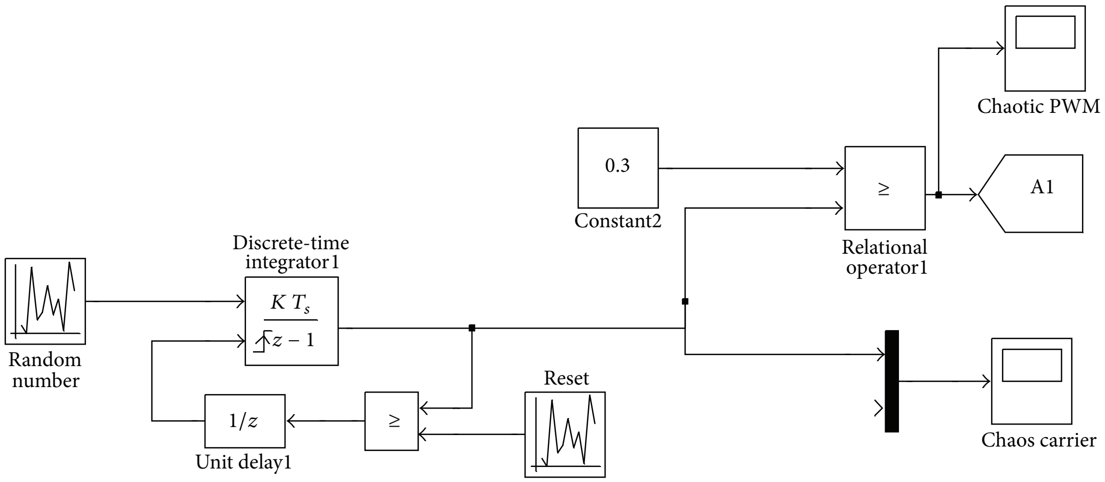

Figure 5: Chaotic PWM pulse generation.

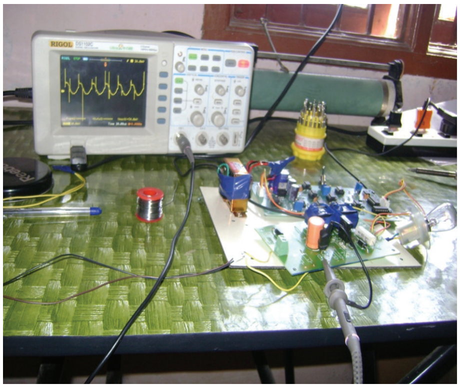

Figure 6: Hardware setup.

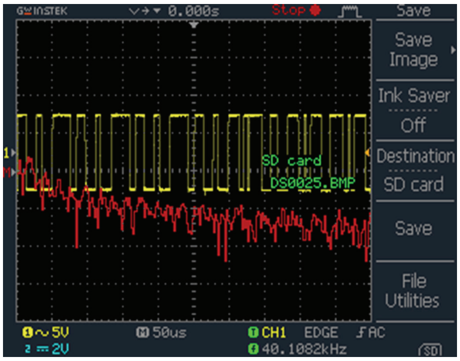

Figure 7: Chaotic PWM.

2.4. Experimental Setup: Standalone PV System. Figure 6 shows the experimental setup of the proposed SEPIC converter-based MPPT for solar PV module, which is constituted by a power stage and a control circuit. The power stage includes an inductor L_1, L_2, capacitor C_1, C_2, a switch S, a load resistance, and a solar PV module (L1235-37Wp). The analog chaotic carrier is generated based on the hardware output of CPWM is in Figure 7.

3. Mathematical Model for Parallel Boost Converter with Active Snubber Circuit

Figure 12 represents the circuit diagram of the parallel boost converter with active snubber. It consists of five inductors L_{fi}, L_{f2}, L_{R1}, L_{R2}, L_n and three capacitors C_s, C_r, C_o, V_g and V_o represents supply and output voltage, respectively; S (S_1, S_2) is an active primary switch, D (D_{f1}, D_{f2}) is a freewheeling diode, D_s (D_1, D_2, D_3) is a Snubber diode, and R_L is the load resistance. S (S_1, S_2, S_3) operates at a switching frequency f_S with duty ratio d.

Choose the switching frequency of switches $S_1 = S_2 = 100$ KHz and $S_3 = 200$ KHz.

When $S_1 = S_2 = 0$ and $S_3 = 1$ as in Figure 8

$$\frac{diL_F}{dt} = \frac{1}{L_F}\left[V_g = V_o\right], \qquad \frac{dV_o}{dt} = \frac{1}{C_o}\left[iL_F - \frac{V_o}{R_L} - iL_S\right]. \tag{18}$$

Also the switches $S_1 = S_2 = S_3 = 1$ as in Figure 9

$$\frac{diL_F}{dt} = \frac{1}{L_F}\left[V_g - V_o\right], \qquad \frac{dV_o}{dt} = \frac{1}{C_o}\left[iL_F - \frac{V_o}{R_L}\right]. \tag{19}$$

Similarly, the switches $S_1 = S_2 = 1$ and $S_3 = 1$ or 0 as in Figure 10

$$\frac{diL_F}{dt} = \frac{V_g}{L_F}, \qquad \frac{dV_o}{dt} = \frac{1}{C_o}\left[-\frac{V_o}{R_L}\right]. \tag{20}$$

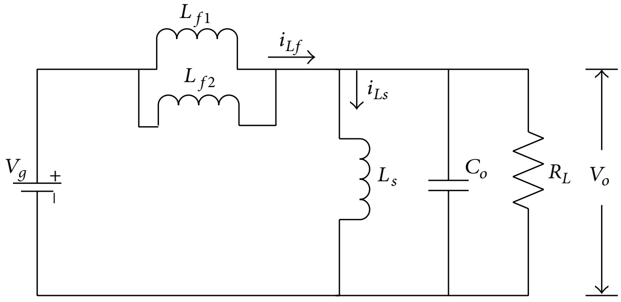

FIGURE 8: When $S_1 = S_2 = 0$ and $S_3 = 1$.

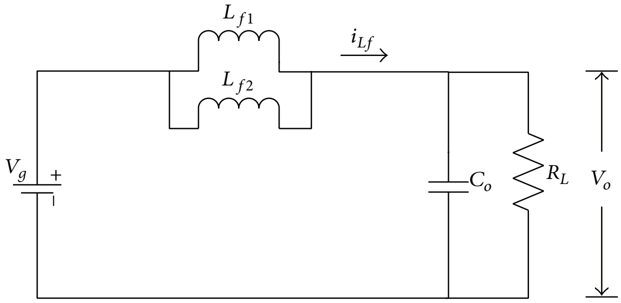

FIGURE 9: When $S_1 = S_2 = S_3 = 1$.

By using state-space averaging method the state equations during switch-on and switch-off conditions are

$$\dot{x}_1 = \frac{-(1-d_1)}{L_F}x_2 - \frac{(1-d_2)}{L_F}x_2 + \frac{V_g}{L_F},$$
$$\dot{x}_2 = \frac{-1}{R_L C_o}x_2 + \frac{(1-d_1)\,d_2}{C_o}x_1 + \frac{(1-d_1)(1-d_2)}{C_o}x_1, \tag{21}$$

where x_1 and x_2 are the moving averages of i_{LF} and V_o, respectively.

4. Proposed Parallel Boost Converter for PV Application

Figure 11 shows the Block Diagram of PV based parallel boost converter with active snubber. It is the combination of new active snubber circuit with parallel boost converter. Three switches S_1, S_2, and S_3 are used; S_1 and S_2 act as main switch and S_3 acts as an auxiliary switch. S_1 and S_2 are controlled by ZVT and ZCT, respectively; also S_3 is controlled by ZCS. This circuit operates with the input of solar power.

Assume both the main switches (S_1 and S_2) operate in the same frequency. The features of proposed parallel boost converter are as follows.

(i) All the semiconductors work with soft switching in the proposed converter.

(ii) The main switches S_1 and S_2 turn on with ZVT and turn off with ZCT.

(iii) The secondary switch is turned on with ZCS and turned off with ZCS.

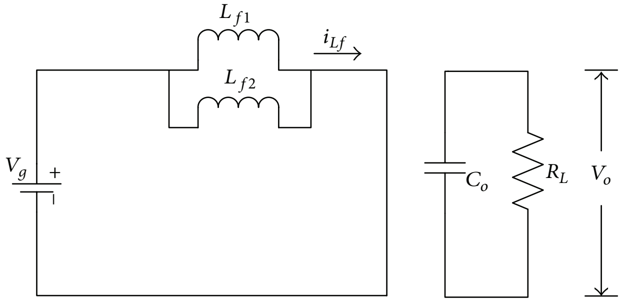

FIGURE 10: When $S_1 = S_2 = 1$ and $S_3 = 1$ or 0.

(iv) All other components of the parallel boost converter functions based on this soft switching.

(v) There is no additional current or voltage force on the main switches S_1 and S_2.

(vi) There is no additional current or voltage force on the secondary switch S_3.

(vii) Also there is no additional current or voltage force on the main diodes D_{f1} and D_{f2}.

(viii) According to the ratio of the transformer, a part of the resonant current is transferred to the output load with the coupling inductance. So there is less current stress on the secondary switch with satisfied points.

(ix) At resistive load condition, in the ZVT process, the main switches voltage falls to zero earlier due to decreased interval time and that does not make a problem in the ZVT process for the main switch.

(x) At resistive load condition, in the ZCT process, the main switches body diode on state time is increased when the input current is decreased. However, there is no effect on the main switch turn off process with ZCT.

(xi) This parallel boost converter operates in high-switching frequency.

(xii) This converter easily controls because the main and the auxiliary switches are connected with common ground.

(xiii) The most attractive feature of this proposed converter is using ZVT and ZCT technique.

(xiv) The proposed new active snubber circuit is easily adopted with other basic PWM converters and also switching converters.

(xv) Additional passive snubber circuits are not necessary for this proposed converter.

(xvi) SIC (silicon carbide) is used in the main and auxiliary diodes, so reverse recovery problem does not arise.

(xvii) The proposed active snubber circuit is also suitable for other DC-DC converters.

4.1. Procedure for Constructing a Proposed Converter. Steps to obtain a system level modeling and simulation of proposed power electronic converter are listed below.

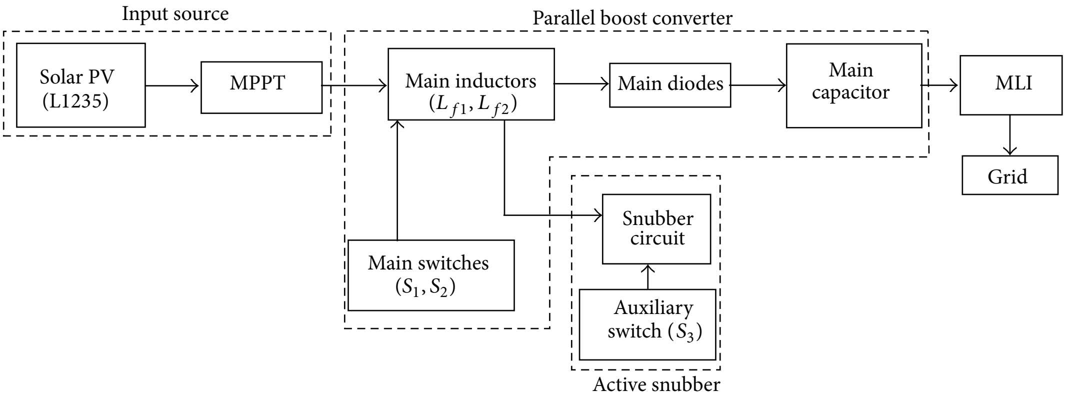

FIGURE 11: Block diagram of PV based parallel boost converter with active snubber.

TABLE 2: Specification of parallel boost converter with active Snubber.

Main inductor L_{f1}	750 μH
Main inductor L_{f2}	750 μH
Upper Snubber inductor L_{R1}	5 μH
Lower Snubber inductor L_{R2} ($L_m + L_d$)	2 μH
Magnetization inductor L_M ($L_n + L_{0l}$)	3 μH
Parasitic capacitor C_s	1 μF
Snubber capacitor C_R	4.7 nF
Output capacitor C_o	330 μF/450 V
Output load resistance $R = R_L$	530 Ω

(i) Determine the state variables of the proposed power circuit in order to write its switched state-space model, for example, inductance current and capacitance voltage.

(ii) Assign integer variables (ON-1 and OFF-0 state) to the proposed power semiconductor to each switching circuit.

(iii) Determine the conditions controlling the states of the proposed power semiconductors or the switching circuit.

(iv) Assume the main operating modes, apply Kirchhoff's Current law and Kirchhoff's Voltage law and combine all the required stages into a switched state-space model, which is the desired system-level of the proposed model.

(v) Implement the derived equations with MATLAB Simulink.

(vi) Use the obtained switched space-state model to design linear or nonlinear controllers for the proposed power converter.

The algorithm for solving the differential equations and the step size should be chosen before running any simulation. This step is only suitable in closed-loop simulations [21].

4.2. Operation of Proposed Boost Converter with Snubber Circuit. The proposed PV based converter is shown in Figure 12, and it is based on a dual boost circuit where the first one (switch S_1 and choke L_{f1}) is used as main chock of boost converter circuit and where the second one (switch S_2 and choke L_{f2}) is used to perform an active filtering. The proposed converter applies active snubber circuit for soft switching. This snubber circuit is built on the ZVT turn on and ZCT turn off processes of the main switches. Specification of proposed parallel boost converter with active snubber is in Table 2.

The power from the solar flows through the two parallel paths. High efficiency was obtained by this method. So as to reach soft switching (SS) for the main and the auxiliary switches, main switches turn on with ZVT and turn off with ZCT. The proposed converter utilizes active snubber circuit for SS. This snubber circuit is mostly based on the ZVT turn on and ZCT turn off processes of the main switch. L_{R2} value is limited with $(V_{\text{out}}/L_{R2})t_{\text{rise}}S_2 \leq I_{i\max}$ to conduct maximum input current at the end of the auxiliary switch rise time $(t_{\text{rise}}S_2)$ and $L_{R1} \geq 2L_{R2}$. To turn off S_1 with ZCT, the duration of t_{ZCT} is at least longer than fall time of $S_1(t_{\text{fall}}S_1)t_{\text{ZCT}} \geq t_{\text{fall}}S_1$. Though the main switches are in off state, the control signal is functional to the auxiliary switch. The parasitic capacitor of the main switch should be discharged absolutely and the main switches antiparallel diode should be turned on. The on state time of the antiparallel diode is named t_{ZVT} and in this time period, the gate signal of the main switch would be applied. So, the main switch is turned on below ZVS and ZCS with ZVT.

Whereas the main switches are in on state and ways input current, the control signal of the auxiliary switch is applied. After the resonant starts, the resonant current should be higher than the input current to turn on the antiparallel diode of the main switch. The on state time of the antiparallel diode (t_{ZCT}) has to be longer than the main switches fall time $(t_{f_{S1}})$. After all these terms are completed, while antiparallel diode is in on state, the gate signal of the main switch should be cutoff to provide ZCT for the main switch. Auxiliary switch turn on with ZCS and turn off with ZCS. The auxiliary switch is turned on with ZCS for the coupling inductance limits the current rise speed.

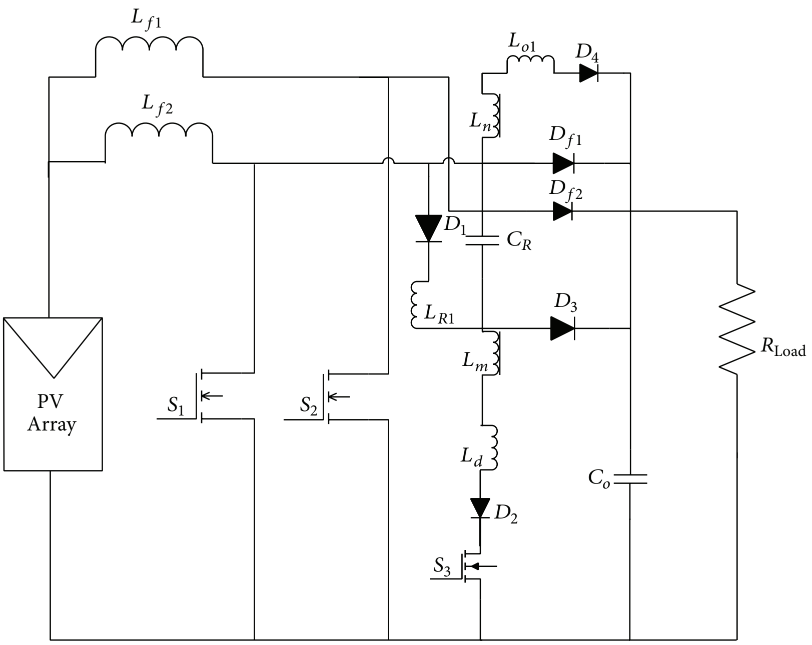

Figure 12: Circuit diagram of PV based parallel boost converter with active snubber with resistive load.

The current passing through the coupling inductance must be partial to conduct maximum input current at the end of the auxiliary switch rise time (t_{rS3}). So, the turn on process of the auxiliary switch with ZCS is offered. To turn off the auxiliary switch with ZCS, though the auxiliary switch is in on state, the current passing through the switch should fall to zero with a new resonant. Then, the control signal can be cutoff. If C_S is ignored, L_{R1} value should be two times added with L_{R2} to make the auxiliary switch current fall to zero. As the current cannot stay at zero as long as the auxiliary switch fall time (t_{fs_3}), the auxiliary switch is turned off nearly with ZCS.

The proposed Simulink topology is shown in Figure 13. The inductors L_{f1} and L_{f2} have the similar values, the diodes D_{f1}-D_{f2} are at the same type and the same guess was for the switches (S_1 & S_2). All the inductors have individual switches and they resemble paralleling of classic converters.

5. Design of MLI Module

A multilevel converter is a power electronic system that synthesizes a desired output voltage levels from the DC inputs supply. Compared with the traditional two-level voltage converter, the primary advantage of multilevel converters is their smaller output voltage step, which results in high power quality, lower harmonic components, better electromagnetic compatibility, and lower switching losses. The functionality verification of the simplified seven-level inverter is done using MATLAB simulation which is shown in Figure 14.

This single-phase simplified seven-level inverter was developed using a single-phase full bridge (H-bridge) inverter, two bidirectional auxiliary switches, and a capacitor voltage divider formed by C_1, C_2, and C_3, as shown in Figure 14. The simplified multilevel inverter topology is significantly advantageous over other topologies. The advantages of simplified topology are requirement of less power switch, power diodes, and less capacitors for this inverter. Photovoltaic arrays were connected to the inverter via a DC-DC SEPIC converter. The power generated by the inverter is to be delivered to the power network, so the utility grid, rather than a load, was used. The DC-DC SEPIC converter was required because the PV arrays had a voltage that was lower than the grid voltage. High DC bus voltages are necessary to ensure that power flows from the PV arrays to the grid. A filtering inductance L_f was used to filter the current injected into the grid. Proper switching of the inverter can produce seven levels of output-voltage (V_{dc}, $2V_{dc}/3$, $V_{dc}/3$, 0, 0^*, $-V_{dc}/3$, $-2V_{dc}/3$, $-V_{dc}$) from the DC supply voltage. Table 3 shows the switching pattern for the single-phase simplified seven-level inverter.

Table 3: Switching pattern for the single-phase seven-level inverter.

V_0	S_1	S_2	S_3	S_4	S_5	S_6
V_{dc}	1	0	0	1	0	0
$2V_{dc}/3$	0	0	0	1	1	0
$V_{dc}/3$	0	0	0	1	0	1
0	0	0	1	1	0	0
0^*	1	1	0	0	0	0
$-V_{dc}/3$	0	1	0	0	1	0
$-2V_{dc}/3$	0	1	0	0	0	1
$-V_{dc}$	0	1	1	0	0	0

6. Grid-Connected Solar Power System

The modelling and simulation of PV, MPPT, CPWMSEPIC converter, simplified seven-level MLI, and controller had

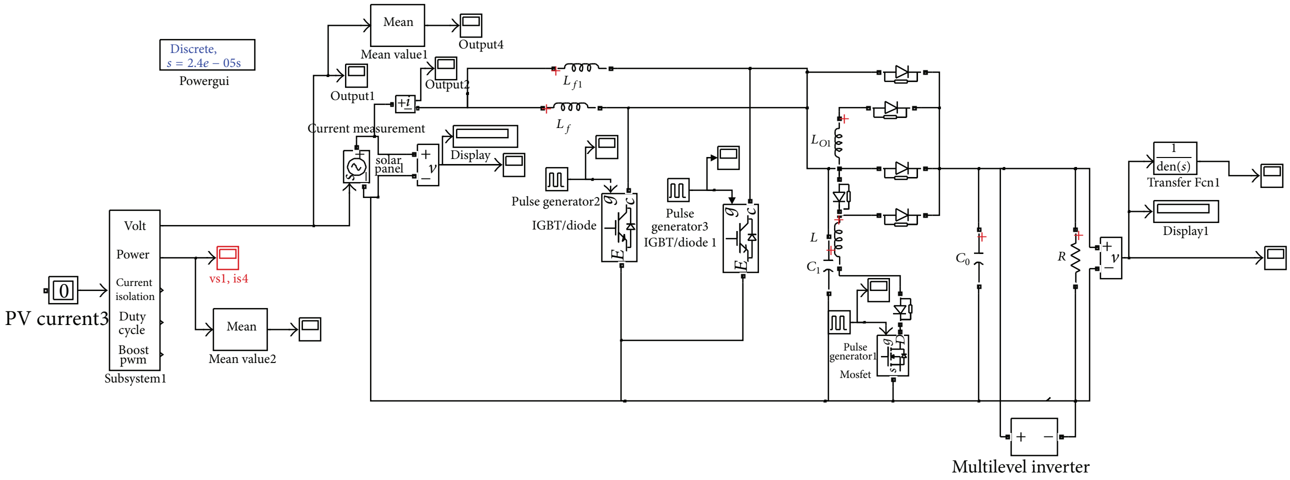

Figure 13: Simulink model of proposed PV based parallel boost converter with active snubber circuit with MLI.

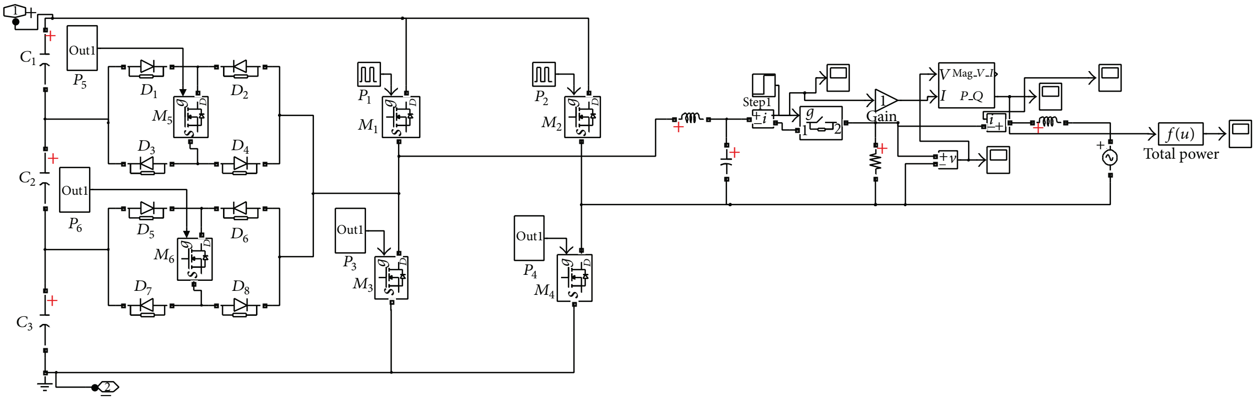

Figure 14: Simulated model for seven-level inverter.

been carried out in MATLAB Simulink environment. The basic block diagram of reliable high efficient grid-connected solar power system has been shown in Figure 15.

The grid-connected PV system consists of MPPT tracking using SEPIC converter which is used to track the maximum voltage. The tracked voltage is boosted in to 325 V. A simplified seven-level MLI is designed to convert into an AC voltage with seven levels which should connect to grid. The simulated results for the MLI output are in Figures 16 and 17.

7. Results and Discussions

A modular solar PV based DC-DC converter using parallel boost converter with active filter of the proposed system is simulated using MATLAB Simulink program. The waveforms of parallel boost converter voltage and MLI filtered output voltage is shown in Figures 18 and 19. The control signals of the switches are shown in Figures 20 and 21, respectively. The simulation results show the proposed PV based soft switched parallel boost DC-DC converter has the proper response. The detailed comparison of SEPIC and parallel boost converter is in Table 4.

Table 4: Comparison of SEPIC and parallel boost converter.

Parameters	SEPIC converter	Parallel boost converter
Duty cycle	45%	47%
No. of switches	7	9
Input	148	148
Output	325 V	448 V
Efficiency	92.15%	98.7%

8. Conclusion

The behaviour of solar module (L1235-37Wp) is studied. The maximum power is extracted from solar PV module using CPWM and PWM for different converters. The spectrum performance is improved when CPWM control is used for MPPT purposes. The performance of MLI is studied and the proto type model of MLI is carried out. The main objective of this research was to improve efficiency of the solar PV based parallel boost converter and reduce the switching losses. Simulations were initially done for conventional boost converter with snubber circuit. The changes in the input current waveform were obtained. A parallel boost converter

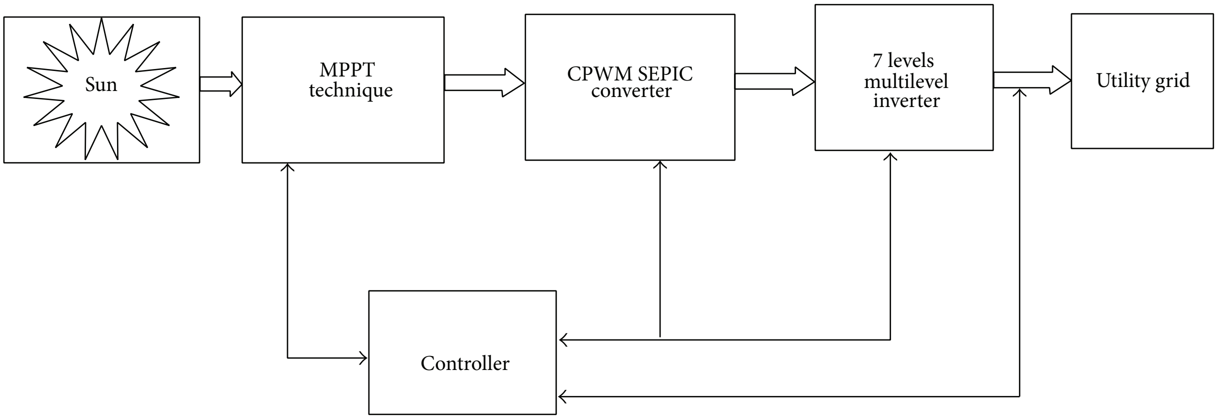

Figure 15: Block diagram of reliable high efficient grid-connected solar power system.

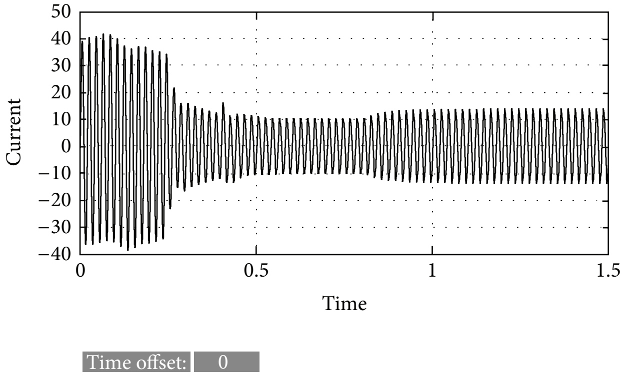

Figure 16: MLI output current.

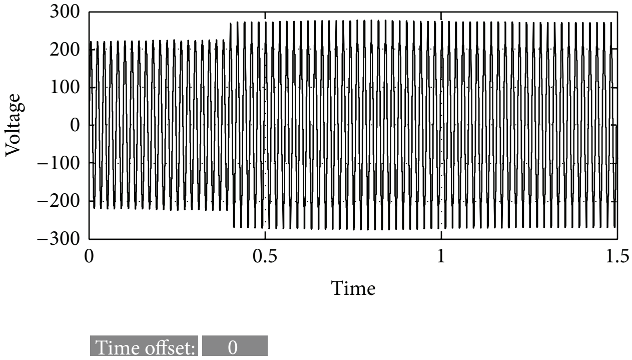

Figure 17: MLI output voltage.

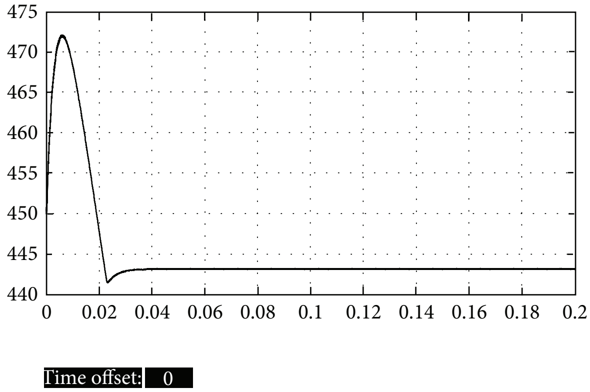

Figure 18: Parallel boost converter output voltage.

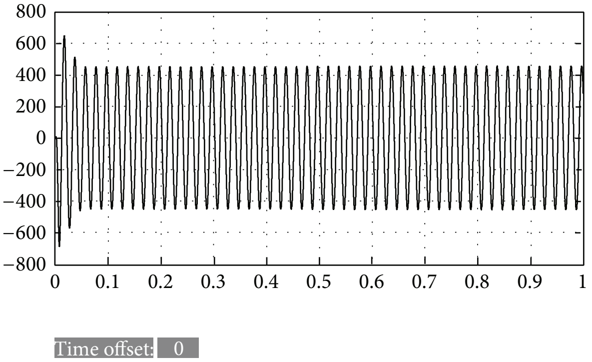

Figure 19: MLI filtered output voltage (V_o).

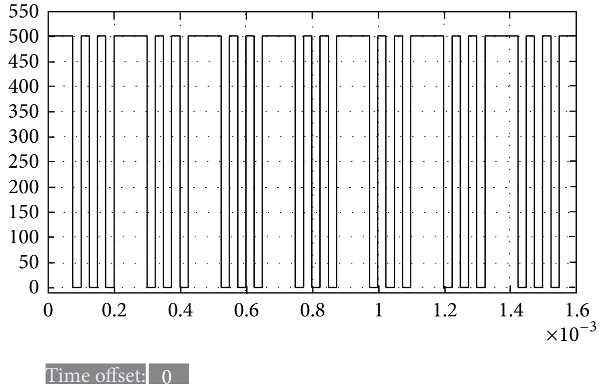

Figure 20: Control signals of switches S_1 and S_2.

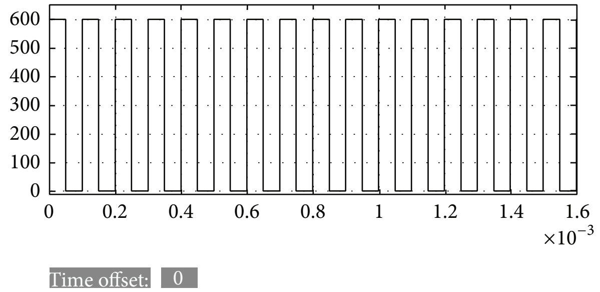

Figure 21: Control signals of switch S_3.

was designed with soft switching which is provided by the active snubber circuit. The main switches and all the other semiconductors were switched by ZVT and ZCT techniques. The active snubber circuit was applied to the parallel boost converter, which is fed by solar input line. This latest converter was achieved with 148 V input. Due to the main and the auxiliary switches have a common ground, the converter was controlled easily. The proposed new active snubber circuit can be simply functional to the further basic PWM converters and to all switching converters thereby increasing efficiency and improving output voltage.

Conflict of Interests

The authors declare that there is no conflict of interests regarding the publication of this paper.

References

[1] J. A. Gow and C. D. Manning, "Development of a photovoltaic array model for use in power-electronics simulation studies," *IEE Proceedings*, vol. 146, no. 2, pp. 193–200, 1999.

[2] H. Patel and V. Agarwal, "MATLAB-based modeling to study the effects of partial shading on PV array characteristics," *IEEE Transactions on Energy Conversion*, vol. 23, no. 1, pp. 302–310, 2008.

[3] M. G. Villalva, J. R. Gazoli, and E. R. Filho, "Comprehensive approach to modeling and simulation of photovoltaic arrays," *IEEE Transactions on Power Electronics*, vol. 24, no. 5, pp. 1198–1208, 2009.

[4] G. Walker, "Evaluating MPPT converter topologies using a matlab PV model," *Journal of Electrical and Electronics Engineering*, vol. 21, no. 1, pp. 49–56, 2001.

[5] H. S.-H. Chung, K. K. Tse, S. Y. Ron Hui, C. M. Mok, and M. T. Ho, "A novel maximum power point tracking technique for solar panels using a SEPIC or Cuk converter," *IEEE Transactions on Power Electronics*, vol. 18, no. 3, pp. 717–724, 2003.

[6] M. Veerachary, "Power tracking for nonlinear PV sources with coupled inductor SEPIC converter," *IEEE Transactions on Aerospace and Electronic Systems*, vol. 41, no. 3, pp. 1019–1029, 2005.

[7] K. K. Tse, B. M. T. Ho, H. S.-H. Chung, and S. Y. R. Hui, "A comparative study of maximum-power-point trackers for photovoltaic panels using switching-frequency modulation scheme," *IEEE Transactions on Industrial Electronics*, vol. 51, no. 2, pp. 410–418, 2004.

[8] K. K. Tse, M. T. Ho, H. S.-H. Chung, and S. Y. R. Hui, "A novel maximum power point tracker for PV panels using switching frequency modulation," *IEEE Transactions on Power Electronics*, vol. 17, no. 6, pp. 980–989, 2002.

[9] M. H. Taghvaee, M. A. M. Radzi, S. M. Moosavain, H. Hizam, and M. Hamiruce Marhaban, "A current and future study on non-isolated DC-DC converters for photovoltaic applications," *Renewable and Sustainable Energy Reviews*, vol. 17, pp. 216–227, 2013.

[10] A. Safari and S. Mekhilef, "Simulation and hardware implementation of incremental conductance MPPT with direct control method using cuk converter," *IEEE Transactions on Industrial Electronics*, vol. 58, no. 4, pp. 1154–1161, 2011.

[11] H. Li, Z. Li, B. Zhang, F. Wang, N. Tan, and W. A. Halang, "Design of analogue chaotic PWM for EMI suppression," *IEEE Transactions on Electromagnetic Compatibility*, vol. 52, no. 4, pp. 1001–1007, 2010.

[12] H. Li, W. K. S. Tang, Z. Li, and W. A. Halang, "A chaotic peak current-mode boost converter for EMI reduction and ripple suppression," *IEEE Transactions on Circuits and Systems II*, vol. 55, no. 8, pp. 763–767, 2008.

[13] Z. Wang, K. T. Chau, and C. Liu, "Improvement of electromagnetic compatibility of motor drives using chaotic PWM," *IEEE Transactions on Magnetics*, vol. 43, no. 6, pp. 2612–2614, 2007.

[14] S.-Y. Tseng and H.-Y. Wang, "A photovoltaic power system using a high step-up converter for DC load applications," *Energies*, vol. 6, pp. 1068–1100, 2013.

[15] V. G. Agelidis and M. Calais, "Application specific harmonic performance evaluation of multicarrier PWM techniques," in *Proceedings of the 29th Annual IEEE Power Electronics Specialists Conference (PESC '98)*, pp. 172–178, 1998.

[16] Y. Cheng, C. Qian, M. L. Crow, S. Pekarek, and S. Atcitty, "A comparison of diode-clamped and cascaded multilevel converters for a STATCOM with energy storage," *IEEE Transactions on Industrial Electronics*, vol. 53, no. 5, pp. 1512–1521, 2006.

[17] L. Zhang, K. Sun, Y. Xing, L. Feng, and H. Ge, "A modular grid-connected photovoltaic generation system based on DC bus," *IEEE Transactions on Power Electronics*, vol. 26, no. 2, pp. 523–531, 2011.

[18] M. E. Ropp and S. Gonzalez, "Development of a MATLAB/simulink model of a single-phase grid-connected photovoltaic system," *IEEE Transactions on Energy Conversion*, vol. 24, no. 1, pp. 195–202, 2009.

[19] N. A. Rahim, K. Chaniago, and J. Selvaraj, "Single-phase seven-level grid-connected inverter for photovoltaic system," *IEEE Transactions on Industrial Electronics*, vol. 58, no. 6, pp. 2435–2443, 2011.

[20] H. S. Patel and R. G. Hoft, "Generalized techniques of harmonic elimination and voltage control in thyristor inverters—1. harmonic elimination," *IEEE Transactions on Industry Applications*, vol. IA-9, no. 3, pp. 310–317, 1973.

[21] T. Esram and P. L. Chapman, "Comparison of photovoltaic array maximum power point tracking techniques," *IEEE Transactions on Energy Conversion*, vol. 22, no. 2, pp. 439–449, 2007.

[22] E. J. Durán, M. Galán, Sidrach-de-Cardona, and J. M. Andújar, "Measuring the I-V curve of photovoltaic generators-analyzing different DC-DC converter topologies," *IEEE Industrial Electronics Magazine*, pp. 4–14, 2009.

[23] J. L. Santos, F. Antunes, A. Chehab, and C. Cruz, "A maximum power point tracker for PV systems using a high performance boost converter," *Solar Energy*, vol. 80, no. 7, pp. 772–778, 2006.

[24] W. Jiang and B. Fahimi, "Active current sharing and source management in fuel cellbattery hybrid power system," *IEEE Transactions on Industrial Electronics*, vol. 57, no. 2, pp. 752–761, 2010.

[25] M. Bhatnagar and B. J. Baliga, "Comparison of 6H-SiC, 3C-SiC, and Si for power devices," *IEEE Transactions on Electron Devices*, vol. 40, no. 3, pp. 645–655, 1993.

[26] Q. Zhang, R. Callanan, M. K. Das, S.-H. Ryu, A. K. Agarwal, and J. W. Palmour, "SiC power devices for microgrids," *IEEE Transactions on Power Electronics*, vol. 25, no. 12, pp. 2889–2896, 2010.

[27] A. Elasser, M. H. Kheraluwala, M. Ghezzo et al., "A comparative evaluation of new silicon carbide diodes and state-of-the-art silicon diodes for power electronic applications," *IEEE Transactions on Industry Applications*, vol. 39, no. 4, pp. 915–921, 2003.

[28] M. M. Hernando, A. Fernández, J. García, D. G. Lamar, and M. Rascón, "Comparing Si and SiC diode performance in commercial AC-to-DC rectifiers with power-factor correction," *IEEE Transactions on Industrial Electronics*, vol. 53, no. 2, pp. 705–707, 2006.

[29] B. Ozpineci and L. M. Tolbert, "Characterization of SiC Schottky diodes at different temperatures," *IEEE Power Electronics Letters*, vol. 1, no. 2, pp. 54–57, 2003.

[30] G. Spiazzi, S. Buso, M. Citron, M. Corradin, and R. Pierobon, "Performance evaluation of a Schottky SiC power diode in a boost PFC application," *IEEE Transactions on Power Electronics*, vol. 18, no. 6, pp. 1249–1253, 2003.

[31] A. M. Abou-Alfotouh, A. V. Radun, H.-R. Chang, and C. Winterhalter, "A 1-MHz hard-switched silicon carbide DC-DC converter," *IEEE Transactions on Power Electronics*, vol. 21, no. 4, pp. 880–889, 2006.

Hindawi Publishing Corporation
International Journal of Photoenergy
Volume 2014, Article ID 692934, 13 pages
http://dx.doi.org/10.1155/2014/692934

Research Article

A Different Three-Port DC/DC Converter for Standalone PV System

Nimrod Vázquez,[1,2] Carlos Manuel Sanchez,[3] Claudia Hernández,[1] Eslí Vázquez,[4] Luz del Carmen García,[1] and Jaime Arau[5]

[1] *Electronics Engineering Department, Technological Institute of Celaya, 38010 Celaya, GTO, Mexico*
[2] *Applied Mathematics Division, Potosino Institute of Scientific and Technological Research, 78216 San Luis Potosi, SLP, Mexico*
[3] *Electrical Engineering Department, Michoacana University, 58030 Morelia, MICH, Mexico*
[4] *Engineering Faculty, Veracruz University, 94294 Boca del Rio, VER, Mexico*
[5] *Electronics Engineering Department, Cenidet, 62490 Cuernavaca, MOR, Mexico*

Correspondence should be addressed to Nimrod Vázquez; n.vazquez@ieee.org

Received 29 November 2013; Revised 17 January 2014; Accepted 17 January 2014; Published 2 March 2014

Academic Editor: Ismail H. Altas

A three-port converter suitable for standalone applications is proposed in this paper. Each port is used for specific input or output, and its functions depend on the port; they are the renewable source, the battery set, and the output port. This proposed converter is considered for standalone operation, but it is not limited to it. Not only the system is able to deliver energy independently from each input source or in a mixed way for the output, but also the battery system may be charged from the renewable source just in case it is required. The battery port is only used when it is required; this allows increasing battery lifetime. Another important feature is that, in case of a renewable source failure, the energy is automatically demanded from the battery set, like an uninterruptible power supply. The system is able to track the maximum power of the renewable source when it is required. Operation, analysis, simulation, and experimental results are described in detail.

1. Introduction

Since fossil fuels are depleting, it is important to study some different choices in order to be able to supply the required worldwide energy. Renewable energy is taken into account more seriously nowadays. There exist applications of renewable energy which employ hundreds of MW (high power) and there are also those which use hundreds of W (low power). Applications may be distinguished depending on if they are connected to the grid or not, also known as cogeneration or standalone systems, respectively; the last one is especially employed in remote places, where utility is not available. The proposed converter can be used in remote places where the utility is not available, but also as satellite power supply, electric vehicles, and other applications that consider a battery set as an input.

Photovoltaic panel arrays should be the main source of energy in standalone systems. Since there is no utility line, which implies that an effective use of energy is very important, a battery set is needed in order to be able to supply energy in case the renewable source is an irregular way; leaving aside the power management a power converter stage is needed in order to assure output power. DC/DC converters suitable for standalone applications can be classified into multistage or integrated-stage topologies (Figure 1).

Multistage converters [1–12] are able to control each input independently but share a single output, with the aid of a common DC bus voltage, as shown in Figure 1(a); for standalone operation this configuration implies a bidirectional converter for the battery port; as a consequence, operation becomes complex because both sources should be able not only to deliver energy but also to manage the battery charging/discharging. In these schemes the energy to charge

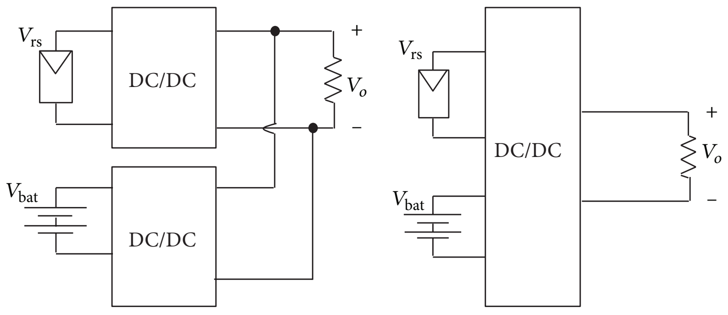

(a) (b)

FIGURE 1: Standalone systems: (a) multistage, (b) integrated stage.

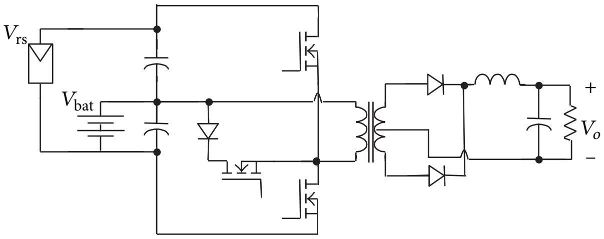

FIGURE 2: Three-port converter proposed in [8].

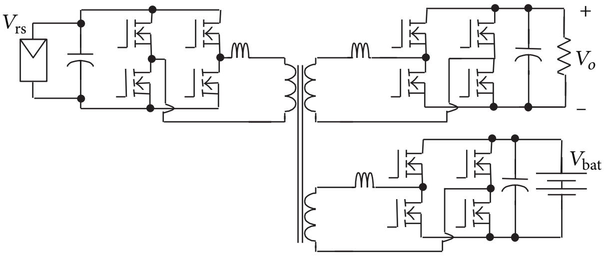

FIGURE 3: Three-port converter proposed in [9].

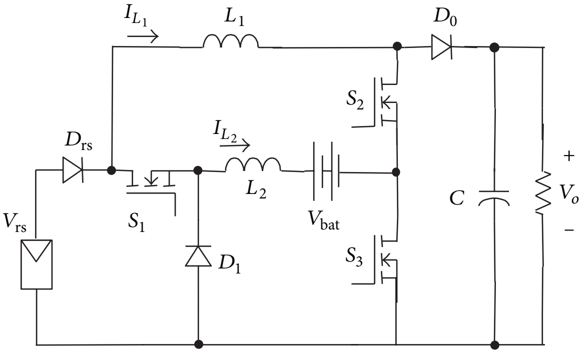

FIGURE 4: Proposed converter.

the battery is processed twice, the first one to deliver energy to the common bus and then to charge the battery.

Integrated-stage converters [1–11] should be able to demand current from both inputs in the easiest way (Figure 1(b)). Some of them do not include bidirectional converters, and the battery charging is not possible unless another converter is considered [5, 6]. There are three-port converters, suggested in the literature, that consider a battery set [7–12].

Proposal in [8] is shown in Figure 2; unfortunately this configuration uses the battery set during all the different modes of operation, which reduces its lifetime. Figure 3 shows a converter based on full-bridge inverter and a transformer [9]; mainly the disadvantage of this topology is the semiconductors count. There are other schemes for three-port converter [10–12], but these are very similar to those two mentioned previously.

A different three-port converter topology is proposed in this paper; not only semiconductors count is reduced and the battery set is used when it is only required to do so, but also the power flow is controlled easily. The system accepts two input voltages and the energy may be supplied from both inputs simultaneously or independently, depending on the availability of the input voltage source. One of these inputs is the battery set, which may be charged from the renewable source if it is necessary. Battery set is involved only when the system requires it, so that its lifetime increases.

Information is organized in this paper as follows: three-port converter proposal is discussed in Section 2, which includes system operation and analysis. Section 3 is addressed for control operation of the proposed system. Experimental results are discussed in Section 4, and some final conclusions are given.

2. Proposed Three-Port Converter

Three-port converter proposal, shown in Figure 4, is suitable for renewable energy application, especially for standalone applications, where a battery set and power flow management are required. This last feature can be carried out easily in the proposed converter.

The system is composed of three switches, three diodes, two inductors, and one capacitor, as shown in Figure 4. Each switch determines the operation of the system; this allows an easy and good power management.

For standalone systems energy is mainly provided from renewable source, which depends on weather conditions. Then the battery set is considered in order to guarantee

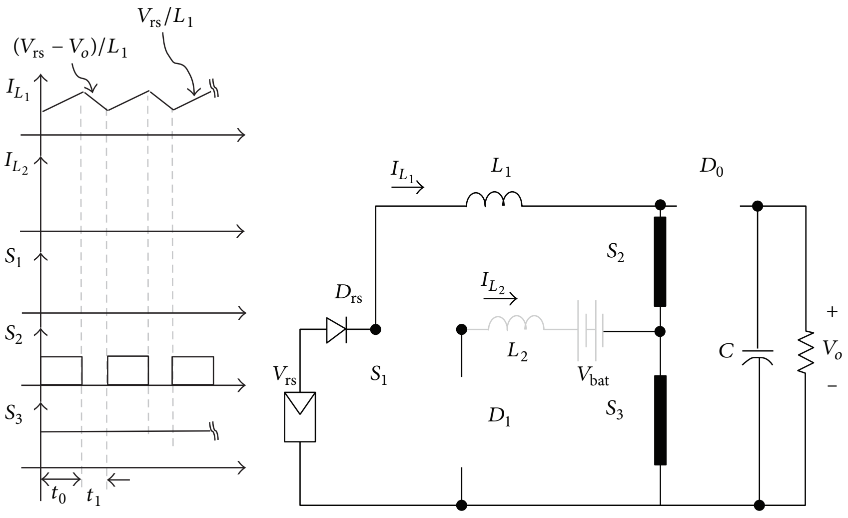

(a) Waveforms (b) Subcircuit for t_0

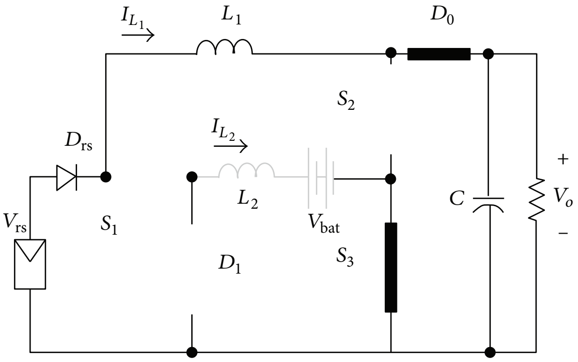

(c) Subcircuit for t_1

Figure 5: Waveforms and subcircuits when the energy is obtained from the renewable source (mode 1, no charging).

energy supply. Since energy consumption is restricted to a maximum limit, this has to be optimized.

When considering a photovoltaic system and a specific load connected in the standalone operation, there exist many different possibilities; these scenarios must be taken into account in the power converter in order to provide a constant and regulated output voltage no matter weather conditions. Each scenario considers different stages depending on the required functions; next are described the operating modes of the system.

2.1. Mode 1: Delivered Energy from the Renewable Source.

2.1. Mode 1: Delivered Energy from the Renewable Source. This mode happens when there is enough energy to feed the load; however the battery set may be charged or not depending on its conditions. Particularly for this operation mode, the switch S_3 is turned on all the time (Figures 5 and 6). Then S_2 is used to regulate the output voltage, and S_1 is used to charge the battery set. The two switches are easily controlled independently, because these are uncoupled.

In this mode the renewable source voltage is higher than the battery set voltage, and then the diode in antiparallel of S_1 is not conducing even if the battery is being charged.

2.1.1. When No Battery Charging. Waveforms for this mode are shown in Figure 5(a). In these conditions the converter operates as described next.

(1) *During* t_0. S_1 is off and S_2 and S_3 are on, the equivalent subcircuit is shown in Figure 5(b), and then the inductor L_1 is being charged with the renewable source; the load is fed only by the output capacitor.

(2) *During* t_1. S_1 remains off and S_3 remains on, but S_2 is turned off, the equivalent subcircuit is shown in Figure 5(c), and then energy stored at the inductor L_1 is delivered to the output capacitor.

2.1.2. When Battery Charging. Waveforms for this mode are shown in Figure 6(a). In these conditions the converter operates as described next.

(1) *During* t_0. S_3 is on, but also S_1 and S_3 are turned on; the equivalent subcircuit is shown in Figure 6(b), so that inductors L_1 and L_2 are charged with the renewable source. Load is only fed from the output capacitor.

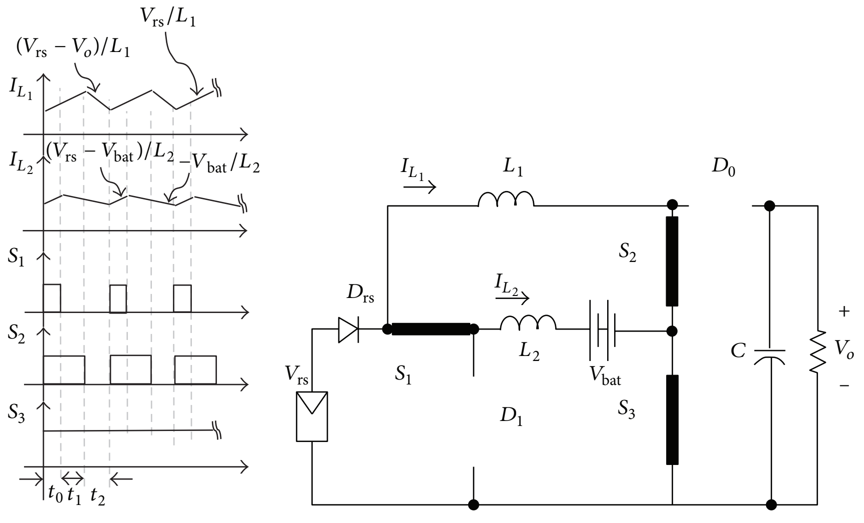

(a) Waveforms (b) Subcircuit for t_0

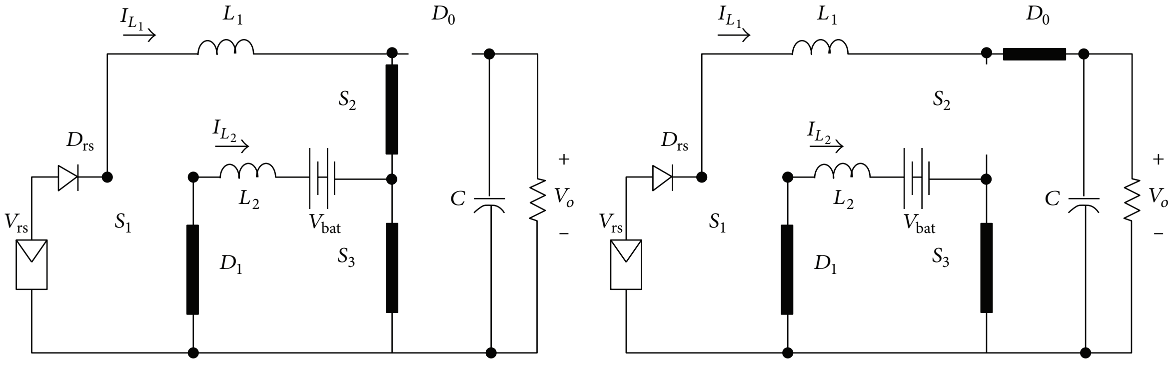

(c) Subcircuit for t_1 (d) Subcircuit for t_2

FIGURE 6: Waveforms and subcircuits when the battery set is being charged (mode 1, charging).

(2) *During* t_1. S_3 remains on and S_1 may be turned off, but S_2 is still on; the equivalent subcircuit is shown in Figure 6(c), so that inductor L_1 is still charged, while inductor L_2 is discharged into the battery set and by the diode D_1.

(3) *During* t_2. S_3 remains on, but now S_1 and S_2 are off; the equivalent subcircuit is shown in Figure 6(d), so that stored energy at inductors L_1 and L_2 is delivered to the output capacitor and the battery set, respectively.

In this mode of operation, the switch S_2 is always used to control the output voltage. And the switch S_1 is used to control the charge of the battery set; a MPPT tracker is used for this purpose; except when the renewable energy available is too high, then the current for charging the battery is limited to a maximum value. The energy is taken from the renewable source.

2.2. Mode 2: Delivered Power from the Battery Set. This mode occurs if the photovoltaic panel has no energy (point A in Figure 7) or if the maximum energy which may be obtained from the panel (point B in Figure 7) is lower than the output power (point C in Figure 7); then it is necessary to use a battery in order to deliver the required amount of energy to the load.

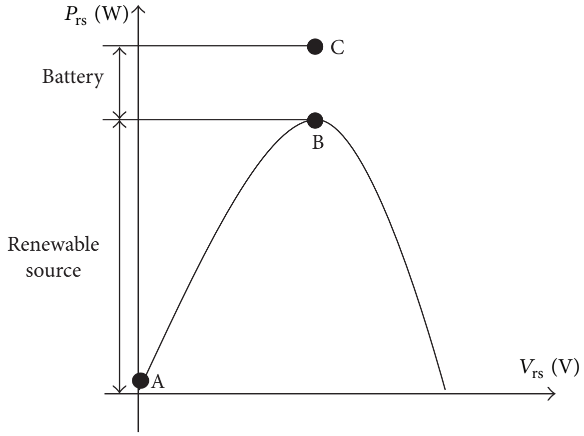

FIGURE 7: Characteristic waveforms of renewable sources and different power outputs.

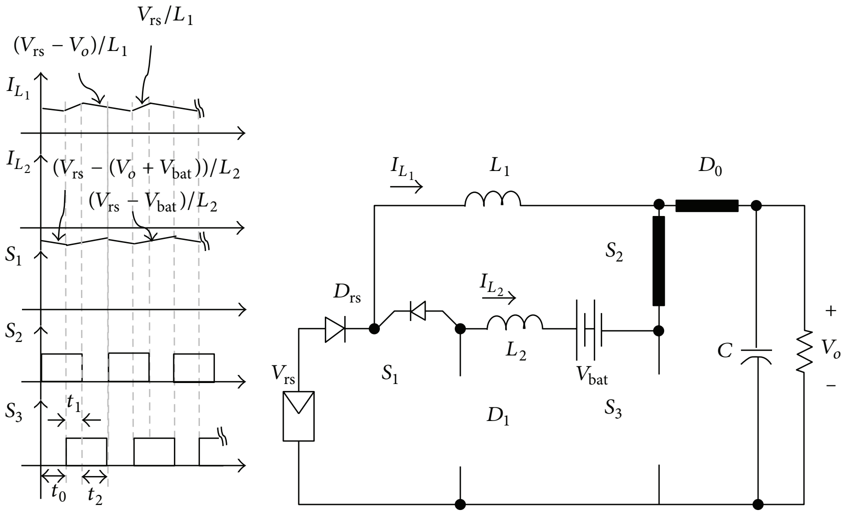

(a) Waveforms

(b) Subcircuit for t_0

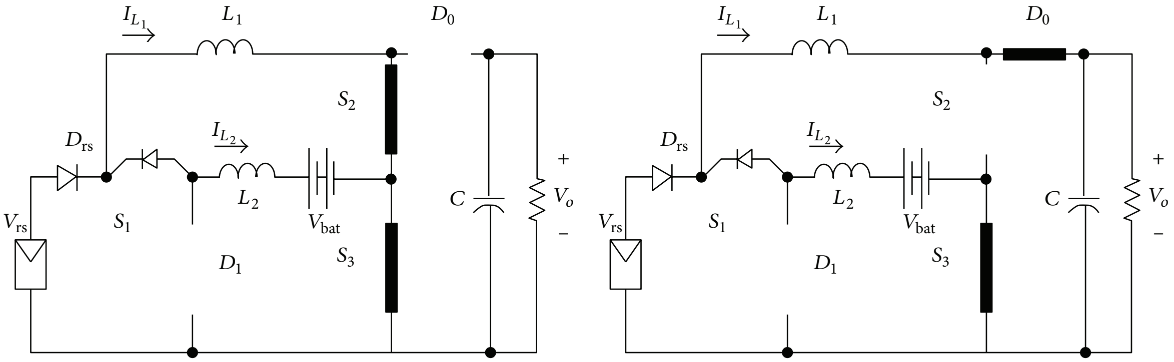

(c) Subcircuit for t_1

(d) Subcircuit for t_2

Figure 8: Waveforms and subcircuits when the energy is obtained from both sources (mode 2, energy available from renewable source).

By assuming that the converter is operated in mode 1 (switch S_3 is on), and suddenly the renewable source suffers a power variation that reduces its power capacity for any circumstance, the battery set is automatically connected to the inductor L_1 through the diode in antiparallel of S_1, acting as uninterruptible power supply; therefore the power to the load is guaranteed, no matter weather conditions.

The above implies that the operation mode 2 occurs without any change to the switch control signals of mode 1. However the energy demanded to the renewable source could not be the maximum available from it; therefore the switch S_3 is used to track the maximum power point during mode 2.

2.2.1. When Energy Available in Renewable Source. Waveforms for this mode are shown in Figure 8(a). In these conditions the converter operates as described next.

(1) *During* t_0. S_1 and S_3 are off, but S_2 is on; the equivalent subcircuit is shown in Figure 8(b); the inductors L_1 and L_2 are discharged.

(2) *During* t_1. S_1 remains off, but S_2 and S_3 are turned on; the equivalent subcircuit is shown in Figure 8(c), and inductors L_1 and L_2 are charged from the renewable source. Load is only fed from the output capacitor.

(3) *During* t_2. S_1 is still off and S_3 remains on, but S_2 is turned off; the equivalent subcircuit is shown in Figure 8(d). Stored energy at inductor L_1 is delivered to the output, while L_2 is charged.

During all these stages the battery set and the renewable source are delivering energy. It should be noticed that the current in L_2 is negative because the battery is delivering energy; therefore the diode D_1, in antiparallel of S_1, is conducting even if control signal of S_1 is off.

2.2.2. When Energy Available Only in Battery Set. Waveforms for this mode are shown in Figure 9(a). In these conditions the converter operates as described next.

(1) *During* t_0. S_1 is off, but S_2 and S_3 are on; the equivalent subcircuit is shown in Figure 9(b), so that both inductors L_1 and L_2 are charged with energy provided from the battery set. Load is only fed from the output capacitor.

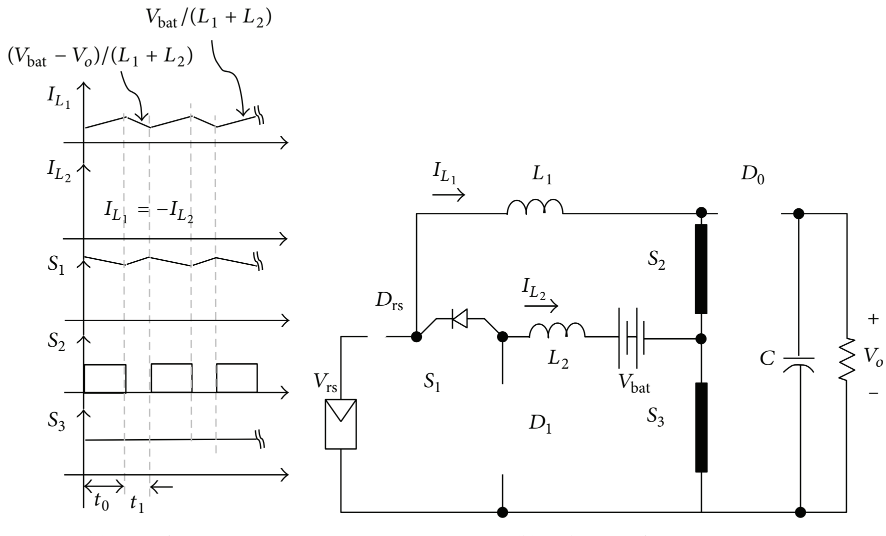

(a) Waveforms

(b) Subcircuit for t_0

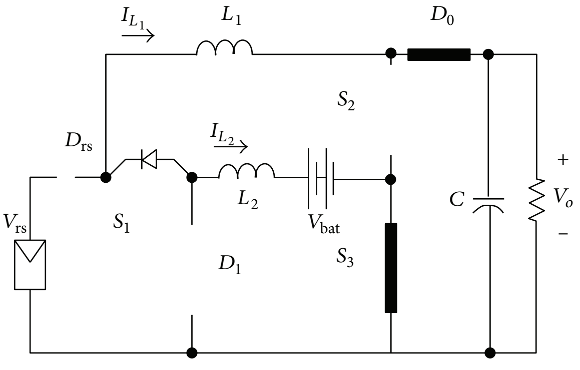

(c) Subcircuit for t_1

Figure 9: Waveforms and subcircuits when energy is supplied from the battery set (mode 2, only battery).

(2) *During* t_1. S_1 remains off and S_3 is still on, but S_2 is turned off; the equivalent subcircuit is shown in Figure 9(c). Stored energy at inductors L_1 and L_2 is delivered to the output capacitor.

Similar to mode 1, the switch S_2 is used to control the output voltage; however energy can be taken from the renewable source and the battery set or only just from the battery set. The switch S_3 is used to track the maximum power point of the photovoltaic panel. If there is no energy in the renewable source, then the battery will deliver all the power to the load.

2.3. Mode 3: No Power Available. This mode occurs when the renewable source and the battery cannot supply the energy requirements to the load, because it should not be forgotten that the amount of energy is finite and it depends on the battery set and weather conditions. When this occurs the system is in idle condition, and only the battery set could be charged (once the renewable source is available).

When the renewable source and the battery set do not have enough energy, the output voltage cannot be kept into its acceptable limits of operation. This mode will remain until the battery set is completely charged. To guarantee no energy is delivered to the load a relay is used to disconnect the load.

Table 1 summarizes different switching states which establish the power flow of the system. The switching frequency of the different states is determined by a single carrier; therefore all the switches work under the same frequency when they are operating; the switching period for the system was selected at 20 μs.

2.4. Analysis of the Converter. Since the converter may be operated in several modes and each one has a different behavior, analysis was made for each specific condition.

In *mode 1* switch S_3 is turned on, but S_1 and S_2 are commuting and then only appear at the equations, where the duty cycle is associated with these switches. State variable representation for the system is then as follows:

$$\frac{di_{L_1}}{dt}=\frac{V_{\text{rs}}}{L_1}-\frac{V_o}{L_1}\left(1-d_{S_2}\right)$$

$$\frac{di_{L_2}}{dt}=\frac{V_{\text{rs}}}{L_2}d_{S_1}-\frac{V_{\text{bat}}}{L_2}$$

Table 1: Switching states of the converter.

Operation mode	Switches			Functions
	S_1	S_2	S_3	
Mode 1	0	X	1	Feeding the load with V_{rs}
	X	X	1	Charging battery and feeding load with V_{rs}
Mode 2	0	X	X	Feeding the load from V_{rs} and V_{bat}
	0	X	1 or 0	Feeding the load only with V_{bat}
Mode 3	X	0	1	Charging battery
	0	0	1	System off

"1" means "on," "0" means "off," and "X" means "commutating."

Table 2: Equilibrium point of the operation mode.

Operation mode	Equilibrium point	Functions
Mode 1	$V_o = \frac{1}{1 - d_{S_2}} V_{\text{rs}}$	Feeding the load with V_{rs}
	$V_{\text{bat}} = d_{S_1} V_{\text{rs}}$	Charging battery if required
Mode 2	$V_o = \frac{1}{1 - d_{S_2} - d_{S_3}} V_{\text{rs}}$ $V_{\text{bat}} = V_{\text{rs}} - (1 - d_{S_3}) V_o$	Feeding the load from V_{rs} and V_{bat}
	$V_o = \frac{1}{1 - d_{S_2}} V_{\text{bat}}$	Feeding the load only with V_{bat}
Mode 3	$V_{\text{bat}} = d_{S_1} V_{\text{rs}}$	Charging battery

$$\frac{dV_o}{dt} = \frac{i_{L_1}}{C}\left(1 - d_{S_2}\right) - \frac{V_o}{RC}, \tag{1}$$

where V_{rs} is the renewable voltage source, V_{bat} is the battery set voltage, V_o is the output voltage, i_{L_1} is the inductor L_1 current, i_{L_2} is the inductor L_2 current, C is the output capacitance, L_1 and L_2 are the inductances, d_{S_1} is the duty cycle of the switch S_1, and d_{S_2} is the duty cycle of the switch S_2.

In *mode 2* S_1 is turned off, S_2 is always commuting, and S_3 may be switching depending on the availability of the renewable source. State variable representation for the system where the renewable source is available is then as follows:

$$\begin{gathered}\frac{di_{L_1}}{dt} = \frac{V_{\text{rs}}}{L_1} - \frac{V_o}{L_1}\left(2 - \left(d_{S_2} + d_{S_3}\right)\right) \\ \frac{di_{L_2}}{dt} = \frac{V_{\text{rs}} - V_{\text{bat}}}{L_2} - \frac{V_o}{L_2}\left(1 - d_{S_3}\right) \\ \frac{dV_o}{dt} = \frac{i_{L_1}}{C}\left(1 - d_{S_2} d_{S_3}\right) d_{S_2}\left(1 - d_{S_3}\right) - \frac{V_o}{RC},\end{gathered} \tag{2}$$

Where d_{S_3} is the duty cycle of the switch S_3.

In this mode, when the renewable source cannot provide energy, the valid equations for the system are then as follows:

$$\begin{gathered}\frac{di_{L_1}}{dt} = \frac{V_{\text{bat}}}{L_1 + L_2} - \frac{V_o}{L_1 + L_2}\left(1 - d_{S_2}\right) \\ \frac{di_{L_2}}{dt} = -\frac{di_{L_1}}{dt} \\ \frac{dV_o}{dt} = \frac{i_{L_1}}{C}\left(1 - d_{S_2}\right) - \frac{V_o}{RC}.\end{gathered} \tag{3}$$

Particularly for this case $i_{L_1} = -i_{L_2}$.

Converter in *mode 3* operates only in charging mode; therefore the system equations are as follows:

$$\frac{di_{L_2}}{dt} = \frac{V_{\text{rs}}}{L_2} d_{S_1} - \frac{V_{\text{bat}}}{L_2}. \tag{4}$$

The equilibrium points of the different operating modes are obtained by making the set of differential equations equal to zero; these are shown in Table 2. As it is easily seen, the output voltage always depends on the duty cycle of S_2; hence it is the switch employed to do it.

Particularly for mode 2, when energy is delivered by both sources, switch S_3, which is related to the battery set, is used for having control of the energy delivered by this source; it should be noticed that S_3 also affects the output voltage, and in order to maintain a regulated output voltage the S_2 must be adjusted by the controller.

It should be noted that S_1 affects only the battery; hence, it is used only when battery requires to be charged.

Table 3: Comparison between converters.

Converter	Reported in [8] Figure 2	Reported in [9] Figure 3	Proposed scheme
Active			
Diode	3	0	3
MOSFET	3	12	3
Passive			
Inductor	1	3	2
Transformer	1	1	0
Battery lifetime	Bad	Good	Good
Operation	Simple	Complex	Simple

2.5. Converter Design Issues. The converter was designed to be operated in continuous conduction mode (CCM). Not only inductors were designed based on the desired ripple but also the capacitor.

Inductors L_1, L_2 and the capacitor may be obtained by considering the operation in mode 1 and using the following equations:

$$L_1 = \frac{V_{\mathrm{rs}} d_{S_2} T_s}{\Delta I_{L_1}}$$

$$L_2 = \frac{\left(V_{\mathrm{rs}} - V_{\mathrm{bat}}\right) d_{S_1} T_s}{\Delta I_{L_2}} \qquad (5)$$

$$C = \frac{V_o\left(1 - d_{S_2}\right) T_s}{\Delta V_C R},$$

where T_S is the switching period, ΔI_{L_1} is the ripple of L_1, ΔI_{L_2} is the ripple of L_2, and ΔV_C is the ripple of C.

2.6. Comparison of Proposal with Previous Schemes. Table 3 shows a brief comparison of this proposed converter; it considers the number of semiconductors, the passive elements, the operation of the battery set, and the general form of operation. Schemes appear illustrated in Figure 2 [8] and Figure 3 [9]; both are the most representative in the literature. It is easily observed that converter in this proposal and the one reported in [8] have not only less components than those reported in [9] but also an easier form of operation. Although this proposal has similar features than those offered in [8], it is not the same with the battery use; this proposal will only employ the battery when it is required to do so; however, the other scheme will use it during all the operating modes, which diminish its lifetime.

The other two schemes consider isolation, which may be a disadvantage in this proposal since it is not taken into account; however, if more components are added it may become suitable.

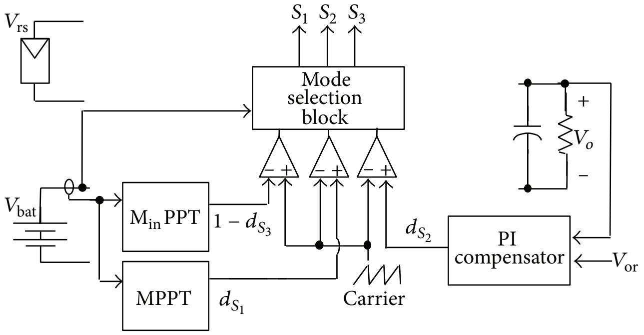

Figure 10: Block diagram of the controller.

3. Controlling the Converter

There are three switches, and each one is used for one purpose, as mentioned before in Section 2.4. Output voltage for this converter is controlled using a traditional controller, but an integrator must be in it; the employed switch for this purpose is S_2. This switch controls the output voltage independently if the converter is operated in mode 1 or 2, even from where the energy is taken; which permits to operate easily the system. It is important to notice that even if the renewable source is suddenly not available, the system operates properly, because in a natural way the energy is taken from the battery set due to the diode D_{rs} and the antiparallel diode of S_1.

For controlling the charge of battery, switch S_1 is used, and this occurs in modes 1 and 3.

Particularly when operating in mode 2, when switches S_2 and S_3 are commuting, S_3 establishes the amount of energy taken from each input source; it comes either from the renewable source or from the battery set. A maximum power point tracker (MPPT) algorithm is used in order to optimize the use of the renewable source; although a traditional maximum power point tracker is reported in the literature, a minimum power point tracker ($\mathrm{M_{in}}$PPT) focused on the battery is suggested in this paper and is only necessary to sense the battery.

In Figure 10 the controller employed is shown,; as it may be observed the voltage compensator (PI), the $\mathrm{M_{in}}$PPT tracker, the battery charger (MPPT), the pulse width modulation (PWM) section, and the mode selection block are used. Battery voltage is considered to determine if the battery requires to be charged or not, while the battery current is used to switch between modes and enable the control signal of each semiconductor.

3.1. Voltage Regulator. A traditional controller, which is a PI compensator, is used in order to regulate the output voltage. The output capacitor voltage and reference are introduced into the compensator in order to obtain the duty cycle, and then d_{S_2} is considered in a typical PWM controller based on a carrier signal, which determines the switching frequency, as shown in Figure 10. The switch used is S_2.

The equation considered is then as follows:

$$u_{S_2} = k_p e_o + k_i \int e_o dt = 0, \tag{6}$$

where e_o is the output voltage error ($e_o = V_o - V_{\text{or}}$) and V_{or} is the voltage reference.

It should be noticed for this controller that, although perturbations may occur, the integral part reduces the steady state error. Actually, output voltage depends on both switches in mode 2, as seen in Table 2, and for reducing the coupling issue, the compensator includes an integral term.

3.2. M_{in}PPT Algorithm. Maximum power point of the renewable source is obtained by centering the algorithm on the battery set, and then instead of a MPPT a different method is used to obtain the maximum energy from the renewable source. This algorithm is used when the battery set provides energy to the load and there is still energy from the renewable source (mode 2).

The system is focused on obtaining the minimum power from the battery set in order to make sure that the maximum power is delivered from the renewable source, where this condition is achieved easily. Therefore a minimum power point tracker (M_{in}PPT) for the battery set is considered; the battery power is not required, since the battery set voltage is almost constant, and then only the current of the battery set may be used.

Flowchart of the proposed M_{in}PPT algorithm is shown in Figure 11. Since current is the only variable, which is measured, the proposed technique becomes simpler than other methods. Once it is detected that the battery set is in use and delivering energy to the load, the algorithm is performed; then the duty cycle of S_3 is changed. At the beginning the duty cycle is equal to one and then decreases until the minimum power is obtained; the system remains oscillating at the M_{in}PP until the current of the battery set is zero; this means that the renewable source is able to deliver all the energy to the load and the battery set is not required.

After obtaining the duty cycle, it is introduced into a PWM; it should be noticed that the comparator inputs are changed and the compliment of the d_{S_2} is used in order to obtain the signals as the proposed operation in mode 2.

3.3. Charging the Battery. A voltage-current mode method, which is similar to methods in uninterruptible power supplies (UPS), was implemented for charging the battery set. Voltage is employed to determine when the battery set either is fully charged or requires to be charged; the current is used to control the battery set charging.

This stage may occur in mode 1 or 3. As the energy is taken from the renewable source, a maximum power point is considered. It is assumed that the battery set voltage is constant, and then only the current is required in the algorithm, similar to that implemented in the previous section; but here the traditional maximum power tracker is used.

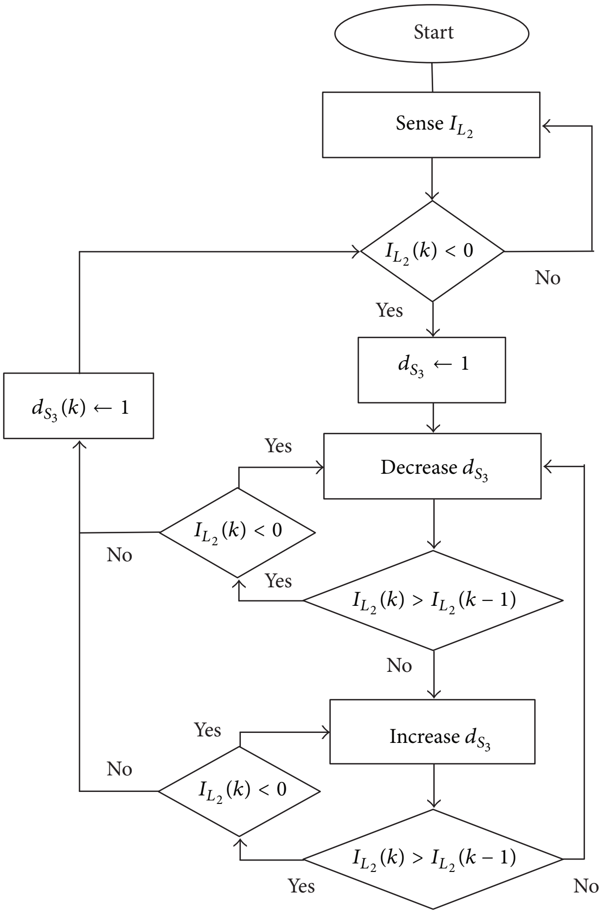

FIGURE 11: Flowchart of the tracking algorithm.

Additionally to the MPPT, the battery current is bounded to a maximum value, which allows avoiding the increase of the power to the battery that may cause damage in it.

3.4. Mode Selection Block. For establishing the mode of operation, a mode selection block is considered; it enables the respective control signal of each mode, and this is made depending on conditions for the system. Basically the battery voltage and current are used.

4. Experimental Results

System functionality was experimentally evaluated with a built prototype, so that the proposed idea was validated. The battery set is of 24 V, the renewable source is a photovoltaic solar panel emulator of Agilent (6131), the output voltage is 100 V, and the converter was designed for an output power of 100 W; the switching frequency is 50 KHz, L_1 and L_2 are 700 μH, and C_o is 100 μF.

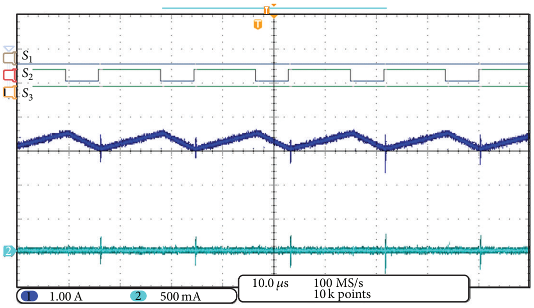

Figure 12: Operation when the energy is obtained from the renewable source. From top to bottom: S_1, S_2, S_3, I_{L_1}, and I_{L_2}. The current reference of both inductors is the same.

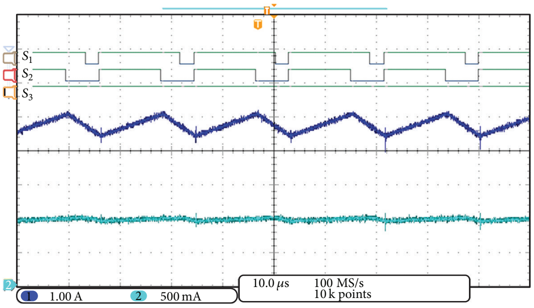

Figure 13: Operation when the battery set is being charged from top to bottom: S_1, S_2, S_3, I_{L_1}, and I_{L_2}. The current reference of both inductors is the same.

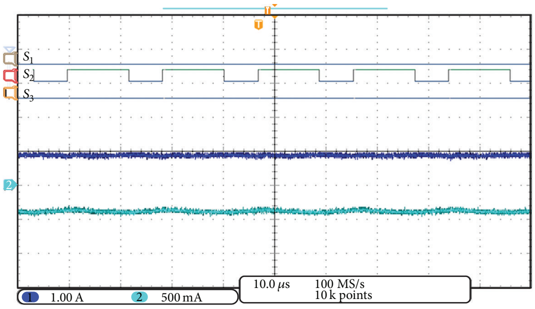

Figure 14: Operation when the energy is obtained from the battery set from top to bottom: S_1, S_2, S_3, I_{L_1}, and I_{L_2}. The current reference of both inductors is the same.

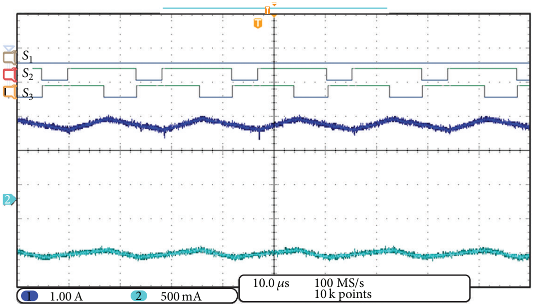

Figure 15: Operation when the energy is obtained from the battery set and the renewable source from top to bottom: S_1, S_2, S_3, I_{L_1}, and I_{L_2}. The current reference of both inductors is the same.

The experimental prototype was tested under different operating conditions. First, the performance of the converter in the different modes in steady state is addressed; second, the performance under power variation of the renewable source is addressed; third, some tests were applied to the system under transitions due to the battery set conditions; and finally a test under load variations is made.

4.1. Steady State Operation. Figures 12 through 15 show experimental results for different operation modes; they were obtained with a mixed signals oscilloscope. For illustration purpose, results were not graphed at the designed conditions, which allow comparing with the theoretical waveforms; this is explained because the ripple values cannot be well appreciated at the full output power and designed conditions. Then the output power in this case is 20 W.

Figure 12 shows operation in mode 1, when the renewable source is available, but no charging is required. For this case the available energy from the photovoltaic panel is higher that the load power, so that no battery needs to be used. As it is easily seen only inductor L_1 provides energy to the load; since inductor L_2 has no current the battery is not in use. The efficiency in this condition is around 93%.

Figure 13 shows system operation in mode 1, when the battery set is charged from the renewable source. For this case it is considered that required energy to the renewable source is able to satisfy the load necessities; it is clearly seen how both inductors have current; L_1 provides energy to the load and L_2 provides to the battery set. The efficiency in this condition is around 93%.

Figure 14 shows operation in mode 2, when the available energy from the renewable source is null; then all the energy is obtained from the battery set. It is seen how both inductors, L_1 and L_2, have the same current in magnitude, but opposite sign; for this case the battery is discharged through both inductors. The efficiency in this condition was around 89%.

Figure 15 shows operation in mode 2; when the available energy from the photovoltaic panel is less than that required by the output, then the battery set is used as a compliment; it is easily seen how both sources deliver energy to the load and how current in both inductors is different; however they are delivering energy to the load. The efficiency in this condition was around 91%.

It is important to notice that the efficiency depends on the devices in use and also the operating conditions; this should be improved if other devices are considered. Different inputs and/or outputs were considered because the battery port is bidirectional; the efficiency was calculated as

$$\eta = \frac{\sum_n P_{\mathrm{on}}}{\sum_m P_{\mathrm{im}}}, \tag{7}$$

where P_{on} is the "n"th output power and P_{im} is the "m"th input power.

4.2. Renewable Power Source Variation. The proposed system was tested under a renewable source variation in order to

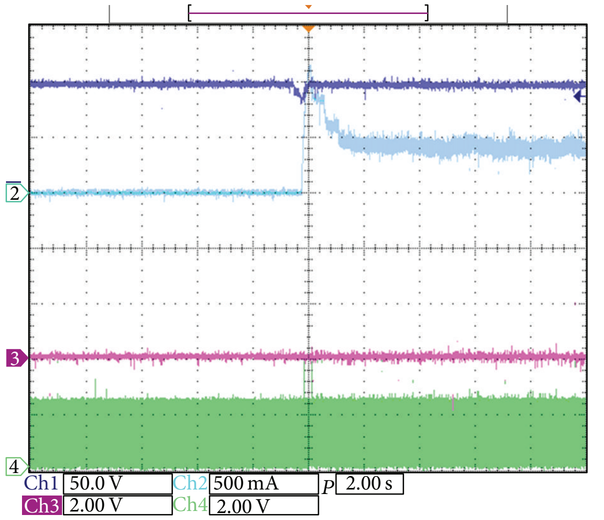

FIGURE 16: Operation when suddenly the maximum power energy of the renewable source becomes lower than the output power from top to bottom V_o, $-I_{L_2}$, S_2, and S_1.

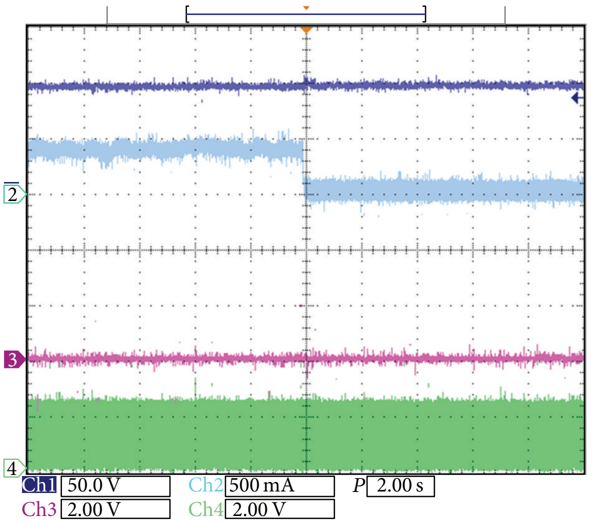

FIGURE 17: Operation when suddenly the maximum power energy of the renewable source becomes higher than the output power from top to bottom: V_o, $-I_{L_2}$, S_2, and S_1.

carry consistently validation. Henceforth the proposed power point tracker algorithm was tested.

Figure 16 shows the system operation when the renewable source suffers a variation. The initial MPP of the renewable source is $V_{\text{mpp}} = 48\,\text{V}$ and $I_{\text{mpp}} = 2.5\,\text{A}$ ($V_{\text{oc}} = 60\,\text{V}$, $I_{\text{sc}} = 3\,\text{A}$), which means a higher output power than the initially considered in the test ($P_o = 100\,\text{W}$); then suddenly the MPP is changed to $V_{\text{mpp}} = 35\,\text{V}$ and $I_{\text{mpp}} = 2.5\,\text{A}$ ($V_{\text{oc}} = 43\,\text{V}$, $I_{\text{sc}} = 3\,\text{A}$); this represents a lower power demanded by the load. It should be noticed that the system automatically demands part of the energy to the battery (see current of inductor L_2); the system is properly maintained in operation.

It is important to notice that after the transition the MPP of the renewable source is not assured, but then M_{in}PPT starts to operate. As it is seen in the figure, the current of the battery set is changed until the minimum battery current is obtained by reaching the MPP of the renewable source; this was made by changing the duty cycle of the switch S_3.

Figure 17 shows the system operation when the renewable source returns to the initial condition; then the energy available from the renewable source is enough to satisfy the load requirements. As it may be noticed, after the transition the battery does not deliver energy.

4.3. Operation under Different Battery Set Conditions. To verify the system operation some tests were made under variation of battery set conditions, when charging starts and when stop is considered and when charging starts and when stop is considered.

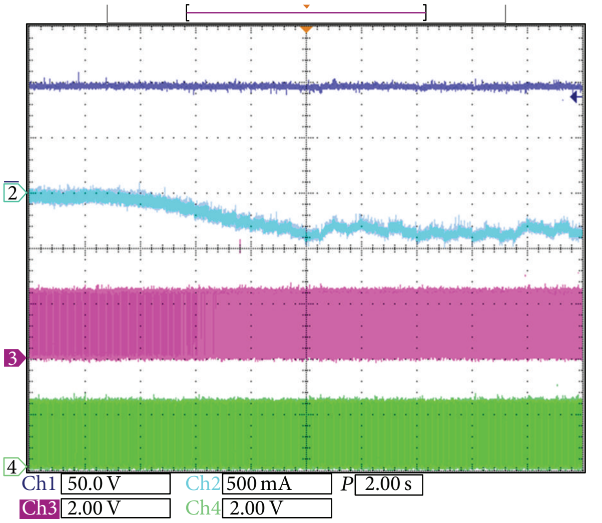

FIGURE 18: Operation when battery set charging starts from top to bottom: V_o, $-I_{L_2}$, S_2, and S_1.

Figure 18 shows the operation of the systems when the battery set is being charged. The MPP of the renewable source is $V_{\text{mpp}} = 48\,\text{V}$ and $I_{\text{mpp}} = 2.5\,\text{A}$ ($V_{\text{oc}} = 60\,\text{V}$, $I_{\text{sc}} = 3\,\text{A}$), this means that initial power is higher than the output power considered in the test ($P_o = 100\,\text{W}$); the battery is required to be charged, and then the system starts to charge it, but demanding the maximum power available from the renewable source.

Figure 19 shows the operation of the systems when the battery set is stopped to be charged. The MPP of the renewable source is $V_{\text{mpp}} = 48\,\text{V}$ and $I_{\text{mpp}} = 2.5\,\text{A}$ ($V_{\text{oc}} = 60\,\text{V}$, $I_{\text{sc}} = 3\,\text{A}$); this means that initial power is higher than the output power considered in the test ($P_o = 100\,\text{W}$); the battery initially is being charged, and when it is detected to be fully charged, then the charging is stopped.

4.4. Load Variation. A load variation was made in order to complete the tests. Figure 20 shows the performance of the system when the load is changed from 50% to 100% of the power; the system was operated under mode 1. The triggering

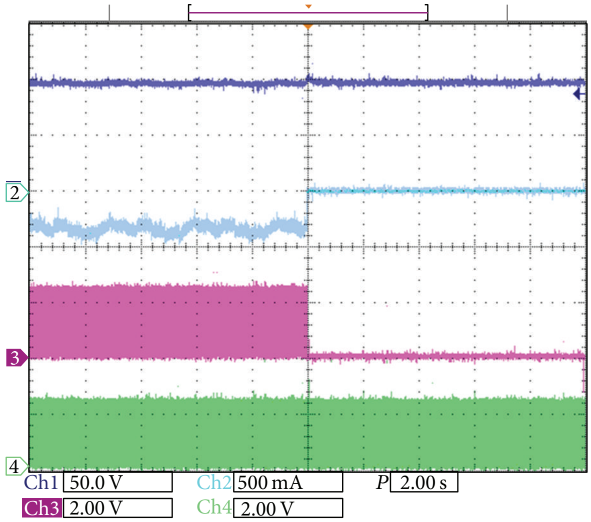

FIGURE 19: Operation when battery set charging stops from top to bottom: V_o, $-I_{L_2}$, S_2, and S_1.

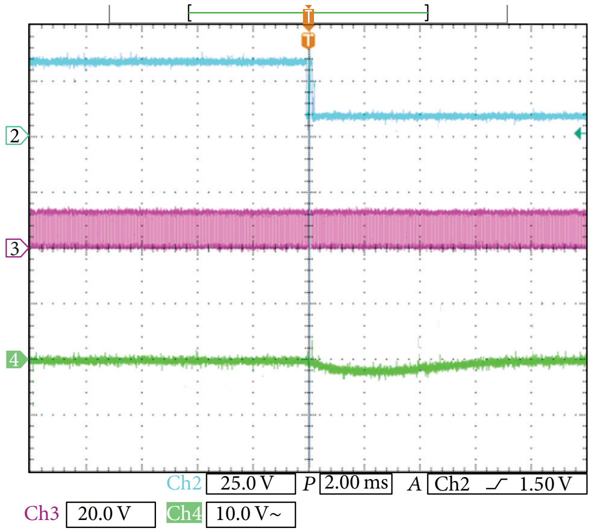

FIGURE 20: Operation under a load variation from top to bottom: triggering signal, S_2, and V_o (AC mode).

signal of the event, the control signal of S_2, and the output voltage put in AC mode are also illustrated. As it is seen, the system operates in a satisfactory manner, the settling time is around 5 ms, and the undervoltage is around 2 V.

5. Conclusion

Three-port DC/DC converter in renewable applications should be able to handle both the renewable source and the battery set; this is because the energy from these sources depends on their availability, and especially for the battery set its utility period of life should be taken into account.

A different three-port DC/DC converter is suggested in this paper, one port for the renewable source, the second for the battery set, and finally the output port. Power may be demanded from both input voltages simultaneously or each one independently. The battery set may also be charged from the renewable source. This proposal has the feature that battery port is used only when it is required; this offers an increase of lifetime. Also when the renewable source suddenly is not available the system automatically takes energy from the battery set without any change, only after an MPPT is used to optimize the use of the renewable source.

The operation and analysis of the converter were given. Experimental results were also shown.

Conflict of Interests

The authors declare that there is no conflict of interests regarding the publication of this paper.

References

[1] Y.-M. Chen, Y.-C. Liu, and F.-Y. Wu, “Multi-input DC/DC converter based on the multiwinding transformer for renewable energy applications,” *IEEE Transactions on Industry Applications*, vol. 38, no. 4, pp. 1096–1104, 2002.

[2] Y.-M. Chen, Y.-C. Liu, and S.-H. Lin, “Double-input PWM DC/DC converter for high-/low-voltage sources,” *IEEE Transactions on Industrial Electronics*, vol. 53, no. 5, pp. 1538–1545, 2006.

[3] B. G. Dobbs and P. L. Chapman, “A multiple-input DC-DC converter topology,” *IEEE Power Electronics Letters*, vol. 1, no. 1, pp. 6–9, 2003.

[4] Y.-M. Chen, Y.-C. Liu, S.-C. Hung, and C.-S. Cheng, “Multi-input inverter for grid-connected hybrid PV/wind power system,” *IEEE Transactions on Power Electronics*, vol. 22, no. 3, pp. 1070–1077, 2007.

[5] N. Vázquez, A. Hernández, C. Hernández, E. Rodríguez, R. Orozco, and J. Arau, “A double input DC/DC converter for photovoltaic/wind Systems,” in *Proceedings of the IEEE Power Electronics Specialists Conference (PESC ’08)*, pp. 2460–2464, Rodes, Greece, 2008.

[6] C. L. Shen and S. H. Yang, “Multi-input converter with MPPT feature for wind-PV power generation system,” *International Journal of Photoenergy*, vol. 2013, Article ID 129254, 13 pages, 2013.

[7] V. M. Pacheco, L. C. Freitas, J. B. Vieira Jr., E. A. A. Coelho, and V. J. Farias, “A DC-DC converter adequate for alternative supply system applications,” in *Proceedings of the 17th Annual IEEE Applied Power Electronics Conference and Expositions*, pp. 1074–1080, Dallas, Tex, USA, March 2002.

[8] H. Al-Atrash, F. Tian, and I. Batarseh, “Tri-modal half-bridge converter topology for three-port interface,” *IEEE Transactions on Power Electronics*, vol. 22, no. 1, pp. 341–345, 2007.

[9] J. L. Duarte, M. Hendrix, and M. G. Simões, “Three-port bidirectional converter for hybrid fuel cell systems,” *IEEE Transactions on Power Electronics*, vol. 22, no. 2, pp. 480–487, 2007.

[10] H. Tao, J. L. Duarte, and M. A. M. Hendrix, “Three-port triple-half-bridge bidirectional converter with zero-voltage switching,” *IEEE Transactions on Power Electronics*, vol. 23, no. 2, pp. 782–792, 2008.

[11] H. Krishnaswami and N. Mohan, “Three-port series-resonant DC-DC converter to interface renewable energy sources with bidirectional load and energy storage ports,” *IEEE Transactions on Power Electronics*, vol. 24, no. 10, pp. 2289–2297, 2009.

[12] Z. Qian, O. Abdel-Rahman, H. Al-Atrash, and I. Batarseh, “Modeling and control of three-port DC/DC converter interface for satellite applications,” *IEEE Transactions on Power Electronics*, vol. 25, no. 3, pp. 637–649, 2010.

Hindawi Publishing Corporation
International Journal of Photoenergy
Volume 2014, Article ID 128327, 10 pages
http://dx.doi.org/10.1155/2014/128327

Research Article

Improved Fractional Order VSS Inc-Cond MPPT Algorithm for Photovoltaic Scheme

R. Arulmurugan[1,2] **and N. Suthanthiravanitha**[2]

[1] *Department of Electrical and Electronics Engineering, Anna University Regional Zone, Coimbatore, India*
[2] *Department of Electrical and Electronics Engineering, Knowledge Institute of Technology, KIOT Campus, NH-47 Salem to Coimbatore Road, Kakapalayam, Salem 637 504, India*

Correspondence should be addressed to R. Arulmurugan; arul.lect@yahoo.com

Received 5 November 2013; Revised 7 January 2014; Accepted 7 January 2014; Published 2 March 2014

Academic Editor: Ismail H. Altas

Nowadays a hot topic among the research community is the harnessing energy from the free sunlight which is abundant and pollution-free. The availability of cheap solar photovoltaic (PV) modules has to harvest solar energy with better efficiency. The nature of solar modules is nonlinear and therefore the proper impedance matching is essential. The proper impedance matching ensures the extraction of the maximum power from solar PV module. Maximum power point tracking (MPPT) algorithm is acting as a significant part in solar power generating system because it varies in the output power from a PV generating set for various climatic conditions. This paper suggested a new improved work for MPPT of PV energy system by using the optimized novel improved fractional order variable step size (FOVSS) incremental conductance (Inc-Cond) algorithm. The new proposed controller combines the merits of both improved fractional order (FO) and variable step size (VSS) Inc-Cond which is well suitable for design control and execution. The suggested controller results in attaining the desired transient reaction under changing operating points. MATLAB simulation effort shows MPPT controller and a DC to DC Luo converter feeding a battery load is achieved. The laboratory experimental results demonstrate that the new proposed MPPT controller in the photovoltaic generating system is valid.

1. Introduction

Renewable energy sources are considered as an important source of energy in the 21st century that is in use to fulfill our needs and growing demands of electricity. Among all renewable energy sources, solar energy is readily available free of cost. The production cost of solar photovoltaic based system is decreased considerably. The advancement in PV technology also causes less cost per unit and thus PV technology do not contribute to global warming [1]. The extraordinary diffusion of solar PV system in electricity generation is evident from the fact that the PV scheme is anticipated to be the largest source of electricity generation among all the accessible nonconventional energy sources. They are considered feasible in residential applications and are suitable for roof top installations [2]. The PV modules are primarily a current source device and the current is produced when light falls on the surface of solar device. The characteristics curve of the PV module shows its nonlinear behavior. The nonlinear V-I curve of PV module has only one point of maximum power extraction. Therefore, the energy harvesting at maximum efficiency is not simple enough. The survival of only one unique point of maximum power requires special techniques to function the scheme at the point of maximum power. These operating techniques are named as MPPT [3]. MPPT techniques control the power electronic interface such that the source impedance is matched with the load impedance and hence maximum power is transferred. In contrast with the nonlinear characteristics, MPPT techniques are vital for any solar PV system.

Different methods have been reported in literature for tracking the maximum power point (MPP). Among the 20 distinct methods reported by [4] the methods such as perturb and observe (P&O), incremental conductance (Inc-Cond), fractional open circuit voltage (FOCV), fractional short circuit current (FSCC), fuzzy logic, and neural network algorithm are widely used by the researchers. Among these methods the FOCV and FSCC are considered as offline MPPT techniques, because they isolate the PV array when they track the MPP and calculate the operating point for MPPT [5, 6]. These techniques adopt both analog as well as digital implementations [7]. However, the periodic isolation of the PV array is power loss and the change in operating point depends on irradiance (G); therefore, the periodic power loss is to be avoided; we need irradiance sensor that can measure the G and hence PV array needs not to be isolated [8]. The fuzzy logic and/or neural network based MPPT technique have good performance under fast changing environmental circumstances and display improved performance than the P&O method [9]. However, the main drawback of this technique is that its efficiency is extremely reliant on the technical information of the engineer in calculating the error and approaching up with the fuzzy rule based table. It is importantly reliant on how a designer assembles the system based on his experience and skill. Perturb and observe algorithm can be failure under fast varying environmental circumstances. The Inc-Cond technique is constructed on the slope of the solar photovoltaic panel power curve. This technique has partly solved divergence of perturb and observe model [10].

In this paper we suggested a novel technique that will tune the online MPPT techniques based on changing weather conditions. The proposed algorithm modifies the existing conventional Inc-Cond controller based on improved fractional order variable step size which differs from the existing. The difference is based on the datasheet of the panel on the novel controller and is constant for any particular PV array. The proposed algorithm is implemented into MATLAB/Simulink environment and it is tested and validated.

The structure of the system is organized as follows. Section 2 discuss the modelling of PV modules, Improved FOVSS Inc-Cond controller and analysis of DC to DC Luo converter. Section 3 provides the simulation and experimental setup; hence results validate the controller performance. Finally Section 4 concludes remarks.

2. Proposed System Description

The schematic circuit diagram for the suggested system is shown in Figure 1. It contains PV panel, designed novel FOVSS Inc-Cond control algorithm, synchronous DC to DC Luo converter, and battery load. The power switches of the designed DC to DC Luo converter are controlled by the gate drivers programmed via a controller module. The designed converter delivers required levels of the output power to the stand alone battery load. The impedance of the battery load should be assumed as a suitable one for subsequent analysis. The DC to DC converters are responsible for MPPT and voltage regulations. Simulation and experimental models are established in MATLAB/Simulink and controller processor environment.

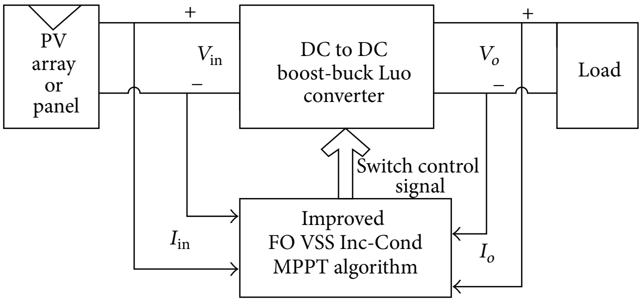

Figure 1: The proposed optimized novel FOVSS Inc-Cond MPPT system.

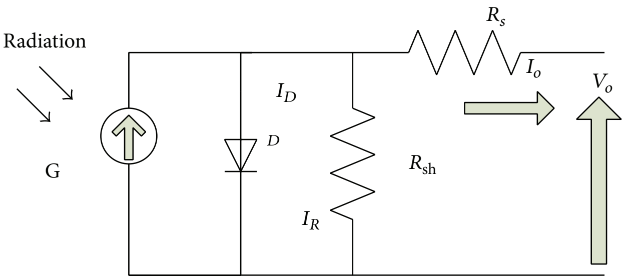

Figure 2: Equivalent circuit model of solar cell.

2.1. Modeling of PV Modules. PV systems convert sunlight into electrical energy without causing any environmental issues. Various equivalent models are available in the literature for better understanding of concept of PV array. Among the models, Figure 2 is considered as good which supports accuracy and user friendliness [11]. For the constant weather conditions the curve has only one unique point of maximum power (MP) and the V-I characteristic of an irradiated cell is nonlinear. It depends on several factors including the temperature and irradiance. With a varying irradiance the short circuit current varies; however, the open circuit voltage changes significantly with changes in temperature. The varying atmospheric conditions make the MPP keep shifting around the PV curve. In the PV simulation, results show the cumulative effect of the nonhomogenous weather conditions on MPP. The analytical expression based on the temperature (T) and irradiance (G) variation can be written as follows:

$$I_{PV} = k \cdot G \cdot S, \tag{1}$$

where I_{PV} is the photovoltaic current source.

I_d is the single exponential junction current and is given by

$$I_d = I_o \cdot \left(e^{AV_d} - 1\right); \tag{2}$$

I is the output current and is given by $I = I_{PV} - I_d - V_d/R_{sh}$.

V is the output voltage and is given by $V = V_d - R_s \cdot I$:

$$I_{sc}(G,T) = I_{sc}(\text{STC}) \cdot \frac{G}{1000} \cdot \left(1 + \alpha I_{sc} \Delta T\right), \tag{3}$$

$$V_{oc}(\text{G},\text{T}) = V_{oc}(\text{STC}) \cdot \left(1 + \beta V_{oc} \Delta T\right), \tag{4}$$

$$P_m(G,T) = P_m(\text{STC}) \cdot \frac{G}{1000} \cdot \left(1 + \gamma \rho \Delta T\right), \tag{5}$$

$$\eta = \frac{P_m}{GA} = \left(P_m(\text{STC}) \cdot \frac{\left(1 + \gamma \rho \Delta T\right)}{A}\right), \tag{6}$$

where $\Delta T = Tc - 25^\circ\text{C}$.

2.2. A New Design of Improved Fractional Order VSS Inc-Cond Controller

2.2.1. Fractional Order Differentiator. A FO system comprised by a fractional differential or an integral equation, and systems covering few equations, has been deliberate in engineering and physical appliances, for example, active control, signal processing, and linear and nonlinear response controller. The generally utilized approaches have been anticipated for numerical assessment of fraction derivatives by Riemann-Lioville and Grunwald-Letnikov definition [12]. It reflects a continuous function $f(t)$, where its αth order derivative can be conveyed as follows [13]:

$$\frac{d^{\alpha} f(t)}{dt^{\alpha}} = \lim_{h \to 0} \frac{1}{h^{\alpha}} \sum_{r=0}^{\alpha} (-1)^{r} \binom{\alpha}{r} f(t - rh),$$
$$\beta = \binom{\alpha}{r} = \frac{\alpha!}{r!\,(\alpha - r)!}, \tag{7}$$

where β is the coefficient binomial and α is an integer positive order. We use the guesstimate approach, arising the Grunwald Letnikov definition as

$$D_t^{\alpha} f(t) \approx h^{-\alpha} \sum_{r=0}^{[t/h]} (-1)^{r} \beta f(t - rh). \tag{8}$$

For generalization, it is suitable to adopt $t = nh$, where "t" is the opinion at which the derivative is appraised and h is the discretization step. We can rewrite the estimate of the αth derivative as follows:

$$D_t^{\alpha} f(t) = \frac{d^{\gamma}}{dt^{\gamma}} \left[D_t^{-(\gamma - \alpha)} \right],$$
$$D_t^{\alpha} f(t) \approx \left(\frac{t}{n} \right)^{-\alpha} \sum_{r=0}^{n-1} \frac{\Gamma(r - \alpha)}{\Gamma(-\alpha)\,\Gamma(r + 1)} f\left(t - r\frac{t}{n} \right), \tag{9}$$

where γ is an integer satisfying $\gamma - 1 < \alpha \leq \gamma$. Clearly the FO calculus leads to an immeasurable dimension, while the integral calculus is a finite dimension. Reflect $f_m(t) = t^m$, $m = 1, 2, 3, 4 \ldots$, and the αth derivative is

$$D_t^{\alpha} t^{m} \approx \frac{t^{m-\alpha}}{\Gamma(-\alpha)} n^{\alpha} \sum_{r=0}^{n-1} \frac{\Gamma(r - \alpha)}{\Gamma(r + 1)} \left(1 - \frac{r}{n} \right)^{m}. \tag{10}$$

If we expand $[1 - (r/n)]^m$ by the binominal theorem [3, 6], (10) becomes

$$D_t^{\alpha} t^{m} \approx \frac{t^{m-\alpha}}{\Gamma(-\alpha)} \sum_{k=0}^{m} (-1)^{k} \binom{m}{k} n^{\alpha - k} \sum_{r=0}^{n-1} \frac{\Gamma(r - \alpha)}{\Gamma(r + 1)} r^{k}, \tag{11}$$

$$K \equiv \sum_{r=0}^{n-1} \frac{\Gamma(r - \alpha)}{\Gamma(r + 1)} r^{k}. \tag{12}$$

If y is an unstipulated and if j is an integer positive, then y, j fractional is defined as

$$y^{(j)} = y(y - 1)(y - 2) \cdots (y - j - 1),$$
$$\Gamma(y + 1) = y^{(j)} \Gamma(y - j + 1). \tag{13}$$

So, an integral power of y can be expressed as a factorial polynomial, as

$$y^{k} = \sum_{j=1}^{k} \xi_j^{k} y^{(j)} = \sum_{j=1}^{k} \xi_j^{k} \frac{\Gamma(y - j + 1)}{\Gamma(y + 1)}, \tag{14}$$

where the ξ is the sterling values. Let $y = r$ in (14) be substituted in (12) and replace n by $n - j$ and α by $\alpha - j$; then

$$K = \sum_{j=1}^{k} \xi_j^{k} \left(\sum_{r=0}^{n-1} \frac{\Gamma(r - \alpha)}{\Gamma(r + 1 - j)} \right) = \sum_{j=1}^{k} \xi_j^{k} \frac{\Gamma(n - \alpha)}{\Gamma(n - j)} \left(\frac{1}{j - \alpha} \right). \tag{15}$$

Equation (11) becomes

$$D_t^{\alpha} t^{m} \approx \frac{t^{m-\alpha}}{\Gamma(-\alpha)} \sum_{k=0}^{m} (-1)^{k} \binom{m}{k} \sum_{j=0}^{k} \frac{\xi_j^{k} n^{\alpha - k} \Gamma(n - \alpha)}{(j - \alpha)\,\Gamma(n - j)},$$
$$\lim_{n \to \infty} n^{\alpha - k} \frac{\Gamma(n - \alpha)}{\Gamma(n - j)} = \begin{cases} 1, & \text{if } j = k, \\ 0, & \text{if } j < k, \end{cases} \tag{16}$$

where

$$\sum_{k=0}^{m} (-1)^{k} \binom{m}{k} \frac{1}{(k - \alpha)} = B(-\alpha, m + 1). \tag{17}$$

A general fractional order differentiator can be expressed as follows:

$$D_t^{\alpha} t^{m} \approx \frac{\Gamma(m + 1)}{\Gamma(m + 1 - \alpha)} t^{m - \alpha}. \tag{18}$$

For all α, positive, negative, and/or zero, $m = 0, 1, 2, 3, 4 \ldots$. Note, the select of α can be seen as selecting the spectacles that will be modeled. By selecting $0 < \alpha < 1$, anomalous phenomena, such as heat conduction, diffusion, viscoelasticity, and electrode-electrolyte polarization, can be described [1].

2.2.2. Design of New Improved VSS Inc-Cond Controller. Generally step size is fixed for the Inc-Cond MPPT technique. The produced power from the PV panel with a higher step size plays to quicker dynamics but results in extreme steady state fluctuations and subsequent poor efficiency [14]. This condition is inverted through the MPPT by operating with a lesser step size. Thus, the tracking with constant step size makes a suitable trade-off among the fluctuation and dynamics. Thus the problem can be resolved with VSS restatement [15, 16]. Even though all the conventional methods are simple perturb and observe method produce oscillations occurring at maximum power point and hence output power is not achieved at desired level and results in poor efficiency. The Inc-Cond method is envisioned to resolve the difficulty of the conventional perturb and observe method under quick varying environment circumstances [17]. Hence, in this paper the performance of the FOVSS Inc-Cond method in quickly varying environment conditions by using voltage versus current graph [18]. Condition 1: the curve power versus voltage is positive and the indication of the altering voltage and current

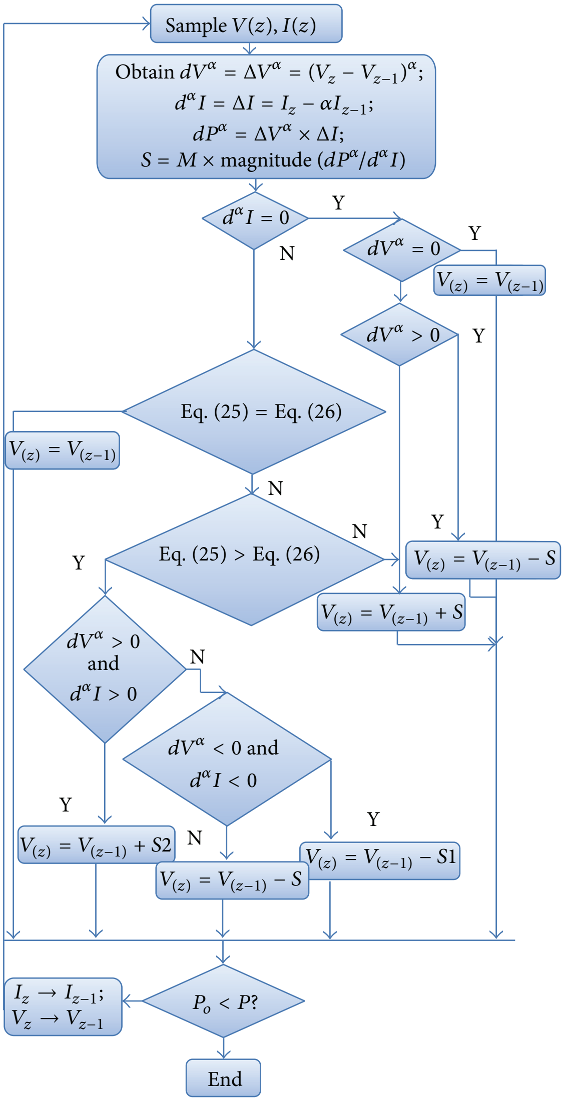

Figure 3: Novel improved FOVSS Inc-Cond MPPT algorithm.

is the same, simultaneously; the algorithm recognizes that G is in quickly accumulative environmental circumstances and reduces the voltage. Condition 2: on the other side, if the slope of the power versus voltage graph is positive, altering current and voltage are opposite; concurrently, the algorithm recognizes that it is quickly reducing environment situations and rises the voltage. Condition 3: lately, if altering I and V are in conflicting directions, the algorithm for tracing supreme power upsurges the V, as the Inc-Cond conventional algorithm. Thus this algorithm eludes difference from the real MPP in quickly varying environmental circumstances.

In this report, a VSS procedure is suggested for the improved Inc-Cond tracking technique and is dedicated to search an easier and active way to increase tracking dynamic as well as correctness. In every tracking application, the possible power follower is attained by joining a DC to DC converter among the PV panel and load system [19]. The power output of the PV is utilized for energetic control of the DC to DC converter pulse width modulation (D) to diminish well the complication of the structure [20]. The flowchart of the FOVSS improved Inc-Cond tracking algorithm is illustrated in Figure 3, where the power DC to DC converter PWM (D) recapitulation step size tuned automatically. The power output of PV panel is involved to regulate the power DC to DC converter PWM (D), donating to a shortened control scheme, where the outputs I and V of the PV array represent $V_{(z)}$ and $I_{(z)}$ at time z, respectively. The VSS implemented to diminish the problem represented above is written in the equation as follows:

$$D(z) = D(z-1) \pm M \times \left|\frac{dP}{dV}\right|. \tag{19}$$

In the above equation M denotes the scaling factor, which is adjusted at the period to regulate the step size. The VSS can also be recognized from the incline of the power versus duty cycle graph in [16] for perturb and observe tracking written as follows:

$$D(z) = D(z-1) \pm M \times \left|\frac{\Delta P}{\Delta V}\right|. \tag{20}$$

In the above written equation ΔD represents the change in stage D at earlier sample period. As illustrated in the power versus voltage, the derivative of (dP/dV) of a PV panel can be seen to be changing efficiently and is suggested in [15] as an appropriate constraint for determining the VSS of the perturb and observe method. So, the derivative (dP/dV) is also working herein to control the VSS for the Inc-Cond tracking method. The modern rule for PWM (D) can be acquired as the following equation:

$$D(z) = D(z-1) \pm M \times \left|\frac{P(z) - P(z-1)}{V(z) - V(z-1)}\right|. \tag{21}$$

The M is necessarily determined by the effectiveness of the tracking structure. Physical fine-tuning of this constraint is boring and resultant output may be effective only for a given structure and operating circumstance [15]. A modest technique is used to determine whether the M is suggested here. Initially higher step size of the maximum duty cycle ($D_{\max}$) for constant step size tracking scheme was selected. By such results, the active development is best adequate but gives poor steady state performance. The stable state assessment instead of dynamic assessment in the start-up development of the magnitude P divided by V of the PV panel output can be estimated under the constant VSS working with maximum duty cycle, which will be selected as the superior controller as VSS Inc-Cond tracking technique. To confirm the conjunction of the tracking superior rule, the variable step (VS) rule should observe the following:

$$M \times \left|\frac{dP}{dV}\right|_{\text{fized step}=\Delta D_{\max}} < \Delta D_{\max}. \tag{22}$$

In the above equation $|dP/dV|_{\text{fized step}=\Delta D_{\max}}$ is the $|dP/dV|$ at FSS operation of maximum duty cycle. The M can be obtained as follows:

$$M < \frac{\Delta D_{\max}}{|dP/dV|_{\text{fized step}=\Delta D_{\max}}}. \tag{23}$$

In the equation above, the VSS improved Inc-Cond tracking will be operating with FSS of the early set superior controller $\Delta D_{\max}$. The above equation delivers an easier supervision to determine the M of the VSS Inc-Cond tracking technique. With the fulfillment of above calculation, superior scaling factor shows a relatively quick reaction than a minor scaling factor. The SW will become minute as derivative power to voltage becomes very slight nearby the maximum power [21].

2.2.3. The Control Process of Improved FOVSS Inc-Cond Algorithm. The V-I characteristics of a single module are resolute and enlarge to control the performance of a PV array, as illustrated in Figure 3. It seems $dI/dV < 0$, with rising V as I, is diminishing. Based on (1)–(3), current and voltage are contingent on environment and electricity transmission. The irregular singularities can be designated as FOD. Thus, the dI/dV can be altered as follows:

$$\frac{d^{\alpha}V(I)}{d^{\alpha}I} = \lim_{\Delta V\to 0}\frac{V^{\alpha}(I) - V_o^{\alpha}(I-\Delta I)}{\Delta I}, \tag{24}$$

$$\frac{dV^{\alpha}}{d^{\alpha}I} \approx \frac{(V-V_o)^{\alpha}}{I-\alpha I_o}. \tag{25}$$

The efficiency of the weighing ΔI is altered as $\alpha > 0$, and α is an even number. If $\alpha = 1$, then it yields to the rate of change quickness. For $\alpha = 2$ outside the range, it yields acceleration. Therefore, for $0 < \alpha < 1$ the appearance can be called as the fractional rate of the alteration of operation. Equation (25) is utilized to direct the FO incremental variations of the I and V of the PV array. The VSS incremental conductance load can be modified as follows:

$$\begin{aligned}
&\frac{d^{\alpha}}{dV^{\alpha}}\left(-\frac{V_o}{I_o}\right)\\
&\quad=\left(-\frac{1}{I_o}\right)\frac{d^{\alpha}V_o^{\alpha}}{d^{\alpha}I}+(-V_o)\frac{d^{\alpha}I_O^{-1}}{d^{\alpha}I}\\
&\quad=\left(-\frac{1}{I_o}\right)\left(\frac{\Gamma(2)}{\Gamma(2-\alpha)}\right)V_o^{\;1-\alpha}+(-V_o)\frac{\Gamma(0)}{\Gamma(-\alpha)}I_O^{1-\alpha},
\end{aligned} \tag{26}$$

where $\operatorname{Res}(\Gamma, -z) = ((-1)^z/z!)Z = 0, -1, -2, -3, -4, \ldots$ with remainder $\Gamma(0) = \operatorname{Res}(\Gamma - 0) = 1$. Thus the procedure of improved FOVSS Inc-Cond method examines the V as a variable at which the MPP has an increasing or diminishing duty cycle.

Figure 3 shows the flowchart of the improved FOVSS Inc-Cond control algorithm. By using the radiation meter, this control technique can modify the working mode in the program. Based on the power output of the PV module MPP varies, hence the suggested control technique increases or diminishes the voltage output of the PV module as a similar path and it can be traced to the MPP. It regulates the D by the immediate values I_z and V_z at existent iteration step and their consistent values of I_{z-1} and V_{z-1} deposited at the end of the foregoing repetition step. The VSS incremental changes in I and V are approached as $d^{\alpha}I \approx (I_z - \alpha I_{z-1}) = \Delta I$ and $dV^{\alpha} \approx (V_z - V_{z-1})^{\alpha} = \Delta V^{\alpha}$, correspondingly. To evade underestimating the employed state under numerous conditions, the first voltage V_z can be set to $0V$ or default values rendering to the T differences. Rendering to the four conclusions, the control process of improved FOVSS Inc-Cond method algorithm can be expressed as follows.

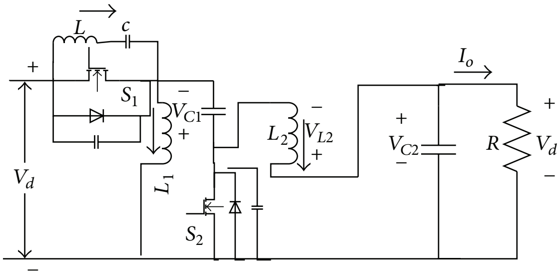

Figure 4: DC to DC Luo converter.

Situation one: if ($\Delta V^{\alpha} = 0$ and $\Delta I = 0$) not any controller accomplishment is required.

Situation two: if ($\Delta I = 0$ and $\Delta V^{\alpha} > 0$) a controller action is required to enhance the ΔV^{α} to present voltage V with a cumulative D step size.

Situation three: if ($\Delta I = 0$ and $\Delta V^{\alpha} < 0$) a controller action is required to decrease the ΔV^{α} to present voltage V with a diminishing D step size.

Situation four: calculated power output is equal to multiplication of voltage and current output, $P = VI$. If $P_o < P$, modernize the $V : V_{z-1} = V_z$ and $I_{z-1} = I_z$ and then dismiss the controller process.

2.3. Analysis of Synchronous DC to DC Luo Converter. When recommending a MPP tracker, the most important process is to choose and analyze a highly suitable converter, which is invented to function as the foremost fragment of the tracker (MPPT). Therefore switching mode power supplies are suitable to operate with high efficiency. Among all the complete topologies existing, the series of buck-boost converters provide the opportunity to have either higher or lower output voltage compared with the input voltage. The conventional buck-boost formation is cheaper than the Luo one, even though some drawbacks occur, such as less efficient, weak transient reaction, high peak current in power apparatuses, and discontinuous current input. On the other side, the Luo converter has the highest efficiency with low switching losses amongst nonisolated DC to DC converters and no negative polarity regulated output voltage compared to the input voltage. It can deliver an improved current output characteristic due to the output stage inductor. Thus, the Luo configuration is an appropriate converter to be active in deceiving the MPPT [21].

The DC to DC Luo converter provides a positive polarity regulated output voltage with respect to the input voltage which is shown in Figure 4. The process of the synchronous Luo converter with ZVS and ZCS technique is for dropping the switching loss of the primary switch. In addition, the freewheeling diode is replaced by power switch to reduce

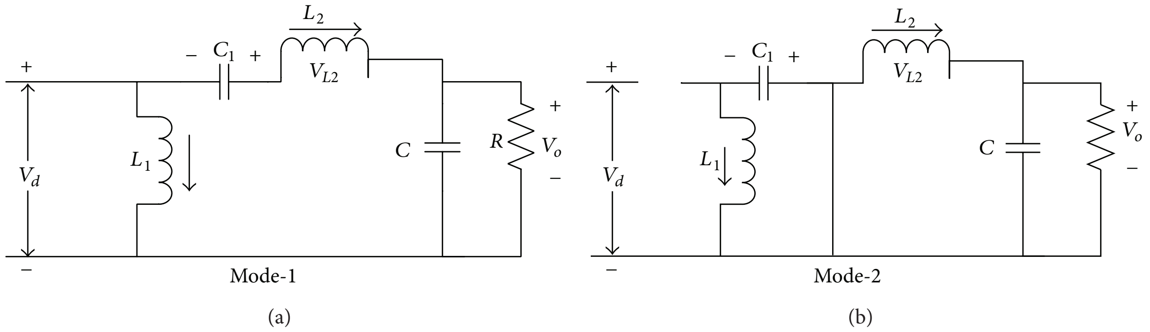

(a)

(b)

Figure 5: Equivalent modes of converter: (a) main switch on; (b) main switch off.

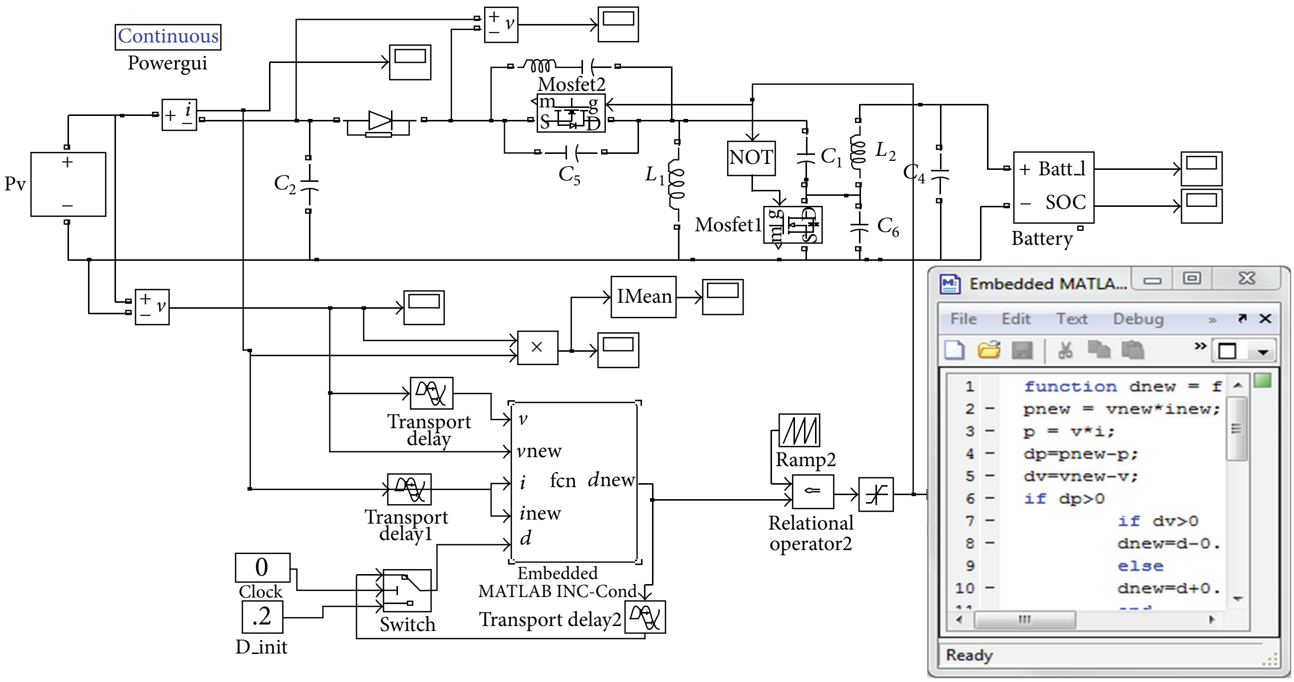

```
function dnew = f
pnew = vnew*inew;
p = v*i;
dp=pnew-p;
dv=vnew-v;
if dp>0
            if dv>0
            dnew=d-0.
            else
            dnew=d+0.
```

Figure 6: Simulation layout of the proposed FOVSS Inc-Cond system.

conduction losses too. The designed circuit, two powers MOSFET switches are utilized to reduce switching and conduction losses. The energy storage elements are capacitors C_1 and C_2 and inductors L_1 and L_2. R is the load resistance. To analyze the process of the DC to DC Luo converter, the circuit can be divided into two equivalent modes [22].

2.3.1. Modes of Operation. In mode one operation, when the power switch S_1 is turned on, the inductor L_1 is charged by the input supply voltage V_{in}. At similar time, the inductor L_2 absorbs the energy from input source and the primary capacitor C_1. The load is delivered by the capacitor C_2. The equivalent method of DC to DC Luo converter operating mode 1 is shown in Figure 5(a).

In the mode 2 process, when the switch is in turned off state, the input current drawn from the source becomes zero, as shown in Figure 5(b). The inductor current I_{L1} flows through the power S_2 to charge the capacitor C_1. The inductor second current I_{L2} flows through C_2 to load resistance circuit and the second switch S_2 to keep it continuous.

3. Simulation Results and Discussion

3.1. Simulation Setup. The PV array is modeled and coupled with the DC to DC Luo converter and is controlled by suggested tracking algorithm. To examine the performance and effectiveness of suggested FOVSS Inc-Cond controller, it is tested on the experimental prototype of the photovoltaic MPPT controller and the complete simulation structure of a proposed system is illustrated in Figure 6 [23]. It is made up of multi and mono crystalline silicon materials of 40 watt PV array. The Table 1 shows the specifications for single 10 watt PV module [10].

3.2. Analysis of PV Results. To confirm the enactment of the suggested system the V-I and V-P characteristics of single PV

Table 1: Electrical parameters of PV module.

Designation	Peak maximum power	Peak maximum voltage	Peak maximum current	Open circuit voltage	Short circuit current
Value [units]	10 Wp	16.4 V	0.610 A	21 V	0.700 A

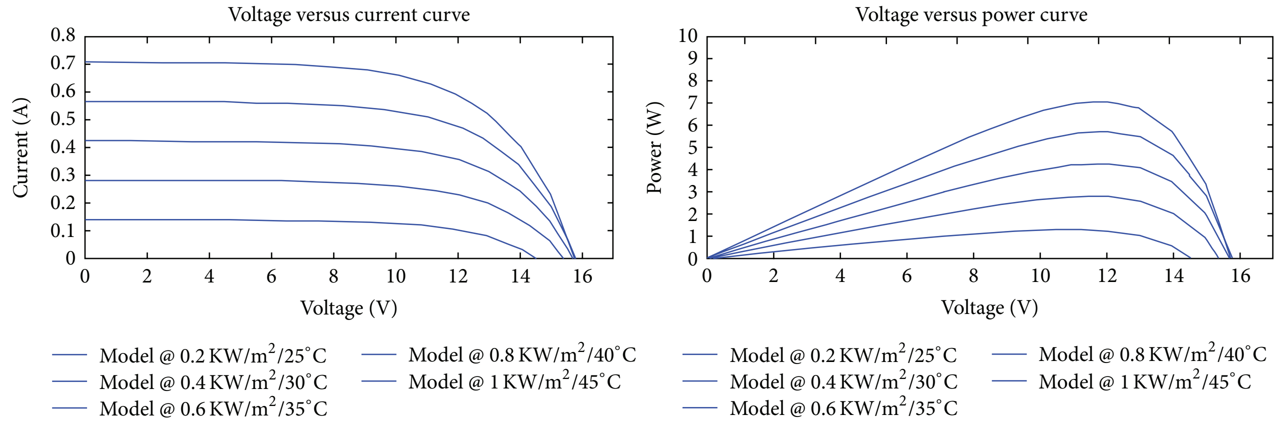

Figure 7: Simulated V-I and V-P characteristics of single PV module with variation of solar G&T, which are installed on the floor of the laboratory at GCE, Salem (sponsored by IIT, Bombay).

module of proposed panel are plotted for different values of solar insulation and cells temperature as shown in Figure 7. Simulation uses the standard design method which shows that an increased number of modules can deliver a nominal level of operating charging current for normal range of G. From this PV curves, it was discovered that the decrease in the maximum power causes increase in temperature. The following operating conditions are observed from this study: (1) when increasing the load current causes drops in the PV voltage; (2) when increase in temperature causes reduction in power output due to rises of internal resistance across the cell; (3) when increasing the insolation, the power output PV increases as more photons hit out electronics and further current flow causing higher recombination. The variation of power output acts as a function of module voltage and is affected by altered working conditions. Also, the output V versus I characteristics of the single PV module is observed under various conditions of T and G [23].

3.3. Results for Proposed System under Dynamic Weather Conditions. To distinguish the enactment of the designed improved FOVSS Inc-Cond MPPT control algorithm which can automatically regulate the step size with the traditional incremental conductance algorithm, the MATLAB simulations are constructed under similar circumstances. The sampling period carried out for the conventional Inc-Cond algorithm was selected as 0.02 second. Consequently, the PWM duty cycle (D) of the DC to DC Luo converter is modernized for each 0.02 seconds. The performance of output power of conventional Inc-Cond maximum tracking control with a fixed size step is 0.02 under an irradiance step various from 200 W/m^2 at temperature 25°C to 800 W/m^2 at temperature 27°C at 0.5 seconds which are shown in Figure 8(a). To differentiate, the consistent photovoltaic power output response of the designed improved FOVSS Inc-Cond maximum tracking control algorithm with allowable possible duty size ΔD is 0.10 and is illustrated in Figure 8(b). It is observed that the fluctuations happening at steady state in conventional Inc-Cond algorithm are nearly eliminated by the design of improved FOVSS Inc-Cond tracking algorithm. Also, the dynamic enactment of the designed method is noticeably quicker than the conventional technique by fixed size step of 0.02. The outcomes point out that the fluctuations at steady state conditions are significantly reduced by using the designed FOVSS Inc-Cond maximum tracking control algorithm.

The performance is compared between conventional Inc-Cond and proposed FOVSS Inc-Cond tracking algorithm and is obtained in Table 2. Compared with the conventional incremental conductance, fixed step size of ΔD is 0.10 which shows good performance but results in greater steady state fluctuation. The proposed FOVSS Inc-Cond technique solves this problem. The fluctuation at the steady state is nearly exterminated by the use of very small magnitude of $(dP^{\alpha}/d^{\alpha}I)$ and the resultant output power of PV array is 39.5 W. Furthermore, the dynamic performance of proposed FOVSS Inc-Cond technique is quicker than conventional Inc-Cond technique which is shown in Figure 8.

3.4. Experimental Setup and Results. The process of improved FOVSS Inc-Cond maximum tracking algorithm has been assessed by experiment. The experimental test was carried out on the laboratory test bench of the standalone PV system installed on the floor of the Electrical and Electronics Engineering at Government College of Engineering, Salem, India, sponsored by IIT, Bombay. A model of the suggested scheme

Table 2: Comparison of conventional and proposed tracking algorithm performance.

Technique	Parameter	Irradiance-200 W/m^2 and temperature is −25°C		Irradiance-800 W/m^2 and temperature is −27°C		Under steady state conditions
		Output power	Sampling period in seconds	Output power	Sampling period in seconds	
Conventional Inc-Cond	$\Delta D = 0.10$	P_o: 12.9 W	0.02 seconds	P_o: 38.7 W	0.5 seconds	More fluctuation takes place
Proposed FOVSS Inc-Cond algorithm	$M = 0.056$	P_o: 13.5 W	0.02 seconds	P_o: 39.5 W	0.5 seconds	Eliminate the fluctuation

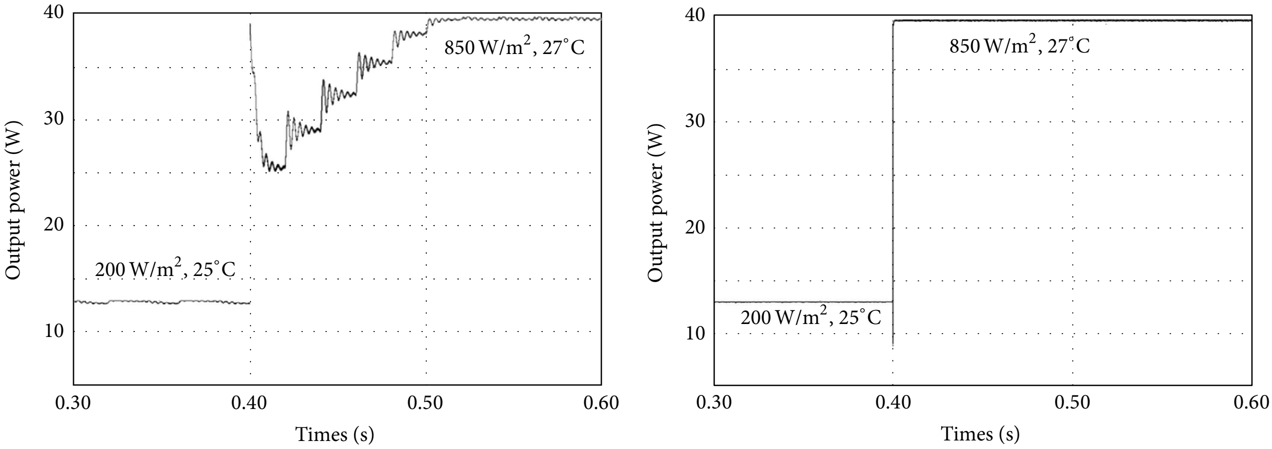

(a)

(b)

Figure 8: Simulated photovoltaic power output response under sudden change in G&T: (a) conventional Inc-Cond algorithm; (b) designed improved FOVSS Inc-Cond tracking technique.

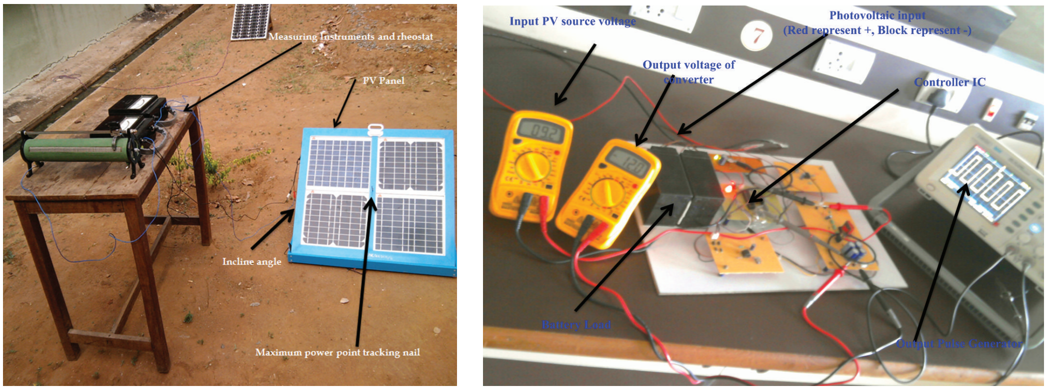

(a)

(b)

Figure 9: Photos of prototype setup: (a) PV array; (b) DC to DC Luo converter with improved FOVSS Inc-Cond MPPT algorithm.

depicted in Figure 9 is composed of (a) photovoltaic panel and (b) DC to DC Luo converter with suggested controlling technique. The DC to DC Luo converter specifications are selected as follows. The input voltage is 21 V, capacitance C_1 and capacitance C_2 are 220 μF, inductances L_1 and L_2 are 1.5 mH and 2 mH, respectively, switching frequency is 10 Khz, and 12 V battery. Note that these passive components are designated to fill design criteria distilled based on equations. In the test, there are four PV modules mounted side by side and connected in series and parallel manner. Atmega 8 microcontroller was used to deliver the control pulses for the DC to DC Luo converter. The *C* language code of

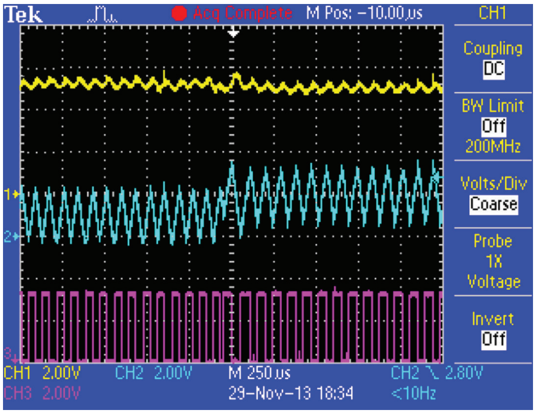

Figure 10: Initial waveforms of MPPT with PV array (channel-1: PV voltage, channel-2: PV current, channel-3: gate pulse).

the improved FOVSS Inc-Cond controller and PWM generator system is constructed, debugged, and executed with the assistance of the Arr studio development tool and Proisp software [16, 17].

The initial graph with improved FOVSS Inc-Cond peak tracking control algorithm is illustrated in Figure 10. When the scheme attains close to the peak power, the size of the step becomes very tiny, outcoming in an excellent power graph. The power and current of the PV rises to a length due to great step size change at the starting. An adjustable resistive load was straight joined with the PV panel as well to investigate the peak power. The peak power distinguishing between the PV panel could be fashioned and the modules outputs with the suggested FOVSS Inc-Cond peak tracking technique are within numerous watts. Thus, the peak tracking efficiency of the suggested technique under the present situation is about 98.92%. The peak tracking efficiency variance is not clear due to the minor step size selected for the fixed step size Inc-Cond algorithm. The reason of this paper is to advance the dynamic reaction and investigate the change in irradiance further [18–20]. A dual switch is familiarized to series with one set of series assembled PV module to simulate the consequence of the irradiance on the PV scheme. When the SW is off or on, both the voltage and power output of the PV panel will hit a step variation, simulating a poor operational condition for the maximum tracking control. When the SW is off, the modules of the PV altered from three to four. The equivalent PV scheme power output graphs with the suggested improved FOVSS Inc-Cond peak tracking algorithm controller are illustrated in Figure 11, while Figure 12 demonstrates individuals graph for the modules of the PV that suddenly varied from four to three. The sampling periods of the improved FOVSS Inc-Cond peak tracking algorithm are selected to achieve almost steady state accuracy. From the outcome of the figures, it can be illustrated that the PV scheme with improved VSS gets the peak power within 1.3 seconds to trace the peak power when the power output of the PV is instantly varied. From the result it is concluded that the improved FOVSS Inc-Cond peak tracking control algorithm has the best dynamic enactment.

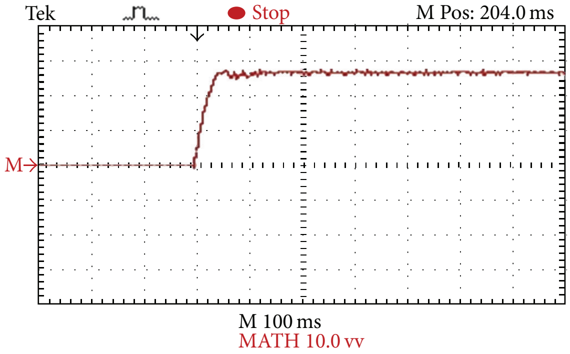

Figure 11: Change in power when the number of PV modules is increased from three to four.

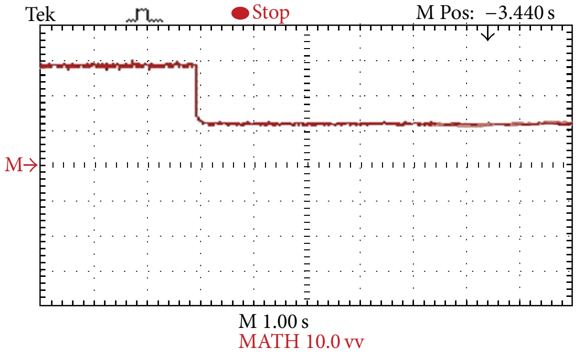

Figure 12: Change in power when the number of PV modules is decreased from four to three.

4. Conclusion

In this paper, a novel improved fractional order variable step size (FOVSS) incremental conductance (Inc-Cond) tracking algorithm is designed and verified with MATLAB simulation and experimental environment. The major difference between the suggested technique and existing tracking technique includes elimination of the additional PI control loop and investigates the effect of novel Improved FOVSS Inc-Cond control technique. This paper includes huge contributions such as how improved VSS Inc-Cond is derived based on fractional order derivative method, how DC to DC soft switching Luo converter is designed, and how comparison between the proposed scheme and existing system is done with the help of simulation and experimental arrangement. The experimental and simulation results demonstrate that the suggested controller tracks the peak power of the photovoltaic scheme in variable insulation with quick transient response. Since current and voltage of the solar photovoltaic are utilized as input elements, it has controller characteristics with variable step size. Thus, fluctuations around peak power are significantly eliminated. Thus the suggested FOVSS Inc-Cond based peak tracking algorithm increase the power output 4.75 times the conventional power output for low load conditions. Accordingly, it is seen that the suggested technique is favorable for quick varying climatic situation.

Nomenclature

T:	Temperature
G:	Irradiance
MPPT:	Maximum power point tracking
MPP:	Maximum power point
PV:	Photovoltaic
Inc-Cond:	Incremental conductance
ADC:	Analog to digital converter
FSS:	Fixed step size
FOVSS:	Fractional order variable step size
D:	Duty cycle
A:	Appendix
SW:	Switch
VSS:	Variable step size
I:	Current
V:	Voltage
MP:	Maximum power
FO:	Fractional order
FOD:	Fractional order derivative
ZVS:	Zero voltage switching
ZCS:	Zero current switching.

Conflict of Interests

The authors declare that there is no conflict of interests regarding the publication of this paper.

References

[1] C.-H. Lin, C.-H. Huang, Y.-C. Du, and J.-L. Chen, "Maximum photovoltaic power tracking for the PV array using the fractional-order incremental conductance method," *Applied Energy*, vol. 88, no. 12, pp. 4840–4847, 2011.

[2] A. Al Nabulsi and R. Dhaouadi, "Efficiency optimization of a DSP-based standalone PV system using fuzzy logic and Dual-MPPT control," *IEEE Transactions on Industrial Informatics*, vol. 8, no. 3, pp. 573–584, 2012.

[3] S. Subiyanto, A. Mohamed, and M. A. Hannan, "Intelligent maximum power point tracking for PV system using Hopfield neural network optimized fuzzy logic controller," *Energy and Buildings*, vol. 51, pp. 29–38, 2012.

[4] N. Patcharaprakiti, S. Premrudeepreechacharn, and Y. Sriuthaisiriwong, "Maximum power point tracking using adaptive fuzzy logic control for grid-connected photovoltaic system," *Renewable Energy*, vol. 30, no. 11, pp. 1771–1788, 2005.

[5] T. Tafticht, K. Agbossou, M. L. Doumbia, and A. Chériti, "An improved maximum power point tracking method for photovoltaic systems," *Renewable Energy*, vol. 33, no. 7, pp. 1508–1516, 2008.

[6] A. A. Ghassami, S. M. Sadeghzadeh, and A. Soleimani, "A high performance maximum power point tracker for PV systems," *Electrical Power and Energy Systems*, vol. 53, pp. 237–243.

[7] T. K. Soon, S. Mekhilef, and A. Safari, "Simple and low cost incremental conductance maximum power point tracking using buck-boost converter," *Journal of Renewable and Sustainable Energy*, vol. 5, pp. 023106–023110, 2013.

[8] L. Guo, J. Y. Hung, and R. M. Nelms, "Comparative evaluation of sliding mode fuzzy controller and PID controller for a boost converter," *Electric Power Systems Research*, vol. 81, no. 1, pp. 99–106, 2011.

[9] D. Rekioua, A. Y. Achour, and T. Rekioua, "Tracking power photovoltaic system with sliding mode control strategy," *Energy Procedia*, vol. 36, pp. 219–230, 2013.

[10] K. Punithaa, D. Devaraj, and S. Sakthivel, "Development and analysis of adaptive fuzzy controllers for photovoltaic system under varying atmospheric and partial shading condition," *Applied Soft Computing*, vol. 13, pp. 4320–4332, 2013.

[11] A. I. Dounis, P. Kofinas, C. Alafodimos, and D. Tseles, "Adaptive fuzzy gain scheduling PID controller for maximum power point tracking of photovoltaic system," *Renewable Energy*, vol. 60, pp. 202–214, 2013.

[12] S. Lalouni and D. Rekioua, "Optimal control of a grid connected photovoltaic system with constant switching frequency," *Energy Procedia*, vol. 36, pp. 189–199, 2013.

[13] A. Safari and S. Mekhilef, "Simulation and hardware implementation of incremental conductance MPPT with direct control method using cuk converter," *IEEE Transactions on Industrial Electronics*, vol. 58, no. 4, pp. 1154–1161, 2011.

[14] F. Liu, S. Duan, F. Liu, B. Liu, and Y. Kang, "A variable step size INC MPPT method for PV systems," *IEEE Transactions on Industrial Electronics*, vol. 55, no. 7, pp. 2622–2628, 2008.

[15] Q. Mei, M. Shan, L. Liu, and J. M. Guerrero, "A novel improved variable step-size incremental-resistance MPPT method for PV systems," *IEEE Transactions on Industrial Electronics*, vol. 58, no. 6, pp. 2427–2434, 2011.

[16] D. A. R. Wati, W. B. Pramono, and R. D. G. Wibowo, "Design and implementation of fuzzy logic controller based on incremental conductance algorithms for photovoltaic power optimization," in *Proceeding of the International Conference on Sustainable Energy Engineering and Application (ICSEEA'12)*, pp. 6–8, Yogyakarta, Indonesia, November 2012.

[17] M. H. Taghvaee, M. A. M. Radzi, S. M. Moosavain, H. Hizam, and M. H. Marhaban, "A current and future study on non-isolated DC-DC converters for photovoltaic applications," *Renewable and Sustainable Energy Reviews*, vol. 17, pp. 216–227, 2013.

[18] M. A. Al-Saffar, E. H. Ismail, and A. J. Sabzali, "Family of ZC-ZVS converters with wide voltage range for renewable energy systems," *Renewable Energy*, vol. 56, pp. 32–43, 2013.

[19] T. Esram and P. L. Chapman, "Comparison of photovoltaic array maximum power point tracking techniques," *IEEE Transactions on Energy Conversion*, vol. 22, no. 2, pp. 439–449, 2007.

[20] K. Ishaque, Z. Salam, M. Amjad, and S. Mekhilef, "An improved particle swarm optimization (PSO)-based MPPT for PV with reduced steady-state oscillation," *IEEE Transactions on Power Electronics*, vol. 27, no. 8, pp. 3627–3638, 2012.

[21] D. P. Hohm and M. E. Ropp, "Comparative study of maximum power point tracking algorithms," *Progress in Photovoltaics: Research and Applications*, vol. 11, no. 1, pp. 47–62, 2003.

[22] R. Arulmurugan and N. V. Suthanthira, "Intelligent fuzzy MPPT controller using analysis of DC to DC novel Buck converter for photovoltaic energy system applications," in *Proceedings of the International Conference on Pattern Recognition, Informatics and Mobile Engineering*, pp. 225–231, February 2013.

[23] R. Rahmani, R. Yusof, and M. Seyedmahmoudian, "Hybrid technique of ant colony and particle swarm optimization for short term wind energy forecasting," *Journal of Wind Engineering and Industrial Aerodynamics*, vol. 123, part A, pp. 163–170, 2013.

Hindawi Publishing Corporation
International Journal of Photoenergy
Volume 2014, Article ID 153428, 7 pages
http://dx.doi.org/10.1155/2014/153428

Research Article

A Simple and Efficient MPPT Method for Low-Power PV Cells

Maria Teresa Penella[1] and Manel Gasulla[2]

[1] *Urbiotica S.L, Parc UPC, Edifici Nexus II, C/Jordi Girona 29, 08034 Barcelona, Spain*
[2] *Universitat Politècnica de Catalunya, C/Esteve Terradas 7, 08860 Castelldefels, Spain*

Correspondence should be addressed to Manel Gasulla; manel.gasulla@upc.edu

Received 31 October 2013; Accepted 28 December 2013; Published 27 February 2014

Academic Editor: Ismail H. Altas

Small-size PV cells have been used to power sensor nodes. These devices present limited computing resources and so low complexity methods have been used in order to extract the maximum power from the PV cells. Among them, the fractional open circuit voltage (FOCV) method has been widely proposed, where the maximum power point of the PV cell is estimated from a fraction of its open circuit voltage. Here, we show a generalization of the FOCV method that keeps its inherent simplicity and improves the tracking efficiency. First, a single-diode model for PV cells was used to compute the tracking efficiency versus irradiance. Computations were carried out for different values of the parameters involved in the PV cell model. The proposed approach clearly outperformed the FOCV method, specially at low irradiance, which is significant for powering sensor nodes. Experimental tests performed with a 500 mW PV panel agreed with these results.

1. Introduction

The advances in electronics and communication protocols have led to a widespread use of wireless sensor networks (WSN). In most applications, the sensor nodes of the WSN are required to be wireless both for communication and powering. As for the power supply, the use of small-size PV cells or modules has been proposed. The power-voltage (P-V) curve of a photovoltaic (PV) cell or panel presents a maximum power point (MPP) that changes with temperature and irradiance. To extract the maximum power under varying conditions an MPP tracker can be used. Several MPP tracking (MPPT) methods have been proposed in the literature [1–4]. Since sensor nodes present limited computing resources, low complexity MPPT methods are preferred for this particular application. Because the location of the sensor nodes is mostly determined by the application, a wide range of irradiance can be expected at the sensor placement. Thus, a high efficiency is desirable over a wide range of irradiance, and specially for low irradiance as the power source is scarce.

One of the simplest and most popular MPPT methods is the fractional open circuit voltage (FOCV) technique, which estimates the MPP voltage (V_{MPP}) from a fraction of the open circuit voltage (V_{OC}); that is,

$$V_{\mathrm{MPP,est}} = kV_{\mathrm{OC}}, \quad (1)$$

where $V_{\mathrm{MPP,est}}$ is the estimated value of the actual V_{MPP} and k is an empirical constant whose value should be set following a thorough characterization of the PV panel under varying meteorological conditions (irradiance and cell temperature). V_{OC} is either measured periodically (by momentarily opening the output of the PV panel) or by using a pilot cell (i.e., an additional solar cell of the same type configured in open circuit voltage configuration). Typical reported values for k range from 0.73 to 0.8 depending on the PV panel type and characteristics [2, 3]. Because of its simplicity, the FOCV method has been recently applied to small-size PV cells in order to power autonomous sensors [5–9].

In this work, we propose to generalize (1) in order to estimate V_{MPP} by using a linear fit; that is,

$$V_{\mathrm{MPP,est}} = aV_{\mathrm{OC}} + b, \quad (2)$$

where a and b are empirical coefficients. The use of (2) will be referred to as the linear open circuit voltage (LOCV) method. In fact, the FOCV method can be considered a particular case of the proposed LOCV method with $b = 0$. Both computed and experimental results of the proposed approach will be presented and compared with the FOCV method. As will be shown, the LOCV method significantly improves the performance of the FOCV method, especially at low irradiance, while maintaining its inherent simplicity. The work presented here builds upon [10], where we first presented (2) and some initial results.

2. Solar Cell Model

Different equivalent circuits have been used in the literature in order to model the current/voltage (I-V) characteristic of a silicon PV cell [11–15]. Among them, the single-diode model, shown in Figure 1, offers a good compromise between simplicity and accuracy [13], whereby I_{PH} is the photogenerated current, I is the cell current, V is the cell voltage, and R_s and R_p are, respectively, the series and shunt resistances. This model will be used here in order to generate computed data of the I-V curve of a PV cell.

The corresponding expression of the I-V characteristic is given by [16]

$$I = I_{SC} - I_O\left[e^{((q(V+R_sI))/n_dKT_{cell})} - 1\right] - \frac{V + R_sI}{R_p}, \qquad (3)$$

where I_{PH} has been approximated by I_{SC}, the short circuit current of the cell; I_O is the saturation current of the diode; q is the electron charge; n_d is the ideality factor of the diode, which, for silicon, is usually between 1 and 2 [5, 7]; K is the Boltzmann constant; and T_{cell} is the cell temperature in Kelvin.

By considering open circuit conditions ($I = 0$ and $V = V_{OC}$) in (3), we can write the parameter I_O as

$$I_O = \frac{I_{SC} - \left(V_{OC}/R_p\right)}{\left[e^{(qV_{OC}/n_dKT_{cell})} - 1\right]}. \qquad (4)$$

The parameters I_{SC} and V_{OC} in (3) and (4) change with the irradiance and temperature as

$$I_{SC}\left(T_{cell}, G\right) = \frac{G}{1000}\left[I_{SC_r} + \alpha\left(T_{cell} - T_r\right)\right], \qquad (5)$$

$$V_{OC}\left(T_{cell}, G\right) = \left[V_{OC_r} + \beta\left(T_{cell} - T_r\right)\right] \times \left[1 + \rho_{OC}\ln\left(\frac{G}{G_{OC}}\right)\ln\left(\frac{G}{G_r}\right)\right], \qquad (6)$$

where T_{cell} is the cell temperature; G is the incident irradiance (in W/m^2); α and β are the current and voltage temperature coefficients, respectively; I_{SC_r} and V_{OC_r} are given at a reference irradiance (G_r) and reference cell temperature (T_r); and ρ_{OC} and G_{OC} are two empirical constants used to model the significant variation of V_{OC} at low G. Typically, G_r = 1000 W/m^2 (=100 mW/cm^2) and T_r = 25°C. Values of $\rho_{OC} = -0.04$ and G_{OC} = 1000 W/m^2 are adequate for many silicon PV cells [17]. When directly illuminated, solar cells heat up above the ambient temperature (T_a), which is known as the self-heating effect, and T_{cell} can be obtained from

$$T_{cell} = T_a + \frac{T_{cell,NOCT} - 20}{800\ \mathrm{W/m^2}}G. \qquad (7)$$

where $T_{cell,NOCT}$, known as the *nominal operating cell temperature* (NOCT), is the temperature of the cell when exposed to 800 W/m^2 at T_a = 20°C and wind speed of 1 m/s. It is empirically determined, and for silicon solar cells range between 42°C and 48°C.

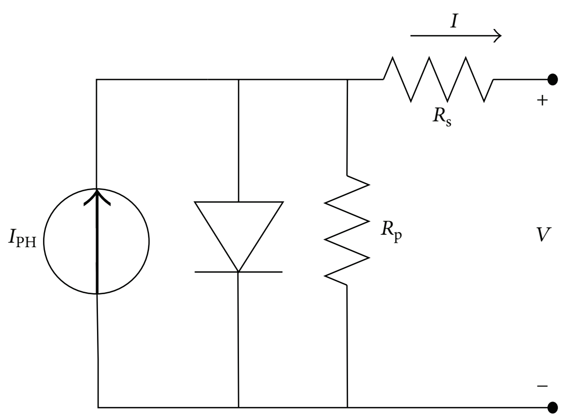

Figure 1: Single-diode model of a solar cell with series (R_s) and shunt (R_p) resistances.

3. Computed Results

We employed (3) to (7) with the following parameter values typical of monocrystalline solar cells [17]: J_{SC_r} = 35 mA/cm^2; V_{OC_r} = 0.6 V; α/A = 12.5 μA/cm^2/°C; β = −2 mV/°C; and $T_{cell,NOCT}$ = 42°C. The parameters I_{SC_r} and α in (5) can be, respectively, obtained by multiplying J_{SC_r} and α/A by the area of the cell. For the computations, a single solar cell with an area of 1 cm^2 was used. Nevertheless, as will be justified at the end of this section, the results and the derived conclusions are equally valid to cells of any area and PV panels composed of an arbitrary number of solar cells disposed in parallel and series. Figure 2 shows the computed I-V and P-V curves at three different levels of irradiance for the particular case of $R_s = 0$, $R_p = \infty$, $n_d = 1.5$, and T_a = 25 °C. To obtain the data we simulated the PV cell model in SPICE. The power values were obtained by multiplying I by V at each data point. As can be seen, both V_{OC} and V_{MPP} slightly decrease at the highest irradiance, which is due to the self-heating effect of the PV cell.

From the data of the I-V and P-V curves, several parameters can be obtained such as V_{OC}, V_{MPP}, and P_{MPP} (power at the MPP). Table 1 shows numerical values of those parameters for an irradiance range from *ca.* 20 W/m^2 to 1000 W/m^2. Fourteen points of irradiance, logarithmically equally spaced, were selected to provide a dynamic range around 100 in P_{MPP}. Other cases that will be discussed throughout this section are also shown in Table 1. Figure 3

Table 1: Computed V_{OC}, V_{MPP}; and P_{MPP} data at fourteen points of irradiance, logarithmically equally spaced, and for different values of the parameters of the PV cell model.

G	$n_d = 1.5$ (Figure 1)			$n_d = 1$			$n_d = 2$			$r_s = 0.1$ (Figure 6)			$r_p = 10$ (Figure 8)		
(W/m^2)	V_{OC} (V)	V_{MPP} (V)	P_{MPP} (mW)	V_{OC} (V)	V_{MPP} (V)	P_{MPP} (mW)	V_{OC} (V)	V_{MPP} (V)	P_{MPP} (mW)	V_{OC} (V)	V_{MPP} (V)	P_{MPP} (mW)	V_{OC} (V)	V_{MPP} (V)	P_{MPP} (mW)
23.7	0.262	0.194	0.135	0.262	0.207	0.153	0.262	0.185	0.121	0.262	0.193	0.134			
31.6	0.311	0.237	0.227	0.311	0.251	0.254	0.311	0.226	0.205	0.311	0.235	0.225			
42.2	0.357	0.277	0.362	0.357	0.293	0.401	0.357	0.264	0.330	0.357	0.275	0.359	0.241	0.126	0.095
56.2	0.398	0.313	0.553	0.398	0.331	0.609	0.398	0.300	0.507	0.398	0.311	0.548	0.306	0.168	0.168
75	0.434	0.347	0.826	0.434	0.365	0.904	0.434	0.332	0.761	0.434	0.343	0.816	0.369	0.221	0.299
100	0.467	0.376	1.2	0.467	0.396	1.312	0.467	0.361	1.113	0.467	0.372	1.186	0.42	0.282	0.524
133.4	0.495	0.402	1.725	0.495	0.422	1.874	0.495	0.385	1.600	0.495	0.395	1.693	0.462	0.337	0.899
177.8	0.518	0.423	2.431	0.518	0.444	2.635	0.518	0.406	2.259	0.518	0.415	2.374	0.494	0.379	1.477
237.1	0.537	0.440	3.38	0.537	0.461	3.657	0.537	0.422	3.146	0.537	0.429	3.279	0.519	0.409	2.321
316.2	0.55	0.452	4.64	0.55	0.474	5.013	0.55	0.434	4.321	0.55	0.437	4.458	0.537	0.43	3.500
421.7	0.558	0.458	6.28	0.558	0.481	6.786	0.558	0.441	5.853	0.558	0.439	5.961	0.548	0.443	5.094
562.3	0.56	0.459	8.386	0.56	0.482	9.067	0.56	0.441	7.812	0.56	0.433	7.821	0.553	0.448	7.185
749.9	0.555	0.454	11.031	0.555	0.477	11.943	0.555	0.436	10.264	0.555	0.42	10.035	0.55	0.446	9.850
1000	0.543	0.442	14.254	0.543	0.464	15.472	0.543	0.424	13.234	0.543	0.398	12.511	0.54	0.436	13.13

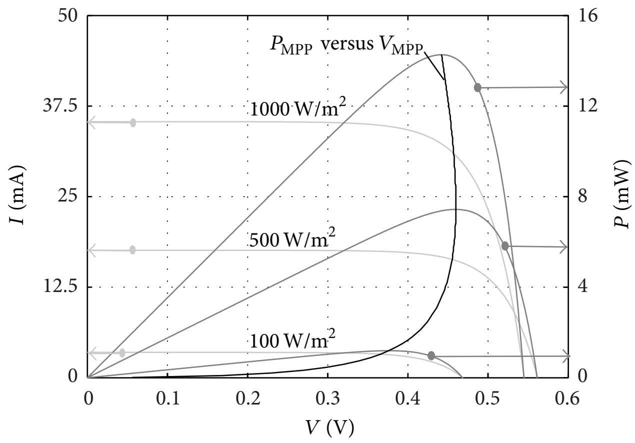

Figure 2: Generic I-V and P-V plots at several values of G and at $T_a = 25\,^\circ$C for a single solar cell with an area of 1 cm^2. A curve joining the MPPs is also plotted.

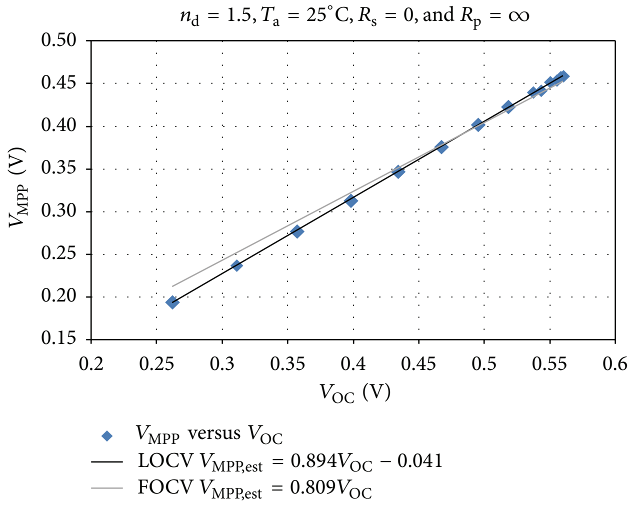

Figure 3: Computed V_{MPP} versus V_{OC} for a single PV cell. Two least-square regression lines are also represented: the grey line corresponds to the FOCV method with $k = 0.809$ whereas the black line corresponds to the LOCV method with $a = 0.894$ and $b = -0.041$. The parameters of the PV cell model are $T_a = 25\,^\circ$C, $n_d = 1.5$, $R_s = 0$, and $R_p = \infty$.

represents the fourteen computed points (diamonds) of V_{MPP} versus V_{OC} and two least-squares regression lines fitted to the computed data corresponding, respectively, to the FOCV method, that is, (1) with $k = 0.809$, and the LOCV method, that is, (2) with $a = 0.894$ and $b = -0.041$. As can be seen, the regression line corresponding to the LOCV method better fits the computed data. The inferred parameters of the regression lines (k, a, and b) were used to obtain $V_{\mathrm{MPP,est}}$ at the fourteen irradiance points for each of the two methods, by using (1) and (2), respectively.

The corresponding power values at $V_{\mathrm{MPP,est}}$, $P_{\mathrm{MPP,est}}$ were inferred from the computed P-V curves in order to obtain the tracking efficiency, which is given by

$$\eta_{\mathrm{MPP}} = \frac{P_{\mathrm{MPP,est}}}{P_{\mathrm{MPP}}}. \tag{8}$$

This parameter is used in the literature to compare the performance among different algorithms. Obviously, a value of 1 (100%) is the ultimate goal. Figure 4 shows the computed values of η_{MPPT} versus G at $T_a = 25\,^\circ$C for the fourteen irradiance points. We added the results at two more temperatures, 0°C and 50°C. For these temperatures, the P-V curves were recalculated but we still used the same regression lines of Figure 3. This makes sense, as a PV panel can be characterized at a single temperature, for example, 25°C, and the calculated regression lines used for

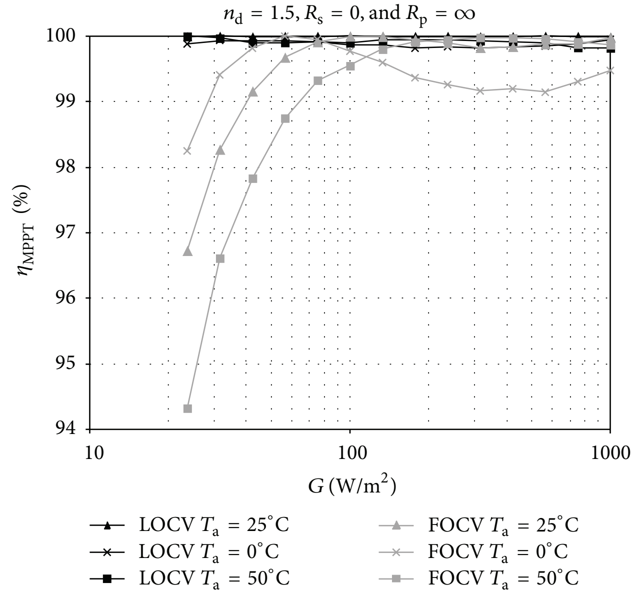

FIGURE 4: Computed η_{MPPT} versus G by using the FOCV and LOCV methods for a single PV cell at different values of T_a and with n_d = 1.5, R_s = 0, and R_p = ∞.

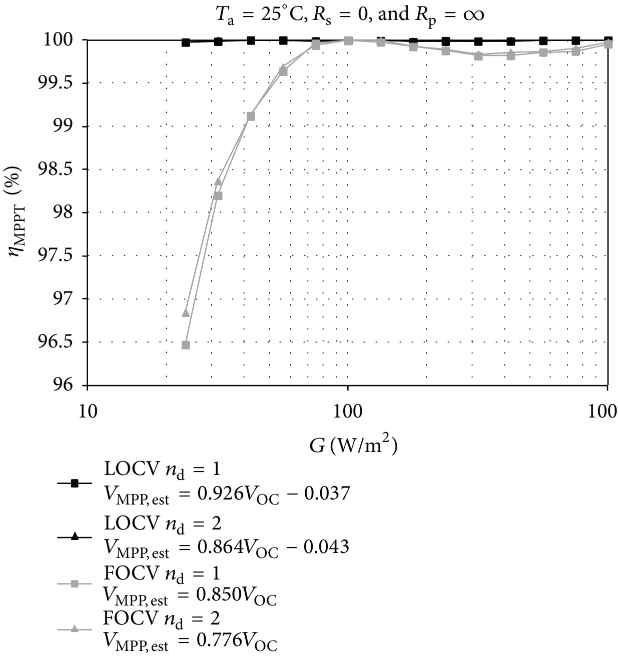

FIGURE 5: Computed η_{MPPT} versus G by using the FOCV and LOCV methods for a single PV cell at different values of n_d and with T_a = 25 °C, R_s = 0, and R_p = ∞.

the full working temperature range. As can be seen, at low irradiance the LOCV method clearly outperforms the FOCV method. At higher irradiance, a rather high value of η_{MPPT} (>99%) is achieved by both methods, although the FOCV method presents the lowest efficiency from *ca.* 100 W/m² to 1000 W/m² at T_a = 0 °C. The value of η_{MPPT} for the LOCV method was always higher than 99.8% at the three computed temperatures.

More computations were carried out at T_a = 25 °C for n_d = 1 and n_d = 2 (see Table 1). Again, better linear fits were obtained with the LOCV method (not shown). Figure 5 shows the corresponding computed values of η_{MPPT}. For each of the cases, the parameters of the corresponding regression lines are provided. Again, the LOCV method clearly outperforms the FOCV method at low irradiance and slightly at medium irradiance.

Finally, computations were performed for n_d = 1.5, T_a = 25 °C, nonzero values of R_s, and finite values of R_p. In [13] normalized values for R_s and R_p were defined as

$$r_s = \frac{R_s}{[V_{OC}/I_{SC}]_{STC}},$$
$$r_p = \frac{R_p}{[V_{OC}/I_{SC}]_{STC}}. \tag{9}$$

This normalization allows for an immediate comparison among different PV modules (of different area and characteristics). Based on [13], in our work we considered the following values: from 0.01 to 0.1 for r_s and from 100 to 10 for r_p. The performance for both r_s = 0.01 and r_p = 100 was almost identical to that shown in Figure 2 (for T_a = 25 °C), with the LOCV method outperforming the FOCV method. So these results are not shown here. Table 1 shows the data for the limiting cases r_s = 0.1 (with r_p = ∞) and r_p = 10 (with r_s = 0). For the case of r_p = 10, the data for the lowest two irradiance levels were not used as they provided negligible values of P_{MPP} (well below of 1% of the resulting P_{MPP} at 1000 W/m²). As for r_s = 0.1, Figure 6 shows the computed values of V_{MPP} versus V_{OC} and the fitted regression lines. Due to the high value of r_s (highest limit), the data values present a folded form at the highest irradiance levels. So the regression lines of the FOCV and LOCV methods cannot fit the data corresponding to the high irradiance levels as well as that in Figure 3. Otherwise, both lines are very similar in this case. Consequently, the computed values of η_{MPPT}, shown in Figure 7 (r_s = 0.1), are quite similar (and indeed relatively high) for both methods.

As for r_p = 10, Figure 8 again shows the computed values of V_{MPP} versus V_{OC} and the fitted regression lines. Due to the low relative value of r_p (lowest limit) the regression line of the LOCV method cannot fit the data corresponding to the low irradiance levels as well as that in Figure 3. Even so, the computed values of η_{MPPT}, also shown in Figure 7, still present a high efficiency, outperforming the FOCV method at all the irradiance levels, but specially at the low ones. Finally, we computed η_{MPPT} for r_s = 0.1 and r_p = 10 (not shown). In that case, the LOCV method also outperformed the FOCV method at low and medium irradiance levels.

Increasing the PV cell area or adding identical PV cells in parallel will scale up the values of currents and thus of powers but the values of V_{OC} and V_{MPP} will remain the same and so the derived tracking efficiencies. Tracking efficency will also

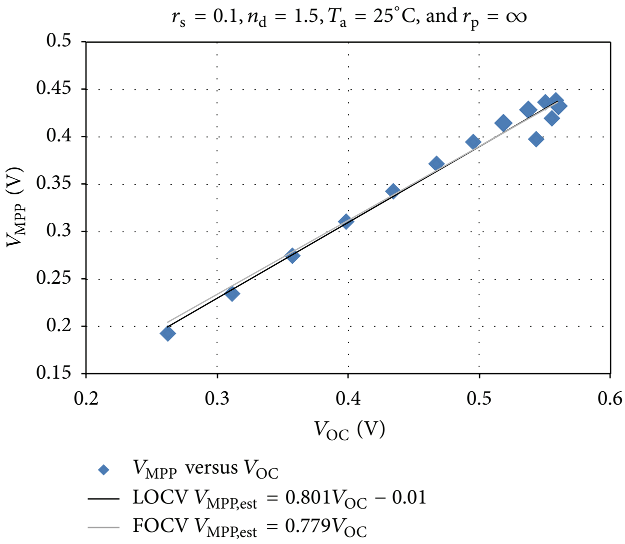

Figure 6: Computed V_{MPP} versus V_{OC} for a single PV cell with $T_a = 25^\circ$C, $n_d = 1.5$, $r_p = \infty$, and $r_s = 0.1$. Two regression lines corresponding to the FOCV and LOCV methods are also represented.

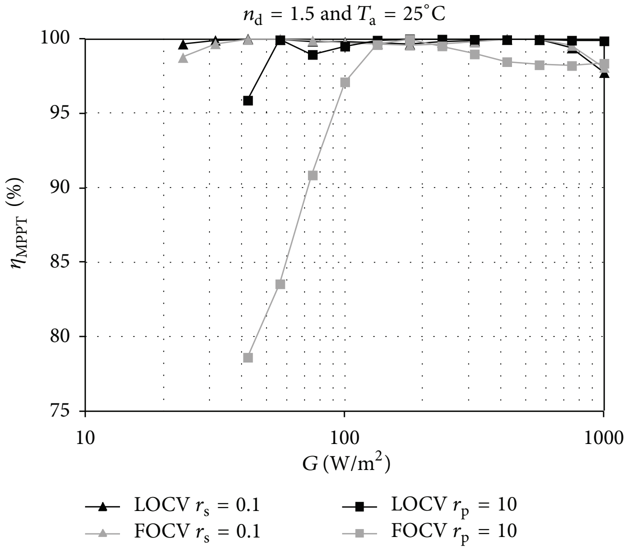

Figure 7: Computed η_{MPPT} versus G by using the FOCV and the LOCV methods for a single PV cell with $T_a = 25^\circ$C, $n_d = 1.5$, and for both $r_s = 0.1$ (and $r_p = \infty$) and $r_p = 10$ (and $r_s = 0$).

remain constant by adding PV cells in series: both V_{MPP} and V_{OC} will scale up by the number of serial cells but their ratio will remain constant and so the derived tracking efficiencies.

4. Experimental Results

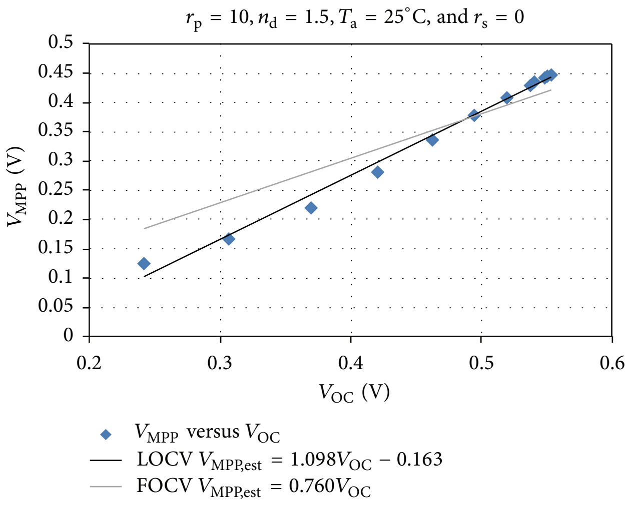

Figure 8: Computed V_{MPP} versus V_{OC} for a single PV cell with $T_a = 25^\circ$C, $n_d = 1.5$, $r_s = 0$, and $r_p = 10$. Two regression lines corresponding to the FOCV and LOCV methods are also represented.

The LOCV method was tested with a 500 mW (I_{SC} = 160 mA, V_{OC} = 4.6 V) PV panel (MSX-005, Solarex) and compared with the FOCV method. These low-power panels are used, for example, to power autonomous sensors [5–10]. In order to achieve reproducible results, we implemented a PV panel simulator by connecting a current source (GS610, Yokogawa) in parallel with the PV panel, which was coated with an opaque cover (Figure 9). In this way, the short circuit current (I_{SC}) of the PV panel was adjusted by the current source, emulating different levels of irradiance. Since the panel was not illuminated, $T_{cellL,NOCT} = 20^\circ$C (i.e., the panel is not overheated). The current source was configured to cover the full range of the PV panel, varying from 5 mA to 158 mA in 9 mA steps. The PV panel simulator was characterized by using the GS610's measurement unit to measure the panel's voltage, a 2001 multimeter (Keithley) to measure the current of the panel, and a programmable voltage source (Agilent E3631A) in parallel with a 10 Ω/1 W resistor acting as a load. Figure 9 shows the experimental setup.

All the instruments were controlled via the GPIB bus with a dedicated program using the graphical development environment LabVIEW. For each current value (I_{SC}), the voltage of the E3631A was increased from 0 V to 5 V in 0.1 V steps. PV output voltages and currents were measured and the corresponding power values were calculated in order to obtain the *I-V* and *P-V* curves. From each *P-V* curve the values of V_{OC}, V_{MPP}, and P_{MPP} were obtained. The limit values for P_{MPP} were, respectively, 8.2 mW (I_{SC} = 5 mA) and 545.9 mW (I_{SC} = 158 mA).

Figure 10 represents the experimental data of V_{MPP} versus V_{OC} and two fitted least-squares regression lines corresponding to the FOCV and LOCV methods. As can be seen, the regression line corresponding to the LOCV method better fits the experimental data. From the two regression lines, the values of $V_{MPP,est}$ corresponding to the FOCV and LOCV methods were derived. Then, from the *P-V* curves, the values of $P_{MPP,est}$ and η_{MPPT} were obtained. Figure 11 shows η_{MPPT} versus P_{MPP}. In agreement with the computed results of Section 3, the LOCV method clearly outperformed the

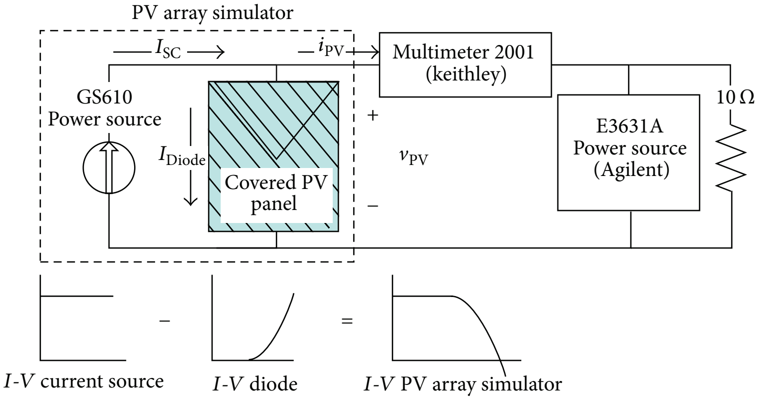

FIGURE 9: The PV array simulator and the setup used for its characterization.

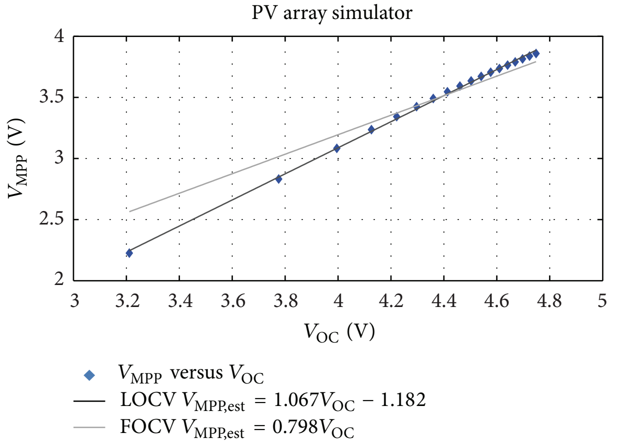

FIGURE 10: V_{MPP} versus V_{OC} for a 500 mW panel simulator at T_a = 25 °C and two fitted least-square regression lines corresponding to the FOCV and LOCV methods.

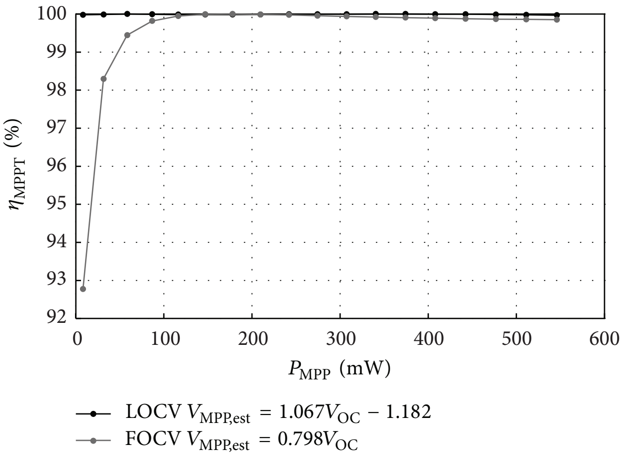

FIGURE 11: Experimental η_{MPPT} versus P_{MPP} by using the FOCV method (grey line), with $k = 0.798$, and the LOCV method (black line), with $a = 1.0674$ and $b = -1.182$, for a 500 mW PV panel.

FOCV method at low irradiance, with η_{MPPT} always being higher than 99.96%. The efficiency increase at low irradiance is of significant importance in order to power sensor nodes.

5. Conclusion

PV cells have been proposed in the literature in order to power the sensor nodes of WSN. Because of the limited computing capabilities of the sensor nodes, simple MPPT methods have to be used. Among them, the FOCV method has been widely proposed and used. Tracking efficiencies, though, are lower than that achieved with more complex methods. In this work, we have proposed the LOCV method, which outperforms the FOCV method while maintaining its inherent simplicity. Computations show that the LOCV method achieves a high efficiency for all the irradiance range whereas the FOCV method fails in achieving a high efficiency at low irradiance levels for most of the cases. The presence of extremely low values of shunt resistance of the PV cell negatively impacts the achieved efficiency on both methods but specially that of the FOCV method. Finally, experimental data from a low-power 500 mW PV panel confirmed the good performance of the LOCV method for a wide range of irradiance, which is of significant value for powering sensor nodes.

Conflict of Interests

The authors declare that there is no conflict of interests regarding the publication of this paper.

Acknowledgment

This work was supported by the Spanish Ministry of Economy and Competitiveness under Contract TEC2011-27397.

References

[1] T. Esram and P. L. Chapman, “Comparison of photovoltaic array maximum power point tracking techniques,” *IEEE Transactions on Energy Conversion*, vol. 22, no. 2, pp. 439–449, 2007.

[2] N. Onat, “Recent developments in maximum power point tracking technologies for photovoltaic systems,” *International Journal of Photoenergy*, vol. 2010, Article ID 245316, 11 pages, 2010.

[3] D. P. Hohm and M. E. Ropp, “Comparative study of maximum power point tracking algorithms,” *Progress in Photovoltaics: Research and Applications*, vol. 11, no. 1, pp. 47–62, 2003.

[4] V. Salas, E. Olías, A. Barrado, and A. Lázaro, “Review of the maximum power point tracking algorithms for stand-alone photovoltaic systems,” *Solar Energy Materials and Solar Cells*, vol. 90, no. 11, pp. 1555–1578, 2006.

[5] D. Dondi, A. Bertacchini, D. Brunelli, L. Larcher, and L. Benini, “Modeling and optimization of a solar energy harvester system for self-powered wireless sensor networks,” *IEEE Transactions on Industrial Electronics*, vol. 55, no. 7, pp. 2759–2766, 2008.

[6] A. S. Weddell, G. V. Merrett, and B. M. Al-Hashimi, “Photovoltaic sample-and-hold circuit enabling MPPT indoors for low-power systems,” *IEEE Transactions on Circuits and Systems I*, vol. 59, no. 6, pp. 1196–1204, 2012.

[7] A. Chini and F. Soci, “Boost-converter-based solar harvester for low power applications,” *Electronics Letters*, vol. 46, no. 4, pp. 296–298, 2010.

[8] F. I. Simjee and P. H. Chou, “Efficient charging of supercapacitors for extended lifetime of wireless sensor nodes,” *IEEE Transactions on Power Electronics*, vol. 23, no. 3, pp. 1526–1536, 2008.

[9] O. Lopez-Lapeña and M. T. Penella, “Low-power FOCV MPPT controller with automatic adjustment of the sample&hold,” *Electronics Letters*, vol. 48, no. 20, pp. 1301–1303, 2012.

[10] M. T. Penella and M. Gasulla, “Optical energy harvesting,” in *Powering Autonomous Sensors*, chapter 5, section 5.5, pp. 101–107, Springer, Dordrecht, The Netherlands, 2011.

[11] J. A. Gow and C. D. Manning, “Development of a photovoltaic array model for use in power-electronics simulation studies,” *IEE Proceedings: Electric Power Applications*, vol. 146, no. 2, pp. 193–200, 1999.

[12] M. G. Villalva, J. R. Gazoli, and E. R. Filho, “Comprehensive approach to modeling and simulation of photovoltaic arrays,” *IEEE Transactions on Power Electronics*, vol. 24, no. 5, pp. 1198–1208, 2009.

[13] C. Carrero, J. Amador, and S. Arnaltes, “A single procedure for helping PV designers to select silicon PV modules and evaluate the loss resistances,” *Renewable Energy*, vol. 32, no. 15, pp. 2579–2589, 2007.

[14] W. de Soto, S. A. Klein, and W. A. Beckman, “Improvement and validation of a model for photovoltaic array performance,” *Solar Energy*, vol. 80, no. 1, pp. 78–88, 2006.

[15] F. Adamo, F. Attivissimo, A. Di Nisio, and M. Spadavecchia, “Characterization and testing of a tool for photovoltaic panel modeling,” *IEEE Transactions on Instrumentation and Measurement*, vol. 60, no. 5, pp. 1613–1622, 2011.

[16] F. Lasnier and T. G. Ang, *Photovoltaic Engineering Handbook*, Adam Hilger, New York, NY, USA, 1990.

[17] A. Luque and S. Hegedus, *Handbook of Photovoltaic Science and Engineering*, 2003.

Hindawi Publishing Corporation
International Journal of Photoenergy
Volume 2014, Article ID 586503, 9 pages
http://dx.doi.org/10.1155/2014/586503

Research Article

BICO MPPT: A Faster Maximum Power Point Tracker and Its Application for Photovoltaic Panels

Hadi Malek[1] **and YangQuan Chen**[2]

[1] *Electrical & Computer Engineering Department, Utah State University, Logan, UT 84321, USA*
[2] *MESA Lab, School of Engineering, University of CA, Merced, California 95343, USA*

Correspondence should be addressed to Hadi Malek; hadi.malek@aggiemail.usu.edu

Received 29 May 2013; Accepted 3 January 2014; Published 27 February 2014

Academic Editor: Ismail H. Altas

This paper develops a maximum power point tracking (MPPT) algorithm to optimize photovoltaic (PV) array performance and make it more compatible to rapidly varying weather conditions. In particular, a novel extremum seeking controller (ESC), which uses a Bode ideal cutoff (BICO) filter in its structure, is designed and tested on a simulated PV array. The new algorithm is compared against the commonly used ESC MPPT algorithm with first-order filters. The BICO extremum seeking controller achieves transient rise to the MPP faster than the common extremum seeking MPPT, which is the faster and more robust method among all other methods. This claim has been discussed and proved mathematically in this paper, in addition to simulation illustrations. This faster extremum seeking algorithm enables PV systems to detect rapid variations in the environmental conditions like irradiation and temperature changes.

1. Introduction

The PV cells exhibit a nonlinear V-I characteristics as shown in Figure 1 and their power output mainly depends on the nature of the connected load. Since connecting the load directly to the PV system results in a poor overall efficiency, to minimize the life cycle cost of any PV system, increasing the efficiency by changing the operating point of the system using an intermediate maximum power point tracker (MPPT) is desirable.

MPPT controls the output current and voltage and consequently output power of the PV panel adaptively to maintain maximum efficiency and better performance in the presence of environmental variations. Typically MPPT algorithms are implemented on a solar array using a switching power converter; for instance, in a grid-tied inverter, the solar array charges a capacitor and then the current is switched out of the capacitor at an optimal varying duty cycle in order to extract maximum power from the PV array.

A number of solar power converter architectures with MPPT are discussed in the literature [1, 2]. As discussed in these works, convergence speed is one of the most important features among all different MPPT algorithms. Brunton et al. have pointed out in their paper that, "as irradiance decreases rapidly, the *IV* curve shrinks and the MPV and MPI decrease. If the MPPT algorithm does not track fast enough, the control current or voltage will fall off the *IV* curve" [3]. Consequently, any improvement in the rise time of MPPT improves the reliability of the system and increases the power extraction and efficiency of the whole system.

1.1. Maximum Power Point Tracking Algorithms.

There are many different maximum power point tracking techniques for photovoltaic systems which are well established in the literature [4–11]. These techniques vary in many aspects as simplicity, convergence speed, digital or analogical implementation, sensors required, cost, range of effectiveness, and other aspects. In analog world, short current (SC), open voltage (OV), and CV are good options for MPPT; otherwise with digital circuits that require the use of microcontroller, Perturb and Observe (P&O), Incremental Conductance (IC), and temperature methods are easy to implement [12]. Table 1 and Figure 2 present the comparison among different MPPT

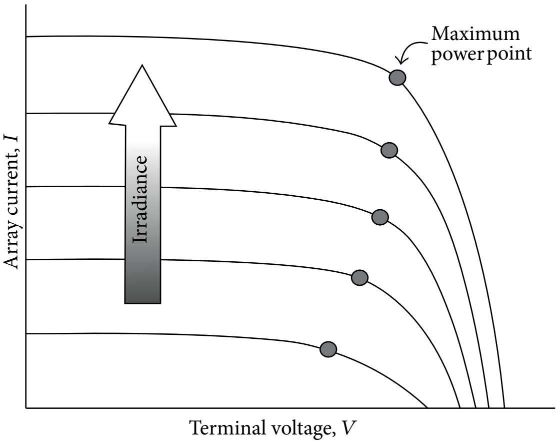

Figure 1: *I-V* curves at various solar irradiances [3].

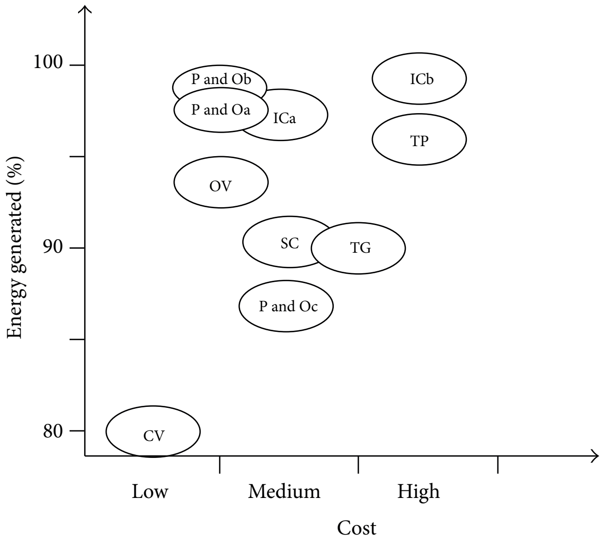

Figure 2: Comparison of the MPPT methods [12].

methods considering the costs of sensors, microcontroller, and additional power components and also their efficiencies. In this table, A means absence, L means low, M means medium, and H means high.

Currently, the most popular and workhorse MPPT algorithm is P&O, because of its balance between performance and simplicity. However, it suffers from the lack of speed and adaptability which is necessary for tracking the fast transients under varying environmental conditions [3]. Recently, another adaptive algorithm, called extremum seeking control, has been developed [13] to overcome these weaknesses.

1.2. Extremum Seeking Control. A promising new robust MPPT algorithm is the method of extremum seeking (ES) control, which carries all P&O's benefits like simplicity and performance, and in addition, improves its weaknesses [3]. Figures 3 and 4 present the comparison between ESC and P&O, where the inverter controls the current and voltage

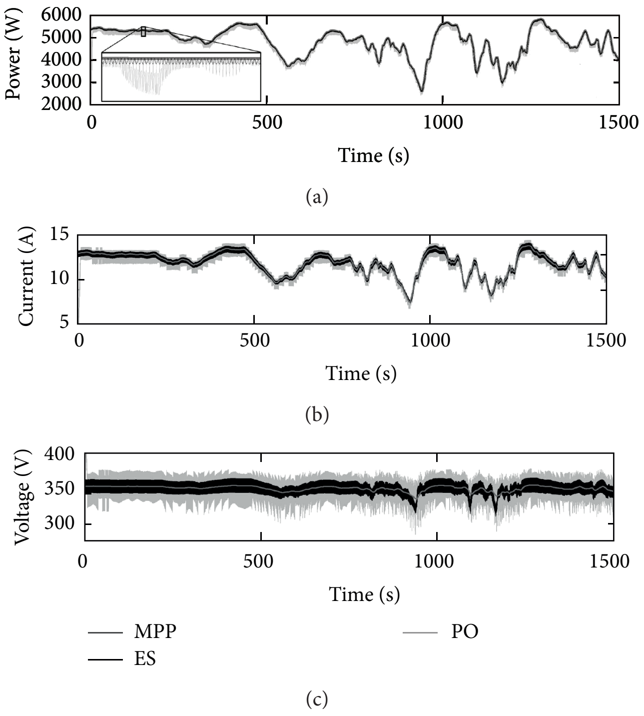

Figure 3: Comparison of current controlled P&O and ESC MPPT controller [3].

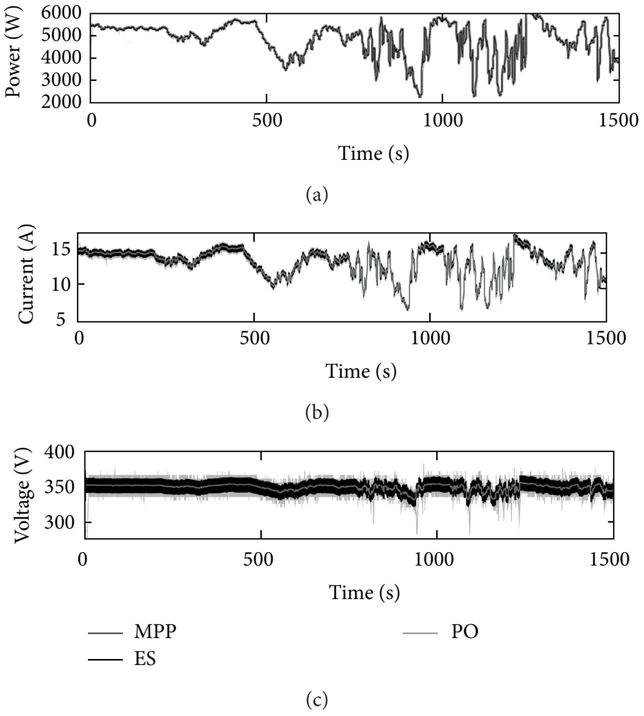

Figure 4: Comparison of voltage controlled P&O and ESC MPPT controller [3].

Table 1: MPPT methods comparison [12].

MPPT algorithm	Additional components	Sensors	Micro-Controller	Total
CV	A	L	A/L	L
SC	H	M	A/L	M
OV	H	L/M	A/L	L/M
P and Oa	A	M	L	L/M
P and Ob	A	M	L	L/M
P and Oc	A	M	M	M
IC	A	M	M	M
TG	A	M/H	M	M/H
TP	A	H	M/H	H

according to the set-points which are provided by these two MPPT algorithms.

The power, current, and voltage are plotted versus time for the ESC and P&O algorithms as well as the true maximum power of the system.

P&O and ESC methods oscillate closely around the real maximum power voltage, as seen in the power versus time plot. Obviously, the ESC method rises to the MPP orders of magnitude more rapidly than the P&O.

ESC MPPT has some advantages from hardware implementation point of view. Brunton et al. have mentioned in their paper that “the ripple-based ES algorithm has good MPPT performance over a range of inverter capacitor sizes. Typically, the choice of capacitor is expensive because it must be well characterized and large enough to maintain a small ripple. However, because the ES control signal exploits the natural inverter ripple, a smaller capacitor allows the tracking of rapid irradiance changes.”

ESC for peak power point tracking method has been successfully applied to biochemical reactors [14, 15], ABS control in automotive brakes [16], variable cam timing engine operation [17], electromechanical valves [18], axial compressors [19], mobile robots [20], mobile sensor networks [21, 22], optical fibre amplifiers [23], and so on. A good survey of the literature on this topic prior to 1980 can be found in [24] and a more recent overview can be found in [25]. Astrom and Wittenmark rated extremum seeking as one of the most promising adaptive control methods [26].

Since extremum seeking control has better features and performance compare to P&O which is the best known MPPT algorithm, in this paper, the improvement of better than the best MPPT algorithm has been investigated.

2. Basic Regular Extremum Seeking Algorithm

As shown in Figure 5, ESC algorithm employs a slow periodic perturbation, $\sin(\omega t)$, which is added to the estimated signal, $\hat{\theta}$. If the perturbation is slow enough, the plant appears as a static map $y = f(\theta)$ and its dynamics do not interfere with the peak seeking scheme [13]. If $\hat{\theta}$ is on either side of θ^*, which is the optimal point, the perturbation signal $a\sin(\omega t)$, will create a periodic response of y which is either in phase or out of phase with $a\sin(\omega t)$. The high-pass filter eliminates the “DC component” of y. Thus $a\sin(\omega t)$ and high-pass filter will be approximately two sinusoids which are in phase if $\hat{\theta} < \theta^*$ or out of phase if $\hat{\theta} > \theta^*$.

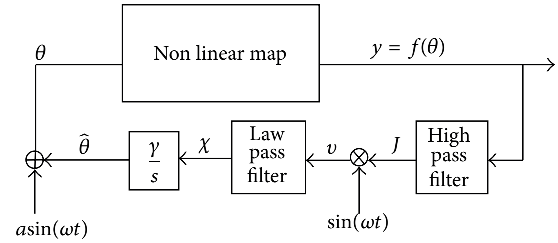

Figure 5: Extremum seeking algorithm scheme.

The integrator $\hat{\theta} = (\gamma/s)\chi$ approximates the gradient update law $\dot{\hat{\theta}} = k(a^2/2)(f)'(\hat{\theta})$ which tunes $\hat{\theta}$ to θ^* [13]. System of Figure 5 can be summarized in mathematical equations as follows:

$$\begin{gathered} y = f\left(\hat{\theta} + a\sin(\omega t)\right), \\ \dot{\hat{\theta}} = -\gamma\chi, \\ \chi = \upsilon * \mathfrak{L}^{-1}\left\{\mathrm{H}_{\mathrm{LPF}}(s)\right\}, \\ \upsilon = \left[y * \mathfrak{L}^{-1}\left\{\mathrm{H}_{\mathrm{HPF}}(s)\right\}\right]\sin(\omega t), \end{gathered} \tag{1}$$

where $*$ is the convolution operator and $\mathfrak{L}^{-1}$ is the inverse Laplace transform operator. The transfer functions for $\mathrm{H}_{\mathrm{HPF}}$ and $\mathrm{H}_{\mathrm{LPF}}$ in the regular SISO ESC scheme are $s/(s+\omega_h)$ and $\omega_l/(s+\omega_l)$ respectively, where $\omega_l < \omega < \omega_h$ [25]. This model will be used for stability analysis in this paper.

In the following sections, after introducing BICO filter [27, 28], the advantages of using this filter in the ESC algorithm from the stability and robustness point of view will be discussed.

3. BICO Extremum Seeking Control MPPT

In this section we are going to introduce a filter which was strongly favored by Bode [29], called Bode’s ideal cutoff

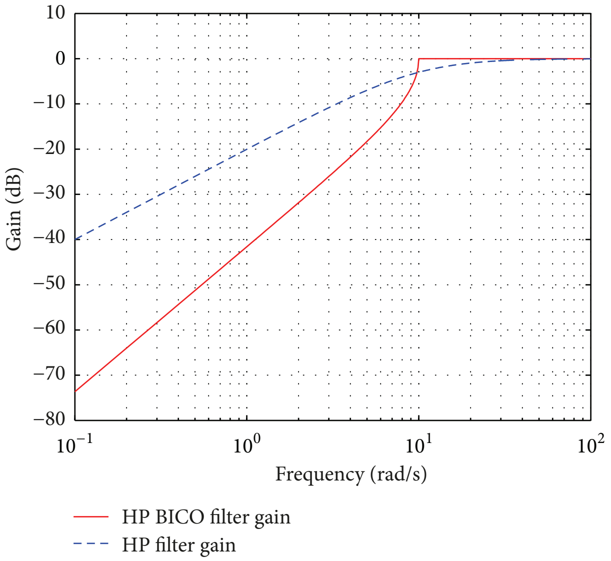

Figure 6: High-pass BICO and regular high-pass filters.

characteristic (BICO) filter [27, 28]. The general transfer function of low-pass BICO filter is,

$$G_{\text{LP-BICO}}(s) = \frac{k}{\left(s/\omega_c + \sqrt{1+(s/\omega_c)^2}\right)^r}, \quad r \in \mathbb{R}^+. \tag{2}$$

Its corresponding time response in the special case ($\omega_c = 1$ rad/s) was derived by Oberhettinger and Baddi [30], but the time response of (2) is presented as,

$$g_{\text{BICO}_{\text{LP}}}(t) = k\frac{rJ_r(\omega_c t)}{\omega_c t}, \tag{3}$$

where J_r is the rth order Bessel function.

By replacing s by $1/s$, high-pass BICO filter is obtained. Figure 6 compares the frequency response of high-pass BICO filter and regular high-pass filter ($s/(s+\omega_c)$) with the same cutoff frequency of $\omega_c = 10$ rad/s.

As seen in this figure, BICO filter has a sharp edge in its cutoff frequency. This great feature causes almost no attenuation for frequencies higher than ω_c and a large attenuation in the lower frequencies. Therefore the behavior of this filter is close to an "ideal" filter. This sharp edge presents in the low-pass BICO filter. By combining high-pass and low-pass BICO filters, the band-pass BICO filter with sharp edges in both sides can be obtained as well.

4. Stability Analysis of Extremum Seeking Control

4.1. Mathematical Modeling of ESC Scheme. The stability analysis of ESC algorithm has been investigated in [13, 31–34]. In these literatures traditional extremum seeking control with regular first-order filters has been considered. In this paper, we have considered the similar stability analysis approach as [34] to compare the stability and robustness of BICO-ESC and regular SISO ESC. The difference between this work and [34] is that in this paper, the stability analysis has been done by considering both low-pass and high-pass filters in the ESC structure but in [34] authors have investigated the stability of simplified ESC with only low-pass filter in its structure.

According to the previous discussion, the nonlinear map in the ESC scheme is considered to be concave and is assumed to have only one extremum point. Since in the PV system applications, MPPT is employed to extract maximum amount of power from PV panels, therefore, extremum point in this case is maximum point (θ^*), where at this point $\partial f(\theta^*)/\partial\theta = 0$, and also $\partial^2 f(\theta^*)/\partial\theta^2 < 0$. In ESC algorithm, the output of the nonlinear map is,

$$y = f\left(\hat{\theta} + a\sin(\omega t)\right), \tag{4}$$

where a and ω are the amplitude and angular frequency of perturbation signal. Since the perturbation signal assumes to be small, therefore the Taylor expansion of (4) is

$$y = f\left(\hat{\theta}\right) + \frac{df\left(\hat{\theta}\right)}{d\hat{\theta}} a\sin(\omega t) + \text{H.O.T.}, \tag{5}$$

where H.O.T. stands for higher order terms and $\hat{\theta}$ is the approximation of θ^*. The high-pass filtered signal will be,

$$\begin{aligned} J \simeq{}& \mathfrak{L}^{-1}\left\{\frac{s}{s+\omega_h}\right\} * f\left(\hat{\theta}\right) \\ &+ \mathfrak{L}^{-1}\left\{\frac{s}{s+\omega_h}\right\} * \left\{\frac{df\left(\hat{\theta}\right)}{d\hat{\theta}} a\sin(\omega t)\right\}. \end{aligned} \tag{6}$$

High-pass filter acts as a derivative opereator in series with a low-pass filter ($s(1/(s+\omega_h))$). By multiplying the modulation signal to the resulted signal from the high-pass filter and passing the modulated signal through the low-pass filter and since $\omega_l < \omega_h$, the output signal of integrator will be

$$\begin{aligned} \hat{\theta} \simeq{}& \frac{a\gamma}{2}\mathfrak{L}^{-1}\left\{\frac{1}{s}\right\} * \mathfrak{L}^{-1}\left\{\frac{\omega_l}{s+\omega_l}\right\} \\ &* \left\{\frac{d}{dt}\left(\frac{df\left(\hat{\theta}\right)}{d\hat{\theta}}\right)\right\}. \end{aligned} \tag{7}$$

Under the assumptions that the amplitude of the sinusoidal perturbation is small and the harmonics of high-pass filter are attenuated by low-pass filter, output of low-pass filter is proportional to the gradient of the nonlinear map with respect to its input and time. Therefore in the neighborhood of the extremum point, the amplitude of the estimated signal is small, since the gradient is small. It can be seen that this amplitude depends on γ and a.

4.2. Stability Analysis of Averaged ESC Scheme. The averaging method is typically used to analyze the periodic steady state solutions of weakly nonlinear systems. Since the amplitude of perturbation in the ESC scheme is small, this system can be evaluated by its averaged model. The averaged form of signal $x(t)$ is,

$$\overline{x(t)} = \frac{1}{T}\int_0^T x(t)\,dt, \tag{8}$$

where $T = 2\pi/\omega$. Therefore the averaged model of ESC scheme is

$$\begin{aligned} \bar{\hat{\theta}} &= \theta, \\ \bar{y} &= \overline{f(\hat{\theta})} = f\left(\bar{\hat{\theta}}\right) = f(\theta), \\ \bar{\hat{\theta}} &= \frac{\gamma a}{2}\frac{d}{dt}\left(\frac{df\left(\hat{\theta}\right)}{d\hat{\theta}}\right) * \mathfrak{L}^{-1}\left\{\mathrm{H}_{\mathrm{LPF}}\right\} * \mathfrak{L}^{-1}\left\{\frac{1}{s}\right\}. \end{aligned} \tag{9}$$

On the other hand, in the neighborhood of the extremum point, $y(t)$ can be approximated as,

$$\begin{aligned} y \simeq{}& f(\theta^*) + \left.\frac{df(\theta)}{d\theta}\right|_{\theta=\theta^*}(\theta-\theta^*) \\ &+ \frac{1}{2}\left.\frac{d^2 f(\theta)}{d\theta}\right|_{\theta=\theta^*}(\theta-\theta^*)^2. \end{aligned} \tag{10}$$

If the difference between the extremum point and averaged point is defined by $\tilde{\theta} = \bar{\theta} - \theta^*$ and since $df(\theta)/d\theta|_{\theta=\theta^*} = 0$, thus,

$$\tilde{y} \simeq \frac{1}{2}\left.\frac{d^2 f(\theta)}{d\theta^2}\right|_{\theta=\theta^*}\tilde{\theta}^2. \tag{11}$$

By defining $(1/2)(d^2 f(\theta)/d\theta^2)|_{\theta=\theta^*} = K$, then, $(df(\theta)/d\theta)|_{\theta=\theta^*} = 2K\theta$. Therefore, $(d/dt)(df(\theta)/d\theta)|_{\theta=\theta^*} = 2(dK/dt)\theta^*$. Substituting this relationship in (9) gives,

$$\bar{\hat{\theta}} = \left(\gamma a\theta^*\frac{dK}{dt}\right) * \mathfrak{L}^{-1}\left\{\mathrm{H}_{\mathrm{LPF}}\right\} * \mathfrak{L}^{-1}\left\{\frac{1}{s}\right\}. \tag{12}$$

Without loss of generality and by assuming that dK/dt is the output signal from a high-pass filter, H_{HPF}, which its cutoff frequency is higher than cutoff frequency of the low-pass filter, H_{LPF}, then (12) can be rewritten as

$$\bar{\hat{\theta}} = (\gamma a\theta^* K)\,\mathfrak{L}^{-1}\left\{\mathrm{H}_{\mathrm{HPF}}\right\} * \mathfrak{L}^{-1}\left\{\mathrm{H}_{\mathrm{LPF}}\right\} * \mathfrak{L}^{-1}\left\{\frac{1}{s}\right\}. \tag{13}$$

This system can be considered as a feedback system as shown in Figure 7, which K can be considered as a perturbation. The loop gain of this system depends on the demodulation gain, a, the integral gain, γ, and the curvature of nonlinear map, K. This result completely matches with the results obtained from other analysis method in the simplified case [13, 31–33].

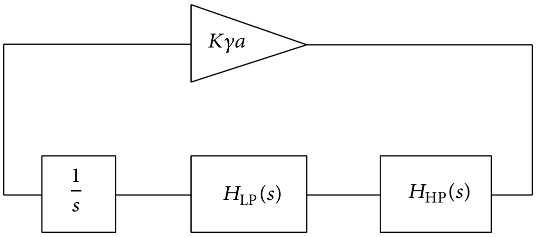

Figure 7: Averaged BICO-ESC scheme.

5. Analysis of ESC MPPT on PV Panels

5.1. PV Cell Model. The PV cell V-I curve $v = f(i, G)$ is modeled using the light emitting diode equations [3]:

$$\begin{aligned} I &= I_L - I_{\mathrm{OS}}\left(\exp\left(\frac{q}{Ak_B T}\right)(V + RI) - 1\right), \\ I_{\mathrm{OS}} &= I_{\mathrm{OR}}\left(\frac{T}{T_R}\right)\exp\left(\frac{qE_G}{Ak_B}\left(\frac{1}{T_R} - \frac{1}{R}\right)\right), \\ I_L &= \frac{G}{1000}\left(I_{\mathrm{SC}} + K_{T,I}(T - T_R)\right), \\ V &= \frac{Ak_B T}{q}\ln\left(\frac{I_L - I}{I_{\mathrm{OS}}} + 1\right) - RI. \end{aligned} \tag{14}$$

Values and definitions for further simulations are shown in Table 2.

5.2. BICO ESC vsersus Regular SISO ESC. In order to compare the qualitative behavior of BICO MPPT with the regular SISO ESC MPPT, the Root-Locus (RL) analysis has been chosen. Clearly, other stability analysis methods are applicable at this point.

Since Root-Locus (RL) method is serving for linear systems, it is important to point out that the curvature constant, K, is an uncertain parameter which depends on different factors like the PV panel manufacturer and weather conditions. According to [33], $K \in [-0.5, -5]$.

As seen in Figure 7, the characteristic polynomial of averaged ESC system is $1 + a\gamma K\mathrm{H}_{\mathrm{HPF}}\mathrm{H}_{\mathrm{LPF}}$, and to analyze the behavior of this system, Root-Locus (RL) analysis method can be employed. Since there is no command in MATLAB to plot Root-Locus (RL) for BICO transfer function, this equation has been solved for different $a\gamma$ and the roots have been plotted. To compare the behavior of regular SISO ESC with BICO ESC, the roots for this system has been plotted with the same method instead of using "rlocus" command.

Figure 8 shows the comparison between the root locus of averaged ESC using BICO and regular first-order filters. In this root locus plot, the constant gain is assumed to be $a\gamma\theta^* = 1$ and cutoff frequencies in both filters are assumed to be $\omega_c = 10$ rad/s. Clearly, by using first-order filters in the averaged ESC scheme, for some values of K, system has complex poles which cause an oscillatory behavior in the response of the system. On the other side, by using BICO filters, roots of the characteristic polynomial (system poles) are always real numbers for any value of K.

TABLE 2: Values of the considered PV model [3].

T_R	298	Reference temperature
I_{OR}	$2.25e-6$	Reverse saturation curent at $T = T_R$
I_{SC}	3.2	Short circuit current
E_G	$1.38e-19$	Silicon band gap
A	1.6	Ideality factor
k_B	$1.38e-23$	Boltzman's constant
q	$1.6e-19$	Electron charge
R	0.01	Resistance
$K_{T,I}$	0.8	I_{SC} Temperature coefficient

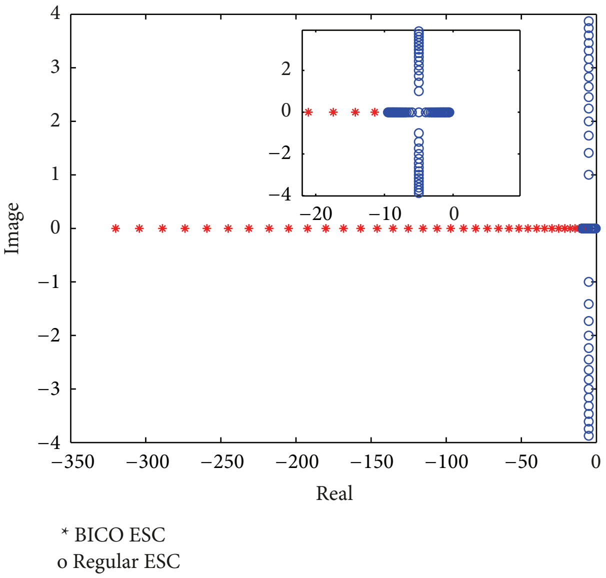

FIGURE 8: Root locus of the averaged BICO and the regular first-order low-pass filters.

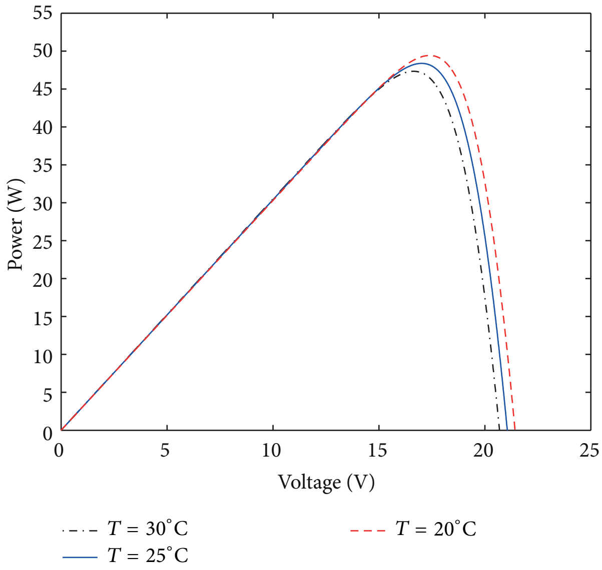

FIGURE 9: *P-V* chart of considered PV model for different temperatures (irradiation = 1000 W/m^2).

Besides the location of the poles, as can be seen in this figure, for the same value of K, BICO filter has farther poles with respect to the origin compared to the first-order filter case. Therefore, the bandwidth of BICO filter is higher than the first-order filter with similar cutoff frequency. Higher bandwidth means faster response for BICO ESC. This feature is justifiable by looking at the frequency response of both filters. Since the bandwidth of BICO is close to the bandwidth of an ideal filter, BICO ESC becomes the fastest achievable MPPT algorithm.

6. Simulation Illustrations

Figures 9 and 10 show the maximum power point of a PV panel with the defined parameters in Table 2. As can be seen in these figures, environmental conditions and especially variations in the sun irradiation will change the nonlinear behavior of PV panels. Shadows, cloudy or dusty weather, and temperature variations cause moving of optimal operating point in PV systems. When temperature increases, the maximum output power of PV panels decreases and vice versa. In Figure 9 the variations of optimal operating point by changing the environmental temperature from 20°C to 30°C are illustrated. As Figure 10 presents, variation of peak output power happens in the wider range when sun irradiation changes. Generally, in PV panels, when sun irradiation increases, the output power increases, but when temperature increases, the maximum extractable power reduces.

To compare the proposed MPPT method which is called BICO MPPT with the ESC MPPT, the working conditions of both algorithms have been defined to be same. For all simulations, the ambient temperature is 25°C and the irradiation is assumed to be 1000 W/m^2. Also the cutoff frequency of high-pass filters is $\omega_h = 100$ rad/s, and for low-pass filter, this frequency is $\omega_l = 50$ rad/s. Under these conditions, from Figure 9, the maximum amount of power which can be extracted from the simulated PV panel is 48 Watts and this maximum happens around 17 Volts. To implement the BICO MPPT, the discrete approximation of this filter in MathWorks, Inc.'s website has been used.

Figure 11 shows the outputs of extremum seeking algorithms resulted from two different MPPT methods. Figure 12

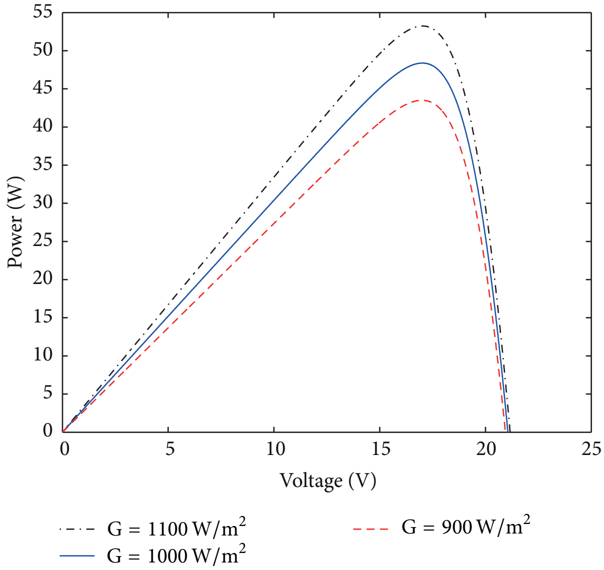

Figure 10: *P-V* chart of considered PV model for different irradiations (temperature = 25°C).

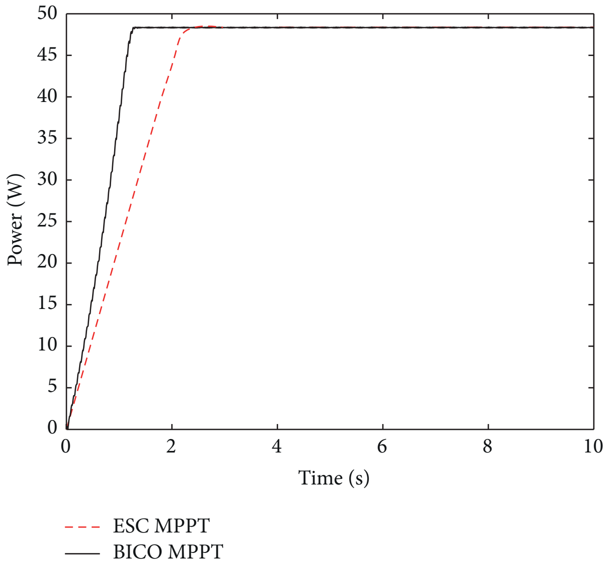

Figure 11: Comparison of power tracking in BICO MPPT and ESC MPPT.

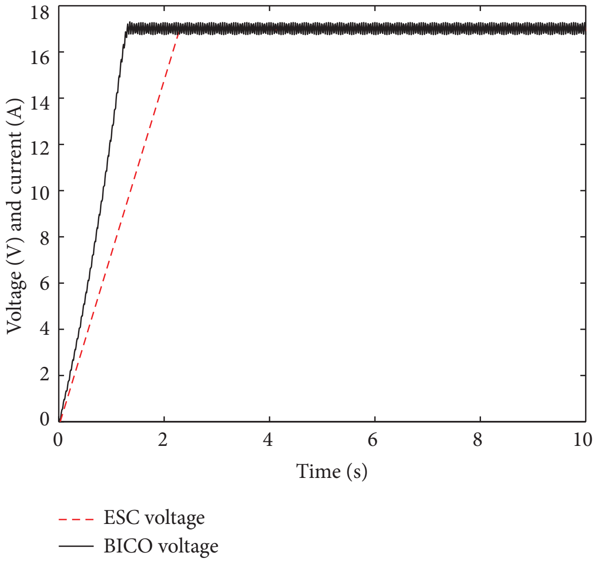

Figure 12: Comparison of voltage tracking in BICO MPPT and ESC MPPT.

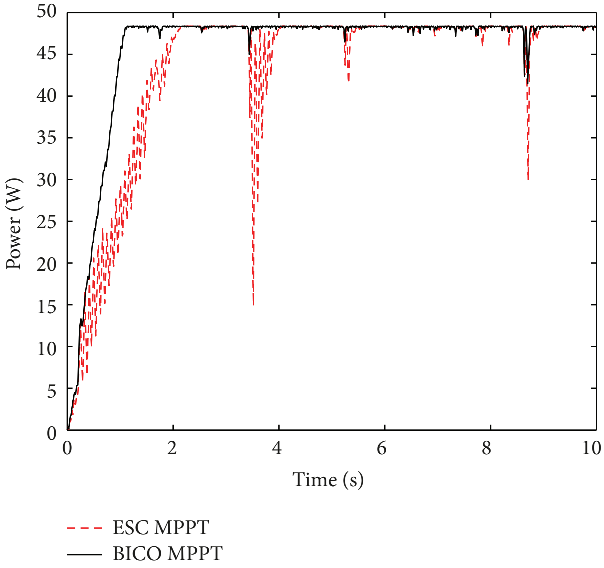

Figure 13: Performance of BICO MPPT and ESC MPPT in the presence of a white noise with noise power 0.04.

represents the maximum voltage tracking in BICO MPPT algorithm and ESC with first-order filters. As expected and proved before, BICO MPPT converges to the peak power point two times faster than the regular ESC MPPT algorithm. Faster convergence speed is due to the higher bandwidth of the averaged BICO system.

Figures 13 and 14 show the performance of the proposed MPPT approach compare to the ESC in the presence of white noise. As can be seen in these figures, in the presences of a white noise (noise power = 0.04), which is considered as the variations in the nonlinear map behavior, K, BICO MPPT preforms better than ESC MPPT from attenuation and tracking point of view.

Another parameter which is considered in these simulations is the robustness of these two methods to the variations of the system gain. Figures 15(a) and 15(b) illustrate the performance of BICO MPPT and regular ESC MPPT to the gain variations, respectively. From these figures, it can be concluded that, BICO MPPT tolerates higher gain variations, but by increasing the gain of the integrator in ESC MPPT, it starts oscillating.

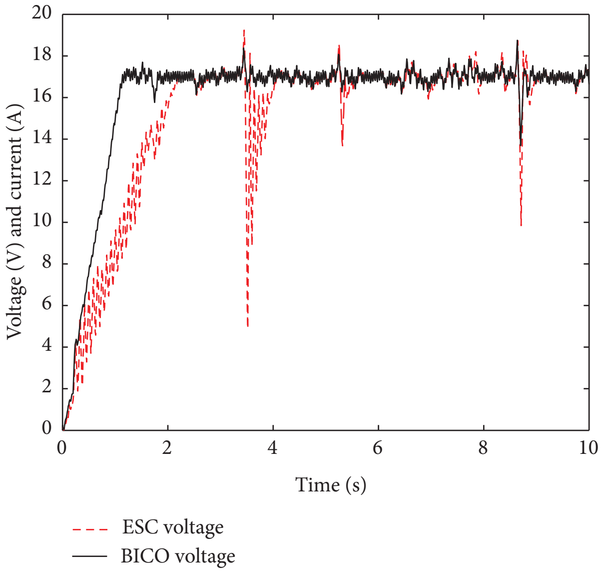

Figure 14: Voltage tracking of BICO MPPT and ESC MPPT in the presence of a white noise with noise power 0.04.

7. Conclusions

The ubiquity of using MPPT in the renewable energy systems has stimulated the persistent development of various MPPT algorithms. According to the comparison in this paper, one of the most popular methods of maximum power tracking method is the P&O method. However, this method fails in those situations when there is a need to track the MPPs rapidly.

ESC is a new robust MPPT algorithm which carries all P&O's benefits and improves its weaknesses. In this paper, a novel ES algorithm has been presented which is called BICO MPPT. This algorithm employs BICO filter in its structure to improve the ESC rise time response even further. BICO filter is a forgotten part of Bode's research that for the first time in this paper was used for PV applications.

BICO filter is the closest filter to the ideal filter and this feature of BICO improves the performance of ESC algorithm. Also, the advantages of BICO has been discussed in this paper. As discussed in this paper, using BICO in the ESC structure increases the bandwidth of the system, which improves the system response.

In addition, applying BICO filter to the ESC algorithm moves all the roots of characteristic polynomial of averaged BICO ESC system to the real axis. Consequently, this system has no pole with imaginary part, and therefore theoretically the system has no oscillatory response by increasing its integrator gain. These poles, however, can have imaginary part by increasing the gain of the system in the regular ESC. This feature increases the robustness of the BICO MPPT compared to regular ESC.

As can be seen in the results, BICO MPPT not only can follow the maximum power point faster than regular ESC, but also it shows more robustness in the presence of disturbance in the system or gain variations.

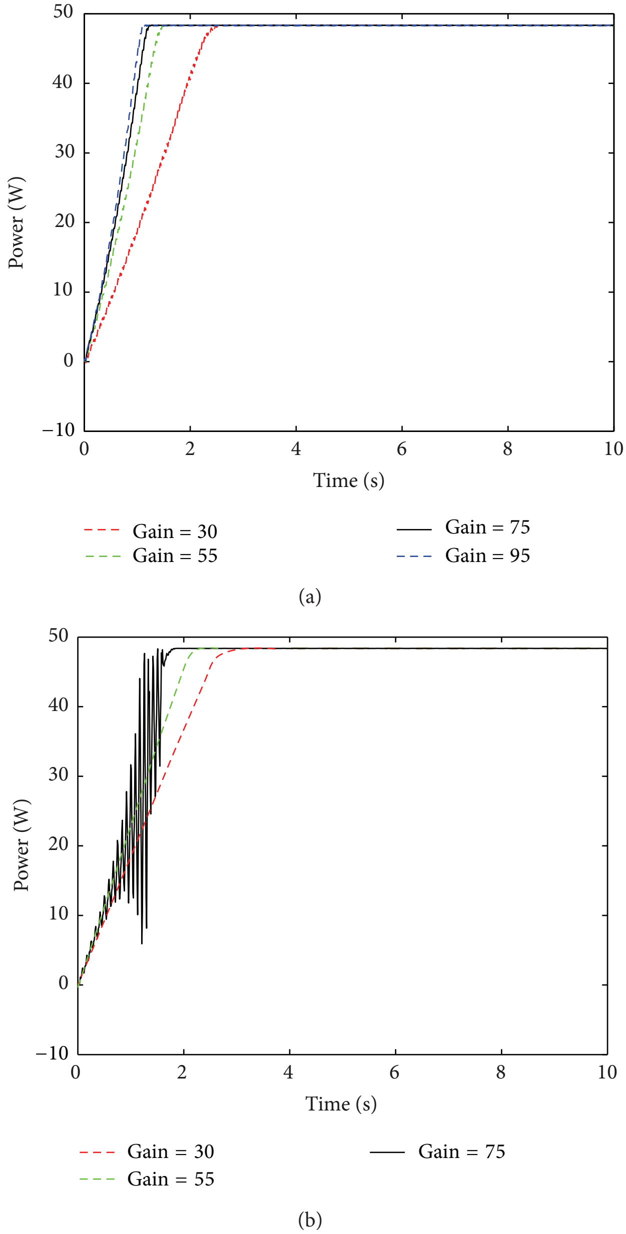

(a)

(b)

Figure 15: Sensitivity of BICO MPPT and ESC MPPT to the gain variation of integrator.

Conflict of Interests

The authors declare that there is no conflict of interests regarding the publication of this paper.

References

[1] B. Bose, P. Szczesny, and R. Steigerwald, "Microcomputer control of a residential photovoltaic power conditioning system," *IEEE Transactions on Industry Applications*, vol. 21, no. 5, pp. 1182–11191, 1985.

[2] R. A. Mastromauro, M. Liserre, T. Kerekes, and A. Dell'Aquila, "A single-phase voltage-controlled grid-connected photovoltaic system with power quality conditioner functionality," *IEEE*

Transactions on Industrial Electronics, vol. 56, no. 11, pp. 4436–4444, 2009.

[3] S. L. Brunton, C. W. Rowley, S. R. Kulkarni, and C. Clarkson, "Maximum power point tracking for photovoltaic optimization using ripple-based extremum seeking control," *IEEE Transactions on Power Electronics*, vol. 25, no. 10, pp. 2531–2540, 2010.

[4] T. Esram and P. L. Chapman, "Comparison of photovoltaic array maximum power point tracking techniques," *IEEE Transactions on Energy Conversion*, vol. 22, no. 2, pp. 439–449, 2007.

[5] J. J. Nedumgatt, K. B. Jayakrishnan, S. Umashankar, D. Vijayakumar, and D. P. Kothari, "Perturb and observe MPPT algorithm for solar PV systems-modeling and simulation," in *Proceedings of the Annual IEEE India Conference: Engineering Sustainable Solutions (INDICON '11)*, pp. 1–6, December 2011.

[6] R. Alonso, P. Ibáñez, V. Martínez, E. Román, and A. Sanz, "An innovative perturb, observe and check algorithm for partially shaded PV systems," in *Proceedings of the 13th European Conference on Power Electronics and Applications (EPE '09)*, pp. 1–8, September 2009.

[7] N. Femia, G. Petrone, G. Spagnuolo, and M. Vitelli, "Optimization of perturb and observe maximum power point tracking method," *IEEE Transactions on Power Electronics*, vol. 20, no. 4, pp. 963–973, 2005.

[8] G. J. Kish, J. J. Lee, and P. W. Lehn, "Modelling and control of photovoltaic panels utilising the incremental conductance method for maximum power point tracking," *IET Renewable Power Generation*, vol. 6, no. 4, pp. 259–266.

[9] A. Safari and S. Mekhilef, "Simulation and hardware implementation of incremental conductance MPPT with direct control method using cuk converter," *IEEE Transactions on Industrial Electronics*, vol. 58, no. 4, pp. 1154–1161, 2011.

[10] H. Malek, S. Dadras, Y. Q. Chen, R. Burt, and J. Cook, "Maximum power point tracking techniques for efficient photovoltaic microsatellite power supply system," in *Proceeding of the Small Satellite Conference*, Logan, Utah, USA, 2012.

[11] H. Malek, S. Dadras, and Y. Q. Chen, "A fractional order maximum power point tracker: Stability analysis and experiments," in *Proceeding of the IEEE 51st Annual Conference on Decision and Control (CDC '12)*, pp. 6861–6866, Maui, Hawaii, USA, 2012.

[12] R. Faranda and S. Leva, "Energy comparison of MPPT techniques for PV systems," *WSEAS Transactions on Power Systems*, vol. 3, no. 6, pp. 1–6, 2008.

[13] M. Krstić and H.-H. Wang, "Stability of extremum seeking feedback for general nonlinear dynamic systems," *Automatica*, vol. 36, no. 4, pp. 595–601, 2000.

[14] M. Guay, D. Dochain, and M. Perrier, "Adaptive extremum seeking control of continuous stirred tank bioreactors with unknown growth kinetics," *Automatica*, vol. 40, no. 5, pp. 881–888, 2004.

[15] G. Bastin, D. Nešić, Y. Tan, and I. Mareels, "On extremum seeking in bioprocesses with multivalued cost functions," *Biotechnology Progress*, vol. 25, no. 3, pp. 683–689, 2009.

[16] S. Drakunov, U. Ozguner, P. Dix, and B. Ashrafi, "ABS control using optimum search via sliding modes," *IEEE Transactions on Control Systems Technology*, vol. 3, no. 1, pp. 79–85, 1995.

[17] D. Popović, M. Janković, S. Magner, and A. Teel, "Extremum seeking methods for optimization of variable cam timing engine operation," in *Proceeding of the American Control Conference*, pp. 3136–3141, Denver, Colo, USA, June 2003.

[18] K. S. Peterson and A. G. Stefanopoulou, "Extremum seeking control for soft landing of an electromechanical valve actuator," *Automatica*, vol. 40, no. 6, pp. 1063–1069, 2004.

[19] H.-H. Wang, S. Yeung, and M. Krstić, "Experimental application of extremum seeking on an axial-flow compressor," *IEEE Transactions on Control Systems Technology*, vol. 8, no. 2, pp. 300–309, 2000.

[20] C. G. Mayhew, R. G. Sanfelice, and A. R. Teel, "Robust source-seeking hybrid controllers for autonomous vehicles," in *Proceedings of the American Control Conference (ACC '07)*, pp. 1185–1190, New York, NY, USA, July 2007.

[21] E. Biyik and M. Arcak, "Gradient climbing in formation via extremum seeking and passivity-based coordination rules," in *Proceedings of the 46th IEEE Conference on Decision and Control (CDC '07)*, pp. 3133–3138, New Orleans, La, USA, December 2007.

[22] P. Ögren, E. Fiorelli, and N. E. Leonard, "Cooperative control of mobile sensor networks: adaptive gradient climbing in a distributed environment," *IEEE Transactions on Automatic Control*, vol. 49, no. 8, pp. 1292–1302, 2004.

[23] P. M. Dower, P. M. Farrell, and D. Nešić, "Extremum seeking control of cascaded Raman optical amplifiers," *IEEE Transactions on Control Systems Technology*, vol. 16, no. 3, pp. 396–407, 2008.

[24] J. Sternby, "Extremum control systems: an area for adaptive control," in *Proceedings of the International Symposium on Adaptive Systems*, vol. 24, pp. 151–160, San Francisco, Calif, USA, 1980.

[25] K. B. Ariyur and M. Krstic, *Real-Time Optimization by Extremum-Seeking Control*, Wiley-Interscience, 2003.

[26] K. J. Astrom and B. Wittenmark, *Adaptive Control*, Addison-Wesley, 2nd edition, 1995.

[27] Y. Luo, T. Zhang, B. Lee, C. Kang, and Y. Q. Chen, "Disturbance observer design with bode's ideal cut-off filter in hard-disc-drive servo system," *Mechatronics*, vol. 23, no. 7, pp. 856–862, 2013.

[28] L. E. Olivier, I. K. Craig, and Y. Q. Chen, "Fractional order and BICO disturbance observers for a run-of-mine ore milling circuit," *Journal of Process Control*, vol. 22, no. 1, pp. 3–10, 2012.

[29] T. T. Hartley and C. F. Lorenzo, "Optimal fractional-order damping," in *Proceedings of the ASME Design Engineering Technical Conferences and Computers and Information in Engineering Conference*, pp. 737–743, Chicago, Ill, USA, September 2003.

[30] Oberhettinger and Baddi, *Tables of Laplace Transforms*, Springer, Berlin, Germany, 1973.

[31] Y. Tan, D. Nešić, and I. Mareels, "On stability properties of a simple extremum seeking scheme," in *Proceedings of the 45th IEEE Conference on Decision and Control (CDC '06)*, pp. 2807–2812, December 2006.

[32] Y. Tan, D. Nešić, and I. Mareels, "On non-local stability properties of extremum seeking control," *Automatica*, vol. 42, no. 6, pp. 889–903, 2006.

[33] R. Leyva, C. Olalla, H. Zazo et al., "Mppt based on sinusoidal extremum-seeking control in pv generation," *International Journal of Photoenergy*, vol. 98, no. 4, pp. 529–542, 2011.

[34] R. Leyva, P. Artillan, C. Cabal, B. Estibals, and C. Alonso, "Dynamic performance of maximum power point tracking circuits using sinusoidal extremum seeking control for photovoltaic generation," *International Journal of Electronics*, vol. 98, no. 4, pp. 529–542, 2011.

Hindawi Publishing Corporation
International Journal of Photoenergy
Volume 2014, Article ID 843617, 14 pages
http://dx.doi.org/10.1155/2014/843617

Research Article

Simulation Analysis of the Four Configurations of Solar Desiccant Cooling System Using Evaporative Cooling in Tropical Weather in Malaysia

M. M. S. Dezfouli,[1] S. Mat,[1] G. Pirasteh,[2] K. S. M. Sahari,[3] K. Sopian,[1] and M. H. Ruslan[1]

[1] *Solar Energy Research Institute (SERI), Universiti Kebangsaan Malaysia, 43600 Bangi, Selangor, Malaysia*
[2] *Department of Mechanical Engineering, Faculty of Engineering, University of Malaya, 50603 Kuala Lumpur, Malaysia*
[3] *Department of Mechanical Engineering, Universiti Tenaga Nasional, Jalan IKRAM-UNITEN, 43000 Kajang, Selangor, Malaysia*

Correspondence should be addressed to M. M. S. Dezfouli; salehi.solar@gmail.com

Received 29 May 2013; Revised 13 November 2013; Accepted 29 November 2013; Published 2 February 2014

Academic Editor: Ismail H. Altas

A high demand for air conditioning systems exists in hot and humid regions because of the warm climate during the year. The high energy consumption of conventional air conditioning system is the reason for our investigation of the solar desiccant cooling system as an energy-efficient cooling system. Four model configurations were considered to determine the best configuration of a solar desiccant cooling system: one-stage ventilation, one-stage recirculation, two-stage ventilation, and two-stage recirculation. These models were stimulated for 8,760 hr of operation under hot and humid weather in Malaysia. Several parameters (i.e., coefficient of performance or COP, room temperature and humidity ratio, and the solar fraction of each system) were evaluated by detecting the temperature and humidity ratio of the different points of each configuration by TRNSYS simulation. The latent and sensible loads of the test room were 0.875 kW and 2.625 kW, respectively. By investigating the simulation results of the four systems, the ventilation modes were found to be higher than the recirculation modes in the one- and two-stage solar desiccant cooling systems. The isothermal dehumidification COP of the two-stage ventilation was higher than that of the two-stage recirculation. Hence, the two-stage ventilation mode desiccant cooling system in a hot and humid area has higher efficiency than the other configurations.

1. Introduction

Because of the high electrical consumption of conventional vapor compression systems, the solar desiccant cooling system has been considered as one of the promising alternatives to cooling air where the sensible and latent heats of air are removed separately [1]. The first desiccant cooling system was presented by Pennington in 1955 [2]. Generally, depending on the dehumidification material used, two kinds of desiccant cooling system exist: solid and liquid. Many scientists and researchers have studied both kinds of desiccant cooling using renewable energy [3]. The common materials used in the solid and liquid desiccant cooling systemwere silica gel and liquid water-lithium chloride. The desiccant cooling system includes three main units, namely, desiccant, heat-source, and cooling units [4]. The elements of each unit are designed depending on the weather conditions. The components of the basic cycle consist of the solid desiccant wheel (DW) as dehumidifier, evaporative cooler as the cooling unit, and the heat recovery wheel as the heater and cooler in the regeneration and process air sides, respectively. In recent years, according to the Pennington cycle, different types of solid desiccant cooling cycles have been designed in the world by different researchers. The coefficient of performance (COP) of the desiccant cooling system, regeneration temperature, mass flow rate, fresh air, and relative humidity of the supply air are the important parameters considered by the researchers. Haddad et al. [5] studied the simulation of a desiccant-evaporative cooling system for residential buildings. They found that the use of solar energy for regeneration of the DW can provide a significant portion of the auxiliary thermal energy needed.

Fong et al. [6] designed a simulation model (TRNSYS) of an integrated radiant cooling by absorption refrigeration and desiccant dehumidification. Salehi Dezfouli et al. [7] investigated the solar hybrid desiccant cooling system in hot and humid weather in Malaysia. They found that a solar hybrid solid desiccant cooling system provided considerable energy savings in comparison with the conventional vapor compression in hot and humid area.

Researchers have studied and compared the COP of ventilation and recirculation cycles. Jain et al. [8] evaluated ventilation and recirculation cycles based on weather data in India to determine the effectiveness of evaporative coolers on the COP of a cooling system. Boundoukan et al. [9] evaluated a comparison between ventilation and recirculation procedure modes; critical values were achieved for cycle component performance specifics required to yield a given supply air temperature condition. Mehmet et al. [10] evaluated First low and second Low for COPs of ventilation and recirculation cycles. Panaras et al. [11] investigated the behavior of the COP of the ventilation and recirculation desiccant cooling systems in terms of the air flow rate. They found that the ventilation cycle presents a higher COP, and the required air flow rate is similar for both cycles. Sphaier et al. [12] studied the simulation of ventilation and recirculation desiccant cooling systems to analyze the impact of cycle component characteristics on the overall system performance. They concluded that, although all components can influence the COP, the COP values of the recirculation cycle are lower than the ventilation cycle.

With regard to the increase in temperature of the process air after dehumidification and the limitation capacity of the dehumidification by the DW, the required regeneration temperature is high, especially in hot and humid regions [13–16]. Many researchers have attempted to determine the best solution for the high required regeneration temperature problem in one-stage desiccant cooling systems. The isothermal dehumidification process is a great solution to solve this problem. The required cool process air after dehumidification and reduced regeneration temperature can be obtained using isothermal dehumidification technology or multistage dehumidification process. Meckler [17] proposed a two-stage solid desiccant air conditioning system integrated with an HVAC system. A two-stage system was also introduced by Henning [18]. A novel rotary desiccant cooling cycle with isothermal dehumidification and regenerative evaporative cooling was proposed by La et al. [19]. They found that the isothermal dehumidification was relatively lower temperature requirement for the heat source because the regeneration temperature is reduced from 80°C to approximately 60°C. Ge et al. [20] evaluated the performance of a two-stage rotary desiccant cooling (TSRDC) system. The required regeneration temperature of the TSRDC system is low, and the COP of the system is high. La et al. [21] performed a theoretical analysis of a solar-driven TSRDC system assisted by vapor compression air conditioning. They concluded that the solar-driven two-stage desiccant cooling system is reliable and energy efficient. Li et al. [22] investigated the TSRDC/heating system driven by evacuated glass tube solar air collectors. Their experimental results indicated that the average thermal COP in the cooling cycle was 0.97, and the cooling capacity was in the range from 16.3 kW to 25.6 kW under hot and humid ambient conditions. Li et al. [23] carried out experimental investigation on a one-rotor two-stage desiccant cooling/heating system driven by solar air collectors. The average thermal COP in the cooling cycle is 0.95 in hot and humid climate conditions.

Given the use of ambient air in solar desiccant cooling systems, the ambient conditions of each region have a significant impact on system performance. Although various studies and publications on the one-stage and two-stage desiccant cooling systems have been based on different weather data, no such study compares one-stage and two-stage solar cooling technologies that have been undertaken in Malaysia. The high demands of air conditioning systems because of hot and humid weather during the year, as well as the high energy consumption of conventional AC systems, have resulted in the investigation of the solar desiccant cooling system as an efficient air conditioning system in Malaysia. The present paper presents a comparison simulation study among the four configurations of solar desiccant cooling system in hot humid weather in Malaysia.

2. Methodology

The comparison performance between the one-stage and two-stage solar desiccant cooling systems under the ventilation and recirculation modes is used as the methodology in this study. The one-stage and two-stage desiccant cooling systems are explained in the following sections.

2.1. Case Study Description. Four kinds of solar desiccant cooling systems were considered to supply air for a test room in a technology park (UKM) in Malaysia. The one-stage desiccant cooling system under two modes of ventilation and recirculation and the two-stage desiccant cooling system under two modes of ventilation and recirculation were considered to evaluate the four types of desiccant cooling system. The latent and sensible loads of the test room were 0.875 and 2.625 kW, respectively. The cooling capacity was 1 ton. According to the American Society of Heating, Refrigerating and Air Conditioning Engineers (ASHRAE) comfort condition, indoor condition designs should consist of temperature of 25°C, relative humidity of 50%, and humidity ratio of 0.0098 kg/kg [24]. According to the Malaysian weather, in outdoor condition design, the temperature should be 30°C, and the humidity ratio should be 0.0200 kg/kg. The cooling system includes four main parts, namely, DW as dehumidifier, heat recovery wheel, evaporative cooler as humidifier, and solar-evacuated tube collector as heat source. Simulation design using the TRNSYS software was carried out to investigate the solar desiccant cooling in the different configurations to find the best operation of the components and the cooling system based on the hot and humid weather in Malaysia. In this study, one stage (ventilation and recirculation modes) and two stages (ventilation and recirculation modes) were simulated under the same effectiveness of the components.

Table 1: Specific assumptions used in simulation.

Item	Factor
DW	Type 683, F_1 = 0.1, F_2 = 0.07, power consumption: 0.2 kW, and speed of rotor rotation: 8 r/h
DEC	Type 506c, saturation efficiency = 0.8, and power consumption: 0.1 kW
HRW	Type 760b, sensible efficiency = 75.6%, latent efficiency = 0%, and power consumption: 0.17 kW
HX	Type 91, effectiveness = 0.7, specific heat of hot side: 4.19 kj/kg·K, and specific heat of hot side: 1.05 kj/kg·K
Pump	Type 3b, maximum power consumption: 60 W and water flow rate: 180 kg/h
Blower	Type 112a, motor efficiency = 0.85 and maximum air flow rate: 870.4 kg/h
Room (load)	Type 690, sensible load: 2.625, latent load: 0.875, SHR = 0.75
Weather data	Type 109-TMY2, all of weather data is based on Kuala Lumpur (Malaysia)
Solar collector	Type 71, evacuated tube, area of collector: 20 m^2 and the efficiency of collector η: 0.60
Hot water tank	Type 4c, the loss coefficient: 0.55 W/m^2 K
Backup heater	Type 6, the maximum heating rate: 10 kW
G	The one year average solar radiation of Malaysia (2012): 500 W/m^2

In the simulation process, the regeneration temperature can be detected by adjusting and setting the required humidity ratio after the dehumidification process in DW as the humidity ratio set point. Three set points (i.e., 0.0100, 0.0080, and 0.0050 kg/kg) for the humidity ratio were considered for the one-stage ventilation and recirculation modes to evaluate the behavior of regeneration temperatures and COPs. In a comparative evaluation between one-stage and two-stage solar desiccant cooling systems, the humidity ratio set points for the first and second DW in the two-stage ventilation and recirculation modes were 0.0100 kg/kg and 0.0050 kg/kg, respectively. The properties of the simulation components used in the four configurations are shown in Table 1. The solar desiccant cooling system was divided into two parts, namely, the one-stage and the two-stage that are explained in Sections 2.2 and 2.3, respectively. The TRNSYS simulation was validated by the measurement data from the experimental setup of the one-stage ventilation solar desiccant cooling system. This system had been installed in the technology park at the Universiti Kebangsaan Malaysia [7]. After the validation of TRNSYS, it was used to simulate the four configurations of the solar desiccant cooling system.

2.2. One-Stage Solar Desiccant Cooling System.

The one-stage solar desiccant cooling includes the ventilation and recirculation modes. The components of the one-stage desiccant cooling are one DW, one heat recovery wheel, two evaporative coolers, one heat exchanger, one auxiliary heater, and an evacuated tube collector.

The air flow rate of the one-stage ventilation and recirculation in the process and regeneration sides of the system was 870.4 kg/hr.

2.2.1. One-Stage Ventilation Mode.

Figure 1 shows that the ventilation mode of the solar desiccant cooling is an open cycle that provides supply air to the room from ambient air.

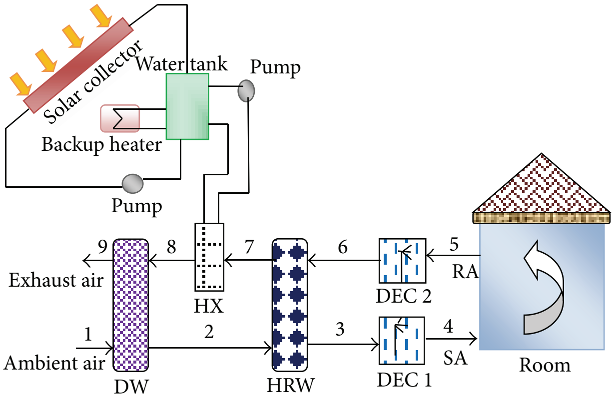

Figure 1: Solar desiccant cooling in ventilation mode schematic.

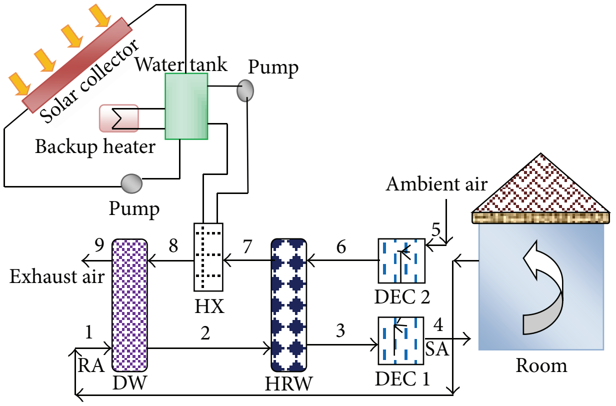

Figure 2: Solar desiccant cooling in recirculation mode schematic.

The returning air from the room after few processes is converted to ambient temperature as exhaust air. Therefore, two kinds of air are present: the process side that produces

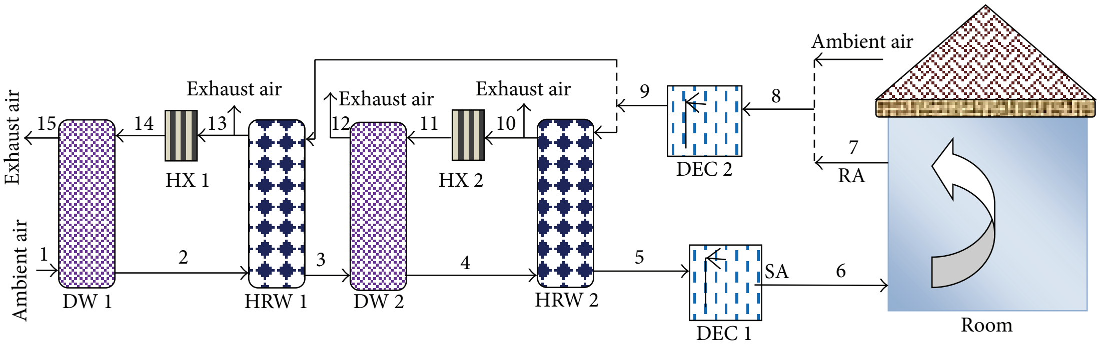

Figure 3: Schematic of two-stage solar desiccant cooling system-ventilation mode.

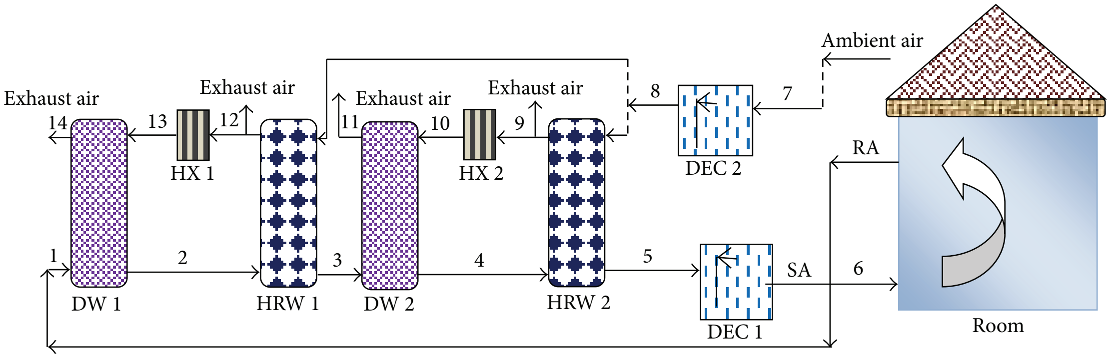

Figure 4: Schematic of two-stage solar desiccant cooling system-recirculation mode.

the supply air, and the regeneration side that releases the returning air from room to ambient temperature. In the process side, first, the ambient air becomes dry because of the DW. Then, the heat recovery wheel cools the air in the process side. In the next step, the air becomes cold because of the evaporative cooler; then, the air moves into the room as supply air. In the regeneration side, the returning air whose latent and sensible loads were left in the room becomes cold because of the evaporative cooler. The heat recovery wheel acts as an energy conservation wheel in the regeneration air side. Then, the heat from the heat exchanger is transferred to the air. In the last step in the regeneration side, the hot air thus absorbed the humidity of the DW and released it outside.

2.2.2. One-Stage Recirculation Mode. Figure 2 shows the recirculation mode of the solar desiccant cooling system. Generally, this system is not an open cycle. The process air side in the recirculation mode is a closed loop, whereas the regeneration air side is an open cycle.

In the process air side, the room air that includes the sensible and latent loads moves to the DW to remove the latent load. The heat recovery wheel acts as a cooler in the process air side. In the next step, the air grows cold because of the evaporative cooler, and it moves into the room as supply air. In the regeneration side, the ambient air grows cold because of the evaporative cooler. In the next step, the heat from the solar collectors and the backup heater is transferred to the air by means of a heat exchanger. Thus, in the last step in the regeneration side, the hot air absorbs the humidity of the DW and is released as exhaust air outdoors.

2.3. Two-Stage Solar Desiccant Cooling System. The two-stage solar desiccant cooling includes the ventilation and recirculation modes. The components of the two-stage desiccant cooling system are two DWs, two heat recovery wheels, two evaporative coolers with different capacities, two heat exchangers, two auxiliary heaters, and an evacuated tube collector. According to the high dehumidification capacity of the two-stage DW and the humid weather in Malaysia, the set point of dehumidification was adjusted at a 0.0050 kg/kg humidity ratio. The air flow rate of the two-stage ventilation and recirculation in the process side was 870.4 kg/hr and 435.2 kg/hr in the regeneration side.

2.3.1. Two-Stage Ventilation Mode. Figure 3 shows the two-step dehumidification of the process air in the solar desiccant cooling system using the evaporative cooling units in ventilation mode. This mode is an open cycle. The air properties of each of the 15 points are characterized by the simulation model. The air properties are explained in Section 3.

The supply air in the process side is produced from the ambient air by undergoing a few stages, such as the two-step dehumidification in the DWs (2 and 4), two-step cooling in the heat recovery wheels (3 and 5), and one-step cooling in the direct evaporative cooler (6). In the regeneration air side, the returning air (7) is mixed with the ambient air (8)

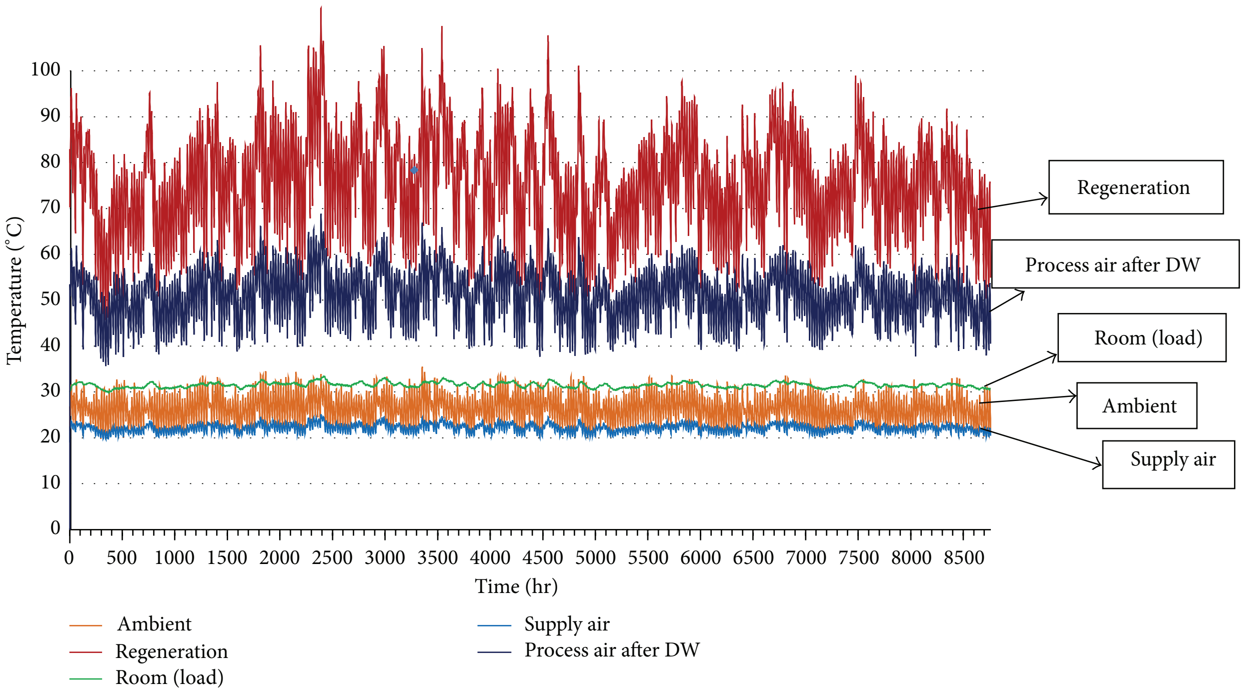

Figure 5: Temperatures (°C) of different components versus time (hr) in ventilation desiccant cooling system.

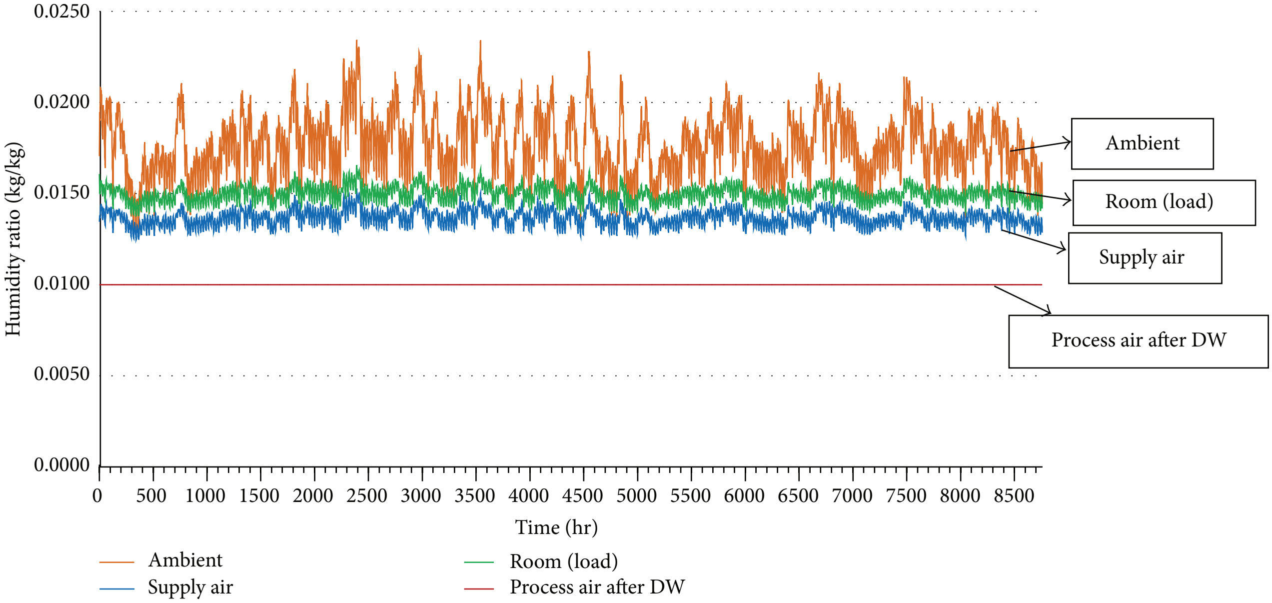

Figure 6: Humidity ratio (kg/kg) of different components versus time (hr) in ventilation desiccant cooling system.

before being cooled in one direct evaporative cooler. Then, the output air from the evaporative cooler (9) is divided into two stages with the same air flow rate. In each stage, air is heated in the heat recovery wheel (10 and 13), heated in the solar heaters (11 and 14), and humidified in the DWs (12 and 15).

2.3.2. Two-Stage Recirculation Mode. Figure 4 shows the schematic of the two-stage solar desiccant cooling system under the recirculation mode. The process air side (1–6) is a closed loop and the regeneration side (7–14) is an open cycle. Supply air is produced from the returning air in the process air side by undergoing a few stages, such as the two-step dehumidification in the DWs (2 and 4), two step cooling in the heat recovery wheels (3 and 5), and one-step cooling in the direct evaporative cooler (6). In the regeneration side, ambient air (7) is mixed from the air in the cooler (8) and then divided into two stages for the heating and humidifying process (8–11 and 8–14). The process air under the ventilation mode is an open loop, whereas it is a closed loop under the recirculation mode.

2.4. Determination of the COP of the Desiccant Cooling System. The COP of the solar desiccant cooling system can be calculated by the rate of heat extracted against the rate of the cooling system driving energy. The rate of heat extracted is the cooling capacity of the system. The rate of the cooling system driving energy is the total thermal energy requirement for the cooling system generated from solar collectors and the backup heater. Therefore, the COP of the system is obtained by the following relationship [4]:

$$\mathrm{COP} = \frac{Q_{\mathrm{cool}}}{Q_T}. \tag{1}$$

2.4.1. One Stage. The COP of the solar desiccant cooling system under the ventilation mode is defined as the ratio of the enthalpy change from ambient air to supply air, multiplied by the mass air flow and external heat delivered to the regeneration heat exchanger. It can be written as follows:

$$\mathrm{COP} = \frac{\dot{m}_s\left(h_1 - h_4\right)}{\dot{m}_r\left(h_8 - h_7\right)}. \tag{2}$$

The COP of the solar desiccant cooling under recirculation mode can be written as

$$\mathrm{COP} = \frac{\dot{m}_s\left(h_1 - h_4\right)}{\dot{m}_r\left(h_8 - h_7\right)}, \tag{3}$$

where $\dot{m}_s$ (kg/hr) is the mass flow rate of the supply air, $\dot{m}_r$ (kg/hr) is the mass flow rate of the regeneration air, and h (kJ/kg) is the enthalpy of air.

2.4.2. Two Stages. The COP of the two-stage solar desiccant cooling under the ventilation mode can be written as [20]

$$\mathrm{COP} = \frac{\dot{m}_{s1}\left(h_1 - h_6\right)}{\dot{m}_{r13}\left(h_{14} - h_{13}\right) + \dot{m}_{r10}\left(h_{11} - h_{10}\right)}. \tag{4}$$

The COP of the two-stage solar desiccant cooling under the recirculation mode can be written as

$$\mathrm{COP} = \frac{\dot{m}_{s1}\left(h_1 - h_6\right)}{\dot{m}_{r12}\left(h_{13} - h_{12}\right) + \dot{m}_{r9}\left(h_{10} - h_9\right)}, \tag{5}$$

where $\dot{m}_s$ (kg/hr) is the mass flow rate of the supply air, $\dot{m}_r$ (kg/hr) is the mass flow rate of the regeneration air, and h (KJ/kg) is the enthalpy of air.

2.5. Solar Fraction. Generally, solar collectors convert solar radiation into thermal energy in solar cooling systems. Considering the insufficient thermal energy from solar collectors in cloudy weather, the backup heater is used to achieve the required thermal energy for the total cooling system driving energy. The percentage ratio of the thermal energy produced by the solar collectors to the total cooling system driving energy is known as the solar fraction, which can be expressed as follows [25]:

$$\mathrm{SF} = \frac{Q_U}{Q_T}, \tag{6}$$

where Q_T is the total cooling system driving energy produced by the solar collectors and the backup heater. Q_U is the thermal energy produced by the solar collectors that can be expressed as [26]

$$Q_U = A \times \eta \times G. \tag{7}$$

Table 2: Air properties of one-stage solar desiccant cooling system in ventilation mode.

Points number	Temperature (°C)	Humidity ratio (kg/kg)
1	30	0.0200
2	49.5	0.0100
3	31.8	0.0100
4	22	0.0137
5	30.8	0.0152
6	24.95	0.0176
7	45.6	0.0176
8	81.6	0.0176
9	50	0.0262

3. Results and Discussion

The results of the four different systems were explained and then compared in the next sections. The temperature and humidity ratio against time of the specified points in the four systems were analyzed.

3.1. Results of the One-Stage Solar Desiccant Cooling System

3.1.1. Ventilation Mode. The temperature of ambient air, process air after the DW, supply air, room (load), and regeneration temperature versus time (hr) are shown in Figure 5. The temperatures at different points were specified for 8,760 h after running the solar desiccant cooling system. The regeneration temperature is one of the important parameters that play a main role in the changes in the COP of the desiccant cooling system. The regeneration temperature under the ventilation mode for 0.0100 kg/kg dehumidification (humidity ratio reduction from 0.0200 kg/kg to 0.0100 kg/kg) was almost 81.6°C (average). Figure 6 shows the humidity ratio of the ambient air, supply air, load, and process air after the DW versus time under the ventilation mode.

The humidity ratio of the supply air is one of the important parameters that play a main role in the amount latent load removed from the room by the desiccant cooling system, especially in hot and humid weather in Malaysia. The average temperature and humidity ratio of the specified points in the one-stage ventilation system for 8,760 h operation are shown in Table 2. The temperature and humidity ratio of the supply air (point 4) are 22°C and 0.0137 kg/kg, respectively, whereas those in the room (point 5) are 30.80°C and 0.0152 kg/kg, respectively.

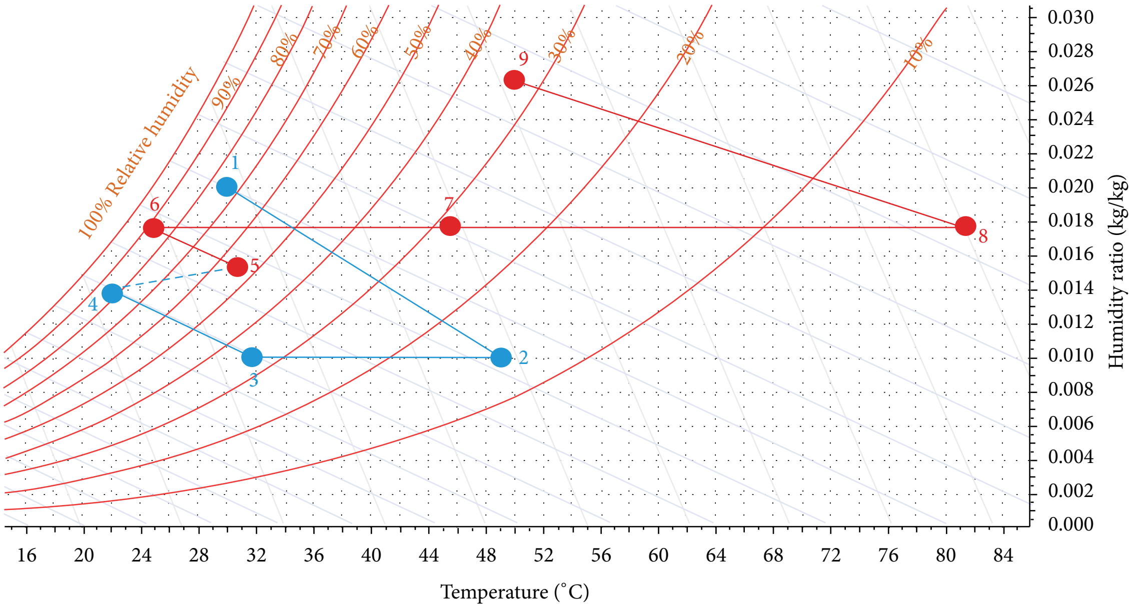

Figure 7: Psychometric chart of the one-stage solar desiccant cooling system under the ventilation mode.

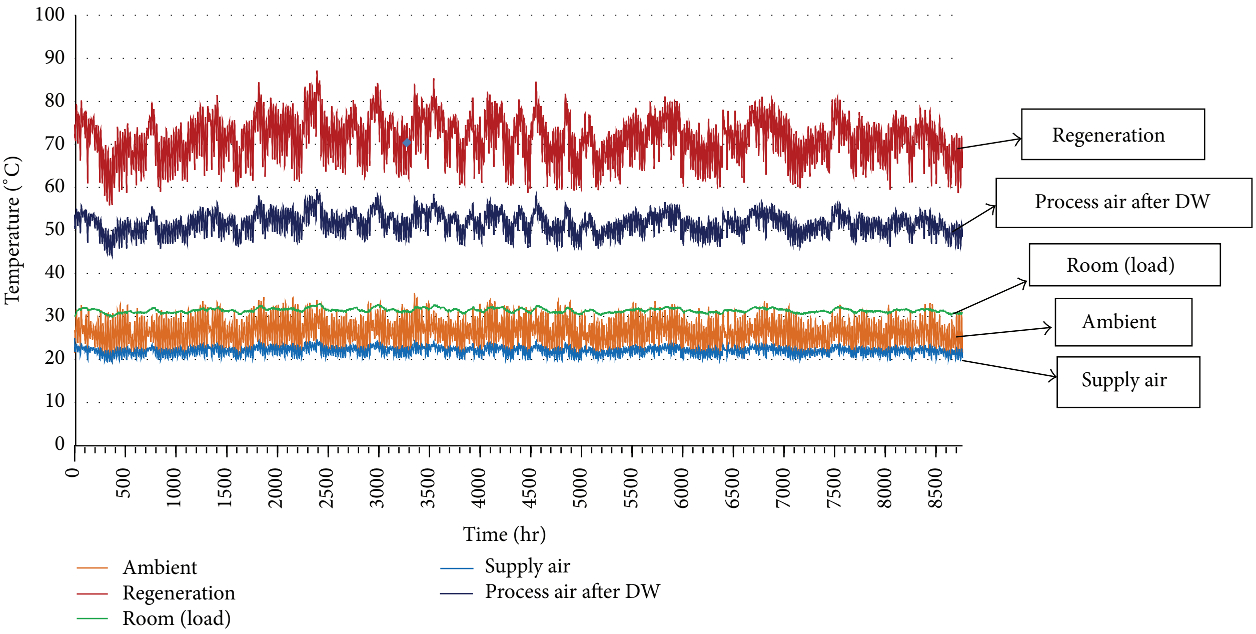

Figure 8: Temperatures (°C) of different components versus time (hr) in recirculation desiccant cooling system.

Figure 7 shows the psychometric chart of the one-stage solar desiccant cooling system under the ventilation mode in which the air property and process air on all points are specified. The process-air and regeneration-air sides are indicated by blue and red lines, respectively. Because of the dehumidification process between points 1 and 2, the air temperature increases, whereas the humidity ratio decreases. By the cooling process between points 2 and 3, the air temperature decreases, whereas the humidity ratio of air in the heat recovery wheel remains constant. The temperature decreases, and the humidity ratio increases because of the evaporative cooling process between points 3 and 4. The line between points 4 and 5 shows that the air property changes from supply air to the returning air inside the room. The regeneration side includes the four stages, namely, the evaporative cooling process between points 5 and 6, heating between points 6 and 7, heating process between points 7 and 8, and process of exhausted air to outdoor between points 8 and 9.

3.1.2. Recirculation Mode. Figure 8 shows the temperatures (°C) of the ambient air, process air after the DW, supply

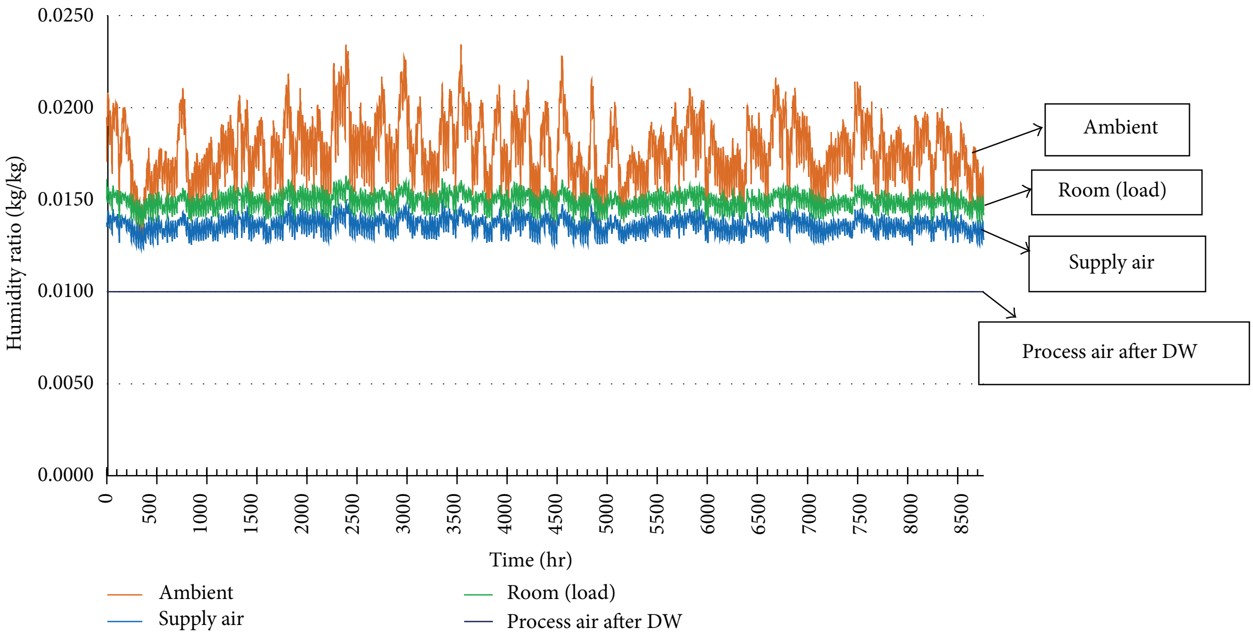

Figure 9: Humidity ratio (kg/kg) of different components versus time (hr) in recirculation mode.

Table 3: Air properties of one-stage solar desiccant cooling system in recirculation mode.

Points number	Temperature (°C)	Humidity ratio (kg/kg)
1	31	0.0150
2	51	0.0100
3	31.4	0.0100
4	21.4	0.0136
5	30	0.0200
6	26.4	0.0215
7	45	0.0215
8	70.2	0.0215
9	55	0.0257

air, the room, and the regeneration versus time (hr) under the recirculation mode. The regeneration temperature under the recirculation mode for 0.0100 kg/kg dehumidification (humidity ratio reduced from 0.0200 kg/kg to 0.0100 kg/kg) is almost 70.2°C (average). The humidity ratios of the ambient air and process air after DW, in the room, and the supply air versus time (hr) in the one-stage recirculation mode are shown in Figure 9.

The average temperature and humidity ratio of the specified points in the one-stage recirculation system for 8,760 h operation are shown in Table 3. The temperature and humidity ratio of the supply air (point 4) are 21.4°C and 0.0136 kg/kg, respectively, whereas those for the room (point 1) are 31°C and 0.0150 kg/kg, respectively. Figure 10 shows the psychometric chart of the one-stage solar desiccant cooling system under the recirculation mode where the air property changes in the different parts of the solar desiccant cooling system are described. In the process side, the air returning from the room to the DW for dehumidification is shown between points 4 and 1. The ambient air temperature is decreased by the evaporative cooling process (5 and 6). The heating process (6 and 7), heating process (7 and 8), and process of exhausted air to outdoor (8 and 9) are performed in the regeneration side.

3.2. Comparison between the One-Stage Ventilation and Recirculation Modes.

Table 4 shows the simulation results of the one-stage ventilation and recirculation modes in three different humidity ratio set points (i.e., 0.0050, 0.0080, and 0.0100 kg/kg). The results show that by increasing the humidity ratio set point in both modes, the trend of the regeneration temperature decreased, whereas the trend of supply air temperature, return air temperature, and COP increased. By increasing the humidity ratio set point because of the decreasing regeneration temperature, the COP of the system increased. The temperature and humidity of the room also increased. In the evolution of air conditioning system parameters, although the COP is the most important parameter, reaching the comfortable condition of the room is another important parameter that must be considered. For example, in ventilation mode, when the humidity ratio decreased from 0.00100 kg/kg to 0.0050 kg/kg, the room temperature and humidity ratio also decreased from 30.80°C to 28.22°C and from 0.0152 kg/kg to 0.0115 kg/kg, respectively. The COP decreased from 0.65 to 0.57. The set point of 0.0050 kg/kg humidity ratio in comparison with another set point thus leads the system to reach near thermal comfort conditions.

By comparing the temperature results of the one-stage ventilation and recirculation in each humidity ratio set point, the regeneration temperature under the ventilation mode is found to be considerably higher than that under the recirculation mode. The temperatures of the supply air under

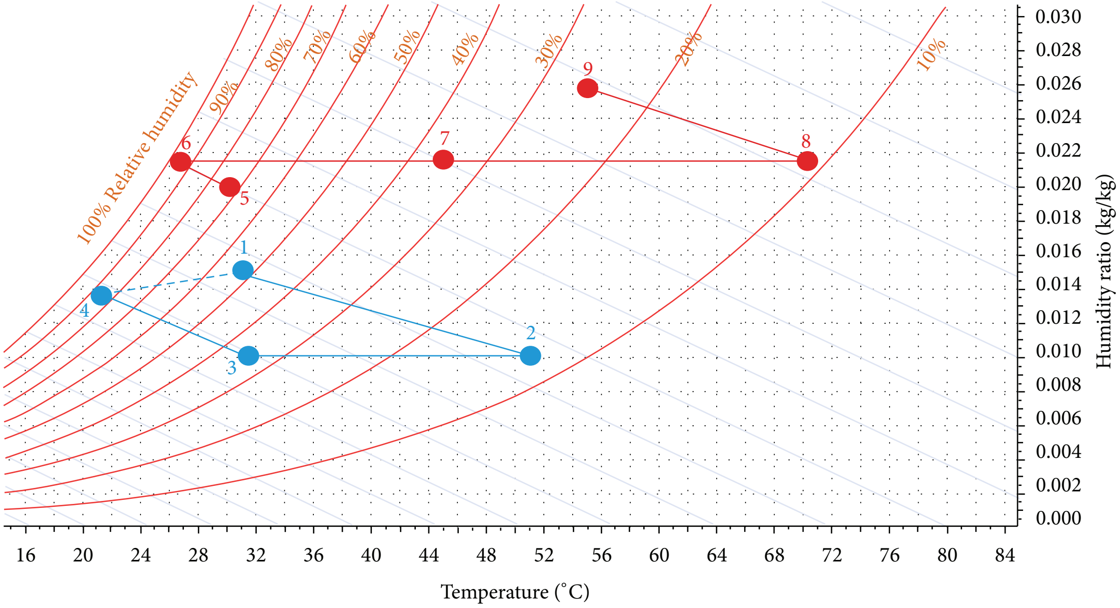

Figure 10: Psychometric chart of one-stage solar desiccant cooling system in recirculation mode.

Table 4: Air properties results of ventilation and recirculation modes based on different humidity ratio set points.

Humidity ratio set point (kg/kg)	Ventilation mode						Recirculation mode					
	Reg T (°C)	SA		RA		COP	Reg T (°C)	SA		RA		COP
		T (°C)	HR (kg/kg)	T (°C)	HR (kg/kg)			T (°C)	HR (kg/kg)	T (°C)	HR (kg/kg)	
0.0050	122.00	19.48	0.0100	28.22	0.0115	0.57	96.90	18.50	0.0100	28.50	0.0115	0.29
0.0080	98.40	20.95	0.0121	30.24	0.0136	0.61	80.30	20.80	0.0121	30.46	0.0135	0.40
0.0100	81.60	22.00	0.0137	30.80	0.0152	0.65	70.20	21.40	0.0136	31.00	0.0150	0.50

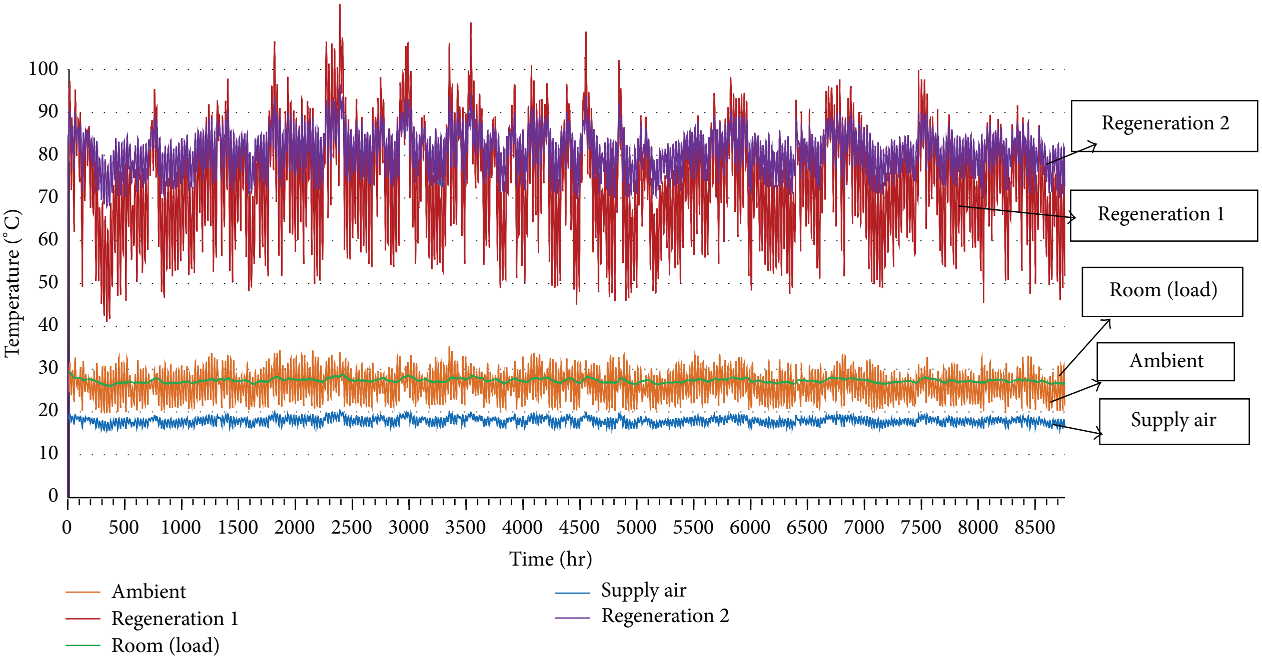

Figure 11: Temperatures (°C) of different components versus time (hr) in two-stage ventilation desiccant cooling system.

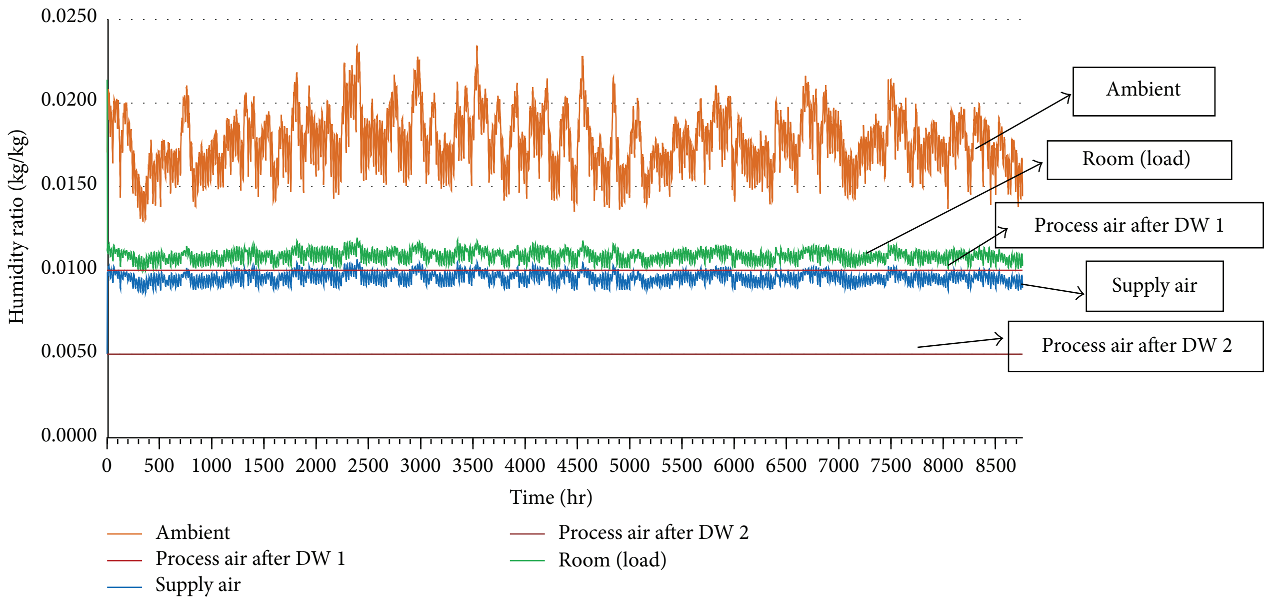

Figure 12: Humidity ratio (kg/kg) of different components versus time (hr) in two-stage ventilation desiccant cooling system.

both modes are almost the same. In addition, the room temperatures under both modes are almost the same.

By comparison, the humidity ratio results of the ventilation and recirculation show that the humidity ratio of the room and the supply air under both modes are almost the same. The COPs under the ventilation and recirculation modes are calculated using (1) and (2). Therefore, the COPs of the desiccant cooling system under the ventilation mode are higher than those under the recirculation mode.

3.3. Result of the Two-Stage Solar Desiccant Cooling System.

The simulation results of the two-stage desiccant cooling system under the two modes of ventilation and recirculation are explained in the following sections.

3.3.1. Two-Stage Ventilation. Figure 11 shows the temperature trend in the different points of the two-stage solar desiccant system, such as the temperatures of the regeneration of the first and second DWs, room, ambient air, and supply air versus time (hr). The first and second regeneration temperatures are approximately 80°C. The humidity ratio of the ambient air, process air after DW, room, and supply air versus time (hr) under the two-stage ventilation mode are shown in Figure 12.

The humidity ratios of the air after the first and second dehumidification are 0.0100 and 0.0050 kg/kg, respectively, during the 8,760 hr system operation. According to the temperature and humidity ratio results under the ventilation mode, the important points of the air property are detected and shown in Table 5.

Figure 13 shows the psychometric chart of the two-stage solar desiccant cooling system under the ventilation mode. The process air side of this system includes the two-step dehumidification process (1 and 2 and 3 and 4) by the two DWs, the two-step cooling process (2 and 3 and 4 and 5) by the two heat recovery wheels, and the one-stage cooling process (5 and 6) by the evaporative cooler. The process from points 1 to 5 is defined as isothermal dehumidification. The regeneration air side includes a few processes such as the mixing of ambient air and returning air process (7 and 8), evaporative cooling process (8 and 9), two-step heating process (9 and 10 and 9–13) by the heat recovery wheels, two-step heating process (10 and 11 and 13 and 14) by the solar heater, and two-step process of exhausted air outdoors (11 and 12 and 14 and 15).

Table 5: Air properties of two-stage solar desiccant cooling system in ventilation mode.

Points number	Temperature (°C)	Humidity ratio (kg/kg)
1	30	0.0200
2	53.7	0.0100
3	30.2	0.0100
4	50	0.0050
5	28.3	0.0050
6	17.62	0.0096
7	27.3	0.0109
8	29.71	0.0145
9	23.4	0.0168
10	45.1	0.0168
11	82.1	0.0168
12	41.5	0.0270
13	48.2	0.0168
14	80	0.0168
15	34	0.0280

3.3.2. Two-Stage Recirculation. The temperature trend in various points in the two-stage recirculation solar desiccant

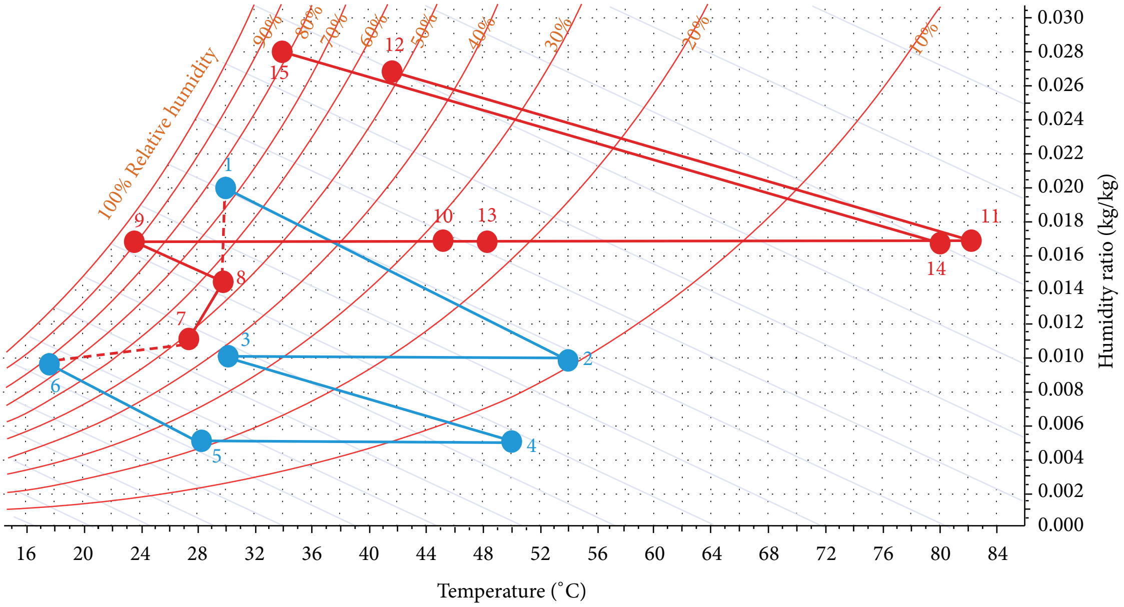

Figure 13: Psychometric chart of two-stage solar desiccant cooling system in ventilation mode.

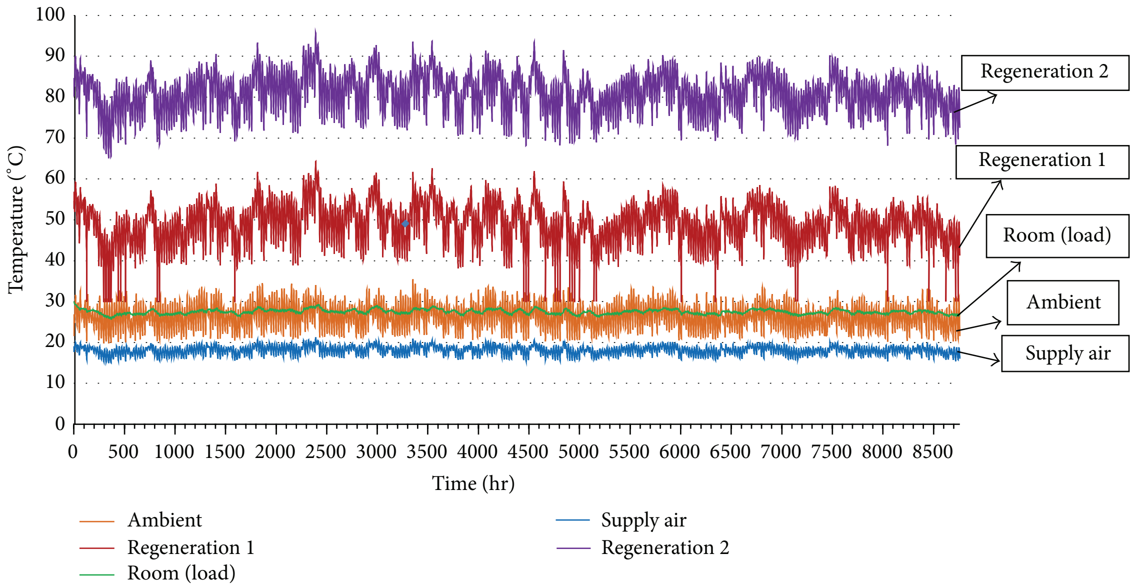

Figure 14: Temperatures (°C) of different components versus time (hr) in two-stage recirculation desiccant cooling system.

cooling system versus time (hr) is shown in Figure 14. The humidity ratio trend of the various points in the two-stage recirculation system versus time (hr) is shown in Figure 15. According to the temperature and humidity ratio results of the simulation model of the two-stage system under the recirculation mode, the important points of air properties are detected and shown in Table 6.

Figure 16 shows the psychometric chart of the two-stage solar desiccant cooling system under the recirculation mode. The process air side of this system includes several processes such as the returning air process from the room to the first DW (6–1), two-step dehumidification process (1 and 2 and 3 and 4) by the two DWs, two-step cooling process (2 and 3 and 4 and 5) by the two heat recovery wheels, and one-stage cooling process (5 and 6) by the evaporative cooler. The regeneration air side includes several processes such as the evaporative cooling process (7 and 8), two-step heating process (8 and 9 and 8–12) by the heat recovery wheel, two-step heating process (9 and 10 and 12 and 13) by the solar heater, and two-step process of exhausted air to outdoor (10 and 11 and 13 and 14).

3.4. Comparison Results between the Two-Stage Ventilation and Recirculation Modes.

The humidity ratios of the process

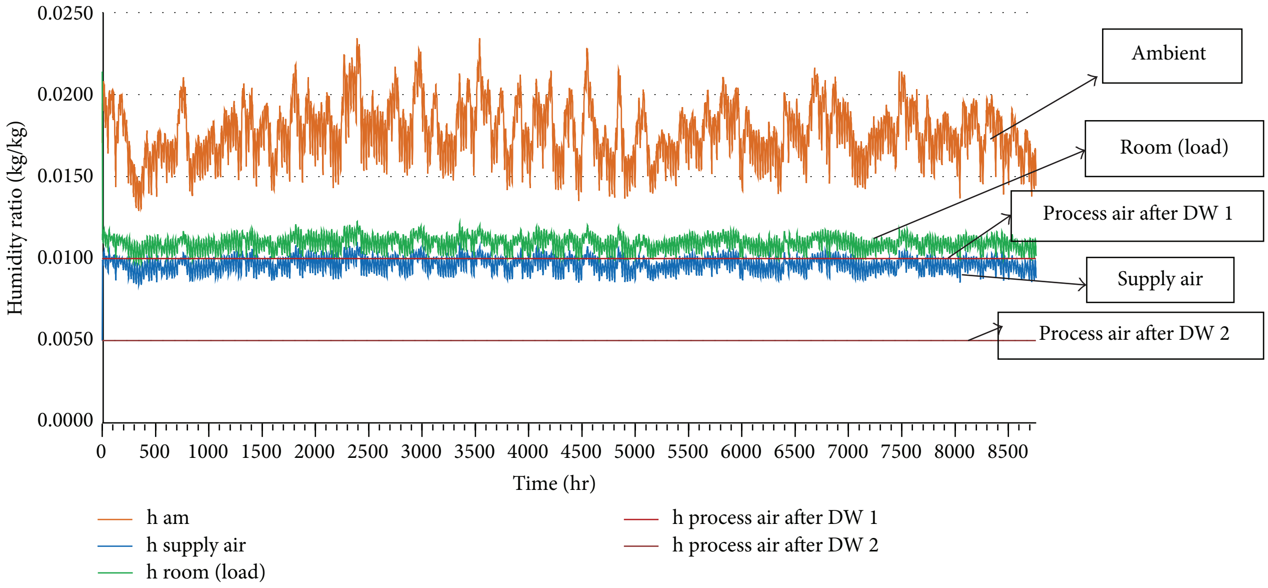

Figure 15: Humidity ratio (kg/kg) of different components versus time (hr) in two-stage recirculation mode.

Table 6: Air properties of two-stage solar desiccant cooling system in recirculation mode.

Points number	Temperature (°C)	Humidity ratio (kg/kg)
1	27	0.0109
2	34.82	0.0100
3	27.3	0.0100
4	49.33	0.0050
5	30.74	0.0050
6	18	0.0096
7	30	0.0200
8	26.1	0.0211
9	41.3	0.0211
10	80	0.0211
11	58.7	0.0253
12	32.9	0.0211
13	50	0.0211
14	42.6	0.0231

air after the first and second DWs under both modes are 0.0100 and 0.0050 kg/kg, respectively. By comparing the temperature results of the two-stage ventilation and recirculation modes, the regeneration temperatures under the ventilation mode are found to be higher than those under the recirculation mode. The supply air temperature and humidity ratio under the ventilation mode are 17.6°C and 0.0096 kg/kg, respectively, whereas those under the recirculation mode are 18°C and 0.0096 kg/kg, respectively. The room air temperature and humidity ratio are 27.3°C and 0.0109 kg/kg, respectively, whereas those under the recirculation mode are 27°C and 0.0109 kg/kg, respectively. The COPs under the ventilation and recirculation modes are calculated by (3) and (4). The COPs of the ventilation and recirculation are 1.06 and 0.43, respectively. Although the cooling system driving energy in ventilation mode was higher than the recirculation mode, the rate of cooling capacity in ventilation mode was higher than the recirculation mode. The COPs of the one-stage and two-stage desiccant cooling systems under the ventilation mode were higher than those under the recirculation mode.

3.5. Comparison Results of the Four Configurations of the Solar Desiccant Cooling Systems. The regeneration temperature, supply air temperature, supply air relative humidity, supply air humidity ratio, room air temperature, room air relative humidity, room air humidity ratio, COP, and solar fraction of the four configurations of the solar desiccant cooling are shown in Table 7. The values are average for one year. The final humidity ratio set point before the evaporative cooler for the four configurations is 0.005 kg/kg humidity ratio. Whereas the one-stage desiccant cooling dehumidification occurs in one step, the two-stage desiccant cooling dehumidification occurs in two steps.

The supply and return air temperatures and humidity ratios of the two-stage system are less than those of the one-stage system. Regarding the thermal comfort condition parameters, the results of the two-stage desiccant cooling system were better than the one-stage desiccant cooling system. Given the isothermal dehumidificationin process in the two stage desiccant cooling systems, the regeneration temperature of the two-stage ventilation and recirculation was lower than the one stage ventilation and recirculation. By comparing the best configuration of the one-stage and two-stage ventilation modes, the two-stage ventilation solar cooling system was selected as the best configuration among the four configurations because of its higher COP, as well as lower room temperature and humidity ratio. By comparing the

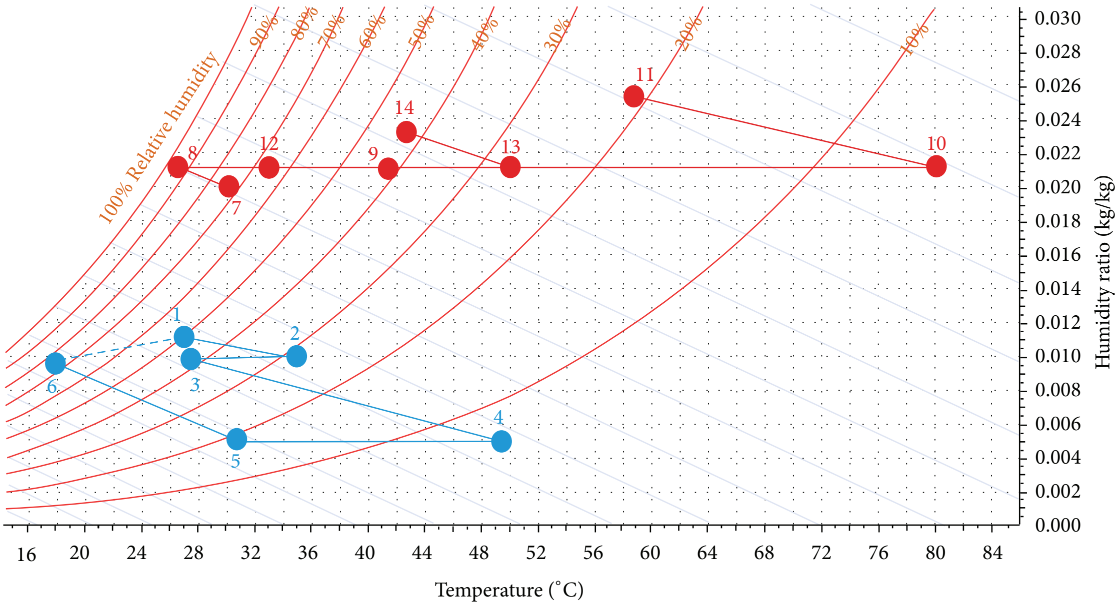

FIGURE 16: Psychometric chart of two-stage solar desiccant cooling system in recirculation mode.

TABLE 7: Performance comparison of four desiccant cooling configurations under 0.005 kg/kg humidity ratio set point in hot and humid climate (30°C, 20 HR).

Type of configurations	T reg (°C)	SA			RA			COP	SF (%)
		T (°C)	HR (kg/kg)	RH (%)	T (°C)	HR (kg/kg)	RH (%)		
One-stage ventilation	122.00	19.48	0.0100	70.4	28.22	0.0115	47.9	0.57	39
One-stage recirculation	96.90	18.50	0.0100	75.0	28.50	0.0115	47.1	0.29	50
Two-stage ventilation	82.10–80.00	17.60	0.0096	76.2	27.30	0.0109	48.0	1.06	69
Two-stage recirculation	80.00–50.00	18.00	0.0096	74.3	27.00	0.0109	48.7	0.43	85

solar fractions of the four configurations, the solar fraction percentage for the two-stage ventilation desiccant cooling system was 69%. The maximum and minimum solar fractions were for the two-stage recirculation and one-stage ventilation systems.

4. Conclusions

This paper has presented a comparison study among four configurations of a solar desiccant cooling system in the hot and humid weather in Malaysia. The four systems, namely, the one-stage ventilation, one-stage recirculation, two-stage ventilation, and two-stage recirculation, were simulated during an 8,760 hr operation by TRNSYS. The COP of the two-stage ventilation mode was higher than those of the other configurations. The two-stage ventilation produced supply air at 17.6°C and 0.0096 kg/kg to remove the sensible load of the room, whereas the supply air temperatures of the other configurations were higher. Therefore, based on the condition of ambient air (30°C and 0.0200 kg/kg), the two-stage solar desiccant cooling system under the ventilation mode is more suitable than the other configurations.

Nomenclature

A:	Collector area [m^2]
AC:	Air conditioning system [-]
ASHRAE:	American Society of Heating, Refrigerating and Air Conditioning Engineers [-]
COP:	Thermal coefficient of performance [-]
DEC:	Direct evaporative cooler [-]
DW:	Desiccant wheel [-]
F1, F2:	Effectiveness of desiccant wheel
G:	Solar radiation [W/m^2]
h:	Enthalpy [kj/kg]
hr:	Time [hour]
HR:	Humidity ratio [kg/kg]
HRW:	Heat recovery wheel [-]
HVAC:	Heating, Ventilation, and Air-Conditioning [-]
HX:	Heat exchanger [-]
Q_{cool}:	Cooling capacity of the system [kW]
Q_T:	The cooling system driving energy
Q_U:	Solar thermal power [kW]
reg:	Regeneration
RA:	Return air [-]
SA:	Supply air [-]

SF:	Solar fraction [%]
T:	Air temperature [°C]
TSRDC:	Two-stage rotary desiccant cooling [-]
$\dot{m}_s$:	Mass flow rate of the supply air [kg/hr]
$\dot{m}_r$:	Mass flow rate of regeneration air [kg/hr]
η:	Solar collector efficiency [-].

Conflict of Interests

The authors of the paper do not have any financial relation with the TRNSYS software company. They confirm that the paper is just a research workwhich has no financial benefit from TRNSYS Company or other companies.

Acknowledgment

The authors would like to thank the Solar Energy Research Institute (SERI), Universiti Kebangsaan Malaysia, for providing the laboratory facilities and technical support.

References

[1] D. La, Y. J. Dai, Y. Li, R. Z. Wang, and T. S. Ge, "Technical development of rotary desiccant dehumidification and air conditioning: a review," *Renewable and Sustainable Energy Reviews*, vol. 14, no. 1, pp. 130–147, 2010.

[2] E. Hürdoğan, O. Büyükalaca, T. Yılmaz, and A. Hepbaşlı, "Experimental investigation of a novel desiccant cooling system," *Energy and Buildings*, vol. 42, no. 11, pp. 2049–2060, 2010.

[3] A. Y. T. Al-Zubaydi, "Solar air conditioning and refrigeration with absorption chillers technology in australia—an overview on researches and applications," *Journal of Advanced Science and Engineering Research*, vol. 1, no. 1, pp. 23–41, 2011.

[4] K. Daou, R. Z. Wang, and Z. Z. Xia, "Desiccant cooling air conditioning: a review," *Renewable and Sustainable Energy Reviews*, vol. 10, no. 2, pp. 55–77, 2006.

[5] K. Haddad, B. Ouazia, and H. Barhoun, "Simulation of a desiccant-evaporative cooling system for residential buildings," in *Proceedings of the 3rd Canadian Solar Building Conference*, pp. 1–8, Fredericton, Canada, August 2008.

[6] K. F. Fong, V. I. Hanby, and T. T. Chow, "HVAC system optimization for energy management by evolutionary programming," *Energy and Buildings*, vol. 38, no. 3, pp. 220–231, 2006.

[7] M. M. Salehi Dezfouli, Z. Hashim, M. H. Ruslan, B. Bakhtyar, K. Sopian, and A. Zaharim, "Experimental investigation of solar hybrid desiccant cooling system in hot and humid weather of malaysia," in *Proceedings of the 10th International Conference on Environment, Ecosystems and Development (WSEAS '12)*, 2012.

[8] S. Jain, P. L. Dhar, and S. C. Kaushik, "Evaluation of solid-desiccant-based evaporative cooling cycles for typical hot and humid climates," *International Journal of Refrigeration*, vol. 18, no. 5, pp. 287–296, 1995.

[9] P. Bourdoukan, E. Wurtz, and P. Joubert, "Comparison between the conventional and recirculation modes in desiccant cooling cycles and deriving critical efficiencies of components," *Energy*, vol. 35, no. 2, pp. 1057–1067, 2010.

[10] K. Mehmet, M. Özdinç Çarpınlıoğlu, and M. Yıldırım, "Energy and exergy analyses of an experimental open-cycle desiccant cooling system," *Applied Thermal Engineering*, vol. 24, no. 5-6, pp. 919–932, 2004.

[11] G. Panaras, E. Mathioulakis, and V. Belessiotis, "Achievable working range for solid all-desiccant air-conditioning systems under specific space comfort requirements," *Energy and Buildings*, vol. 39, no. 9, pp. 1055–1060, 2007.

[12] L. A. Sphaier and C. E. L. Nóbrega, "Parametric analysis of components effectiveness on desiccant cooling system performance," *Energy*, vol. 38, no. 1, pp. 157–166, 2012.

[13] Z. Huan and N. Jianlei, "Two-stage desiccant cooling system using low-temperature heat," *Building Services Engineering Research and Technology*, vol. 20, no. 2, pp. 51–55, 1999.

[14] Z. Q. Xiong, Y. J. Dai, and R. Z. Wang, "Development of a novel two-stage liquid desiccant dehumidification system assisted by CaCl2 solution using exergy analysis method," *Applied Energy*, vol. 87, no. 5, pp. 1495–1504, 2010.

[15] S. Techajunta, S. Chirarattananon, and R. H. B. Exell, "Experiments in a solar simulator on solid desiccant regeneration and air dehumidification for air conditioning in a tropical humid climate," *Renewable Energy*, vol. 17, no. 4, pp. 549–568, 1999.

[16] K.-H. Yang and S.-H. Wang, "The analysis of a solar-assisted desiccant evaporative cooling system and its application," *Journal of the Chinese Institute of Engineers*, vol. 11, no. 3, pp. 227–234, 1988.

[17] G. Meckler, "Two-stage desiccant dehumidification in commercial building HVAC systems," *Ashrae Transactions*, vol. 95, no. 2, pp. 1116–1123, 1989.

[18] H.-M. Henning, "Solar assisted air conditioning of buildings—an overview," *Applied Thermal Engineering*, vol. 27, no. 10, pp. 1734–1749, 2007.

[19] D. La, Y. Dai, Y. Li, T. Ge, and R. Wang, "Case study and theoretical analysis of a solar driven two-stage rotary desiccant cooling system assisted by vapor compression air-conditioning," *Solar Energy*, vol. 85, no. 11, pp. 2997–3009, 2011.

[20] T. S. Ge, Y. Li, R. Z. Wang, and Y. J. Dai, "Experimental study on a two-stage rotary desiccant cooling system," *International Journal of Refrigeration*, vol. 32, no. 3, pp. 498–508, 2009.

[21] D. La, Y. Li, Y. J. Dai, T. S. Ge, and R. Z. Wang, "Development of a novel rotary desiccant cooling cycle with isothermal dehumidification and regenerative evaporative cooling using thermodynamic analysis method," *Energy*, vol. 44, no. 1, pp. 778–791, 2012.

[22] H. Li, Y. J. Dai, Y. Li, D. La, and R. Z. Wang, "Case study of a two-stage rotary desiccant cooling/heating system driven by evacuated glass tube solar air collectors," *Energy and Buildings*, vol. 47, pp. 107–112, 2012.

[23] H. Li, Y. J. Dai, Y. Li, D. La, and R. Z. Wang, "Experimental investigation on a one-rotor two-stage desiccant cooling/heating system driven by solar air collectors," *Applied Thermal Engineering*, vol. 31, no. 17-18, pp. 3677–3683, 2011.

[24] *ASHRAE Handbook—HVAC Systems and Equipment*, American Society of Heating, Refrigerating, and Air Conditioning Engineers, Atlanta, Ga, USA, 1996.

[25] A. M. Baniyounes, G. Liu, M. G. Rasul, and M. M. K. Khan, "Analysis of solar desiccant cooling system for an institutional building in subtropical Queensland, Australia," *Renewable and Sustainable Energy Reviews*, vol. 16, no. 8, pp. 6423–6431, 2012.

[26] *Solar-Assisted Air-Conditioning in Buildings: A Handbook For Planners*, Springer, New York, NY, USA, 2004.

Hindawi Publishing Corporation
International Journal of Photoenergy
Volume 2013, Article ID 843615, 9 pages
http://dx.doi.org/10.1155/2013/843615

Research Article

Solution-Processed Bulk Heterojunction Solar Cells with Silyl End-Capped Sexithiophene

Jung Hei Choi,[1] Mohamed E. El-Khouly,[2] Taehee Kim,[1] Youn-Su Kim,[1] Ung Chan Yoon,[3] Shunichi Fukuzumi,[4] and Kyungkon Kim[1,5]

[1] *Photo-Electronic Hybrids Research Center, Korea Institute of Science and Technology, Hwarangno 14-gil 5, Seongbuk-gu, Seoul 136-791, Republic of Korea*
[2] *Department of Chemistry, Faculty of Science, Kafrelsheikh University, Kafr ElSheikh 33516, Egypt*
[3] *Department of Chemistry, Pusan National University, Jangjeon-dong Kumjeong-gu, Busan 609-735, Republic of Korea*
[4] *Department of Material and Life Science, Graduate School of Engineering, Osaka University, ALCA, Japan Science and Technology Agency (JST), Suita, Osaka 565-0871, Japan*
[5] *Department of Chemistry and Nanoscience, Ewha Womans University, 52 Ewhayeodae-gil, Seodaemun-gu, Seoul 120-750, Republic of Korea*

Correspondence should be addressed to Shunichi Fukuzumi; fukuzumi@chem.eng.osaka-u.ac.jp

Received 15 July 2013; Accepted 25 November 2013

Academic Editor: Adel M. Sharaf

We fabricated solution-processed organic photovoltaic cells (OPVs) using substituted two sexithiophenes, a,w-bis(dimethyl-*n*-octylsilyl)sexithiophene (**DSi-6T**) and a,w-dihexylsexithiophene (**DH-6T**), as electron donors, and [6,6]-phenyl-C_{61}-butyric acid methyl ester (PCBM) as an electron acceptor. Solution-processed OPVs using **DH-6T** and **DSi-6T** showed good photovoltaic properties in spite of their poor solubility. The best performance was observed on **DSi-6T** : PCBM 1 : 5 (w/w) blend cell with an open circuit voltage (V_{oc}) of 0.63 V, short circuit current density (J_{sc}) of 1.34 mA/cm^2, fill factor (FF) of 55%, and power conversion efficiency of 0.44% under AM 1.5 G illumination. Although **DH-6T** has higher hole mobility than **DSi-6T**, the **DSi-6T** : PCBM blend cell showed higher hole mobility than **DH-6T** : PCBM cell. Therefore, **DSi-6T** cell showed higher device performance than **DH-6T** cell due to its silyl substitutions, which lead to the increase of the solubility. The incorporation of solution-processed TiO_2 interfacial layer in the **DSi-6T** : PCBM devices significantly enhances FF due to the reduced charge recombination near active layer/Al interface.

1. Introduction

Organic solar cells have received strong attention due to the possibility to realize flexible and low-cost large photovoltaic cells [1–5]. Polymer based organic photovoltaic cells (OPVs) demonstrated power conversion efficiencies (PCEs) in excess of 7% by the results of synthesis of low bandgap polymers [6, 7]. However, the polymers still have high batch-to-batch variations and difficulty in purification, and there have been many efforts to discover solution-processed small molecules. Recently, oligothiophenes have received much attention as donor materials in OPVs because of their high hole mobility, easy multigram synthesis, high purity, and simple chemical modification [8–10]. Some studies on oligothiophene based solar cells have already been reported using bilayer heterojunction solar cells [11–15]. By controlling the film morphology using coevaporation of excess fullerene (C_{60}), bulk heterojunction organic photovoltaic cells consisting of sexithiophene (6T) as a donor and C_{60} as an acceptor showed good photovoltaic properties [16]. However, the small molecules based on sexithiophene have not been investigated solution-processed OPVs. The low performance of sexithiophene-based solar cells was mainly attributed to the difficulties encountered in fabricating solution-processed bulk heterojunction cells.

We choose α,ω-dihexylsexithiophene (**DH-6T**) as the oligothiophene material because it is well known to exhibit high field-effect mobility as high as 1.0 cm^2/Vs and a representative oligothiophene material [17]. Recently, we reported α,ω-bis(dimethyl-n-octylsilyl)sexithiophene (**DSi-6T**) for vacuum-deposited or solution processable organic thin film transistor application [18]. The silyl end-capped sexithiophene (**DSi-6T**, 2.2 g/L in $CHCl_3$) was more soluble than hexyl substituted sexithiophene (**DH-6T**, 1 g/L in $CHCl_3$) [19]. Thus, the silyl end-capped sexithiophene may be a good candidate for solution processable solar cell application.

In regard to our continuing interest for sexithiophene-based organic solar cells, we report herein analysis of the performance of solution-processed organic solar cells based on α,ω-functionalized linear sexithiophene: PCBM systems. We fabricated the solution-processed OPVs using two linear sexithiophenes, α,ω-dihexylsexithiophene (**DH-6T**) and α,ω-bis(dimethyl-n-octylsilyl)sexithiophene (**DSi-6T**) as donors and [6, 6]-phenyl-C_{61}-butyric acid methyl ester (PCBM) as an acceptor (Figure 1). Solution-processed bulk heterojunction (BHJ) solar cells using **DH-6T** and **DSi-6T** with PCBM showed good photovoltaic properties in spite of their poor solubility. Although **DH-6T** has higher hole mobility than **DSi-6T**, the **DSi-6T** : PCBM blend cell showed higher hole mobility than **DH-6T** : PCBM cell. Therefore, **DSi-6T** cell showed higher device performance than **DH-6T** cell due to their silyl substitutions, which lead to the increase of the solubility. The higher photovoltaic performance of **DSi-6T** cell can be explained by the film morphology dependence on the solubility of donor. In addition, utilizing the nanosecond transient absorption spectroscopy in polar media in the visible and near-IR region proved electron-transfer reactions in DH-6T : PCBM and DSi-6T : PCBM mixtures.

2. Experimental Section

2.1. Instruments. The absorption spectra were measured using a Perkin Elmer Lambda 35 UV-vis spectrometer in spin-coated films at room temperature. The morphology of the **DSi-6T** : PCBM and **DH6T** : PCBM was determined using atomic force microscopy (AFM) (Park systems) operating in a noncontact mode, under ambient conditions. Steady-state fluorescence measurements were carried out on a Shimadzu spectrofluorophotometer (RF-5300PC). Phosphorescence spectra were obtained by a SPEX Fluorolog τ_3 spectrophotometer. Emission spectra in the visible region were detected by using a Hamamatsu Photonics R5509-72 photomultiplier. A deaerated 2-MeTHF solution containing **DH-6T** and **DSi-6T** at 77 K was excited at indicated wavelengths. Cyclic voltammograms (CV) and differential pulse voltammograms (DPV) techniques were carried on a BAS CV 50 W Voltammetric Analyzer. A platinum disk electrode was used as working electrode, while a platinum wire served as a counter electrode. SCE electrode was used as a reference electrode. All measurements were carried out in deaerated benzonitrile containing tetra-n-butylammonium hexafluorophosphate ($TBAPF_6$; 0.10 M) as a supporting electrolyte. The scan rate = 50 mV/s.

DSi-6T and **DH-6T** were excited by a Panther OPO pumped by Nd:YAG laser (Continuum, SLII-10, 4–6 ns fwhm) at $\lambda = 440$ nm with the powers of 1.5 and 3.0 mJ *per* pulse. The transient absorption measurements were performed using a continuous xenon lamp (150 W) and an InGaAs-PIN photodiode (Hamamatsu 2949) as a probe light and a detector, respectively. The output from the photodiodes and a photomultiplier tube was recorded with a digitizing oscilloscope (Tektronix, TDS3032, 300 MHz). All measurements were conducted at 298 K. The transient spectra were recorded using fresh solutions in each laser excitation.

2.2. Fabrication of BHJ Cells. BHJ solar cells were fabricated on patterned ITO (indium tin oxide) coated glass substrates as the anode. ITO on glass substrates was sequentially cleaned with isopropyl alcohol, acetone, and isopropyl alcohol in ultrasonic baths. Afterwards, it was dried in oven at 80°C for 10 min and then treated with UV-ozone for 20 min. The surface of the ITO substrate was modified by spin-coating conducting poly(3,4-ethylenedioxythiophene) : poly(styrenesulfonate) (PEDOT : PSS, H. C. Starck Baytron P VP Al 4083) with a thickness of around 40 nm, followed by baking at 120°C for 10 min in oven. The molecular structures of the donor (**DSi-6T** and **DH-6T**) and acceptor materials (PCBM) and their energy band diagram are shown in Figure 1. **DSi-6T** was synthesized according to literature procedures [18]. **DH-6T** was purchased from Aldrich Chemical Co. and was used without further purification. **DSi-6T** : PCBM (1 : 4, 1 : 5, 1 : 6 w/w) and **DH-6T** : PCBM (1 : 4, 1 : 6 w/w) were blended together and dissolved in chloroform at a total concentration of 20 mg mL^{-1}. And then **DSi-6T** : PCBM blended solution was no filtration, but **DH-6T** : PCBM solution was filtered out through a 0.45 μm filter. The active layer was spin-cast at 4000 rpm from the solution of **DSi-6T** or **DH-6T** and PCBM (Nano-C) in chloroform. The thickness of the active layers was around 80 nm, as measured with an Alpha-step IQ. A solution containing 0.5 wt% TiO_2 nanoparticles in ethanol was spin-coat at a rate of 4000 rpm on top of the active layer. The synthesis of TiO_2 nanoparticles is described elsewhere [20, 21]. The cathode consists of 100 nm of aluminum and was thermally evaporated on top of the film through the use of a shadow mask to define an active area of 0.12 cm^2 under a base pressure of 1×10^{-6} Torr (1 Torr = 133.32 Pa). The devices were annealed at 60°C for 10 min in the thermal evaporator. The current density-voltage curves were obtained using a Keithley 2400 source-measure unit. The photocurrent was measured under illumination using a Newport class-A 100 mW cm^{-2} solar simulator (AM 1.5 G) and the light intensity was calibrated with an NREL-calibrated Si solar cell with KG-1 filter for approximating one sun light intensity. External quantum efficiency (EQE) was measured in range from 300 to 800 nm using a specially designed EQE system (PV Measurements, Inc.). A 75 W xenon lamp was used as a light source for the generating monochromatic beam. A calibration was performed using a silicon photodiode, which was calibrated using the NIST-calibrated photodiode G425 as a standard, and IPCE values were collected under bias light at a low chopping speed of 10 Hz.

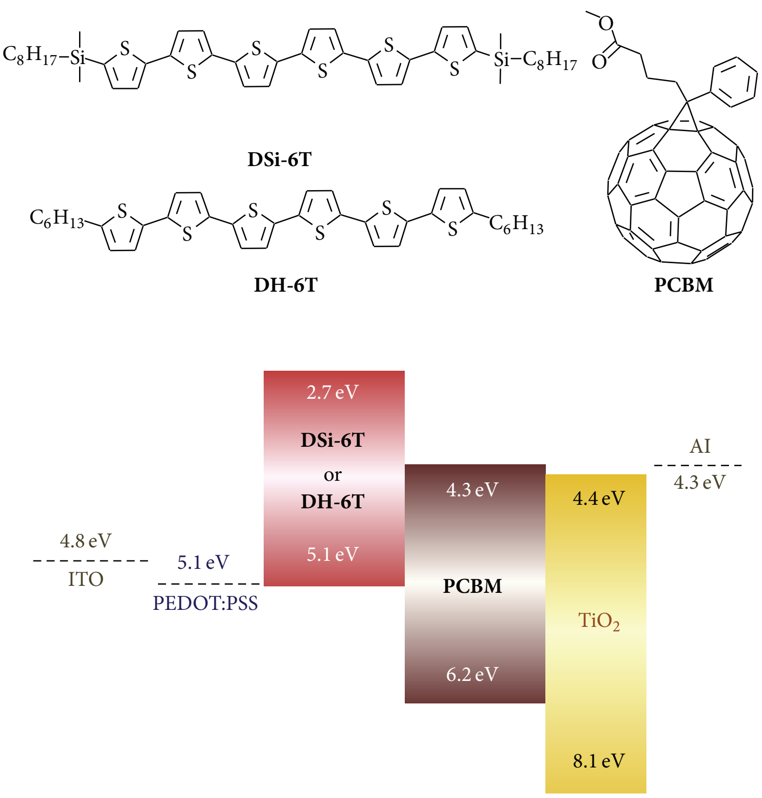

FIGURE 1: Chemical structures and energy band diagram of **DSi-6T**, **DH-6T**, and **PCBM**.

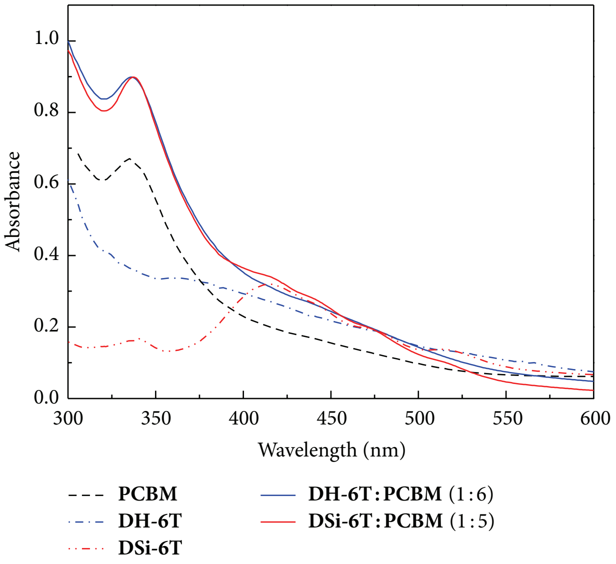

FIGURE 2: UV-vis absorption spectra of the **DSi-6T : PCBM** (1 : 5 w/w) and **DH-6T : PCBM** (1 : 6 w/w) blend films.

3. Results and Discussion

3.1. Electron-Transfer Reaction of DSi-6T/PCBM and DH-6T/PCBM. The UV-vis absorption spectra of spin-coated films of **DSi-6T** and **DH-6T** blended with PCBM are shown in Figure 2. Both **DH-6T** and **DSi-6T** exhibited similar absorption spectra in a dilute chloroform solution, with absorption maxima observed at 440 nm and 442 nm, respectively. The absorption spectra of sexithiophene films exhibited a noteworthy blue shift with respect to that in solution for both compounds, but this shift is more significant for **DH-6T** than for **DSi-6T**. While the **DH-6T** film showed the strongly blue-shifted absorption spectrum with maxima at 362 nm, the **DSi-6T** film showed an absorption peak at 415 nm. Such feature is attributed to molecular excitons formed as a consequence of the intermolecular interactions in the solid state [22] and is found to be blue-shifted by about 0.6 eV with respect to the characteristic absorption peaks of the isolated molecules. The PCBM film has an absorption band of about 340 nm and significantly greater absorption in the visible region (350–750 nm) compared to the PCBM solution, consistent with the literature [23]. The UV-vis absorption spectra of **DSi-6T : PCBM** (1 : 5 w/w) and **DH-6T : PCBM** (1 : 6 w/w) blend films showed similar shape due to their same backbone of donor and strong absorption of PCBM.

Fluorescence spectra of the singlet-excited state of **DH-6T** and **DSi-6T** in benzonitrile exhibited emission bands at 514 and 520 nm, respectively, from which the energy of the singlet state of **DH-6T** and **DSi-6T** were estimated as 2.41 and 2.39 eV, respectively (See Supporting Information, Figure S1 of Supplementary Material available online at http://dx.doi.org/10.1155/2013/843615). Fluorescence quantum yields of **DH-6T** and **DSi-6T** was determined as 0.13 and 0.36, respectively. Fluorescence lifetimes of the singlet states of **DH-6T** and **DSi-6T** were determined as 1.0 and

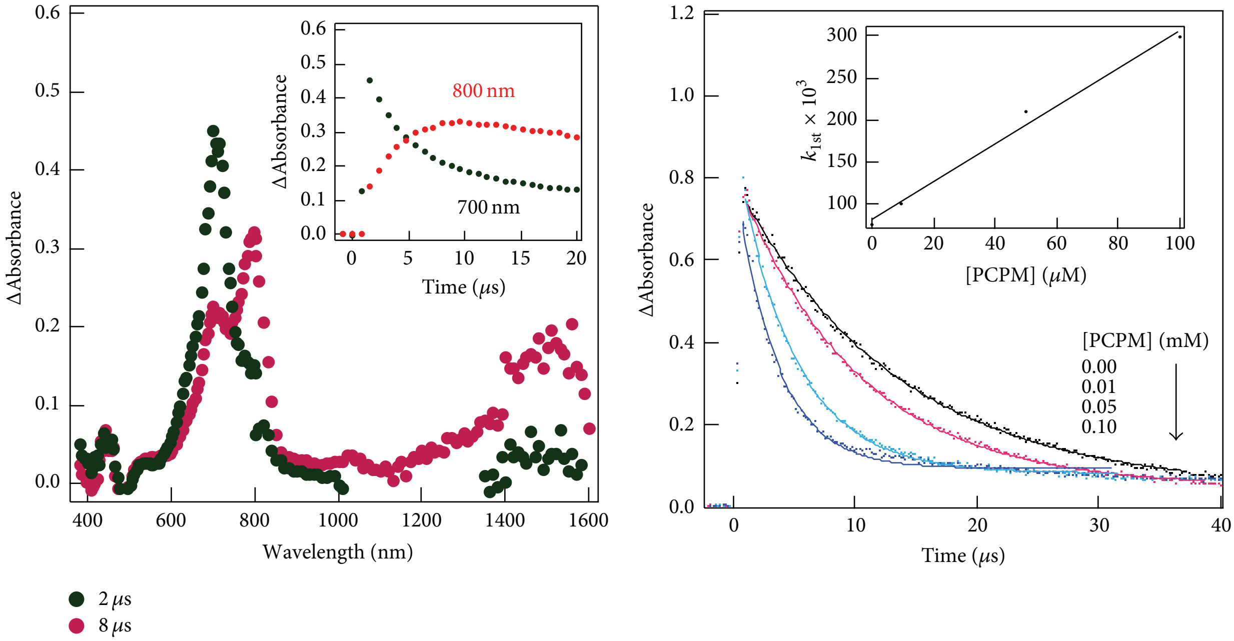

(a)

(b)

FIGURE 3: (a) Nanosecond transient spectra of **DSi-6T** (0.05 mM) in the presence of PCBM (0.05 mM) in deaerated benzonitrile; λ_{ex} = 440 nm. Inset: Decay time profile of ^{3}**DSi-6T*** (700 nm) and rise and decay profiles of **DSi-6T**$^{\bullet+}$(800 nm). (b) Dependence of rate constant of the formation of **DSi-6T**$^{\bullet+}$ at 800 nm on concentration of PCBM in deaerated benzonitrile. Inset: first-order plot.

1.8 ns, respectively. In the case of the DH-6T/PCBM and DSi-6T/PCBM mixtures, it was found that the fluorescence intensities and the lifetimes are quite close to those of the DH-6T and DSi-6T, respectively. This observation suggests the intermolecular electron transfer between the **DH-6T** and **DSi-6T** with PCBM, but not the intramolecular electron transfer.

The redox potentials of the examined **DH-6T**, **DSi-6T** and PCBM have been examined by using cyclic voltammetry (CV) and differential pulse voltammetry (DPV) techniques to evaluate the driving forces for the electron transfer ($-\Delta G_{\mathrm{et}}{}^{T}$). The first reduction potential (E_{red}) of the PCBM was located at –856 mV versus Ag/AgNO$_3$, while the oxidation potentials (E_{ox}) of **DH-6T** and **DSi-6T** were located at 732 and 600 mV versus Ag/AgNO$_3$ (see Supporting Information, Figure S2–S5). The redox potential measurements of the **DH-6T**/PCBM and **DSi-6T**/PCBM mixtures did not show significant interaction suggesting no interaction in the ground state. The redox potentials of the examined **DH-6T**, **DSi-6T**, and PCBM suggest their potentials as promising materials in the photovoltaic cells. The feasibility of the electron-transfer process via the triplet-excited states is controlled by the free energy change ($\Delta G_{\mathrm{et}}{}^{T}$), which can be expressed by the Rehm-Weller relation [24] (1):

$$\Delta G_{\mathrm{et}}{}^{T} = E_{\mathrm{ox}} - E_{\mathrm{red}} - E_{T} + E_{c}, \tag{1}$$

where E_{ox} is the first oxidation potential of the **DH-6T** and **DSi-6T**, E_{red} is the first reduction potential of PCBM, E_{T} is the triplet energy of **DH-6T** (1.78 eV) and **DSi-6T** (1.79 eV) (we found from phosphorescence measurements in deaerated benzonitrile that energy level of the triplet **DH-6T** and **DSi-6T** at 1.78 and 1.79 eV, resp.), and E_{c} is the Coulomb energy term (approximately 0.06 eV in the polar benzonitrile) [25]. The free energy change ($\Delta G_{\mathrm{et}}{}^{T}$) values *via* the triplet **DH-6T** and **DSi-6T** were estimated as −0.05 and −0.17 eV, respectively. The negative $\Delta G_{\mathrm{et}}{}^{T}$ values suggest that the quenching process should be close to the diffusion-controlled limit (k_{diff}) [26].

By photoexcitation of **DSi-6T** in deaerated benzonitrile using 440 nm laser photolysis, the transient absorption spectrum immediately after the laser pulse exhibited only an absorption band at 700 nm, which assigned to the triplet-excited state of **DH-6T** (^{3}**DH-6T***) (See Supporting Information; Figure S6). By fitting the decay profile of ^{3}**DSi-6T***, the decay rate constant was found to be $6.60 \times 10^4\ \mathrm{s}^{-1}$, from which the lifetime of ^{3}**DSi-6T***was estimated as 15.2 μs. By photoexcitation of **DSi-6T** in the presence of PCBM [0.01–0.10 mM] in Ar-saturated benzonitrile using 440 nm laser photolysis, the transient spectra exhibit the characteristic band of ^{3}**DSi-6T*** at 700 nm. With its decay, the concomitant rises of the **DSi-6T** radical cation (**DSi-6T**$^{\bullet+}$) at 800 and 1500 nm and the PCBM radical anion (PCBM$^{\bullet-}$) at 1000 nm were observed (Figure 3(a) and Figure S7). These observations show clear evidence of occurrence of intermolecular electron transfer from the triplet-excited state of **DSi-6T** to PCBM. In oxygen-saturated solutions, an intermolecular energy transfer from ^{3}**DSi-6T*** to oxygen emerges, suppressing the electron-transfer process. Similar

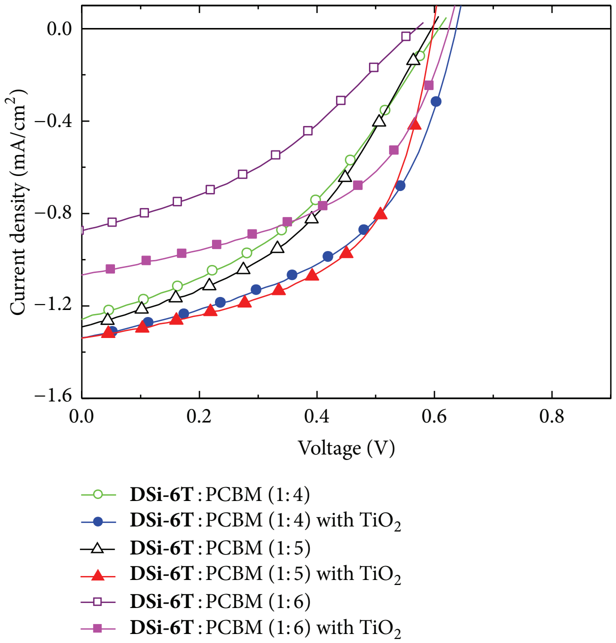

Figure 4: *J-V* characteristics of ITO/PEDOT : PSS/DSi-6T : PCBM/Al (active layer DSi-6T : PCBM 1 : 4, w/w (○), 1 : 5 w/w (△), 1 : 6 w/w (□)) and ITO/PEDOT : PSS/DSi-6T : PCBM/TiO$_2$/Al (active layer DSi-6T : PCBM 1 : 4, w/w (•), 1 : 5 w/w (▲), 1 : 6 w/w (■)) under illumination of AM 1.5, 100 mW cm^{-2}.

electron-transfer features were recorded in the case of **DH-6T**/PCBM mixture in deaerated benzonitrile (See supporting information, Figure S8).

A more detailed picture of the kinetic is shown in Figure 3(b), where the rate constant of the electron-transfer process (k_{et}) was evaluated by monitoring the formation of the **DSi-6T**$^{\bullet +}$ as function of the concentrations of PCBM. The formation of **DSi-6T**$^{\bullet +}$ was fitted with clean first-order kinetics; each rate constant is referred to (k_{1st}). The linear concentration dependence of the observed k_{1st} values gives the k_{et}, which is calculated as $2.24 \times 10^9\ \mathrm{M}^{-1}\ \mathrm{s}^{-1}$, which is near the diffusion-controlled limit ($k_{\mathrm{diff}} = 5.6 \times 10^9\ \mathrm{M}^{-1}\ \mathrm{s}^{-1}$) in benzonitrile [27]. Similarly, the k_{et} value of ^{3}**DH-6T***/PCBM mixture was found to be $2.65 \times 10^9\ \mathrm{M}^{-1}\ \mathrm{s}^{-1}$, which is slightly larger than that of ^{3}**DSi-6T***/PCBM mixture (See supporting information, Figure S9).

3.2. Photovoltaic Properties of DSi-6T/PCBM and DH-6T/PCBM. For investigating the photovoltaic properties of sexithiophenes, OPVs were fabricated with the configuration of ITO/PEDOT : PSS/Donor (**DSi-6T** or **DH-6T**) : PCBM/Al. **DSi-6T** : PCBM and **DH-6T** : PCBM were blended together and dissolved in chloroform at a total concentration of 20 mg/mL. After Al deposition, the devices were thermally annealed at 60°C for 10 min. Figures 4 and 5 show the current density-voltage (*J-V*) curves of the OPV devices with **DSi-6T** : PCBM and **DH-6T** : PCBM using different blended ratios under AM 1.5 illumination, 100 mW cm^{-2}. Table 1 summarizes the photovoltaic performance of the functionalized sexithiophene based solar cells. The sexithiophene **DSi-6T** was mixed with PCBM to form bulk heterojunction active layers, for use as a donor with PCBM as an acceptor. The weight ratios of the donor to acceptor were 1 : 4, 1 : 5, and 1 : 6. For comparison, the OPV devices based on **DH-6T** : PCBM were also fabricated with commercial **DH-6T** as a donor and the weight ratio of 1 : 4 and 1 : 6. The short circuit current density (J_{sc}) values of the **DSi-6T** : PCBM BHJ solar cells increase as the weight ratio of donor to acceptor increases. However, the weight ratio of donor to accepter could not be larger than 1 : 4, due to low solubility of sexithiophenes. The photovoltaic performance was observed on **DSi-6T** : PCBM 1 : 5 (w/w) blend cell with an open circuit voltage (V_{oc}) of 0.60 V, a J_{sc} of 1.29 mA/cm^2, a fill factor (FF) of 42%, and power conversion efficiency of 0.32%. Under the same conditions, **DH-6T** : PCBM 1 : 6 (w/w) blend cell showed a V_{oc} of 0.63 V, a J_{sc} of 0.60 mA/cm^2, a FF of 44%, and PCE of 0.17%. The J_{sc} values of the **DH-6T** : PCBM cells were constant with 0.60 mA/cm^2 regardless of the weight ratio of **DH-6T** to acceptor. This result could be ascribed to the saturated solution of **DH-6T** : PCBM (1 : 6 w/w). In fact, a factor strongly affecting the J_{sc} of **DSi-6T** : PCBM cells is the filtration of the active solution. The J_{sc} of solar cell with the filtration of **DSi-6T** : PCBM solutions is 20% lower than that of solar cell without filtration. The most **DSi-6T** donors remained in the filter due to their strong π-π interaction. However, the **DH-6T** cells without filtration of active solutions showed the poor photovoltaic performance.

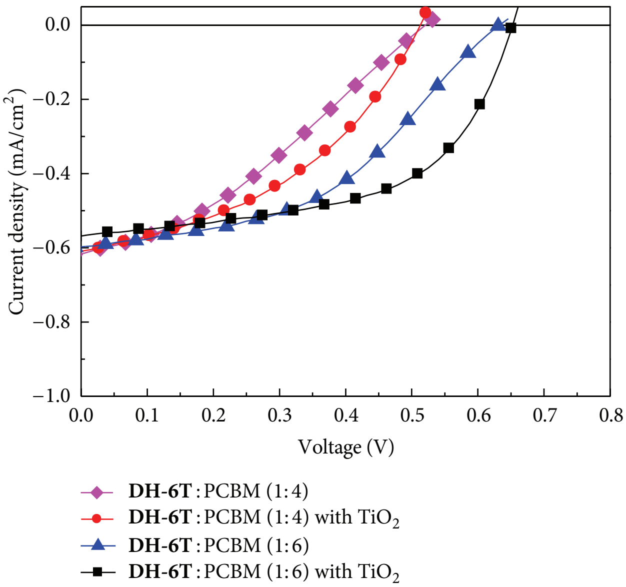

Figure 5: *J-V* characteristics of ITO/PEDOT : PSS/DH-6T : PCBM/Al (active layer DH-6T : PCBM 1 : 4, w/w (◆), 1 : 6 w/w (▲)) and ITO/PEDOT : PSS/DH-6T : PCBM/TiO$_2$/Al (active layer DH-6T : PCBM 1 : 4, w/w (•), 1 : 6 w/w (■)) under illumination of AM 1.5, 100 mW cm^{-2}.

For the development of OPVs with increased PCE and lifetime, OPVs with the TiO$_2$ interfacial layer between the active layer and the Al electrode were fabricated together with typical OPVs without TiO$_2$. According to the literature,

Table 1: Photovoltaic characteristics of **DSi-6T** : PCBM and **DH-6T** : PCBM blended cells.

Device name	V_{oc} (V)	J_{sc} (mA/cm^2)	FF	PCE (%)
DSi-6T : PCBM				
1 : 4	0.61	1.26	0.39	0.30
1 : 5	0.60	1.29	0.42	0.32
1 : 6	0.57	0.88	0.37	0.18
DSi-6T : PCBM (with TiO_2)				
1 : 4	0.64	1.34	0.50	0.42
1 : 5	0.60	1.34	0.55	0.44
1 : 6	0.62	1.07	0.49	0.32
DH-6T : PCBM				
1 : 4	0.52	0.62	0.33	0.11
1 : 6	0.63	0.60	0.44	0.17
DH-6T : PCBM (with TiO_2)				
1 : 4	0.51	0.61	0.42	0.13
1 : 6	0.65	0.57	0.56	0.21

[a] Open circuit voltage (V_{oc}), short circuit current density (J_{sc}), fill factor (FF), and PCE at DSi-6T and DH-6T as electron donors: PCBM at weight ratio. The device performance was consistent and reproducible. The active area is 0.12 cm^2.

the TiO_2 interfacial layer improved the PCEs and reduced the sensitivity of such devices to oxygen and water vapour [21, 28]. As shown in Figure 4, the FF of **DSi-6T** : PCBM cells with TiO_2 layer is enhanced up to 0.55 which is 30% higher than that of the solar cell. The best performance was observed on **DSi-6T** : PCBM 1 : 5 (w/w) blend cell with V_{oc} of 0.63 V, J_{sc} of 1.34 mA/cm^2, FF of 55%, and power conversion efficiency of 0.44%. Also the FF of **DH-6T** cells is exactly 27% higher than that of solar cells. The **DH-6T** : PCBM 1 : 6 (w/w) blend cell with TiO_2 layer exhibited a V_{oc} of 0.65 V, J_{sc} of 0.57 mA/cm^2, FF of 56%, and PCE of 0.21% (Figure 5). The incorporation of solution processed TiO_2 interfacial layer in the sexithiophene : PCBM BHJ devices significantly enhances FF, mainly due to the reduced charge recombination near active layer/Al interface.

Figure 6 shows the external quantum efficiency (EQE) plot for the **DSi-6T** : PCBM (1 : 5 w/w) and **DH-6T** : PCBM (1 : 6 w/w) cells. The sexithiophene-based cells absorb the solar light in narrow visible range and show low EQEs due to a small amount of donor by limited solubility. For the **DH-6T** : PCBM solar cell, the maximum EQE is 11.3% at 340 nm that is caused by strong absorption of PCBM. When the **DSi-6T** was used, the **DSi-6T** : PCBM solar cell shows a higher EQE in the all wavelength, with a maximum of 16.1% at 410 nm. The absorption of the **DSi-6T** donor was increased in the EQE spectrum to be different from the UV-vis spectrum. It is expected that horizontal intermolecular packing due to the bulky silyl side chains of **DSi-6T** may increase the charge transfer at the interfaces, so the EQE increases.

To investigate the charge transporting property of the OPV devices, we measured hole mobility of the donor: PCBM blend layers with the space-charge limited-current (SCLC) model. Hole-only devices were fabricated with a device configuration of ITO/PEDOT : PSS/Donor : PCBM/MoO_3/Al, because high work function of molybdenum oxide (MoO_3) blocks the injection of electrons from the Al cathode. The blend ratios of the Donor: PCBM layers were 1 : 5 (w/w) and 1 : 6 (w/w) for **DSi-6T** : PCBM and **DH-6T** : PCBM, respectively.

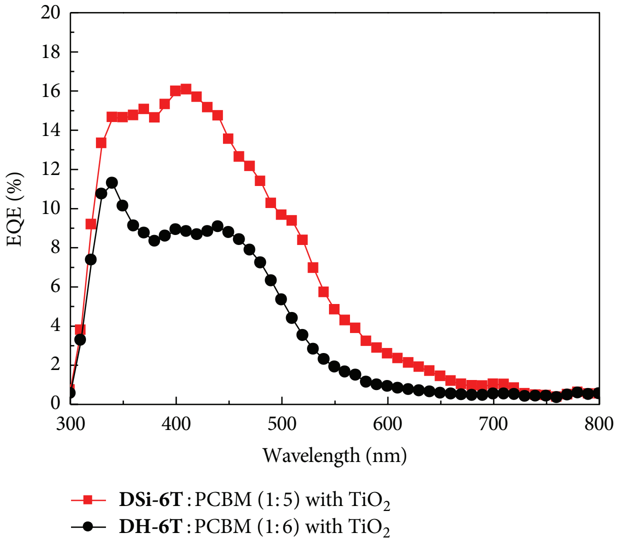

Figure 6: EQE curves of **DSi-6T** : PCBM (1 : 5) and **DH-6T** : PCBM (1 : 6) blend cells.

The hole transport through the active layers is limited by the space charge and the SCLC is described by

$$J = \frac{9}{8}\varepsilon_r \varepsilon_0 \mu_h \frac{V^2}{L^3}, \tag{2}$$

where J is the current density, ε_0 is the permittivity of vacuum, ε_r is the dielectric constant of the material (assumed to be 3), μ_h is the mobility, V is the applied voltage (V_{applied}) corrected from built-in voltage (V_{bi}) arising from difference in the work function of the contacts and voltage drop (V_r) due to the series resistance of the electrodes, and L is the thickness of the blend layer [29]. Equation (1) is valid when the mobility

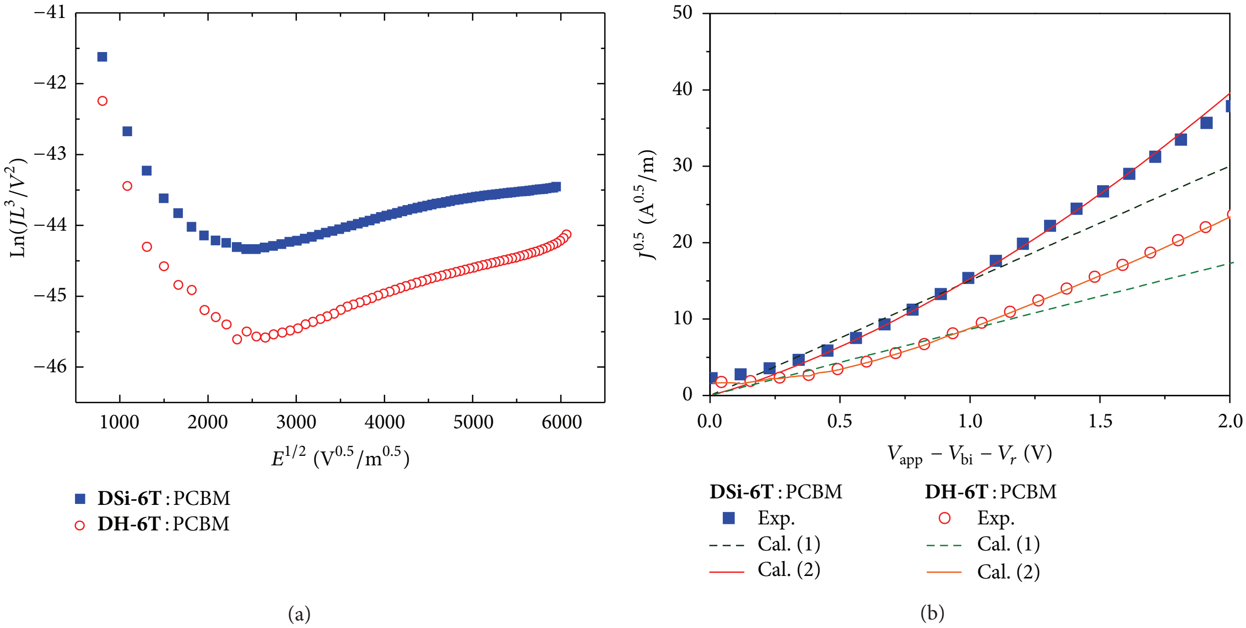

FIGURE 7: (a) ln (JL^3/V^2) versus $E^{1/2}$ curves according to the SCLC equation (2). (b) $J^{1/2}$ versus V curves showing the electric-field-dependence of hole mobilities at highly biased region. Dotted and solid lines are calculated curves with (1) and (2), respectively.

is field independent. It has been found that the behaviour of electric field dependence of the mobility can be described by an empirical rule; $\mu_h = \mu_{h0} \exp(\gamma E^{1/2})$, where μ_{h0} is the hole mobility at zero field, γ is field dependence prefactor, and E is the electric field. Therefore, the electric field dependent SCLC model can be expressed by

$$J = \frac{9}{8}\varepsilon_r\varepsilon_0\mu_{h0} \exp\left(\gamma\sqrt{E}\right)\frac{V^2}{L^3}. \tag{3}$$

The zero-field hole mobility μ_{h0} and the prefatory γ of **DSi-6T** : PCBM (1 : 5 w/w) and **DH-6T** : PCBM (1 : 6 w/w) blend films were obtained from (2) as shown in Figure 7(a) ($\mu_{h0} = 7.7 \times 10^{-6}\,\mathrm{cm^2/Vs}$, $\gamma = 3.3 \times 10^{-4}\,\mathrm{m^{0.5}\,V^{-0.5}}$ for **DSi-6T** : PCBM, and $\mu_{h0} = 1.6 \times 10^{-6}\,\mathrm{cm^2/Vs}$, $\gamma = 4.5 \times 10^{-4}\,\mathrm{m^{0.5}\,V^{-0.5}}$ for **DH-6T** : PCBM). The low γ of **DSi-6T** : PCBM indicates low energetic disorder related to the interaction of each hopping charge in randomly oriented dipoles [30, 31]. Figure 7(b) shows the SCLC fitting of **DSi-6T** : PCBM (1 : 5 w/w) and **DH-6T** : PCBM (1 : 6 w/w) blend films according to (1) and (2). It is observed that the SCLC calculated from the field independent model deviates from the experimental data at the high voltage region. In actual operating devices, the active materials are in the effective bias of ~1 V (corresponding to the energy level difference of HOMO and LUMO of an electron donor and acceptor) at the short circuit conditions. Taking this into consideration, we estimated the field dependent hole mobility of the active blend layers at 1 V; $\mu_h = 2.7 \times 10^{-5}\,\mathrm{cm^2/Vs}$ for **DSi-6T** : PCBM, and $\mu_h = 8.8 \times 10^{-6}\,\mathrm{cm^2/Vs}$ for **DH-6T** : PCBM. The higher hole mobility of the **DSi-6T** : PCBM blend film than that of the **DH-6T** : PCBM film is a key property of the enhanced photovoltaic performance. It seems that the higher hole mobility of **DSi-6T** : PCBM blend layer is inconsistent with the pure donor's field-effect mobility. However, it should be noted that the mobility in organic thin-film transistors strongly depends on the molecular orientation due to the highly anisotropic charge carrier mobility. In the OPV device configuration, the **DSi-6T** : PCBM BHJ layer yielded the better vertical charge transport than the **DH-6T** : PCBM due to the improved solubility of **DSi-6T**.

To study the thermal annealing effect of this system, the morphologies of sexithiophene: PCBM films before and after annealing at 60°C were studied by atomic force microscopy (AFM) (Figure 8). The morphological studies indicate the more amorphous nature of **DSi-6T** : PCBM compared to **DH-6T** : PCBM films. The root-mean-square (rms) roughness is 47, 38, and 23 nm for **DSi-6T** : PCBM 1 : 4, 1 : 5, and 1 : 6 (w/w), respectively, and 7.1 nm for **DH-6T** : PCBM 1 : 6 (w/w). In **DSi-6T** : PCBM films, the weight ratio donor to acceptor increased as the roughness of films decreased. After thermal annealing, the roughness was 37, 29, and 14 nm for **DSi-6T** : PCBM 1 : 4, 1 : 5, 1 : 6 (w/w), respectively, and 7.6 nm for **DH-6T** : PCBM 1 : 6 (w/w). For the solar cell based on the **DSi-6T** : PCBM cell, the rms roughness of films after thermal annealing at 60°C was significantly reduced as compared to that of films. In the case of **DH-6T** : PCBM cell, the morphological change after annealing was slightly observed. Unfortunately, all films were quite rough compared to the polymer solar cells. The inferior morphologies of sexithiophene based BHJ solar cells may be related to the solubility of donors, which is expected to influence the photovoltaic performance. For a comparison, the **DSi-6T** : PCBM cell was thermally annealed at 135°C which was the temperature employed for the P3HT : PCBM cell. When a film was annealed at a high temperature, the decrease in

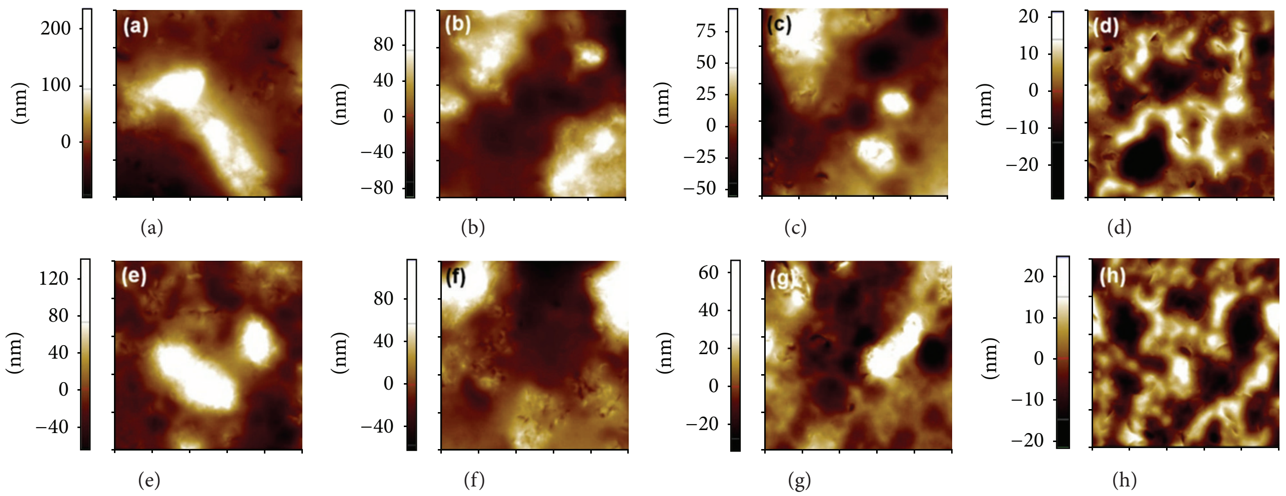

(a) (b) (c) (d)

(e) (f) (g) (h)

FIGURE 8: AFM images of the blended films under various ratios (a) **DSi-6T** : PCBM 1 : 4 w/w nonannealed (e) annealed and (b) **DSi-6T** : PCBM 1 : 5 w/w non-annealed (f) annealed and (c) **DSi-6T** : PCBM 1 : 6 w/w non-annealed (g) annealed and (d) **DH-6T** : PCBM 1 : 6 w/w non-annealed (h) annealed. The image scan sizes is 5 μm × 5 μm.

PCE (0.034%) became more significant. The future work may concentrate on optimization of the annealing temperature of the **DSi-6T** : PCBM devices to allow better efficiency.

4. Conclusion

In conclusion, we have demonstrated solution processed organic photovoltaic cells that incorporate sexithiophene derivatives having silyl side chain or hexyl chain in the end of thiophene ring as donor materials and PCBM as an acceptor. Owing to the particular electronic properties of **DSi-6T**, **DH-6T**, and PCBM, such combinations seem to be perfectly suited for the study of electron-transfer processes in the polar media via the triplet states. The electron-transfer process from the triplet states of **DSi-6T**, **DH-6T** to PCBM was confirmed in this study by utilizing the nanosecond laser photolysis technique in the visible and NIR regions. **DSi-6T** showed higher photovoltaic performance than **DH-6T**, despite its poor quality film morphology. The optimal **DSi-6T** : PCBM blend ratio was found to be 1 : 5, and its power conversion efficiency was 0.44% under AM 1.5 G illumination. Although the power conversion efficiency remains to be improved, the present study provides valuable insight into the further development of the solution-processed efficient OPV devices.

Conflict of Interests

The authors declare that they have no conflict of interests.

Acknowledgments

This research was supported by Grants-in-Aid (No. 20108010) from the Ministry of Education, Culture, Sports, Science and Technology, Japan, and NRF/MEST of Korea through WCU (R31-2008-000-10010-0) and GRL (2010-00353) Programs.

References

[1] G. Yu, J. Gao, J. C. Hummelen, F. Wudl, and A. J. Heeger, "Polymer photovoltaic cells: enhanced efficiencies via a network of internal donor-acceptor heterojunctions," *Science*, vol. 270, no. 5243, pp. 1789–1791, 1995.

[2] N. S. Sariciftci, L. Smilowitz, A. J. Heeger, and F. Wudl, "Photoinduced electron transfer from a conducting polymer to buckminsterfullerene," *Science*, vol. 258, no. 5087, pp. 1474–1476, 1992.

[3] S. Günes, H. Neugebauer, and N. S. Sariciftci, "Conjugated polymer-based organic solar cells," *Chemical Reviews*, vol. 107, no. 4, pp. 1324–1338, 2007.

[4] P. W. M. Blom, V. D. Mihailetchi, L. J. A. Koster, and D. E. Markov, "Device physics of polymer: fullerene bulk heterojunction solar cells," *Advanced Materials*, vol. 19, no. 12, pp. 1551–1566, 2007.

[5] W. Tang, J. Hai, Y. Dai et al., "Recent development of conjugated oligomers for high-efficiency bulk-heterojunction solar cells," *Solar Energy Materials and Solar Cells*, vol. 94, no. 12, pp. 1963–1979, 2010.

[6] H.-Y. Chen, J. Hou, S. Zhang et al., "Polymer solar cells with enhanced open-circuit voltage and efficiency," *Nature Photonics*, vol. 3, no. 11, pp. 649–653, 2009.

[7] Y. Liang, Z. Xu, J. Xia et al., "For the bright future-bulk heterojunction polymer solar cells with power conversion efficiency of 7.4%," *Advanced Materials*, vol. 22, no. 20, pp. E135–E138, 2010.

[8] *Electronic Materials: The Oligomer Approach*, edited by K. Müllen and G. Wegner, Wiley-VCH, Weinheim, Germany, 1998.

[9] *Handbook of Oligo- and Polythiophenes*, edited by D. Fichou, Wiley-VCH, Weinheim, Germany, 1999.

[10] A. Mishra, C.-Q. Ma, and P. Bäuerle, "Functional oligothiophenes: molecular design for multidimensional nanoarchitectures and their applications," *Chemical Reviews*, vol. 109, no. 3, pp. 1141–1176, 2009.

[11] N. Noma, T. Tsuzuki, and Y. Shirota, "α-thiophene octamer as a new class of photoactive material for photoelectrical conversion," *Advanced Materials*, vol. 7, no. 7, pp. 647–648, 1995.

[12] C. Videlot, A. El Kassmi, and D. Fichou, "Photovoltaic properties of octithiophene-based Schottky and p/n junction cells: influence of molecular orientation," *Solar Energy Materials and Solar Cells*, vol. 63, no. 1, pp. 69–82, 2000.

[13] P. Liu, Q. Li, M. Huang, W. Pan, and W. Deng, "High open circuit voltage organic photovoltaic cells based on oligothiophene derivatives," *Applied Physics Letters*, vol. 89, no. 21, pp. 213501–213503, 2006.

[14] K. Schulze, C. Uhrich, R. Schüppel et al., "Efficient vacuum-deposited organic solar cells based on a new low-bandgap oligothiophene and fullerene C_{60}," *Advanced Materials*, vol. 18, no. 21, pp. 2872–2875, 2006.

[15] J. Ah Kong, E. Lim, K. K. Lee, S. Lee, and S. Hyun Kim, "A benzothiadiazole-based oligothiophene for vacuum-deposited organic photovoltaic cells," *Solar Energy Materials and Solar Cells*, vol. 94, no. 12, pp. 2057–2063, 2010.

[16] J. Sakai, T. Taima, and K. Saito, "Efficient oligothiophene:fullerene bulk heterojunction organic photovoltaic cells," *Organic Electronics*, vol. 9, no. 5, pp. 582–590, 2008.

[17] M. Halik, H. Klauk, U. Zschieschang et al., "Relationship between molecular structure and electrical performance of oligothiophene organic thin film transistors," *Advanced Materials*, vol. 15, no. 11, pp. 917–922, 2003.

[18] J. H. Choi, D. W. Cho, H. J. Park et al., "Synthesis and characterization of a series of bis(dimethyl-n-octylsilyl)oligothiophenes for organic thin film transistor applications," *Synthetic Metals*, vol. 159, no. 15-16, pp. 1589–1596, 2009.

[19] F. Garnier, A. Yassar, R. Hajlaoui et al., "Molecular engineering of organic semiconductors: design of self-assembly properties in conjugated thiophene oligomers," *Journal of the American Chemical Society*, vol. 115, no. 19, pp. 8716–8721, 1993.

[20] E. Scolan and C. Sanchez, "Synthesis and characterization of surface-protected nanocrystalline titania particles," *Chemistry of Materials*, vol. 10, no. 10, pp. 3217–3223, 1998.

[21] W.-S. Chung, H. Lee, W. Lee et al., "Solution processed polymer tandem cell utilizing organic layer coated nano-crystalline TiO_2 as interlayer," *Organic Electronics*, vol. 11, no. 4, pp. 521–528, 2010.

[22] A. Sassella, R. Tubino, A. Borghesi et al., "Optical properties of oriented thin films of oligothiophenes," *Synthetic Metals*, vol. 101, no. 1, pp. 538–541, 1999.

[23] S. Cook, H. Ohkita, Y. Kim, J. J. Benson-Smith, D. D. C. Bradley, and J. R. Durrant, "A photophysical study of PCBM thin films," *Chemical Physics Letters*, vol. 445, no. 4-6, pp. 276–280, 2007.

[24] D. Rehm and A. Weller, "Kinetik und mechanismus der elektronübertragung bei der fluoreszenzlöschung in acetonitril," *Berichte der Bunsengesellschaft für physikalische Chemie*, vol. 73, pp. 834–839, 1969.

[25] R. J. Sension, A. Z. Szarka, G. R. Smith, and R. M. Hochstrasser, "Ultrafast photoinduced electron transfer to C_{60}," *Chemical Physics Letters*, vol. 185, no. 3-4, pp. 179–183, 1991.

[26] *Handbook of Photochemistry*, edited by S. I. Murov, Marcel Dekker, New York, NY, USA, 1985.

[27] M. E. El-Khouly, O. Ito, P. M. Smith, and F. D'Souza, "Intermolecular and supramolecular photoinduced electron transfer processes of fullerene-porphyrin/phthalocyanine systems," *Journal of Photochemistry and Photobiology C*, vol. 5, no. 1, pp. 79–104, 2004.

[28] K. Lee, J. Y. Kim, S. H. Park, S. H. Kim, S. Cho, and A. J. Heeger, "Air-stable polymer electronic devices," *Advanced Materials*, vol. 19, no. 18, pp. 2445–2449, 2007.

[29] P. W. M. Blom, M. J. M. de Jong, and M. G. van Munster, "Electric-field and temperature dependence of the hole mobility in poly(p-phenylene vinylene)," *Physical Review B*, vol. 55, no. 2, pp. R656–R659, 1997.

[30] D. H. Dunlap, P. E. Parris, and V. M. Kenkre, "Charge-dipole model for the universal field dependence of mobilities in molecularly doped polymers," *Physical Review Letters*, vol. 77, no. 3, pp. 542–545, 1996.

[31] G. G. Malliaras, J. R. Salem, P. J. Brock, and C. Scott, "Electrical characteristics and efficiency of single-layer organic light-emitting diodes," *Physical Review B*, vol. 58, no. 20, pp. R13411–R13414, 1998.

Hindawi Publishing Corporation
International Journal of Photoenergy
Volume 2013, Article ID 583163, 6 pages
http://dx.doi.org/10.1155/2013/583163

Research Article

Maximum Power Point Tracking Method Based on Modified Particle Swarm Optimization for Photovoltaic Systems

Kuei-Hsiang Chao, Long-Yi Chang, and Hsueh-Chien Liu

Department of Electrical Engineering, National Chin-Yi University of Technology, No. 57, Section 2, Zhongshan Road, Taiping Distatrict, Taichung 41170, Taiwan

Correspondence should be addressed to Kuei-Hsiang Chao; chaokh@ncut.edu.tw

Received 9 June 2013; Accepted 20 September 2013

Academic Editor: Adel M. Sharaf

This study investigated the output characteristics of photovoltaic module arrays with partial module shading. Accordingly, we presented a maximum power point tracking (MPPT) method that can effectively track the global optimum of multipeak curves. This method was based on particle swarm optimization (PSO). The concept of linear decreases in weighting was added to improve the tracking performance of the maximum power point tracker. Simulation results were used to verify that this method could successfully track maximum power points in the output characteristic curves of photovoltaic modules with multipeak values. The results also established that the performance of the modified PSO-based MPPT method was superior to that of conventional PSO methods.

1. Introduction

The output power of photovoltaic (PV) systems is heavily influenced by irradiation and temperature. Thus, the output power of these systems presents nonlinear changes. Maximum power point tracking (MPPT) must be incorporated to stabilize the output power at maximum power points. This research topic is critical for photovoltaic power generation systems.

The voltage feedback method [1] is the simplest of conventional MPPT methods. However, this method requires prior testing of maximum power point (MPP) voltage. In addition, MPPs cannot be tracked when the photovoltaic modules deteriorate and cause the MPPs to change unless remeasurement is performed. The framework of the constant voltage tracking method [2, 3] is simple and does not require complex formulas. This method employs the extreme similarity of MPP voltages under varying amounts of irradiation, using MPP voltage under standard test conditions as reference points to set the operation of the photovoltaic module arrays at these points. However, when the amount of irradiation is low or when photovoltaic module temperatures change, the difference in values between the MPP voltage and the reference voltage becomes substantial, reducing tracking accuracy. The perturb and observe method [4] uses periodical increases or decreases in voltage to perturb the system. If these perturbations increase the output power, the same trend is used to change (i.e., increase or decrease) voltage the following time. If output power decreases, the reverse trend is used to change voltage. However, this method is unable to track MPPs accurately. In addition, the method oscillates near the MPP and increases tracking losses, thereby affecting power generation efficiency. These conventional methods only perform MPPT on module arrays with single-peak characteristic curves. When multipeak values appear in the characteristic curves, these methods frequently track local MPPs and miss global MPPs.

Recently, numerous scholars have presented intelligent MPPT methods [5–11] for photovoltaic module arrays, both to track MPPs accurately and to improve the dynamic and steady-state tracking performance. However, these methods are applicable only to MPPT in photovoltaic module arrays without shading. Nevertheless, the appearance of multipeak output curves because of partial module shading in photovoltaic module arrays is common. Therefore, the development of an algorithm for accurately tracking the true MPPs of complex and nonlinear output curves is crucial. Reference [12] presented a MPP tracker based on particle

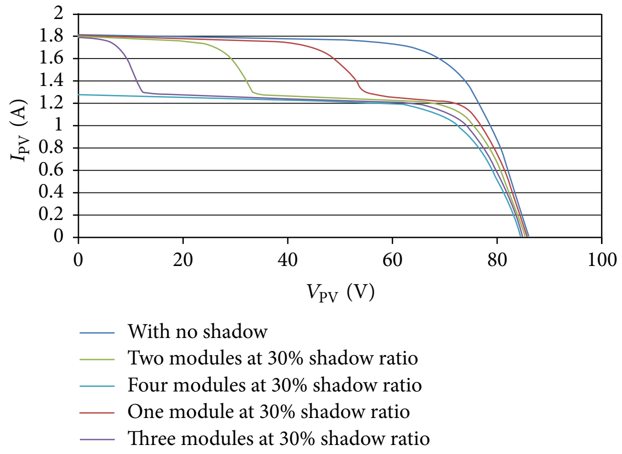

Figure 1: I-V output characteristic curves in the four-series one-parallel module array with varying numbers of modules and shade ratios of 30%, as simulated by Solar Pro software.

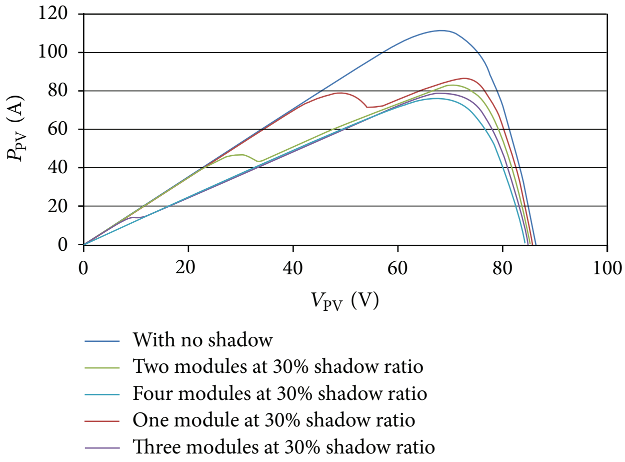

Figure 2: P-V output characteristic curves in the four-series one-parallel module array with varying numbers of modules and shade ratios of 30%, as simulated by Solar Pro software.

swarm optimization (PSO) for photovoltaic module arrays. Although this tracker was capable of tracking global MPPs of multipeak characteristic curves because fixed values were adopted for weighing within the algorithm, the tracking performance lacked robustness, causing low success rates when tracking global MPPs. Even though the MPPs were tracked successfully, the dynamic response speed was low.

Therefore, this study used PSO and added improvements, preventing it from being trapped in local MPPs (i.e., searching only local MPPs) and enabling it to track global MPPs quickly and consistently on the multipeak characteristic curves of photovoltaic module arrays.

2. PV Module Array Characteristic Analysis

Within photovoltaic power generation systems, photovoltaic modules are typically connected to form module arrays using series and parallel methods. When certain modules malfunction or are shaded, their electric current flow is impeded and hot spots occur, damaging the photovoltaic modules. Thus, bypass diodes, through which electric current circulates, are generally installed. This enables the other photovoltaic modules to operate normally. However, when some modules malfunction or are shaded, the output voltage and current of the module arrays decrease, producing multipeak values in the P-V and I-V output characteristic curves.

To find out the output characteristics of series and parallel module arrays when some modules are shaded, a four-series one-parallel photovoltaic module array consisting of HIP 2717 modules produced by Sanyo was investigated. Figures 1 and 2 show the I-V and P-V output characteristic curves of one, two, three, and four modules with 30% shading in the four-series one-parallel module array, simulated using Solar Pro software [13]. The figures show that shading on some modules within the array causes the emergence of multipeak values in the output characteristic curves. In addition, the maximum output power points showed growing declines as the number of shaded modules increased.

3. Particle Swarm Optimization

PSO is an optimization theory presented by Kennedy and Eberhart in 1995 [14]. The theory is an algorithm that uses collective intelligence; it belongs to a branch of evolutionary computation. The two scholars were inspired by the foraging behavior of birds and applied this phenomenon to resolve problems related to search and optimization [15, 16]. Each bird flying in a space is called a particle. All particles moving in the space have fitness values mapped by an objective function and individual velocities, which are used to determine the direction and distance of their movement. Two memory values influence the movement of the particles: P_{best} and G_{best}. Each particle stores the best position it is currently seeking in an individual best memory position (P_{best}). Furthermore, memory intercommunication is present among the particles; the particle swarm compares individual positions to locate the best position and stores this as the swarm best position (G_{best}). The particle swarm uses this method to revise the direction and velocity of its movement continuously, thereby rapidly converging toward a global optimum.

The PSO calculation process is as follows.

(1) Set the number of particles, the maximum number of iterations, the weight, and the learning factors.

(2) Initialize the particle swarm and randomly assign positions and velocities for each particle.

(3) Substitute the initial positions into the objective function to assess the fitness values for each particle.

(4) Compare the fitness values and the individual best memory positions (P_{best}) of each particle to select better positions and update P_{best}.

(5) Compare P_{best} and the swarm best memory value G_{best}. If P_{best} is superior to G_{best}, update G_{best}.

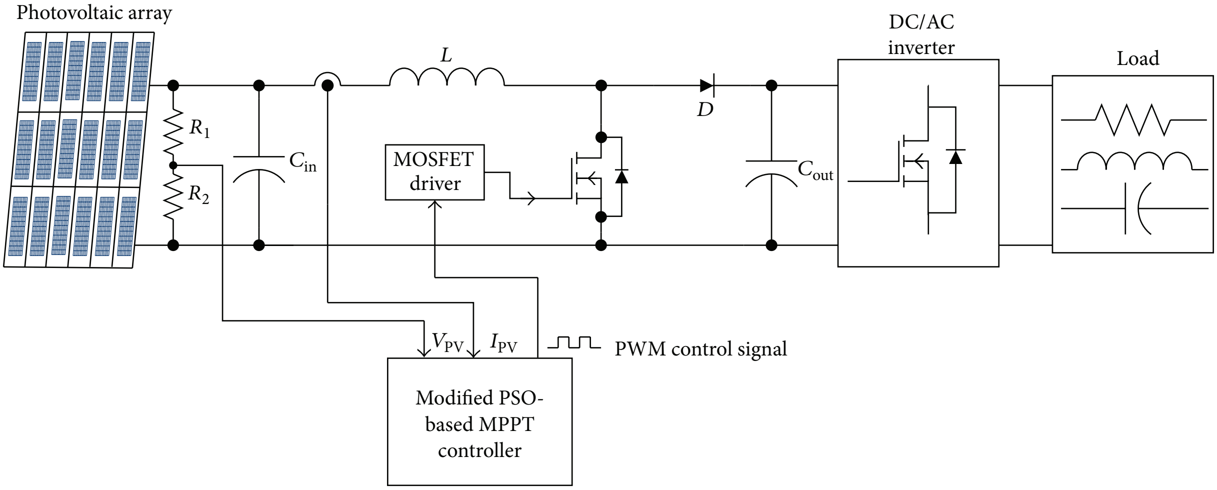

Figure 3: System architecture for modified PSO-based MPPT control.

(6) Use the core PSO formulas to update particle velocities and positions. These formulas are shown as follows:

$$V_i^{j+1} = W \times V_i^j + C_1 \times \text{rand1}(\bullet) \times \left(P_{\text{best}} - P_i^j\right) + C_2 \times \text{rand2}(\bullet) \times \left(G_{\text{best}} - P_i^j\right), \quad (1)$$

$$P_i^{j+1} = V_i^{j+1} + P_i^j. \quad (2)$$

In (1) and (2), V_i^j and P_i^j are the velocity and position of particle i at iteration j, respectively. Variables rand1(•) and rand2(•) are random number generators that generate real numbers between 0 and 1 randomly; these numbers are used to strengthen the variability of the particle swarm. W is the weight; C_1 and C_2 are the learning factors; P_{best_i} is the individual optimum of particle i; and G_{best} is the swarm or global optimum.

(7) Stop tracking if the stop conditions are met. Otherwise, rerun Steps 4 through 6. The stop conditions are either locating the global optimum or reaching the maximum number of iterations.

The search efficiency and success rate of PSO are determined primarily by the values assigned for the weights and the learning factors [17]. When the weight is too high, the particle search might lack accuracy because the movement step sizes are too large. However, if the weight is low, particle movement becomes slow, and the local optimum trap might be unavoidable when facing multipeak values. Thus, weighting is typically based on the objective function.

4. PSO-Based MPPT for PV Systems

Conventional PSO is fast and accurate when searching for the output characteristic curves of PV module arrays with single peak values. However, when some modules are shaded, weights in conventional PSO must be readjusted appropriately based on various multipeak curve characteristics. If this is not performed, excessively high or low weights result in tracking failure. Thus, conventional PSO-based MPPT must be modified when some of the modules in a photovoltaic module array are shaded.

To solve these problems, linear decreases in line with increasing iteration numbers were adopted in this study for the weighting of the PSO kernel formulas. The modified weighting formula is as follows:

$$W = \left(W_{\max} - W_{\min}\right) \times \frac{(n-j)}{n} + W_{\min}, \quad (3)$$

where $W_{\max}$ is the maximum weight, $W_{\min}$ is the minimum weight, n is the maximum number of iterations, and j is the current iteration number.

The physical meaning of this modified weighting formula is that greater step sizes are used to increase the particle search velocity during the initial search because the distance to the global optimum is relatively large. This prevents an excessively small step size from making local optimum traps unavoidable. However, W decreases gradually as the number of iterations increases. Because the particles are now approaching the MPP, these decreases in W cause the steps in the particle movements to shrink, enabling the particles to track the MPP more accurately.

In addition, the output curve of the photovoltaic module array appears only in the first quadrant. Therefore, regions with output power below zero cannot be optimum positions, and the lower limit for particle tracking is set to zero; that is, particles automatically return to zero when tracking regions with values of less than zero. This greatly reduces the time wasted by particles tracking in erroneous regions. The predicate for these conditions is as shown in (4):

$$P_{\text{best}_i} = \begin{cases} P_{\text{best}_i}, & P_{\text{best}_i} > 0, \\ 0, & P_{\text{best}_i} \le 0. \end{cases} \quad (4)$$

The P_{best_i} value obtained in (4) is the solution of (2):

$$P_{\text{best}_i} = P_i^{j+1}. \quad (5)$$

Figure 3 shows the proposed system architecture for modified PSO-based MPPT control. This system contains

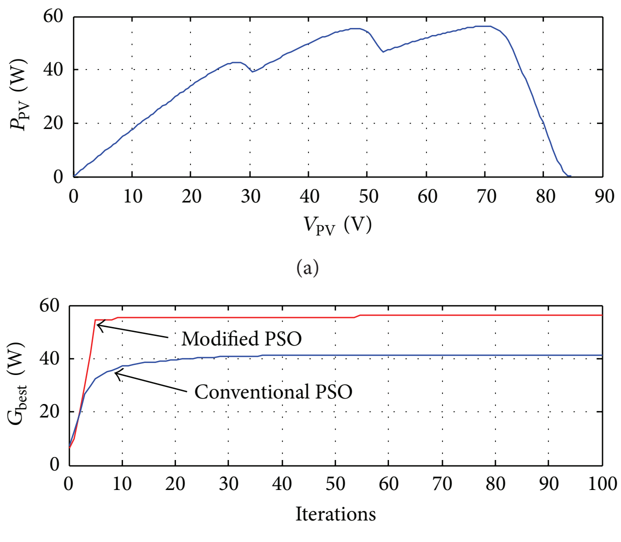

(a)

(b)

Figure 4: Simulation results for a four-series one-parallel module array with one module shaded 30% and one module shaded 55% and(a) P-V characteristic curve. (b) tracking comparison results between the conventional PSO ($W = 0.4$) and modified PSO-based MPPT methods.

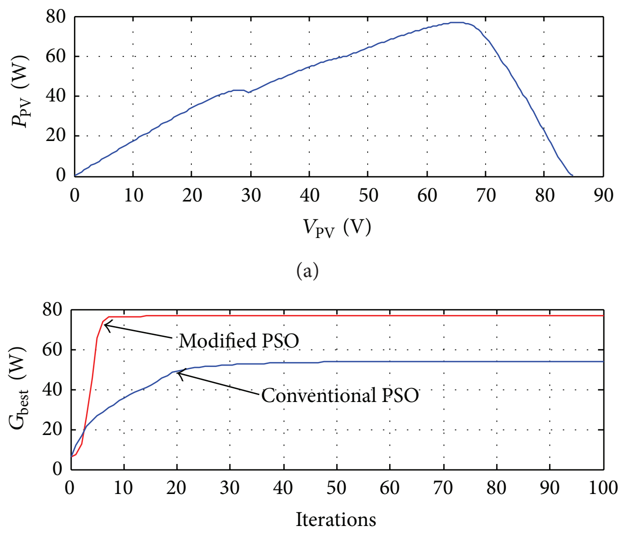

(a)

(b)

Figure 5: Simulation results for a four-series one-parallel module array with one module shaded 25% and one module shaded 30% and (a) P-V characteristic curve. (b) tracking comparison results between the conventional PSO ($W = 0.4$) and modified PSO-based MPPT methods.

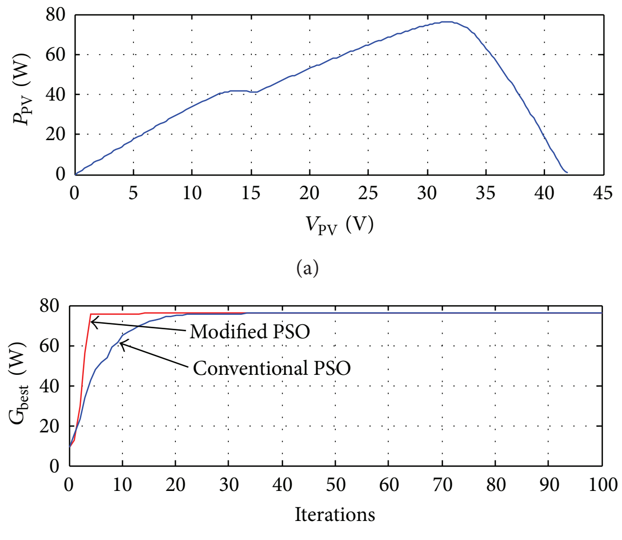

(a)

(b)

Figure 6: Simulation results for a two-series two-parallel module array with one module shaded 25% and one module shaded 30%: (a) P-V characteristic curve; (b) tracking comparison results between the conventional PSO ($W = 0.4$) and modified PSO-based MPPT methods.

two major subsystems: (1) a boost converter and (2) a MPPT controller. The MPPT controller is used to control the duty cycle of the boost converter [18], allowing the photovoltaic module array to output maximum power despite partial shading of some modules.

5. Simulation Results

MATLAB software [19] was used to simulate and compare the application of the conventional and modified PSO-based MPPT control methods to track photovoltaic module arrays in four shading situations. The first test situation involved one module with 30% shading and one module with 55% shading in a four-series one-parallel module array. Figure 4(a) shows this P-V characteristic curve, and Figure 4(b) shows the results of a comparison between the conventional (with a weight of 0.4) and modified PSO-based MPPT methods. The figures indicate that the P-V characteristic curve exhibited three peak values when the two modules in the same series had differing amounts of shade. In this situation, the conventional PSO-based MPPT method could track only local maxima, whereas the modified PSO method could track global MPPs. The modified PSO method also had a faster response speed than the conventional PSO method. In the second test situation, one module was shaded 25% and the other (in another series) was shaded 30% in the four-series one-parallel module array. Figure 5(a) shows the P-V characteristic curve, and Figure 5(b) shows the results of a comparison between the conventional (with a weight of 0.4) and modified PSO-based MPPT methods. Under these working conditions, the P-V characteristic curve had two peaks. The MPPT results in Figure 5(b) indicate that the conventional PSO method tracked the local optimum for the first peak and was unable to avoid the local maximum trap. In contrast, the modified PSO method successfully tracked the global MPP. In the third test situation, one module was shaded 25% and the other was shaded 30% in a two-series two-parallel module array. Figure 6(a) shows the P-V characteristic curve, and Figure 6(b) shows the results of a comparison between the conventional (with a weight of

Table 1: Parameter settings for the two PSO methods.

Methods	Parameter values		
	Weight (W)	Learning factors (c_1, c_2)	Maximum number of iterations
Conventional PSO method	(i) 0.4 with module shading (ii) 0.7 without module shading	(2, 2)	100
Modified PSO method	Linearly decreasing: $W_{\max}$: 0.9; $W_{\min}$: 0.4	(2, 2)	100

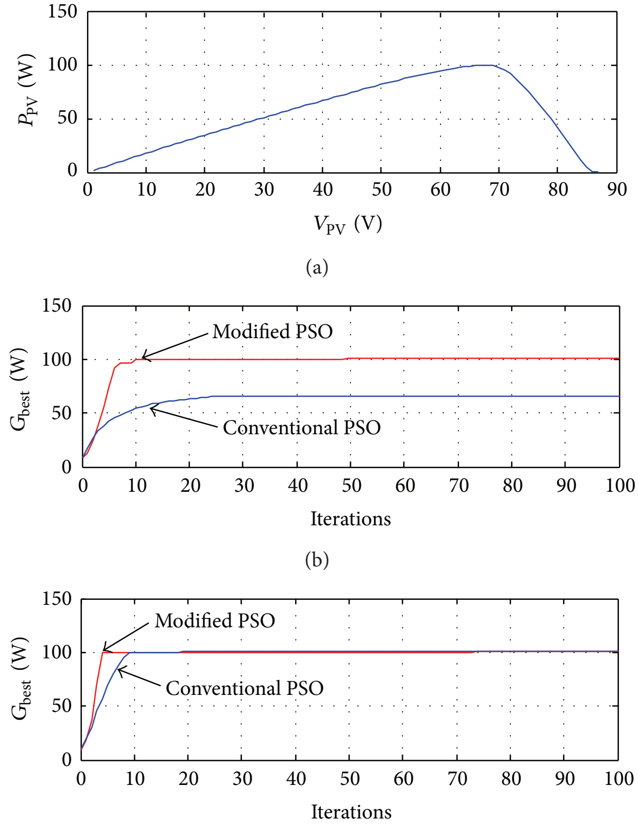

(a)

(b)

(c)

Figure 7: Simulation results for a four-series one-parallel module array without any shading: (a) P-V characteristic curve; (b) tracking comparison results between the conventional PSO ($W = 0.4$) and modified PSO-based MPPT methods; (c) tracking comparison results between the conventional PSO ($W = 0.7$) and modified PSO-based MPPT methods.

0.4) and modified PSO-based MPPT methods. Figure 6(b) indicates that although the conventional PSO method was also able to track the true MPP successfully, its response speed was substantially slower than that of the modified PSO method. The fourth test situation involved a four-series one-parallel module array without any shading. Figure 7(a) shows the P-V characteristic curve, and Figure 7(b) shows the results of a comparison between the conventional (with a weight of 0.4) and modified PSO-based MPPT methods. The figures indicate that the modified PSO method was also able to track the true MPP accurately without the occurrence of multipeak characteristic curves. In contrast, because weighing was maintained at 0.4, the conventional PSO method was unable to track the true MPP. Figure 7(c) shows that both the conventional and the modified PSO methods could track the true MPP when the weighting of conventional PSO method was adjusted to 0.7. However, the modified PSO method still had better response performance in dynamic tracking.

The weight of the conventional PSO method tested in this study was set at 0.4, with which its tracking success rate was the highest when the modules were shaded. Without shading, because output power increased substantially, the weight of the conventional PSO method was reset to 0.7 to increase step size during tracking, thereby allowing the tracking success rate to reach 100%. Linear decreases from 0.9 to 0.4 were used for weighting the modified PSO method in both situations. For both tracking methods, the learning factors C_1 and C_2 were set to a fixed value of 2, and the maximum number of iterations was set to 100. Table 1 shows the detailed parameter settings, and Table 2 shows the comparison results for the success rates of the two methods after 100 tracking attempts. Table 2 indicates that the success rate of the modified PSO method for tracking true MPPs was significantly greater compared to the conventional PSO method regardless of whether, modules were shaded. This is because the modified PSO method employed linearly-adjusted weighting, which enabled it to track true MPPs at a 100% success rate under various shading conditions. In contrast, for the conventional PSO method to reach a 100% success rate regarding single-peak curves and no shading, appropriate weights based on output power were required. Furthermore, tracking using the conventional PSO method frequently became trapped in local MPPs when multipeak characteristic curves appeared.

6. Conclusion

The modified PSO-based MPPT method presented in this study is a novel algorithm based on conventional PSO. The primary feature of this method is the linear decreases used to adjust weighting, in contrast to the fixed weights adopted by conventional PSO. The modified PSO method was applied to maximum power tracking in photovoltaic module arrays, successfully solving the inability to track true MPPs because of partial module shading in photovoltaic module arrays. The tracking success rate reached 100% for the modified method, and the tracking speed was superior to that of conventional PSO. This could reduce energy loss during the MPPT process, thereby substantially enhancing the power generation efficiency of photovoltaic power generation systems.

Table 2: Comparison of the tracking success rates for the conventional and modified PSO methods.

MPPT methods	Module array configuration and shade conditions Four-series one-parallel: one module with 30% shading and one module with 55% shading	Four-series one-parallel: one module with 25% shading and one module with 30% shading	Two-series two-parallel: one module with 25% shading and one module with 30% shading	Four-series one-parallel: no module shading
Conventional PSO method	75/100 attempts*	72/100 attempts	71/100 attempts	(i) With weight set to 0.4: 49/100 attempts (ii) With weight set to 0.7: 100/100 attempts
Modified PSO method	100/100 attempts	100/100 attempts	100/100 attempts	100/100 attempts

*Note: Number of successes/total number of attempts.

Conflict of Interests

The authors of the paper declare that there is no conflict of interest with any of the commercial identities mentioned in the paper.

Acknowledgment

This work was supported by the National Science Council, Taiwan, Republic of China, under the Grant NSC 102-ET-E-167-001-ET.

References

[1] A. Barchowsky, “A comparative study of MPPT methods for distributed photovoltaic generation,” in *Proceedings of the IEEE Innovative Smart Grid Technologies Conference*, pp. 1–7, January 2012.

[2] M. A. S. Masoum, H. Dehbonei, and E. F. Fuchs, “Theoretical and experimental analyses of photovoltaic systems with voltage- and current-based maximum power-point tracking,” *IEEE Transactions on Energy Conversion*, vol. 17, no. 4, pp. 514–522, 2002.

[3] Y. S. Xiong, S. Qian, and J. M. Xu, “Research on constant voltage with incremental conductance MPPT method,” in *Proceedings of the Power and Energy Engineering Conference*, March 2012.

[4] N. Femia, D. Granozio, G. Petrone, G. Spagnuolo, and M. Vitelli, “Predictive and adaptive MPPT perturb and observe method,” *IEEE Transactions on Aerospace and Electronic Systems*, vol. 43, no. 3, pp. 934–950, 2007.

[5] K. H. Chao and Y. H. Lee, “A maximum power point tracker with automatic step size tuning scheme for photovoltaic systems,” *International Journal of Photoenergy*, vol. 2012, Article ID 176341, 10 pages, 2012.

[6] R. Ramaprabha, V. Gothandaraman, K. Kanimozhi, R. Divya, and B. L. Mathur, “Maximum power point tracking using GA-optimized artificial neural network for solar PV system,” in *Proceedings of the 1st International Conference on Electrical Energy Systems (ICEES ’11)*, pp. 264–268, Newport Beach, Calif, USA, January 2011.

[7] A. H. Besheer, “Ant colony system based PI maximum power point tracking for stand alone photovoltaic system,” in *Proceedings of the IEEE International Industrial Technology Conference*, pp. 693–698, March 2012.

[8] M. Adly, “An optimized fuzzy maximum power point tracker for stand alone photovoltaic systems: ant colony approach,” in *Proceedings of the 7th IEEE Industrial Electronics and Applications Conference*, pp. 113–119, July 2012.

[9] K. H. Chao and C. L. Chiu, “Design and implementation of an intelligent maximum power point tracking controller for photovoltaic systems,” *International Review of Electrical Engineering*, vol. 7, no. 2, pp. 3759–3768, 2012.

[10] H. T. Yau and C. U. Wu, “Comparison of extremum-seeking control techniques for maximum power point tracking in photovoltaic systems,” *Energies*, vol. 4, no. 12, pp. 2180–2195, 2011.

[11] H. Zazo, E. del Castillo, J. F. Reynaud, and R. Leyva, “MPPT for photovoltaic modules via newton-like extremum seeking control,” *Energies*, vol. 5, pp. 2653–2666, 2012.

[12] L. R. Chen, C. H. Tsai, Y. L. Lin, and Y. S. Lai, “A biological swarm chasing algorithm for tracking the PV maximum power point,” *IEEE Transactions on Energy Conversion*, vol. 25, no. 2, pp. 484–493, 2010.

[13] K. H. Tang, K. H. Chao, Y. W. Chao, and J. P. Chen, “Design and implementation of a simulator for photovoltaic modules,” *International Journal of Photoenergy*, vol. 2012, Article ID 368931, 6 pages, 2012.

[14] J. Kennedy and R. C. Eberhart, “Particle swarm optimization,” in *Proceedings of the IEEE International Conference on Neural Networks*, vol. 4, pp. 1942–1948, December 1995.

[15] R. C. Eberhart and J. Kennedy, “A new optimizer using particle swarm theory,” in *Proceedings of the 6th International Symposium on Micro Machine and Human Science*, pp. 39–43, October 1995.

[16] D. Srinivasan, W. H. Loo, and R. L. Cheu, “Traffic incident detection using particle swarm optimization,” in *Proceedings of the IEEE Swarm Intelligence Symposium*, pp. 144–151, April 2003.

[17] W. H. Han, P. Yang, H. Ren, and J. Sun, “Comparison study of several kinds of inertia weights for PSO,” in *Proceedings of the 1st IEEE International Conference on Progress in Informatics and Computing (PIC ’10)*, pp. 280–284, Shanghai, China, December 2010.

[18] M. Elshaer, A. Mohamed, and O. Mohammed, “Smart optimal control of DC-DC boost converter in PV systems,” in *Proceedings of the IEEE/PES Transmission and Distribution Conference and Exposition: Latin America (T and D-LA ’10)*, pp. 403–410, Sao Paulo, Brazil, November 2010.

[19] MATLAB Official Website, http://www.mathworks.com/products/matlab/.

Hindawi Publishing Corporation
International Journal of Photoenergy
Volume 2013, Article ID 713791, 8 pages
http://dx.doi.org/10.1155/2013/713791

Research Article

Effect of Subgrains on the Performance of Mono-Like Crystalline Silicon Solar Cells

Su Zhou, Chunlan Zhou, Wenjing Wang, Yehua Tang, Jingwei Chen, Baojun Yan, and Yan Zhao

The Key Laboratory of Solar Thermal Energy and Photovoltaic System, Institute of Electrical Engineering, Chinese Academy of Sciences, Beijing 100190, China

Correspondence should be addressed to Wenjing Wang; wangwj@mail.iee.ac.cn

Received 4 June 2013; Accepted 11 September 2013

Academic Editor: Adel M. Sharaf

The application of Czochralski (Cz) monocrystalline silicon material in solar cells is limited by its high cost and serious light-induced degradation. The use of cast multicrystalline silicon is also hindered by its high dislocation densities and high surface reflectance after texturing. Mono-like crystalline silicon is a promising material because it has the advantages of both mono- and multicrystalline silicon. However, when mono-like wafers are made into cells, the efficiencies of a batch of wafers often fluctuate within a wide range of >1% (absolute). In this work, mono-like wafers are classified by a simple process and fabricated into laser doping selective emitter cells. The effect and mechanism of subgrains on the performance of mono-like crystalline silicon solar cells are studied. The results show that the efficiency of mono-like crystalline silicon solar cells significantly depends on material defects that appear as subgrains on an alkaline textured surface. These subgrains have an almost negligible effect on the optical performance, shunt resistance, and junction recombination but significantly affect the minority carrier diffusion length and quantum efficiency within a long wavelength range. Finally, an average efficiency of 18.2% is achieved on wafers with hardly any subgrain but with a small-grain band.

1. Introduction

Most current industrial solar cells are made of Czochralski (Cz)-grown monocrystalline silicon material and cast multicrystalline silicon substrates [1]. However, Cz monocrystalline silicon material has a high cost and undergoes serious light-induced degradation (LID) of efficiency under sunlight. Defects with very high dislocation densities and high surface reflectance after texturing can limit the application of multicrystalline silicon [2–4]. Mono-like crystalline silicon, which has the advantages of both Cz and multicrystalline silicon, is fabricated using a Cz monoseed layer or by optimized growth nucleation during ingot casting [5, 6]. Recently, these square mono-like crystalline wafers have gained considerable attention because of their low structural defect density, low fabrication cost, and weak LID [7, 8]. Several approaches to improve the quality of mono-like crystalline silicon have been presented [9–11]. However, an important remaining issue is that when mono-like wafers are made into cells, the range of efficiencies of a batch of wafers fluctuates within a wide range of >1% (absolute) [12].

This paper aims to explain the abnormal efficiency fluctuation of mono-like wafers. Mono-like wafers were classified by the subgrain content after alkaline texturing and then fabricated into laser doping selective emitter (LDSE) cells. The optical and electrical performances of these cells were analyzed, and several measurements were performed to estimate the effects of subgrains on solar cells. Finally, semi-mono-like crystalline silicon wafers, which have almost no sub-grain but have a small-grain band, are chosen to prepare LDSE cells to demonstrate the effect of subgrains on cell performance.

2. Experimental

All wafers used in this study were commercial grade, 1 Ω·cm, p-type mono-like crystalline Si wafers with an area of 6 square inches (243.4 cm^2) and thickness of ~200 μm. Wafers

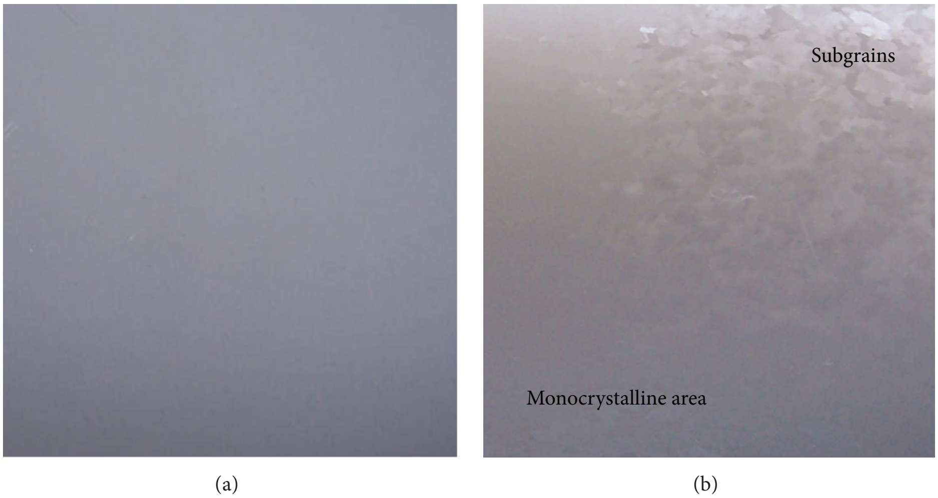

(a) (b)

Figure 1: Optical image of a part of the alkaline textured wafer with sub-grain regions: (a) vertical view and (b) with a tilt angle of 45°.

are typically optically perfect and appear like square Cz monowafers. After texturing in a mixture of 1% NaOH and 4% isopropyl alcohol, some subgrains appeared on some parts of the mono-like wafers, as shown in Figure 1. Figure 1(a) shows an alkaline textured surface like monocrystalline wafer. However, when the image was taken at a tilt angle of 45°, subgrains with an estimated size of 3–7 mm can be observed as shown in Figure 1(b).

According to the content of these subgrains, the wafers were divided into three classes. Wafers with ratios of subgrains area to total wafer area of <10%, ~50%, and >90% on their surface were defined as grades A, B, and C, respectively. All wafers after alkaline texturing were phosphorus diffused to a sheet resistance of 80 Ω/□ with $POCl_3$ liquid source. An industrial wet chemical etching process was then performed to achieve edge junction isolation. A SiN_x antireflection coating (ARC) was deposited onto the front surface of the wafers using an industrial remote plasma-enhanced chemical vapor deposition system. Aluminum (Al) paste was then screen printed on the rear surface of the wafers and fired in a belt furnace at 900°C to form the back surface field of the cells. Diluted phosphoric acid was spin coated on the SiN_x film. A 532 nm Q-switched Nd:YAG laser was used to remove the dielectric layer and pattern laser-doping n+ finger patterns on the *n*-type surface simultaneously. Nickel (Ni) and silver (Ag) were then plated onto the patterned fingers by light-induced plating and sintered to form Ni silicate, which provided low-resistance contact.

The surface reflectance of textured and passivated samples and internal quantum efficiency (IQE) of cells within the range of 300 nm to 1200 nm were measured using a solar cell spectral response/quantum efficiency measurement system (QEX7, PV Measurement). The electroluminescence (EL) images, light beam-induced current (LBIC), and diffusion length of fabricated solar cells were characterized using an infrared defect inspection tool (ELT C02, ASIC) and tabletop PV measurement system (WT-2000, Semilab). A current-voltage (I–V) tester was used to obtain both dark and illuminated I–V curves and to assess the electrical performances of the laser-doped *p*-type mono-like crystalline Si solar cells with different sub-grain amounts.

3. Results and Discussion

3.1. Optical Performances and IQE. Figure 2 shows an experimental comparison of the percentage reflectance of textured and ARC-coated wafers with the IQE of cells with sub-grain and monocrystalline areas within a wavelength range of 300 nm to 1200 nm. The overall reflectance of sub-grain areas is similar to that of monocrystalline areas, except for a slight increase within the short wavelength range of 300 nm to 400 nm. The weighted reflectances of sub-grain and monocrystalline areas after ARC coating are 4.03% and 4.04%, respectively. The similar weighted reflectance means that the subgrains have minimal effect on the light trapping of the pyramid texture. However, as shown in Figure 2, the IQE of cells with sub-grain areas is significantly decreased within the range of 600 nm to 1100 nm wavelength compared with the result of monocrystalline areas. According to the deep penetration of long wavelength light in silicon, the reduction of IQE may be attributed to the recombination in silicon substrate. Thus, the recombination rate is likely to be higher in sub-grain areas than in monocrystalline areas, which decreases the IQE of fabricated cells within the long wavelength range under the same light condition.

3.2. Analysis on Solar Cell Parameters. Table 1 compares various cell parameters fabricated by wafers with different sub-grain contents. For each type of silicon wafer, 10 solar cells were fabricated and measured. With increased sub-grain content from <10% to >90%, the cell efficiency decreases from 17.6% to 16.0%. With increased sub-grain content, the open-circuit voltage (V_{oc}) of the cell decreases from 628.9 mV to 615.9 mV, and the short-circuit current density (J_{sc}) of the cell decreases from 36.87 mA/cm^2 to 34.35 mA/cm^2. The decrease in the efficiency can be attributed to the significant decrements in V_{oc} and J_{sc}.

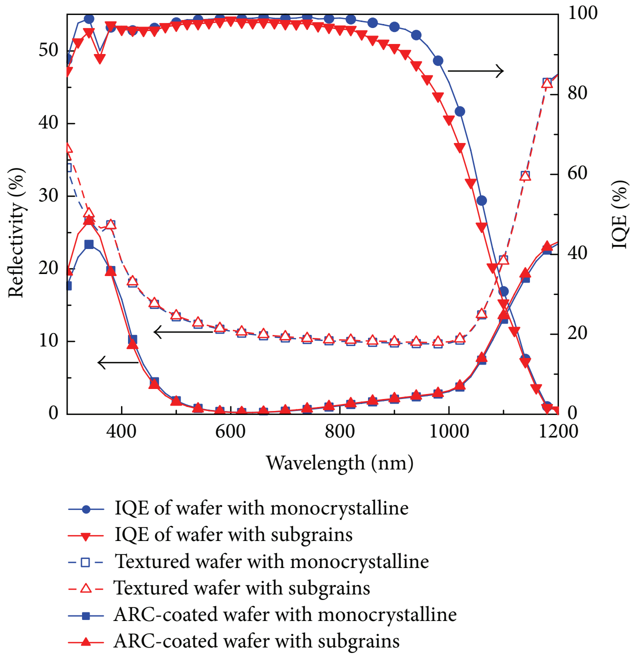

Figure 2: Reflectance of textured and ARC-coated wafers and IQE of cells with subgrains and monocrystalline areas.

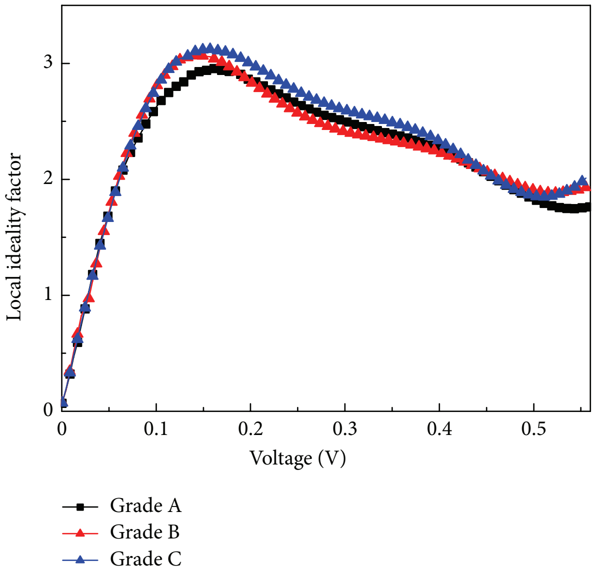

Figure 3: Local ideality factor curves derived from the dark I-V curves of monocrystalline LD solar cells fabricated on different substrates.

The local ideality factor, m, of a solar cell in the dark is given by

$$m = \frac{1}{V_T}\left(\frac{dV}{d\ln(I)}\right), \tag{1}$$

where V and I are the measured dark voltage and current, respectively, and $V_T = 0.026$ eV. The local ideality factors in different voltage regions indicate different mechanisms which may have an effect on cell performance [13, 14]. Figure 3 shows the local ideality factor curves derived from the dark I-V curves of mono-like crystalline laser-doping (LD) solar cells fabricated on different substrates. The local ideality factors of different-grade wafers are similar (>2) around the low-voltage region (<0.4 V), indicating that shunting may have occurred in all these cells. This shunting problem may be caused by insufficient edge isolation. The local ideality factors of different-grade wafers around the medium-voltage region (near the maximum power point) are also similar, indicating that the subgrains hardly affect the formation of localized Schottky contacts. The result shows that the shunting property and metal contact of mono-like crystalline LD solar cells are independent of the subgrains.

Table 1: Average electrical parameters of 10 solar cells fabricated on different substrates.

Grade	V_{oc} (mV)	J_{sc} (mA/cm^2)	FF (%)	Eta (%)
A	628.9 ± 1.2	36.9 ± 0.1	75.8 ± 0.6	17.6 ± 0.2
B	621.6 ± 2.3	35.9 ± 0.2	75.2 ± 0.4	16.8 ± 0.2
C	615.9 ± 3.0	34.4 ± 0.2	75.7 ± 0.6	16.0 ± 0.3

3.3. EL Image. Figure 4 shows the EL images of cells fabricated with different sub-grain contents. With increased sub-grain content, dark line clusters spread from a small part to almost the entire surface. These dark line clusters indicate a low EL intensity which can be caused by series resistance variations or locally enhanced recombination. These dark line clusters are also closely correlated with subgrains observed on the wafer surface. This finding indicates that these subgrains, which can represent material defects such as grain boundaries and dislocations, play an important role in enhancing series resistance or recombination of minority carriers. Grain boundaries and dislocations are known to be easily generated during casting, and the dislocation density increases from bottom to top of the ingots [15, 16]. The dislocation density, especially dislocation clusters correlated with subgrains, has been found to affect the recombination of light-generated minority carriers significantly and thus the solar cell efficiencies of cast multicrystalline silicon [17, 18]. Therefore, dislocations caused by sub-grain formation can be inferred to result in the recombination of minority carriers and the dark line clusters found in the EL images.

3.4. Minority Carrier Diffusion Length. Figure 5 shows various spatial distributions of cells with different sub-grain contents. Red represents the regions with a minority carrier diffusion length (MCDL) of ~130 μm, and black represents those with an MCDL of ~420 μm. Strong local variations in MCDL can be clearly seen in different regions from Figures 5(a) to 5(c). With increased sub-grain content, the diffusion length significantly decreases and the diffusion length distribution changes from uniform to nonuniform. Moreover, these regions of low diffusion length in Figures 5(b) and 5(c) also correspond with subgrains observed on the wafer surface. These reduced diffusion length regions, which indicate locally enhanced recombination, may lead to

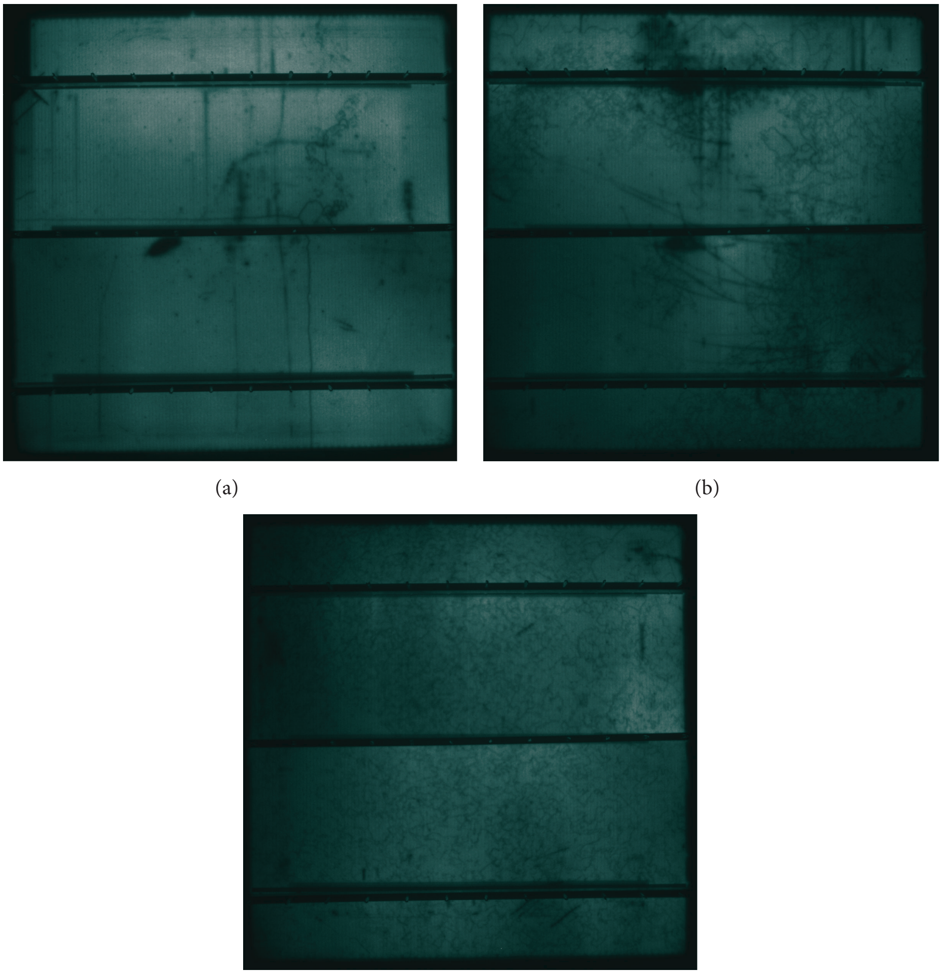

(a)

(b)

(c)

Figure 4: EL images of solar cells fabricated on different substrates: ((a)–(c)) grades A–C, respectively.

decreased V_{oc}. Those longitudinal lines in figures are resulted from fingers of solar cells by blocking the testing laser spot light during the test.

3.5. LBIC Measurement. Further characterizations were performed to determine the influence of subgrains on recombination. The IQE distribution, which was measured by the two-dimensional LBIC method, can represent recombination activity in different regions at different wavelengths of light [19–21]. The IQE distributions measured at 405 and 979 nm are shown in Figures 6 and 7. The uniform and similar IQE distributions of cells with different sub-grain contents in Figure 5 indicate that the locally enhanced recombination caused by subgrains has hardly any effects on the light-induced current at 405 nm. The penetration depth of 405 nm wavelength light is about 500 nm in crystalline silicon. Therefore, the IQE measured at this wavelength indicates the information of emitter and PN junction. The strong field passivation effect caused by the PN junction and the dominating auger recombination caused by the highly doped *n*-type emitter may result in uniform light-induced current and IQE at 405 nm.

However, the result measured at 979 nm shows a significant difference. With increased sub-grain content, the IQE significantly decreases, and the IQE distribution changes from uniform to non-uniform. These non-uniform areas in Figure 7 correspond with sub-grain regions. The penetration depth of 979 nm wavelength light is about 99 μm in crystalline silicon. Therefore, the IQE measured at this wavelength indicates information on the bulk material. The locally enhanced recombination caused by defects and grain boundaries shown as subgrains significantly affects the light-induced current in the bulk silicon.

3.6. Solar Cell Performance of Wafers without Subgrains. To illustrate the effect of subgrains on cell performance, wafers with hardly any sub-grain but with a small-grain band, which means an area with many small grains, were chosen to prepare LDSE cells. Figures 8(a) and 8(b) show optical and EL images of fabricated solar cells, respectively. Hardly any

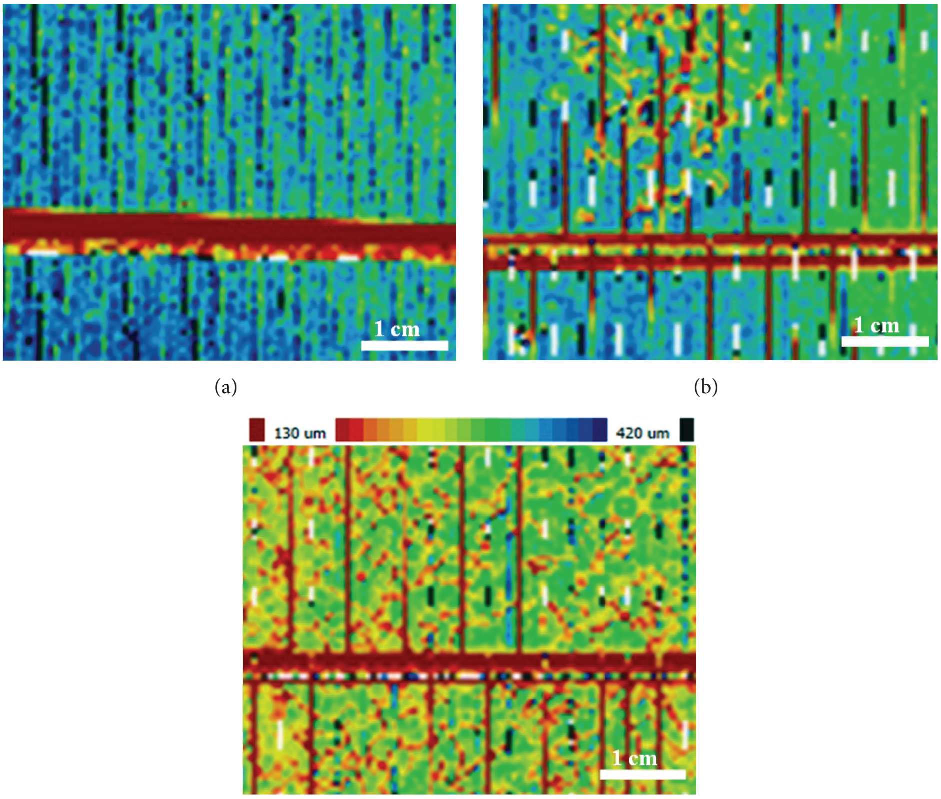

(a) (b)

(c)

Figure 5: Spatial distribution of minority carrier diffusion length of solar cells fabricated on different substrates: ((a)–(c)) grades A–C, respectively.

Table 2: Average electrical parameters of 10 solar cells fabricated on wafers with hardly any sub-grain but with a small-grain band.

V_{oc} (mV)	J_{sc} (mA/cm^2)	FF (%)	Eta (%)
634.1 ± 1.4	37.2 ± 0.1	76.9 ± 0.5	18.2 ± 0.1

dark line clusters can be observed in the EL image. The small straight line dark regions are caused by the slight peeling of grid lines. The average electrical performance results are shown in Table 2. As shown in Figure 8(a), the small-grain band becomes a high-reflectivity area after alkaline texturing, leading to more optical loss. Despite the high reflectivity of the small-grain band, V_{oc} and J_{sc} of cells with a small-grain band are still higher than that of the grade A mono-like cells which have a ratio of subgrains area to total wafer area of <10%. Average V_{oc} increases from 628.9 mV to 634.1 mV, and average J_{sc} increases from 36.9 mA/cm^2 to 37.2 mA/cm^2, respectively. These increments in V_{oc} and J_{sc} indicate that the grain boundaries and defects represented by subgrains have more effects on the electrical performance of mono-like solar cells than high-reflectivity small-grain band.

4. Conclusions

The application of optically perfect mono-like wafers can be challenging because of abnormal efficiency fluctuations. This study showed that cell efficiency decreases with increased sub-grain content. The reflectance of monocrystalline and sub-grain areas after texturing and ARC coating is the same. However, the IQE of cells with sub-grain areas significantly decreases within 600 nm to 1100 nm compared with monocrystalline areas. The local ideality factor result shows that the shunting property and metal contact of mono-like crystalline LD solar cells are independent of subgrains. However, subgrains shown as dark line clusters in the EL image significantly decrease the diffusion length and the IQE at long wavelengths in these regions. This finding indicates that defects caused by subgrains act as the recombination center for minority carriers, degrading the IQE in middle- and long-wavelength range and further affecting the solar cell performance. Finally, an average efficiency of 18.2% was achieved on wafers with hardly any sub-grain but with a small-grain band to indicate that the negative effect of sub-grain on cell performance would be more serious than that of small-grain band. This average efficiency also illustrates the promising application potential of mono-like wafers. It can be inferred that higher efficiency would be obtained on the mono-like wafers without any sub-grain areas and small-grain bands. Thus, defects appeared as subgrains significantly affect cell performance, and dislocations must be eliminated by optimizing the casting process for the industrial application of mono-like crystalline silicon.

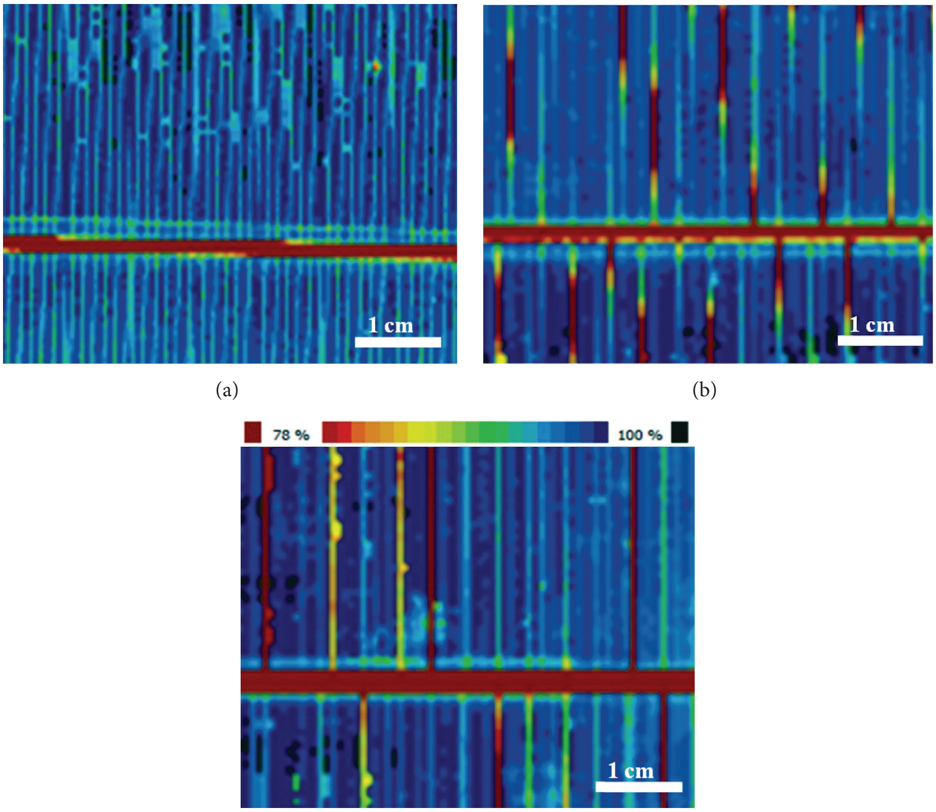

(a) (b)

(c)

Figure 6: IQE distribution of solar cells fabricated on different substrates at 405 nm wavelength: ((a)–(c)) grades A–C, respectively.

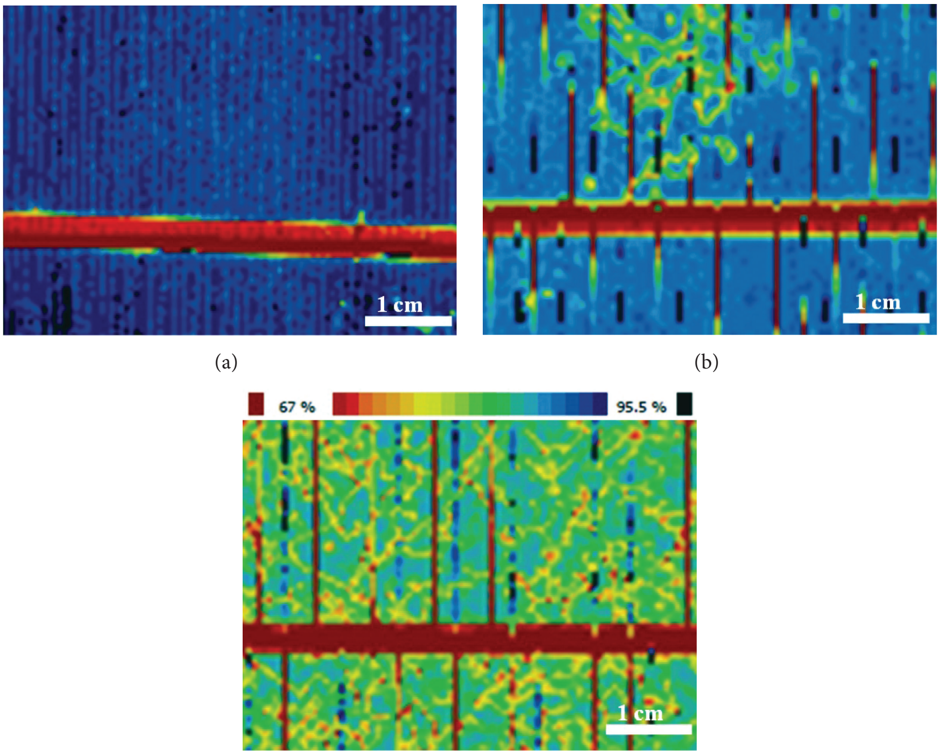

(a) (b)

(c)

Figure 7: IQE distribution of solar cells fabricated on different substrates at 979 nm wavelength: ((a)–(c)) grades A–C, respectively.

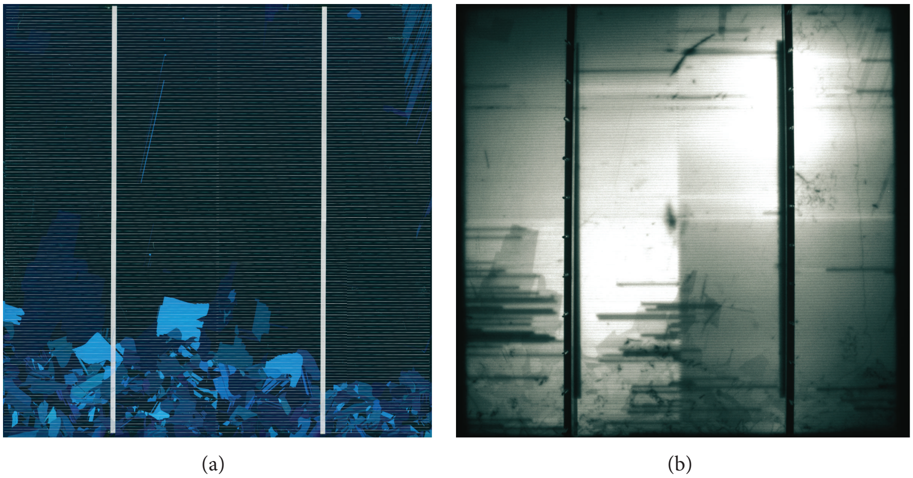
(a) (b)

Figure 8: Optical (a) and EL (b) images of solar cells fabricated on wafers with hardly any sub-grain but with a small-grain band.

Acknowledgments

This work was supported by the National High Technology Research and Development Program of China (Grant no. 2011AA050515) and National Basic Research Program of China (Grant no. 2012CB934204).

References

[1] N. Asim, K. Sopian, S. Ahmadi et al., "A review on the role of materials science in solar cells," *Renewable and Sustainable Energy Reviews*, vol. 16, no. 8, pp. 5834–5847, 2012.

[2] D. Cunningham, A. Parr, J. Posbic, and B. Poulin, "Performance comparison between BP solar mono2 and traditional multicrystalline modules," in *Proceedings of 23rd European Photovoltaic Solar Energy Conference and Exhibition(EUPVEC '08)*, pp. 2829–2833, Valencia, Spain, 2008.

[3] A. Jouini, D. Ponthenier, H. Lignier et al., "Improved multicrystalline silicon ingot crystal quality through seed growth for high efficiency solar cells," *Progress in Photovoltaics: Research and Applications*, vol. 20, no. 6, pp. 735–746, 2012.

[4] K. Nakajima, K. Morishita, R. Murai, and K. Kutsukake, "Growth of high-quality multicrystalline Si ingots using noncontact crucible method," *Journal of Crystal Growth*, vol. 355, no. 1, pp. 38–45, 2012.

[5] N. Stoddard, B. Wu, I. Witting et al., "Casting single crystal silicon: novel defect profiles from BP solar's mono^2 wafers," *Solid State Phenomena*, vol. 131-133, pp. 1–8, 2007.

[6] V. Prajapati, E. Cornagliotti, R. Russell et al., "High efficiency industrial silicon solar cells on silicon Mono2 cast material using dielectric passivation and local BSF," in *Proceeding of 24th European Photovoltaic Solar Energy Conference and Exhibition (EUPVSEC '09)*, pp. 1171–1174, Hamburg, Germany, 2009.

[7] X. Gu, X. Yu, K. Guo, L. Chen, D. Wang, and D. Yang, "Seed-assisted cast quasi-single crystalline silicon for photovoltaic application: towards high efficiency and low cost silicon solar cells," *Solar Energy Materials and Solar Cells*, vol. 101, pp. 95–101, 2012.

[8] Y. Tsuchiya, H. Kusunoki, N. Miyazaki et al., "Correlation between carbon incorporation and defect formation in quasi-single crystalline silicon," in *Proceedings of the 38th IEEE, Photovoltaic Specialists Conference (PVSC '12)*, pp. 000297–000301, 2012.

[9] Q. Yu, L. Liu, W. Ma, G. Zhong, and X. Huang, "Local design of the hot-zone in an industrial seeded directional solidification furnace for quasi-single crystalline silicon ingots," *Journal of Crystal Growth*, vol. 358, pp. 5–11, 2012.

[10] W. Ma, G. Zhong, L. Sun, Q. Yu, X. Huang, and L. Liu, "Influence of an insulation partition on a seeded directional solidification process for quasi-single crystalline silicon ingot for high-efficiency solar cells," *Solar Energy Materials and Solar Cells*, vol. 100, pp. 231–238, 2012.

[11] A. Black, J. Medina, A. Piñeiro, and E. Dieguez, "Optimizing seeded casting of mono-like silicon crystals through numerical simulation," *Journal of Crystal Growth*, vol. 353, no. 1, pp. 12–16, 2012.

[12] D. Hu, T. Zhang, L. He et al., "The characteristics of subgrains in the mono-like silicon crystals grown with directional solidification method," in *Proceedings of the 38th IEEE, Photovoltaic Specialists Conference (PVSC '12)*, pp. 002735–002738, Austin, Tex, USA, 2012.

[13] B. Tjahjono, S. Wang, A. Sugianto et al., "Application of laser doped contact structure on multicrystalline solar cells," in *Processding of 23rd European Photovoltaic Solar Energy Conference*, pp. 1995–2000, Valencia, Spain, 2008.

[14] K. R. McIntosh, Lumps, humps, and bumps, *Three detrimental effects in the current-voltage curve of silicon solar cells [Ph.D. thesis]*, Center of Excellence for Advanced Silicon Photovoltaics and Photonics,University of New South Wales, Sydney, Australia, 2001.

[15] T. Y. Wang, S. L. Hsu, C. C. Fei, K. M. Yei, W. C. Hsu, and C. W. Lan, "Grain control using spot cooling in multi-crystalline silicon crystal growth," *Journal of Crystal Growth*, vol. 311, no. 2, pp. 263–267, 2009.

[16] C. W. Lan, W. C. Lan, T. F. Lee et al., "Grain control in directional solidification of photovoltaic silicon," *Journal of Crystal Growth*, vol. 360, pp. 68–75, 2012.

[17] T. F. Li, K. M. Yeh, W. C. Hsu, and C. W. Lan, "High-quality multi-crystalline silicon (mc-Si) grown by directional solidification using notched crucibles," *Journal of Crystal Growth*, vol. 318, no. 1, pp. 219–223, 2011.

[18] H. Sugimoto, K. Araki, M. Tajima et al., “Photoluminescence analysis of intragrain defects in multicrystalline silicon wafers for solar cells,” *Journal of Applied Physics*, vol. 102, no. 5, Article ID 054506, 2007.

[19] W. Dimassi, L. Derbali, M. Bouaïcha, B. Bessaïs, and H. Ezzaouia, “Two-dimensional LBIC and Internal-Quantum-Efficiency investigations of grooved grain boundaries in multicrystalline silicon solar cells,” *Solar Energy*, vol. 85, no. 2, pp. 350–355, 2011.

[20] W. S. M. Brooks, S. J. C. Irvine, V. Barrioz, and A. J. Clayton, “Laser beam induced current measurements of $Cd_{1-x}Zn_xS/CdTe$ solar cells,” *Solar Energy Materials and Solar Cells*, vol. 101, pp. 26–31, 2012.

[21] S. Litvinenko, L. Ilchenko, A. Kaminski et al., “Investigation of the solar cell emitter quality by LBIC-like image techniques,” *Materials Science and Engineering: B*, vol. 71, no. 1-3, pp. 238–243, 2000.